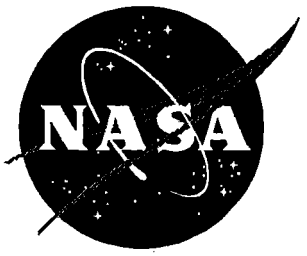

NASA Conference Publication 3336
Part 1

Third International Symposium on Magnetic Suspension Technology

Edited by
Nelson J. Groom and Colin P. Britcher

Proceedings of a symposium sponsored by the
National Aeronautics and Space Administration,
Washington, D.C., and held in
Tallahassee, Florida
December 13–15, 1995

July 1996

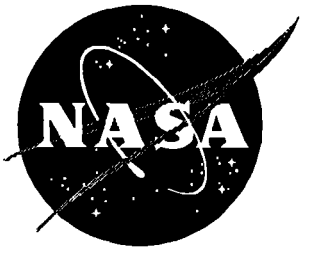

NASA Conference Publication 3336
Part 1

Third International Symposium on Magnetic Suspension Technology

Edited by
Nelson J. Groom
Langley Research Center • Hampton, Virginia

Colin P. Britcher
Old Dominion University • Norfolk, Virginia

Proceedings of a symposium sponsored by the
National Aeronautics and Space Administration,
Washington, D.C., and held in
Tallahassee, Florida
December 13–15, 1995

National Aeronautics and Space Administration
Langley Research Center • Hampton, Virginia 23681-0001

July 1996

INTRODUCTION

The 3rd International Symposium on Magnetic Suspension Technology was held at The Holiday Inn Capital Plaza in Tallahassee, Florida on December 13-15, 1995. The symposium was sponsored by the Guidance and Control Branch of the Langley Research Center in coordination with NASA Headquarters and was hosted by the National High Magnetic Field Laboratory (NHMFL) operated by Florida State University. The symposium was chaired by the following people:

Nelson J. Groom, Symposium Co-Chairman
NASA
Langley Research Center
Hampton, VA 23681-0001

Dr. Jack E. Crow, Symposium Co-Chairman
National High Magnetic Field Laboratory
Tallahassee, FL 32306-4005

Dr. Colin P. Britcher, Technical Program Co-Chairman
Dept. of Aerospace Engineering
Old Dominion University
Norfolk, VA 23529-0247

Dr. Hans Schneider-Muntau, Technical Program Co-Chairman
National High Magnetic Field Laboratory
Tallahassee, FL 32306-4005

Kendall Sherman, Administrative Co-Chairman
NASA
Langley Research Center
Hampton, VA 23681-0001

Sandy Johnson, Administrative Co-Chairman
NASA
Langley Research Center
Hampton, VA 23681-001

Janet Patten, Administrative Co-Chairman
National High Magnetic Field Laboratory
Tallahassee, FL 32306-4005

Merry Ann Johnson, Administrative Co-Chairman
National High Magnetic Field Laboratory
Tallahassee, FL 32306-4005

An international steering committee assisted in selecting and reviewing submitted abstracts and in structuring the symposium sessions. The steering committee consisted of the following people:

Dr. Isaiah Blankson
NASA Headquarters
Code RT
300 E Street SW
Washington, DC 20546-0001
USA

Dr. Karl Boden
KFA-IGV
PF-1913
W-5170 Julich
GERMANY

Dr. James Downer
SatCon Technology Corporation
161 First Street
Cambridge, MA 02142-1207
USA

Dr. Michael J. Goodyer
Department of Aeronautics and Astronautics
University of Southampton
Southampton, S09 5NH
ENGLAND

Dr. Robert A. Kilgore
CES-Hampton
P. O. Box 4006
Hampton, VA 23664-0006
USA

Dr. Alexander V. Kuzin
Microprocessor Systems, Electronics & Electrical Engineering
Moscow Aviation Technological Institute
Petrouka, 27
103737, Moscow, K-31
RUSSIA

Dr. Chin E. Lin
Institute of Aeronautics and Astronautics
National Cheng Kung University
Tainan, Taiwan
REPUBLIC OF CHINA

Dr. John Miller
National High Magnetic Field Laboratory
1800 E. Paul Dirac Drive
Tallahassee, FL 32306-4005

Dr. Hideo Sawada
Aircraft Aerodynamics Division
National Aerospace Laboratory
7-44-1 Jindaiji-higashi-machi
Chofu
Tokyo 182
JAPAN

Dr. Justin Schwartz
National High Magnetic Field Laboratory
1800 E. Paul Dirac Drive
Tallahassee, FL 32306-4005

Dr. Steve Van Sciver
National High Magnetic Field Laboratory
1800 E. Paul Dirac Drive
Tallahassee, FL 32306-4005

Dr. Roland Siegwart
Mecos Traxler AG
Gutstrasse 38
Winterthur S CH-8400
SWITZERLAND

Dr. David Trumper
Department of Electrical Engineering
Massachusetts Institute of Technology
Cambridge, MA 02139
USA

The goal of the symposium was to examine the state of technology of all areas of magnetic suspension and to review recent developments in sensors, controls, superconducting magnet technology, and design/implementation practices. The symposium included 19 sessions in which a total of 55 papers were presented. The technical sessions covered the areas of bearings, superconductivity, vibration isolation, maglev, controls, space applications, general applications, bearing/actuator design, modelling, precision applications, electromagnetic launch & hypersonic maglev, applications of superconductivity, and sensors. A list of attendees begins on page xv.

The first symposium in this series was organized by NASA Langley Research Center and held at Langley Research Center, Hampton, Virginia on August 19-23, 1991. The proceedings of the first symposium are available as NASA Conference Publication 3152, Parts 1 and 2. The second symposium in the series, also organized by NASA Langley Research Center, was held at the Westin Hotel in Seattle, Washington on August 11-13,

Research Center, was held at the Westin Hotel in Seattle, Washington on August 11-13, 1993. The proceedings of the second symposium are available as NASA Conference Publication 3247, Parts 1 and 2.

CONTENTS

SESSION 4--Maglev 1
Chairman: Harry Jones, Oxford University

SESSION 5--Controls 1 – Continued
Chairman: Bibhuti B. Banerjee, Premag Inc.

SESSION 6--Space Applications
Chairman: Nelson J. Groom, NASA Langley

SESSION 7--Superconductivity 2
Chairman: Hans Schneider-Muntau, NHMFL

SESSION 8--Applications 1
Chairman: Steven Van Sciver, NHMFL

*Part 2 is presented under separate cover.

SESSION 12--Precision Applications
Chairman: Karl Boden, KFA-IGV/Hideo Sawada, NAL

SESSION 13--Applications 2
Chairman: Steven Van Sciver, NHMFL

SESSION 14--Maglev 2
Chairman: Tim Lynch, Florida State University

SESSION 18--Modelling 2
Chairman: Gerald Foshage, Honeywell Corporation

SESSION 19--Sensors
Chairman: Colin P. Britcher, Old Dominion University

LIST OF ATTENDEES

Markus Ahrens
Int. Center for Magnetic Bearings
Technopark PFA F16
Pfingstweidstr. 30
Zurich 8005
SWITZERLAND
41-1-445 13 32

Nathaniel G. Albritton
Auburn University
Electrical Engineering Dept.
200 Brown Hall
Auburn University, AL 36849
334-844-1800

Dave L. Alderson
IGC Advanced Superconductors
1875 Thomaston Avenue
Waterbury, CT 06704
203-753-5215

Paul E. Allaire
University of Virginia
Mechanical Engineering Department
Thornton Hall/McCormick Road
Charlottesville, VA 22903-2442
804-924-7421

David E. Andrews
Oxford Superconducting Technology
600 Milik Street
Carteret, NJ 07008
908-541-1300

Bibhuti Banerjee
Precision Magnetic Bearing Systems
36 Green Mountain Drive
Cohoes, NY 12047
518-783-4343

Natale Barletta
EEK
Pfingstweidstr. 30
Technopark E44
Zurich CH-8005
SWITZERLAND
41-1-445 13 81

Clayton C. Bear
Revolve Technologies Inc.
300 207 10th Avenue SW
Calgary, Alberta T2ROB
CANADA
403-232-9262

Martin E. Beck
TRW
1 Space Park R9-2873
Redondo Beach, CA 90278
310-814-8013

Urs Bikle
ETH Institut IEM
ETH Zentrum
ETL G14
Zurich CH 8092
41-1-632-28-17

Mark D. Bird
NHMFL-FSU
1800 E. Paul Dirac Drive
Tallahassee, FL 32306
904-644-7709

Laurence E. Blow
Strategic Insight
1745 Jefferson Davis Hwy #511
Arlington, VA 22202
703-413-0700

Kenneth A. Blumenstock
NASA Goddard Space Flight Center
Code 723.2
Greenbelt, MD 20771
301-286-4268

Karl Boden
Forschungszentrum Juelich
GMBH KFA IGV
PF 1913
Juelich 52425
GERMANY
02461-55712

Hans J. Bornemann
Forschugszentrum Karlsruhe
Postfach 3640
D-76021 Karlsruhe
GERMANY
49-7247-82-4389

Colin P. Britcher
Old Dominion University
Dept. of Aerospace Engineering
Norfolk, VA 23529-0247
804-683-4916

Thomas C. Britton
Lockheed Martin Eng. & Sciences
NASA Langley Research Center
Mail Stop 161
Hampton, VA 23681-0001
804-864-6619

Donato Cardarelli
Milli Sensor Systems & Actuators, Inc.
93 Border Street
West Newton, MA 02165
617-965-1346

David C. Carpenter
Vector Fields, Inc.
1700 N. Farnsworth Ave.
Suite 28
Aurora, IL 60505
708-851-1734

H. Ming Chen
Mohawk Innovative Technology, Inc.
1059 Belridge Road
Niskayuna, NY 12309-4717
518-372-9547

Juan C. Cockburn
FAMU-FSU College of Engineering
Dept. of Electrical Engr.
2525 Pottsdamer Street
Tallahassee, FL 32310-6046
904-487-6462

Howard Coffey
Argonne National Laboratory
Building EES/363
9700 S. Cass Avenue
Argonne, IL 60439

Emmanuel G. Collins
FAMU/FSU
Department of Mechanical Engineering
2525 Pottsdamer Street
Tallahassee, FL 32310-6046
904-487-6373

Thomas C. Cosmus
Intermagnetics General Corporation
450 Old Niskayuna Road
Latham, NY 12110-0461
518-782-1122

David E. Cox
NASA Langley Research Center
Mail Stop 161
Hampton, VA 23681-0001
804-864-8149

Joyanne L. Craft
Rockwell
P. O. Box 21105
Kennedy Space Center, FL 32815
407-799-5507

Michael J. Cronin
Mechanical Technology Inc.
968 Albany-Shaker Road
Latham, NY 12110
518-785-2469

Jack E. Crow
National High Magnetic Field Lab
Florida State University
1800 E. Paul Dirac Dr., B-223
Tallahassee, FL 32306-4005
904-644-0311

Charles R. Dauwalter
Milli Sensor Systems & Actuators Inc.
93 Border Street
West Newton, MA 02165
617-965-1346

Kent R. Davey
American Maglev Technology Inc.
P. O. Box 10
Edgewater, FL 32132
904-427-6643

Daniel A. Davidson
GMSA Systems, Inc.
2730 Kirby Avenue NE #5
Palm Bay, FL 32905
407-728-3800

Peter C. Dent
Everson Electric Company
2000 City Line Road
Bethlehem, PA 18017-2167
610-266-2834

James R. Downer
SatCon Technology Corp.
161 First Street
Cambridge, MA 02142-1207
617-661-0540

George S. Dulikravich
The Pennsylvania State University
Dept. of Aerospace Engineering
233 Hammond Blvd.
University Park, PA 16802
814-863-0134

Horst Ecker
Duke University
Mechanical Engineering
Box 90300
Durham, NC 27708-0300
919-660-5339

Y. M. Eyssa
National High Magnetic Field Lab.
1800 E. Paul Dirac Drive
Tallahassee, FL 32306

Edmund Farino
PMS390T222
c/o NAVSEA
2531 Jefferson Davis Hwy
Arlington, VA 22202
703-602-6255

Roger A. Farrell
Intermagnetics General Corporation
450 Old Niskayuna Road
P. O. Box 461
Latham, NY 12110
518-782-1122

Salah E. Feteih
Florida State University
2525 Pottsdamer Street
Tallahassee, FL 32310
904-487-6164

Gordon Findlay
Tunnel Vac Inc.
3567 W. 117th Street
Cleveland, OH 44111-5270
216-251-3030

Gerald K. Foshage
Honeywell Satellite Systems Div.
19019 North 59th Avenue
Glendale, AZ 85308-9650
602-561-3178

Bruce H. Friedman
Allied Signal, Inc.
Route 46
Mail Stop E/D12
Teterboro, NJ 07608-1173
201-393-3262

Satoru Fukata
Kyushu University 36
Dept. of Energy and Mech. Eng.
6-10-1 Hakozaki, Higashiku
Fukuoka 812-81
JAPAN
81-92-641-1101

James R. Gaines
Superconductive Components Inc.
1145 Chesapeake Ave.
Columbus, OH 43212-2238
614-486-0261

Jameson A. Garrett
Rockwell International Space Sys. Div.
Mail Code AC59
12214 Lakewood Blvd.
Downey, CA 90241-7009
310-922-3432

Nelson J. Groom
NASA Langley Research Center
Mail Stop 161
Hampton, VA 23681-0001
804-864-6613

Cynthia Haffey
Museum of Science & Industry
4801 E. Fowler Avenue
Tampa, FL 33617-2099
813-987-6341

Joseph W. Haney
Rockwell International
12214 Lakewood Blvd.
Mail Stop AA40
Downey, CA 90241-7009
310-922-1057

Mary M. Harman
Cryomagnetics
1006 Alvin Weinberg Drive
Oak Ridge, TN 37830
615-482-9551

Yusuf S. Hascicek
NHMFL
1800 E. Paul Dirac Drive
Tallahassee, FL 32306
904-644-0859

Leo Holland
General Atomics
P. O. Box 85608
San Diego, CA 92186
619-455-3043

Benjamin Joffe
Jet Propulsion Laboratory
4800 Oak Grove Drive
MS 251
Pasadena, CA 91109-8099
818-354-6444

Graham Jones
AVCON
5210 Lewis Road #14
Agoura Hills, CA 91301
818-865-0250

Harry Jones
University of Oxford
Clarendon Laboratory
Oxford OX1 3PU
ENGLAND
44-1865-272326

Patrick S. Keogh
University of Bath
School of Mech. Engineering
Bath BA27AY
UNITED KINGDOM
44 (0) 1225 826826

Jongwon Kim
Seoul National University
Dept. of Mech. Des. & Prod.
San 56-1 Shinlim-Dong, Kwanak-Ku
Seoul, 151-742
KOREA
82-2-880-7181

Ronald W. Kipp
Kingsbury, Inc.
10385 Drummond Road
Philadelphia, PA 19154
215-824-4887

Carl R. Knospe
University of Virginia
Dept. of Mech., Aero., & Nuclear Eng.
Thorton Hall
Charlottesville, VA 22903
804-982-2603

Stewart M. Kohler
Sandia National Laboratories
P. O. Box 5800
Mail Stop 0501
Albuquerque, NM 87185
505-844-0328

Valentine N. Komarov
Scientific Research Institute
for Applied Math. & Cybernetics
10 Uljanov Str.
Nizhny Novgorod 603005
RUSSIA

Anthony S. Kondoleon
The Charles Stark Draper Lab
Mail Stop 23
555 Technology Square
Cambridge, MA 02139-3563
617-258-1537

Ladislav Kucera
Int. Center for Magnetic Bearings
Technopark PFA F16
Pfingstweidstr. 30
Zurich 8005
SWITZERLAND
41 1 445 13 33

Robert Kuklinski
NUWC DIV NPT
Code 8233 Building 1302
Newport, RI 02841
401-841-6034

Alexander V. Kuzin
Moscow Aviation-Technological Inst.
Microprocessor Systems, Electronics
& Electrical Eng., Petrovka, 27
Moskow, K-31 103737
USSR
7-095-313-5551

Bernard Lechable
Aerospatiale Espace et Defense
66 Route de Verneuil BP 2
Les Mureaux 78133
FRANCE
33-1-34 92 32 16

Yyng-Ming Lee
MSE, TA Inc.
P. O. Box 4078
Butte, MT 59701
406-494-7235

Melissa K. Less
846th Test Squadron
1521 Test Track Road
Holloman AFB, NM 88330-7847
505-679-2674

Enrico Levi
Polytechnic University
Six Metrotech Center
333 Jay Street
Brooklyn, NY 11201
718-260-3416

John Liedl
Vector Fields
4917 Water's Edge Drive
Suite 272
Raleigh, NC 27606
919-859-9364
Anders L. Lindskog
SKF Nova AB
Chalmers Teknikpark
Goteborg 41288
SWEDEN
46-31-772-4053

Tim Lynch
Florida State University
1800 E. Paul Dirac Drive
Tallahassee, FL 32306

Ki B. Ma
Texas Center for Superconductivity
University of Houston
3201 Cullen Blvd.
Houston, TX 77204-5932
713-743-8254

Eric H. Maslen
University of Virginia
Mech., Aero., & Nuclear Eng.
Thornton Hall
Charlottesville, VA 22903
804-924-6227

Manabu Matsui
Dept. of Mech. & Envir. Engr.
371-H Cannon Green Dr.
Santa Barbara, CA 93106-5070
805-893-4711

David C. Meeker
University of Virginia
Mech., Aero., & Nuclear Engr.
Thornton Hall
Charlottesville, VA 22903-2442
804-924-3292

Allan D. Miller
MSE, Inc.
P. O. Box 4078
Butte, MT 59702
406-494-7319

John J. Morena
American Maglev Star, Inc.
425 California Ave.
Stuart, FL 34994
407-288-9996

Shin-ichi Moriyama
Kyushu Institute of Technology
Dept. of Control Engineering & Science
Kawazu 680-4
Iizuka, Fukuoka 820
JAPAN
81-948-29-7700

Atsushi Nakajima
National Aerospace Laboratory
7-44-1 Jindaiji-Higashi-machi
Chofu-shi
Tokyo 182
81-422-47-5911 X2548

David R. Noakes
Virginia State University
Physics Department
P. O. Box 9325
Petersburg, VA 23806
804-524-5063

Janet Patten
National High Magnetic Field Lab.
1800 E. Paul Dirac Drive
Tallahassee, FL 32306-4005
904-644-9651

Richard F. Post
Lawrence Livermore National Lab
P. O. Box 808, L-644
7000 East Avenue
Livermore, CA 94551
510-422-9853

Douglas B. Price
NASA Langley Research Center
Mail Stop 161
Hampton, VA 23681-0001
804-864-6605

Ian L. Pykett
Intermagnetics General Corporation
450 Old Niskayuna Road
Latham, NY 12110
518-782-1122

Ronald Rohner
Sulzer Electronics AG
Hegifeldstr. 30
Winterthur SH-8409
SWITZERLAND
41-52-2625284

Dick Rozycki
Lockheed Martin
P. O. Box 179
MS T320
Denver, CO 80201
303-977-1043

Alain Samuel
Aerospatiale Espace et Defense
66 Route de Verneuil BP2
Les Mureaux 78133
FRANCE
33 1 34 92 1825

Michele S. Sapuppo
Milli Sensor Systems & Actuators, Inc.
93 Border Street
West Newton, MA 02165
617-965-1346

Hideo Sawada
National Aerospace Laboratory
7-44-1 Jindaijihigashi-machi
Chofu-shi
Tokyo 182
JAPAN
81-0422-47-5911

Jim C. Schaaf
BDM International
950 Explorer Blvd.
Huntsville, AL 35806
205-922-5159

Harold J. Schmidt
Univ. of Tennessee Space Institute
B. H. Goethart Parkway
Tullahoma, TN 37388
615-393-7422

Hans Schneider-Muntau
National High Magnetic Field Lab.
1800 E. Paul Dirac Drive
Tallahassee, FL 32306-4005
904-644-0863

Venkat Selvamanickam
Intermagnetics General Corp.
450 Old Niskayuna Road
Latham, NY 12110
518-782-1122

Sevankar Sengupta
Superconductive Components Inc.
1145 Chesapeake Ave.
Columbus, OH 43212-2238
614-486-0261

Mark W. Senti
Advanced Magnet Lab, Inc.
425 California Ave.
Palm Bay, FL 34994

Yih R. Sheu
Nan-Tai College
Dept. of Electrical Eng.
No. 1 Nan-Tai Street
Jia-Ding Lane
Taiwan 701
886-06-2741820

Dongwon Shin
Seoul National University
Dept. of Mech. Des. & Prod.
San 56-1 Shinlim-Dong, Kwanak-Ku
Seoul, 151-742
KOREA
82-2-880-7144

John Stekly
Field Effects
Intermagnetic General Corporation
6 Eastern Road
Acton, MA 01720
508-264-4099

Richard E. Stelter
Dexter Magnetic Materials Division
48460 Kato Road
Fremont, CA 94538
510-656-5700, x3050

L. Scott Stephens
Louisiana State University
2508 CEBA
Baton Rouge, LA 70803-6413
504-388-5905

Haga Takahide
Ebara Research Co., Ltd.
2-1 Honfujisawa 4-chome
Fujisaw Kanagawa 251
JAPAN
0466-83-7639

R. Torti
SatCon Technology Corp.
161 First Street
Cambridge, MA 02142-1207
617-349-0875

Dau K. Tran
TRW Space & Defense
One Space Park
Redondo Beach, CA 90278
310-814-8012

David L. Trumper
Massachusetts Institute of Tech.
Room 35-016
77 Massachusetts Avenue
Cambridge, MA 02139
617-253-3481

Wilfred T. Ussery
Ussery & Associates
690 Market Street
Suite 514
San Francisco, CA 94104
415-788-6580

Steve Van Sciver
National High Magnetic Field Lab.
1800 E. Paul Dirac Drive
Tallahassee, FL 32306-4005

Don J. Wade
Hypersonic Maglev Group
1720 Orange Hill Drive
Brandon, FL 33510
813-654-5610

Roy Weinstein
Institute for Beam Particle Dyn.
University of Houston
Room 632 SR1
Houston, TX 77204-5506
713-748-0461

Philip W. Winkler
Government Systems
Air Products & Chemicals Inc.
7201 Hamilton Blvd.
Allentown, PA 18195-1501
610-481-4284

Katsuya Yamashita
Mitsubishi Heavy Industries, Ltd.
Dept. of Mech., Aero., & Nuclear Eng.
Univ. of Virginia, Thornton Hall
Charlottesville, VA 22902
804-924-6234

Kinjiro Yoshida
Kyushu University
Faculty of Engineering
10-1, 6 Chome, Hakozaki, Higashi-ku
Fukuoka 812
JAPAN
092-641-1101 X5307

John Zhang
University of Houston
Dept. of Mechanical Engineering
Houston, TX 77204-4792
713-743-4543

Dawei Zhou
General Superconductor Inc.
1663 Technology Ave.
Alachua, FL 32615
904-462-5977

Ronald B. Zmood
Royal Melbourne Institute of Tech.
124 Latrobe Street
Dept. of Electrical Eng.
Melbourne, Victoria 3000
AUSTRALIA
613-660-2100

PART 1

Session 1 -- Bearings 1

Chairman: David L. Trumper
Massachusetts Institute of Technology (MIT)

MAGNETIC BEARINGS AT DRAPER LABORATORY

Anthony S. Kondoleon
William P. Kelleher
Peter D. Possel

C.S. Draper Laboratory
Cambridge, Ma. 02139

ABSTRACT

Magnetic bearings, unlike traditional mechanical bearings, consist of a series of components mated together to form a stabilized system. The correct design of the actuator and sensor will provide a cost effective device with low power requirements. The proper choice of a control system utilizes the variables necessary to control the system in an efficient manner. The specific application will determine the optimum design of the magnetic bearing system including the touch down bearing. Draper for the past 30 years has been a leader in all these fields. This paper summarizes the results carried out at Draper in the field of magnetic bearing development. A 3-D radial magnetic bearing is detailed in this paper. Data obtained from recently completed projects using this design are included. One project was a high radial load (1000 pound) application. The second was a high speed (35,000 RPM), low loss flywheel application. The development of a low loss axial magnetic bearing is also included in this paper.

INTRODUCTION

The present state-of-the-art magnetic bearings are a result of continuing development. Operational units are emerging for large pipeline and refinery gas compressors where safety, reliability and low maintenance are a high priority. Commercial applications include high speed spindles for precision machining, sealed pumps and compressors for safety and environmental concerns, turbomolecular vacuum pumps for elimination of oil systems and high speed flywheels for energy storage. A large number of prototype systems have been developed to meet these specialized needs. From these applications, many side benefits have been recognized. One such benefit is in equipment monitoring and diagnostics from both on-site and remote locations. Failure prediction and analysis are the by-products. The feedback data from the field equipment has resulted in improved new equipment designs. *A close relationship between equipment maker, magnetic bearing supplier and user is required to develop the full potential of this technology.* The present off-the-shelf magnetic bearing systems are large compared to the mechanical bearings they replace. This has led to their use in equipment where size and weight are not of primary importance. Momentum is building for commercial use, but the high initial cost

has limited magnetic bearings to niches where there is significant cost/benefit improvement. The keys to greatly expanded use of this technology is a reduction in size, weight, power and cost of the total system.

Draper has been developing magnetic suspensions for over 30 years, initially for inertial instrument suspensions and later for other military and space applications. The emphasis in recent years at Draper has been the investigation and proto-typing of active magnetic bearing systems for main shaft support in gas turbine engines. Off-the-shelf magnetic bearings were unsuitable for this application because of their excessive size and weight. Their limitations on operating temperature, speed range and the high power requirements and inefficient and expensive controllers were also a draw back. Draper has addressed all of these issues. *We have made significant advances in digital controllers, reduced the size, weight and power requirements of the actuator and have reduced the eddy current losses in the actuator which limits the rotational speed of the system.* Bearing actuator designs are simple and the control methodologies have been developed and simplified using low cost mass produced electronics. Patent applications have been filed for the actuator designs and the control techniques.

BACKGROUND

Initial work at Draper on magnetic suspensions was applied to floated inertial instruments. The first of these suspensions was an active suspension developed in the early fifties. In 1953 it was discovered that passive suspensions using tuned AC fields were possible and the technology was applied to floated instrument designs. These passive suspensions have been a mainstay in all precision inertial instruments for the last 30 years. In parallel, work has continued at Draper on active magnetic suspensions. In 1975, Draper began to apply this technology to a flywheel energy storage problem (low loss bearings) under a grant from the National Science Foundation (NSF). Since 1975, both analytical and hardware development activities have been continued toward developing actuators and associated controls with emphasis on a total magnetic suspension system.

Five-Axis Active Flywheel Bearing

This project in the mid 1970's resulted in a system which magnetically suspended a twelve pound flywheel at operating speeds to several thousand rpm's. The magnetic bearing system actively controlled five degrees of freedom during operation. The actuators chosen for this system were permanent magnet biased electromagnets. Analog circuitry provided the control.

Electromagnetic Isolator

This 1970's program produced two major results. The first was the understanding of the performance limits of a system based on electromagnetic isolation (e.g., sensors, modeling, actuators, power). The second was to examine actuator performance in a single degree of freedom system. The single degree of freedom system allowed experiments to be run more directly. This system

suspended a ten pound mass using pure electromagnetics. Both analog and digital controls were evaluated.

Flywheel Energy Systems

The CARES project was organized in the early 1980's for the development of a system that simultaneously stored energy in a flywheel and was capable of transferring the associated stored momentum for attitude control. A Lorentz force large angle magnetic suspension (LAMS), motor-generator, power electronics, flywheel, and controls were developed. A hybrid analog/digital controller actively controlled the five degrees of freedom. Draper also conducted extensive work on rotor dynamics on this project. Emphasis on the ability of magnetic bearings to change their dynamic performance in providing forces to the rotor was examined. Benefits from this approach include: suppression of whirl-mode instabilities, reduction of synchronous (mass imbalance) vibrations and eliminating gyroscopic torque couplings.

Slew Actuator-Isolator Development

This 1987 program was to determine the feasibility of using a large angle magnetic suspension system to meet the high torque, low noise requirements for a retarget and slew application. A result from this program was the development of a permanent magnet axial bearing actuator and the demonstration of the torquing and the vibration isolation capabilities of a magnetic bearing system.

Jet Engine Magnetic Bearing Effort

In 1987, a joint effort with MIT's Gas Turbine Laboratory and Draper was formed to investigate the feasibility of using magnetic bearings for main shaft support in gas turbine engines. Included here was an assessment of then state-of-the-art magnetic bearing technology to quantify load carrying capability and maximum operating temperatures.

Magnetic Bearing Test Bed

The objective of this 1988 project was to develop magnetic bearing technology for larger rotating machinery, as a means to control and minimize transmitted vibration. An approach to centralized control design methodology, involving de-coupling algorithms was developed. This Adapted Force Balancing (AFB) algorithm demonstrated significant vibration reduction. A low power radial actuator was developed and constructed with an integrated sensor assembly.

MAGNETIC BEARING SYSTEM

A magnetic bearing is comprised of a number of components when mated together form a suspension system. The major components are the Magnetic Bearing Actuator, the Magnetic Bearing Controller, the Sensor System and the Touchdown Bearing. The difficulty in the design of a total system is the determination of where and when to use magnetic suspensions. Figure 1 shows a graph of rotor speed vs. rotor support weight. The figure shows low speeds and small shaft diameters are an area where mechanical bearings are better suited for support than a magnetic bearing system. As the speeds increase, the load the shaft can support decreases because of the internal loads generated in the

bearings. To increase the load carrying capacity, a larger bearing is required which in turn lowers the speed limit of the shaft. At a point, mechanical bearings become unsuitable. Table I lists area comparisons and the support system suitable for these areas.

ACTUATOR SIZING - FIRST STEP

The basic design equation used to determine the amount of pole area required to magnetically support an object is:

$$\text{Pole Force } (F) = 57 * \text{Pole Area } (A) * B^2 \qquad (1)$$

where F is in pounds, A is in inches and B is in Tesla. If the B in the air gap and the B in the material is the same, then the following equation holds:

$$N * I = B * go / mo \qquad (2)$$

where go is the air gap length (meters), mo = 4p * 10-7 (MKS), N is the number of turns and I is the current (amps). To determine the inductance of a coil, the following holds:

$$L = N^2 \, mo \, A / go \qquad (3)$$

where L is in Henry. The last of the basic equations is

$$V / L = di / dt \qquad (4)$$

where V is in volts and t is in seconds.

These four equations when used together are the first steps in determining the size of a magnetic actuator. These equations also show that while all the equations are independent, when some parameters are chosen, then others become dependent. As an example, if the pole force and the maximum flux density are chosen, then the pole area is calculated (equation 1). For a given air gap and flux density, the required NI is calculated (equation 2). Given a maximum current, the number of turns is determined (equation 2), as well as the inductance of the coil (equation 3). For a maximum voltage, the maximum slew rate of the actuator is calculated (equation 4).

If the above equations were all that were necessary when designing a magnetic actuator, everyone would be doing it. The fact that more is involved can be seen in Figure 2. This figure shows a typical B-H cure for a soft magnetic material. Point P is where B becomes more difficult to obtain from a change in H. How much to the right of P an actuator is designed is one of the main design considerations. If the internal design is not correct, then areas of saturation will occur and the operation of the device will be further to the right of point P than expected. This point will also change depending on the heat treatment of the material. Internal magnetic leakage is also not accounted for with these equations and it can be as high as 20% in some designs.

PARAMETRIC STUDIES

The primary objective to any magnetic bearing design is to produce the maximum force in the minimum volume which will still be controllable over the

entire operational range. In order to accomplish this goal, extensive use of electromagnetic finite element codes are used. While the answers these codes produce are precise for the objects modeled, they do not lend themselves well in the initial design stage. At this initial stage, after the above equations are used, trade-off studies are required which FEM codes do not handle well. By using the traditional approach of a lumped parameter reluctance network, a simple linear model of the magnetic circuit is possible. Figure 3 shows a flux plot of one half of an 8 pole bearing. Figure 4 shows the same plot in cylindrical coordinates. Figure 5 shows the lumped parameter reluctance network for this same model. Using standard field equations, the reluctance values for the resistors can be calculated and the network solved using any standard electronic package. Table II shows a comparison of the results for the FEM and the lumped models. By varying the parameters in the lumped model, optimizing the actuator for maximum force for minimum volume is possible. Refining the linear analysis to include nonlinear effects due to varying parameters is also possible with this technique. The resulting model can then be used as the transfer function for interface with the control system.

DRAPER RADIAL MAGNETIC BEARING ACTUATOR (FOUR POLE-3-D)

Present off-the-shelf radial magnetic bearing actuators use motor-like configurations having two dimensional flux paths with 8 or 12 poles. These designs have two major drawbacks. The first is their high reluctance flux paths which require high input power to the control coils during operation. The second is the large number of poles create high frequency flux cycling in the rotor at rotational speed producing high eddy current loss and heating of the rotor. Both of these conditions limit the rotational speed and efficiency of the suspension system. *Draper has developed and built a radial actuator which produces high force at low power and with low rotational losses at high operating speed.*

Figure 6 shows a magnetic bearing we developed for a 1000 pound static radial load. It is a four pole design with endplates providing a continuous 360 degree return path for the three dimensional flux flow between poles, rotor and end plates. The end plate air gap area is large compared to the main pole area which provides a low reluctance return path for the bias flux. Control coils produce attractive forces at the pole gaps in two perpendicular axes. The reduced pole count, reduces the frequency of rotor currents and biasing the poles at the same magnetic polarity (Homo-Polar) reduces the cyclical flux density peak-to-peak amplitude in the rotating rotor. Both of these conditions reduce eddy current heating. The reduction of eddy currents in the rotor is an increase in efficiency of the bearing.

Magnetic bearings are operated in the biased mode to linearize the control function. This operation is the condition where the pole gaps contain one half the flux density that is required at the maximum operating condition. At no load, with all poles attracting the rotor with equal force, a state of equilibrium exists. Biasing may be achieved by either the use of permanent magnets (PM) in the magnetic

circuit or by current in coils (EM). Each of these methods have advantages. With PM biasing, the no load power requirements will be limited to the power loss due to eddy currents in the magnetic circuit. This is a desired condition where input power is at a premium, applications like space based flywheels or range extender systems. EM biased designs are attractive where the static forces are high or are desired to be adjustable during operation of the actuator.

An inside-out radial magnetic bearing actuator was developed at Draper in 1993 based on a PM biased design. This actuator was to be a part of a range extender flywheel system which was to operate up to 35,000 rpms. Figure 7 shows the rotor and stator components of the actuator. Figure 8 shows a plot of the control current vs. pole force for this design.

AXIAL MAGNETIC BEARING

A double acting axial magnetic bearing actuator was developed in 1993 as part of a range extender flywheel system. The performance goal of the axial bearing was to support a static flywheel weight of 53 Lbs. under dynamic loads of +/-120 Lbs. The design was satisfied with the unique actuator shown in Figure 9. Static load capacity was achieved using a P.M. biased design provided by high energy neodymium iron boron magnets supported by a titanium structure. The low loss actuator design contributed towards an overall high system bandwidth. Figure 10 shows the plot of control current vs. axial force for one of the delivered units.

MAGNETIC BEARING CONTROL SYSTEM

The control system is one of the features which makes the Draper Magnetic Bearing system unique. A computer based fault tolerant system can be constructed about either a Texas Instrument C40 or an Analog Device 21020 processor. The control frequency required for rotor speeds up to 60,000 rpms is 40 to 50 Khz. This assumes a bandwidth of the power amplifiers to be 4 Khz. The control system would be designed to operate in a "centralized" configuration. Past analysis at Draper has shown a magnetic bearing run in a "decentralized" configuration is subject to bandwidth limitations which makes it unacceptable to a moving platform system. Analysis has also shown the "centralized" approach produces a system with significant bandwidth and thereby performance improvements over the "decentralized" approach. One technique used at Draper for control of a magnetic bearing system was with an approach called "Linear Quadratic Regulator with Loop Transfer Recovery (LQG/LTR).

A sub-topic of control was one which dealt with synchronous vibration compensation, referred to as auto balancing. Notch filters are one such technique, but this is bandwidth limited. A Draper patented technique called "Adaptive Force Balancing" effectively compensates for synchronous vibrations over the entire control system bandwidth without producing any de-stabilizing effects. This adaptive algorithm simultaneously tracks and compensates mass

unbalance amplitude, phase and frequency, forcing the rotating shaft to spin about its center of mass rather then the geometric center. This saves enormous amounts of power during high speed operations.

An additional topic in the control system for magnetic bearings is in the use of the suspended mass to damp out vibrations at a remote location. This innovative approach to do active control of tonal vibrations is shown in Figure 11. The information from a remote vibration sensor is supplied to the controller along with tone sensor and tracker information which can be gained from the position sensors in the suspension system. The use of a phase shifter and variable gain algorithm is superimposed on the control amplifiers to vibrate the mass with the magnetic actuators. The phase, frequency and amplitude of the vibration is such, that it cancels out the vibration at the desired remote location. This remote location can be a sensitive piece of instrumentation for sighting or data collection. This approach does not require "a priori" knowledge of the sensor / actuator transfer function. This low bandwidth loop has been demonstrated at Draper. The use of this technique requires no additional hardware to the basic magnetic suspension system, but only some additional code to the control system.

In applications where high reliability is essential, such as an aircraft engines, fault tolerant controllers are necessary. Draper has been a leader in this field for over twenty years. In 1990 a prototype single board fault tolerant controller, based on Transputer Technology was designed and built.

TOUCHDOWN BEARINGS

Draper has been a leader in the design and development of precision bearing assemblies since the 1950's. This includes ball bearings, gas bearings and journal bearings. At this time, over one million space based hours have been accumulated on Draper built ball bearing assemblies without a failure. Hemispherical gas bearings assemblies designed and built by Draper into precision inertial instruments have an estimated MBTF of over 250,000 hours. A Draper designed journal bearing is contained in a pump 2 inches long by two inches in diameter which runs at 20,000 rpm's and produces 90 watts of hydraulic power. Draper has developed machining techniques and technologies which enable the wide spread use of ceramics to be utilized in precision roller bearing designs. The development of a touchdown bearing comprised of a ceramic material with a dry lubricant base has been researched at Draper.

The technology used for a touchdown bearing is dependent on the application. If fluid is present, a journal bearing may be the most cost effective approach. If vapors are present, then a gas bearing may be the design of choice. If these options are not practical then a roller element bearing would be necessary. Draper has and continues to maintain the expertise in all these fields to properly design and manufacture an optimum touchdown bearing for most applications.

CONCLUSIONS

To produce a cost effective magnetic bearing requires a full systems approach to the problem. Having just the actuator on hand will not provide a magnetic bearing. The mating of the magnetic actuator technology with control techniques and touchdown bearing designs will produce the desired effect of having a cost effective long life, low power magnetic bearing. Other important issues for the successful application of magnetic bearings include power drive systems, digital control computers and sensors which are light weight, fault tolerant and compact. Draper has been and continues to be a leader in the pioneering fault tolerant systems. Draper has the unique ability to apply these critical technologies to the design and development of magnetic bearings.

References

Beal, S., May 1991, Ph.D thesis, Northeastern University, "Directions on the Application of Modern Control Theory for Flexible Rotor-shaft Dynamics via Electromagnetic Bearings"

Johnson, B., September 1986, PhD thesis, MIT, "Active Control of a Flexible Two Mass Rotor"

LaRocca, P., May 1988, SM thesis, "A Multivariable Controller for an Electromagnetic Bearing-shaft System"

McCallum, D., May 1988, SM thesis, MIT, "Dynamic Modeling and Control of a Magnetic Bearing Suspended Rotor System"

G. Oberbeck, MIT Press 1974, Magnetic and Electric Suspensions

Sacoman, T., May 1991, SM thesis, MIT, "Characterization of High Speed Magnetic Bearings"

Silverman, B., May 1989, SM thesis, MIT, "Validation of Finite Element Solution for Timoshenko Rotors with Disk"

Table I
Rotor Support System Trade-off

GROUND BASE SYSTEMS	VEHICLE BASE SYSTEMS	SPACE BASED SYSTEMS
Medium Production Volume	High Production Volume	Low Production Volume
Large Supported Mass	Small to Medium Mass	Small to Medium Mass
Low Env. Input	Large Env. Input	Large at Launch Small During Mission
Size Secondary	Size & Power Prime	Size & Power Prime
Magnetic Suspension System of Choice	Mechanical Suspension System of Choice	Magnetic Vs Mechanical Suspension Trade-off: Power, Speed, Size, Life

Table II
Comparison of FEM & Lumped Parameter Model

B in Gap	Lumped Parameter Model	Finite Element Model
Pole 1	1.71	1.74
Pole 2	.51	.55
Pole 3	.08	.10

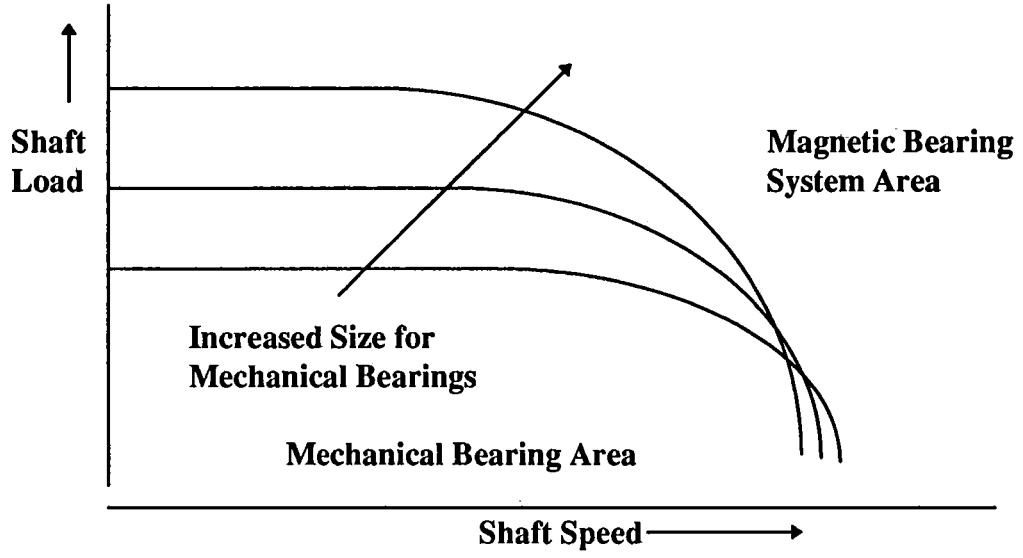

FIGURE 1

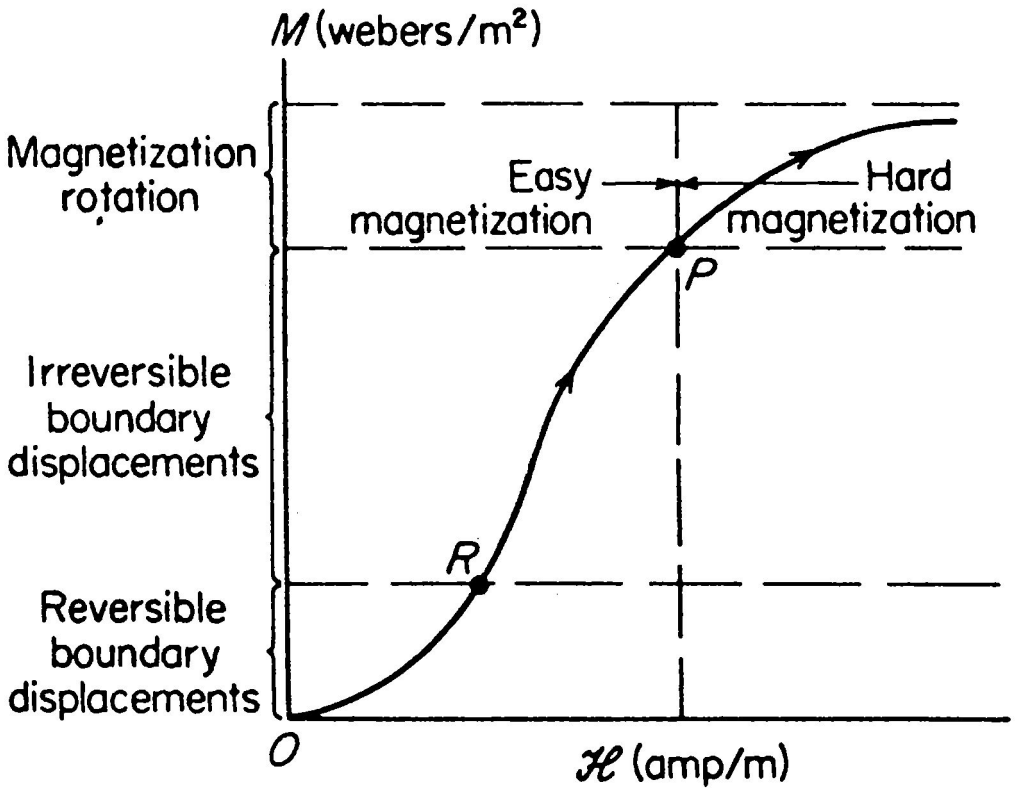

FIGURE 2

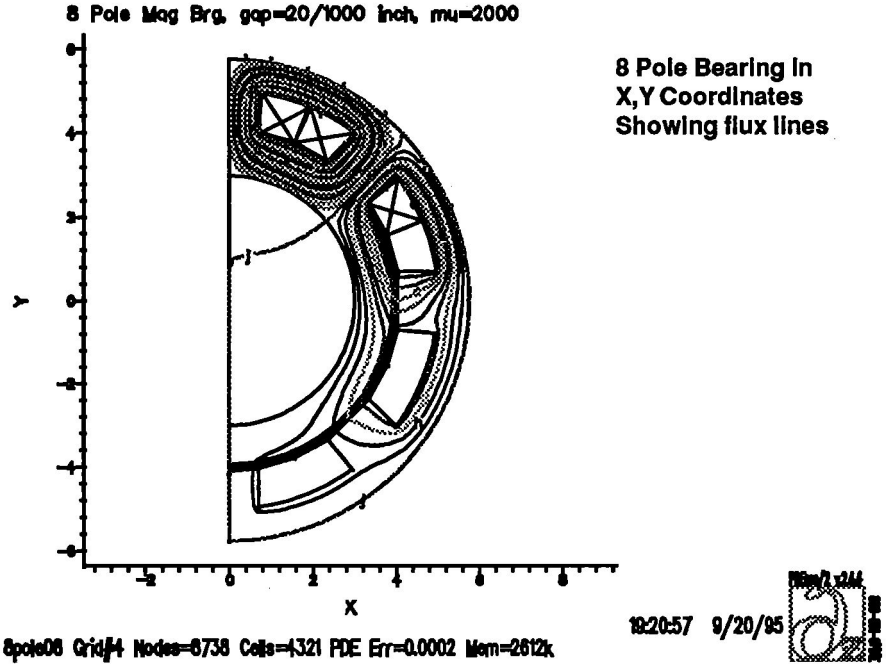

FIGURE 3

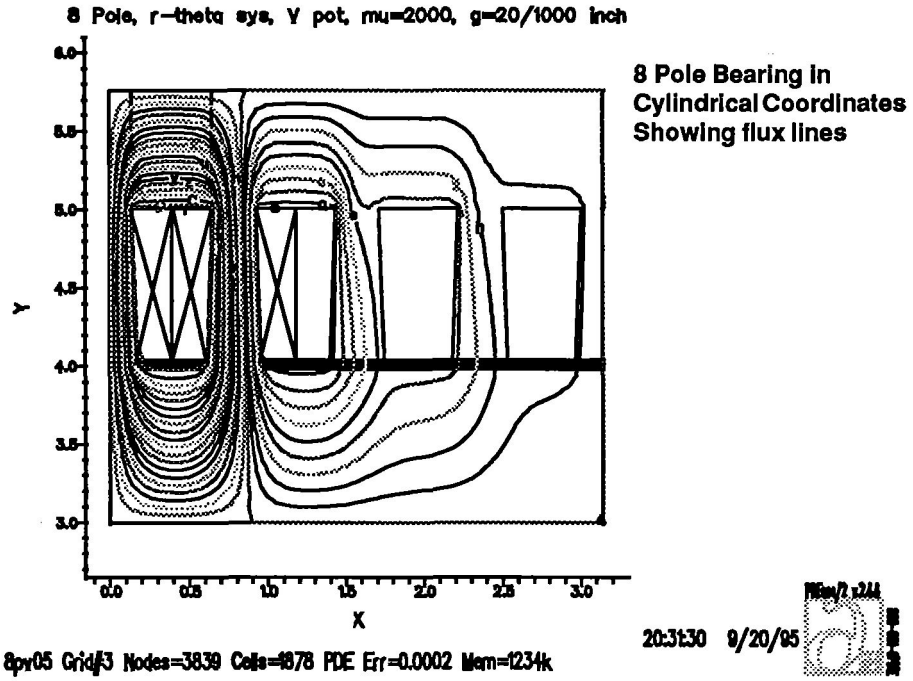

FIGURE 4

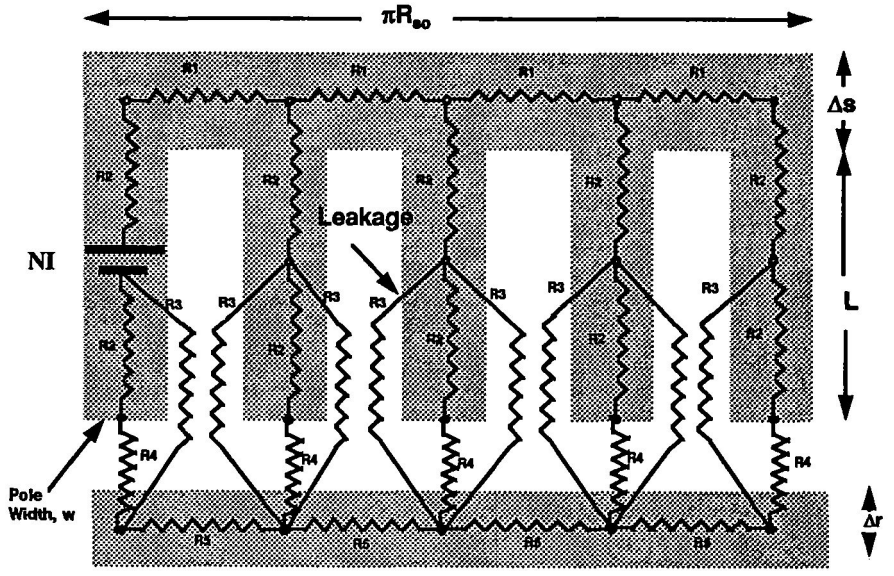

Δs=.75" L=1" Δr=1" W=1.4" R_{so}=5.75" μ_r=2000 μ_o=4πe-7

FIGURE 5

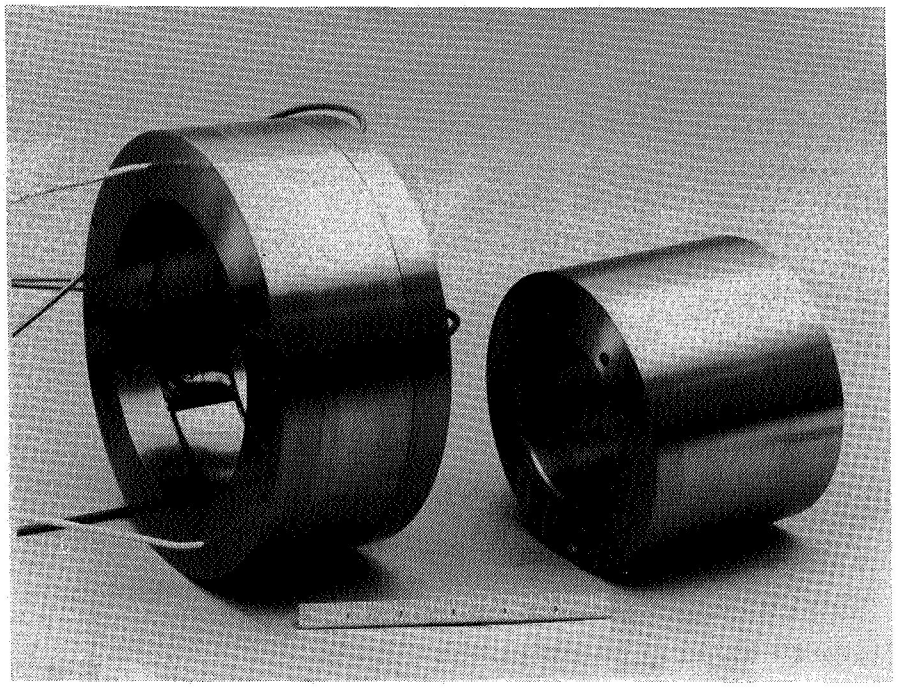

FIGURE 6

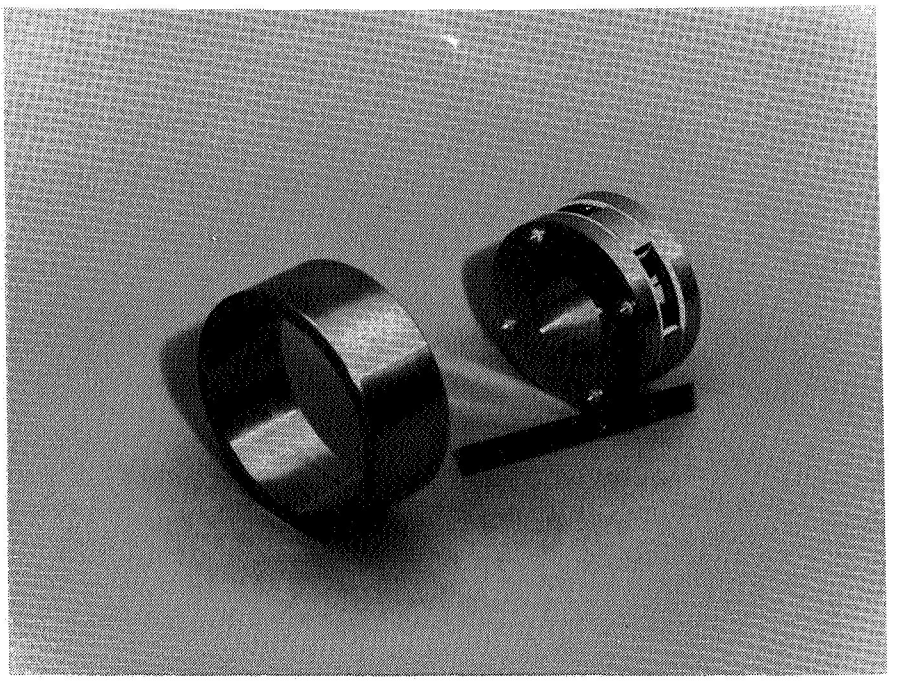

FIGURE 7

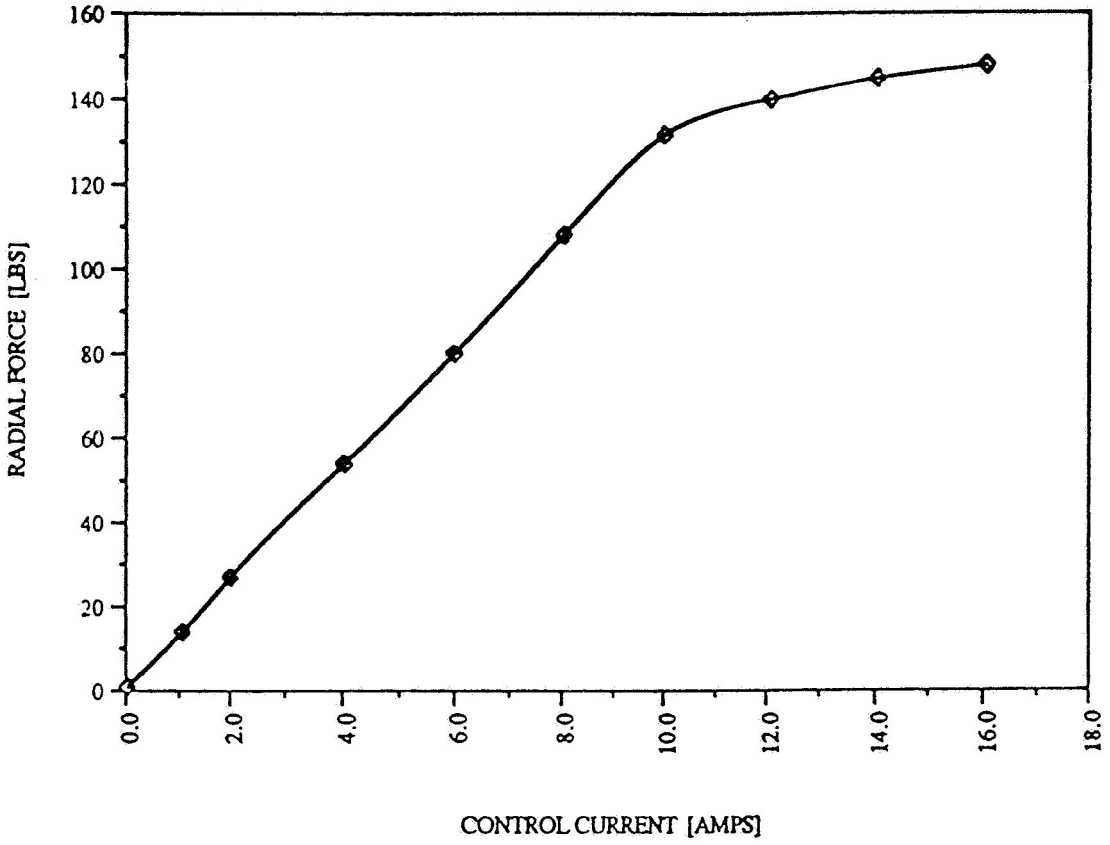

FIGURE 8

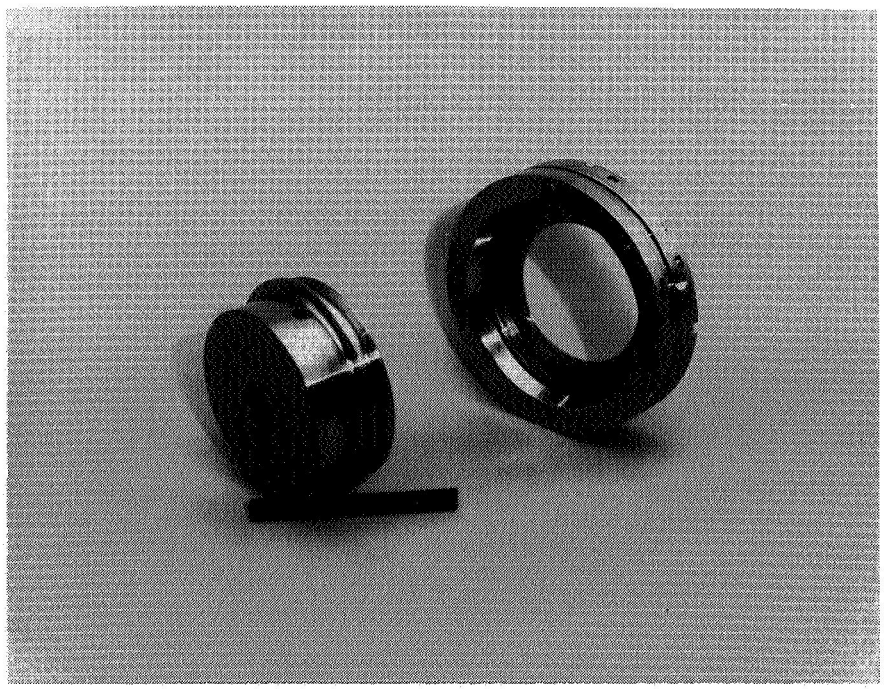

FIGURE 9

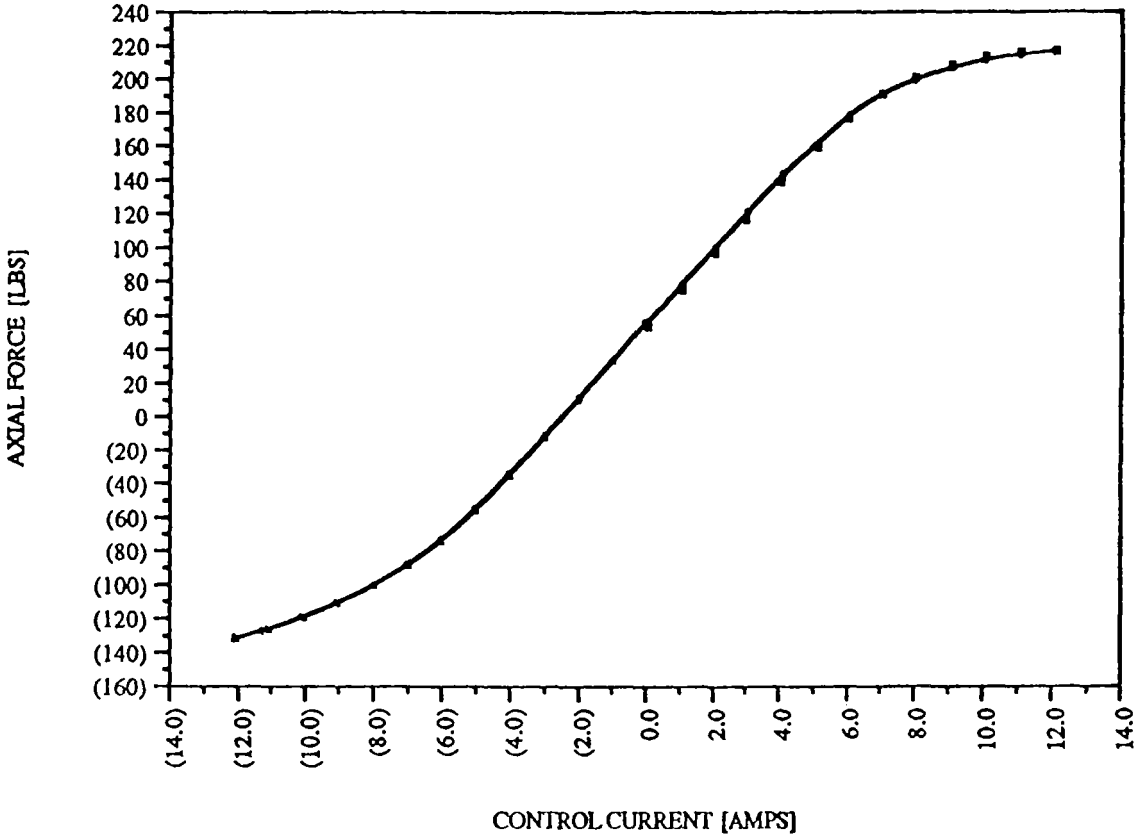
AXIAL FORCE [LBS]
240
220
200
180
160
140
120
100
80
60
40
20
0
(20)
(40)
(60)
(80)
(100)
(120)
(140)
(160)
(14.0)
(12.0)
(10.0)
(8.0)
(6.0)
(4.0)
(2.0)
0.0
2.0
4.0
6.0
8.0
10.0
12.0
14.0
CONTROL CURRENT [AMPS]

FIGURE 10

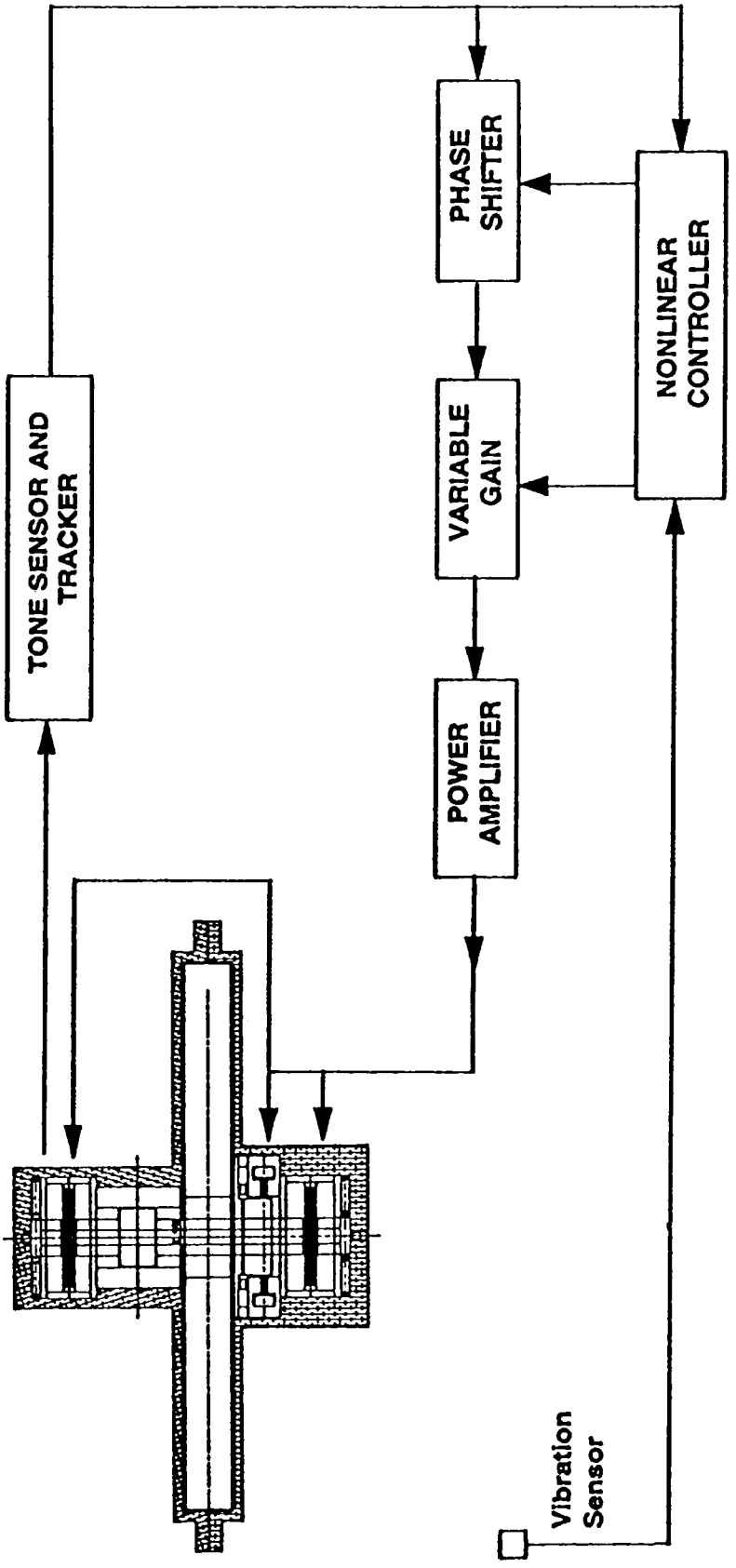
TONE SENSOR AND TRACKER
PHASE SHIFTER
VARIABLE GAIN
POWER AMPLIFIER
NONLINEAR CONTROLLER
Vibration Sensor

FIGURE 11

THE AVOIDANCE OF SATURATION LIMITS IN MAGNETIC BEARING SYSTEMS DURING TRANSIENT EXCITATION*

Neil K. Rutland, Patrick S. Keogh and Clifford R. Burrows
School of Mechanical Engineering
University of Bath
Bath BA2 7AY, UK

SUMMARY

When a transient event, such as mass loss, occurs in a rotor/magnetic bearing system, optimal vibration control forces may exceed bearing capabilities. This will be inevitable when the mass loss is sufficiently large and a conditionally unstable dynamic system could result if the bearing characteristics become non-linear. This paper provides a controller design procedure to suppress, where possible, bearing force demands below saturation levels whilst maintaining vibration control. It utilizes H_∞ optimisation with appropriate input and output weightings. Simulation of transient behaviour following mass loss from a flexible rotor is used to demonstrate the avoidance of conditional instability. A compromise between transient control force and vibration levels was achieved.

INTRODUCTION

Magnetic bearings are being used in increasing numbers in rotating machinery applications, both for the support of static loads and for the control of rotor vibration. However, the advantages of negligible frictional heating and wear are offset against the disadvantage of reduced load carrying capacity when compared with conventional bearings. Also, most applications are limited to relatively small rotors that are rigid in the sense that the rotational speed remains below the first rotor bending mode frequency.

Maximum force characteristics of a magnetic bearing are constrained by material saturation limits.

* **Work done under EPSRC Grant GR/J15575**

When such a bearing forms a component in an active rotor dynamic system, the associated controller is invariably designed on the assumption that the system behaves in a linear manner. Also, most industrial implementations configure magnetic bearings to act as decentralised springs and viscous dampers. Nonetheless, significant research progress has been made towards improved controller designs. An open loop technique for the control of steady synchronous vibration is now well established (ref. 1). The feedforward concept has been developed further (refs 2, 3) and applied to a turbo expander. Interest in the dynamic behaviour of synchronous vibration amplitudes has led to the control of transient rotor vibration through relatively slow acting closed loop controllers that utilise open loop influence coefficients (refs 4-8). Recent research published in the open literature has been directed towards the development of higher order centralised state space controllers (refs 9, 10). However, the non-linear influences of bearing saturation on controller design have received only limited attention.

During a rotor mass loss event, the following situations may arise during the transient rotor vibration response:

(a) The rotor dynamic system remains linear, without magnetic bearing saturation.
(b) The rotor dynamic system becomes non-linear, without magnetic bearing saturation.
(c) The magnetic bearing saturates with no possibility of the system returning to a linear steady state.
(d) The magnetic bearing saturates, though the system may have a linearly stable steady state.

For example, in case (c), the mass loss may be so large that the magnetic bearing cannot deliver sufficient control force and contact is made with emergency bearings. In cases (b) and (d), the controller design is important. A deficient controller for case (d) could result in a long period of saturation or even an unacceptable limit cycle response. Alternatively, a well designed controller would limit the transient saturation period. The proposition of the present paper is that the saturation time may be eliminated so that the controller ensures that case (d) is avoided completely.

NOMENCLATURE

A	system matrix
B_f , B_u	disturbance force, control force distribution matrices
c_d	derivative feedback gain
C_e , C_y , C_z , C_{zq}	coefficient matrices
$\boldsymbol{e}$, $\boldsymbol{e}_1$	control variable vectors
E_f , E_u	disturbance force, control force distribution matrices
$\boldsymbol{f}(t)$, $\boldsymbol{F}(s)$	vector of rotor external disturbance forces (time, Laplace domain)
$H(s)$	vibration controller transfer function matrix
$\boldsymbol{i}_c$	vector of magnetic bearing control currents
J	rotor gyroscopic matrix
k_p	proportional feedback gain
K	rotor stiffness matrix
k_i , k_z	magnetic bearing current, displacement coefficients
$\boldsymbol{m}^+$, $\boldsymbol{m}^-$	mass-eccentricity vectors
M	rotor mass matrix
$\boldsymbol{n}(t)$, $\boldsymbol{N}(s)$	vector of measurement errors (time, Laplace domain)
$\boldsymbol{q}$	vector of rotor lateral displacements and angular deflections
s	Laplace transform variable
t	time
T_{ef}, T_{uf}, T_{en}, T_{un}	closed loop transfer function matrices
$\boldsymbol{u}(t)$, $\boldsymbol{U}(s)$	control force vector (time, Laplace domain)
W_e, W_f, W_n, W_u	weighting function matrices
$\boldsymbol{x}$	state vector ($\boldsymbol{x} = [\boldsymbol{q}^T, \dot{\boldsymbol{q}}^T]^T$)
$\boldsymbol{y}(t)$, $\boldsymbol{Y}(s)$	vector of rotor displacements at transducer locations (time, Laplace domain)
$\boldsymbol{z}(t)$, $\boldsymbol{Z}(s)$	vector of rotor lateral displacements at magnetic bearings (time, Laplace domain)
τ	time constant
ω	frequency
Ω	rotational speed

SYSTEM DYNAMIC BEHAVIOUR

A project is being undertaken at the University of Bath to investigate vibration controller designs for flexible rotor systems. A rig has been constructed and the schematic form is shown in figure 1. It consists of a flexible rotor mounted on two magnetic bearings. The rotor was designed to have a mass of 100 kg with first and second rotor bending modes at around 26 Hz and 66 Hz respectively. A finite element rotor model leads to a discretized linear rotor dynamic system equation having the form

$$M\ddot{\boldsymbol{q}} + \Omega J\dot{\boldsymbol{q}} + K\boldsymbol{q} = E_f\boldsymbol{f} + E_u\boldsymbol{u} \tag{1}$$

Each magnetic bearing consists of two opposing pole pairs arranged at 45° to the vertical. The coils are powered by current amplifiers and, assuming a linear relation, the bearing control forces on the rotor are given by

$$\boldsymbol{u} = k_i\boldsymbol{i}_c + k_z\boldsymbol{z} \tag{2}$$

where

$$\boldsymbol{z} = C_{zq}\boldsymbol{q} \tag{3}$$

It follows that the system behaviour is governed by

$$M\ddot{\boldsymbol{q}} + \Omega J\dot{\boldsymbol{q}} + (K - E_u k_z C_{zq})\boldsymbol{q} = E_f\boldsymbol{f} + E_u k_i\boldsymbol{i}_c \tag{4}$$

For control design purposes, equation (4) is converted to the first order state space form

$$\begin{aligned} \dot{\boldsymbol{x}} &= A\boldsymbol{x} + B_f\boldsymbol{f} + B_u\boldsymbol{u} \\ \boldsymbol{y} = C_y\boldsymbol{x} \quad , \quad \boldsymbol{z} &= C_z\boldsymbol{x} \quad , \quad \boldsymbol{e} = C_e\boldsymbol{x} \end{aligned} \tag{5}$$

Here, $\boldsymbol{y}$ is a vector of lateral displacements of the rotor at the outer disks and magnetic bearings, corresponding to displacement transducer locations. The magnetic bearing force components $\boldsymbol{u}$ are to be used for levitation and vibration control. In order that the vibration control performance can be defined, the vector $\boldsymbol{e}$ is chosen to consist of variables that are to be minimised. In the Laplace transform domain the magnetic bearing forces are written as

$$\boldsymbol{U}(s) = H(s)\boldsymbol{Y}(s) - (-k_z + k_p + sc_d/(1+\tau s))\boldsymbol{Z}(s) \qquad (6)$$

where the levitation components consist of a practical implementation of proportional and derivative control.

A block diagram of the rotor/magnetic bearing system is shown in figure 2, which includes measurement noise and a reference position vector for the rotor at the bearings. Bearing saturation is also incorporated in figure 2 with the simple limiter on $\boldsymbol{u}$. It is now evident that, although the linear system may be stable, the non-linear system may only be conditionally stable. For example, mass loss from the rotor can be represented by a step change in the unbalance condition by

$$\boldsymbol{f}(t) = \begin{cases} \mathbf{0} & , \quad t \le 0 \\ \Omega^2 \boldsymbol{m}^+ e^{i\Omega t} + \Omega^2 \boldsymbol{m}^- e^{-i\Omega t} & , \quad t > 0 \end{cases} \qquad (7)$$

If the level of mass loss, represented by a norm of $\boldsymbol{m}^+$, is sufficiently small, the saturation limits will not be reached. Otherwise, an amplitude dependent response is likely and it is in this case that the vibration controller $H(s)$ can be used to influence the region of linear behaviour.

The system dynamic characteristics without vibration control ($H(s) = 0$) are evident from the steady synchronous unbalance responses of figure 3. The system unbalance corresponded to a nominal 10 g mass on the outer rim of the non-driven end disk with low/high values of the derivative gain. In figure 3(a), rigid body modes are apparent at around 45 rad/s. First order rotor flexure (164 rad/s) has a sharp response since the bearings are close to vibration nodes. The other critical speed involves second order rotor flexure around 420 rad/s and the broader peak indicates greater modal damping and controllability. In figure 3(b), modes involving rigid body rotor motion are well damped and do not exhibit any peaks in the response curves. The increased derivative gain has little effect on the first rotor flexural frequency, in contrast to the significant reduction of the second rotor flexural critical speed.

Mass loss simulations at a speed $\Omega = 500$ rad/s are shown in figure 4, starting from a perfect balance condition and with a mass of 60 g removed from the non-driven end disk at time $t = 0$.

Bearing saturation and clearance limits were not set so that the system remained linear. For low damping, the rotor displacement response at the non-driven end bearing exhibits transient responses of the critical speed modes. The rigid body response is significant and in any practical system the rotor would collide with emergency retainer bearings for displacements amplitudes above around 1mm. The high damping case of figure 4(b) reduces the rotor overshoot, though at the expense of substantially increased control forces. With the inclusion of control force limits of (-1700, 1000) N, biased by static loading, saturation is bound to occur in the high damping case. The simulated results are shown in figure 5, though still without clearance limits. The rotor responses at the bearings suffer from drift when compared with figure 4(b). Of course, in a practical system, the rotor would collide with an emergency bearing at the driven end magnetic bearing. Clearly, transient vibration control is not effective due to the passive configuration of the magnetic bearings.

VIBRATION CONTROLLER DESIGN

To define the level of vibration control, the variables in $\boldsymbol{e}$ were chosen to consist of lateral rotor velocities at the end disks and magnetic bearing locations, coincident with the measurement locations. Without stating the precise details, it is clear from figure 2 that a closed loop transfer function relation exists to relate the external disturbances to the control variables:

$$\boldsymbol{E}(s) = [\,T_{ef}(H;s)\,W_f(s)\,,\,T_{en}(H;s)\,W_n(s)\,]\begin{bmatrix} W_f(s)^{-1}\boldsymbol{F}(s) \\ W_n(s)^{-1}\boldsymbol{N}(s) \end{bmatrix} \tag{8}$$

The weighting $W_f(s)$ was selected as a diagonal matrix with a frequency response characteristic that recognises the nature of mass loss unbalance forcing. Singular value bode plots are shown in figure 6. The weighting $W_n(s)$ reflects the level of anticipated measurement noise and was chosen to have a flat spectrum of small amplitude. A basis on which to evaluate the controller is through the H_∞ optimisation problem

$$\underset{H}{minimise}\ \|[\,T_{ef}(H;s)\,W_f(s)\,,\,T_{en}(H;s)\,W_n(s)\,]\|_\infty \tag{9}$$

However, this optimisation provides no means of accounting for the bearing saturation limits since it

assumes that unconstrained levels of control force are available.

To overcome the saturation problem, the control force vector $\boldsymbol{u}$ is now included in the control variables:

$$\boldsymbol{e}_1 = \begin{bmatrix} \boldsymbol{e} \\ \boldsymbol{u} \end{bmatrix} \tag{10}$$

A revised version of the closed loop system given by equation (8) is

$$\begin{bmatrix} W_e(s)\boldsymbol{E}(s) \\ W_u(s)\boldsymbol{U}(s) \end{bmatrix} = \begin{bmatrix} W_e(s)T_{ef}(H;s)W_f(s) & W_e(s)T_{en}(H;s)W_n(s) \\ W_u(s)T_{uf}(H;s)W_f(s) & W_u(s)T_{un}(H;s)W_n(s) \end{bmatrix} \begin{bmatrix} W_f(s)^{-1}\boldsymbol{F}(s) \\ W_n(s)^{-1}\boldsymbol{N}(s) \end{bmatrix} \tag{11}$$

with the H_∞ optimisation

$$\underset{H}{minimise} \left\| \begin{bmatrix} W_e(s)T_{ef}(H;s)W_f(s) & W_e(s)T_{en}(H;s)W_n(s) \\ W_u(s)T_{uf}(H;s)W_f(s) & W_u(s)T_{un}(H;s)W_n(s) \end{bmatrix} \right\|_\infty \tag{12}$$

Here the weightings $W_e(s)$ and $W_u(s)$ are introduced to allow design influences on control performance and control force respectively.

For the present problem, the rotor was modelled using 12 beam elements, including shear deformation. The levitation parameters were set at $k_p = 1.05\ k_z$, $c_d = 7.5\times10^3$ Ns/m and $\tau = 10^{-3}$ s to produce well damped low frequency rigid body modes without undue influence on the rotor flexural modes. The following weighting forms were arrived at after an iterative process to achieve required levels of vibration attenuation and control force output:

$$W_n(s) = 10^{-8}I \quad , \quad W_e(s) = I \quad , \quad W_u(s) = 10^{-4}I \tag{13}$$

In practice, some shaping would also be applied to these weightings in order that problems such as spillover may be avoided. A controller $H(s)$ may be determined in state space form using standard algorithms. For numerical efficiency, dominant mode techniques were employed to reduce the full

order 104 states rotor model to a 24th order state space model.

The significance of the revised vibration controller is shown in the simulated mass loss plots of figure 7. The rotational speed and mass loss correspond with those of figures 4 and 5. It is seen that synchronous steady state vibration levels are reduced below those of the high damping case in figure 4(b), yet magnetic bearing forces are now within saturation limits. There is an initial transient response involving mainly rigid body motion, though the vibration amplitudes would be well within clearance limits. Any attempt to reduce this transient would require increased transient control force levels. Thus a compromise between magnetic bearing saturation and clearance constraints is always necessary. There is scope for further design to influence steady state force components with alternative weighting functions, but the consideration of this paper has been focused on the transient behaviour. Some generalisation for mass losses at different locations and over a range of rotational speeds is also possible.

CONCLUSIONS

This paper has been used to show that there are circumstances in which vibration control may be achieved without magnetic bearing saturation in a rotor dynamic system. One of the consequences of this is that conditional system instability, caused by non-linear bearing behaviour, may be overcome. However, the ultimate level of achievable vibration control will still depend on the saturation limits and large unbalance conditions will result in significant residual vibration amplitudes. In particular, if the magnetic bearings are situated close to vibration nodes, low controllability will prevent significant reduction around certain critical speeds.

The control design included H_∞ optimisation to minimise both vibration responses and control force levels. Mass loss simulations were used to demonstrate the avoidance of saturation during transient conditions. The success of the method depends on a judicious choice of weighting functions appropriate to the anticipated levels of mass loss that are likely to occur. The weighting functions must be normalised to enable the optimisation problem to achieve desired performance levels. If the mass loss is greater than the levels accounted for in the design, bearing saturation may still occur.

REFERENCES

1. Burrows, C.R. and Sahinkaya, M.N.: Vibration Control of Multi-Mode Rotor Bearing Systems. *Proc.R.Soc.Lond.*, A386, 1983, pp. 77-94.
2. Larsonneur, R., Siegwart, R. and Traxler, A.: Active Magnetic Bearing Control Strategies for Solving Vibration Problems in Industrial Rotor Systems. *Proceedings (IMechE) of the Fifth International Conference on Vibrations in Rotating Machinery*, Bath, UK, September 7-10, 1992, pp. 83-90.
3. Larsonneur, R. and Herzog, R.: Feedforward Compensation of Unbalance: New Results and Experiences. *IUTAM Symposium on the Active Control of Vibration*, Bath, UK, September 8-11, 1994, pp. 45-52.
4. Berry, T., Burrows, C.R., and Keogh, P.S.: Active Control of Synchronous and Transient Vibration with Minimal System Modelling. ASME Winter Annual Meeting, New Orleans, paper 93-WA/DSC-4, 1993.
5. Knospe, C., Hope, R., Fedigan, S., and Williams, R.: New results in the Control of Rotor Synchronous Vibration. *Proceedings of the Fourth International Symposium on Magnetic Bearings*, Zurich, Switzerland, August 23-26, 1994, pp. 119-124.
6. Knospe, C., Hope, R., Fedigan, S., and Williams, R.: Experiments in the Control of Unbalanced Response using Magnetic Bearings. *Mechatronics*, vol. 5, no. 4, 1995, pp. 385-400.
7. Rutland, N.K., Keogh, P.S., and Burrows, C.R.: Comparison of Controller Designs for Attenuation of Vibration in a Rotor-Bearing System under Synchronous and Transient Conditions. *Proceedings of the Fourth International Symposium on Magnetic Bearings*, Zurich, Switzerland, August 23-26, 1994, pp. 107-112.
8. Shafai, B., Beale, S., LaRocca, P., and Cusson, E.: Magnetic Bearing Control Systems and Adaptive Force Balancing. *IEEE Control Systems*, vol. 14, no. 2, 1994, pp. 4-13.
9. Herzog, R. and Bleuler, H.: On Achievable H^{∞} Disturbance Attenuation in AMB Control. *Third International Symposium on Magnetic Bearings*, Washington D.C., 1992.
10. Keogh, P.S., Mu, C., and Burrows, C.R. Optimized Design of Vibration Controllers for Steady and Transient Excitation of Flexible Rotors. *Proc.I.Mech.E.Part C*, 1995, pp. 155-168.

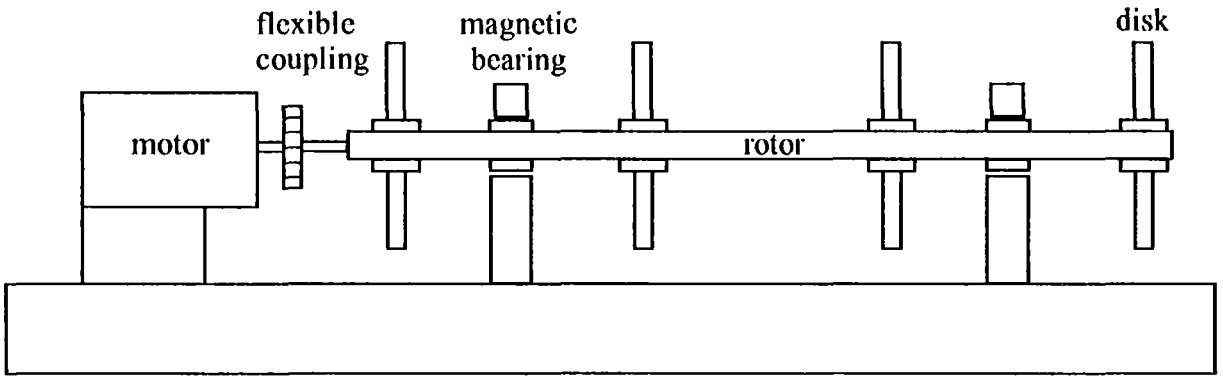

Figure 1. Schematic diagram of rotor / magnetic bearing system.
The steel rotor is 2m long with a shaft diameter of 50mm.
Disks are of 250mm diameter and 35mm wide.

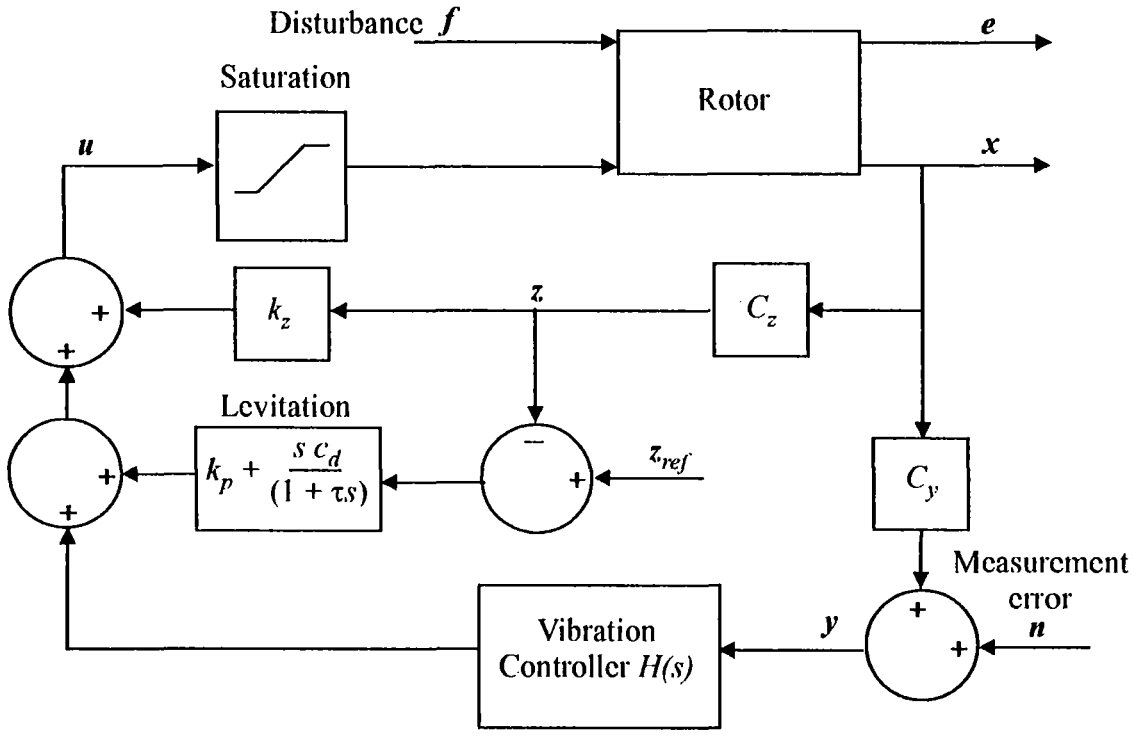

Figure 2. Block diagram of system including levitation and vibration control.

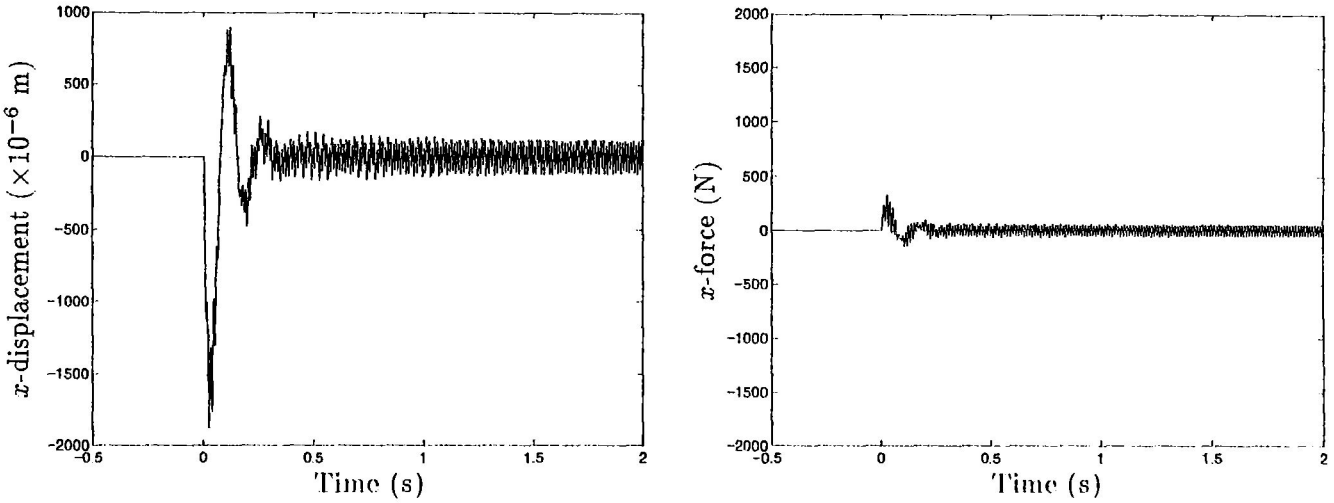

(a) Low damping ($c_d = 10^3$ Ns/m)

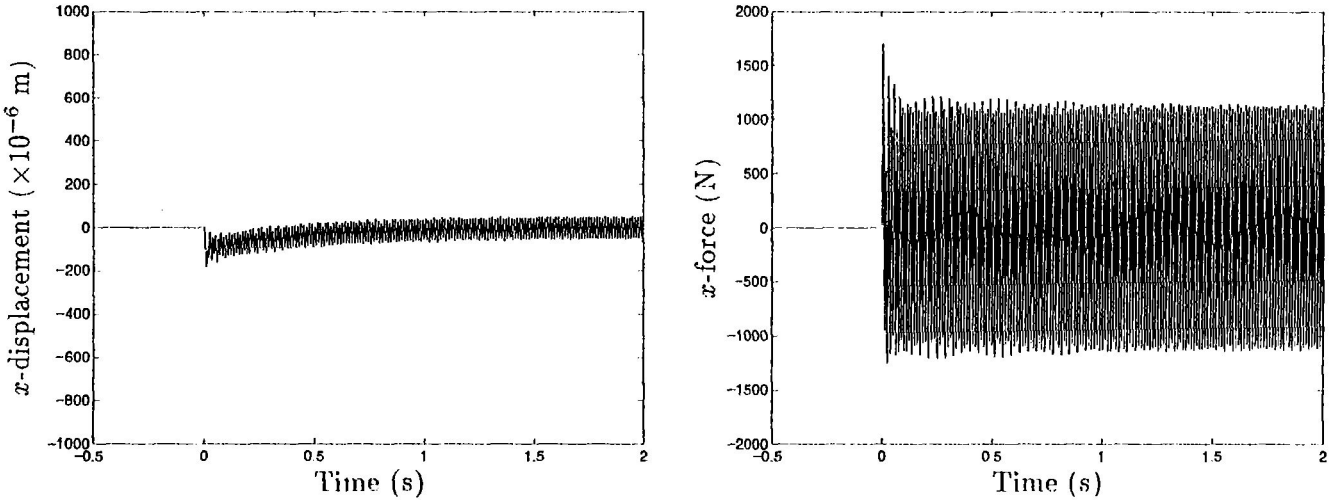

(b) High damping ($c_d = 5 \times 10^4$ Ns/m)

Figure 4. Mass loss simulations at a speed $\Omega = 500$ rad/s with a 60 g mass removed from the non-driven end disk rim in the x direction (45° to vertical against rotation) at $t = 0$ ($k_p = 1{\cdot}05k_z$, $k_z = 2{\cdot}05 \times 10^6$ N/m, $\tau = 10^{-3}$ s). Vibration components of rotor amplitude and bearing force are shown at the non-driven end magnetic bearing. Saturation and clearance limits were not set. The vibration controller of figure 2 is not present.

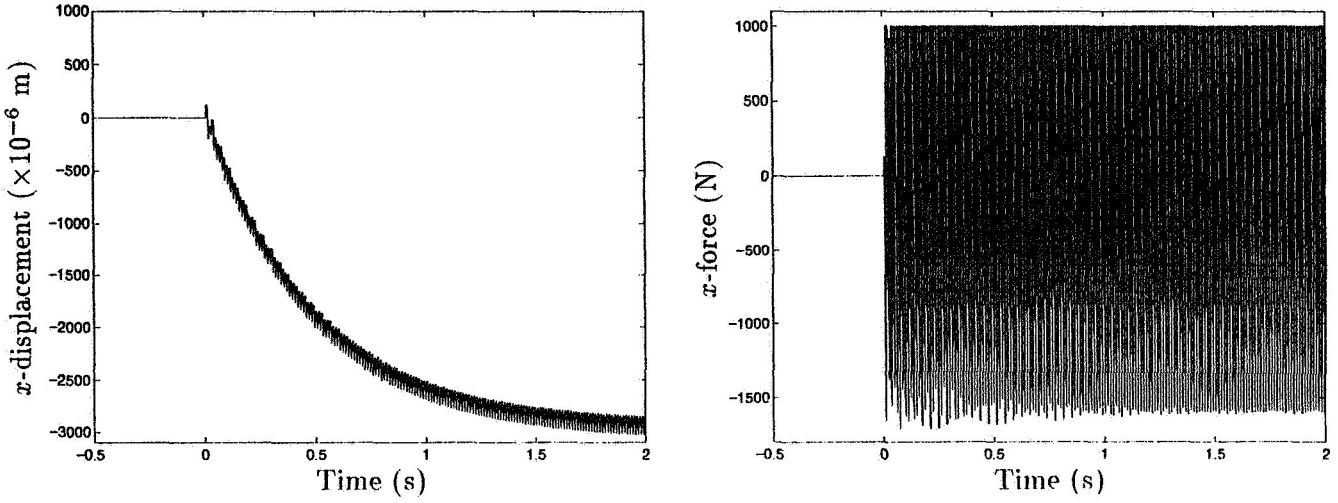

(a) Driven end magnetic bearing

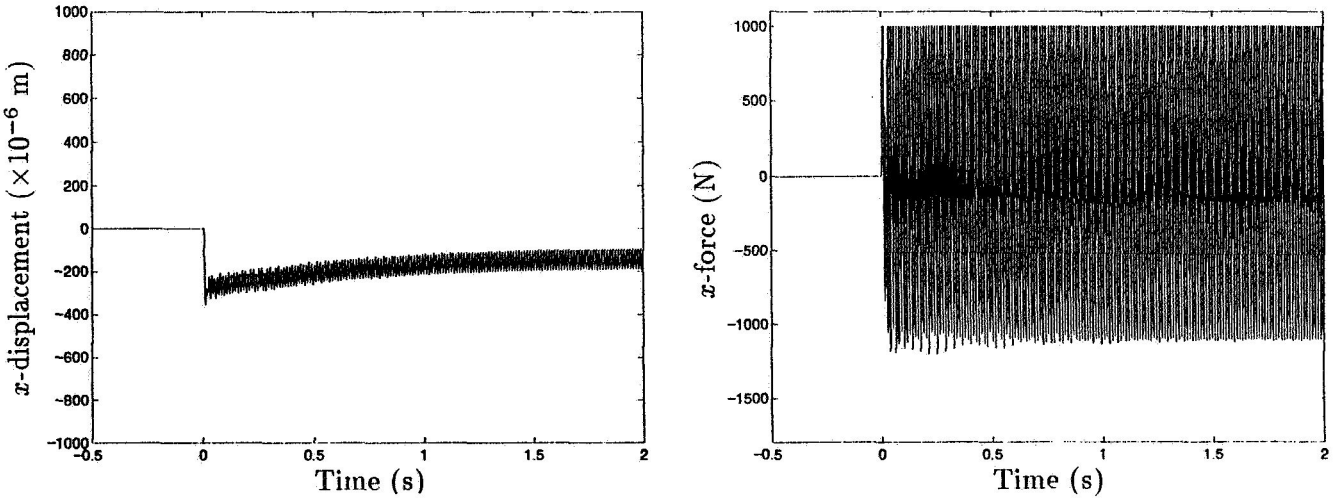

(b) Non-driven end magnetic bearing

Figure 5. Mass loss simulations at a speed $\Omega = 500$ rad/s with a 60 g mass removed from the non-driven end disk rim in the x direction at $t = 0$ ($k_p = 1{\cdot}05k_z$, $c_d = 5 \times 10^4$ Ns/m, $k_z = 2{\cdot}05 \times 10^6$ N/m, $\tau = 10^{-3}$ s). Vibration components of rotor amplitude and bearing force are shown at the magnetic bearings. Saturation force limits were set at 1000 and -1700 N. The vibration controller of figure 2 is not present.

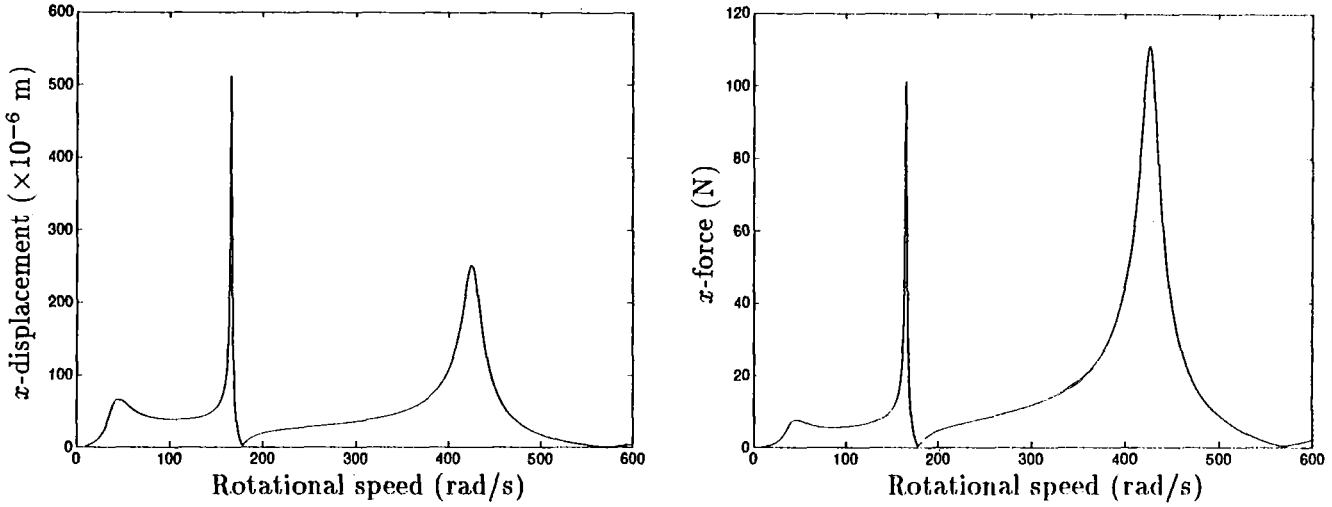

(a) Low damping ($c_d = 10^3$ Ns/m)

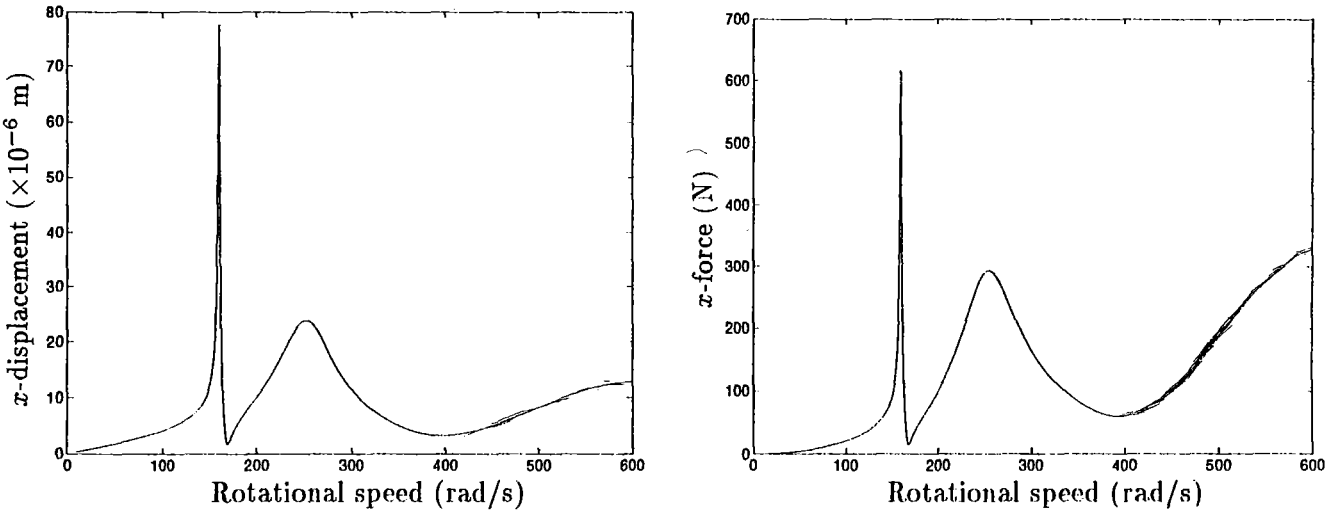

(b) High damping ($c_d = 5 \times 10^4$ Ns/m)

Figure 3. Linearized synchronous response amplitudes at non-driven end magnetic bearing in the x direction (45° to vertical against rotation) ($k_p = 1{\cdot}05k_z$, $k_z = 2{\cdot}05 \times 10^6$ N/m, $\tau = 10^{-3}$ s). The nominal unbalance was a 10 g mass on the rim of the non-driven end disk. The vibration controller of figure 2 is not present.

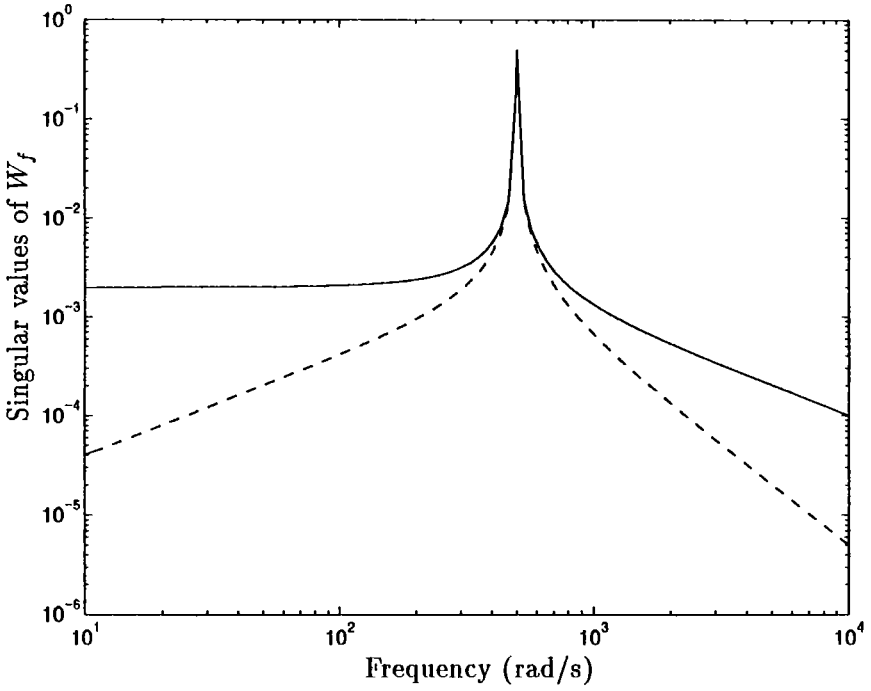

Figure 6. Singular values of weight function matrix $W_f(\mathrm{i}\omega)$.

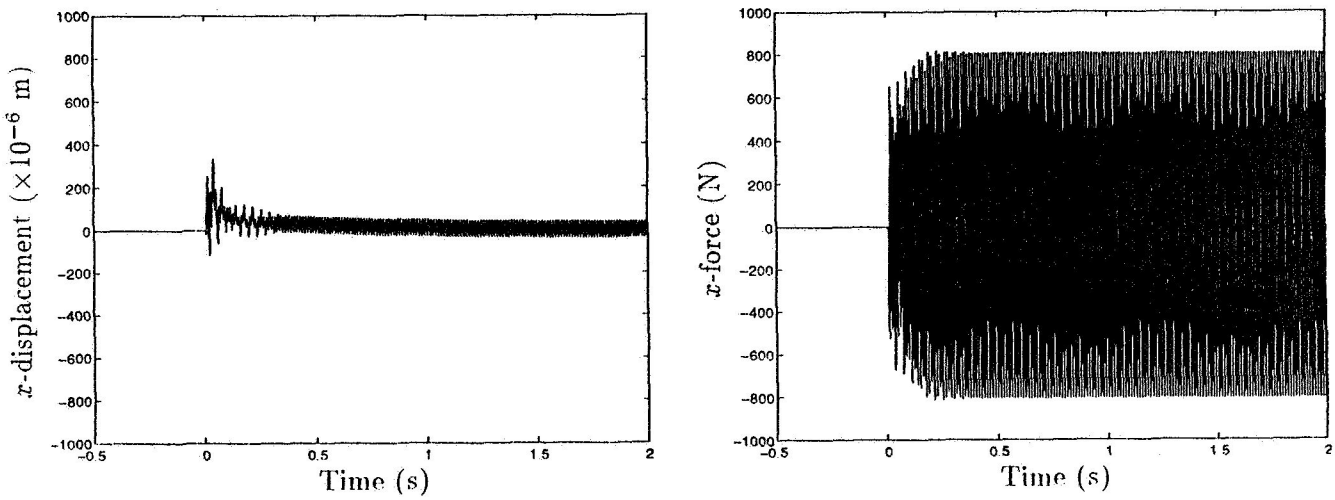

(a) Driven end magnetic bearing

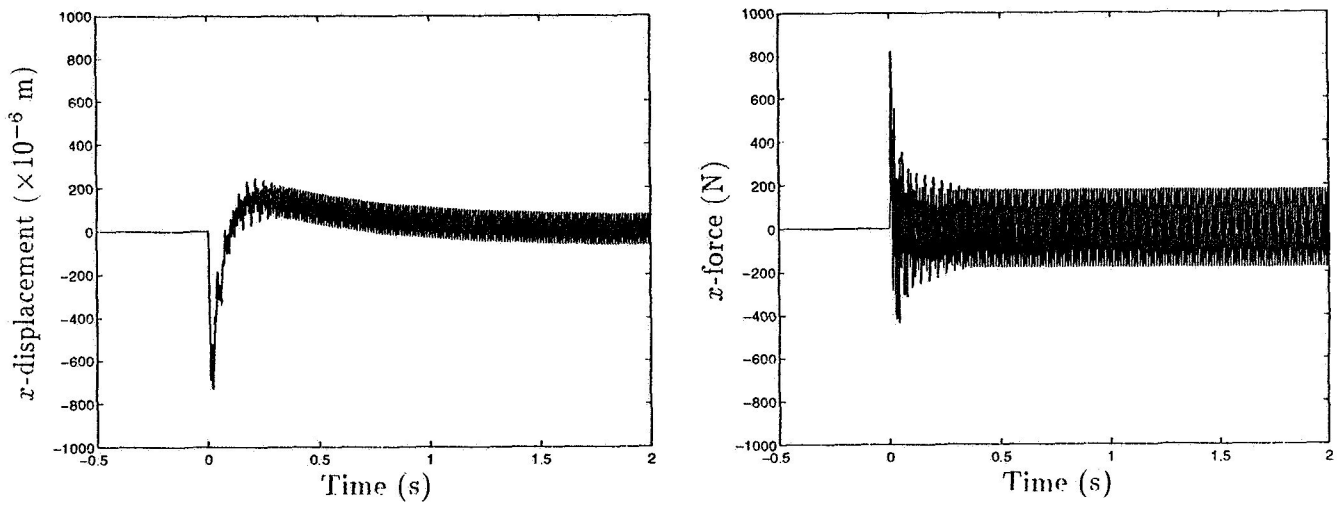

(b) Non-driven end magnetic bearing

Figure 7. Mass loss simulations at a speed $\Omega = 500$ rad/s with a 60 g mass removed from the non-driven end disk rim in the x direction at $t = 0$ ($k_p = 1{\cdot}05k_z$, $c_d = 7{\cdot}5\times10^3$ Ns/m, $k_z = 2{\cdot}05\times10^6$ N/m, $\tau = 10^{-3}$ s). Vibration components of rotor amplitude and bearing control force are shown at the magnetic bearings. Saturation force limits were set at 1000 and -1700 N. The vibration controller of figure 2 is present.

Session 2 -- Superconductivity 1

Chairman: Jack E. Crow
National High Magnetic Field Laboratory (NHMFL)

DESIGN OF A SUPERCONDUCTING MAGNETIC SUSPENSION SYSTEM FOR A LIQUID HELIUM FLOW EXPERIMENT

Michael R. Smith, Yehia M. Eyssa, and Steven W. Van Sciver
National High Magnetic Field Laboratory
Tallahassee, FL

SUMMARY

We discuss a preliminary design for a superconducting magnetic suspension system for measurement of drag on rotationally symmetric bodies in liquid helium. Superconducting materials are a natural choice for liquid helium studies, since temperatures are well below most critical temperatures, so that the resulting heat load is negligible. Also, due to its diamagnetic properties, a superconducting model (for example made or coated with Nb) is inherently stable against disturbances. Issues which we consider include model placement during initial cool-down, maintaining placement during anticipated drag and lift forces, and force measurement. This later can be achieved by a passive technique, where the body is allowed to deflect under the influence of drag from its neutral position. The resulting shift in flux is detected via a superconducting pickup coil. The pickup coil may be connected either to a SQUID, or a secondary loop wound around a Hall probe. Both options are discussed. The objective of this work is to gain a better understanding of the nature of turbulent fields in normal and superfluid helium for potential application to problems in classical high Reynolds number turbulence.

INTRODUCTION

The design and construction of non-intrusive force balance systems has long been an important aspect of dynamic studies carried out in wind tunnels. Early research concentrated on understanding the interaction of physical struts or stings with the flow field under examination, in an effort to subtract these effects for the relevant measurements [1]. With the advent of Magnetic Suspension and Balance Systems (MSBS), the problem of physical intrusion into the flow field has been eliminated at the cost of a formidable controls problem [2,3,4]. Simplification may come as a by-product of using liquid helium as a test fluid. Because its kinematic viscosity is over 800 times smaller than that of air, liquid helium offers the potential of extending the range of Reynolds numbers available in wind tunnel testing of high performance aircraft and marine vessels [5]. Liquid helium also offers operating temperatures well below the critical temperature of most superconductors, thus allowing a superconducting MSBS. Such a system offers several advantages over its resistive counterparts. First, a superconducting MSBS dissipates no heat resistively, and so may be operated in the helium bath. Operated in persistent mode (as a closed system disconnected from external supplies and noise sources), such a 'passive' MSBS may be constructed, as compared with the active systems traditionally built. A passive MSBS eliminates the need for continuous

control/feedback and reduces noise. A superconducting system is then potentially quieter and more sensitive. Second, superconductors in a magnetic field behave as strongly diamagnetic materials which reject flux, and so are repelled by regions of high magnetic field intensity. A superconducting MSBS would then have improved coupling between the model and support field and be inherently stable, again improving sensitivity and simplifying the control problem. Finally, since flux through a superconducting loop in persistent operation is perfectly conserved, one may envision a completely magnetic MSBS, without resorting to optical position sensing schemes. With the MSBS coils operated in persistent mode, and the body is allowed to deflect with applied drag from its neutral or 'no flow' position. The resulting flux shift could then be detected with a superconducting loop wound around the test section. The degree to which this may be carried out depends upon the symmetry of the body and flow field.

In this paper, we consider the design of a superconducting MSBS for supporting and measuring the drag on a sphere in a liquid helium flow field. Current levels and signal output are presented, together with a discussion of certain practical issues which must be considered in the actual construction and operation of a prototype. The optimum design was selected to take advantage of existing facilities at the National High Magnetic Field Laboratory at Florida State University.

GENERAL CONSIDERATIONS

As a first step, we need to estimate the scale of the experiment together with anticipated forces. A conservative estimate of the maximum mass flow available with our equipment is $\dot{m} \approx 50$ g/sec, so long as the pressure drop across the test section is not too large. For fixed mass flow, the drag and Reynolds number vary as

$$F_D = \frac{2\dot{m}^2 C_D}{\pi \rho d_s^2 (A^2 - 1)^2} \tag{1}$$

$$\mathrm{Re} = \frac{4\dot{m}}{\pi \rho \nu d_s (A^2 - 1)} \tag{2}$$

where d_s is the diameter of the sphere, and A is an aspect ratio ($A \equiv d_{tunnel} / d_s$). For a fixed mass flow rate, the largest drag and Reynolds number are achieved for a small A and d_s (note that velocity is not constant in this situation). The coefficient of drag C_D~0.4 over the range of Reynolds numbers considered here, and ρ and ν are the density and kinematic viscosity, respectively. If the body being tested takes up too much space within the test section, the streamlines no longer approximate their behavior in an infinite flow field. The velocity around the model increases due to the reduced flow area associated with the presence of the model within the tunnel. Pressure, drag, and other forces all exhibit anomalous behavior attributed to this 'blockage'. To minimize blockage effects, most wind tunnel users try to maintain $A \geq 10$. Blockage effects however, are manageable for A=4, and the corresponding drag is boosted by a factor of $(99/15)^2$=43.56. Additionally, we will soon measure drag on a sphere with A=4 by other means, and this will serve as a useful point for evaluating the performance of the superconducting MSBS. With A=4, this leaves d_s as the defining scale of the experiment. From the beginning, in order to save weight, we chose to use a glass or quartz sphere with a thin Nb film applied to the outside (as opposed to solid super-conductor). Making d_s too small not only makes it difficult to apply such a film, it also increases the

pressure drop over the test section ($d_{tunnel} = A \cdot d_s$) and leads to problems in detecting the sphere's position during the experiment. In an effort not to make things too difficult, we chose an easily obtainable d_s=9.525 mm (0.375 in). Then the maximum drag and Reynolds number are of order 2.15×10^{-4} N and 3×10^5, respectively. A glass sphere of this size will weigh approximately 10^{-2} N, though a heavier sphere of solid niobium may be required if the plating process proves too difficult. In all subsequent calculations, we assume that such a sphere acts as a perfect diamagnet.

With an estimate of the forces in hand, one may consider whether to orient the experiment horizontally or vertically. In the vertical configuration, the weight and flow/drag are co-axial. While this appears to be a simplification, it places the experimentalist in the position of accurately resolving a small fluctuating signal against a large dc background to better than 1 part in 10^4. Further, it is difficult to imagine how one might calibrate such a system or recover in the event of the MSBS 'losing its grip' on the sphere (hereafter called 'blow-by'). In the horizontal configuration however, the drag and support fields are orthogonal, so that sensitive drag measurements may be made with minimal interference from the support coils.

The final issue which had to be resolved up front was whether to use active feedback or a passive system for measuring the drag. In the case of a conventional ferromagnetic MSBS, the support field is attractive by nature, and thus is fundamentally unstable. An active system continuously senses the model's position and makes corrections in the support field to maintain the neutral position. These corrections are calibrated and then read off as forces and moments. Such a system is indispensable for a conventional MSBS. In the passive system, one operates all the superconducting coils in the persistent mode, and the diamagnetic material in or on the model is repelled to the point of lowest field intensity. This system is fundamentally stable, as well as being free from sources of instrument noise in the lab. The sphere deflects slightly from its neutral position under applied drag. This re-distributes the flux in the test section, which may be detected by a superconducting sensing coil around the test section. Having selected the passive approach for the benefits discussed in the introduction, we designed the drag coils as a Helmholtz pair with a linear drag/displacement response over the anticipated range of drag. The field produced by this pair should be reasonably homogeneous over the region which the sphere is allowed to deflect, with the maximum allowed field kept well below the critical field at which superconductivity breaks down (B_c~0.15 T for Nb).

SUPPORT AND DRAG COIL DESIGN

The general configuration selected is illustrated in Figure 1, which shows cross-sections of the flow experiment together with the coil components. The vertical support coils are of a counterwound racetrack configuration designed to produce a quadrapole field in the plane perpendicular to the flow. Higher current in the coils results in a stiffer field, but also a higher maximum field intensity to which the sphere is exposed. The sphere then displaces slightly under the influence of its weight. This vertical displacement is plotted against the applied field strength in Figure 2, where the radius of the windings was taken to be 43 mm. Since we wish to limit the total maximum field which the sphere experiences (including the contribution from the drag coils, discussed below) to below the critical field, the applied field strength B_s=0.018 T was selected, requiring a total 8.68 kA turns flowing around each coil. The corresponding vertical displacement of the sphere within the field is 1 mm. The associated maximum field on the surface of the sphere was $B_{s,max}=2.5 \cdot B_s$=0.045 T. Thus, one should offset the support coils 1 mm with respect to

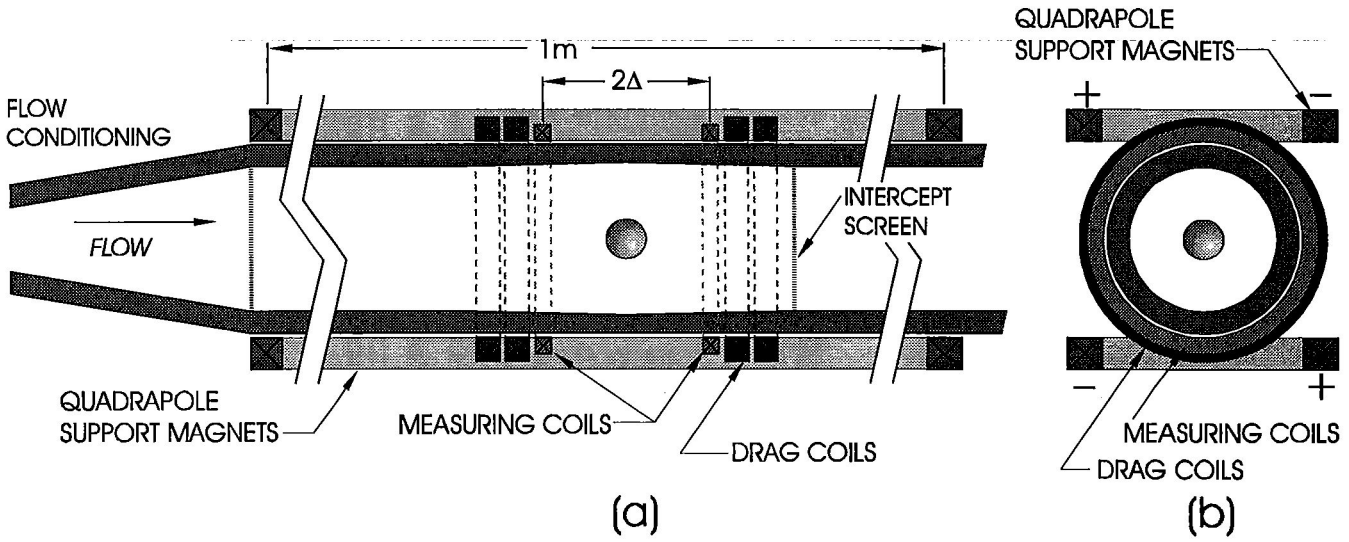

Figure 1. Schematic of the proposed Superconducting MSBS. Support is accomplished by means of two independent magnet assemblies operated in persistent mode. The support coils are of a counter-wound race track configuration, designed to produce a quadrapole field. The drag coil assembly is composed of sets of Helmholtz coils, tuned to provide a particular B_0 and dB/dz. The screen located down stream of the neutral position intercepts the sphere in the event of blow by. The walls form a very slight conical taper, extending up and down stream from the neutral position. This provides a passive mechanism for controlling the location of the sphere without the MSBS energized.

the test section in order to maintain the sphere in the center of the flow field. Figure 3 shows the field lines around the superconducting sphere in a quadrapole field. The plane of this illustration is perpendicular to the flow as in Figure 1b. Arrows point to the regions of highest field intensity.

The drag coils are built up from Helmholtz pairs, designed to produce a particular applied field B_0 and field gradient dB/dz along the direction of drag/flow. In principle, a system of coils may be designed to produce any B_0 and dB/dz desired, so we will not dwell on the details. If the sphere is allowed to deflect a distance δ under the influence of drag, the restoring force (drag) may be expressed

$$F_D = \frac{2\pi\, d_s^3}{\mu_0} B_o \frac{dB}{dz} \tag{3}$$

where dB/dz, and therefore F_D, varies linearly with the displacement. Figure 4 shows a plot of B_0 vs. dB/dz for various values of F_D. In measuring drag (as discussed in the next section), the optimum signal is achieved for dB/dz as small as possible, or equivalently B_0 as large as possible, while maximizing the displacement δ corresponding to a given F_D. To keep the maximum total field below the critical field, the largest practical B_0= 0.067 T. For F_D=2.15x10^{-4} N, this value of B_0 corresponds to the field gradient dB/dz=0.742 T/m at the point of maximum displacement. The maximum field experienced by the sphere due to the drag coils is $B_{0,max}$=1.5 · B_0=0.101 T. Note that one may still adjust the stiffness of the field, since dB/dz~ C_2 · δ, where C_2 is a constant. A measurable signal is generated in the sensing coils for δ_{MAX}=10 mm, corresponding to F_D=2.15x10^{-4} N.

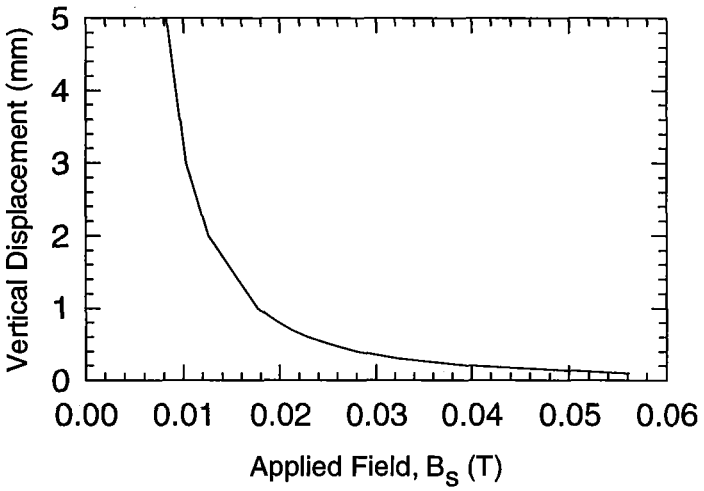

Figure 2. Support field stiffness. The sphere displaces slightly in the support field under the influence of its weight. The maximum field experienced by the sphere should remain well below the critical field for the niobium coating. For B_s=0.018 T, the support coils should be offset 1 mm with respect to the test section in order for the sphere to remain centered in the flow field.

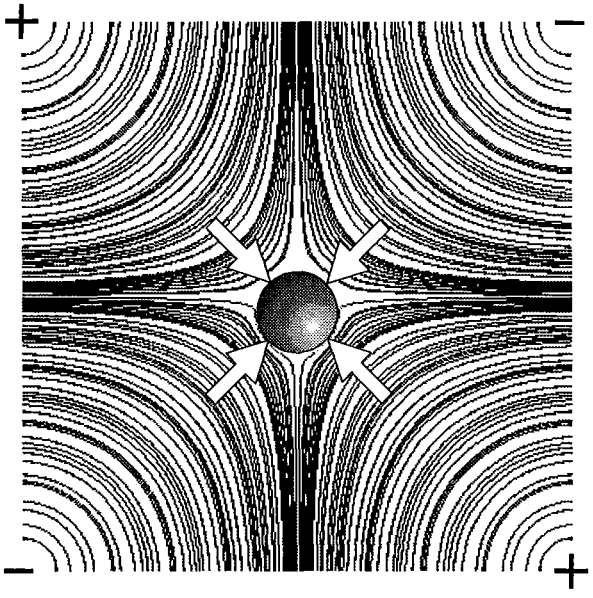

Figure 3. Field lines in the quadrapole support system. Arrows indicate regions of highest field intensity. Note the slight asymmetry due to the vertical displacement of the sphere under the influence of its own weight. (courtesy, Soren Prestemon, NHMFL/FSU)

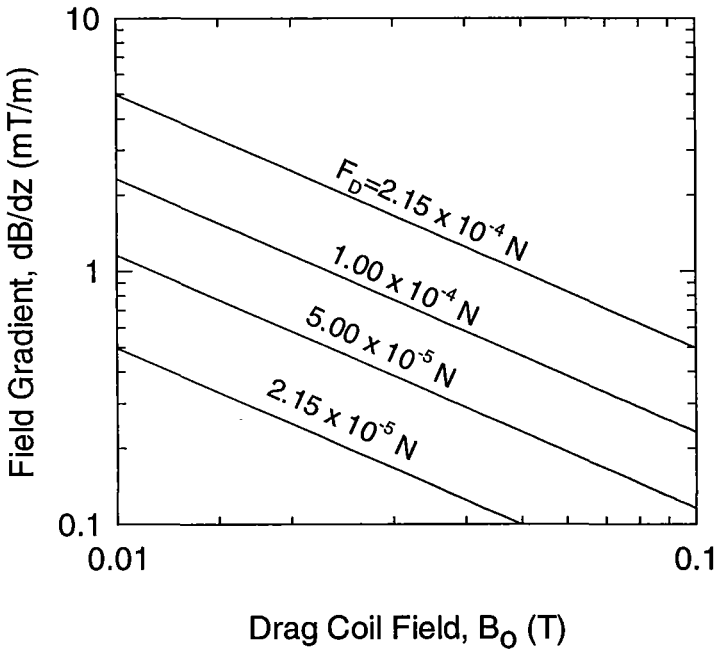

Figure 4. Drag coil field gradient vs. applied field B_0. The optimum signal for drag measurement is achieved for dB/dz as small as possible for a particular drag, while remaining well below the critical field B_c~0.15 T.

DRAG MEASUREMENT SCHEMES

The proposed drag measurement is accomplished by allowing the sphere to deflect a small amount δ, under applied drag. Sensor coils, placed as illustrated in Figures 1 and 5, will then detect a flux change $\delta\phi$. These sensor coils should be counterwound to increase the flux change through the circuit, as well as to decrease the total inductance of the sensor coil pair. Counterwinding also makes the system insensitive to stray field fluctuations in the laboratory. The flux change detected by two single loops placed 2Δ apart and having a radius R_1 is

$$\delta\phi = \pi d_s^3 B_0 R_1^2 (R_1^2 + \Delta^2)^{-3/2} \{[1 + \frac{\delta(2\Delta + \delta)}{R_1^2 + \Delta^2}]^{-3/2} - [1 + \frac{\delta(-2\Delta + \delta)}{R_1^2 + \Delta^2}]^{-3/2}\}. \quad (4)$$

Figure 6 plots this equation as $\delta\phi/B_0$ vs. 2Δ for different values of δ. For small δ, the optimum flux change occurs for $2\Delta=R_1$. For the experiment proposed here, R_1=30 mm. An approximate expression for this optimum flux is shown in Equation 5, underlining the linear dependence of $\delta\phi$ upon δ for small displacements.

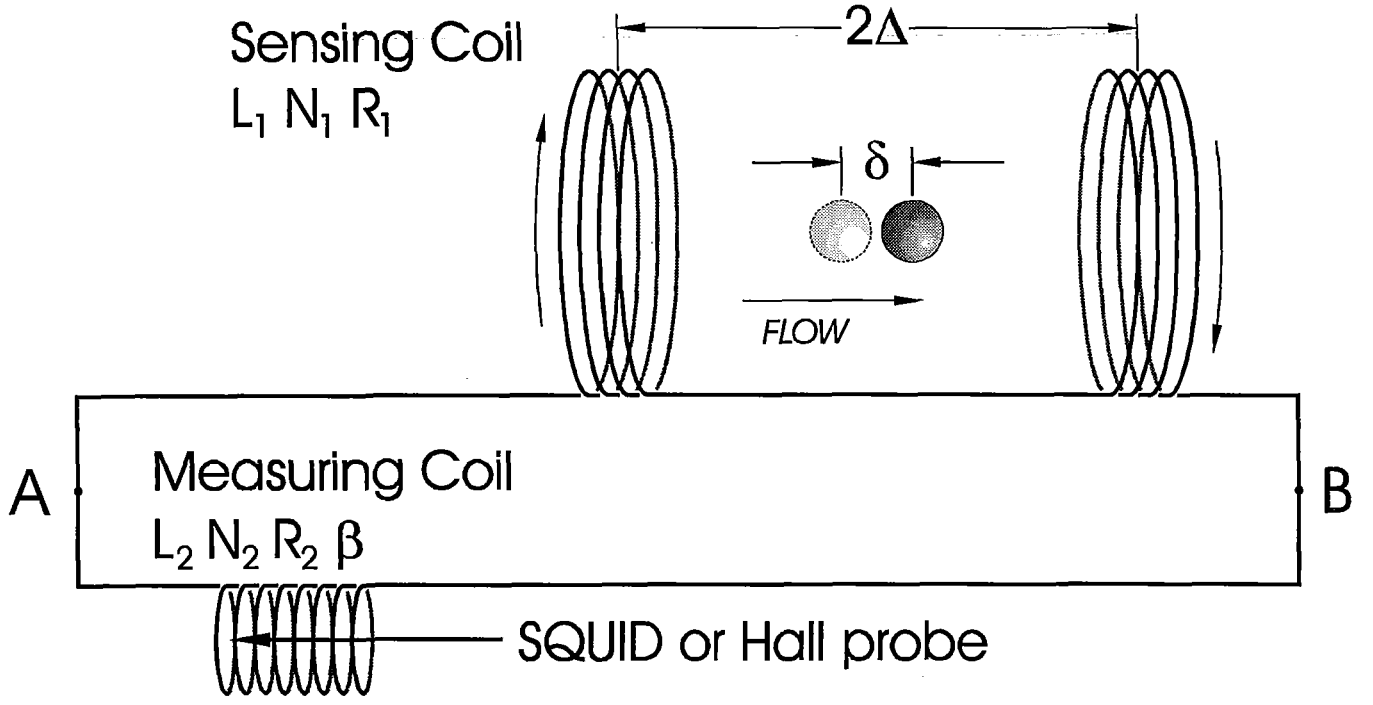

Figure 5. Drag measurement scheme. In the passive magnetic drag measurement, the sphere is allowed to deflect slightly under applied drag. This results in change in the magnetic flux contained by the superconducting sensing coils, which in turn induces current flow in the closed superconducting loop. The current flow creates a field in the secondary, or measuring coil which may be measured by several methods.

$$\delta\phi_{MAX}(at\ R_1 = 2\Delta) = 5.3950\frac{d_s^3 B_o \delta}{R_1^2} \tag{5}$$

The changing flux $\delta\phi/dt$ induces a voltage, which can in principle be measured across open connections as A and B in Figure 5. The total flux change then follows from integrating $V_{AB}(t)$. Since $V_{AB}(t)$ depends upon the rate at which the sphere responds to changing flow conditions however, displacements which evolve over 10 seconds or more may produce signals too small to record. One needs a measurement scheme which depends only on the distance δ, independent of the response time; in effect, the perfect integrator. Such performance may be achieved via a closed superconducting circuit, as illustrated in Figure 5. The secondary, or measuring coil may be either a small solenoid wrapped around a hall probe, or a SQUID (Superconducting QUantum Interference Device) to measure the current induced in the circuit. In either case, the flux in the circuit is conserved, so that

$$N_1(\delta\phi + \phi_1) + N_2\phi_2 = 0 \tag{6}$$

and

$$\frac{N_1\phi_1}{L_1} = \frac{N_2\phi_2}{L_2} = I \tag{7}$$

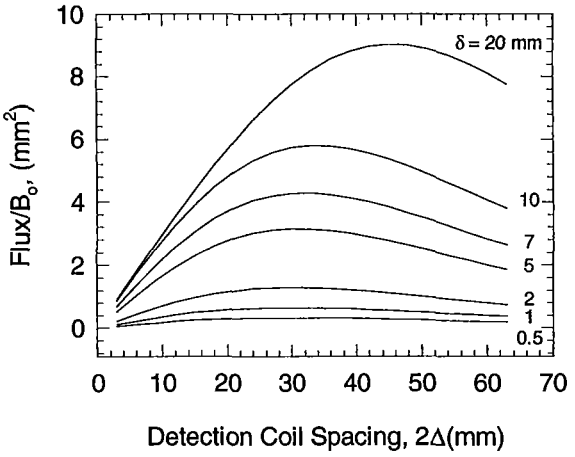

Figure 6. Measured flux vs. detection coil spacing. The optimum flux change occurs for a coil spacing $2\Delta=R_1$. A greater signal also results from allowing a larger deflection δ for a given drag F_D. This is also apparent in Equation 10.

where N_1 is the number of turns/loop in the sensing coil, and N_2 is the number of turns in the measuring coil. Thus, $N_1(\phi_1+\delta\phi)$ and $N_2\phi_2$ are the fluxes linked by the turns of the sensing and measuring coils, respectively. The inductance L_1 is the total inductance of the sensing coils, including mutual inductance. We now consider the two measurement options in greater detail.

1. Drag Measurement Using a Hall Probe

From Equations 6 and 7, the total flux in the measurement coil is

$$N_2\phi_2 = \frac{N_1\delta\phi}{1+\frac{L_1}{L_2}} \tag{8}$$

where the hall probe records approximately $B=\phi_2\pi R_2^2$. The maximum field B is obtained when $L_1=L_2$, so that

$$\mu_o R_1 N_1^2 f_1 = \mu_o R_2 N_2^2 f_2 \tag{9}$$

where f_1 and f_2 are inductance shape factors. For particular R_1 and R_2, this effectively constrains the ratio of turns N_1/N_2. Figure 7 shows B/B_0 plotted against 2Δ for different values of δ, with $R_2=1$ mm. It should come as no surprise to the reader that the optimum measured field occurs for approximately $2\Delta=R_1$. For this coil spacing, the measured field has an analytic form:

$$B = \frac{0.21446\,\mu_o}{\sqrt{\beta^2+1}} \frac{F_D}{dB/dz} \frac{\delta}{\sqrt{f_1 f_2}} \frac{1}{R_1^{2.5} R_2^{1.5}} \tag{10}$$

where $\beta = l/2R_2$ is an aspect ratio for the measuring solenoid. Larger values of β yield more uniform fields in the cross-section, however $\beta=1$ results in only a 15% variation in B across the area of the solenoid (Hall probe), which we deemed an acceptable price for a larger nominal value of B. This was the value used in generating Figure 7. The optimal signal is achieved for R_2, β, and dB/dz as small as possible, while allowing a large displacement δ for a given drag F_D. Note once again, that B varies linearly with the drag.

For $\beta=1$, $R_2=1$ mm, and $\delta=10$ mm, the maximum $B/B_0=7.69\times10^{-2}$, corresponding to the peak drag $F_D=2.15\times10^{-4}$ N. The experimentalist then realizes a maximum signal $B_{MAX}=B_0 \cdot 7.69\times10^{-2}=50$ gauss. For $R_1=30$ mm (fixed by the physical dimensions of the test section), and $R_2=1$ mm $N_2/N_1=15.32$, so that $N_1=3$ allows a nearly optimum $N_2=46$. Axial Hall probes this size are readily available with sensitivities of order 0.01 mV/gauss. Thus, we expect an unamplified maximum output of 0.5 mV. Such measurements are within the reach of the experimentalist, though one could wish for better resolution of small drag forces.

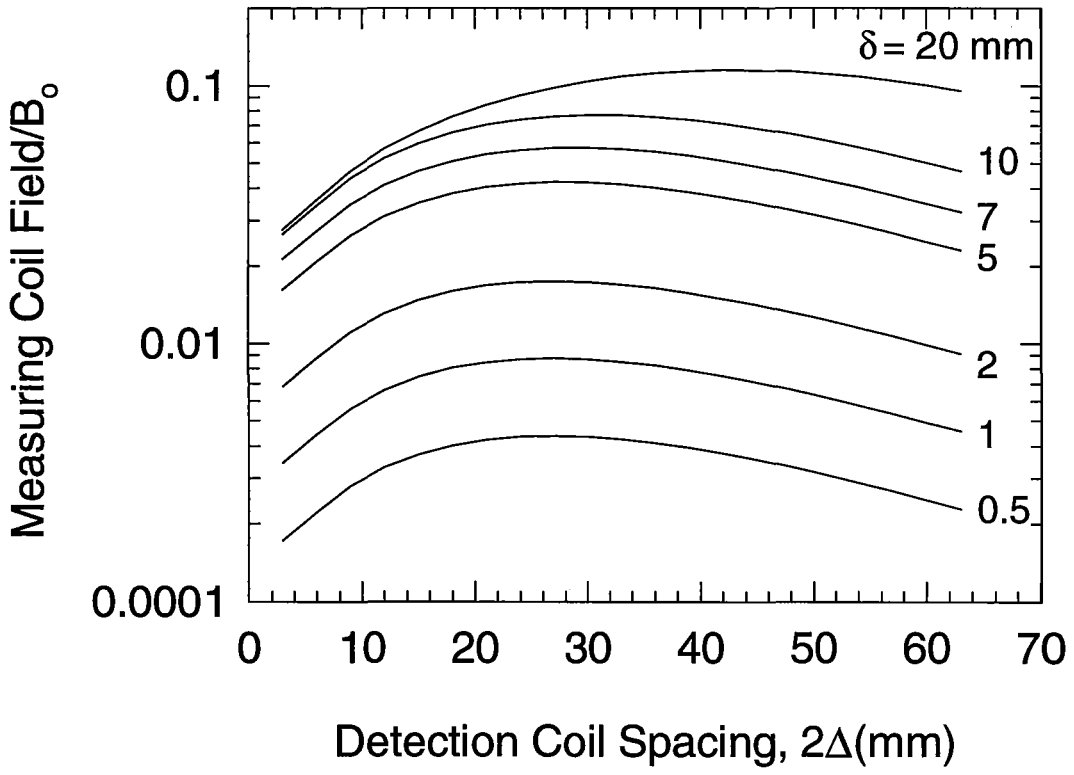

Figure 7. Induced field in the measuring coil vs. detection coil spacing. The maximum field measured by the Hall probe, B_{MAX}~50 gauss, is achieved for $\beta=1$, $R_2=1$ mm, and $\delta=10$ mm, corresponding to a maximum drag $F_D=2.15\times10^{-4}$ N. Again, the optimal spacing is $2\Delta=R_1$.

For greater resolution in measuring small drag forces, one may use SQUID technology. The closed superconducting circuit of Figure 5 appears the same, but the SQUID provides a sensitive measurement of the current. This current is expressed using Equations 6 and 7 as

$$I = \frac{N_1 \delta\phi}{L_1 + L_2} \approx \frac{N_1 \delta\phi}{L_1}, \tag{11}$$

where the approximation holds for small $L_1 >> L_2$. In fact, a SQUID has too *much* sensitivity for use with the optimized field gradient discussed above. This is compensated for by building a much stiffer drag field, with smaller B_0 (equivalently, a much larger gradient dB/dz). Additionally, the circuit is 'de-tuned' such that $L_1 >> L_2$. Our SQUID has a maximum continuous range of 0.1-50 μA with 0.1 μA resolution over the entire span, and L_2=2 μH. Using these values, Figure 8 plots N_1/B_0 against coil spacing 2Δ, for various δ. Though one may be tempted to select a large coil spacing, this tends to de-couple the coils from the sphere, as well as increase the noise from stray field fluctuations. With 2Δ=15 mm, B_0=0.01 T, and a stiff field (say, δ=0.5 mm for $F_D = 2.15 \times 10^{-4}$ N), N_1=300 turns/loop is sufficient to limit the maximum signal to 50 μA. Such a system will reliably resolve drag forces on the sphere as small as F_D=4.3 μN.

Although the pickup coils are counterwound in an attempt to eliminate noise form stray fields in the laboratory, the sensitive nature of the SQUID requires additional shielding of all wires, coils, and electronics. It may even be necessary to build a superconducting shield around the entire experiment.

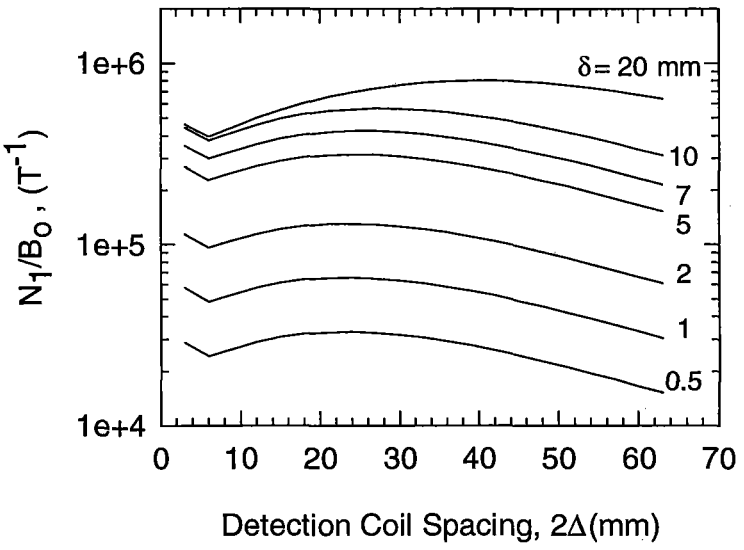

Figure 8. Turns/loop in the sensing coil to 'de-tune' the sensing circuit for use with a SQUID. For a stiff field gradient, B_0=0.01 T (allowing a maximum δ=0.5 mm) and N_1=300 turns/loop limits the maximum induced current to the 50 μA required for our SQUID.

PRACTICAL CONSIDERATIONS AND CONCLUSION

In evaluating the different options and possible configurations for a superconducting MSBS, we have tried to keep in mind the practical implications on building and operating such an experiment. We conclude with a brief discussion of two of these; sphere position management, and calibration. The vertical orientation initially considered had impractical consequences for both of these.

In the horizontal orientation, calibration of the superconducting MSBS is not difficult. By carefully weighing the sphere initially, one may then tilt the experiment slightly out of horizontal with the MSBS energized, so that the weight has some small component directed along the tunnel. In the absence of flow, this becomes the only force measured by the MSBS. For a 1m long test section in which a 0.01 N sphere is suspended, raising the upstream end by 21.5 mm (0.846 in) with respect to the outlet results in 2.15×10^{-4} N resolved along the drag direction.

The issue of sphere position management is more complicated. Due to the vacuum and thermal isolation required for a liquid helium experiment, the sphere must be sealed inside the apparatus as it is assembled at room temperature, limiting access during the course of the experiment. Since the superconducting MSBS does not function above the critical temperature, the sphere must rest within some mounting or controlled position upon the lower surface of the tunnel while the experiment is inserted in the cryostat and cooled down. If the sphere somehow becomes displaced from this initial or rest position, it must relocate itself. Furthermore, this relocation process must be robust, since access is limited. This is especially true when the apparatus reaches its operating temperature. Finally, all of this must be accomplished so as not to disturb the flow. One promising solution is to construct the test section with walls bowed out *very* slightly, as with a slight conical taper extending up and down stream from the sphere's neutral position (its position in the center of the tunnel with the MSBS energized and without flow). This preserves the axisymmetric nature of the flow, and if done carefully may act to correct somewhat the blockage effects. With the walls bowed out slightly and the sphere resting upon the lower surface, there is a low-point on the tunnel wall directly adjacent to the neutral position, to which the sphere will settle. With the experiment cold, ramping the current up from zero lifts the ball gently from its rest position to the neutral position in the center of the tunnel.

As previously mentioned, once such an experiment is cold, access to the test section is limited. Thus, one should plan for every contingency, particularly the possibility of blow-by. One must have a passive, non-destructive, non-intrusive mechanism in place to intercept the sphere and return it to its rest position. One option would be to place a large-mesh fiberglass screen several inches downstream of the sphere's neutral/rest position. In the event of blow-by, the screen intercepts the sphere without scratching (damaging the Nb film). The MSBS may then be de-energized, allowing the sphere to roll along the lower tunnel wall back to the rest position.

In the present paper, we describe the theoretical and practical issues associated with designing, building and operating a superconducting MSBS for a liquid helium wind tunnel. Such a system could be developed as part of a modest effort in high Reynolds liquid helium flow testing. The approach is most easily applied for the suspension of symmetrical bodies, but with further modifications could be extended to asymmetrical objects where active control may be incorporated. With such an effort it would be possible to develop much of the technology necessary to apply magnetic suspension systems in large scale liquid helium flow facilities which could be utilized for a variety of studies at very high Reynolds number ($Re > 10^6$).

ACKNOWLEDGMENTS

We wish to acknowledge the support of the Naval Undersea Warfare Center under contract number N66604-96-C-A093. We also wish to acknowledge partial support from the National High Magnetic Field Laboratory at Florida State University. Finally, we would like to thank Soren Prestemon for his work in plotting the magnetic field lines for the quadrapole field shown in Figure 3.

REFERENCES

1. Pope, A.; and Harper, J. J.: *Low Speed Wind Tunnel Testing*. John Wiley and Sons, New York, 1966 [Second Edition: Rae, W. H.; and Pope, A.: John Wiley and Sons, 1984].

2. Goodyear, M. J. in *High Reynolds Number Flows Using Liquid and Gaseous Helium*, R. J. Donnelly, ed.; Springer-Verlag, New York, 1991, pp. 131-152.

3. Lawing, P. L. in *High Reynolds Number Flows Using Liquid and Gaseous Helium*, R. J. Donnelly, ed.; Springer-Verlag, New York, 1991, pp. 153-164.

4. Britcher, C. P. in *High Reynolds Number Flows Using Liquid and Gaseous Helium*, R. J. Donnelly, ed.; Springer-Verlag, New York, 1991, pp. 165-180.

5. Donnelly, R. J., ed.: *High Reynolds Number Flows Using Liquid and Gaseous Helium*. Springer-Verlag, New York, 1991, pp. 131-152.

54-33

82141

035607

10P.

DEVELOPMENT OF PROTOTYPE HTS COMPONENTS FOR MAGNETIC SUSPENSION APPLICATIONS

P. Haldar, J. Hoehn, Jr., V. Selvamanickam, R. A. Farrell
Intermagnetics General Corporation
Latham, NY

U. Balachandran, A. N. Iyer
Energy Technology Division
Argonne National Laboratory
Argonne, IL

E. Peterson, K. Salazar
Los Alamos National Laboratory
Los Alamos, NM

ABSTRACT

We have concentrated on developing prototype lengths of bismuth and thallium based silver sheathed superconductors by the powder-in-tube approach to fabricate high temperature superconducting (HTS) components for magnetic suspension applications. Long lengths of mono and multi filament tapes are presently being fabricated with critical current densities useful for maglev and many other applications. We have recently demonstrated the prototype manufacture of lengths exceeding 1 km of Bi-2223 multi filament conductor. Long lengths of thallium based multi-filament conductor have also been fabricated with practical levels of critical current density and improved field dependence behavior.

Test coils and magnets have been built from these lengths and characterized over a range of temperatures and background fields to determine their performance. Work is in progress to develop, fabricate and test HTS windings that will be suitable for magnetic suspension, levitation and other electric power related applications.

INTRODUCTION

Significant effort has been made over the past few years in the development of superconducting wires and tapes, through use of the powder-in-tube technique for possible electric power and high field magnet applications. Several research groups have demonstrated high critical

current density (J_c) in short length Ag-clad BSCCO tapes fabricated by the powder-in-tube (PIT) technique [1-7]. The tapes were fabricated in a series of uniaxial pressing and heat treatment schedules. Because this technique cannot be adopted for fabricating high quality long-length conductors a modified processing technique was required. Using a more practical approach such as rolling, Intermagnetics General Corporation has fabricated mono- and multi-filament BSCCO conductors in lengths of up to several hundred meters [4,8-9]. These conductors have been co-wound into prototype pancake coils. Currently, research is underway to improve superconducting performance and to reduce the cost of HTS tapes [10-13]. Details of high field magnets, coils, conductor fabrication and the development of the next generation thallium based HTS conductors will be discussed in the present paper.

To fabricate the Bi-2223 HTS tapes, partially reacted precursor powder for the PIT process was prepared by a solid-state reaction of high-purity oxides and carbonates of Bi, Pb, Sr, Ca, and Cu. The powder was then packed into Ag tubes, swaged, drawn through a series of dies, and then rolled to a thickness of ~0.1 mm. Multi filament conductors containing 37 and 61 filaments were fabricated by stacking mono-filament wires in a larger Ag tube and then drawing and rolling to final size.

Short lengths of tapes were cut and heat treated at ~850°C in air with a repeated thermo-mechanical routine. After each thermo-mechanical step, the tapes were characterized by X-ray diffraction (XRD), scanning electron microscopy, and critical current measurements. Transport properties of the resulting tapes were measured by the four probe technique, with a 1 μV/cm criterion. Long-length mono- and multi filament conductors were fabricated by implementing a carefully designed two-step rolling and heat treatment schedule. Figure 1 shows winding of a long length of conductor (about 1,260 meters) onto a spool during the mechanical deformation operation. After final reaction these conductors were co-wound in parallel to form pancake coils. HTS magnets were fabricated by stacking together and connecting in series a set of such coils. The magnets were characterized at various temperatures and applied magnetic fields.

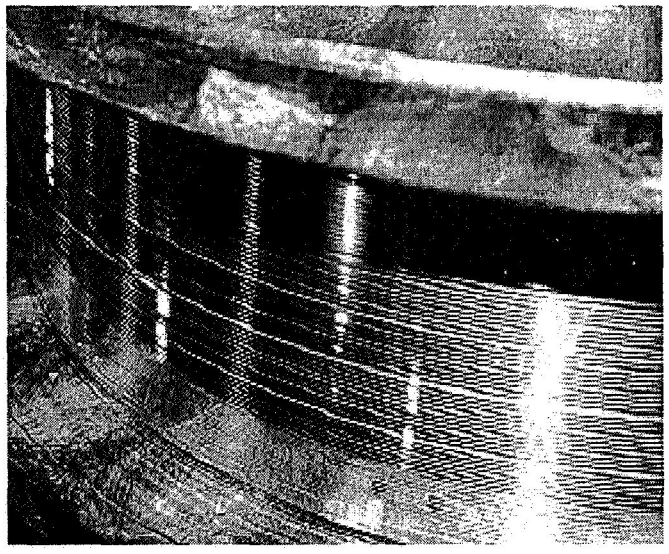

Fig. 1. Fabrication of a 1,260 m length of Bi-2223 conductor.

RESULTS AND DISCUSSION

High critical current (I_c) values in short samples of Bi-2223 tapes have been achieved by a combination of uniaxial pressing and heat treatments. I_c values above 40 A were typically attained at 77 K, with the highest being 51 A (corresponding to a J_c of 45,000 A/cm^2), in short mono filament samples subjected to three or four cycles of uniaxial pressing and heat treatment. For fabricating long length conductors, however a more practical approach such as rolling has been adopted. More recent multi-filament tapes with 61 filaments have been processed and measured in short samples to carry 58 Amps of current at 77 K, zero field. Table 1 summarizes the transport current properties, at 77 K, of both short and long mono- and multi-filament conductors. At 77 K, core J_c values of approaching 2 x 10^4 A/cm^2 have been achieved in a 90 m long multi-filament conductor.

	Length (meters)	Ic (A)	Core Jc (A/cm²)	Overall Jc (A/cm²)	SC %
MONOFILAMENT					
Short Pressed	0.03	51	~45,000	9,000	20
Short Rolled	0.03	51	~29,000	7,800	27
Long Length	70	23	~15,000	3,500	24
Long Length	114	20	~12,000	3,200	27
MULTIFILAMENT (37)					
Long Length	20	42	~21,000	6,800	32
Long Length	90	35	~17,500	5,600	32
Long Length	850	16	~10,500	2,500	24
Long Length	1,260	18	~12,000	3,500	30

Table 1. Summary of transport current properties of short and long mono- and multi-filament Ag-clad BSCCO conductors

Figure 2 shows the critical current density along the length of a 1,260 m long multi filament conductor containing 37 filaments. This tape was mechanically processed in a single piece length. To measure its current carrying properties small samples from the long length were sectioned and heat treated. The results of the tests of these samples are shown in Figure 2. The average I_c was 18A, corresponding to a J_c of =1.2 x 10^4 A/cm^2. These results indicate that considerable progress has been made in the development of Ag-clad BSCCO superconductors by the PIT technique. Pancake coils were fabricated from long Ag-clad BSCCO conductors. HTS magnets were fabricated by stacking the pancake coils and connecting them in series.

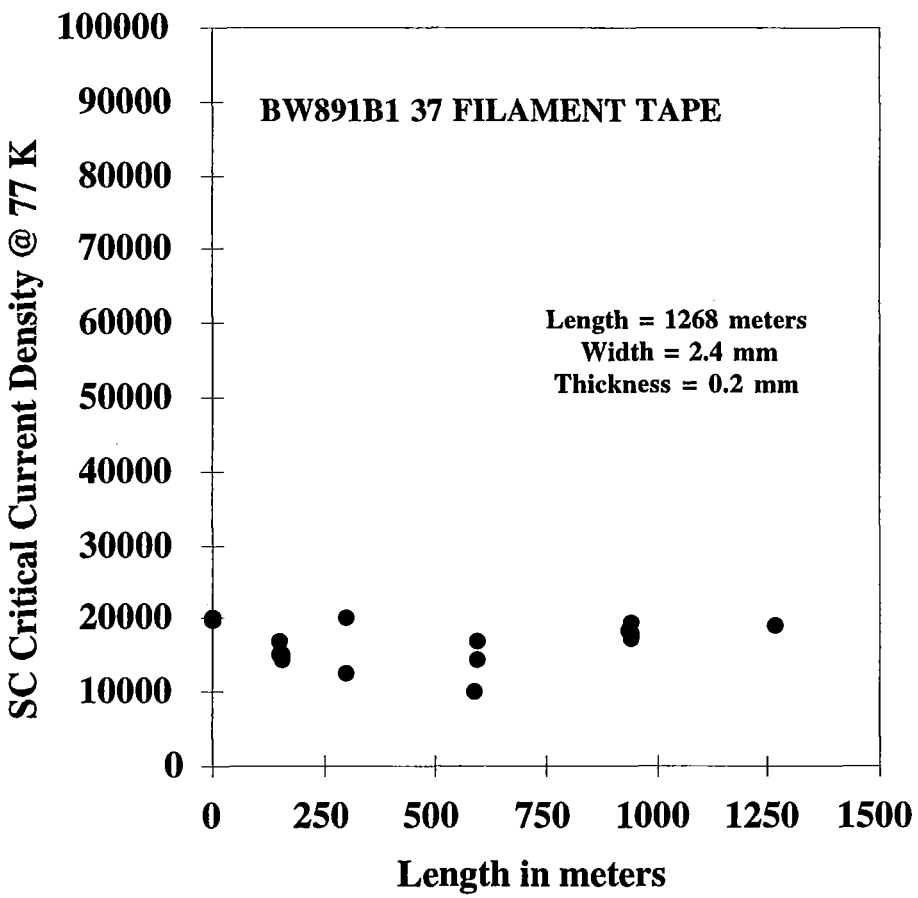

Fig. 2. J_c vs. length at 77K of multi filament conductor containing 37 filaments. Average J_c of ~1,260 m long conductor was ~1.2 x 10^4 A/cm^2.

A test magnet (Fig. 3) fabricated by stacking 20 pancake coils generated a self-field of ~3.2 T at 4.2 K and zero applied field. Total length of the conductor in the magnet was 2,400 m. The outer and inner winding diameters of the coil were 0.203 and 0.040 m, respectively. Ampere turns at 4.2K were >250,000. Another test magnet fabricated with a 40 mm room temperature bore was designed, fabricated and assembled for use in a dry or liquid cryogen free mode. Using the wind and react approach the coils were fabricated and assembled using copper supporting flanges and a copper base block. A schematic of this setup is shown in Figure 4. This magnet was able to generate a field of 0.8 T when cooled with a cryocooler down to 20 K.

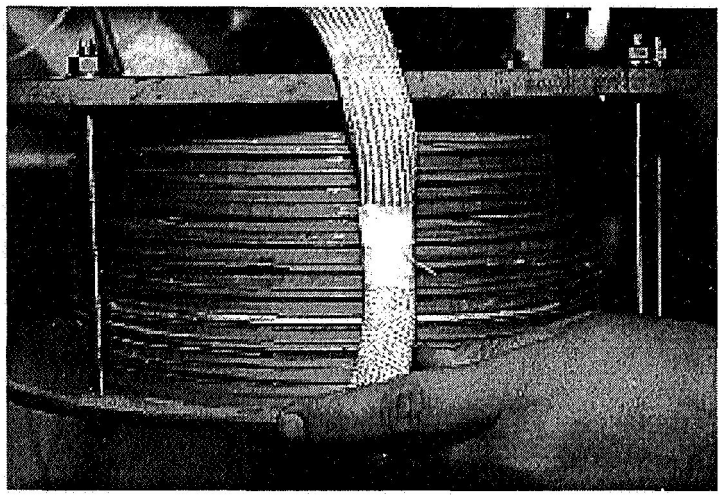

Fig. 3. Test magnet that generated a field of ~3.2T at 4.2K and zero applied field

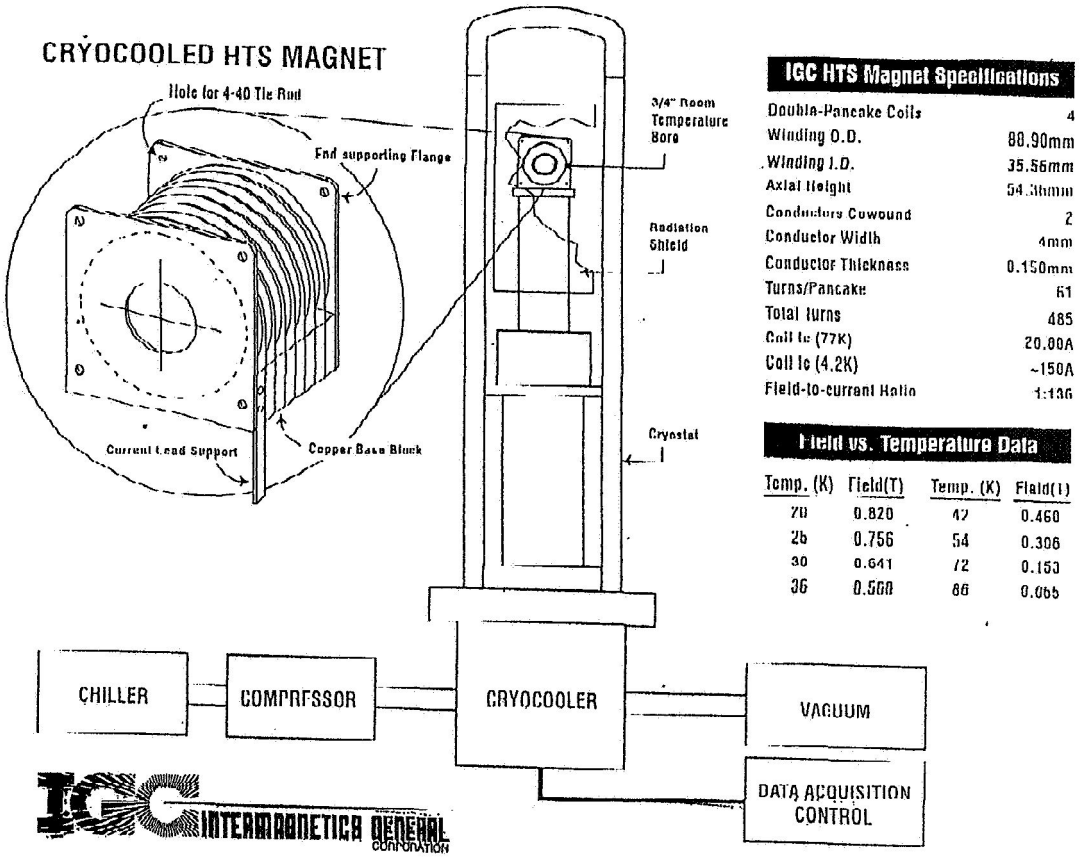

Fig 4. Schematic of a pancake magnet installed in a cryocooler assembly.

Another important advance that has recently been achieved is in the area of active magnetic bearing technology [4]. Using HTS coils fabricated by Intermagnetics, NASA Lewis Research Center has completed a proof-of-feasibility demonstration that showed the use of HTS coils in

high load, active magnetic bearings operating at liquid nitrogen temperature. A homopolar radial bearing wound with Bi-2223 four control coils (about 1,000 Amp-turns each) produced over 890 N (200 lb.) radial load capacity and supported a shaft at 14,000 rpm. It was shown that HTS coils could operate stably with ferromagnetic cores in a feedback controlled system at a current density that was superior to that for Cu in liquid nitrogen. A photograph of the parts that were used to fabricate the system is shown in Figure 5.

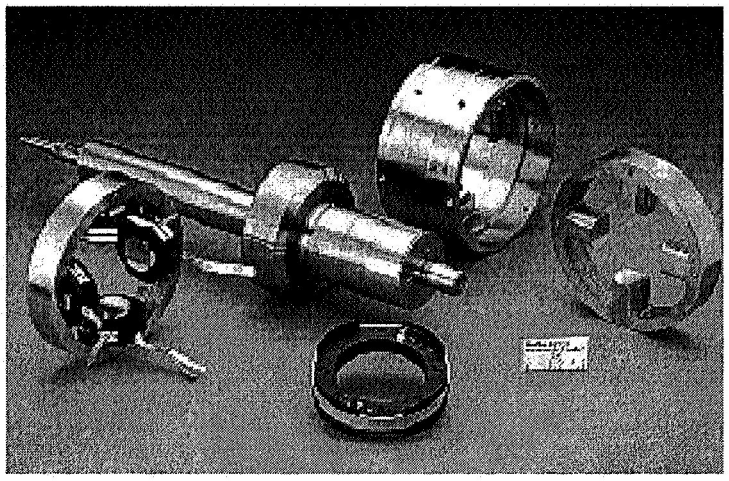

Fig 5. Parts of an active magnetic bearing using HTS control coils and developed by NASA.

The next generation of thallium based HTS conductors is being developed at Intermagnetics [15] for high field, high temperature operation. Both powder-in-tube and thick film approaches are being developed. We have concentrated on single thallium layer compounds mainly the Tl-1223 which is sometimes doped with Pb, Bi or Sr. Table 2 summarizes the performance levels of PIT Tl-1223 mono and multi filament tapes that have been fabricated at Intermagnetics. The highest critical current densities were achieved in tapes fabricated using unreacted precursors. An I_c in excess of 25 A has been achieved in zero field at 77 K in these tapes that correspond to Jc's of over 20,000 A/cm^2. Figure 6 shows the magnetic field dependence of the J_c of a PIT tape that is compared to a dip-coated tape. The Jc of the PIT tapes tend to drop rapidly at low fields but remain constant up to fields of 5 T at 77 K. Work is continuing to improve the characteristics of these materials further.

	Length (m)	I_c (A)	Core J_c (A/cm²)	Overall J_c (A/cm²)
Monofilament				
Pressed	0.04	25	20000	4500
Rolled	0.14	8	8400	1600
Rolled	1.5	6	6300	1200
Multifilament (19)				
Pressed	0.04	16	11000	2500
Pressed (sequential)	0.14	12	12000	2400
Pressed (sequential)	1.0	9.2	9200	1800
Rolled	1.5	8	8000	1600
Rolled	7.2	6.2	6200	1300
Multifilament (37)				
Rolled	1.5	13	13000	2600

Table 2. Summary of transport current properties of short and long mono- and multi- filament Ag-clad TBCCO conductors

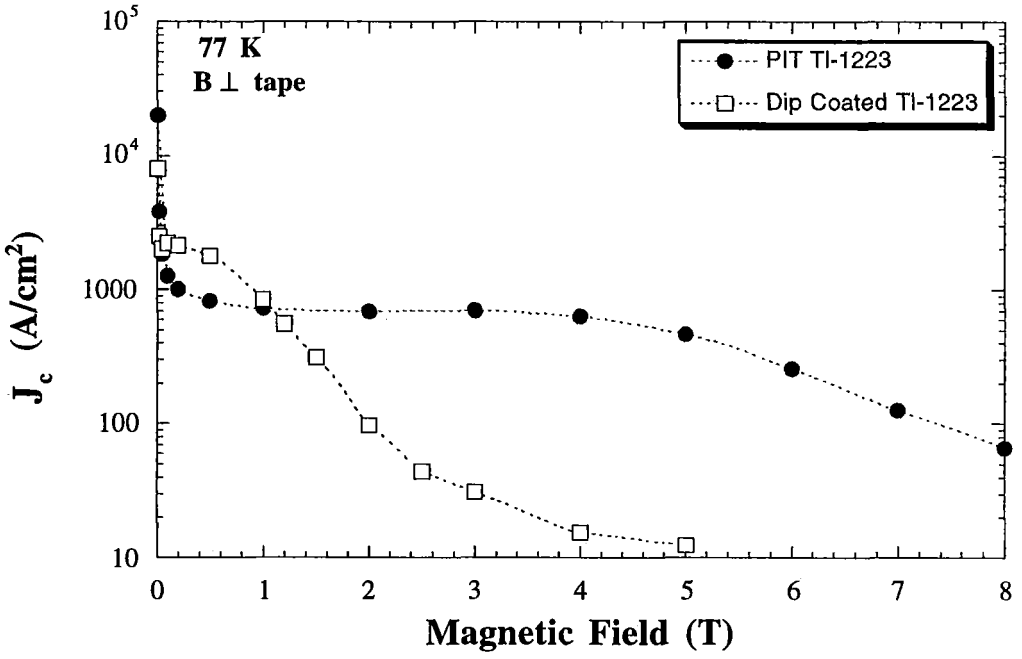

Fig 6. Magnetic field dependence of the current density of Tl-1223 tapes fabricated by the PIT and dip coating approaches.

SUMMARY

High quality mono- and multi filament conductors up to several hundred meters in length have been successfully fabricated by the PIT technique in both the Bi-2223 and Tl-1223 systems.

These conductors have been used to develop HTS superconducting magnets suitable for use in maglev applications. A long length of 1,260 meters of Bi-2223 tape was fabricated and an HTS magnet containing 20 pancake coils generated a self-field of =3.2 T at 4.2 K. A liquid cryogen free HTS magnet has been demonstrated to work effectively and produce a field of 0.8 T at 20 K. Small control coils have been fabricated and used by NASA to develop an active magnetic bearing with ferromagnetic cores that was used to support a 200 lb. radial load rotating at 14000 rpm. Work in developing the next generation HTS conductor based on thallium for higher temperature operation is showing considerable promise. Significant progress has been made in improving the superconducting properties of HTS materials that can potentially be used in a wide variety of maglev and electric power applications.

ACKNOWLEDGMENTS

Work at Argonne National Laboratory, Los Almos National Laboratory and part of the work at Intermagnetics General Corporation is supported by the U.S. Department of Energy (DOE), Energy Efficiency and Renewable Energy, as part of a DOE program to develop electric power technology, under Contract W-31-109-Eng-38.

REFERENCES

1. Sato S, Hikata T, Mukai H, Ueyama M, Shibuta N, Kato T, Masuda T, Nagata M, lwata K, Mitsui T (199 1) *IEEE Trans.* Mag. 27: 1231
2. Flukiger R, Hensel B, Jeremle A, Peiin A, Grivel LC (1993) *Appl. Supercond.* 1: 709
3. Dou S X, Liu H K (1993) Supercond. Scl. Technol. 6: 297
4. Balachandran U, Iyer A N, Haldar P, Hoehn J G, Motowidlo L R, Galinski G (1994) *Appl. Supercond.* 2: 251
5. Li Q, Brodersen K, Hjuler H A, Freltoft T (1993) *Physica* C 217: 36
6. Larbaleister D C, Cal X Y, Feng Y, Edelman H. , Umezawa A, Riley, G N, Carter VV-L, (1993) *Physica* C 221: 229
7. Lelovic M, Krishnaraj P, Eror N G, Balachandran U, (1995) *Physica* C 242: 246
8. Haldar P, Hoehn J G, Motowidlo LR, Balachandran U, Twasa Y, (1994) *Adv. Cryo. Eng.* 40: 313
9. Motowidlo L R, Gregory E, Haldar P, Rice J A, Balugher R D, (1991) *Appl. Phys. Lett.* 59: 736
10. Ekin J W (1983) In : Reed R P, Clark A F (eds) Materials at low temperatures. *American Society of Metals*, Materials Park, Ohio, pp 494-496
11. Dou S X, Liu H K, Guo YC, Bhasale R, Hu Q Y, Babic E, Kusevic I, (1994) *Appl. Supercond.* 2:191
12. Schwartz J, Heuer J K, Goretta K C, Poeppel R B, Guo J, Raban G (1994) *Appl. Supercond.* 2:271
13. Dou S X, Guo Y. C., Yau J., and Liu H. K. *Supercond. Sci. Technol.* (1993) 6:195
14. Brown G.V., DiRusso E., and Provenza A.J., *Proc. of the 1995 ICMC meeting* at Columbus, OH, July 17-21, 1995, to be published in *Adv. in Cryogenic Eng.*
15. Selvamanickam V., et al to be published.

Session 3 -- Vibration Isolation 1/Controls 1

Chairman: David E. Cox
NASA Langley Research Center

POSITIONING AND MICROVIBRATION CONTROL BY ELECTROMAGNETS OF AN AIR SPRING VIBRATION ISOLATION SYSTEM

Katsuhide Watanabe , Weimin Cui , Takahide Haga
Ebara Research Co., Ltd.
2-1 , Honfujisawa 4-chome , Fujisawa-shi , Kanagawa pref. , Japan

Yoichi Kanemitsu
Kyushu University
10-1 , Hakozaki 6-chome , Higashi-ku , Fukuoka-shi , Fukuoka pref. , Japan

Kenichi Yano
Kajima Technical Research Institute
19-1 , Tobitakyu 2-chome , Chofu-shi , Tokyo , Japan

SUMMARY

Active positioning and microvibration control has been attempted by electromagnets equipped in a bellows-type, air-spring vibration isolation system. Performance tests have been carried out to study the effects. The main components of the system's isolation table were four electromagnetic actuators and controllers. The vibration isolation table was also equipped with six acceleration sensors for detecting microvibration of the table. The electromagnetic actuators were equipped with bellows-type air springs for passive support of the weight of the item placed on the table, with electromagnets for active positioning, as well as for microvibration control, and relative displacement sensors. The controller constituted a relative feedback system for positioning control and an absolute feedback system for vibration isolation control. In the performance test, a 1,490 kg load (net weight of 1,820 kg) was placed on the vibration isolation table, and both the positioning and microvibration control were carried out electromagnetically. Test results revealed that the vibration transmission was reduced by 95 %.

INTRODUCTION

Semiconductor manufacturing is making quantum leaps in recent years, consequent to which higher precision is sought in semiconductor manufacturing systems and detection devices. In line with this, measures against vibration occurring in such systems and devices are becoming factors of utmost importance.

Conventional measures against such vibration had mainly consisted of passive type vibration isolation systems featuring air and coil springs. However, such passive systems are inappropriate for *mgal* order vibration levels and low frequency regions. Moreover, swift vibration isolation control is necessary for not only vibration that is transmitted from the floor on which the system is installed, but also for vibration that is generated by the system itself, including vibration that is caused by disturbance in the periphery of the system, such as the vibration from an air conditioner. To satisfy such conditions, studies have been in recent years actively carried out on pneumatic actuators[1], linear motors, piezoelectric actuators, and electromagnetic actuators[2][3], as part of the research and development of active-control vibration isolation systems. A paper by the authors on the development of a vibration isolation system, featuring electromagnetic actuators which use both air springs and electromagnets, had been submitted previously[2]. This paper discusses microvibration isolation achieved by PID control of the air spring pressure, positioning control in the vertical direction, and control of the electromagnetic force by absolute velocity feedback. Such control made it possible to reduce the vibration transmissibility, under a load of 1,250 *kg*, for both horizontal and vertical directions, by 90%. However, as no positioning control was being done in the horizontal direction, and due to influences by the center-of-gravity position when the load was increased, by the property of rubber used for the air spring, and by the unbalanced force generated by the bias electric current, the precise position (attitude) of the table in relation to the floor could not be determined. In the worst case, no control was able to be made due to contact, as the clearance between the electromagnet poles and the yoke was small. Table positioning constituted an important factor when attempting control by electromagnets.

The following discusses active positioning and microvibration control by electromagnets equipped in a bellows-type, air-spring vibration isolation system. The system comprised an isolation table, electromagnetic actuators and controllers. The electromagnetic actuators were equipped with bellows type air springs for passive support of the weight of the item placed on the table, with electromagnets for active positioning, as well as for microvibration control, and displacement sensors for detecting the relative displacement between the table and the floor. The controller constituted a relative feedback system for positioning control and an absolute feedback system for vibration isolation control. Detected relative displacement and absolute acceleration data was applied for feedback control of electromagnets. A performance test was carried out, in which a 1,490 *kg* load (net weight of 1,820 *kg*) was placed on the vibration isolation table, and both the positioning and microvibration control were carried out electromagnetically. Test results revealed that the vibration transmission was reduced by 95 %.

Definition of symbols

G	Center of gravity
F_x , F_y , F_z	Actuator controlling force
F_{xi} , F_{yi} , F_{zi} (i=1 $\sim$ 4)	Controlling force of each actuator
M_α , M_β , M_γ	Controlling force moment
k_{xi} , k_{yi} , k_{zi} (i=1 $\sim$ 4)	Constant of each air spring
c_{xi} , c_{yi} , c_{zi} (i=1 $\sim$ 4)	Damping coefficient of each air spring
x , y , z	Isolation table displacement
α , β , γ	Rotational displacement of isolation table
u , v , w	Floor displacement
ξ , η , ζ	Rotational displacement of floor
m	Mass
I_α , I_β , I_γ	Moment of inertia for each axial rotation
W	Disturbance vector
k_e	Constant determined by number of coil windings, magnetic permeability, & cross-sectional area of magnetic pole
i_1 , i_2	Excitation current of both opposing electromagnets
h_1 , h_2	Void of both opposing electromagnets
h_0 , i_0	Void under balanced condition (center of void) & bias current
x_r , i_c	Micro-fluctuating part under balanced condition

TEST APPARATUS

Microvibration Isolation System

Figure 1 shows the configuration of the microvibration isolation system, while Table 1 shows the specifications of the same. The main components shown are the isolation table, on which a device subject to vibration isolation is placed, four electromagnetic actuators and controllers. The table has an overhanging configuration due to its relation with the center-of-gravity of the device which would be placed on it. A total of six acceleration sensors are installed on the table for detecting vibration on the table.

Figure 2 shows the analog control system used for vibration isolation. Displacement sensors detect relative displacement, in the horizontal and vertical directions, between the isolation table, supported by air springs, and the floor. There are two feedback systems. One is a relative feedback system by which relative displacement data is fed back for positioning of the isolation table. The other is an absolute feedback system by which absolute acceleration data, detected on the isolation table, is fed back for vibration isolation control in the horizontal and vertical directions. Electromagnets are used for the control. The absolute acceleration speed is detected by six acceleration sensors installed on

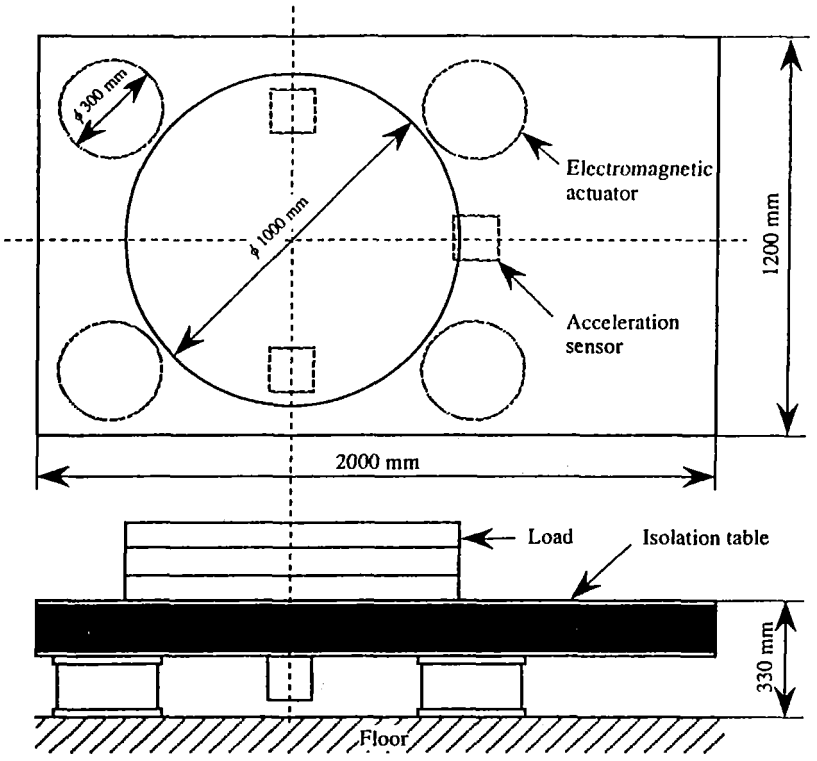

Figure 1. Configuration of microvibration isolation system.

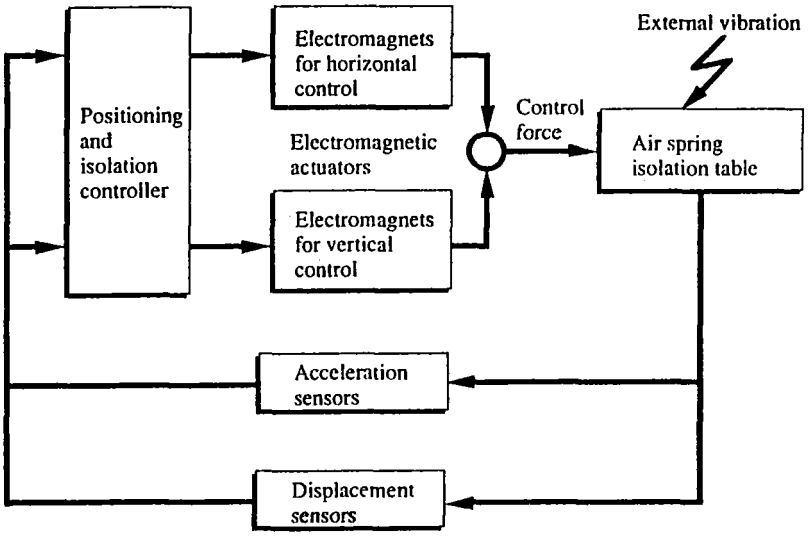

Figure 2. Components of control system.

Table 1. Specification of microvibration isolation system

Mass	Total	Table	Load	Actuator
	$1820kg$	$210kg$	$1490kg$	$120kg$
Size	Total		Actuator	
	$900mm \times 1200mm \times 150mm$		$\phi\ 300mm \times 150mm$	
Electromagnet		Max. magnetic foce	Current	
	Hrizontal	$177N$	$3.8A$	
	Vertical	$1209N$	$10A$	
Air spring		Standard load capacity	Natural frequency	
	Hrizontal	—	—	
	Vertical	$530kg$ $(0.5Mpa)$	$2.7Hz$	

the isolation table, and is coordinate-transformed into accelcration signals for six degrees of freedom.

Electromagnetic Actuators

Figure 3 shows a cross-section view of the electromagnetic actuator. It contains a bellows-type air spring for supporting the item placed on the table; DC electromagnets which generate magnetism in the vertical and horizontal directions, for positioning the isolation table supported by an air spring, also for isolating vibration; displacement sensors for detecting relative displacement between the installation floor and the isolation table. The air spring, compact yet capable of excellent support, was installed in the center of the actuator, around which were installed electromagnets.

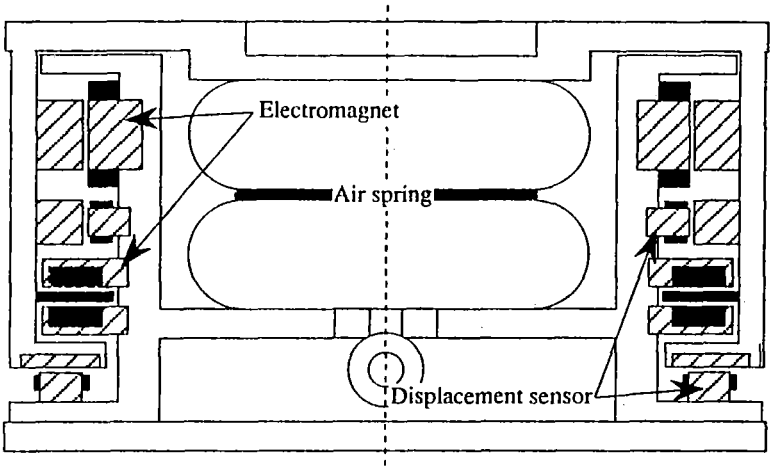

Figure 3. Cross-sectional view of electromagnetic actuator.

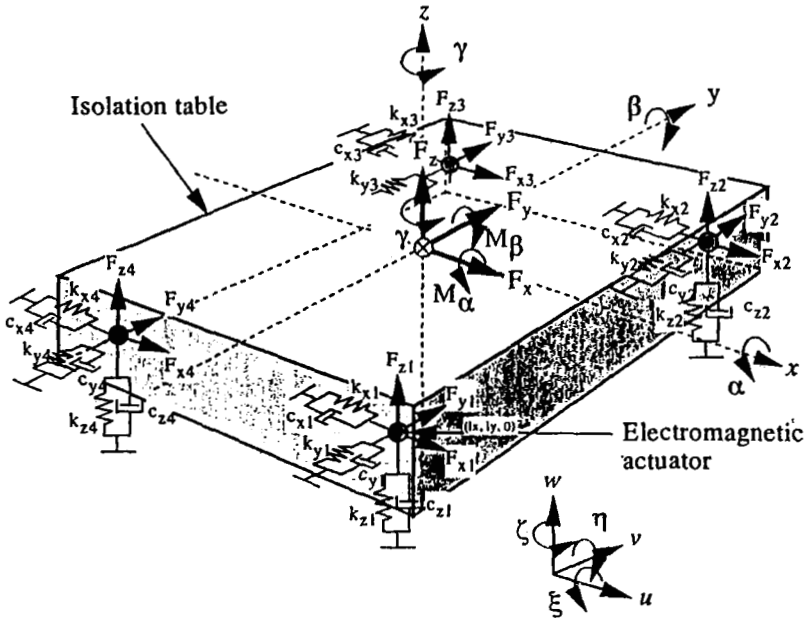

Figure 4. Model of microvibration isolation system.

As for the characteristics of the air spring and electromagnets, detailed studies had already been made by the authors[2].

MODELS

Isolation System Model

Figure 4 shows the isolation system model. A balanced situation is shown, with the isolation table being supported by four electromagnetic actuators. The directions of each electromagnet force matches the coordinate axes, the working points being inside the x and y plane surfaces (plane surfaces including the center of gravity), identical to those of the air springs.

This model was made assuming that an ideal rigid body was completely non-coupled supported, making it possible to design a control system for controlling each degree of freedom independently. Consequently, the model featured the following:

1. Inertial coupling was eliminated by matching the coordinate axes with the inertial main axes of the system.

2. The center of elasticity and elastic main axis of the four air springs were matched with the center of gravity and the coordinate axes.

From the above, the equation of motion for the isolation system is the following Equation 7, by way of Equations 1 - 6.

$$
\begin{aligned}
m\,\ddot{x} + C_x\,\dot{x} + K_x\,x &= F_x + W_x && (1)\\
m\,\ddot{y} + C_y\,\dot{y} + K_y\,y &= F_y + W_y && (2)\\
m\,\ddot{z} + C_z\,\dot{z} + K_z\,z &= F_z + W_z && (3)\\
I_\alpha\,\ddot{\alpha} + C_\alpha\,\dot{\alpha} + K_\alpha\,\alpha &= M_\alpha + W_\alpha && (4)\\
I_\beta\,\ddot{\beta} + C_\beta\,\dot{\beta} + K_\beta\,\beta &= M_\beta + W_\beta && (5)\\
I_\gamma\,\ddot{\gamma} + C_\gamma\,\dot{\gamma} + K_\gamma\,\gamma &= M_\gamma + W_\gamma && (6)\\
M\,\ddot{X} + C\,\dot{X} + K\,X &= F + W && (7)\\
X &= [x\ y\ z\ \alpha\ \beta\ \gamma\ ]^T\\
M &= diag\,[m_x\ m_y\ m_z\ I_\alpha\ I_\beta\ I_\gamma]\\
C &= diag\,[C_x\ C_y\ C_z\ C_\alpha\ C_\beta\ C_\gamma]\\
K &= diag\,[K_x\ K_y\ K_z\ K_\alpha\ K_\beta\ K_\gamma]\\
F &= [F_x\ F_y\ F_z\ M_\alpha\ M_\beta\ M_\gamma]^T\\
W &= [W_x\ W_y\ W_z\ W_\alpha\ W_\beta\ W_\gamma]^T
\end{aligned}
$$

Model of Electromagnets

The magnetic attraction force of the controlling electromagnets is expressed in Equation 8. If this force is linearized in the proximity of a balanced condition, it becomes as expressed in Equation 9.

$$
\begin{aligned}
f &= k_e\left\{\left(\frac{i_1}{h_1}\right)^2 - \left(\frac{i_2}{h_2}\right)^2\right\} && (8)\\
& i_1 = i_0 + i_c\ ,\ i_2 = i_0 - i_c\\
& h_1 = h_0 - x_r\ ,\ h_2 = h_0 + x_r\ ,\ x_r = x - x_0\\
& i_0 \gg i_c\ ,\ h_0 \gg x_r\\
f &= k_e\left\{4\frac{i_0^2}{h_0^3}X_r - 4\frac{i_0}{h_0^2}i_c\right\}\\
&= k_u x_r + k_c i_c && (9)
\end{aligned}
$$

Thus, the controlling force, vector F, becomes

$$
\begin{aligned}
F &= K_u\,(X - X_0) + K_c\,I_c && (10)\\
K_u &= diag\,[K_{ux}\ K_{uy}\ K_{uz}\ K_{u\alpha}\ K_{u\beta}\ K_{u\gamma}]\\
K_c &= diag\,[K_{cx}\ K_{cy}\ K_{cz}\ K_{c\alpha}\ K_{c\beta}\ K_{c\gamma}]\\
I_c &= diag\,[I_x\ I_y\ I_z\ I_\alpha\ I_\beta\ I_\gamma]^T
\end{aligned}
$$

The controlling electric current is distributed to each of the 12 electromagnets. If the control matrix is set as $B(6 \times 12)$

$$\begin{aligned} I_c &= B\, I_{ca} \\ I_{ca} &= diag\,[i_{x1}\ i_{y1}\ i_{z1}\ i_{x2}\ i_{y2}\ i_{z2}\ i_{x3}\ i_{y3}\ i_{z3}\ i_{x4}\ i_{y4}\ i_{z4}]^T \end{aligned} \tag{11}$$

DESIGNING OF THE CONTROL SYSTEM

The control system was designed so as to achieve both the positioning control and vibration-isolation control of the vibration isolation system. The control system for increasing the vibration control performance, versus direct disturbance, featured the same design as that for the vibration isolation performance.

As for positioning control, the magnetic poles were positioned in the center of void of the electromagnets, and attitude control was carried out for the isolation table. This control system was constituted as a relative feedback system, by which relative displacement data, of detected displacement between the installation floor and the isolation table, were fed back by a PID controller. The vibration isolation control system was constituted as an absolute feedback system, by which absolute speed on the isolation table was fed back. The controllers are thus

$$G_r(s) = [g_{rij}(s)]\ ,\ g_r = -\left(k_P + \frac{k_I}{s} + k_D(s)\right) \tag{12}$$

$$\begin{aligned} G_a(s) &= [g_{aij}(s)]\ ,\ g_a = -k_a(s) \\ &\quad (i = 1 \sim 6\ ,\ j = 1 \sim 6) \end{aligned} \tag{13}$$

Regarding Equation 7 as a relative system, let us consider a servo system controlled by controller $G_r(s)$ and which follows up command value X_{ref}. The servo performance becomes better along greater $G_r(s)$, as the transfer function of the closed loop is

$$\frac{X_r}{X_{ref}} = \frac{K_c\, G_r(s)}{Ms^2 + Cs + K - (K_u + K_c\, G_r(s))} \tag{14}$$

Considering an absolute feedback system which includes a controller $G_r(s)$ for positioning control, regarding disturbance vector W in Equation 7 as the disturbance caused by floor vibration X_0, we get

$$\begin{aligned} M\ddot{X} + C\dot{X} + KX &= F + C\,\dot{X}_0 + K\,X_0 \\ &\quad X_0 = [u\ v\ w\ \xi\ \eta\ \zeta]^T \end{aligned} \tag{15}$$

Accordingly, the equation of movement, when Laplace transformed, becomes as Equation 16, and the vibration transmissibility becomes as Equation 17. The $G_r(s)$ and $G_a(s)$ were designed so that the desired vibration isolation performance could be obtained, as much as possible from the low frequency side. This involved making the controller operate at extremely low frequencies, and eliminating differentiating elements ($k_D = 0$).

$$\begin{aligned} Ms^2 X(s) + Cs X(s) + K X(s) &= Cs X_0(s) + K X_0(s) + F(s) \\ &= Cs X_0(s) + K X_0(s) + [K_u (X(s) - X_0(s)) \\ &\quad + K_c \{G_r(s) (X(s) - X_0(s)) + G_a(s) X(s)\}] \qquad (16) \end{aligned}$$

$$\frac{X(s)}{X_0(s)} = \frac{Cs + K - (K_u + K_c G_r(s))}{Ms^2 + Cs + K - \{K_u + K_c (G_r(s) + G_a(s))\}} \qquad (17)$$

It is acknowledged here that the $G_r(s)$ and $G_a(s)$ constitute a trade-off relationship, for satisfying both the positioning and the vibration isolation performance simultaneously.

PERFORMANCE TESTS

Figure 5 (a), (b), and (c) show displacement data of the isolation table for directions X, Y, and Z, respectively. Each case represents a start with no positioning control and a duration where positioning control was applied. The isolation table was able to be positioned within 50 μm of the void center of the electromagnets by this positioning control, justifying the validity of the attitude control.

Figures 6 and 7 show the isolation performance and vibration transmissibility, respectively, of cases where control was being made. It is acknowledged from these figures that vibration of the isolation table (for directions X, Y, and Z) was able to be reduced to 1/20 of that on the installation floor, and that a performance almost equal to that indicated in the simulation was attained.

Figures 8 (a) and (b) show the vibration control performance versus impulse disturbance. The case of 8 (a), where passive vibration isolation was implemented, indicated a slow transient damping characteristics. In contrast, the case of 8 (b), where active vibration isolation was implemented, indicated a convergence within a short time.

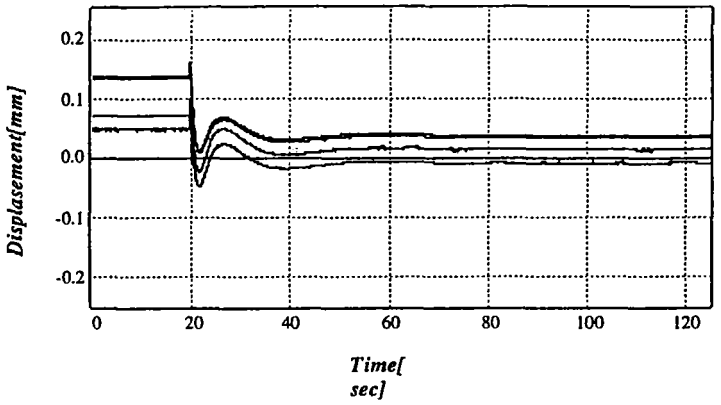

(a). X direction.

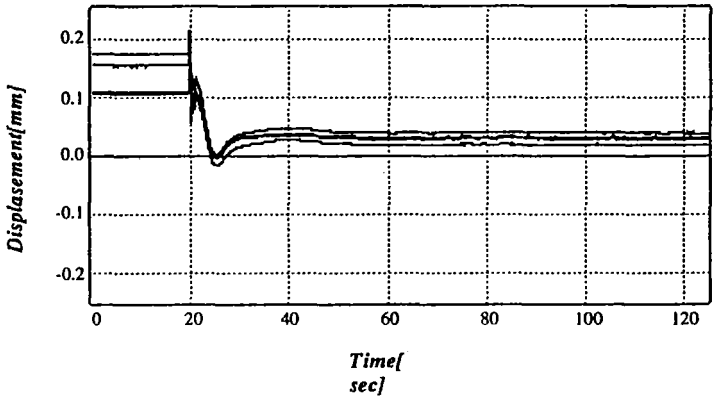

(b). Y direction.

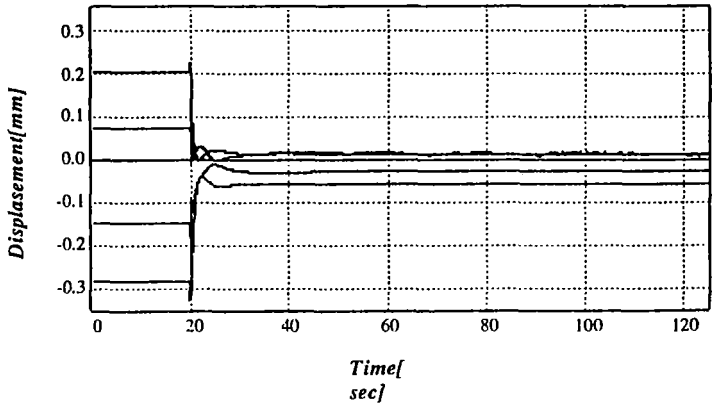

(c). Z direction.

Figure 5. Displacement of isolation table.

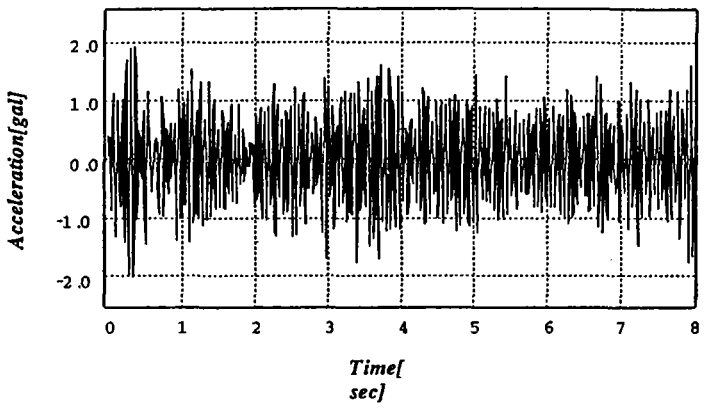

(a). Acceleration of floor.

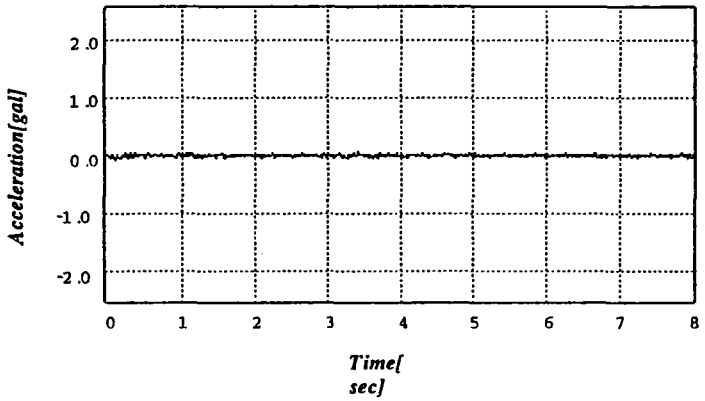

(b). Acceleration of isolation table (Simulation).

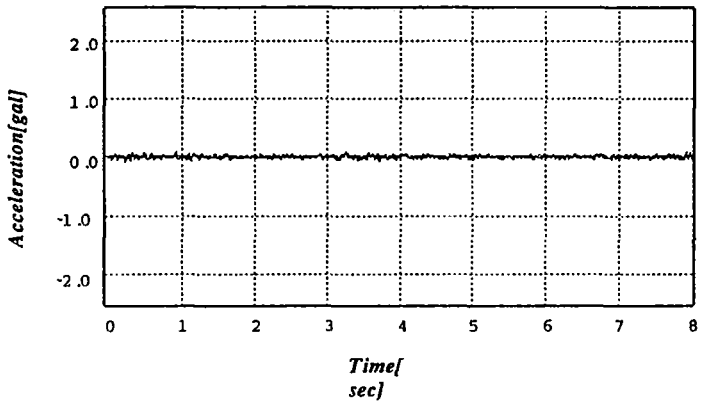

(c). Acceleration of isolation table.

Figure 6-1. Isolation performance of microvibration isolation system in horizontal(X) direction.

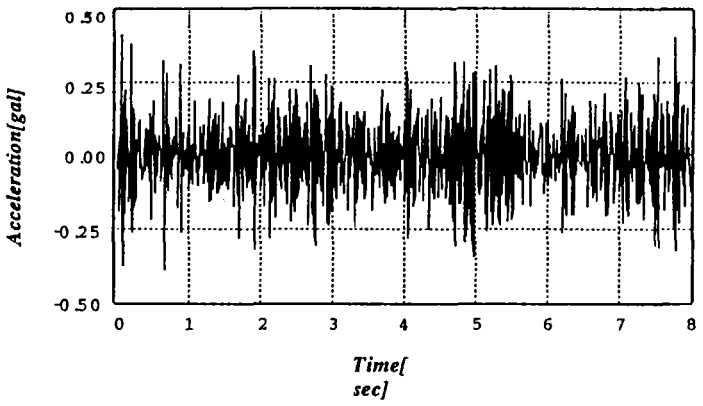

(a). Acceleration of floor.

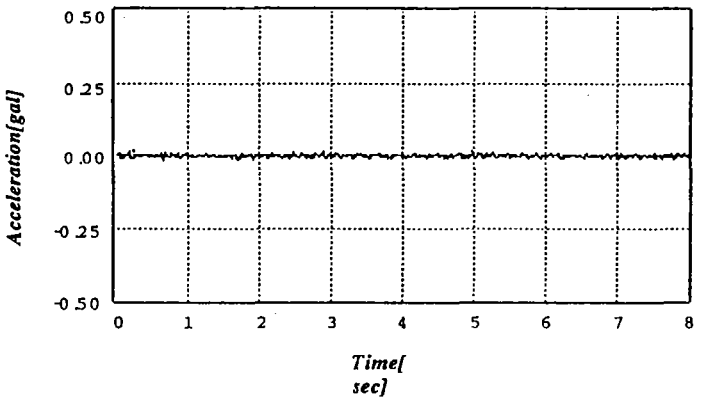

(b). Acceleration of isolation table (Simulation).

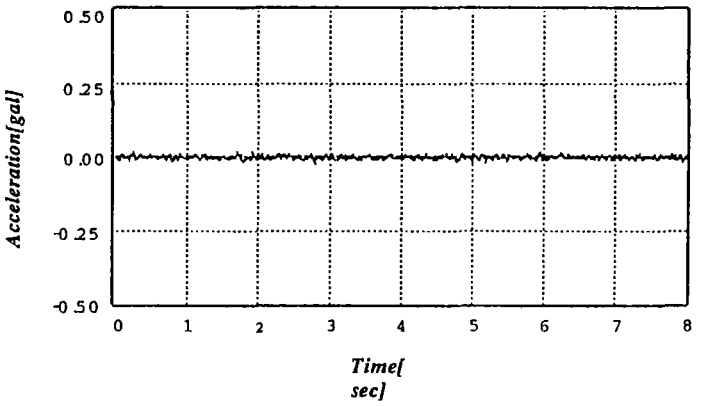

(c). Acceleration of isolation table.

Figure 6-2. Isolation performance of microvibration isolation system in vertical(Z) direction.

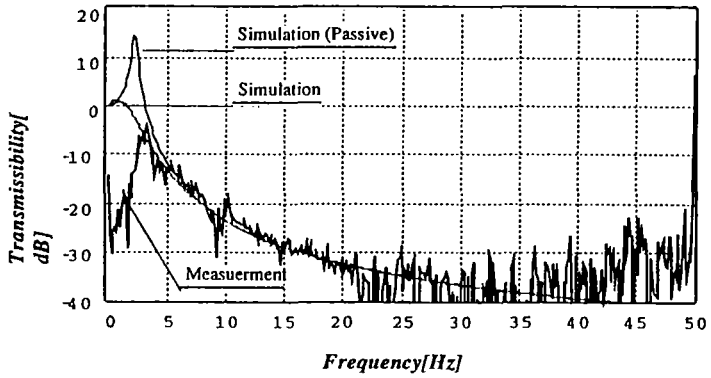

(a). Horizontal(X) direction.

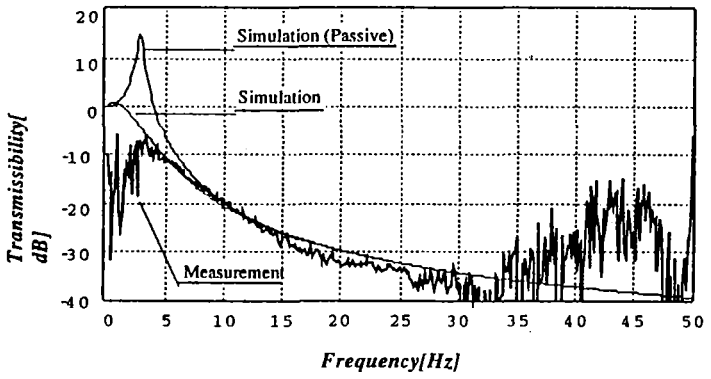

(b). Vertical(Z) direction.

Figure 7. Transmissibility of microvibration isolation system.

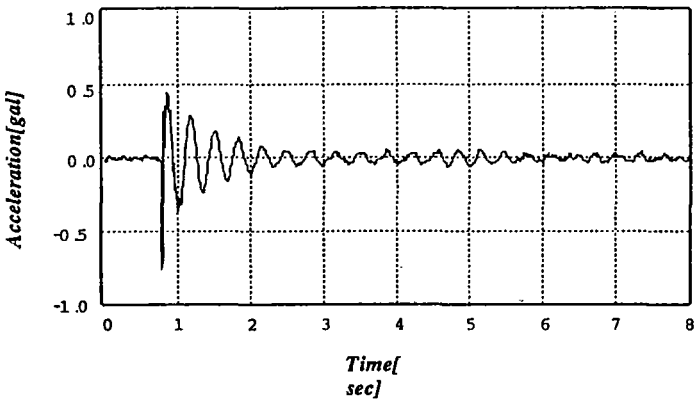

(a). Passive.

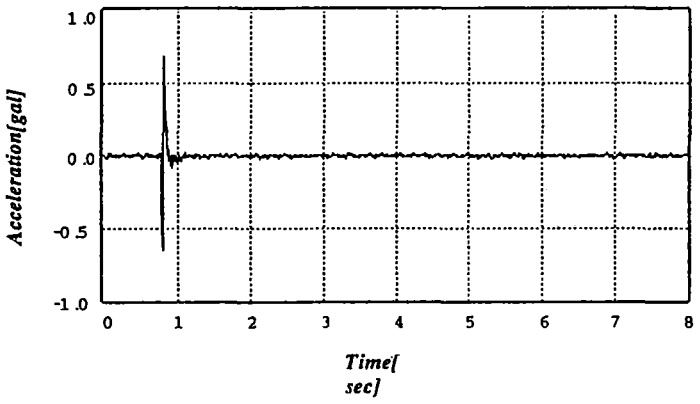

(b). Active.

Figure 8. Impulse response on the table.

CONCLUSION

Active positioning and microvibration control has been attempted by electromagnets equipped in a bellows-type, air-spring vibration isolation system. Performance tests have been carried out to access the control method and study the vibration isolation performance. The following are results obtained from this research.

1. An isolation table, passively supported by bellows-type, air-springs, was controlled by electromagnets, the result of which was an achievement of both stable positioning control and microvibration isolation.

2. Vibration transmissibility, in the horizontal and vertical directions, was able to be reduced to below 1/20 in performance tests. Vibration control was also possible for external disturbances that had direct effect.

REFERENCES

1. Yasuda, M., Osaka, T., Ikeda, M., Study of Active Isolation Added Feedforward Control, Trans. of JSME, 58-552C (1992), 2381.

2. Cui, W., Nonami, K., Kanemitsu, Y., Watanabe, K., Active Microvibration Control System Using Both Air Springs and Magnetic Bearings (1st Report: Control Performance with Absolute Velocity Feedback),Trans. of JSME, 60-575C (1994),2227.

3. Watanabe, K., Kanemitsu, Y., Yano, K., Mizuno, T., Research on Electromagnetically Levitated Vibration Isolation System (2nd Report: Isolation Performance on 3-D Vibration Isolation System), Proceedings of JSME,No.930-39 (1993-7), 42.

Active Vibration Isolation of Microgravity Experiments With Spring Umbilicals Using An Electrodynamic Actuator

B. B. Banerjee
Precision Magnetic Bearing Systems, Inc.
Cohoes, New York

P. E. Allaire
University of Virginia
Charlottesville, Virginia

C. M. Grodsinsky
St. Gobain/Norton Industrial Ceramics Corp.
Newbury, Ohio

ABSTRACT

Microgravity experiments will require active vibration isolation in the low to mid frequency range of 0.1 Hz to 10 Hz. Approximately two orders of acceleration reduction (40 dB) will be required. Previous works have reported results for accelerations transmitted through the umbilical. This paper describes experimental and theoretical results for vibration isolation in one dimension (horizontal) where the simulated experiment is connected to the spacecraft by a spring umbilical. The experiment consisted of a spacecraft (shaker), experiment (mass), umbilical, accelerometer, control electronics, and Lorentz actuator. The experiment mass was supported in magnetic bearings to avoid any stiction problems. Acceleration feedback control was employed to obtain the vibration isolation. Three different spring umbilicals were employed. Acceleration reductions on the order of 40 dB were obtained over the frequency range of 0.1 Hz to 10 Hz. Good agreement was obtained between theory and experiment.

INTRODUCTION

Microgravity science experiments have often yielded poor results due to the presence of wideband vibration sources aboard the orbiter. These vibration disturbances are produced by astronaut movements, on-board machinery, thruster firings and other unavoidable factors, as noted by Nelson [1]. Typical acceleration environments on Skylab [2,3] and Spacelab [4] have been found to be of the order of 10^{-3} g_0 (g_0 is the gravitational constant for earth), while experiment specifications have been in the range of 10^{-5} to 10^{-6} g_0. Figure 1 shows the amplitude and frequency for a typical microgravity vibration specification (monochromatic) and an anticipated acceleration environment [5]. Note that a comparison of these environmental levels and the specifications indicate the need for vibration isolation on the order of 40 dB over the intermediate frequency range from 0.1 to 10 Hz.

The degree of isolation that can be obtained onboard the orbiter is fundamentally constrained by the actuator stroke. Knospe and Allaire have characterized the limits of microgravity isolation for both monochromatic sinusoidal [6] and stochastic [7] vibration disturbances. The actuator stroke most seriously affects the isolation of the payload from low frequency (in the quasi-steady range below 0.1 Hz) orbiter disturbances due to gravity gradient and atmospheric drag forces. Fortunately, most microgravity experiments do not require isolation in this range. For mid to high frequency vibrations (above 10 Hz) microgravity experiments can be isolated using passive techniques. It should be noted that passive devices cannot isolate microgravity payloads from both direct disturbances, where the disturbance is on the experiment platform, and indirect disturbances, those transmitted through the umbilicals or other connections to the spacecraft.

Further, payload isolation over the low to intermediate range cannot be achieved using passive isolation. Typically, the stiffness of umbilicals results in a corner frequency too high for effective passive isolation [1]. These issues are discussed in more detail in Knospe, et. al [8] where feedback controller design issues are explored. If the transfer function G(s) represents the plant, a loop shaping approach is proposed where the control loop feedback transfer function H(s) must be chosen so that G(s)H(s) is large. Also, gain and phase margins for system stability are discussed.

The choice of actuator to be employed is important. Non-contacting magnetic actuators, utilizing electromagnets or permanent magnets, are the best actuator solution for vibration isolation in the low to intermediate frequency range [9]. One reason for the use of non-contacting actuators is the avoidance

of friction and stiction associated with contacting actuators. Electrostatic levitation has also been considered for this application but typically, the size and force requirements preclude their use [10].

Several isolation systems have been built by researchers in the past decade. A single-axis electromagnetic actuator, similar to a magnetic thrust bearing, has been described by Havenhill and Kral [11]. Flux feedback was employed to accurately control the force produced independently of the air gap. Due to shaker and accelerometer limits, the lowest recorded frequency of their measured data was 5 Hz. Also umbilicals were not considered. This concept was extended to a six degree of freedom system called the Fluids Experiment Apparatus Magnetic Isolation System (FEAMIS) as reported in [12]. The system did not isolate disturbances below 2 Hz and did not consider umbilicals.

Grodsinsky [13] has reported a six degree of freedom active isolation system that employs relative and inertial sensors. A digital feedforward control system activated nine electromagnetic actuators with a stroke of ±0.3 in (0.76 cm). Another six degree of freedom system was developed by Fenn and Johnson [14] with a stroke of 0.4 in (1.002 cm). Nonlinear controls were also tested for a one degree of freedom testbed. Hibble, et. al [15] reported a Magnetic Isolation and Pointing System (MIPS) for the Space Station's Payload Pointing System. This system met the requirement of 0.01 g_0. The effect of umbilicals were not considered in any of these isolation systems.

Several researchers have employed a theoretical approach to examine the use of feedback control for active vibration isolation. Knospe, et. al [8] discussed the control issues of microgravity vibration when umbilicals are included and examined stability robustness. An investigation of acceleration control to reject disturbances caused by the compliance of an umbilical was considered by Jones, et. al [16]. The umbilical was assumed to have stiffness but not damping. As umbilical stiffness increased, the microgravity isolation quality deteriorated, as expected. Acceleration control was found to improve disturbance rejection significantly as compared to position control but at a cost of larger required gaps and forces. Hampton, et. al [17] presented a method for the design of robust feedback controllers using modern control synthesis methods. Constant state feedback gains and a quadratic cost function was employed used with an inverse frequency weighting approach which attenuates low frequency accelerations, below 50 Hz, by two orders of magnitude more than high frequency accelerations.

The purpose of this paper is to report on one dimensional long stroke microgravity vibration isolation results in the presence of spring umbilicals. Both a theoretical treatment and experimental results are presented. The objectives were three

fold: 1) construction of a one dimensional experimental test rig for microgravity vibration isolation, 2) achievement of mirocravity levels (1 to 10 μg_0) with spacecraft excitation levels on the order of 1 mg_0, and 3) a study of spring umbilical effects.

EXPERIMENTAL SET-UP

Figure 2 shows a one dimensional schematic diagram of a spacecraft (base), experiment (mass), umbilical with stiffness and damping coefficients, and an active isolator. A cylindrical mass, representing the experiment, is connected via springs, representing experiment umbilicals, to a shaker, representing the vibrating orbiter. An electrodynamic actuator is used to supply an active force creating the desired payload vibration isolation from disturbances produced by the shaker [18]. Figure 3 is a block diagram of the test rig. A non-contacting radial magnetic bearing support system ensures that the cylinder is free to move horizontally along its axis without stiction [19]. A large concrete base was employed to support the experiment and isolate the experiment from external building excitations.

The isolated mass (microgravity experiment) is a solid cylindrical mass with dimensions 58.4 cm (23 in) long and 9.6 cm (3.8 in) weighting 34 kg (75 lb). The shaker had a continuous force rating of 133.4 N (30 lb) in the frequency range from 0.1 to 20 Hz. It was operated in the voltage mode producing a constant velocity motion of the armature up to approximately 8 Hz where it had a resonance. Spring umbilicals were used to simulate experiment umbilicals. These are connected to both the experiment (mass) and spacecraft (shaker).

In the orbiter, there is a very high impedance at mid to low frequencies between the experiment and the orbiter due to the very large mass of the orbiter. The electrodynamic shaker employed in the laboratory experiment does not have a high impedance at low frequencies. Thus, in the laboratory experiment, the actuator was connected to an inertial plate, rather than directly to the shaker, to simulate experiment conditions in space. Connection directly to the shaker would change the impedance of the shaker armature and thus strongly influence the measurements.

The active isolation system consists of an accelerometer, accelerometer amplifier, controller, transconductance amplifier, and Lorentz actuator. A low frequency accelerometer, a Sundstrand Q-Flex QA-700, was used to sense the acceleration of the experiment. Another one was employed to monitor the acceleration of the shaker armature. These accelerometers use a quartz flexure seismic suspension system with a measured level of noise at 0.204 μg_0 and a signal to noise ratio of 4.9 at 1 μg_0. An acceleration amplifier is supplied with the unit. The analog

controller incorporates a continuously adjustable gain and some other components described in more detail in the later sections. The controller output drives a linear, bipolar transconductance amplifier. The one dimensional Lorentz actuator provides a force which is linear in response to the applied current. Because of the low frequencies involved, a long stroke was needed. The actuator was designed with a stroke of 2 inches. Experimental measurements showed that the stroke was nearly independent of position [18], as shown in Fig 4.

ACTIVE ISOLATION THEORY

The single degree of freedom isolation system described above for the spacecraft/experiment is considered here. The equation of motion for the system is

$$m\,\ddot{x} + c\,(\dot{x}-\dot{u}) + k(x-u) = F_d - F_a \qquad (1)$$

The experiment is subject to accelerations due to their transmission through the connecting umbilicals from the spacecraft as well as direct force excitation F_d by a source on the experiment platform. Taking the Laplace transform yields

$$(m\,s^2 + c\,s + k)\,X(s) = (c\,s + k)\,U(s) + F_d(s) - F_a(s) \qquad (2)$$

We are interested in accelerations rather than displacements yielding

$$\frac{(m\,s^2 + c\,s + k)}{s^2}\,\ddot{X}(s) = \frac{(c\,s + k)}{s^2}\,\ddot{U}(s) - F_a(s) \qquad (3)$$

where the double dot over the symbol denotes acceleration. Figure 5 shows a block diagram of the control loop.

The direct disturbance force F_d is important for microgravity isolation and is treated in several works as discussed in the introduction so it will not be discussed in this paper. Thus the $F_d(s)$ term is set to zero. The open loop transfer function between the shaker (orbiter) acceleration and mass (microgravity experiment) acceleration (also called the open loop acceleration transmissibility) T_{OL} is

$$T_{OL} = \frac{\ddot{X}_{OL}(s)}{\ddot{U}(s)} = \frac{c\,s + k}{m\,s^2 + c\,s + k} \tag{4}$$

where X_{OL} denotes the open loop experiment displacement. In dimensionless pole-zero form this becomes

$$T_{OL} = \frac{2\zeta\omega_n\left(s+\frac{\omega_n}{2\zeta}\right)}{\left(s+2\zeta\omega_n-2i\omega_n\sqrt{1-\zeta^2}\right)\left(s+2\zeta\omega_n+2i\omega_n\sqrt{1-\zeta^2}\right)} \tag{5}$$

where the denominator is easily factored.

With acceleration feedback, the actuator force is given by

$$F_a(s) = H(s)\,\ddot{X}(s) \tag{6}$$

Substituting in Eq. (3) and solving for the closed loop transfer function (closed loop acceleration transmissibility) T_{CL} yields

$$T_{CL} = \frac{\ddot{X}_{CL}(s)}{\ddot{U}(s)} = \frac{c\,s + k}{[m + H(s)]\,s^2 + c\,s + k} \tag{7}$$

The closed loop transmissibility indicates the effectiveness of the feedback control loop in reducing the transmitted accelerations through the umbilicals. The objective is to find H(s) so that the magnitude of T_{CL} is small (at least -40 dB) in the frequency range where isolation is needed, 0.1 to 10 Hz.

Another effectiveness measure of the microgravity isolation system is the reduction ratio R of the open loop experiment acceleration to the closed loop experiment acceleration. R has the form

$$R = \frac{\ddot{X}_{OL}(s)}{\ddot{X}_{CL}(s)} = \frac{[m + H(s)]\,s^2 + c\,s + k}{m\,s^2 + c\,s + k} \tag{8}$$

This indicates how much improvement in the experiment acceleration level is achieved through active feedback control. Here the objective is to make R large, at least 100 (+40 dB), in the frequency range of 0.1 to 10 Hz. Note that the reduction ratio R indicates the improvement obtained with active control,

it does not directly indicate whether the overall isolation objective has been achieved.

FEEDBACK LOOP

The actuator force F_a is produced by a feedback loop which is examined next. The elements in the feedback loop are: 1) accelerometer, 2) controller circuit, 3) transconductance amplifier, and 4) Lorentz actuator.

An accelerometer and its associated amplifier can be considered a pure gain in this frequency range with the voltage/acceleration constant K_a. The analog controller has the transfer function

$$\frac{V_c(s)}{V_a(s)} = \frac{K_c}{(1 + \tau_1 s)^2} \tag{9}$$

Here, K_c is the gain constant and the denominator represents a second order low pass filter, necessary to avoid exciting lightly damped high frequency modes of the space platform/experiment, with time constant τ_1 which has the value of 0.0072 sec. For the frequency range of interest, the transconductance amplifier has the gain constant K_t

$$\frac{I(s)}{V_c(s)} = K_t \tag{10}$$

and the Lorentz actuator has the gain constant α. The actuator provides a force which is very linear with respect to current and insensitive to displacement [18,19].

Combining all of these terms, the overall feedback transfer function is

$$\frac{F_a(s)}{\ddot{X}(s)} = \frac{V_a(s)}{\ddot{X}(s)} \frac{V_c(s)}{V_a(s)} \frac{I(s)}{V_c(s)} \frac{F_a(s)}{I(s)} \tag{11}$$

for the feedback part of the loop. Substituting for the individual components yields

$$\frac{F_a(s)}{\ddot{X}(s)} = H(s) = \frac{K_a K_c K_t \alpha}{(1 + \tau_1 s)^2} = \frac{K}{(1 + \tau_1 s)^2} \tag{12}$$

where all of the constants can be condensed into one acceleration feedback gain K. In the actual control loop some additional compensation was employed at high frequency to avoid exciting high frequency modes of the system. The additional compensation was necessary to increase the system gain and phase margins [18] but did not affect the isolation properties in the frequency range of interest. Thus, due to length restrictions in the paper, a detailed discussion of that aspect is not presented here.

REDUCTION RATIO

The final open loop/closed loop acceleration ratio is given by

$$R = \frac{R_{num}}{R_{den}} \tag{13}$$

where the numerator is

$$R_{num} = m\,\tau_1^2\,s^4 + (2\,m\,\tau_1 + c\,\tau_1^2)\,s^3 + (m + K + 2\,c\,\tau_1 + k\,\tau_1^2)\,s^2 + (c + 2\,k\,\tau_1)\,s + k \tag{14}$$

and the denominator is

$$R_{den} = m\,\tau_1^2\,s^4 + (2\,m\,\tau_1 + c\,\tau_1^2)\,s^3 + (m + 2\,c\,\tau_1 + k\,\tau_1^2)\,s^2 + (c + 2\,k\,\tau_1)\,s + k \tag{15}$$

This is the theoretical model of the active isolation system.

EXPERIMENTAL MEASUREMENTS

Experimental data was obtained by exciting the shaker with pseudo-random noise, band limited to 12.5 Hz. High resolution auto spectra were obtained providing 512 lines of frequency resolution. An averaged spectra were taken in each case presented with one hundred auto spectra per averaged plot.

The objective of the experimental measurements was to obtain acceleration auto spectra with a spring umbilical in place to determine the acceleration reduction and transmission ratios. A flat top window weighting function was chosen on the analyzer to make the time waveform be exactly periodic within the sample record length. The recorded plots are somewhat "jittery" due to

the nature of the shaker armature motion excited by the broadband pseudo-random noise input signal.

Three different cylindrical springs made of carbon steel were tested as umbilicals. The were connected from the shaker armature to the experiment mass. Each spring was in tension initially and throughout the testing in each case. It is assumed that the levitation magnetic bearings have negligible axial stiffness and damping because the simulated experiment mass was very long compared with the magnetic bearing length - there were no magnetic end effects.

The first case involved a spring umbilical with stiffness of 876 N/m (5 lb/in), verified by independent measurement. The overall gain constant was 9,000 and the calculated natural frequency ω_n, as in Eq. (5), equal to 0.81 Hz, and the damping ratio was equal to zero for the case of a spring. Figure 6 shows the acceleration of the mass with the controller off (top line) and on (bottom line) where the vertical axis is plotted in terms of the acceleration in decibels compared to 1 g_0. The upper line indicates spacecraft milligravity levels averaging about -80 dB (10^{-4} g_0) while the lower line indicates experiment microgravity levels approximately -120 dB (10^{-6} g_0).

Figure 7 plots the acceleration transmissibility T_{CL}, the ratio of experiment acceleration to spacecraft acceleration as transmitted by the spring umbilical, for the same case as above. With feedback control, over 30 dB of isolation is achieved over the entire frequency range from 0.1 to 10 Hz. Figure 8 shows a plot of the experimental reduction ratio R obtained from the ratio of the closed loop experiment acceleration to the open loop experiment acceleration. The reduction ratio is approximately 30 dB in the low frequency range, from 0.1 to 0.3 Hz and increases to approximately 50 dB in the range from 1 to 10 Hz. The theoretical results, based upon Eq. (16), are also plotted for comparison purposes, with relatively good agreement.

The second spring had a stiffness of 1226 N/m (7 lb/in). The overall controller gain constant was set at 9,000 and the calculated natural frequency of ω_n of 0.96 Hz. As with the first spring umbilical, the reduction is approximately 30 dB in the low frequency range and approximately 50 dB at higher frequencies [18]. Figure 9 gives the experiment/spacecraft acceleration transmissibility which is close to that for the first spring case. Figure 10 shows the reduction ratio for this case. The peak of reduction occurs at approximately 1 Hz. At 0.1 Hz, R = 26 dB and at 10 Hz R = 48 dB indicating that the desired reduction of 40 dB has been obtained for most of the frequency range. An overall controller gain constant of 9,000 produced an effective ratio of dynamic mass to actual mass of approximately 31.6 (30 dB).

The third spring had stiffness of 1488 N/m (8.5 lb/in). A gain of 9,000 was used again and the calculated natural frequency ω_n of 1.05 Hz. Acceleration plots and reduction ratio plots were generated for these cases [18]. They are rather similar to the previous two cases so they are not presented here. Figure 11 shows both the experimental transmissibility ratio and theoretical results from Eq. (16) for comparison purposes. Again, the results are in good agreement.

CONCLUSIONS

Microgravity experiments will require active vibration isolation in the expected acceleration environment for spacecraft. This paper has demonstrated the reduction of milli-g spacecraft acceleration levels, transmitted to the experiment via spring umbilicals, to μ-g_0 levels. A magnetic bearing supported experiment mass was constructed to simulate a zero-g environment and avoid stiction problems that would be encountered with other support systems. An acceleration feedback control system using an accelerometer, controller, and non-contacting actuator to implement the control force was developed. Experimental results were presented demonstrating over 30 dB attenuation for a tethered microgravity experiment in the low to mid frequency range of 0.1 to 10 Hz. This is the first combined theoretical/experimental study that the authors are aware of to carry out such isolation as a function of different umbilicals.

Three different spring umbilicals were used in the study, with spring stiffnesses of 876, 1226, and 1488 N/m (5, 7, and 8.5 lbf/in). Accelerations of the simulated spacecraft were at milli-g levels averaging about -80 dB (10^{-4} g_0) due to shaker excitations. With the controller on, experiment accelerations were at microgravity levels of approximately -120 dB (10^{-6} g_0). These isolation levels were obtained for all of the three spring umbilicals tested. The controller attained an average level of transmissibility reduction of two orders of magnitude over the frequency range from 0.1 to 10 Hz with somewhat lower levels in the lower end of this frequency range. The controller also attained reduction ratios averaging approximately 40 dB over the same frequency range. A linear theoretical model of the system was developed and agreed reasonably well with the experimental results. It is expected that this model could be used to design microgravity controllers in general, if umbilical nonlinearities are not too large.

ACKNOWLEDGEMENTS

This work was funded in part by NASA Lewis Research Center under a grant monitored by the late Joseph Lubomski. This paper is dedicated to his memory.

NOMENCLATURE

c	Umbilical Damping
F_a	Actuator Force
F_d	Disturbance Force
H	Feedback Transfer Function
I	Actuator Current
k	Umbilical Spring Stiffness
K	Acceleration Feedback Gain
K_c	Controller Gain
K_t	Transconductance Amplifier Gain
m	Experiment Mass
R	Reduction Ratio
s	Complex Frequency
T	Acceleration Transmissibility
u	Spacecraft Displacement
V_a	Accelerometer Voltage
V_c	Controller Voltage
x	Experiment Displacement
α	Lorentz Actuator Constant
τ	Controller Time Constant
ω_n	Natural Frequency = $(k/m)^{1/2}$
ζ	Damping Ratio = $c/2m\omega_n$

REFERENCES

1. Nelson, E. S., "An Examination of Anticipated g-Jitter on Space Station and Its Effect on Materials Processes," NASA TM-103775, April (1991).

2. Teledyne Brown Engineering, "Low Acceleration Characterization of Space Station Environment," Report No. SP85 MSFC 2928, October, (1985).

3. Chase, T. L., "Report on Micro-g Measurements for Space Shuttle Experiments," NASA Lewis Research Center, Cleveland, Ohio, December (1985).

4. Hamacher, H., Jilg, R., and Merbold, U., "Analysis of Microgravity Measurements Performed During D1," 6th European Symposium on Materials Sciences Under Microgravity Conditions," Bordeau, France, December 2-5, (1986).

5. Hoshi, Seiko, "Summary of NASDA Acitivities in Vibration Isolation Technology," Proceedings of the International Workshop on Vibration Isolation Technology for Microgravity Science Applications, NASA Lewis Research Center, Cleveland, Ohio, April 23-25, (1991).

6. Knospe, C. R. and Allaire, P. E., "Limitations on Vibration Isolation for Microgravity Space Experiments," Journal of Space Craft and Rockets, Vol. 27, No. 6, pp. 642-646, (1990).

7. Knospe, C. R., and Allaire, P. E., "Limitations on the Isolation of Stochastic Vibration for Microgravity Space Experiments," Journal of Spacecraft and Rockets, Vol. 28, No. 2, pp. 229-237, (1991).

8. Knospe, C. R., Hampton, R. D., and Allaire, "Control Issues of Microgravity Vibration Isolation," Acta Astronautica, Vol. 25, No. 11, pp 687-697, (1991).

9. Grodsinsky, C. M. and Brown, G. V., "Nonintrusive Inertial Vibration Isolation Technology for Microgravity Space Experiments," NASA TM-102386, January (1990).

10. Watkins, J. L., Jackson, H. W., and Barmatz, "Microwave Dieletrophoretic Levitation in Microgravity," NASA Technical Support Package for NASA Tech Briefs, Vol. 17, No. 10, Item No. 70, October (1993).

11. Havenhill, D. D., and Kral, K. D., "Payload Isolation Using Magnetic Suspension," AAS 85 014, Annual AAS Guidance and Control Conference, Keystone Coloroda, Feb 2-6, (1985).

12. Allen, T. S., Havenhill, D. D., and Kral, K. D., "FEAMIS: A Magnetically Suspended Isolation for Space Based Materials Processing," AAS 86 017, Annual AAS Guidance and Control Conference, Keystone, Colorado, Feb. 1-5, (1986).

13. Grodsinsky, C., "Vibration Isolation Technology Development to Demonstration," International Workshop on Vibration Isolation Technology for Microgravity Science Applications, NASA Lewis Research Center, Cleveland, Ohio, April (1991).

14. Fenn, R., and Johnson, B., "A Six Degree of Freedom Lorentz Force Vibration Isolator with Nonlinear Control," International Workshop on Vibration Isolation Technology for Microgravity Science Applications, NASA Lewis Research Center, Cleveland, Ohio, April (1991).

15. Hibble, W. P., Wolke, P. J., and Smith, M., "A Magnetic Isolation and Pointing System for the Astrometric Telescope Facility," Workshop on Magnetic Suspension Technology, NASA Langley, Hampton, VA, Feb 2-4, (1988).

16. Jones, D. I., Owens, A. R., Owen, R. G., and Roberts, G., "Microgravity Isolation Mount: Design Report," Technical Note No. BTN 009, University of North Wales, School of Electronic Engineering, Bangor, Gwynedd, Sept (1989).

17. Hampton, R. D., Grodsinski, C. M., Allaire, P. E., Lewis, D. W., and Knospe, C. R., "Optimal Microgravity Vibration Control Isolation: An Algebraic Introduction," Journal of the Astronautical Sciences, Vol. 40, No. 2, April-June, pp. 241-259, (1992).

18. Banerjee, B. B., "Active Vibration Isolation of Microgravity Experiments with Umbilicals Using Magnetic Actuators," Ph. D. Thesis, University of Virginia, (1994).

19. Banerjee, B. B., and Allaire, P. E., "Design of a Long-Stroke Noncontact Electrodynamic Actuator for Active Vibration Isolation", NASA Third International Conference on Magnetic Suspension Technology, Tallahassee, Florida, December 13-15, (1995).

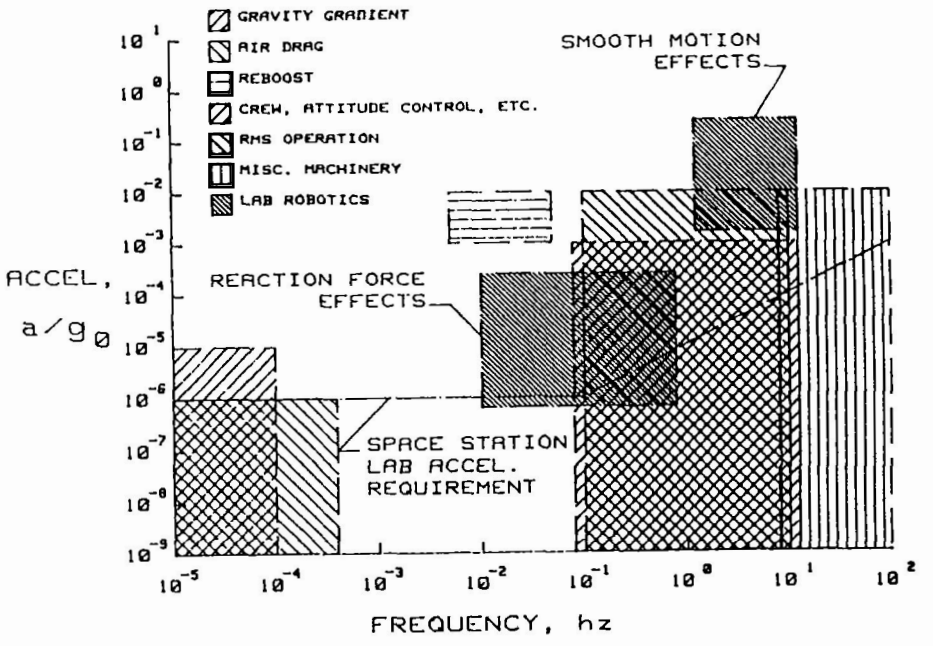

Figure 1. Typical Microgravity Experiment Requirements and Anticipated Acceleration Environment

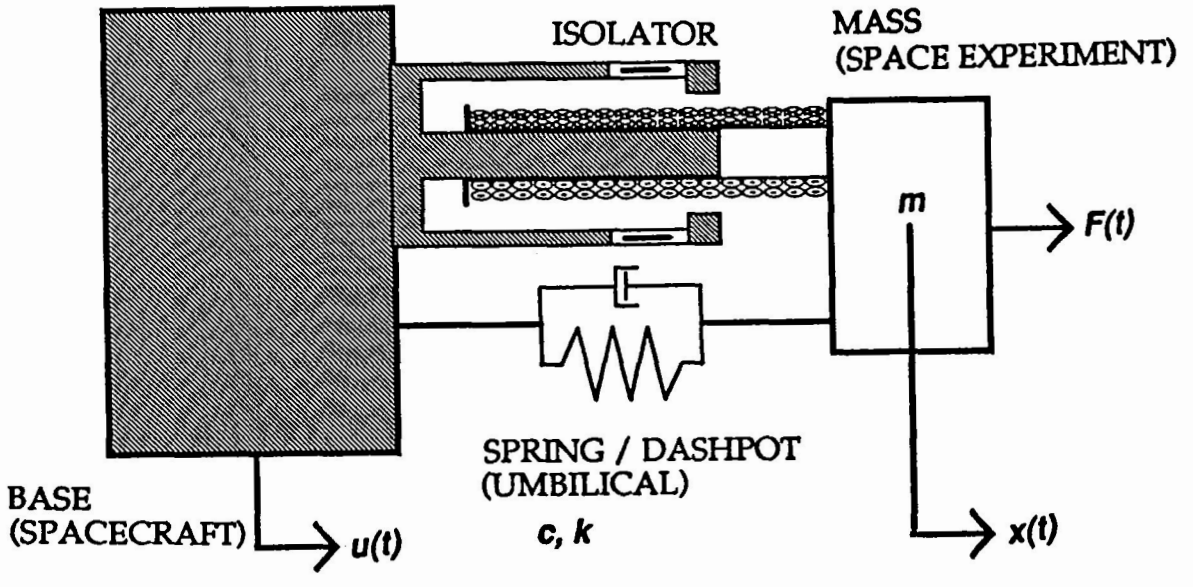

Figure 2. One Dimensional Acceleration Isolation Test Rig for Microgravity Experiments with an Umbilical

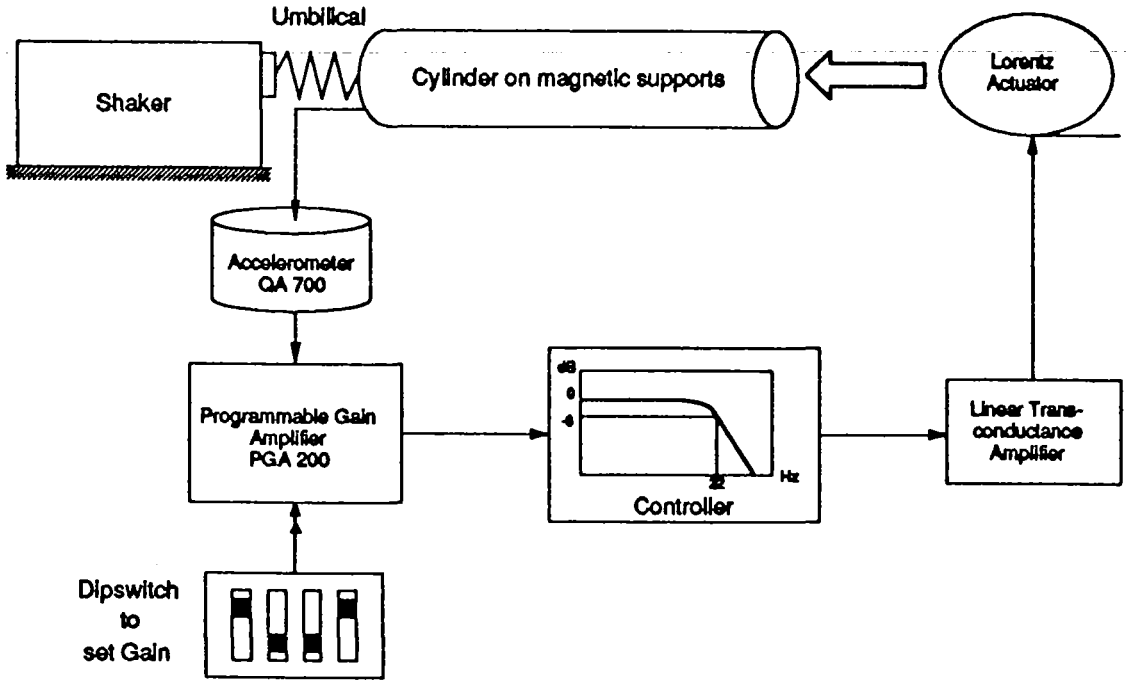

Figure 3. Block Diagram of Microgravity Isolation Test Rig

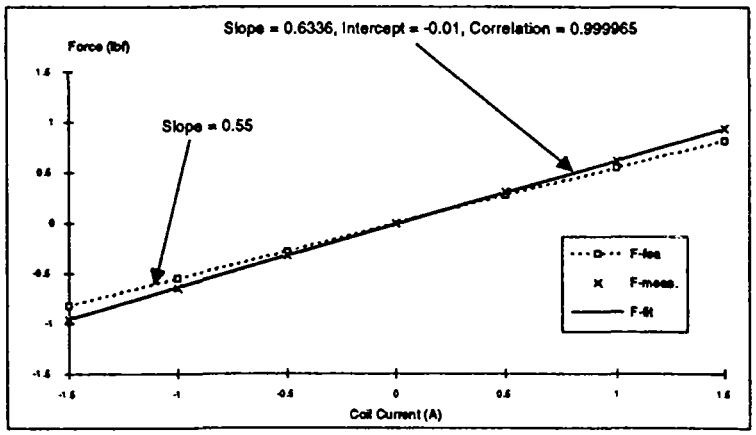

Figure 4. Force vs. Current In Lorentz Actuator of Microgravity Isolation Test Rig

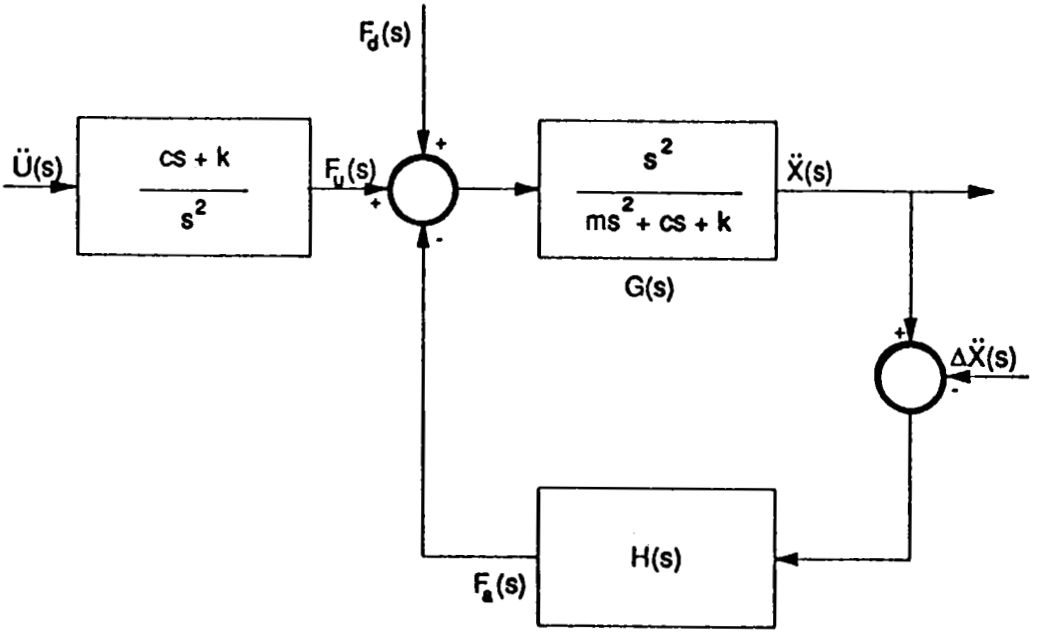

Figure 5. Control Loop Block Diagram

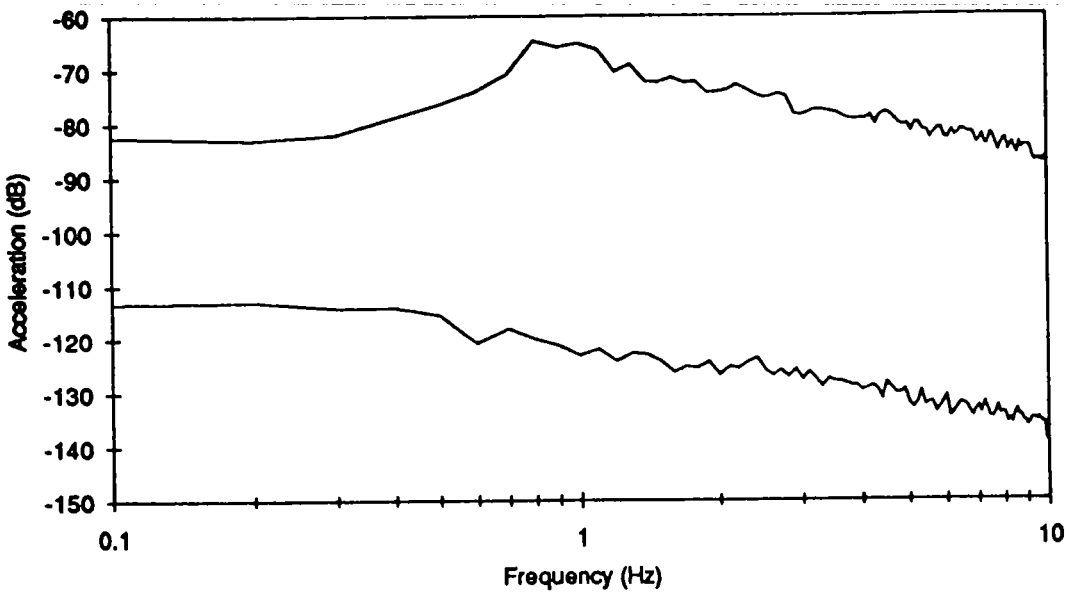

Figure 6. Microgravity Experiment Accelerations without Isolation Controller (Top Line) and with Isolation Controller (Bottom Line) for Umbilical Spring Stiffness of 876 N/m (5 lbf/in). Note: 0 dB equals 1.0 g_0 and -120 dB equals 1.0 μg_0.

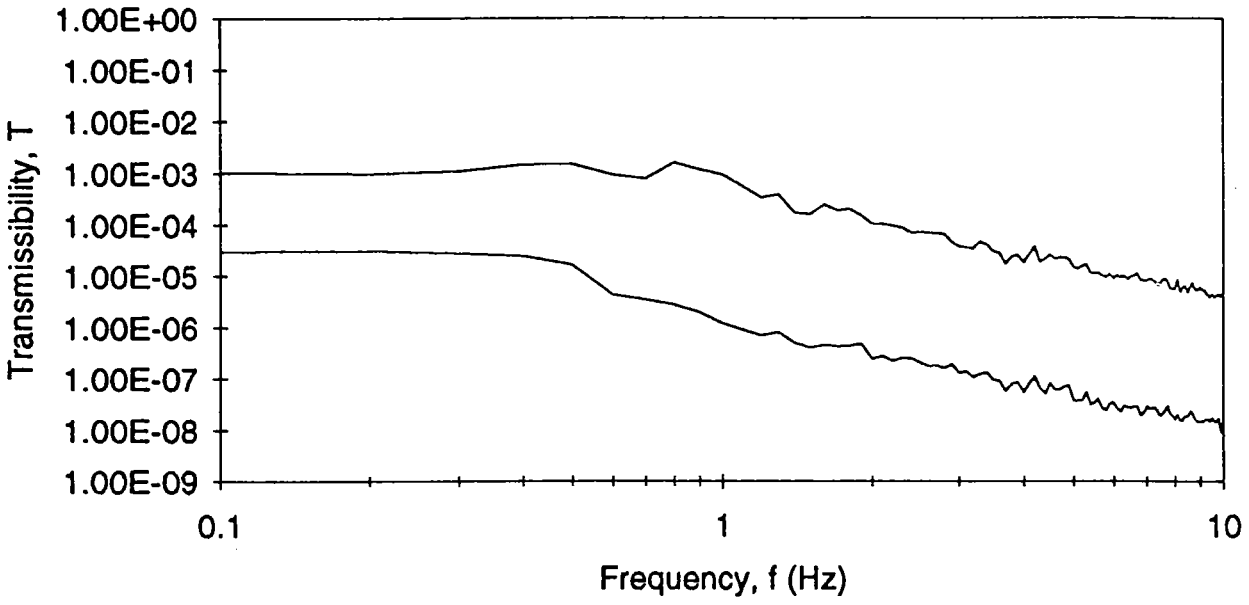

Figure 7. Microgravity Experiment Transmissibility Between Spacecraft and Experiment without Isolation Controller (Top Line) and with Isolation Controller (Bottom Line) for Umbilical Spring Stiffness of 876 N/m (5 lbf/in).

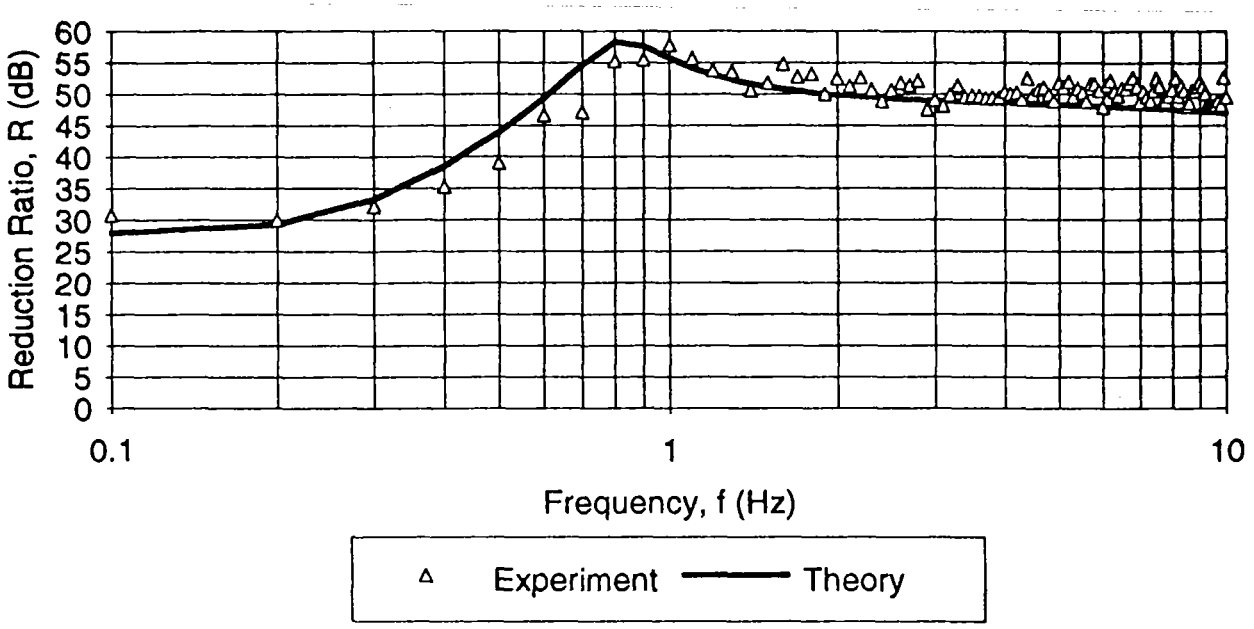

Figure 8. Microgravity Reduction Ratio for Experiment with Isolation Controller vs. Frequency for Umbilical Spring Stiffness of 876 N/m (5 lbf/in).

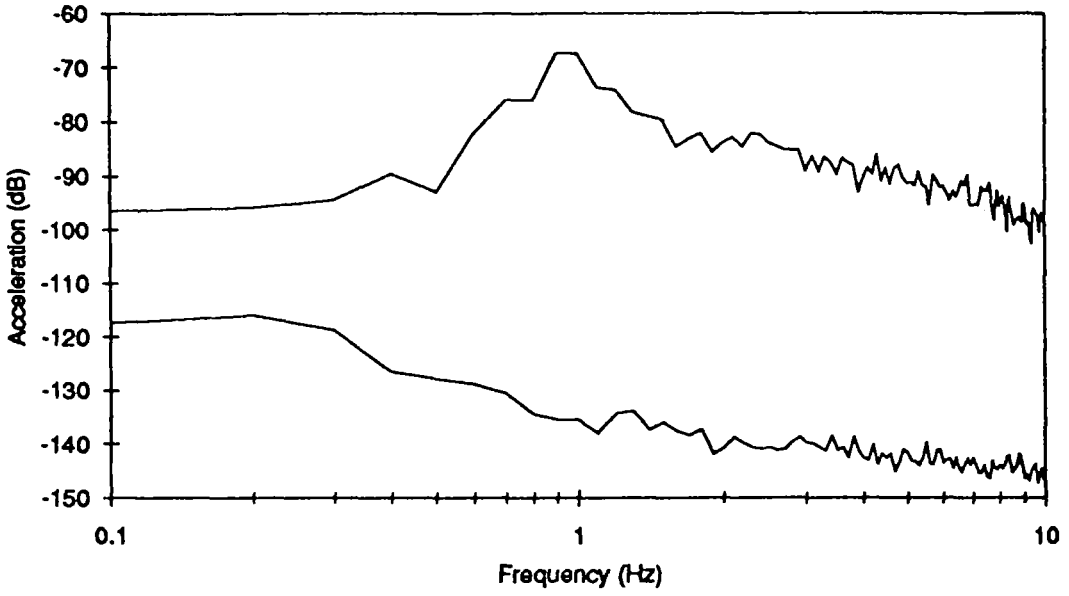

Figure 9. Microgravity Experiment Accelerations without Isolation Controller (Top Line) and with Isolation Controller (Bottom Line) for Umbilical Spring Stiffness of 1226 N/m (7 lbf/in). Note: 0 dB equals 1.0 g_0 and -120 dB equals 1.0 μg_0.

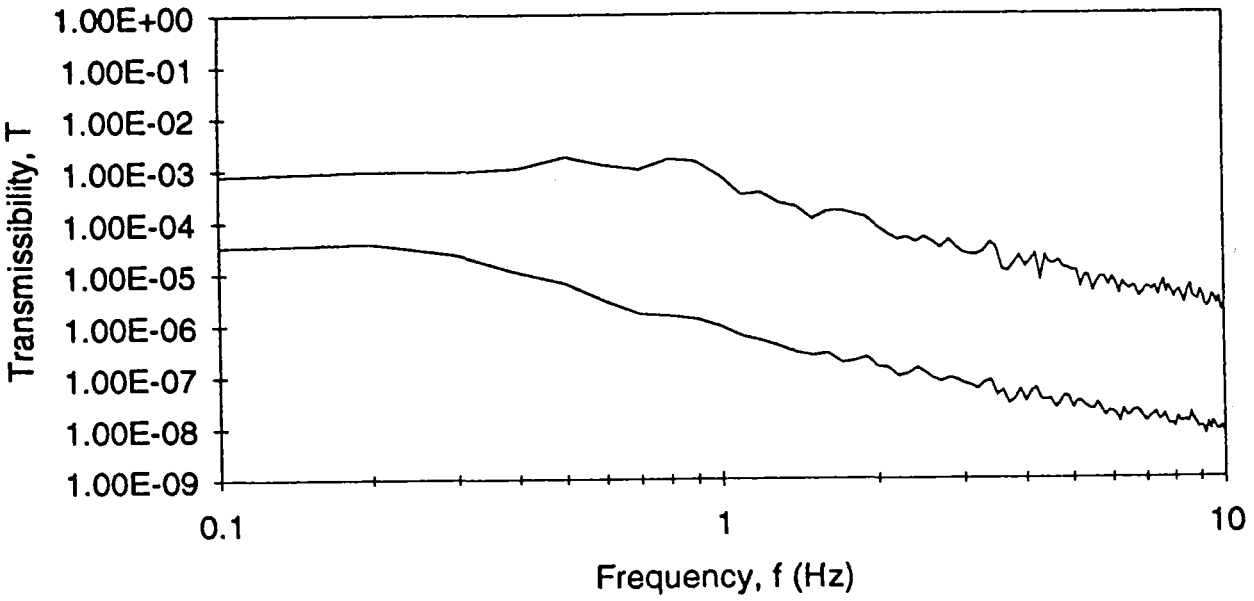

Figure 10. Microgravity Experiment Transmissibility Between Spacecraft and Experiment without Isolation Controller (Top Line) and with Isolation Controller (Bottom Line) for Umbilical Spring Stiffness of 1226 N/m (7 lbf/in).

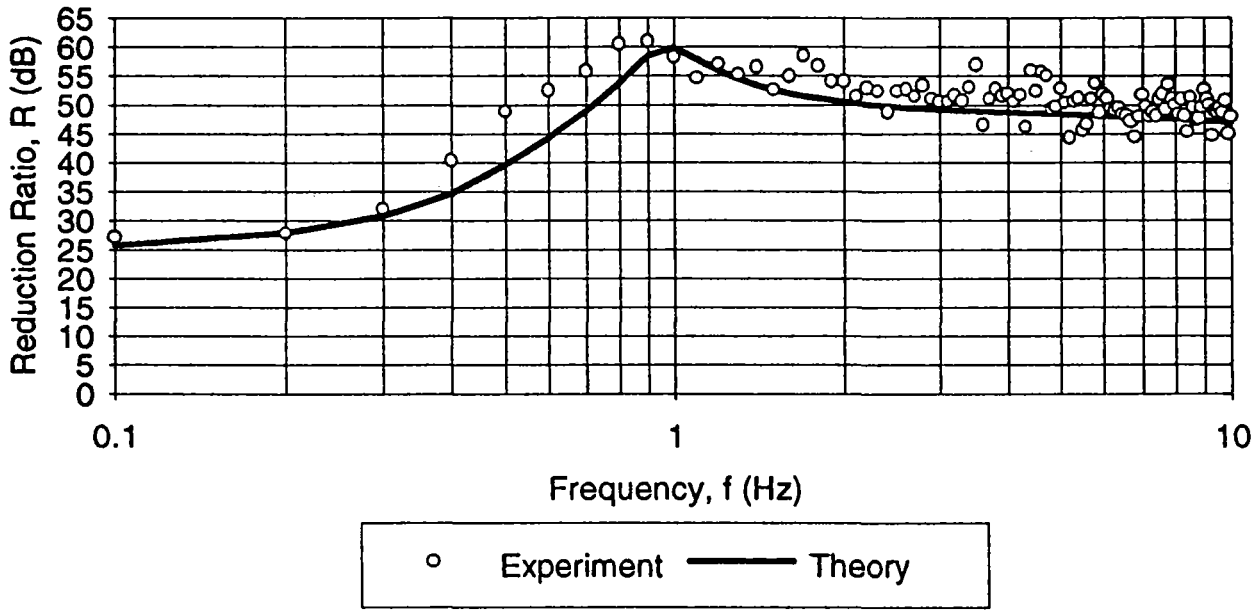

Figure 11. Microgravity Reduction Ratio for Experiment and with Isolation Controller for Umbilical Spring Stiffness of 1226 N/m (7 lbf/in).

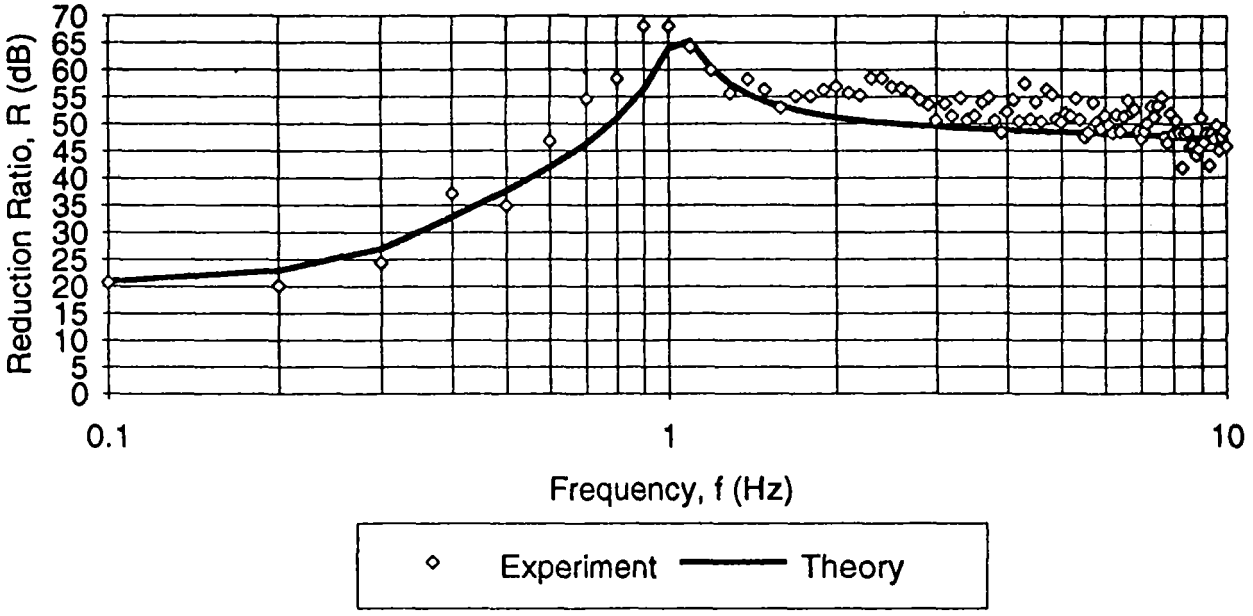

Figure 12. Microgravity Reduction Ratio for Experiment with Isolation Controller for Umbilical Spring Stiffness of 1488 N/m (8.5 lbf/in).

FEEDBACK LINEARIZATION IN A SIX DEGREE-OF-FREEDOM MAG-LEV STAGE

Stephen J. Ludwick
Department of Mechanical Engineering
Massachusetts Institute of Technology
Cambridge, Massachusetts

David L. Trumper
Department of Mechanical Engineering
Massachusetts Institute of Technology
Cambridge, Massachusetts

Michael L. Holmes
Department of Electrical Engineering
University of North Carolina at Charlotte
Charlotte, North Carolina

ABSTRACT

A six degree–of–freedom electromagnetically suspended motion control stage (the Angstrom Stage) has been designed and constructed for use in short-travel, high-resolution motion control applications. It achieves better than 0.5 nm resolution over a 100 micron range of travel. The stage consists of a single moving element (the platen) floating in an oil filled chamber. The oil is crucial to the stage's operation since it forms squeeze film dampers between the platen and the frame. Twelve electromagnetic actuators provide the forces necessary to suspend and servo the platen, and six capacitance probes measure its position relative to the frame. The system is controlled using a digital signal processing board residing in a '486 based PC. This digital controller implements a feedback linearization algorithm in real-time to account for nonlinearities in both the magnetic actuators and the fluid film dampers. The feedback linearization technique reduces a highly nonlinear plant with coupling between the degrees of freedom into one that is linear, decoupled, and setpoint independent. The key to this procedure is a detailed plant model. The operation of the feedback linearization procedure is transparent to the outer loop of the controller, and so a proportional controller is sufficient for normal operation. We envision applications of this stage in scanned probe microscopy and for integrated circuit measurement.

INTRODUCTION

The Angstrom Stage is a motion control device that utilizes electromagnetic actuators in combination with squeeze film dampers to achieve sub-nanometer resolution with travel in a cube of 100 microns. Details concerning the mechanical design of the stage are found in [1]. In addition, [2] gives examples of atomic resolution images that were generated when the stage was paired with a scanning tunneling microscope. Rather than emphasizing the mechanical design of the stage, this paper instead concentrates on the feedback linearization algorithm that is key to the controller design. Using a model of the plant, this algorithm linearizes and decouples the six degrees of freedom. Linearizing the electromagnetic actuators with this technique is a standard procedure in our group's design process [3] [4] [5] [6]. In this paper, we expand the technique to include reducing the plant itself to six decoupled integrators with transfer functions of $1/s$ each. Hunt [7] and Su [8] provide a more general, mathematically rigorous description of the feedback linearization procedure.

MECHANICAL DESIGN AND MODELING

The Angstrom Stage consists of a platen floating in an oil–filled[1] chamber formed by an outer frame. Figure 1 shows a photograph of the device seated on a tabletop vibration isolation table. This frame has exterior dimensions of approximately $30 \times 30 \times 20$ cm, and is constructed from 6061-T6 aluminum. The platen is also made from aluminum, measures $17 \times 17 \times 8$ cm, and is designed with a hollow interior. This lightweighting of the platen is designed so that the platen's mass approximately equals the mass of the fluid it displaces. In practice, the oil supports better than 98% of the 3.09 kg mass of the platen. This reduces the bias currents required to keep the platen suspended, and thus reduces the associated thermal distortions of the frame. However, the most important function of the oil is the forming of squeeze film dampers between the platen and the frame. This will be described in more detail later in the paper. The end result is a highly overdamped and vibration resistant design. A cross section and an isometric view of the stage are shown in Figure 2.

Electromagnetic Actuators

Twelve electromagnetic actuators provide the forces necessary to suspend and servo the platen. Each actuator is fabricated with 230 turns of 22 gauge copper wire around 50-50 Ni-Fe E–Core laminations. The actuators are potted directly into the frame and act upon corresponding 50-50 Ni-Fe I–laminations epoxied into the platen. The actuators are

[1]Dow Corning FS-1265 fluorosilicone oil, density = 1.28 g/cm^3, viscosity = 1.323 kg/ms

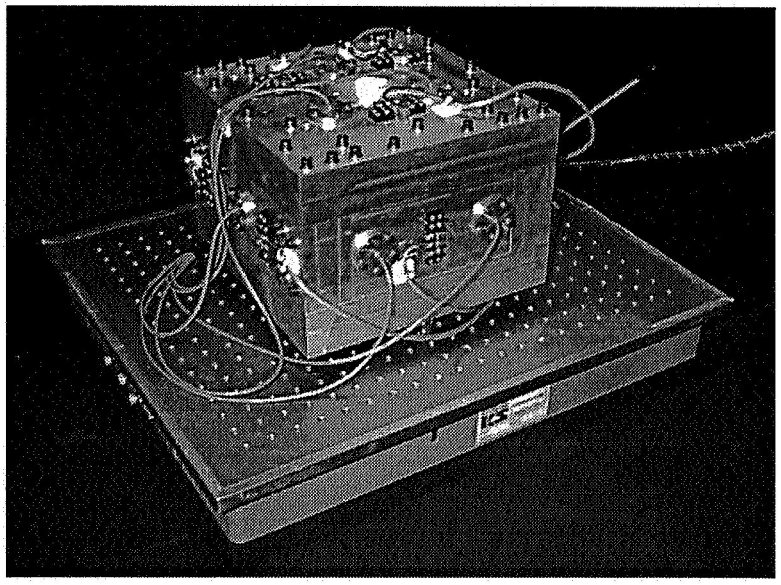

Figure 1: Photograph of the Angstrom Stage.

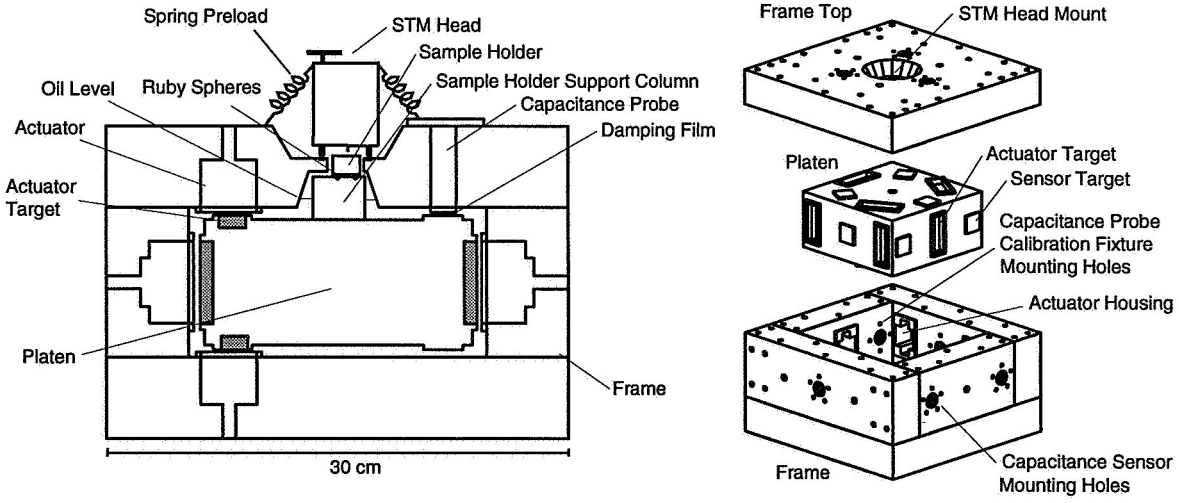

Figure 2: Angstrom Stage Cross Section and Isometric View.

designed to operate at a nominal gap of 300 μm, and are capable of producing over 50 N of force at this gap. However, normal operating forces are less than 1 N. The relationship between force, current, and gap is nonlinear, and is well modeled in the low–current region by

$$F(i, g_a) = C\left(\frac{i}{g_a}\right)^2. \tag{1}$$

Low currents are those for which the electromagnet has not begun to enter saturation, i.e., less than about 1 A in this application. In eq.(1), F represents the electromagnetic force, i is the coil current, and g_a is the target separation gap. The constant C is experimentally determined with our magnetic bearing calibration fixture [9], and equals approximately 2.5×10^{-6} Nm^2/A^2 for this design.

Squeeze Film Dampers

The dominant components of the stage, with respect to the system dynamics, are the squeeze film dampers formed by the thin film of oil located between the platen and the actuators and capacitance probes. The relationship between force and velocity at each capacitance probe comes from a direct application of the Navier–Stokes equation for viscous fluid flow [10],

$$F = \frac{3\pi\mu R^4}{2g_c^3}V. \tag{2}$$

The key fact to note here is that the damping changes with the inverse cube of the gap. The oil viscosity ($\mu = 1.323$ kg/ms), and the capacitance probe radius ($R = 0.01$ m) combine into a single characteristic constant b_c for the capacitance probe dampers. This reduces the force–velocity relationship to

$$F = \frac{b_c}{g_c^3}V, \tag{3}$$

where $b_c = 6.2 \times 10^{-8}$ Nsm^2. At the nominal oil film thickness of $g_c = 100$ μm, each probe contributes a damping term of $B_c = 6.2 \times 10^4$ Ns/m. However, this value changes significantly over the ± 50 μm range of travel due to the g_c^{-3} dependence.

The relationship between force and velocity for the actuator dampers is more difficult to model in a closed form because of their rectangular shape. It instead results in an infinite series solution [11],

$$F = \frac{192\mu l^3 V}{\pi^4 g_a^3} \sum_{n=1,3,5}^{\infty} \left(\frac{b}{2n^4} - \frac{l}{n^5\pi}\tanh\frac{n\pi b}{2l}\right). \tag{4}$$

The summation contains only the known width ($b = 0.06$ m) and length ($l = 0.025$ m) of the damping pad, and so evaluates to a constant independent of the gap. Thus the

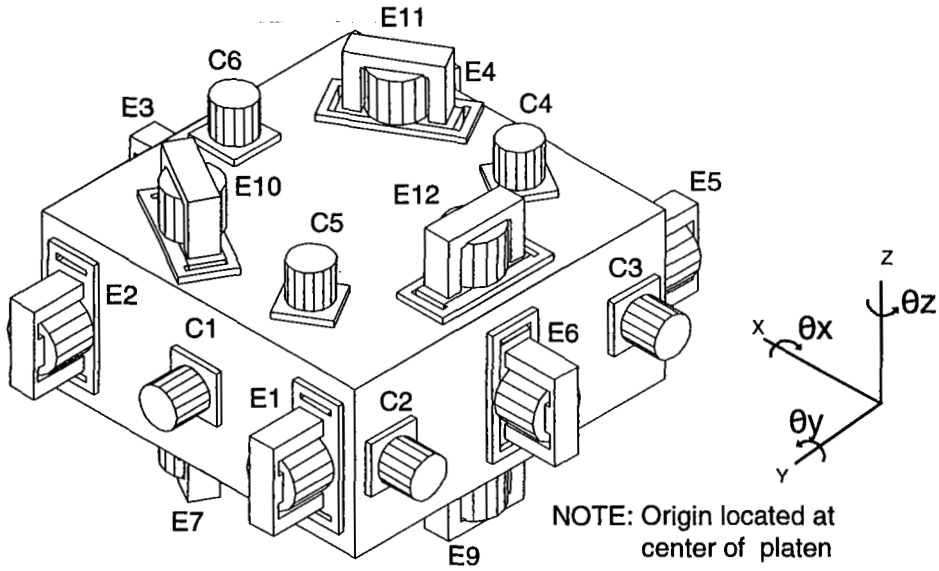

Figure 3: Location of Probes and Actuators Relative to the Platen.

damping due to an actuator in our system can be expressed as

$$F = \frac{b_a}{g_a^3} V, \tag{5}$$

with $b_a = 9.1 \times 10^{-7}$ Nsm^2. At the nominal oil film thickness of $g_a = 300$ μm, each actuator then contributes a damping term to the system of $B_a = 3.4 \times 10^4$ Ns/m. Again though, this factor changes significantly as the platen moves.

Equations (2) and (4) give the damping values for a single probe and actuator. In the stage operation, multiple dampers act on the platen with every motion. Figure 3 shows the the positions of the actuators and capacitance probes relative to the platen. It now becomes easier to express the force–velocity relationship in a matrix format,

$$\mathbf{F} = \mathbf{B}\mathbf{V}. \tag{6}$$

The forces (and torques) $\mathbf{F}$ and velocities $\mathbf{V}$ are defined as

$$\mathbf{F} = \begin{bmatrix} F_x & F_y & F_z & T_x & T_y & T_z \end{bmatrix}^T, \tag{7}$$

and

$$\mathbf{V} = \begin{bmatrix} \dot{x} & \dot{y} & \dot{z} & \dot{\theta}_x & \dot{\theta}_y & \dot{\theta}_z \end{bmatrix}^T. \tag{8}$$

The 6×6 damping matrix $\mathbf{B}$ is an instantaneous function of the stage position, and couples motions in the different axes. Its components are algebraically complex even though it is derived simply from free body diagrams of the platen motion. These relationships are given in the Appendix. For perspective on the magnitude of the damping values in the combined model, Figures 4 and 5 shows the damping in each degree of freedom as the stage moves from plus to minus full scale in that axis.

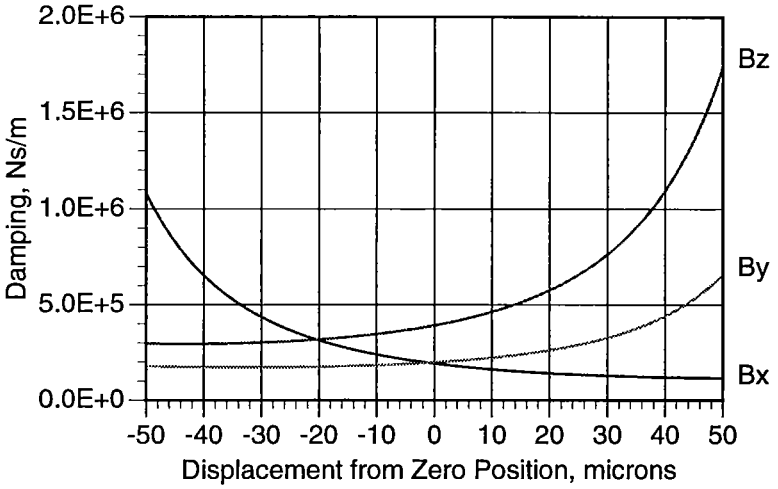

Figure 4: Damping Coefficients as the Stage Moves in the Translational Directions.

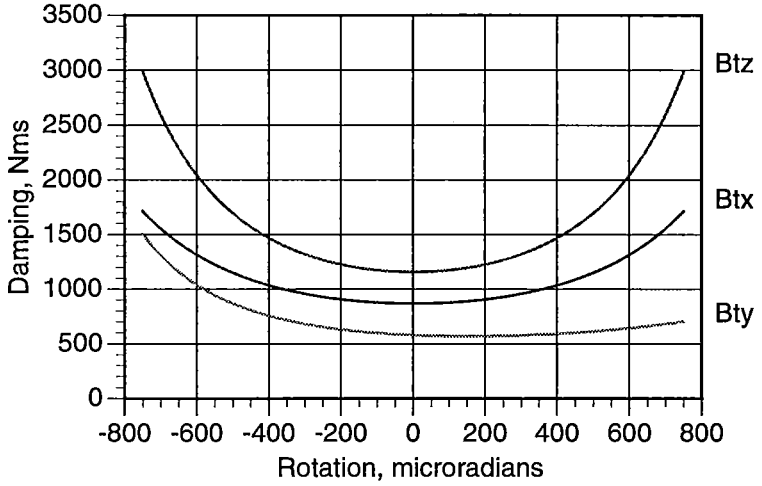

Figure 5: Damping Coefficients as the Stage Moves in the Rotational Directions.

CONTROLLER

A digital computer controls the operation of the Angstrom Stage. A 16-bit analog–to–digital conversion board reads the six capacitance probe voltages (as well as a Z-servo voltage from a scanning tunneling microscope) into a '486-based PC . Each channel is sampled at 22.3 kHz, which brings the overall sampling rate for the board close to the board's maximum throughput of 160 ksamples/second. A TMS320C30–based digital signal processing board implements a 100 point finite impulse response filter in order to increase the position resolution and lessen the noise magnitude. Finite processor speed requires that the resulting waveform be downsampled by thirty points before the remainder of the controller operates on filtered position measurements. This reduces the controller update rate to about 744 Hz. The C30 performs the control calculations and writes the required voltages to a 12-bit digital–to–analog converter board. Finally, twelve linear transconductance power amplifiers transduce these voltages into actuator currents.

The controller design begins with a model of the stage. In this case, the fluid film dampers dominate the dynamics to the point where the stage can be modeled as a pure integrator. The velocity along any axis is thus simply proportional to the force applied by the electromagnetic actuators along that axis. However, the applied force is a nonlinear function of the gaps and the current, and the damping is also a nonlinear function of the gaps. Closing the loop with a typical Proportional (P) or Proportional-Integral (PI) controller will stabilize the plant. However, the response to a commanded change in position will depend upon where the platen is located. Also, a typical controller will not lead to constant velocity motion as is required in a scanning stage.

As an alternative, we approach the design with a set of desired velocities in each of the six directions (three translational and three rotational). The controller utilizes a model of the plant,

$$\mathbf{F}_d = \hat{\mathbf{B}}\mathbf{V}_d, \tag{9}$$

that calculates the forces and torques that will produce these target velocities. The plant model is derived by calculating the damping coefficients for each of the fluid film dampers, and relating these to the cartesian axes. Off–diagonal terms in the $\hat{\mathbf{B}}$ matrix indicate the inherent coupling between the axes. Its component elements are calculated in real–time by the digital signal processor on the basis of the damping models presented earlier.

The second step of the feedback linearization is to determine what currents should be applied in order to generate the desired forces. This is accomplished by inverting the actuator dynamics, leading to

$$i = \hat{g}_a\sqrt{\frac{F_d}{\hat{C}}}. \tag{10}$$

If the estimates of the gaps, force constants, and damping factors are accurate, the velocity of the plant will match the reference velocity. At this point, the controller can use the linearized plant in two ways. One is to simply command constant velocities in order to generate a scanning motion. The accuracy of the model determines the performance of this

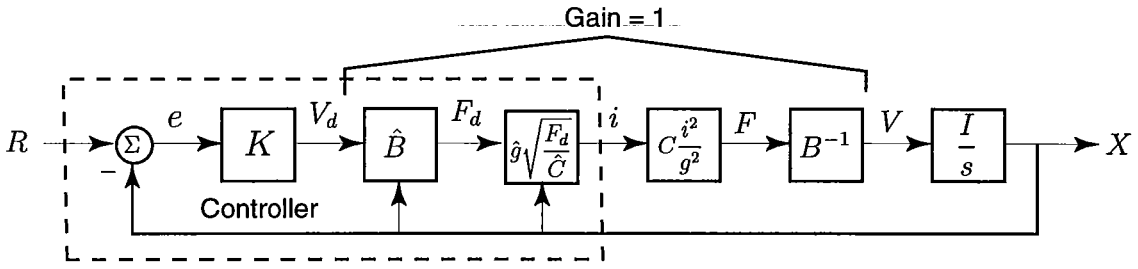

Figure 6: Block Diagram of Feedback Linearization Scheme.

open loop velocity controller. More typically, we can feed back the position readings in a PI control scheme. In this case, the operation of the linearization component of the controller is transparent. The main outer loop can simply be designed to control a decoupled plant with transfer functions of 1/s in each of six degrees of freedom. This control mode is useful for small displacements and maintaining stability about a setpoint. The block diagram of this feedback control scheme is shown in Figure 6.

RESULTS

As was stated in the previous section, the stage operates in both an open loop velocity control mode and in a closed loop position control mode. The velocity control is important for providing motion in the fast direction of a scanning pattern. Using closed loop position control in this case would result in an exponential approach to a target position, and therefore a non-uniform velocity. However, closed loop control on the position in the slow scan direction allows the stage to move a set distance for each new scan. Maintaining position stability in that axis ensures that the repeated scans lie parallel to each other. The magnitude of the position error determines in which control mode the stage is operating. Large position errors cause the stage to move with a constant velocity while small errors are handled by closed loop position control.

Experimental data from the open loop constant velocity control mode is shown in Figure 7. This figure illustrates the accuracy of the plant model and the effectiveness of the open loop velocity control. The stage moves with a commanded velocity of -2 μm/s from a position at $x = +25$ μm to one at $x = -20$ μm. Over that span, the damping coefficient in the x-direction increases over 2.7 times from 135,300 Ns/m to 369,200 Ns/m. Figure 8 contains a plot of the error between the data in Figure 7 and the best–fit line. The maximum error at any time is less than 20 nm, but more importantly, the error follows a repeatable pattern. This shape is due to manufacturing errors which changed the null actuator and capacitance probe gaps from their nominal values of 300 μm and 100 μm respectively. By fitting responses such as these to the plant models, we were able to generate better estimates of the true gaps. Figure 8 shows both the success of this approach, and that there is still room to improve the model. In the future we plan to add

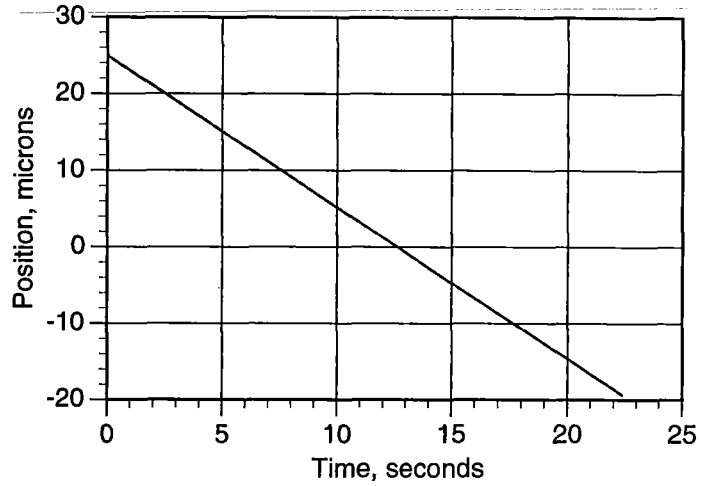

Figure 7: Examples of a constant velocity scan.

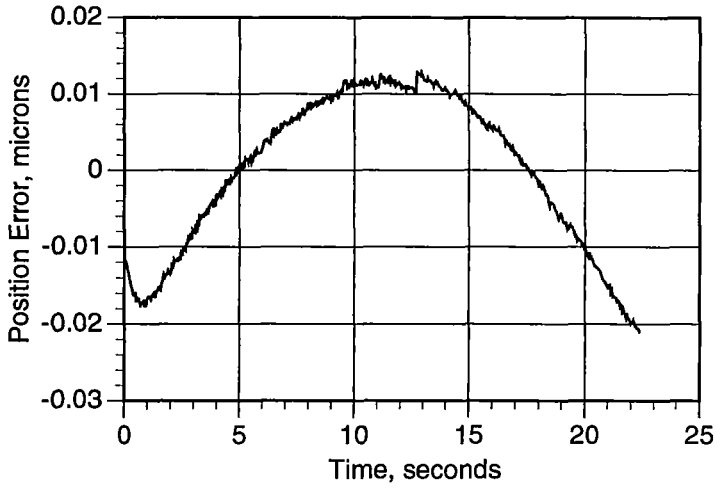

Figure 8: Error in a constant velocity scan.

closed loop velocity control to the plant. To date, this has not been implemented simply because processor time has been devoted to the more immediate goal of position resolution.

Once the position error in an axis is less than 100 nm, the controller switches to the closed loop position control mode for that axis. An example of multiple 0.5 nm steps is shown in Figure 9. For this measurement, the control bandwidth is set at 5 Hz, and the measurement is taken through a differential amplifier with a bandwidth of 1 Hz. In the steady stage condition, the standard deviation of the stage position (measured through a 1 Hz filter) is about 0.05 nm.

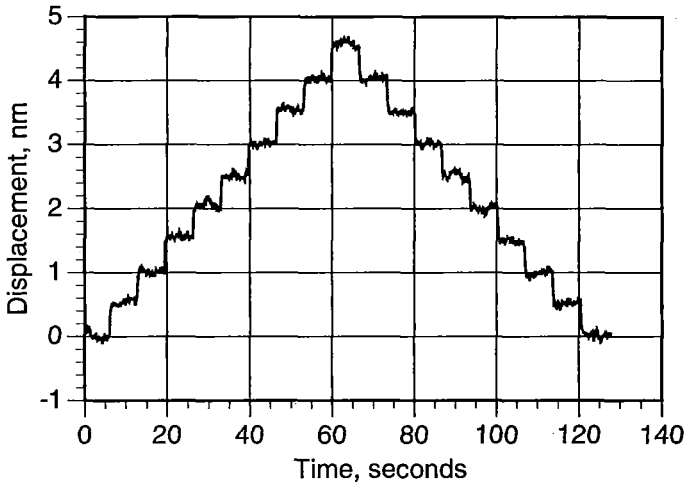

Figure 9: Repeated 0.5 nm step responses.

CONCLUSIONS

This version of the Angstrom Stage has demonstrated the feasibility of a magnetically levitated stage for use in atomic-scale motion control applications. The squeeze film dampers provide the high level of disturbance rejection necessary for a high resolution stage, but do so at the cost of a nonlinear plant with inherent coupling between the axes. The electromagnetic actuators are capable of applying precisely controlled forces, but these are again a nonlinear function of current and position. In both cases, these nonlinearities can be well modeled analytically. Including these models in a feedback linearization scheme yields a linear plant with decoupled motion in all six degrees of freedom. This stage has achieved a position noise standard deviation of 0.05 nm over a travel of 100 μm, and thus has a dynamic range of about 10^6. We believe this to be the highest-resolution magnetic suspension which has yet been constructed.

ACKNOWLEDGMENTS

Portions of this work are part of a thesis submitted by Stephen Ludwick for the degree of Master of Science in Mechanical Engineering at the Massachusetts Institute of Technology. Other portions of this work form part of a thesis submitted by Michael Holmes for the degree of Master of Science in Electrical Engineering at the University of North Carolina at Charlotte. This work was supported by the National Science Foundation under grants DDM-9396605, DMI-9414778, and through David Trumper's Presidential Young Investigator Award, DDM-9496102. We gratefully acknowledge the assistance provided by the ADE Corporation in the development of the capacitance gaging system.

BIBLIOGRAPHY

[1] M. L. Holmes: "Analysis and Design of a Magnetically Suspended Precision Motion Control Stage." M.S. Thesis, Department of Electrical Engineering, University of North Carolina at Charlotte, Charlotte, NC, 1994.

[2] M. L. Holmes; D. L. Trumper; and R. Hocken: "Atomic-Scale Precision Motion Control State (The Angstrom Stage)." *Annals of the CIRP*, 44(1):455-460, 1995.

[3] D. L. Trumper. *Magnetic Suspension Techniques for Precision Motion Control.* Ph.D. Thesis, Department of Electrical Engineering and Computer Science, Massachusetts Institute of Technology, Cambridge, MA, Sept. 1990.

[4] S. M. Alson: "Nonlinear Compensation of a Single Degree of Freedom Magnetic Suspension System." M.S. Thesis, Department of Mechanical Engineering, Massachusetts Institute of Technology, Cambridge, MA, June 1994.

[5] K. S. Chen: "A Spring-Dominated Regime Design of a High Load Capacity, Electromagnetically Driven x-y-θ stage." M.S. Thesis, Department of Mechanical Engineering, Massachusetts Institute of Technology, Cambridge, MA, June 1995.

[6] M. E. Williams; D. L. Trumper; and R. Hocken: "Magnetic Bearing Stage for Photolithography." *Annals of the CIRP*, 42(1):607-610, 1993.

[7] L. Hunt; R. Su; and G. Meyer. "Global Transformations of Nonlinear Systems." *IEEE Transactions on Automatic Control*, AC-28(1);24-30, Jan. 1983.

[8] R. Su: "On the Linear Equivalents of Nonlinear Systems." *Systems and Control Letters*, 2(1):48-52, July 1982.

[9] T. Poovey; M. L. Holmes; and D. L. Trumper: "A Kinematically Coupled Magnetic Calibration Fixture." *Precision Engineering*, 16(2), April 1994.

[10] J. A. Fay. *Introduction to Fluid Mechanics.* MIT Press, Cambridge, MA, 1994.

[11] O. Pinkus and B. Sternlicht. *Theory of Hydrodynamic Lubrication.* McGraw Hill, New York, 1961.

APPENDIX

Damping Model

The damping model is derived simply by drawing free body diagrams of the platen with all of the nonlinear dampers around it in each degree of freedom. The six forces and torques relate to the velocities through:

$$\begin{aligned}
F_x &= b_{xx}\dot{x} + b_{x\theta_z}\dot{\theta}_z \\
F_y &= b_{yy}\dot{y} + b_{y\theta_z}\dot{\theta}_z \\
F_z &= b_{zz}\dot{z} + b_{z\theta_x}\dot{\theta}_x + b_{z\theta_y}\dot{\theta}_y \\
T_x &= b_{\theta_x z}\dot{z} + b_{\theta_x\theta_x}\dot{\theta}_x + b_{\theta_x\theta_y}\dot{\theta}_y \\
T_y &= b_{\theta_y z}\dot{z} + b_{\theta_y\theta_x}\dot{\theta}_x + b_{\theta_y\theta_y}\dot{\theta}_y \\
T_z &= b_{\theta_z x}\dot{x} + b_{\theta_z y}\dot{y} + b_{\theta_z\theta_z}\dot{\theta}_z
\end{aligned}$$

where the individual damping components are defined as

$$\begin{aligned}
b_{xx} &= b_a\left(\frac{1}{g_{a3}^3}+\frac{1}{g_{a6}^3}\right)+b_c\left(\frac{1}{g_{c2}^3}+\frac{1}{g_{c3}^3}\right) \\
b_{x\theta_z} &= b_c\ell\left(\frac{1}{g_{c3}^3}-\frac{1}{g_{c2}^3}\right) \\
b_{yy} &= b_a\left(\frac{1}{g_{a1}^3}+\frac{1}{g_{a2}^3}+\frac{1}{g_{a4}^3}+\frac{1}{g_{a5}^3}\right)+b_c\left(\frac{1}{g_{c1}^3}\right) \\
b_{y\theta_z} &= b_a\ell\left(-\frac{1}{g_{a1}^3}+\frac{1}{g_{a2}^3}+\frac{1}{g_{a4}^3}-\frac{1}{g_{a5}^3}\right) \\
b_{zz} &= b_a\left(\frac{1}{g_{a7}^3}+\frac{1}{g_{a8}^3}+\frac{1}{g_{a9}^3}+\frac{1}{g_{a10}^3}+\frac{1}{g_{a11}^3}+\frac{1}{g_{a12}^3}\right)+b_c\left(\frac{1}{g_{c4}^3}+\frac{1}{g_{c5}^3}+\frac{1}{g_{c6}^3}\right) \\
b_{z\theta_x} &= \frac{b_a\ell\sqrt{3}}{2}\left(\frac{1}{g_{a7}^3}-\frac{1}{g_{a8}^3}+\frac{1}{g_{a10}^3}-\frac{1}{g_{a11}^3}\right)+\frac{b_c\ell\sqrt{3}}{2}\left(-\frac{1}{g_{c4}^3}+\frac{1}{g_{c5}^3}\right) \\
b_{z\theta_y} &= \frac{b_a\ell}{2}\left(-\frac{1}{g_{a7}^3}-\frac{1}{g_{a8}^3}+\frac{2}{g_{a9}^3}-\frac{1}{g_{a10}^3}-\frac{1}{g_{a11}^3}+\frac{2}{g_{a12}^3}\right)+\frac{b_c\ell}{2}\left(\frac{1}{g_{c4}^3}+\frac{1}{g_{c5}^3}-\frac{2}{g_{c6}^3}\right) \\
b_{\theta_x z} &= \frac{b_a\ell\sqrt{3}}{2}\left(\frac{1}{g_{a7}^3}-\frac{1}{g_{a8}^3}+\frac{1}{g_{a10}^3}-\frac{1}{g_{a11}^3}\right)+\frac{b_c\ell\sqrt{3}}{2}\left(-\frac{1}{g_{c4}^3}+\frac{1}{g_{c5}^3}\right) \\
b_{\theta_x\theta_x} &= \frac{3b_a\ell^2}{4}\left(\frac{1}{g_{a7}^3}+\frac{1}{g_{a8}^3}+\frac{1}{g_{a10}^3}+\frac{1}{g_{a11}^3}\right)+\frac{3b_c\ell^2}{4}\left(\frac{1}{g_{c4}^3}+\frac{1}{g_{c5}^3}\right)
\end{aligned}$$

$$
\begin{aligned}
b_{\theta_x\theta_y} &= \frac{b_a\ell^2\sqrt{3}}{4}\left(-\frac{1}{g_{a7}^3}+\frac{1}{g_{a8}^3}-\frac{1}{g_{a10}^3}+\frac{1}{g_{a11}^3}\right)+\frac{b_c\ell^2\sqrt{3}}{4}\left(-\frac{1}{g_{c4}^3}+\frac{1}{g_{c5}^3}\right)\\
b_{\theta_y z} &= \frac{b_a\ell}{2}\left(-\frac{1}{g_{a7}^3}-\frac{1}{g_{a8}^3}+\frac{2}{g_{a9}^3}-\frac{1}{g_{a10}^3}-\frac{1}{g_{a11}^3}+\frac{2}{g_{a12}^3}\right)+\frac{b_c\ell}{2}\left(\frac{1}{g_{c4}^3}+\frac{1}{g_{c5}^3}-\frac{2}{g_{c6}^3}\right)\\
b_{\theta_y\theta_x} &= \frac{b_a\ell^2\sqrt{3}}{4}\left(-\frac{1}{g_{a7}^3}+\frac{1}{g_{a8}^3}-\frac{1}{g_{a10}^3}+\frac{1}{g_{a11}^3}\right)+\frac{b_c\ell^2\sqrt{3}}{4}\left(-\frac{1}{g_{c4}^3}+\frac{1}{g_{c5}^3}\right)\\
b_{\theta_y\theta_y} &= \frac{b_a\ell^2}{4}\left(\frac{1}{g_{a7}^3}+\frac{1}{g_{a8}^3}+\frac{2}{g_{a9}^3}+\frac{1}{g_{a10}^3}+\frac{1}{g_{a11}^3}+\frac{2}{g_{a12}^3}\right)+\frac{b_c\ell^2}{4}\left(\frac{1}{g_{c4}^3}+\frac{1}{g_{c5}^3}+\frac{2}{g_{c6}^3}\right)\\
b_{\theta_z x} &= b_c\ell\left(-\frac{1}{g_{c2}^3}+\frac{1}{g_{c3}^3}\right)\\
b_{\theta_z y} &= b_a\ell\left(-\frac{1}{g_{a1}^3}+\frac{1}{g_{a2}^3}-\frac{1}{g_{a4}^3}+\frac{1}{g_{a5}^3}\right)\\
b_{\theta_z\theta_z} &= b_a\ell^2\left(\frac{1}{g_{a1}^3}+\frac{1}{g_{a2}^3}+\frac{1}{g_{a4}^3}+\frac{1}{g_{a5}^3}\right)+b_c\ell^2\left(\frac{1}{g_{c2}^3}+\frac{1}{g_{c3}^3}\right)
\end{aligned}
$$

The entire damping model can be describe more compactly through a matrix representation where $\mathbf{F} = \mathbf{BV}$ and $\mathbf{B}$ is defined as

$$
\mathbf{B} = \begin{bmatrix}
b_{xx} & 0 & 0 & 0 & 0 & b_{x\theta_z} \\
0 & b_{yy} & 0 & 0 & 0 & b_{y\theta_z} \\
0 & 0 & b_{zz} & b_{z\theta_x} & b_{z\theta_y} & 0 \\
0 & 0 & b_{\theta_x z} & b_{\theta_x\theta_x} & b_{\theta_x\theta_y} & 0 \\
0 & 0 & b_{\theta_y z} & b_{\theta_y\theta_x} & b_{\theta_y\theta_y} & 0 \\
b_{\theta_z x} & b_{\theta_z y} & 0 & 0 & 0 & b_{\theta_z\theta_z}
\end{bmatrix}.
$$

Session 4 -- Maglev 1

Chairman: H. Jones
Oxford University

DESIGN OPTIMIZATION FOR A MAGLEV SYSTEM EMPLOYING FLUX ELIMINATING COILS

Dr. Kent R. Davey
American MAGLEV Technology
Edgewater, FL

ABSTRACT

Flux eliminating coils have received no little attention over the past thirty years as an alternative for realizing lift in a MAGLEV system. When the magnets on board the vehicle are displaced from the equilibrium or null flux point of these coils, they induce current in those coils which act to restore the coil to its null flux or centerline position. The question being addressed in this paper is that of how to choose the best coil for a given system. What appears at first glance to be an innocent question is in fact one that is actually quite involved, encompassing both the global economics and physics of the system. The real key in analyzing that question is to derive an optimization index or functional which represents the cost of the system subject to constraints, the primary constraint being that the vehicle lift itself at a certain threshold speed. Outlined in this paper is one scenario for realizing a total system design which uses sequential quadratic programming techniques.

INTRODUCTION

Figure 1 shows a simple magnet and coil layout involving null flux and flux eliminating coils. In inset (a), a pair of null flux coils is being moved past a set of magnets which direct flux in a single direction through the coil. When the coil is displaced vertically downward with respect to the magnet, the upper window of the null flux coil begins to link more flux than the lower window. Because that flux is also changing with time, an induced voltage causes a current to flow which acts to restore the coil to its centerline position, yielding a force in the upward direction of the coil. A similar process is involved in the lower inset (b) of that figure. Here the magnets are stacked, unlike poles above each other, unlike those in inset (a). The coils now form single loops. When the single loop coil is offset from its null flux position, it begins to link flux in a similar fashion to the null flux coil. As drawn, it is clear that the left most coil has more south pole shadowing it than north pole. It will therefore have a net flux linking it which induces a current to again restore it to its null flux position. The one advantage that the stacked magnet design has over the null flux design is that the closure path for the magnetic field is shorter and therefore more efficient.

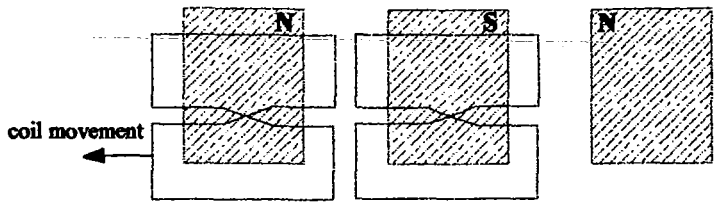

(a) Null Flux Coil

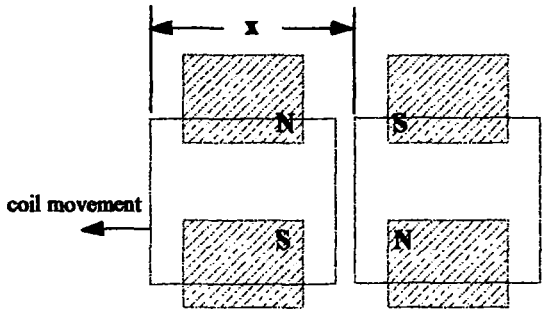

(b) Flux Eliminating Coils

Figure 1 Magnet and coil geometry used for getting lift for null flux and flux eliminating coils.

Figure 2 shows a cross-section of the second embodiment, the flux eliminating coil. In this cross-section is clear that there are two loops or "O" rings that are arranged side by side, one of the "O"

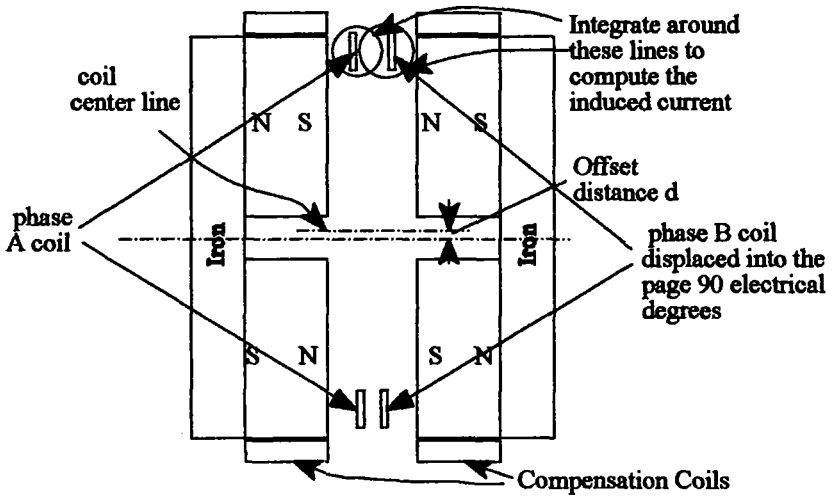

Figure 2 Overlapped Composite coils analyzed with a compensation winding.

rings is in fact displaced into the page with respect to the other, so that the two form a phase shifted pair. The lift associated with the coil pattern shown in Figure 2 is a function of both the offset displacement d of the centerline of the coils with respect to the centerline of the magnets and the excitation frequency. The excitation frequency is in fact specified by the velocity of the coils past the magnets, i.e., $f = \frac{v}{\lambda}$, *where* $\lambda \equiv$ *wavelength into the page*. Note that the coils that are displaced electrically axially into the paper 90^0 with respect to the first set, link no flux at the instant in time when the phase A coil links maximum flux. The objective is to suggest the best track design based on the information realized through a computational analysis, delivering force as a function of displacement and frequency. Specifically the objective would be to define the following:

1. The number of magnet c-sets on the vehicle.
2. The spacing of the magnets and the coils in the track.
3. Displacement distance d at lift off.
4. The commensurate properties associated with these parameters including the system cost per mile, the vehicle weight, the drag forces, and the lift to weight ratio.

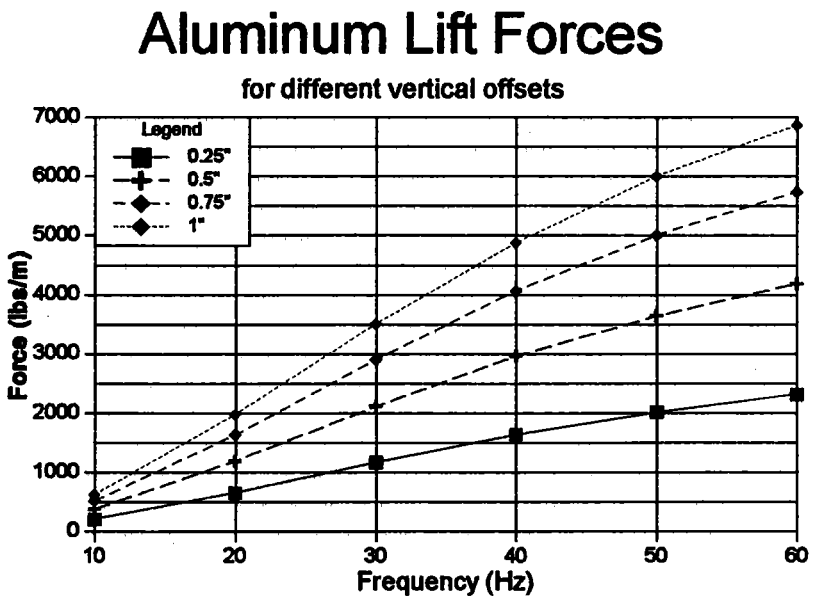

Figure 3 *Lift force on overlapped aluminum composite coils.*

The forces on the coils in Figure 2 are analyzed for a range of displacements and frequencies for both aluminum and copper using a Boundary Element eddy current package (Oersted from Integrated Engineering Software in Winnipeg, Canada). Shown in Figure 3 are the lift forces on aluminum overlapped composite coils. The reader should recognize the familiar induction motor torque/speed profile within these shapes. Because the forces were analyzed in 2D, all forces are reported in lbs/m of depth. Connectivity of the coils is specified by constraining the vector potential within each of the coils, and demanding that the $\oint \vec{H} \cdot \vec{dl}$ around a closed-loop surrounding the coils be constrained so that the induced current within the top two coils is opposite in sign to that in the lower two coils. In addition, the induced current was constrained to be the same for each conductor cross-section.

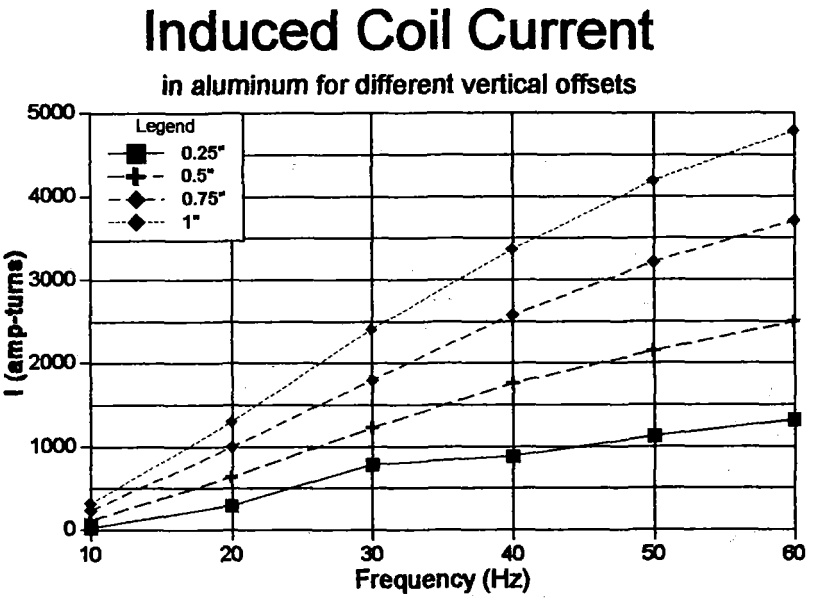

Figure 4 Current induced in the aluminum overlapped composite.

After the field is found everywhere, the induced current within the coils is determined also by integrating $\oint \vec{H} \cdot \vec{dl}$ around each of the coils. Shown in Figure 4 is the current induced in the coils as a function of the same parameters. Note that this current is independent of depth since both the inductance/resistance and flux linkage scale the same with depth extension.

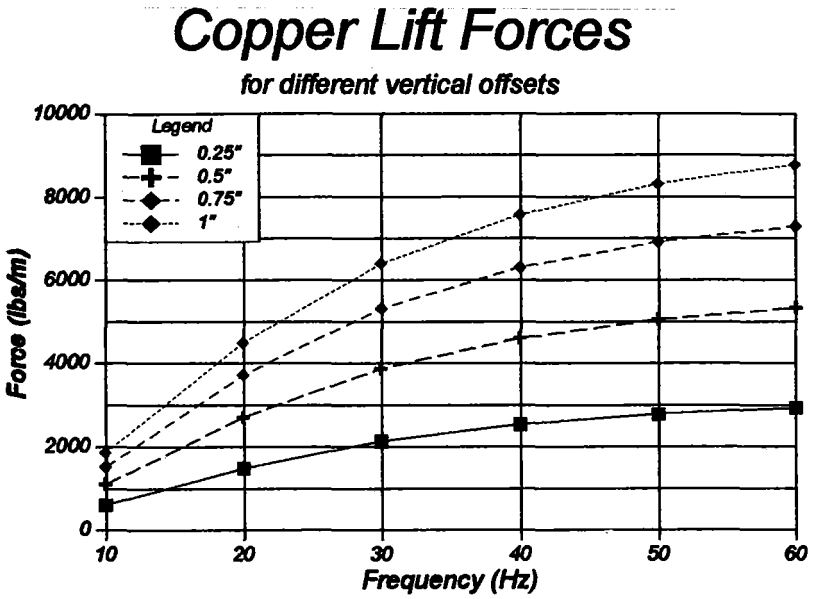

Figure 5 Lift forces on copper overlapped composite coils.

The primary reason why the force using aluminum coils is low is due to timing. The current is not peaking at the right time. If the coil were resistance dominated, the current would be 90 ° out of phase with the inducing current in the magnet, and no net current would result. Changing the coils to copper roughly doubles the L/R time constant and greatly helps the force as witnessed by Figure 5.

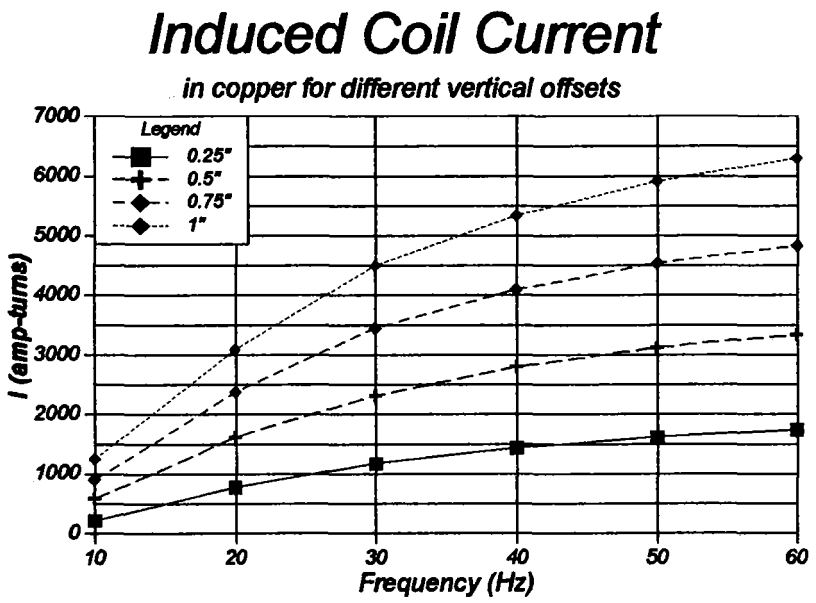

Figure 6 Current induced in copper composite coils.

The commensurate current induced in these coils is displayed in Figure 6. As expected, the force and current follow the same pattern.

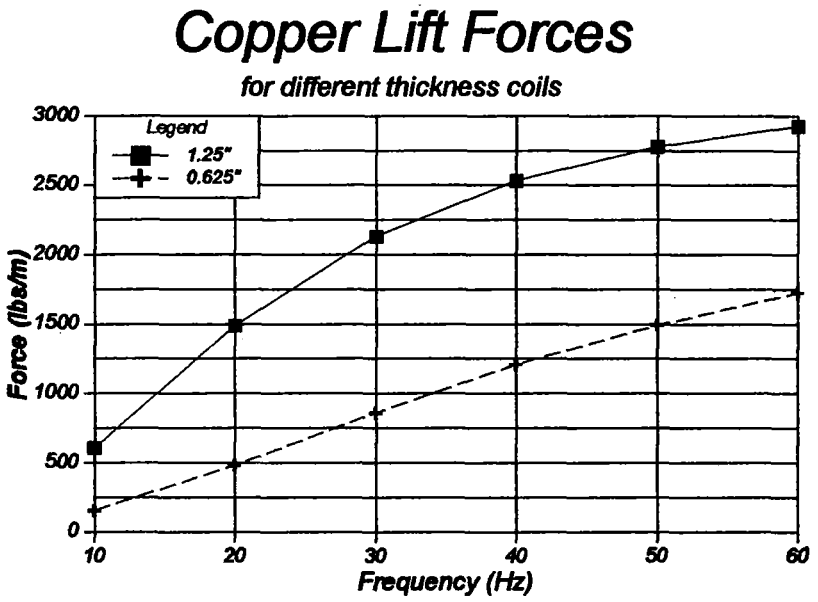

Figure 7 Lift force on two copper coils each with a different thickness.

The ultimate objective is to minimize the cost of the long member, the track. Two coil thicknesses were examined, one having a cross-section of 0.625" by 0.25" (10 turns of #9 wire) and a second having a cross-section of 1.25" by 0.25" (20 turns of #9 wire). By way of underscoring the importance of the larger 1.25" coils over the previous 0.625" coils, Figure 7 displays the different forces expected when 1.25" copper coils are condensed to 0.625" in height. The force reduction results from two issues. First, the timing due to the L/R ratio is such that the currents do not come on opposite in phase to their source. Second, the currents are physically positioned closer to the outer periphery of the field, where the fields are reduced in magnitude.

OPTIMIZATION SETUP

The optimization objective will be to minimize the cost of the magnets and wire in the track as well as the drag at lift off,

$$\mathcal{F} = (\$wire + \$magnets) * drag \qquad (1)$$

subject to the constraint that lift ≥ weight at lift off. **The system design is dictated by the desired liftoff speed**. Once the desired liftoff is defined, the four objective parameters listed on page 3 are known. The approach adopted is as follows:

1. Predict the forces and induced currents as a function of both offset distance d and frequency f.
2. Fit a complex polynomial involving d and f to the force and induced current.
3. Use a sequential quadratic program to determine the best design topology.

The equivalent frequency seen by the coils is dictated by the product of wave number k and velocity v as

$$kv=\omega \Rightarrow \frac{2\pi}{2x}v = 2\pi f. \tag{2}$$

Where x is the axial distance between coils (see Figure 1). Thus the equivalent frequency is related to the spacing between coils x as

$$f = \frac{v}{2x}. \tag{3}$$

The process begins by fitting the force F per C set and induced current I to a vector of unknowns c_f and c_I such that

$$A\vec{c}_f = \vec{F}/C \tag{4}$$

$$A\vec{c}_I = \vec{I}. \tag{5}$$

The actual current for each is fitted as

$$F=c_1+c_2x+c_3x^2+c_4x^3+c_5d+c_6d^2+c_7xd+c_8x^2d+c_9xd^2+c_{10}(xd)^2+c_{11}x^4. \tag{6}$$

with a similar fit for the induced current I. A total of m=24 trials were investigated, allowing the construction of a matrix equation to determine the coefficients based on the m trials,

$$\begin{bmatrix} 1 & x_1 & x_1^2 & \dots & x_1^4 \\ 1 & x_2 & x_2^2 & \dots & x_2^4 \\ \vdots & \vdots & \vdots & \vdots & \vdots \\ 1 & x_m & x_m^2 & \dots & x_m^4 \end{bmatrix} \begin{bmatrix} c_1 \\ c_2 \\ \vdots \\ c_{11} \end{bmatrix} = \begin{bmatrix} F_1 \\ F_2 \\ \vdots \\ F_m \end{bmatrix} \tag{7}$$

Equation (5) was found to accurately track both force and induced current.

THE DESIGN SETUP

The objective function (1) involves 3 parameters which serve as the unknowns - the axial winding displacement x, the offset distance d of the coils with respect to the magnets, and the

number of magnet C-sets N. The magnet costs, wire costs, and drag at liftoff must be represented in terms of these three parameters. The distance x represents the outside axial distance of the coils. In terms of the average height of the coils (h=7.325") and the average width (x-1.25"), the wire density ρ, the price per pound P, and the length L of the track, the cost of the wire is

$$\$wire = 2_{sides/coil}(h+(x-1.25))*4_{coils/Cset}*0.22*1.25*(2L/x)\rho P*4_{rails/system}. \quad (8)$$

The factor 2 multiplying L accounts for the half pole pitch placed coil. Each of the 12" magnets employed cost $10,000. To allow room for the placement of the compensation winding, the magnets must be 0.75" shorter than the pole pitch distance x. Thus the cost of N magnets for vehicles is

$$\$magnets = N*\$10{,}000*Veh*(x-0.75)/12. \quad (9)$$

From the induced current in each coil, it is possible to compute the drag force in terms of the average B field in the air gap. This drag of course depends on the relative offset distance d of the coils with respect to the magnets. For the 4 sets of coils (2 sets being displaced a half pole pitch axially), the drag force in pounds is

$$Drag = N*8*d*0.0254_{m/in}*I*B/4.48_{N/lb}. \quad (10)$$

Each brush set for a 12" section of magnet is estimated to weigh 100# with an additional 50# being needed to account for the weight of the air cylinder controlling the actuators, yielding a brush weight

$$brush = 100\,x/12+50. \quad (11)$$

Each magnet C set weighs approximately 400 lbs with an additional 150 lbs required to account for the support struts. In terms of the burden, the vehicle weight is

$$wt = burden+N*[650*(x-0.75)/12+50]. \quad (12)$$

The burden for the test sled is only 640 lbs, whereas the burden for a typical people mover is 27,000 lbs. The expected burden for the fully deployed 90' long high speed cruiser is 43,000 lbs. The lift to drag ratio l/d is

$$l/D = wt/drag. \quad (13)$$

The cost per mile for a length L of track is

$$cost/mile = (\$magnets+\$wire)/L*5280_{ft/mile}*12_{in/ft}. \quad (14)$$

RESULTS

Table I System Design with a 700lb load/C set

L	Mat.	spd	# veh	x	d	N	drag /1000	f/D	wt /1000	$wire *10^6	$mag *10^6	cost/ mile *10^6	I kA	F/C /1000
4000'	Cu	30	6	12	1	51	4.35	14	60.7	1.13	2.87	5.28	3.42	1.19
4000'	Al	35	6	12.3	1	38.2	3.71	14.3	52.86	1.12	2.21	4.4	3.87	1.38
4000'	Al	40	2	12	1	145	8.83	13.9	123.1	0.331	2.73	4.04	2.43	0.846
10 miles	Al	40	2	"	"	"	"	"	"	4.36	"	0.709	"	"
4000"	Cu	40	2	14.8	0.906	35.6	2.74	20.4	55.9	1.06	0.834	2.50	3.4	1.57
10 miles	Cu	40	2	17.12	0.82	45.9	2.55	27.4	70.0	13.42	1.25	1.47	2.70	1.53
4000'	Al	40	6	12	1	145	8.83	13.9	123.1	0.33	8.21	11.26	2.43	0.846
10 miles	Al	40	6	12	1	145	8.83	13.9	123.1	4.36	8.21	1.25	2.43	0.846
4000'	Cu	40	6	13.77	.969	32	2.99	17.1	51.2	1.08	2.09	4.18	3.86	1.60
4000'	Al	80	2	14.7	0.929	29.3	2.55	19.8	50.6	0.31	0.683	1.31	3.76	1.73
10 miles	Al	80	2	16.98	0.795	38.4	2.18	29	62.7	3.93	1.04	0.497	2.85	1.63
4000'	Cu	80	2	26.2	0.77	17.1	1.07	48	51.4	0.924	0.725	2.18	3.26	3.07
10 miles	Cu	80	2	29.3	0.66	23.2	977	65.6	64.1	11.95	1.11	1.31	2.55	2.76

Table I shows the results for a variety of liftoff speeds, coil materials, lengths of track, and number of vehicles for a 4 rail people mover system based 27,000 lb burden system. The design variables are chosen to minimize (1) subject to the constraint that the vehicle lift itself at the specified liftoff speed. Because the winding end turns become comparable to the coil length for x<12", the additional constraint that $x \geq 12$" was also enforced. As expected, when the design is asked to lift at low speeds, x is forced to the smallest axial extension in an attempt to drive the effective frequency up. In addition, the vehicle is forced to ride "low in the water" at a large "d"; this of course translates into a

low lift/drag ratio, but the system has no choice at these low speeds. The superior L/R time constant of the copper allows it to deliver a solution when none is available for aluminum at low speeds. As the lift threshold rises, the optimization algorithm attempts to pick the number of magnets N to decrease both d and the drag as desired. The following trends are also registered as expected

1. As the length of the track L increases, the algorithm drives the cost of the wire down by extending x.
2. As the number of vehicles increases, the algorithm drives N down to reduce the total expenditure required for the magnets.
3. As x is increased to reduce wire cost, the vehicle will lift with a greater d; the lift/drag ratio is compromised at the expense of track cost reduction.

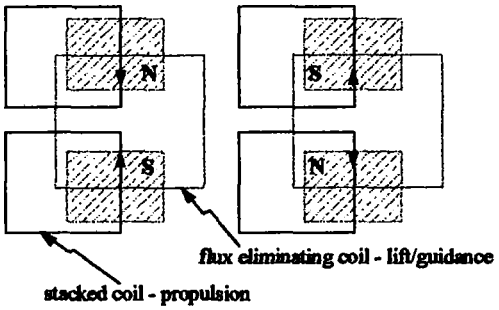

(a) Side view - lift and propulsion coils

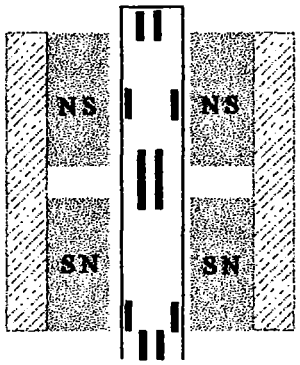

(b) side view

Figure 8 Combination of flux eliminating and stacked coils for lift and propulsion.

SYSTEM STAGING-A 3 STAGE RAIL BUILDUP

It should be apparent that the flux eliminating coil presented in Figure 8 (b) is not useful for realizing propulsion forces. A separate stacked coil is recommended for propulsion with this design. Figure 8 shows the incorporation of stacked coils for propulsion as well. American MAGLEV is however testing a proprietary coil at present which performs all three functions - lift, guidance, and propulsion. The first section of track up to 40 MPH where lift is unnecessary should use only stacked coils centered on the magnets. The centered stacked coil makes the best use of the field for propulsion. The lift coils in the track section between 40 and 80 MPH should be copper, while above 80 MPH they should be aluminum. The stacked coils remain aluminum throughout. With the proprietary single composite coil system being tested at present, the same sequence should be followed - aluminum stacked 0 - 40 MPH, copper composite (40 MPH - 80 MPH), aluminum composite (> 80 MPH).

Table II Distance staging @ 1.5m/s^2 acceleration

Stage	velocity range (m/s)	δ time (s)	distance (m)	distance ft	Accumulate Distance ft
acceleration 0 - 40 MPH	0 - 18	12	108	354	354
St. lift-off copper 40 - 80MPH	18 - 36	12	324	1063	1417
lift-off Al 150MPH	36 - 66.96	20.6	1063	3487	4,904

Table II shows the appropriate distance for each of these stages assuming the vehicle accelerates at a speed of 1.5m/s^2. In this scenario, the stacked coils would be used for the first 108m, then copper composites for the next 324m, and overlapped aluminum composites for the remainder of the track.

Table III Distance staging @ 1 m/s^2 acceleration

Stage	velocity range (m/s)	δ time (s)	distance m	distance ft	Accumulated Distance ft
acceleration 0 - 40MPH	0 - 18	18	162	531	531
1st lift off copper 40 - 80MPH	18 - 36	18	486	1,594	2126
lift off Al 150MPH	36 - 66.96	30.96	1594	5,229	7355 (1.4 miles)

Table III suggests the corresponding lengths if the vehicle accelerates at only $1 m/s^2$.

In such a hybrid system, a different optimization must be enforced, one in which a single coil span distance x is selected which reflects the use of both copper and aluminum overlapped coils. The modified merit function corresponding to (1) is

$$\mathcal{F} = \$wire_{Cu} * drag_{Cu} + \$wire_{Al} * drag_{Al} + \$magnets\sqrt{drag_{Cu} * drag_{Al}} \quad . \tag{15}$$

Note that the modified merit function must separately account for the drag during the copper stage drag $_{Cu}$ and the aluminum stage drag$_{Al}$. The dual constraint is that the vehicle lift itself at 40MPH with the copper coils and also at 80MPH using the aluminum coils.

The results of the hybrid optimization are summarized in Table IV

Table IV Hybrid System 10 miles 486m copper @ each end, 4 vertical rails
Cu lift @ 40MPH, Al lift @ 80MPH

$$Minimize[\$wire_{Cu} * drag_{Cu} + \$wire_{Al} * drag_{Al} + mags * \sqrt{drag_{Cu} * drag_{Al}}]$$

Row	Burden	L	veh	x	d_{Cu}	d_{Al}	N	$\frac{Drag\ Cu}{1000}$	$\frac{Drag_{Al}}{1000}$	ℓ/D_{Cu}
1	27000	10 mile	6	15.84	0.94	0.82	35.1	2.72	2.25	21.1
2	43000	10 mile	6	15.35	0.96	0.84	53.1	4.46	3.7	24.3
3	*640	1.4miles	1	13.99	0.46	0.42	4	0.087	0.077	43

Row	wt/ 1000	ℓ/D_{Al}	wire Cu	wire Al	I_{Cu}	I_{Al}	cost/ mile	F/C set 1000
1	57.4	25.4	0.827	3.76	3.3	3.14	0.724	1.64
	87.7	23.7	0.835	3.8	3.48	3.31	0.851	1.65
3	3.77	48.4	0.429	.165	1.88	1.84	0.456	0.927

* 2 rails only

The 3 rows of the lower table inset correspond to those in the upper one. The weight burden for the third row corresponds to that for the test sled given the weight associated with each magnet as dictated by (12) . This would suggest that the ideal spacing x of the coils for the test track is 13.99", but is closer to 16" for a 10 mile people mover having a burden of 27,000 lbs.

To what extent are the results sensitive to the weight load associated with each magnet C set? As suggested by (12), the weight associated with each 12" C set is 386-lbs self weight, 164-lbs support structure, and 150-lbs of brush hardware for a total load of 700 lbs. By more efficient support of both the brush mechanisms and perhaps carbon composite struts, this weight could be substantially reduced. If 150-lbs could be shed from this figure, the modified vehicle weight would become

$$wt = burden + N^*[550^*(x-0.75)/12]. \quad (16)$$

Table V System design with a 550lb load/Cset

L	Mat.	speed	# veh	x	d	N	drag/ 1000	//D	wt/ 1000	$wire *10^6	$mag *10^6	cost/ mile *10^6	I kA	F/C 1000
4000ft	Cu	30	6	12.0	.943	42.7	3.26	15.04	49.1	1.13	2.41	4.67	3.24	1.15
4000ft	Al	35	6	12.0	1	153	7.6	13.9	105.9	0.33	8.61	11.8	1.99	0.69
4000ft	Cu	35	6	12.8	0.87	36.7	2.65	17.8	47.23	1.11	2.21	4.37	3.31	1.29
4000ft	Al	40	2	12.0	1	82	4973	14	69.3	0.33	154	2.47	2.43	0.85
10 mile	Al	40	2	12.0	0.995	83	4963	14.1	69,6	4.36	1.55	0.59	2.42	0.84
4000ft	Cu	40	2	15.4	0.778	36	1.964	26	50.9	1.05	0.867	2.53	2.84	1.43
10 mile	Cu	40	2	26	0.932	45	1,793	45	81.1	12.1	1.97	1.41	1.71	1.80
4000ft	Al	40	6	12.0	1	82.0	4973	13.9	69.3	0.33	4.62	6.53	2.43	0.846
10 mile	Al	40	6	12.0	1	82.0	4973	13.9	69.3	4.36	4.62	0.90	2.93	0.846
4000ft	Cu	40	6	14.2	0.844	31.4	2180	21.3	46.7	1.07	2.116	4.21	3.3	1.48
4000ft	Al	80	2	15.2	0.815	28.5	1,880	24.2	45.9	0.31	0.688	1.31	324	1.61
10 mile	Al	80	2	17.5	0.674	39.3	1,562	36.6	57.2	3.91	1.1	0.50	2.36	1.45
4000ft	Cu	80	2	27	0.67	17.5	0.82	58.7	48.1	0.92	0.767	2.22	2.79	2.79
10 mile	Cu	80	2	30.5	0.56	25	0.73	83	60.8	11.9	1.23	1.31	2.10	2.45

Table V shows how the design parameters change if such a reduction could be realized. The lift to drag ratios are greatly enhanced and the overall weight of the vehicle is reduced by 10,000-lbs. The advantages underscore the importance of expending every effort to keep the support and brush weight burden per magnet C set to a minimum. The column marked I indicates the current induced in any one (1 turn) coil of the overlapped coil.

CONCLUSIONS

The design of a complete MAGLEV system is indeed somewhat complicated, involving most critically the desired threshold speed as an input parameter. The directive to minimize cost is of course integral to the design. Towards this end a constrained optimization using sequential quadratic programming is employed to great benefit for minimizing an energy functional. A high order polynomial fit easily obtained using QR decomposition, proves to have a smoothly differentiable function to be operated on by the optimization program. The end result is a process that allows for the characterization of a pole pitch of the winding in the track and the cost for the entire system.

REGARDLESS-OF-SPEED SUPERCONDUCTING LSM CONTROLLED-REPULSIVE MAGLEV VEHICLE

Kinjiro Yoshida, Tatsuya Egashira and Ryuichi Hirai
Department of Electrical Engineering
Faculty of Engineering, Kyusha University
10 - 1 6-chome Hakozaki Higashi - ku
Fukuoka, 812 JAPAN

SUMMARY

This paper proposes a new repulsive Maglev vehicle which a superconducting LSM can levitate and propel simultaneously, independently of the vehicle speeds. The combined levitation and propulsion control is carried out by controlling mechanical-load angle and armature-current. Dynamic simulations show successful operations with good ride-quality by using a compact control method proposed here.

INTRODUCTION

As a superconducting linear synchronous motor (LSM) repulsive Maglev vehicle, MLU002 in Japan is well-known all over the world [1]. This type of repulsive Maglev system is based on the electrodynamic repulsive forces which are generated on superconducting magnets moving over a series of short-circuited conducting coils. This Maglev system is simple but passive and also needs additional coils or sheets for levitation. The generated levitation forces are strongly dependent on the speed of moving magnets. In the speed range from a standstill to relatively high speeds, this Maglev system cannot levitate the vehicle. MLU002 takes off at the speed of about 150 Km/h.

This paper proposes a new repulsive Maglev vehicle system using a superconducting LSM which can propel and levitate simultaneously. This paper also presents a fundamental simulation study on a superconducting LSM Maglev vehicle which can produce repulsive force even at a standstill. With a concept proposed here, the vehicle can be levitated regardless of the vehicle speed. When the mechanical load-angle is controlled to be at a suitable position between half the pole-pitch and the pole-pitch, propulsion and levitation forces are produced simultaneously [2] in the superconducting LSM which has horizontally arranged armature windings on a guideway and horizontally-mounted superconducting magnets on the vehicle. The levitation force as well as the propulsion force are quite independent of the speed of superconducting magnets on the vehicle. By controlling the mechanical load-angle to be the pole-pitch and regulating the

armature-currents, the vehicle is levitated while it remains at a standstill [3]. After that, the vehicle starts running. The dynamic simulations show that the vehicle can run stably at the height of 15 cm, following a given speed pattern.

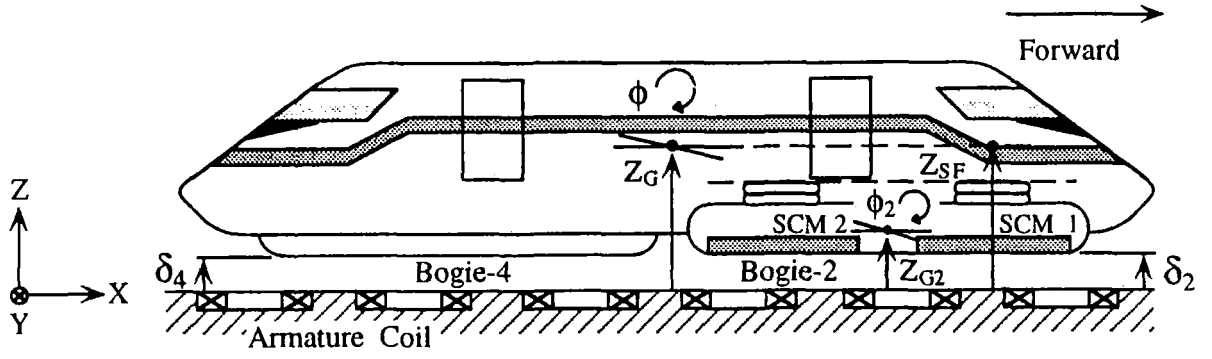

Figure.1 A Model for vehicle dynamics analysis

EQUATIONS OF MOTION

Heave motions of the bogies and the cabin of the vehicle, which is illustrated in Fig. 1, are given as follows:

$$M_B \frac{d^2}{dt^2} Z_{G\,i} = \sum_{j=1}^{2} (F_{Z,\,ij} - f_{s,\,ij} - f_{d,\,ij}) - M_B\, g\,, \quad (i = 1,\ 2,\ 3,\ 4) \tag{1}$$

$$M_C \frac{d^2}{dt^2} Z_G = \sum_{i=1}^{4} \sum_{j=1}^{2} (f_{s,\,ij} + f_{d,\,ij}) - M_C\, g \tag{2}$$

$$f_{s,\,ij} = K_S\, \Delta l_{s,\,ij} \tag{3}$$

$$f_{d,\,ij} = K_D \frac{d}{dt} \Delta l_{s,\,ij} \tag{4}$$

where M_B = mass of bogie
M_C = mass of cabin
$Z_{G\,i}$ = height of CG of bogie-i
Z_G = height of CG of cabin
$F_{Z,\,ij}$ = levitation force
$f_{s,\,ij}$ = restoring force of secondary suspension
$f_{d,\,ij}$ = damping force of secondary suspension
$\Delta l_{s,\,ij}$ = change of length in secondary suspension
K_S = stiffness of secondary suspension
K_D = damping constant of secondary suspension
g = acceleration of gravity

Propulsion motion of the vehicle is described by

$$M \frac{d}{dt} v_x = \sum_{i=1}^{4} \sum_{j=1}^{2} F_{X,ij} - K_A v_x^2 \qquad (5)$$

where $M = 4 M_B + M_C$ = mass of vehicle
v_x = vehicle speed
$F_{X,ij}$ = thrust force acting on each superconducting magnet (SCM)
K_A = coefficient of aerodynamic drag force

The pitching motions of bogies are

$$\begin{aligned} I_{\phi B} \frac{d^2}{dt^2} \phi_i = & - F_{X,i1} L_{BM} \sin(\phi_M + \phi_i) - F_{Z,i1} L_{BM} \cos(\phi_M + \phi_i) \\ & - F_{X,i2} L_{BM} \sin(\phi_M - \phi_i) + F_{Z,i2} L_{BM} \cos(\phi_M - \phi_i) \\ & + (f_{s,i1} - f_{d,i1}) L_{BS} \cos(\phi_S - \phi_i) - (f_{s,i2} - f_{d,i2}) L_{BS} \cos(\phi_S + \phi_i) \qquad (6) \\ & \qquad (i = 1, 2, 3, 4) \end{aligned}$$

where L_{BM} = length between CG's of bogie and SCM
L_{BS} = length between CG of bogie and joint of bogie to secondary suspension
ϕ_M = angle between L_{BM} and X-axis
ϕ_S = angle between L_{BS} and X-axis
$I_{\phi B}$ = moment of inertia of bogie for pitching motion
ϕ_i = pitching angle of bogie-i.

The pitching motion of the cabin is described by

$$\begin{aligned} I_{\phi C} \frac{d^2}{dt^2} \phi = & - \sum_{i=1}^{2} (f_{s,i1} - f_{d,i1}) L_f \cos(\phi + \phi_f) \\ & + \sum_{i=3}^{4} (f_{s,i2} - f_{d,i2}) L_f \cos(\phi + \phi_f) \\ & - \sum_{i=1}^{2} (f_{s,i2} - f_{d,i2}) L_n \cos(\phi + \phi_n) \\ & + \sum_{i=3}^{4} (f_{s,i1} - f_{d,i1}) L_n \cos(\phi + \phi_n) \\ & - \sum_{i=1}^{2} \frac{F_{X,i1} + F_{X,i2}}{2} \left\{ L_f \sin(\phi_f + \phi) + L_n \sin(\phi_n + \phi) \right\} \\ & - \sum_{i=3}^{4} \frac{F_{X,i1} + F_{X,i2}}{2} \left\{ L_f \sin(\phi_f - \phi) + L_n \sin(\phi_n - \phi) \right\} \qquad (7) \end{aligned}$$

where L_f, L_n = length between CG of cabin and joint of cabin to secondary suspensions measured far and near from CG of cabin
ϕ_f, ϕ_n = angles between L_f and X-axis and between L_n and X-axis
$I_{\phi C}$ = moment of inertia of cabin for pitching motion
ϕ = pitching angle of cabin.

In this paper, the equations of motion are solved on the assumption that bogie-1 and 3 make the same motions as those of bogie-2 and 4, respectively.

CONTROL METHOD

Propulsion System

The demand patterns of effective value of armature-current I_1 and the mechanical load-angle x_0 are obtained as shown in equations (8) and (9), by applying the command acceleration-pattern a_{x0} to the analytical equations for LSM Maglev system.

$$I_1^* = \frac{M}{4}\sqrt{\left(\frac{a_{x0}}{K_X}\right)^2 + \left(\frac{g}{K_Z}\right)^2} \tag{8}$$

$$x_0^* = \frac{\tau}{\pi}\tan^{-1}\left(-\frac{a_{x0}K_Z}{g K_X}\right) + \tau \tag{9}$$

where K_X, K_Z = thrust and levitation-force coefficients
I_1^* = demand pattern of effective value of armature-current
x_0^* = demand pattern of mechanical load-angle
τ = pole-pitch.

In a repulsive-mode of the combined levitation and propulsion systems, x_0^* should be controlled within the range $\frac{\tau}{2} \sim \frac{3}{2}\tau$. In order to accomplish LSM operation at the demand mechanical load-angle x_0^*, the control law for x_0 based on PID regulator becomes equation (10).

$$\Delta x_0 = G_P(v_x - v_{x0}) + G_I\int(v_x - v_{x0})\,dt + G_D(\dot{v}_x - \dot{v}_{x0}) \tag{10}$$

$$x_0 = x_0^* + \Delta x_0 \tag{11}$$

where Δx_0 = deviation of x_0
G_P, G_I, G_D = feedback gains
v_{x0} = command speed-pattern of vehicle.

Levitation System

In the levitation system with all the pitching motions neglected, equations of states, which are linearized about steady-state (I_1^*, $x_0^* = \tau$, Z_{G0}, Z_{GB0}) are expressed in the following matrix form:

$$\dot{X} = A X + B U \tag{12}$$

$$Y = C X = [\Delta Z_G] \tag{13}$$

with

$$X = [\ \Delta Z_G \quad \Delta Z_{GB} \quad \Delta \dot{Z}_G \quad \Delta \dot{Z}_{GB}\ ]^T \tag{14}$$

$$U = [\Delta I_1] \tag{15}$$

$$A = \begin{bmatrix} 0 & 0 & 1 & 0 \\ 0 & 0 & 0 & 1 \\ \frac{4K_S}{M_C} & \frac{2K_S}{M_C} & -\frac{8K_D}{M_C} & \frac{4K_D}{M_C} \\ \frac{K_S}{M_B} & \frac{K_{\delta Z} - K_S}{M_B} & \frac{2K_D}{M_B} & \frac{2K_D}{M_B} \end{bmatrix} \tag{16}$$

$$B = \begin{bmatrix} 0 & 0 & \frac{K_{IZ}}{M_B} & 0 \end{bmatrix}^T \tag{17}$$

$$C = [1\ 0\ 0\ 0] \tag{18}$$

where ΔI_1 = deviation of I_1

ΔZ_G = change in height of cabin from Z_{G0}

Z_{G0} = steady-state height of cabin

ΔZ_{GB} = change in height of bogie from Z_{GB0}

Z_{GB0} = steady-state height of bogie

$K_{\delta Z}$, K_{IZ} = linearized coefficients of levitation-force with respect to airgap length and armature-current.

The control law of the levitation system is given by applying the theory of optimal servo control in the following form:

$$\Delta I_1(t) = - K_1 \Delta Z_G - K_2 \Delta Z_{GB} - K_3 \Delta \dot{Z}_G - K_4 \Delta \dot{Z}_{GB} - K_5 \int \Delta Z_G dt \qquad (19)$$

where $K_1, K_2, ..., K_5$ = feedback gains.

$K_1, K_2, ..., K_5$ are determined by solving the following performance index J based on LQ control theory.

$$J = \int_0^\infty \{ q_1 \Delta Z_G(t)^2 + q_2 \Delta Z_{G1}(t)^2 + q_3 \Delta \dot{Z}_G(t)^2 + q_4 \dot{Z}_{G1}(t)^2 + r \Delta I_1(t)^2 \} dt \qquad (20)$$

where q_1, q_2, q_3, q_4, r = weighting coefficients.

Therefore, the effective value of armature-current is calculated from

$$I_1 = I_1^* + \Delta I_1 \qquad (21)$$

The demand instantaneous value of the u-phase of armature-current can be obtained by

$$i_u^* = \sqrt{2}\, I_1 \cos\left(\frac{\pi}{\tau}\int_0^t v_{x0}\, dt + \frac{\pi}{\tau} x_0 + \frac{\pi}{2}\right) \qquad (22)$$

Note that $\frac{\pi}{2}$ in equation (22) is used for a starting position of the vehicle to coincide with the left-hand conductor of the u-phase coil.

MAGLEV RUNNING SIMULATIONS

Basic behavior of the new Maglev vehicle which is levitated and propelled independently of vehicle speed according to a principle of the combined levitation and propulsion are analyzed numerically using equations (1) - (7) subject to the control method expressed by equations (10), (11), (19) and (21). The vehicle parameters are summarized in Table 1.

Case Study for Acceleration and Deceleration of 1 m/s^2

Figure 2 shows numerical experiments to show response to the command patterns which are given with dotted lines in Figs. 2 (a) - (d) for the speed and acceleration of the vehicle and airgap-lengths of the bogies. Just before 1 s and just after 69 s, the vehicle levitates steadily at standstill. The vehicle starts running in a levitated state with airgap lengths $\delta_2 = 15$ mm and $\delta_4 = 15$ mm.

Table 1. Superconducting LSM Vehicle

Superconducting Magnet :			
No. of Poles per one Bogie	P	=	2
Coil Length	L_{SC}	=	2.2 m
Coil Width	W_{SC}	=	0.5 m
Pole-Pitch	τ	=	2.7 m
MMF	I_{SC}	=	700 kAT
Armature Winding :			
Coil Length	L_{AC}	=	1.5 m
Coil Width	W_{AC}	=	0.6 m
Number of Turn	T_a	=	30 turns
Mass :			
Mass of one Bogie	M_B	=	2 t
Mass of Cabin	M_C	=	10 t
Secondary Suspension :			
Stiffness	K_S	=	1.3×10^6 N/m
Damping Constant	K_D	=	2.3×10^5 N • s/m
Natural Length	l_0	=	0.3 m
Vehicle Size :			
Cabin Length	L_C	=	10.8 m
Cabin Width	W_C	=	1.5 m
Cabin Height	H_C	=	2.0 m
Bogie Height	H_B	=	0.5 m
The Moment :			
the Moment of Inertia of Bogie for Pitching Motion	$I_{\phi B}$	=	4208 kg • m^2
the Moment of Inertia of Cabin for Pitching Motion	$I_{\phi C}$	=	100533 kg • m^2
Coefficient of aerodynamic force :	K_A	=	1.305 N • s^2/m^2

Figures 2 (a) and (b) show that the vehicle follows very well the command speed- and acceleration-patterns. Figures 2 (c) and (d) also show that the rear SCM2 of the bogie-2 and the front SCM1 of the bogie-4 follow very well the command airgap-length patterns, but the front SCM1 of the bogie-2 and the rear SCM2 of the bogie-4 do not follow that command patterns. During the acceleration phase, the SCM1's of the bogie-2 and 4 are higher and lower than the command value by about 1.5 cm, respectively, and during the deceleration phase vice versa. This is the reason why thrust and braking forces as shown in Fig. 2 (g) produce the pitching motions in the inverse direction of each other during acceleration and deceleration phases, respectively. Those pitching motions influence strongly only the front and rear SCM's in the vehicle. But, though the distance between the neighboring bogies is quite short, the secondary suspensions reduce the pitching motions of the cabin to about 67% as shown in Fig. 2 (I). Figures 2 (j), (k) and (m) show that the center of gravity (CG) of the vehicle does not change due to lack of heave motions in the SCM2 of the bogie-2 and the SCM1 of the bogie-4, which the heave motions of the CG's of bogie-2 and 4 cause as shown in Fig. 2 (n). It is thus found that the ride-quality is

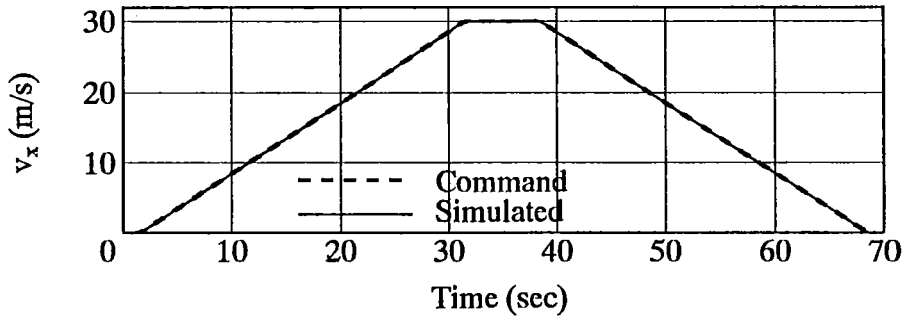

(a) Command and simulated vehicle speeds

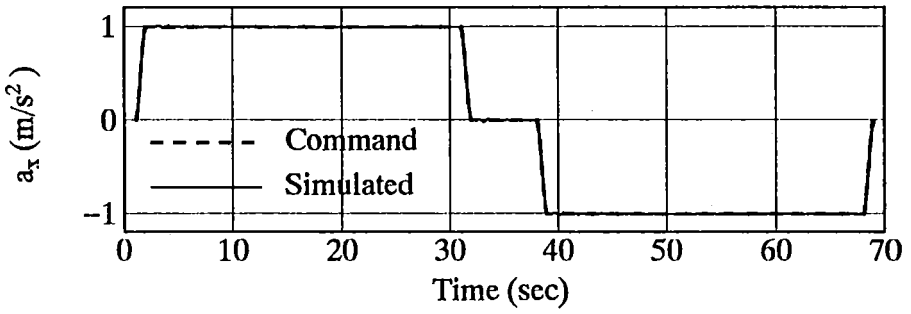

(b) Command and simulated vehicle accelerations

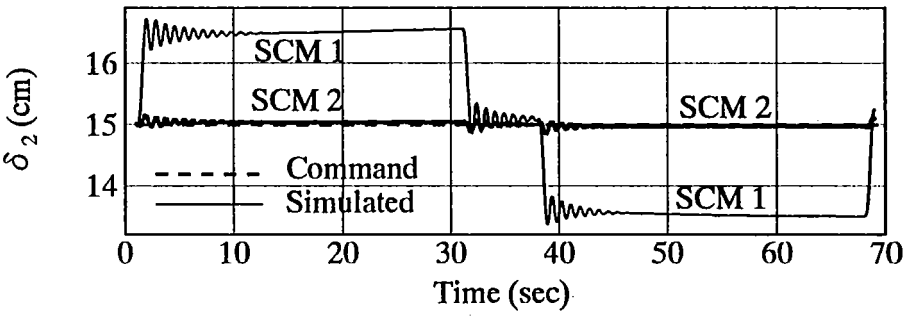

(c) Airgap length of bogie−2

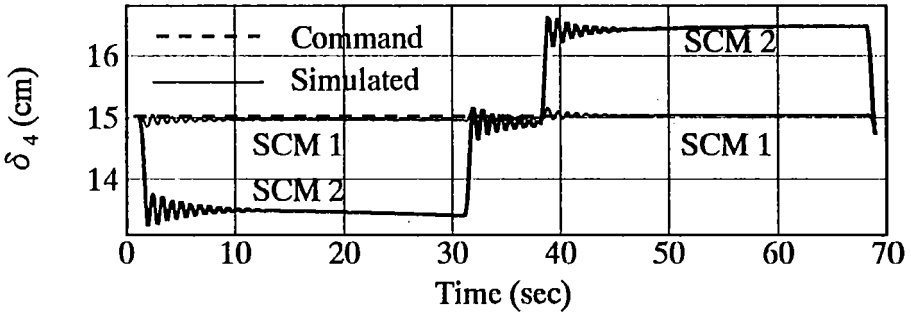

(d) Airgap length of bogie−4

Figure. 2 Levitation and propulsion control for acceleration and deceleration of 1 m/s^2

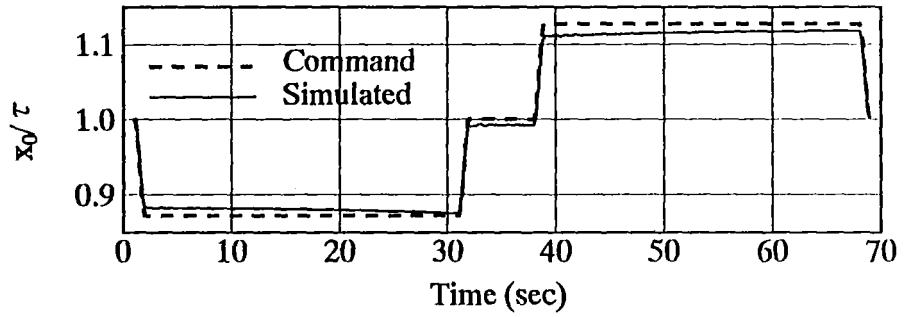

(e) Command and simulated mechanical load-angles

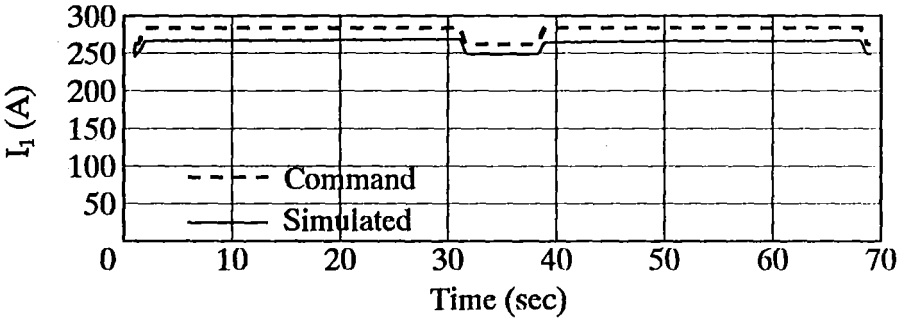

(f) Command and simulated stator-currents

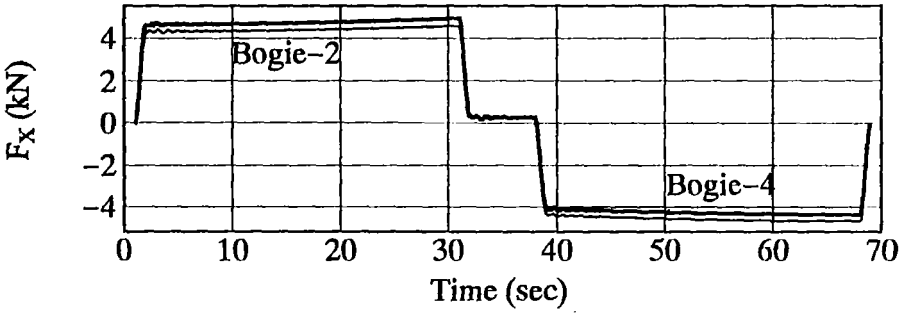

(g) Thrust force

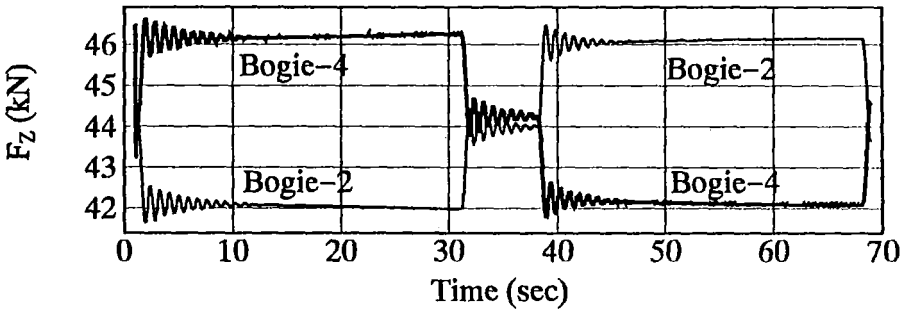

(h) Lift force

Figure. 2 Levitation and propulsion control for acceleration and deceleration of 1 m/s^2

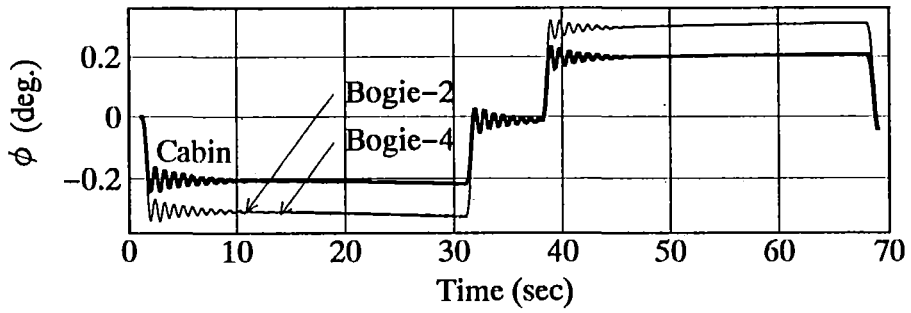

(i) Pitching angles of cabin and bogie−2 and 4

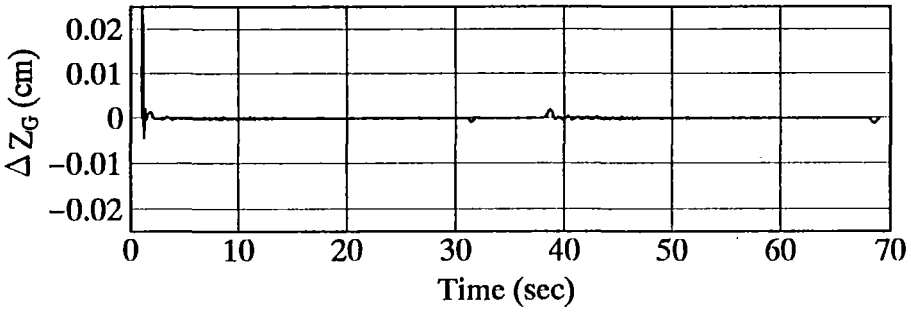

(j) Heave variation of cabin

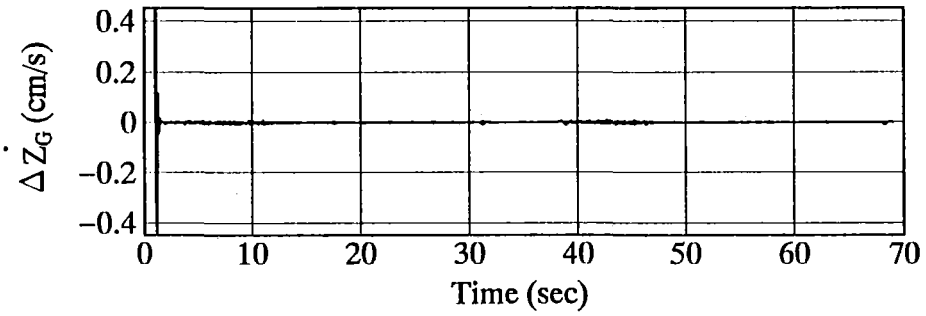

(k) Heave velocity of cabin

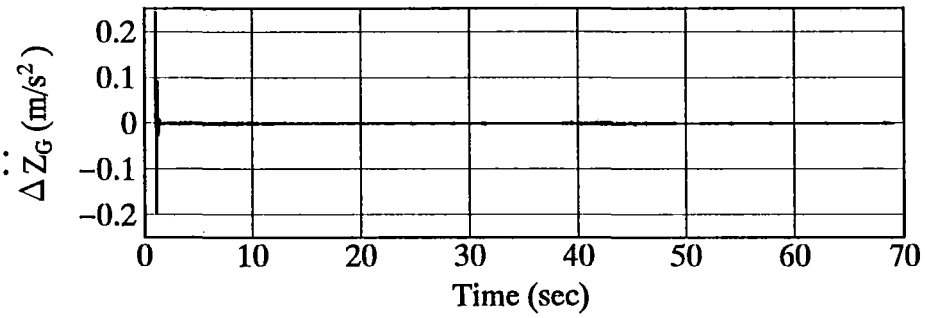

(l) Heave acceleration of cabin

Figure. 2 Levitation and propulsion control for acceleration and deceleration of 1 m/s^2

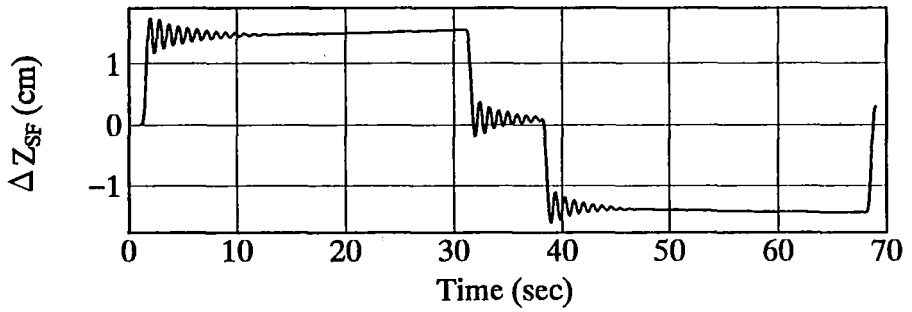

(m) Heave variation of front cabin above the secondary suspension

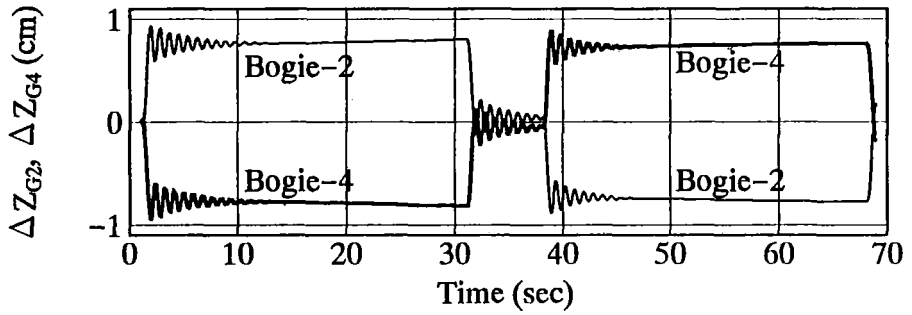

(n) Heave variations of CG of bogie-2 and 4

Figure. 2 Levitation and propulsion control for acceleration and deceleration of 1 m/s^2

very good around the CG of the cabin. Figure 2 (m) shows the heave variation of the front portion of the cabin above the secondary suspension measured far from the CG of the cabin which is about the same variation as +/- 1.5-cm-variation of SCM1 of the bogie-2 as shown in Fig. 2 (c). This variation is not so important, and its acceleration is much smaller than 0.1g. Therefore, the ride-quality near the front and rear portions of the vehicle is also very good.

Concerning the control of mechanical load-angle and armature-current, it is known from Figs. 2 (e) and (f) that, though a compact control method proposed here is used, the simulated results show a good agreement with the command patterns within a small error of about 6%. Figure 2 (f) also shows that the simulated current is smaller than the command one. This is due to the fact that the SCM2 of the bogie-4 heaved upward by 1.5 cm producing larger levitation-force than the SCM1 of the bogie-2 heaved downward by 1.5 cm.

Case Study for Acceleration and Deceleration of 3 m/s^2

Figure 3 shows numerical experiments for the case where the levitated vehicle is propelled with 3 times larger acceleration than that in Fig. 2. As shown in Figs. 3 (c) and (d), during the acceleration phase, airgap-length variations of the SCM1 of the bogie-2 and the SCM2 of the bogie-4 are proportionally 3 times larger and smaller than those of Fig. 3. It is known from Fig. 3 (f) that the armature-current is also controlled with about 3 times larger error than that in Fig. 2. But Figs. 3 (a) and (b) show for the vehicle to follow very well the command patterns. Figures 3 (j), (k) and (l) show the good ride-quality which is almost similar with that in Fig. 2. It is confirmed that a compact control method enables the vehicle to run stably even in this case.

CONCLUSIONS

A new type of superconducting LSM Maglev vehicle system is proposed which can levitate and propel independently of the vehicle speeds. A compact control method is developed which is based on the concept of controlling the levitation system with armature-current and the propulsion system with mechanical load-angle. It is verified from dynamic simulations that the vehicle is controlled to follow very well the command speed pattern in both cases for accelerations of 1 m/s^2 and 3 m/s^2. Though the compact control method is applied, the vehicle is operated with very high ride-quality.

Operation in the range of $\frac{\tau}{2} \sim \frac{3}{2}\tau$ have never previously been used, but have recently been successfully demonstrated experimentally by us [4]. The present study gives a base for a large-scale new Maglev vehicle.

ACKNOWLEDGMENTS

We appreciate the help of Hiroshi Takami in preparing the manuscript.

REFERENCES

1. Fujie: Running Characteristics of the MLU002 Maglev Vehicle and Future Development Plan, Proc. Inter. Conf. Maglev '88 in Hamburg, June 1988, pp. 281-287.

2. K. Yoshida: Magnetic Levitation and Linear Motor, Science of Machine, Vol. 42, No. 4, 1990, pp. 468-474.

3. K. Yoshida and S. Nagao: Levitation and Propulsion Control Simulation of Regardless-of-Speed Superconducting LSM Repulsive Maglev Vehicle, Proc. of the 3rd Symposium on Electromagnetic Forces, June 1991, pp. 201-206.

4. K. Yoshida; H. Takami; N. Shigemi; and A. Sonoda: Repulsive-Mode Levitation and Propulsion Control of a Land Traveling Marine-Express Model Train ME03, Proc. of LDIA '95 Nagasaki, 1995, pp. 41-44.

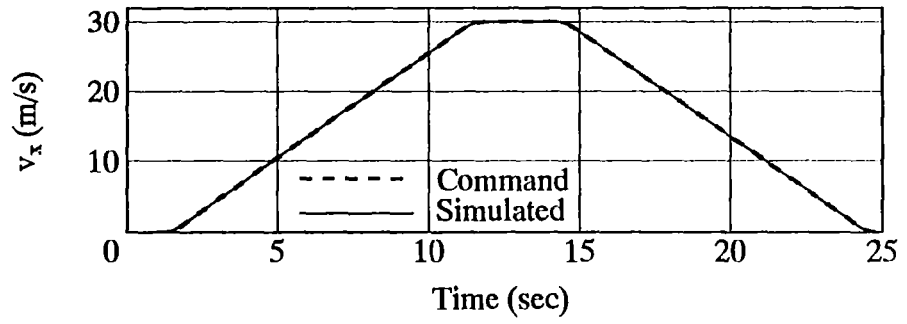

(a) Command and simulated vehicle speeds

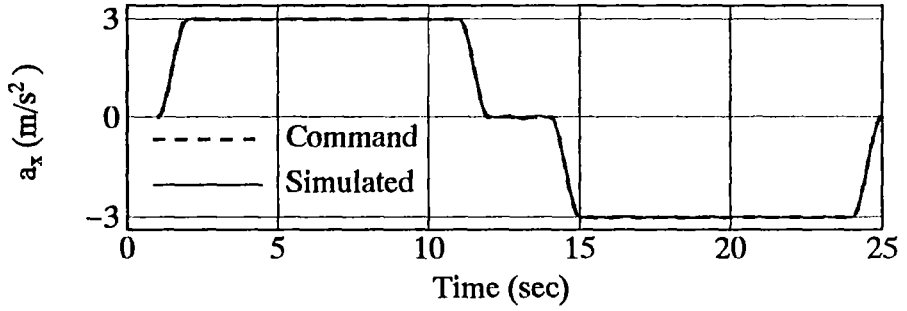

(b) Command and simulated vehicle accelerations

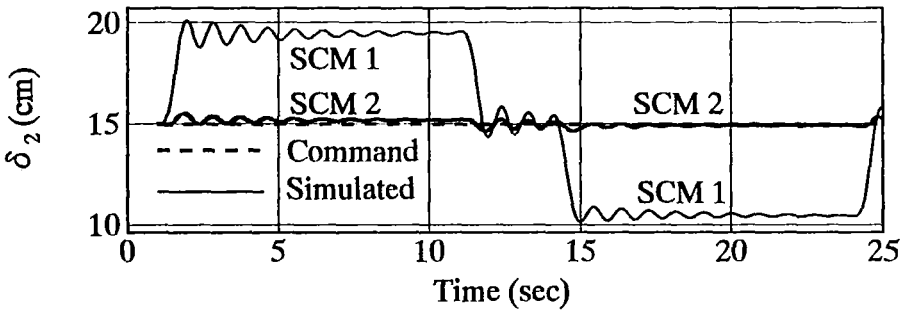

(c) Airgap length of bogie−2

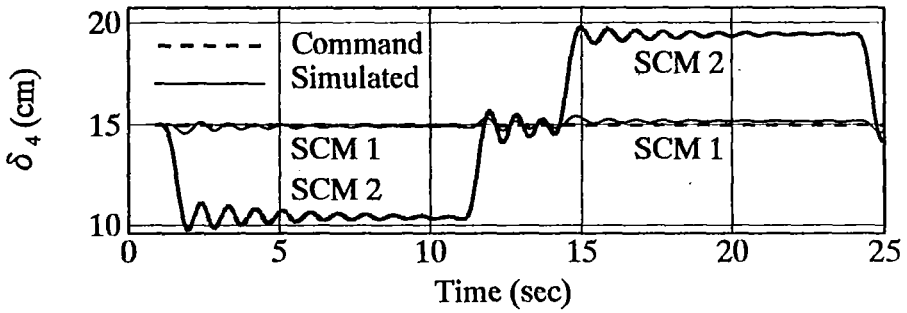

(d) Airgap length of bogie−4

Figure. 3 Levitation and propulsion control for acceleration and deceleration of 3 m/s^2

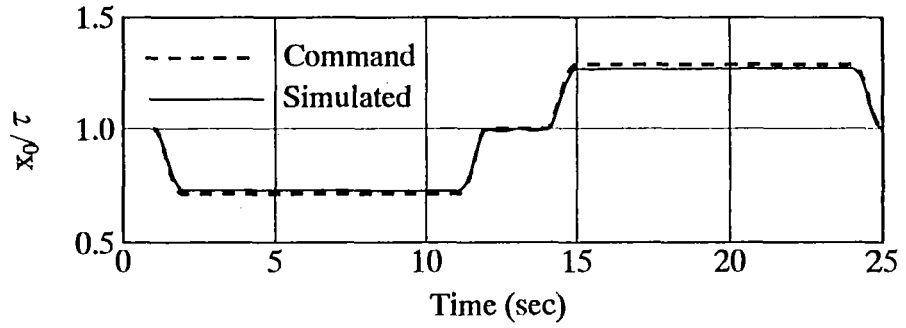

(e) Command and simulated mechanical load-angles

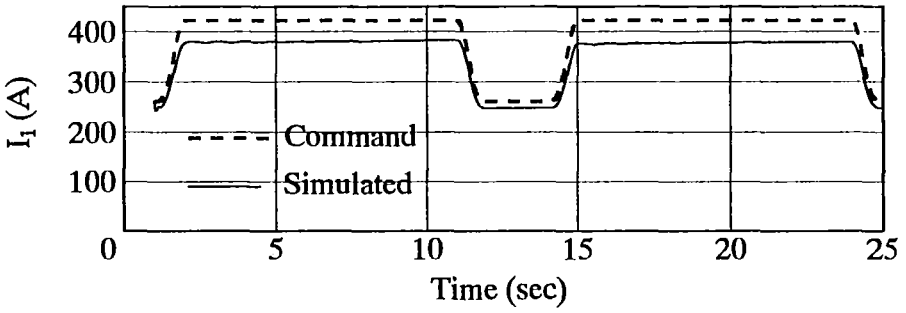

(f) Command and simulated stator-currents

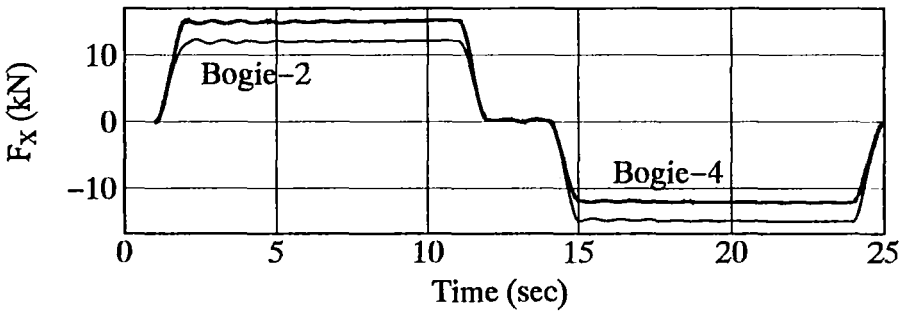

(g) Thrust force

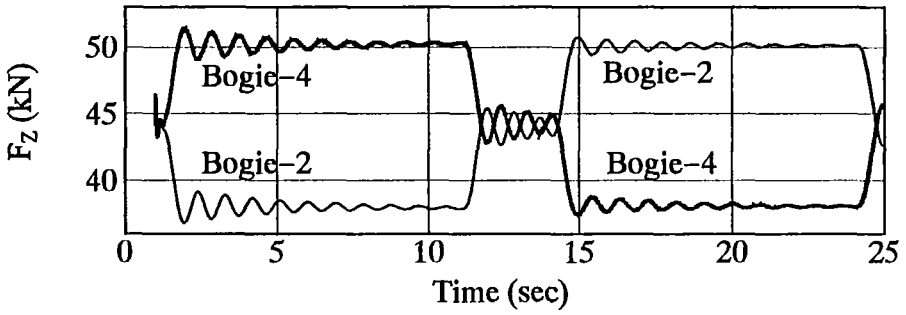

(h) Lift force

Figure. 3 Levitation and propulsion control for acceleration and deceleration of 3 m/s^2

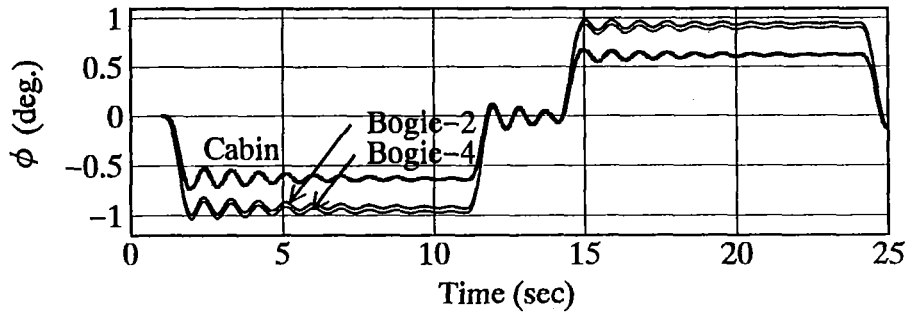

(i) Pitching angles of cabin and bogie-2 and 4

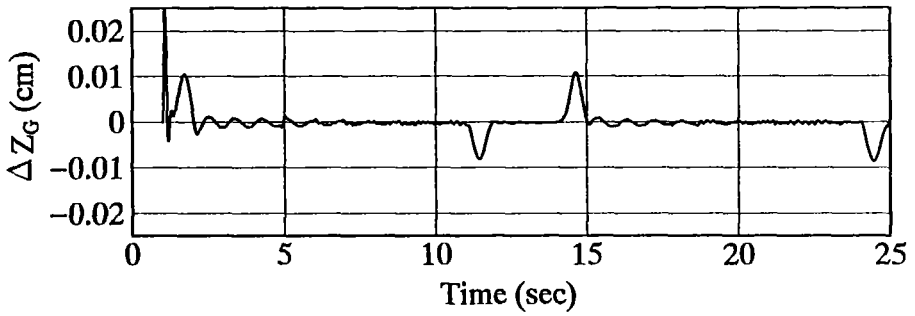

(j) Heave variation of cabin

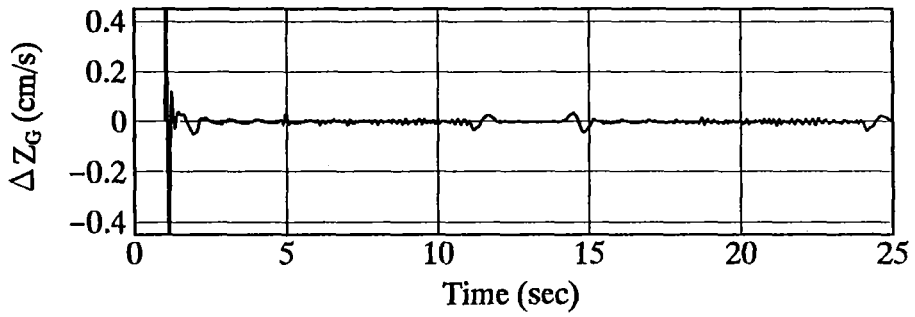

(k) Heave velocity of cabin

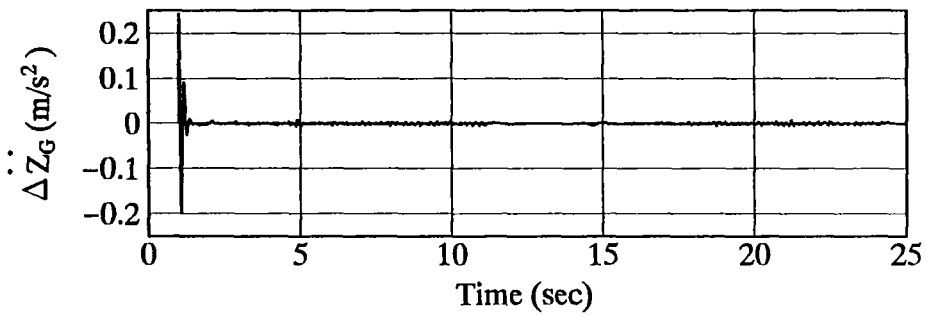

(l) Heave acceleration of cabin

Figure. 3 Levitation and propulsion control for acceleration and deceleration of 3 m/s^2

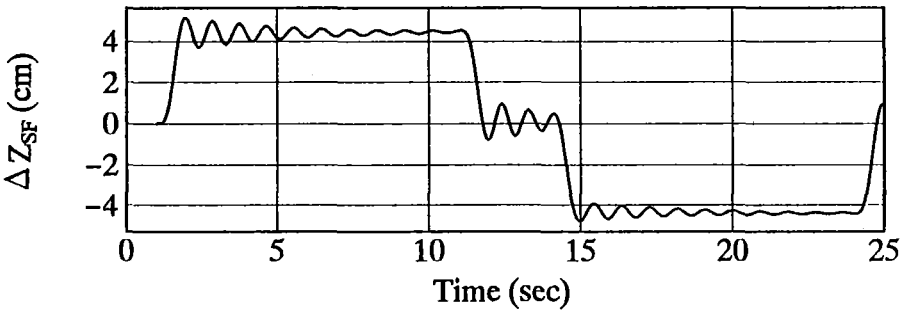

(m) Heave variation of front cabin above the secondary suspension

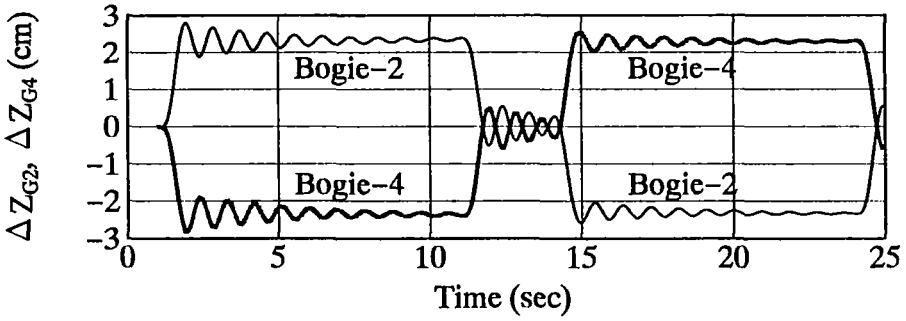

(n) Heave variations of CG of bogie-2 and 4

Figure. 3 Levitation and propulsion control for acceleration and deceleration of 3 m/s^2

U.S. ADVANCED FREIGHT AND PASSENGER MAGLEV SYSTEM

John J. Morena
Gordon Danby
James Powell
American Maglev Star Inc.
Stuart, FL 34994

SUMMARY

Japan and Germany will operate first generation Maglev passenger systems commercially shortly after 2000A.D. The United States Maglev systems will require sophisticated freight and passenger carrying capability. The U.S. freight market is larger than passenger transport. A proposed advanced freight and passenger Maglev Project in Brevard County Florida is described. Present Maglev systems cost 30 million dollars or more per mile. Described is an advanced third generation Maglev system with technology improvements that will result in a cost of 10 million dollars per mile.

Global Maglev Technology

Gordon Danby and James Powell proposed the first practical Maglev concept in 1966. This first generation transport concept included lightweight and powerful superconducting magnets that would levitate and propel a vehicle by inductive interaction with a guideway that contained normal aluminum wire loops at ambient temperature. During 1969 through 1971 they also developed and described the concepts of the null flux configuration and linear synchronous motor which have been developed by Japan into their Superconducting Linear Motor Express System.

Superconducting Maglev systems such as the recent and third generation American Maglev Star Inc. (AMS) system achieve large 6 to 8 inch clearances between the vehicle and guideway.

The magnetic fields are inherently and strongly stable against any external force such as wind gusts, up and down land grades, curves, etc. This type of system can be designed to have very low magnetic drag and switch to different guideways at full operating speed while being propelled at high efficiency using a small AC current in the guideway.

Japan is presently building, in Yamanishi Perfecture, the initial 25 miles of a 300 mph, 300 mile long Tokyo to Osaka Maglev route. Germany has developed an alternate Maglev technology approach based on attracting magnetic forces between conventional electromagnets and ferromagnetic iron rails operating at ambient temperature. Electromagnets as compared to superconducting magnets are severely constrained by electric power consumption. The clearance between the guideway and vehicle therefore is only about 3/8 inch. Superconducting Maglev is strongly stable against all conceivable external forces. Electromagnetic Maglev is inherently strongly unstable. Guideway contact is only prevented by sensing the gap and adjusting current by milliseconds in the vehicle electromagnet windings so as to counteract any movement towards or away from normal suspension points. Plans to build a 175 mile Transrapid line between Hamburg and Berlin should result in system operations around 2004 AD.

During the late 60's to early 70's the United States started several small Maglev study programs that were discontinued. The U.S. restarted several small study efforts a few years ago under the National Maglev Initiative and authorized under ISTEA a full scale prototype development program, but due to budget deficit constraints, work on U.S. Maglev has again been halted. The only Maglev development work currently under way is taking place in the state of Florida as a direct result of the efforts of the Florida Department of Transportation.

Benefits and Capabilities of Maglev Systems

Benefits of Maglev transport systems include 1) more energy efficiency than automobiles and airplanes (Figure 1); 2) much less polluting to the environment (Figure 2); 3) independent of oil supply and imports; 4) much lower transport costs; 5) capable of carrying larger capacity of passengers along given corridors; 6) shorter travel times over moderate distances; and 7) not affected by bad weather.

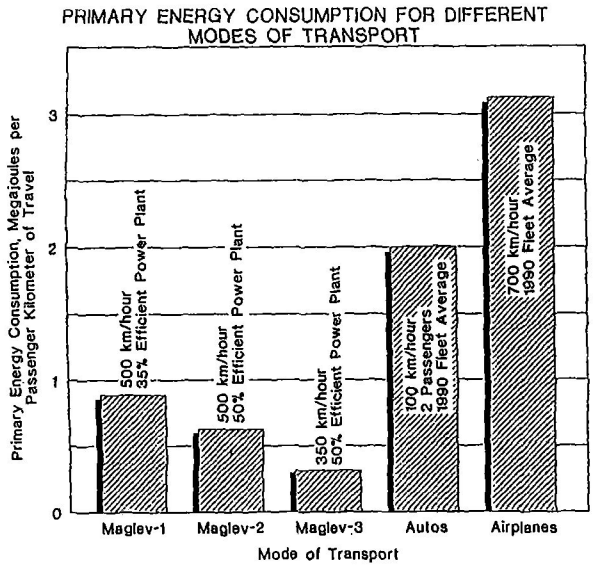

Figure 1
Transport Energy Consumption

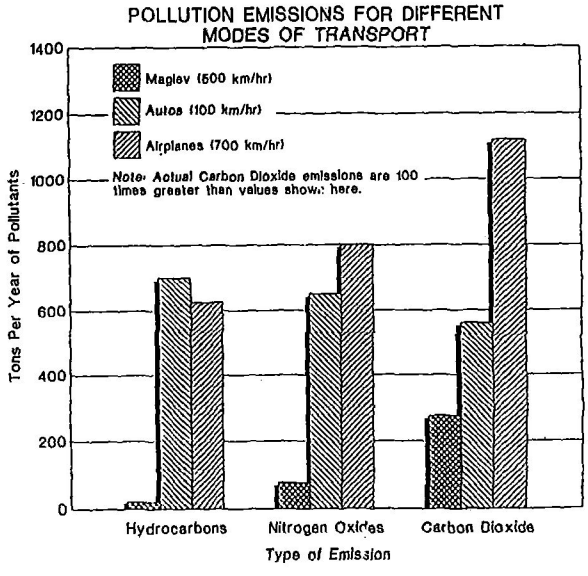

Figure 2
Transport Pollution Emissions

Figure 3 shows that intercity transport accounts for slightly more than one-half of the current annual U.S. outlay. Intercity freight transport out-lay is almost 4 times greater than that of air passenger travel. At 177 billion dollars per year versus 50 billion dollars, Maglev market potential is much greater for intercity truck type freight than intercity passengers. Policy makers, transportation proponents including analysts, Maglev designers and builders should realize this fundamental fact. Maglev is still being viewed primarily as a passenger carrier instead of a freight carrier with the secondary role as a passenger carrier.

Average intercity passenger trip distance is around 600 miles. Average intercity truck haul distance is 400 miles. AMS vehicles could carry containerized freight as well as passengers. A Maglev vehicle carrying truck trailers or containers would be about 10% heavier but it could travel on a common guideway along with passenger vehicles. This type of vehicle comparison is shown in Figure 4. "Roll-on, roll-off" trailer and container technology is common both domestically and internationally. Channel trains take advantage of the concept. Operating costs including energy, vehicle amortization and system, for freight and passenger transport are shown in Figure 5. These costs are approximately 20 to 25% of the air and truck transport operating costs. The guideway amortization costs are inversely proportional to the traffic carried and are not included.

U.S. OUTLAY AND DEMAND BY TRANSPORT MODE

INTERCITY TRANSPORT MODE	1992 OUTLAY (B $ / YEAR)	1992 DEMAND (BILLION TON MILES OR PASSENGER MILES/YEAR)	NOTES
Passenger Auto	260	1683	½ of Total Auto 46¢ Per Vehicle Mile
Truck Freight	177	815	22¢ Per Ton Mile 400 Mile Avg. Haul
Air Passengers	49	367	12.5¢ Per Passenger Mile 1000 Miles Avg. Trip
Rail Freight	31	1107	3¢ Per Ton Mile (Bulk) 700 Mile Avg. Haul
Air Freight	15	11	1.30$ Per Ton Mile
Rail/Bus *Passenger*	4	38	10¢ Per Passenger Mile

Source - 1994 Statistical Abstracts

Figure 3
U.S. Outlay and Demand

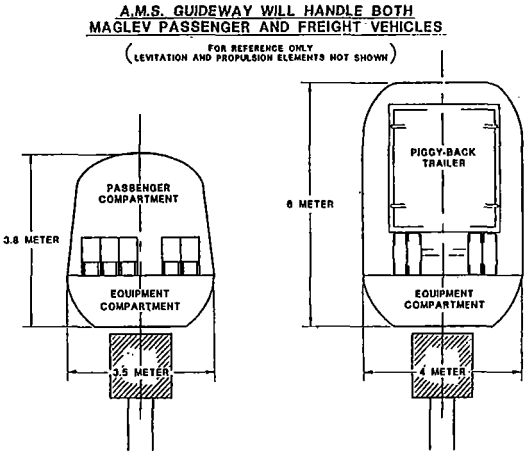

Figure 4
AMS Guideway Will Handle Both Freight and Passengers

Guideway payback depends on the traffic volume as shown in Figure 6. Traffic loading as shown above is achievable in many locations in the United States. Freight and passenger systems that carry on the order of 1,000 trailer equivalents a day and 10,000 passengers a day result in a pay back period of about 4 years. Figure 7 shows a 16,000 mile National Maglev Network that connects virtually all of the 100 largest metropolitan areas in the U.S. Present transport systems operate as networks and so Maglev systems should be viewed in the same way. The Network indicates that 70% of the population live within 15 miles of a maglev station and 95% in the states served by the network.

OPERATING COSTS FOR MAGLEV TRANSPORT

COST COMPONENT	PASSENGERS CENTS/PASSENGER MILE)	TRAILER FREIGHT (CENTS/TON MILE)
PROPULSION ENERGY (80% EFFICIENT LSM)	0.53	3.5
VEHICLE AMORTIZATION	1.14	2.7
MISCELLANEOUS (INCL. PERSONNEL)	1.3	1.0
TOTAL	3.0	7.2
BASIS:	5 M $ VEHICLE 5 YEAR WRITE-OFF 100 PASSENGERS (2/3 OF MAX. CAPACITY) 40% DUTY FACTOR 250 MPH AVERAGE SPEED C_D = 0.20 L/D_{MAG} = 100 A_F = 10 M_2	3 M $ VEHICLE SAME 1 TRAILER (25 T PAYLOAD) SAME SAME SAME SAME A_F = 18 M^2

Figure 5
Maglev Transport Operating Costs

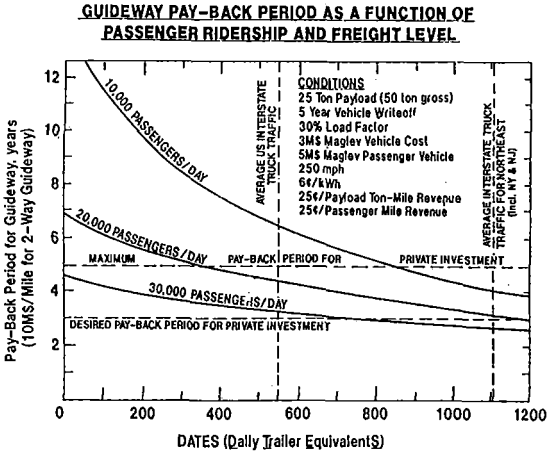

Figure 6
Guideway Pay-Back Period

Two principal Maglev implementation requirements are needed. One is cost and the other is ability to switch vehicles off-line that are traveling at full operating speed on the main guideway. Both requirements are achievable.

First generation Maglev guideway costs are on the order of 30 million dollars per mile. AMS designs are based on narrow beam and pier guideway technology which can be mass produced and prefabricated at local factories and shipped to construction sites for rapid assembly. This is shown in Figure 8. A projected AMS guideway cost for two way travel is around 10 million dollars per mile.

Figure 9 shows the AMS format for high speed switching technology which is the second requirement. It includes a specially shaped guideway at high speed switch locations and it is possible to divert 300 mph vehicles from the main guideway onto the secondary guideway where deceleration, unloading and loading would take place. After operations are complete the vehicles would accelerate up to 300 mph and enter the main guideway. In this way vehicles could either stop at or skip stations.

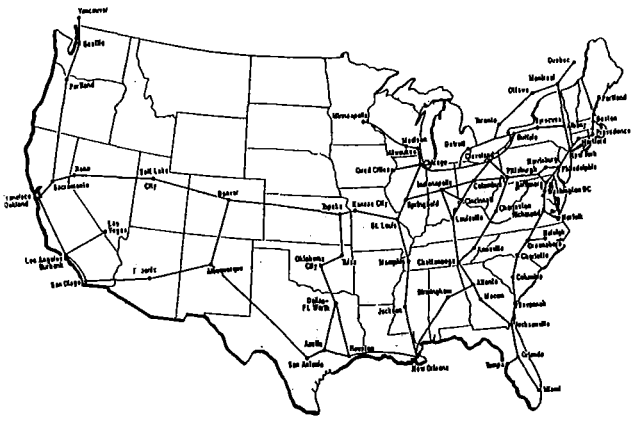

Figure 7
National Maglev Network

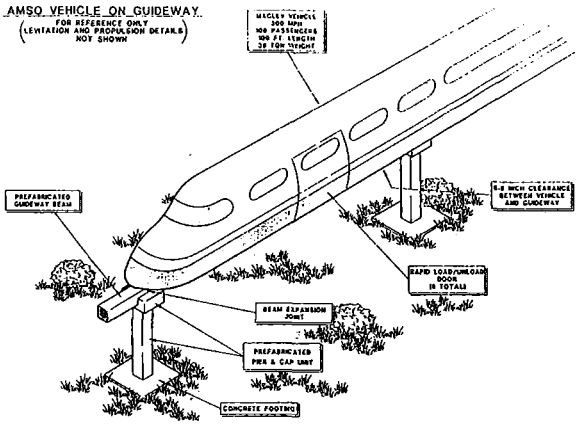

Figure 8
Narrow Beam Guideway

Development of an Advanced Maglev Industry in the United States

Although the U.S. was the leader in establishing the concepts for advanced superconducting magnet Maglev it starts from far behind in the Global Maglev race. However high speed transportation technologies are being incubated in the state of Florida and if a vigorous program were to be pursued, there is still time to catch up and "leap-frog" to a more advanced third generation system. The U.S. has advanced engineering and industrial capability to achieve this more advanced system, but budget problems appear to prevent the government from taking the leading role. The only alternative is private, public partnerships where the private sector assumes the role of technology developer and shares the burden with the public sector.

American Maglev Star Inc. is following this approach in the Brevard Count Florida Project. AMS has proposed a 20 mile Maglev transportation system to demonstrate the new advanced technology. The system would run between Port Canaveral in the east to TICO airport in the west with an intermediate stop planned at the Kennedy Space Center Visitors Center, as shown in Figure 10. This route appears to have sufficient ridership potential that it could return its investment in a reasonable period and it has strong local and state backing.

The project is planned to start with a phased program. The AMS technology development is already benefiting Brevard County and the state with spin-off industrial applications in the area of advanced superconducting and normal magnets, conductor and related electromagnetic applications that include transportation, medical MRI, power storage (SMES), high energy physics accelerators and others.

The phased program will contain three levels in the development work plan. Level 1A will include the development of electromagnetics and a full scale mockup. Level 2A will result in the fabrication of approximately 85 meters of smart guideway including advanced infrastructure. The National High Magnetic Field Lab in Tallahassee will provide support for the development of high temperature superconductors as coils for Maglev magnets. The National Aviation and Transportation Center will provide multimodal simulation support and local Brevard County as well as national industry will provide additional technology development support.

In the level 2 phase AMS proposes to lengthen the guideway to 250 meters and construct a full scale, short and light Maglev vehicle that will operate at speeds to around 100Km/h.

In the level 3 work plan phase a full demonstration of Maglev transportation system components is planned. A high speed switch would be installed on an extended guideway of 2,500 meters. A full scale freight and passenger simulator vehicle would be fabricated and operated through the switch at 300 Km/h. At the completion of level 3 of the phased program the AMS technology would be ready for certification and validation of the system operating and safety parameters.

Then with private and other investments to start the 20 mile project, it appears that this system could be the demonstrator for an advanced U.S. Maglev System that could then be implemented at many locations throughout the Nation.

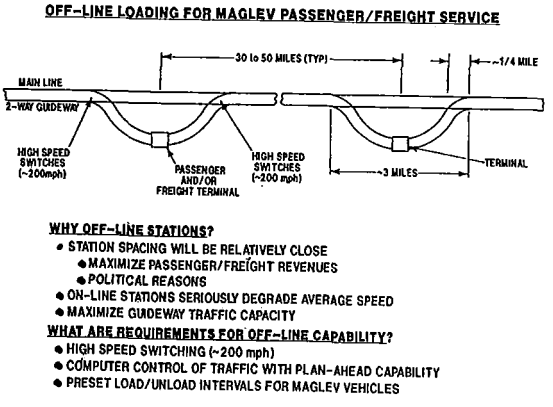

Figure 9
High Speed Switch

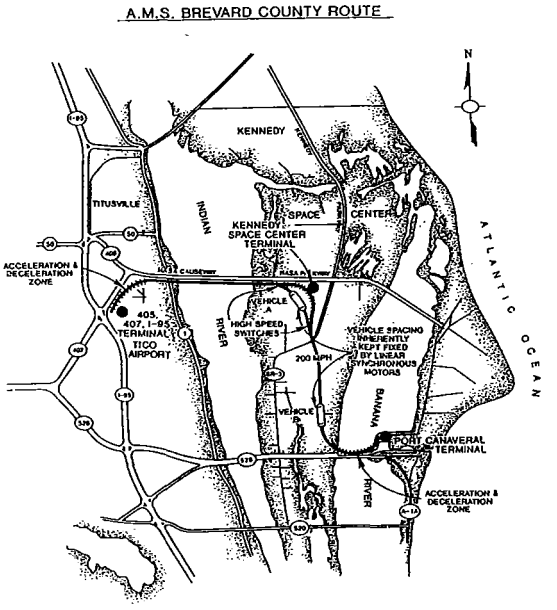

Figure 10
Proposed AMS Brevard County Maglev Route

Session 5 -- Controls 1

Chairman: Bibhuti Banerjee
Premag Incorporated

DESIGN OF ROBUST ADAPTIVE UNBALANCE RESPONSE CONTROLLERS FOR ROTORS WITH MAGNETIC BEARINGS

Carl R. Knospe
Samir M. Tamer
Stephen J. Fedigan
Department of Mechanical, Aerospace and Nuclear Engineering
University of Virginia
Charlottesville, Virginia, 22903

ABSTRACT

Experimental results have recently demonstrated that an adaptive open loop control strategy can be highly effective in the suppression of unbalance induced vibration on rotors supported in active magnetic bearings. This algorithm, however, relies upon a predetermined gain matrix. Typically, this matrix is determined by an optimal control formulation resulting in the choice of the pseudo-inverse of the nominal influence coefficient matrix as the gain matrix. This solution may result in problems with stability and performance robustness since the estimated influence coefficient matrix is not equal to the actual influence coefficient matrix. Recently, analysis tools have been developed to examine the robustness of this control algorithm with respect to structured uncertainty. Herein, these tools are extended to produce a design procedure for determining the adaptive law's gain matrix. The resulting control algorithm has a guaranteed convergence rate and steady state performance in spite of the uncertainty in the rotor system. Several examples are presented which demonstrate the effectiveness of this approach and its advantages over the standard optimal control formulation.

INTRODUCTION

The active control of unbalance vibration in rotating machinery using magnetic bearings has generated a great deal of interest in the last decade [1-10]. Recently, research in this area has focused on the application of adaptive open loop (or feedforward) strategies. This type of control has the advantage of not placing any constraint on the design of the stabilizing feedback control loop for the rotor. Thus, the transient performance of the machine can be optimized without considering its unbalance response.

An important issue in the application of the adaptive open loop control (AOLC) to industrial machines is the stability and performance robustness of the unbalance control algorithm employed. Recently, the authors have demonstrated that the stability and performance robustness of an AOLC algorithm can be analyzed using structured singular value methods [11]. In this paper, these methods are extended to provide a synthesis procedure for the design of the AOLC gain matrix. Several examples are

presented which demonstrate the effectiveness of the design procedure and its advantage over the standard approach that uses a gain matrix derived from optimal control theory.

Mathematical Notation

The two-norm of a vector v is indicated by the notation $\|v\|$. The maximum singular value of a matrix P is denoted by $\overline{\sigma}(P)$ and the spectral norm by $\rho(P)$. The lower and upper linear fractional transformations [12] of P are given the notations $\mathcal{F}_l(P,Q)$ and $\mathcal{F}_u(P,R)$ respectively where the matrices Q and R are assumed to be appropriately dimensioned. The Redheffer star-product [13] of appropriately dimensioned matrices P and Q will be denoted by $\mathbf{S}(P,Q)$. The structured singular value [12,14] of a matrix P is indicated by the notation $\mu_\Delta(P)$. The symbol S_Δ is used to denote the set of all matrices of a defined block structure.

ADAPTIVE OPEN LOOP CONTROL

Adaptive open loop control has been shown to provide excellent vibration attenuation over an operating speed range, to quickly respond to sudden changes in unbalance, and to be computationally simple [10].

The concept of adaptive open loop control is quite simple. Synchronous perturbation control signals are generated and added to the feedback control signals. The magnitudes and phases of these sinusoids are periodically adjusted so as to minimize the rotor unbalance response. In this paper, a particular form of adaptive open loop control, referred to as *convergent control*, will be examined. The convergent control algorithm uses a model of the rotor system where vibration is related to the applied open loop signals via

$$X = TU + X_0$$

where X is a n-vector of the complex synchronous Fourier coefficients of the n vibration measurements, U is a m-vector of the complex synchronous Fourier coefficients of the m applied open loop signals, X_0 is a n-vector of the complex synchronous Fourier coefficients of the uncontrolled vibration, and T is a $n \times m$ matrix of complex influence coefficients relating the open loop signals to the vibration measurements. The influence coefficient matrix is the transfer function matrix of the supported rotor (with feedback control) from perturbation forces at the bearings to the displacements at the sensors, evaluated at the rotor operating speed Ω,

$$T = G_{f\to d}(j\Omega) \equiv \mathbf{C}(j\Omega\mathbf{I} - \mathbf{A})^{-1}\mathbf{B} + \mathbf{D}$$

where the rotor/bearing system is described by the state space model $(\mathbf{A},\mathbf{B},\mathbf{C},\mathbf{D})$:

$$G_{f\to d}(s) \equiv \left[\begin{array}{c|c} \mathbf{A} & \mathbf{B} \\ \hline \mathbf{C} & \mathbf{D} \end{array}\right]$$

Since the convergent control algorithm updates the control vector U periodically, the subscript i will be used to denote the i'th update. The time between the i'th and i+1'th update is referred to as cycle i of the algorithm. During cycle i, the control U_i is applied resulting in the vibration X_i. This vibration vector is computed during cycle i using the measurements from the position sensors. The vibration vector is related to the control vector by

$$X_i = TU_i + X_{0i} \tag{1}$$

where T is assumed to be changing slowly and therefore is not subscripted. During cycle i the next update of the control vector U_{i+1} must be computed from the available information (i.e., U_i and X_i). Convergent control uses the control update or *adaptation* law

$$U_{i+1} = U_i + AX_i \tag{2}$$

where A is a gain matrix. The standard approach for determining the gain matrix A is through the formulation of an optimal control problem. Minimizing the quadratic performance function

$$J = E\left\{X_{i+1}^* X_{i+1}\right\} \tag{3}$$

where $E\{\}$ is the expected value operator, results in the optimal gain matrix [10]

$$A \equiv -\left[T^* T\right]^{-1} T^* \tag{4}$$

For implementation, the matrix T for a particular operating speed can be estimated either on-line or off-line. When on-line estimation is employed, the gain matrix A is based upon a recently measured influence coefficient matrix. If the estimator can track the changes in this matrix, the estimate will be accurate and the robustness of the algorithm is not an important issue. However, as the authors have experimentally demonstrated [10], the use of continuous on-line estimation may result in large synchronous response when there is a sudden change in rotor speed or unbalance.

An off-line estimate may be obtained through either (1) the injection of test forces using the bearings, or (2) modeling of the machine's dynamics (rotor, amplifiers, sensors, and feedback controller). Either of these estimates, $\hat{T}$ can be considered to correspond to a nominal state space model of the system given as follows

$$\overline{G}_{f\to d}(s) \equiv \left[\begin{array}{c|c} \overline{\mathbf{A}} & \overline{\mathbf{B}} \\ \hline \overline{\mathbf{C}} & \overline{\mathbf{D}} \end{array}\right]$$

where the estimate is related to this nominal model via the equation

$$\hat{T} = \overline{G}_{f\to d}(j\Omega)$$

If the influence coefficient matrix estimate is used to compute the gain matrix A, the *nominal system optimal gain matrix* results

$$A_{nso} = -\left[\hat{T}^{*}\hat{T}\right]^{-1}\hat{T}^{*} \tag{5}$$

Because of the possible inaccuracy of the off-line determined estimate, the robustness of the algorithm must be considered. With sufficient error, the nominal system optimal gain matrix may result in unstable adaptation. In this paper, an alternative design method is proposed for the determination of the gain matrix A. This method results in a gain matrix which has a worst case performance that is guaranteed to be within a specified factor of the optimal performance.

The best synchronous performance that can be obtained through active control (open loop or feedback) as measured by the minimum value of the quadratic performance index denoted J_{opt} is

$$J_{opt} = X_{opt}^{*}X_{opt}$$

where the minimal vibration vector X_{opt} is given by the expression

$$X_{opt} = \left[I - T\left(T^{*}T\right)^{-1}T^{*}\right]X_{o}$$

When the estimate used in the adaptation of the control schedule, $\hat{T}$, is equal to the actual influence coefficient matrix, T, this performance is achieved by the convergent control algorithm (with A given by Eqn. 5) in one update. When the estimate is in error, the adaptation process, governed by Eqns. (1) and (2), results in the control vector either growing unbounded or converging to a control vector U_n that may not be equal to the optimal control vector. If the control vector converges to a equilibrium vector U_n, then the adaptation process is said to be stable. A necessary and sufficient condition for stability is $\rho(I + AT) < 1$. A sufficient condition for adaptation process stability is given by the following condition [9]:

$$\overline{\sigma}(I + AT) < 1 \tag{6}$$

This stability condition requires that the distance of the control vector from the equilibrium control vector, $\|U_i - U_n\|$, decrease with each update. This more conservative condition, exponential convergence, is required to obtain an upper bound on worst case performance. Therefore, Eqn. (6) will be used as the stability criterion throughout this paper. If the adaptation process is stable, the steady state value of the vibration vector is given by

$$X_n = \left[I - T(AT)^{-1}A\right]X_{opt} \tag{7}$$

ROBUSTNESS

In application of the algorithm, only an estimate of the matrix T can be used in determining the gain matrix A. If this estimate, $\hat{T}$, was obtained through testing, it may differ from the actual T due to

inaccuracies in the estimation process, and/or to changes in the machine's dynamics since the estimate was obtained. If the estimate was obtained from a computer model of the rotor, it may differ due to modeling errors.

Both changes in the machine's dynamics and modeling errors usually can be represented by a structured uncertainty representation. That is, several parameters $\theta_1,\theta_2,\ldots\theta_i,\cdots\theta_p$ of the dynamic model (e.g., the effective stiffness or damping of a seal) are different from those that produced the influence coefficient estimate $\hat{T}$. Furthermore, a structured representation of uncertainty indicates how each of these parameter affects the elements of the influence coefficient matrix T. Each parameter θ_i may differ from its nominal value $\overline{\theta}_i$ (i.e., the value which produced the estimate $\hat{T}$) with this difference bounded as follows

$$\theta_i = \overline{\theta}_i + \delta_i \qquad |\delta_i| \le d_i$$

Thus, each parameter remains in some known neighborhood about its nominal value. Each of these parameters may be either real or complex, and therefore this neighborhood may be either a real interval or a complex "ball" centered on the nominal value.

If the state space model matrices $(\mathbf{A},\mathbf{B},\mathbf{C},\mathbf{D})$ are affinely dependent on the uncertain parameters $\delta_1,\delta_2,\ldots\delta_i,\cdots\delta_p$, then the influence coefficient matrix of the rotor/bearing system can be represented by a linear fractional transformation (LFT) of the following form [11]

$$T = \mathcal{F}_u\left(G(j\Omega),\Delta_s\right) \equiv G_{22}(j\Omega) + G_{21}(j\Omega)\Delta_s\left[I - G_{11}(j\Omega)\Delta_s\right]^{-1}G_{12}(j\Omega)$$

where the nominal influence coefficient matrix is given by

$$G_{22}(j\Omega) = \overline{G}_{f\to d}(j\Omega) = \hat{T}$$

and Δ_s is a block diagonal matrix of the uncertain parameters. The uncertainties considered determine the particular block structure. The set of all matrices of a given block structure is denoted by S_Δ. Note that through appropriate scaling of the matrices $G_{11}(j\Omega)$ and $G_{12}(j\Omega)$, the uncertain parameters can all be considered to satisfy

$$|\delta_i| \le 1$$

Throughout the remainder of this paper, the notation $(j\Omega)$ will be suppressed. It will be understood that G_{ij} represents a transfer function matrix evaluated at the operating speed of the rotor.

Stability Robustness

The adaptation process is said to have exponential convergence to steady state control vector U_n with convergence rate ε_c if

$$\|U_{i+1} - U_n\| \le \varepsilon_c \|U_i - U_n\|$$

This is achieved for all T given by the family of matrices

$$T = \mathcal{F}_u(G, \Delta_s) \qquad \Delta_s \in S_{\Delta_s}: \ \bar{\sigma}(\Delta_s) \le 1 \tag{8}$$

if and only if $\mu_\Delta(\mathbf{S}_a) < 1$ where

$$\mathbf{S}_a \equiv \mathbf{S}(G, V) \qquad V \equiv \begin{bmatrix} 0 & I \\ \frac{1}{\varepsilon_c} A & \frac{1}{\varepsilon_c} I \end{bmatrix} \tag{9}$$

and the uncertainty structure is given by

$$\Delta = \begin{bmatrix} \Delta_s & \\ & \Delta_f \end{bmatrix}$$

where Δ_s is a structured block representing the parametric uncertainty, $\Delta_s \in S_{\Delta_s}$, and Δ_f is a full complex block, $\Delta_f \in C^{m \times m}$ [11].

Performance Robustness

As discussed previously, an error in the influence coefficient estimates may cause a decrease in performance (unbalance response attenuation). Performance is measured using a quadratic performance index of the steady state vibration

$$J_n \equiv X_n^* X_n = \|X_n\|^2 \tag{10}$$

As shown by the authors [11], the steady state performance for an uncertain rotor system given by Eqn. (8) is bounded as follows

$$J_n < \kappa^2 J_{opt} \tag{11}$$

where

$$\kappa = \beta + \upsilon \vartheta \bar{\sigma}(A) \frac{\vartheta}{\alpha - \vartheta} \tag{12}$$

In this equation, α is a free parameter ($\alpha > \vartheta$), and β, υ, and ϑ are given by the expressions

$$\beta \equiv \left\{ \min_{\gamma > 0} \gamma: \ \mu_\Delta(\mathbf{S}(G, W)) < 1, \ W \equiv \begin{bmatrix} \alpha A & A \\ \frac{\alpha}{\gamma} I & \frac{1}{\gamma} I \end{bmatrix}, \ \Delta = \begin{bmatrix} \Delta_s & \\ & \Delta_f \end{bmatrix}, \ \Delta_f \in C^{n \times n} \right\} \tag{13a}$$

$$\upsilon \equiv \left\{ \min_{\gamma>0} \gamma:\ \mu_{\Delta}\left(\begin{bmatrix} G_{11} & G_{12} \\ \frac{1}{\gamma}G_{21} & \frac{1}{\gamma}G_{22} \end{bmatrix} \right) < 1,\ \Delta = \begin{bmatrix} \Delta_s & \\ & \Delta_f \end{bmatrix},\ \Delta_f \in C^{m\times n} \right\} \tag{13b}$$

$$\vartheta \equiv \left\{ \frac{1}{1-\min_{0<\gamma<1}\gamma}:\ \mu_{\Delta}\left(\mathbf{S}(G,V)\right) < 1,\ V \equiv \begin{bmatrix} 0 & I \\ \frac{1}{\gamma}A & \frac{1}{\gamma}I \end{bmatrix},\ \Delta = \begin{bmatrix} \Delta_s & \\ & \Delta_f \end{bmatrix},\ \Delta_f \in C^{m\times m} \right\} \tag{13c}$$

As Eqn. (12) indicates, the variable κ can be decreased so that it is very close to the value of β through increasing α. For large α, β can be considered a good approximation to κ. If this approximation holds, then $\mu_{\Delta}\left(\mathbf{S}(G,W)\right) < 1$ implies that $J_n < \beta^2 J_{opt}$. The derivation of Eqn. (12) requires that the stability condition, Eqn. (6), be satisfied.

Convergence Rate and Performance

Both a convergence rate of ε_c and an (approximate) performance of $J_n < \beta^2 J_{opt}$ can be "guaranteed" if the following condition holds

$$\mu_{\Delta}\left(\overline{\mathbf{S}}\right) < 1 \qquad\qquad \overline{\mathbf{S}} \equiv \begin{bmatrix} \mathbf{S}(G,V) & \\ & \mathbf{S}(G,W) \end{bmatrix} \tag{14}$$

where the structure of the uncertainty block Δ is given by

$$\Delta = \begin{bmatrix} \Delta_s^1 & & & \\ & \Delta_f^1 & & \\ & & \Delta_s^2 & \\ & & & \Delta_f^2 \end{bmatrix} \qquad \begin{matrix} \Delta_s^1, \Delta_s^2 \in S_{\Delta_s} \\ \Delta_f^1 \in C^{m\times m} \\ \Delta_f^2 \in C^{n\times n} \end{matrix} \tag{15}$$

where V and W are as defined in Eqns. (9) and (13a). Note that both V and W in Eqn. (14) are affinely dependent on the gain matrix A.

An upper bound on the structured singular value μ is available via the equation

$$\mu_{\Delta}\left(\overline{\mathbf{S}}\right) \le \left\{ \min_{\substack{\mathcal{D}_L,\mathcal{D}_R,\tilde{q} \\ \mathcal{G}_L\mathcal{G}_M\mathcal{G}_R}} q\ :\ q \equiv \overline{\sigma}\left(\left(I+\mathcal{G}_L^2\right)^{-\frac{1}{4}} \left(\mathcal{D}_L \overline{\mathbf{S}} \mathcal{D}_R^{-1} - j\tilde{q}\mathcal{G}_M\right) \left(I+\mathcal{G}_R^2\right)^{-\frac{1}{4}} \right),\ q < \tilde{q} \right\} \tag{16}$$

where $\{\mathcal{D}_L, \mathcal{D}_R, \mathcal{G}_L, \mathcal{G}_M, \mathcal{G}_R\}$ must be chosen from sets of appropriately structured block diagonal matrices [12] and $\tilde{q}$ is a positive scalar. The minimization problem given in Eqn. (16) is convex, and therefore the upper bound can be determined very quickly and easily [15].

SYNTHESIS OF ROBUST GAIN MATRICES

The result of Eqns. (14) and (16) gives rise to a design algorithm for adaptive open loop control gain matrices. If the upper bound on $\mu_\Delta(\overline{\mathbf{S}})$, Eqn. (16), is minimized through choice of A to be less than one, then the convergence and performance robustness specifications will be achieved. The actual performance robustness must be checked after this design procedure since the performance specification is only approximate. In practice, however, α can be chosen to be very large, so that the design method using the approximation produces a gain matrix satisfying the desired performance specification.

The design problem is as follows:

$$\underset{\substack{A,\mathcal{D}_L,\mathcal{D}_R,\tilde{q}\\ \mathcal{G}_L\mathcal{G}_M\mathcal{G}_R}}{\text{minimize}}\ q\ :\ q \equiv \overline{\sigma}\left(\left(I+\mathcal{G}_L^2\right)^{-\frac{1}{4}} \left(\mathcal{D}_L \overline{\mathbf{S}}(A) \mathcal{D}_R^{-1} - j\tilde{q}\mathcal{G}_M\right) \left(I+\mathcal{G}_R^2\right)^{-\frac{1}{4}} \right),\ q<\tilde{q} \tag{17}$$

While the individual minimization with respect to $\{\mathcal{D}_L,\mathcal{D}_R,\mathcal{G}_L,\mathcal{G}_M,\mathcal{G}_R,\tilde{q}\}$ and with respect to A are both convex, the combined minimization with respect to $\{A,\mathcal{D}_L,\mathcal{D}_R,\mathcal{G}_L,\mathcal{G}_M,\mathcal{G}_R,\tilde{q}\}$ is not convex. Therefore, the minimization of Eqn. (17) is handled via an iteration between the two convex problems. First, $\{\mathcal{D}_L,\mathcal{D}_R,\mathcal{G}_L,\mathcal{G}_M,\mathcal{G}_R,\tilde{q}\}$ will be fixed (starting with $\mathcal{D}_L,\mathcal{D}_R = I$, $\mathcal{G}_L,\mathcal{G}_M,\mathcal{G}_R = 0$) and the minimization is carried out with respect to A. Then, A is fixed and the minimization is carried out with respect to $\{\mathcal{D}_L,\mathcal{D}_R,\mathcal{G}_L,\mathcal{G}_M,\mathcal{G}_R,\tilde{q}\}$. This second step is just the computation of the upper bound on $\mu_\Delta(\overline{\mathbf{S}}(A))$ given in Eqn. (16) with $\tilde{q}$ as the resulting upper bound on $\mu_\Delta(\overline{\mathbf{S}}(A))$. This iterative synthesis procedure is analogous to that used in D-K iteration for μ-synthesis [15]. The minimization is stopped when the upper bound on $\mu_\Delta(\overline{\mathbf{S}}(A))$ is less than one.

EXAMPLE PROBLEMS

Example #1

First, the two mass system, shown in Figure 1, is considered. While this system is very simple, its vibration behavior is analogous to that of a rotor supported in magnetic bearings. For this example, the spring between the masses has a uncertain stiffness, k_1, with a nominal value of 1. The values of the other parameters are: $m_1 = 0.5$, $m_2 = 1$, $k_2 = 1$, and $c = 1$. The "operating speed" of 1.2 radian/s is first considered for this example problem. This is nominally between the first and second critical speeds of the system. With a 40% decrease in stiffness, the second natural frequency approaches the operating speed. The first natural frequency is relatively insensitive to this variation in stiffness.

A gain matrix was first designed to meet the following requirements:

$$J_n \le 1.25 J_{opt} \qquad \|U_{i+1} - U_n\| \le 0.9\|U_i - U_n\|$$

with an uncertainty in the stiffness k_1 of ± 50%. From these specifications, the values $\beta = \sqrt{1.25}$ and $\varepsilon_c = 0.9$ were used in the synthesis procedure. The free parameter α was set at 10^5 so as to make the

$\beta \approx \kappa$ approximation accurate. The procedure was successful in synthesizing a gain matrix which meets all of the specifications.

The time response of the adaptive open loop vibration control was simulated using Eqns. (1) and (2). A comparison of the behavior of the system was conducted using the nominal system optimal gain matrix, Eqn. (5), and the gain matrix obtained by the synthesis procedure. In both cases, the convergent control algorithm was started with U=0 (no open loop control forces applied). With an actual stiffness $k_1 = 0.5$, the quadratic performance index time history with the nominal system optimal control and with the robust control are shown in Figure 2. Both time histories have been normalized by the minimum value of the performance index J_{opt}. Note that the robust control results in very little degradation in the converged value of the performance index in comparison with the optimal value. However, the nominal system optimal gain matrix resulted in unstable adaptation.

To fully examine the performance robustness of the robust gain matrix control, 100 simulations were conducted with the actual stiffness varying from 0.5 to 1.5. Each performance index history was normalized by the optimal performance. Figure 3 shows the results of these simulations. In each case, the adaptive open loop control converges to a steady state satisfying $J_n \le 1.25 J_{opt}$.

Example #2

A more complex rotordynamic system is considered in the second example problem. Figure 4 shows a diagram of a rotor considered for a boiler feedpump application. The rotor has a length of 2.54 m, a diameter of 57 mm, and a mass of 226 kg. Two magnetic bearings are used with proportional-derivative feedback control for stabilization. The rotor also has a fluid film bearing. For the purposes of this example, the magnetic bearing feedback control as well as the fluid film bearing will be modeled as a stiffness and a damping at each bearing location as shown in the diagram (stiffness k_1, k_2, k_5 and damping c_1, c_2, c_5). Parameters k_3 and k_4 represent the motor's stiffness which is due to both magnetic and fluid dynamic effects. The nominal values of each of these parameters and the uncertainty in each considered in this example are shown in Table 1. The two lowest critical speeds of the nominal rotor system are 2600 and 4970 rev/min. The balancing forces are injected at bearings #1 and #3 (the magnetic bearings) so as to reduce the vibration at bearings #1 and #3 and the motor locations. These inputs and outputs are indicated in Figure 4. For this example, the operating speed of the rotor is 3000 rev/min.

A robust gain matrix was synthesized to meet the following specifications:

$$J_n \le 1.4 J_{opt} \qquad \|U_{i+1} - U_n\| \le 0.95 \|U_i - U_n\|$$

Figure 5 shows the time histories of the normalized performance index for convergent control with the robust and nominal system optimal gain matrices. In these simulations, the errors in the nominal stiffnesses were:

$$\delta_1 = 0.525,\ \delta_2 = 0.525,\ \delta_3 = 0.613,\ \text{and}\ \delta_4 = 0.088\ \text{N/}\mu\text{m}.$$

which is within the uncertainty bounds given for the parameters. The nominal system optimal gain matrix resulted in unstable adaptation for this variation. However, the robust gain matrix produced very good performance. The robustness of the synthesized gain matrix was also examined through 1000 time simulations with the system's uncertain stiffnesses chosen as uniformly distributed random numbers

within the ranges given in Table 1. The results of these simulations are shown in Figure 6. In all cases, the robust convergent control was stable and produced a steady state performance that was bounded as originally prescribed in the synthesis specification.

CONCLUSIONS

The robustness of adaptive open loop control algorithms for suppression of synchronous vibration can be significantly improved through the application of a simple synthesis procedure. This procedure can be used to design gain matrices which have both stability and steady state performance robustness to real and complex structured uncertainties.

As the example problems demonstrate, the nominal system optimal gain matrix usually employed in adaptive open loop control can have a significant performance degradation and even instability when variations occur in the system parameters. In contrast, the performance of the robustly-synthesized gain matrix degraded significantly less from the optimal. Its worst case performance is known and was significantly better than that produced by the nominal system optimal gain matrix.

REFERENCES

1. Haberman, H.; and Brunet, M.: The Active Magnetic Bearing Enables Optimum Damping of Flexible Rotors. ASME Paper 84-GT-117, 1984.

2. Matsumura, F.; Fujita, M.; and Okawa, K.: Modeling and Control of Magnetic Bearing Systems Achieving a Rotation around the Axis of Inertia. *Proceedings of the 2nd International Symposium on Magnetic Bearings*, Tokyo, Japan, July 12-14, 1990.

3. Burrows, C.R.; and Sahinkaya, M. N.: Vibration Control of Multi-Mode Rotor-Bearing Systems. *Proceedings of the Royal Society of London*, vol. 386, 1983, pp. 77-94.

4. Burrows, C.R.; Sahinkaya, M.N.; and Clements, S.: Active Vibration Control of Flexible Rotors: an Experimental and Theoretical Study. *Proceedings of the Royal Society of London*, vol. 422, 1989, pp. 123-146.

5. Higuchi, T.; Otsuka, M.; Mizuno, T.; and Ide, T.: Application of Periodic Learning Control with Inverse Transfer Function Compensation in Totally Active Magnetic Bearings. *Proceedings of the 2nd International Symposium on Magnetic Bearings*, Tokyo, Japan, July 12-14, 1990.

6. Larsonneur, R.; and Herzog, R.: 1994, Feedforward Compensation of Unbalance: New Results and Application Experiences. *IUTAM Symposium on the Active Control of Vibration*, Bath, UK, Sept. 1994.

7. Shafai, B.; Beale, S.; LaRocca, P.; and Cusson, E.: Magnetic Bearing Control Systems and Adaptive Forced Balancing. *IEEE Control Systems*, volume 14, no. 2, April 1994, pp. 4-13.

8. Knospe, C.; Hope, R.; Fedigan, S.; and Williams, R.: New Results in the Control of Rotor Synchronous Vibration. *Proceedings of the Fourth International Symposium on Magnetic Bearings.* vdf Hochschulverlag AG, Zurich, Switzerland, August 23-26, 1994

9. Hope, R.: *Adaptive Open Loop Control of Synchronous Rotor Vibration using Magnetic Bearings.* M.S. Thesis, University of Virginia, August 1994.

10. Knospe, C.; Hope, R.; Fedigan, S.; and Williams, R.: Experiments in the Control of Unbalance Response Using Magnetic Bearings. *Mechatronics*, vol. 5, no. 4, 1995, pp. 385-400.

11. Knospe, C.; Tamer, S.; and Fedigan, S.: Robustness of Adaptive Rotor Vibration Control to Structured Uncertainty. Submitted to *ASME Journal of Dynamic Systems, Measurement, and Control.*

12. Doyle, J.; Packard, A.; and Zhou, K.: Review of LFTs, LMIs and μ. *Proceedings of the 30th IEEE Conference on Decision and Control*, England, 1991, pp. 1227-1232.

13. Redheffer, R.; Inequalities for a Matrix Riccati Equation. *Journal of Mathematics and Mechanics*, vol. 8, no. 3, 1959.

14. Doyle, J.: Analysis of Feedback Systems with Structured Uncertainties. *IEEE Proceedings - Part D*, vol. 133, 1982, pp. 45-56.

15. Mathworks, Inc.: *μ-Analysis and Synthesis Toolbox*, Natick, Mass. 01760-1500, January 1994.

Table 1. Nominal Values and Uncertainties for Example #2

Parameter	Nominal Value	Uncertainty
Stiffness (N/μm)		
k_1	55	1.75
k_2	55	1.75
k_3	0	0.875
k_4	0	0.875
k_5	55	1.75
Damping (Ns/mm)		
c_1	91.3	0
c_2	91.3	0
c_3	91.3	0

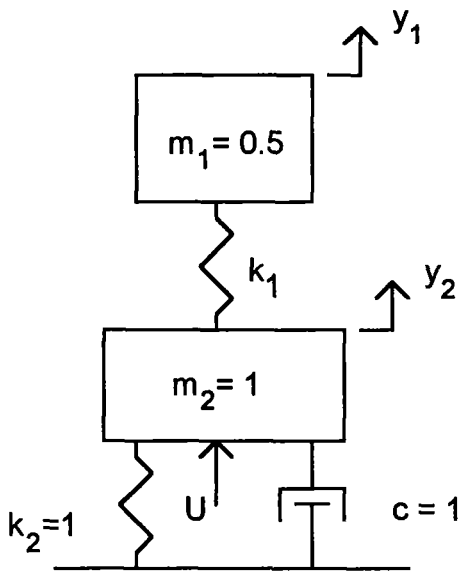

Figure 1: Simple system considered in example #1.

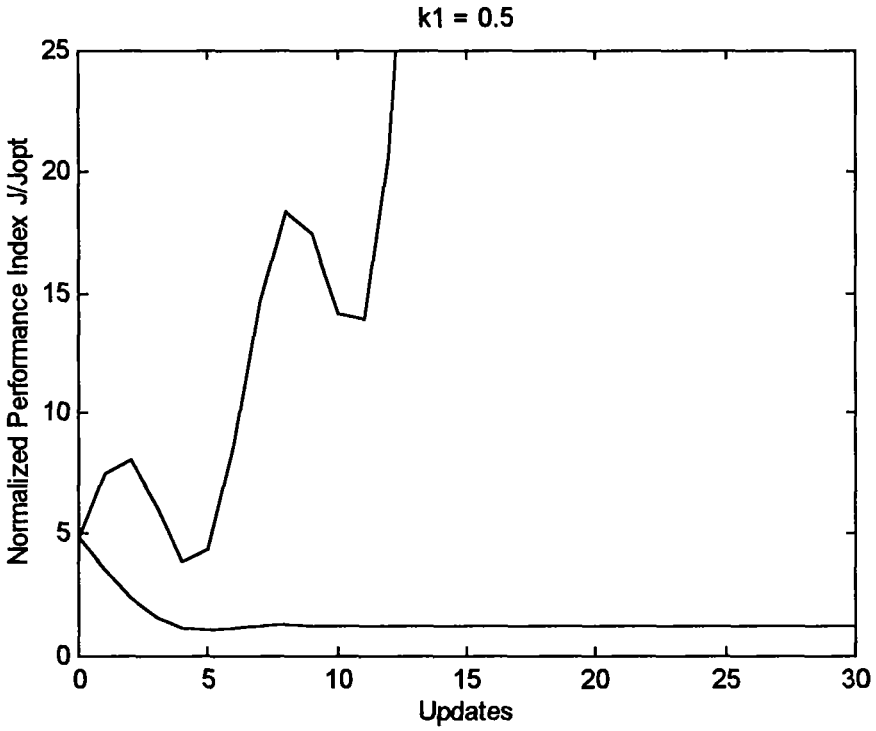

Figure 2: History of performance indices for simulation with robust and nominal system optimal gain matrices, $k_1 = 0.5$.

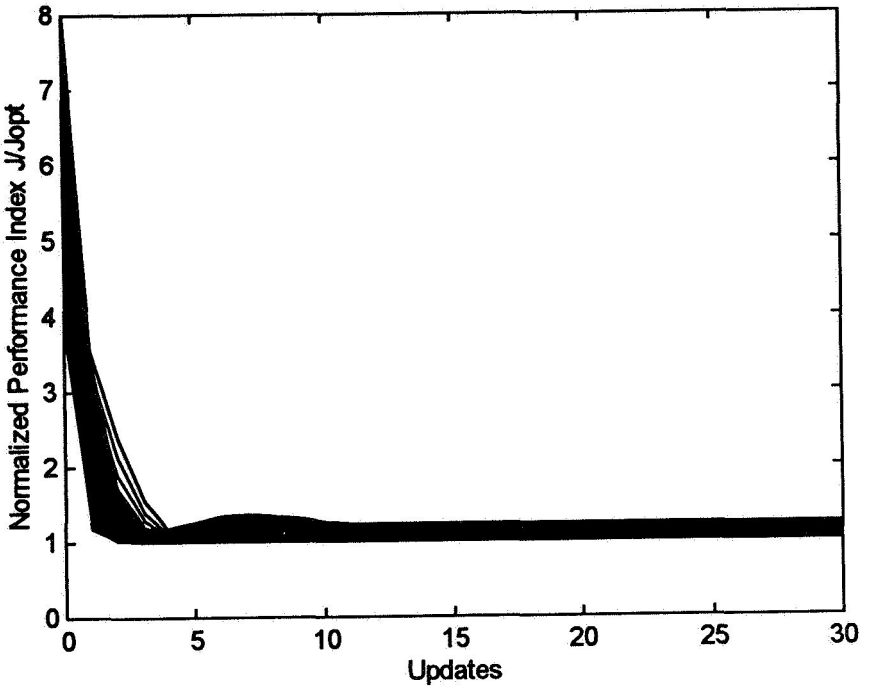

Figure 3: History of performance index for 100 simulations with robust gain matrix, stiffness varies from 0.5 to 1.5.

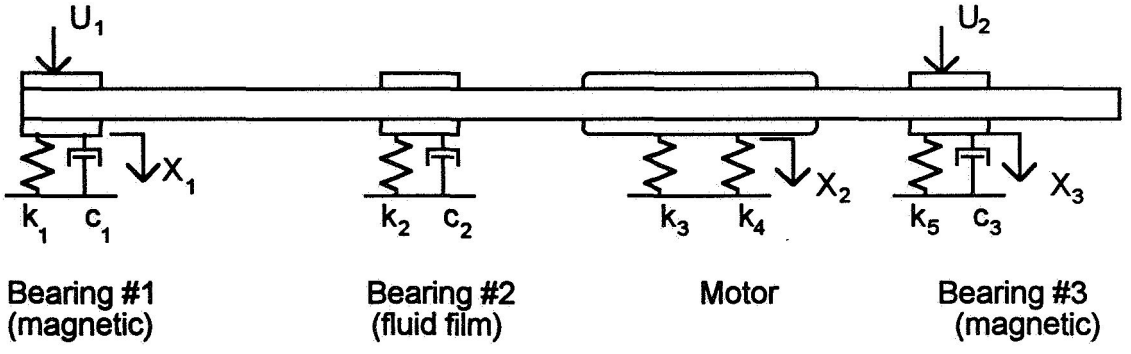

Figure 4: Rotor model considered in example #2.

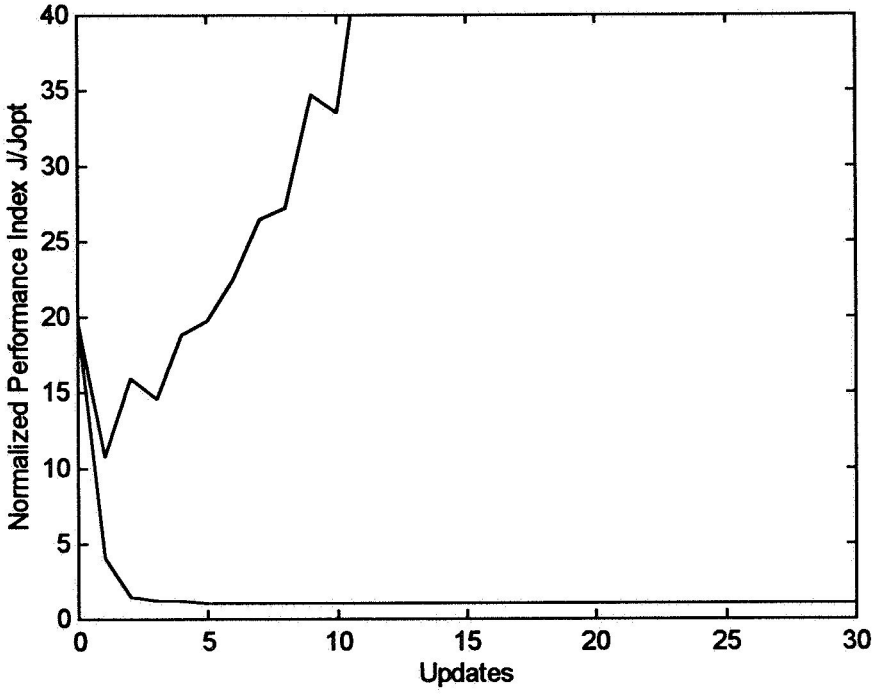

Figure 5: History of performance indices for simulation with robust and nominal system optimal gain matrices, example #2.

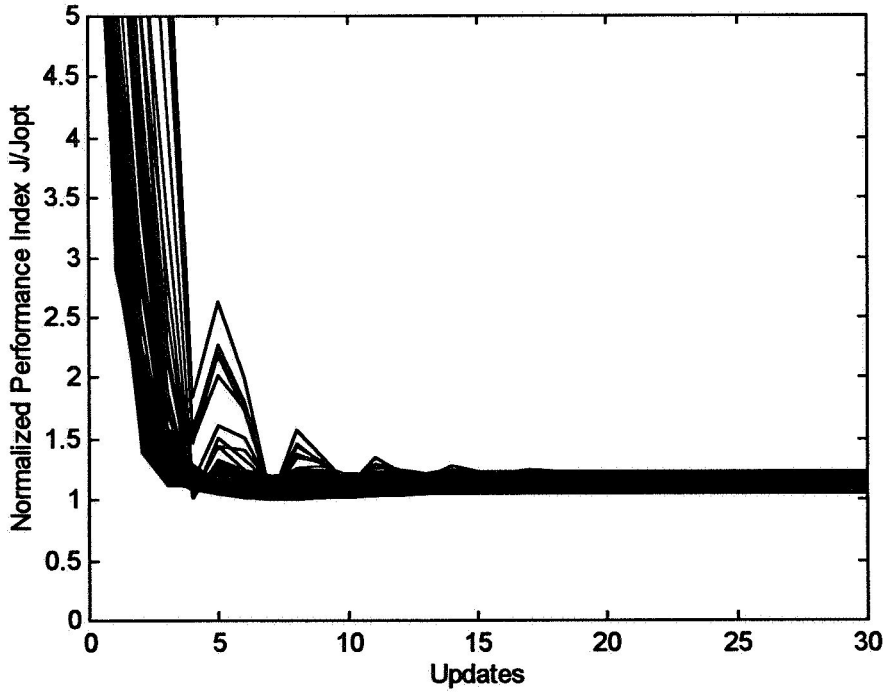

Figure 6: History of performance index for 1000 simulations with robust gain matrix, example #2, maximum $J_n < 1.24 J_{opt}$.

H∞ CONTROL OF MAGNETIC BEARINGS TO ENSURE BOTH SYSTEM AND EXTERNAL PERIODIC DISTURBANCE ROBUSTNESS

Yuhong Jiang and R. B. Zmood

Department of Electrical Engineering
Royal Melbourne Institute of Technology
Melbourne Victoria 3000, Australia

SUMMARY

Both self-excited and forced disturbances often lead to severe rotor vibrations in a magnetic bearing systems with long slender shafts. This problem has been studied using the H∞ method, and stability with good robustness can be achieved for the linearized model of a magnetic bearing when small transient disturbances are applied. In this paper, the H∞ control method for self-excited and forced disturbances is first reviewed. It is then applied to the control of a magnetic bearing rotor system. In modelling the system, the shaft is first discretized into 18 finite elements and then three levels of condensation are applied. This leads to a system with three masses and three compliant elements which can be described by six state variable coordinates. Simulation of the resultant system design has been performed at speeds up to 10,000 rpm. Disturbances in terms of different initial displacements, initial impulses, and external periodic inputs have been imposed. The simulation results show that good stability can be achieved under these different transient disturbances using the proposed controller while at the same time reducing the sensitivity to external periodic disturbances.

1. INTRODUCTION

Magnetic bearings, because of their absence of physical contact with the bearing journal are well suited for high speed rotating machines (ref. 1). Additional advantages of magnetic bearings are the absence of mechanical wear and the need for lubrication. A system of magnetic bearings with a long slender shaft can often have severe vibrations due to rotor unbalance or self excited instabilities; especially when the shaft rotates at high speed. In the case of forced vibrations, such as due to unbalanced mass, the shaft will deflect from its axis of rotation as a result of these forces. Self excited rotor instability will also lead to severe rotor vibrations. The control task is, therefore, to restore the bearing journals to the central axes of the magnetic bearings within a short period of time after a transient disturbance, to minimise rotor vibration, and to exhibit

low sensitivity to external periodic disturbances. Thus the design of a controller for a magnetic bearing system poses a significant challenge. While PID controllers have been used extensively with magnetic bearings they do not easily satisfy the robust performance requirements of these systems. The application of LQG methods for bearing control also have their limitations as they are unable to adequately treat systems with plant uncertainty (ref. 2). So H^{∞} control design methods (refs. 3 and 5) have attracted attention for designing the control systems of magnetic bearings, because H^{∞} control theory includes frequency shaping techniques as used for conventional PID controllers as well as the optimisation methods used in modern LQG control design methods.

The present work concerns the application of the H^{∞} control method to a magnetic bearing system as shown in Figure 1. The beam is supported horizontally by two magnetic bearings. The rotor is attached to the shaft midway between the two bearings. In applying H^{∞} control, the system is considered to be a mixed sensitivity control problem, where the weighting functions are selected to assure a robust controller design. An algorithm for arriving at suitable weighting functions using the MATLAB software package for the controller design, is described and is applied to the above system. The designed system has been simulated for speeds up to 10,000 rpm. The results show the proposed magnetic bearing controller using this design method works well when the bearing system is subjected to various transient disturbances while at the same time it reduces the sensitivity of the system to external periodic disturbances.

2. MATHEMATICAL MODEL OF THE MAGNETIC BEARING SYSTEM

The magnetic bearing suspension system being considered has a flexible shaft as shown in Fig. 1. The shaft is supported at its left and right ends by the magnetic bearings

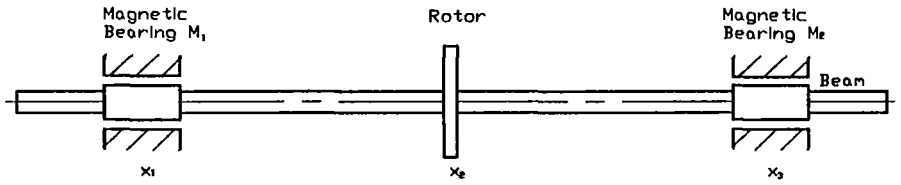

Figure 1. The rotor of the system.

M_1 and M_2 with the rotor being positioned on the shaft midway between the two magnetic bearings. The displacements of the bearing journals are defined to be x_1, and x_3. The flexible shaft in this study is assumed to have a length L=600 mm and a diameter D=10 mm. In this system the bearing forces are generated by electro-magnet coils and the shaft position is detected by a displacement sensor. The sensor signals are fed through the controllers in to the power amplifiers which finally supply the excitation currents to the electro-magnet coils.

In the system model, the rotor flywheel structure was divided into 18 elements. The finite element method was used to calculate the mass and stiffness of the shaft. Three levels of condensation were applied to the 18 finite elements which led to a mathematical model of the shaft having 6 coordinates$\{x\} = \{x_1, x_2, x_3, \dot{x}_1, \dot{x}_2, \dot{x}_3\}$as shown in Fig. 1. The shaft mass and shaft stiffness were calculated to be

$$M_S = \begin{bmatrix} 0.6067 & -0.1465 & 0.0451 \\ -0.1465 & 2.2674 & -0.1465 \\ 0.0451 & -0.1465 & 0.6067 \end{bmatrix} \text{ and } K_S = \begin{bmatrix} 0.0454 & -0.0943 & 0.0472 \\ -0.0943 & 0.1943 & -0.0942 \\ 0.0472 & -0.0942 & 0.0466 \end{bmatrix}$$

respectively. The equations of motion for the simulation of the magnetic bearing system are given in Appendix I.

For the simulations, it is necessary to simulate the system dynamics using a set of first order differential equations. In this study, the magnetic bearing system is modelled using the state-space model of the continuous-time, equation (1)

$$\begin{aligned} \dot{x}_g &= A_g x_g + B_g u_g \\ y_g &= C_g x_g \end{aligned} \tag{1}$$

where$\{x_g\} = \{x_1, x_2, x_3, x_1, x_2, x_3\}$are the displacements and velocities of the flywheel and shaft, and $u_g = \{u_1, u_2, u_3\}$ are the output currents of the power amplifiers. The coefficient matrices for A_g, B_g, C_g are

$$A_g = \begin{bmatrix} 0_{3\times3} & I_{3\times3} \\ -M_s^{-1}(K_s + K_x) & 0_{3\times3} \end{bmatrix} \quad B_g = \begin{bmatrix} 0_{3\times3} \\ M_s^{-1}K_i \end{bmatrix}$$

$$C_g = \begin{bmatrix} 1 & 0 & 0 & 0 & 0 & 0 \\ 0 & 1 & 0 & 0 & 0 & 0 \\ 0 & 0 & 1 & 0 & 0 & 0 \end{bmatrix}$$

From the above parameter matrices, the matrices A_g and B_g can be shown to be

$$A_g = \begin{bmatrix} 0 & 0 & 0 & 1 & 0 & 0 \\ 0 & 0 & 0 & 0 & 1 & 0 \\ 0 & 0 & 0 & 0 & 0 & 1 \\ -0.095 & 0.179 & -0.06 & 0 & 0 & 0 \\ 0.028 & -0.033 & .029 & 0 & 0 & 0 \\ -0.064 & 0.172 & -0.10 & 0 & 0 & 0 \end{bmatrix} \qquad B_g = \begin{bmatrix} 0 & 0 & 0 \\ 0 & 0 & 0 \\ 0 & 0 & 0 \\ -0.9299 & 0.0565 & 0.0555 \\ -0.0565 & -0.251 & -0.0565 \\ 0.0555 & -0.056 & -0.9299 \end{bmatrix}$$

with (A_g, B_g) being controllable, and (A_g, C_g) being observable. The system transfer function is $G(s)=C_g(sI-A_g)^{-1}B_g$.

If external periodic disturbances are applied to the magnetic bearing system, the system equations of motion are shown in Appendix II. In this case the state-space model for the system is

$$\begin{aligned} \dot{x}_g &= A_g x_g + B_g u_g + B_{1g} F_d \\ y_g &= C_g x_g \end{aligned} \tag{2}$$

where $B_{1g} = \begin{bmatrix} 0_{3\times3} \\ M_s^{-1} \end{bmatrix}$

Plant uncertainty, air gap growth with high speed shaft rotation, shaft parameter estimation errors and the effect of eddy-currents in the electromagnets will all affect the coefficient matrices in the above equations, and thus will influence the magnetic bearing control system stability and periodic disturbance robustness.

3. CONTROLLER DESIGN

H^∞ optimal control design offers a robust performance by addressing disturbances and plant uncertainty. The H^∞ optimal controller takes into consideration the plant uncertainty bandwidth, and disturbance attenuation, and achieves the best system performance (ref. 4). The design will be carried out using the computer package ROBUST CONTROL TOOLBOX with MATLAB (ref. 6).

3.1 Mixed-Sensitivity Robust Control

The augmented plant and controller diagram is shown in Fig. 2. The transfer function S from u_1 to e is termed the sensitivity function and the transfer function T from u_2 to y_2 is called the complementary function, also F is the controller for the system. The functions S and T are defined as

$$S = (I + GF)^{-1} \qquad T = I - S = GF(I + GF)^{-1}$$

In the case of the mixed sensitivity problem, the cost function is shown to be

$$\left\| T_{y_1 u_1} \right\| = \left\| \begin{matrix} W_1(s)S(s) \\ W_3(s)T(s) \end{matrix} \right\|_\infty < 1$$

where $\|\cdot\|_\infty$ denotes the H-infinity norm. $W_3(s)$ is the frequency weighting function used for robustness stabilisation at high frequencies and $W_1(s)$ is used for sensitivity reduction at low frequencies. Both of these matrices need to be selected according to the

requirements of system performance, plant uncertainty bandwidth, and the input and output disturbances of the plant. The augmented plant $P(s)$ of the plant $G(s)$ with the weighting functions $W_1(s)$ and $W_3(s)$ is shown in Fig. 2, where u_1 is the disturbance input at the input of the plant, u is the control input vector, y_{11} and y_{12} are the closed-loop system output vectors, and y_2 is the measured output vector. The state vector x of the plant $G(s)$ is not shown on this diagram.

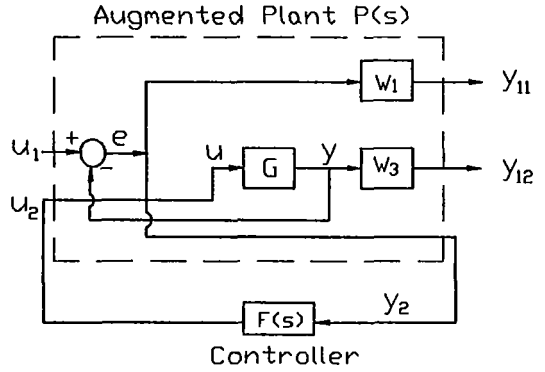

Figure 2. Closed-loop control diagram.

3.2 H∞ Method Design

The magnetic bearing system is subject to different types of disturbances as discussed above. For the disturbances which act on the plant at low frequencies, the performance can be calculated using the sensitivity function S. This can be specified using the performance weighting function $W_1(s)$ so that

$$\left\| W_1(s)S(s) \right\|_\infty < 1$$

$W_1(s)$ is taken as a low pass filter in order to choose the bandwidth of the closed loop and to reduce the output deviation at low frequencies by introducing a quasi-integral action in the controller. A weighting function $W_1(s)$ satisfying these requirements is given by

$$W_1(s) = \frac{\gamma(s+10^4)}{10^2(s+100)}[1 \quad 1 \quad 1]^T$$

where γ is an adjustable parameter which can be set by the designer. Initially it is useful to take γ=1 and then to increase it according to the system performance requirements. It has been found that γ=2.86 is the most appropriate value for this design.

As the magnetic bearing system has air gap growth at high speeds this causes the bearing characteristics to change. To make the stability of the magnetic bearings more robust at high frequencies, the stability robustness can be specified using the uncertainty weighting function $W_3(s)$ so that

$$\left\| W_3(s)T(s) \right\|_\infty \leq 1$$

The weighting function $W_3(s)$ is taken as a high pass filter in order to reduce the control effect at high frequencies. An uncertainty weighting function $W_3(s)$ satisfying these needs is

$$W_3(s) = \frac{s^2}{10^5}[1 \;\; 1 \;\; 1]^T$$

The H$^\infty$ optimal controller design can be analysed using the Robust-Control Toolbox in MATLAB. With the weighting functions $W_1(s)$ and $W_3(s)$, an augmented plant can be formed which is shown in Fig. 3, and then we can use MATLAB to calculate the state-space realisation of the augmented plant as follows

$$\dot{x} = Ax + B_1 u_1 + B_2 u_2$$
$$y_1 = C_2 x + D_{11} u_1 + D_{12} u_2$$
$$y_2 = C_2 x + D_{21} u_1 + D_{22} u_2$$

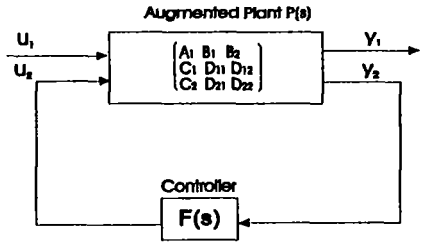

Figure 3. H$^\infty$ feedback diagram.

External periodic disturbances, different initial condition disturbances, and transient disturbances will be applied to the input u_1 after the controller has been obtained.

3.3. The Closed-Loop Transfer Function *T(s)*

The model reduction algorithm (ref. 6) in the Robust Control Toolbox in MATLAB was applied to the H$^\infty$ feedback system to find a reduced 6 state variable model that satisfied the "robustness criterion". Fig. 3 shows a standard H$^\infty$ optimal control system, which has an augmented plant $P(s)$ and a feedback controller $F(s)$. The stabilising feedback control law $u_2=F(s)y_2(s)$ was found so that the H$^\infty$ norm of the closed-loop transfer function matrix

$$T_{y_1 u_1} = P_{11}(s) + P_{12}(s)(1 - F(s)P_{22}(s))^{-1} F(s)P_{21}(s)$$

is small. The H$^\infty$ control problem thus reduces to finding $F(s)$ so as to satisfy the inequality $\left\| T_{y_1 u_1} \right\| < 1$. The closed-loop frequency responses of the bearing system represented by the singular value of $T_{y_1 u_1}$ is shown in Fig. 4. With the selected controller $F(s)$, the system has good performance for frequencies up to 1000 rad/sec, which corresponds to speeds of 10,000 rpm.

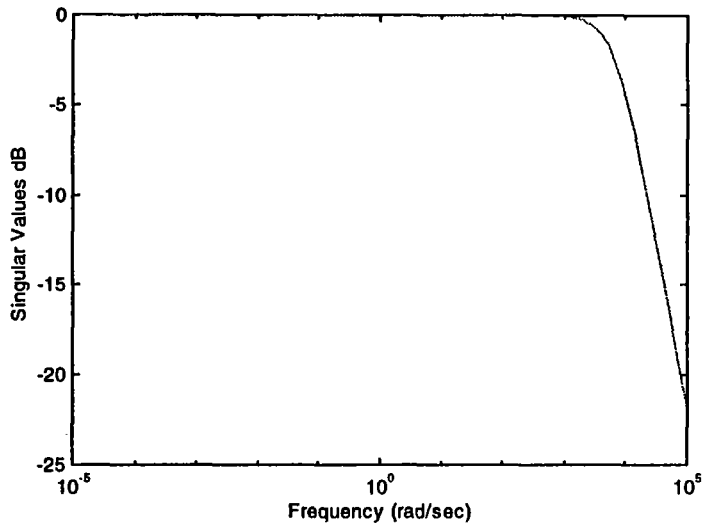

Figure 4. Closed-loop frequency response (Singular value of $T_{y_1 u_1}$).

4. SIMULATION RESULTS

4.1 Simulation Results for Self-Excited Disturbances

In this section we evaluate the stability of the designed control system by studying the transient time response for impulse disturbances and non zero initial conditions. These disturbances have been applied to the augmented plant, and the simulated responses computed using the Robust-Control Toolbox in MATLAB, are shown in Figs. 5 and 6. From the simulation results for an impulse input, we can see that it takes 0.025 seconds to restore the shaft to its rest position while for non-zero initial conditions the settling time is approximately 0.02 seconds. From these time response plots it will also be noted that the performance of the bearing control is very well damped.

4.2 Simulation Results for External Periodic Disturbances

In this section we examine the operation of the H^{∞} magnetic bearing control systems while the rotor experiences external periodic disturbances. A number of cases of periodic disturbances using unbalance eccentricities have been simulated as shown in Table 1.

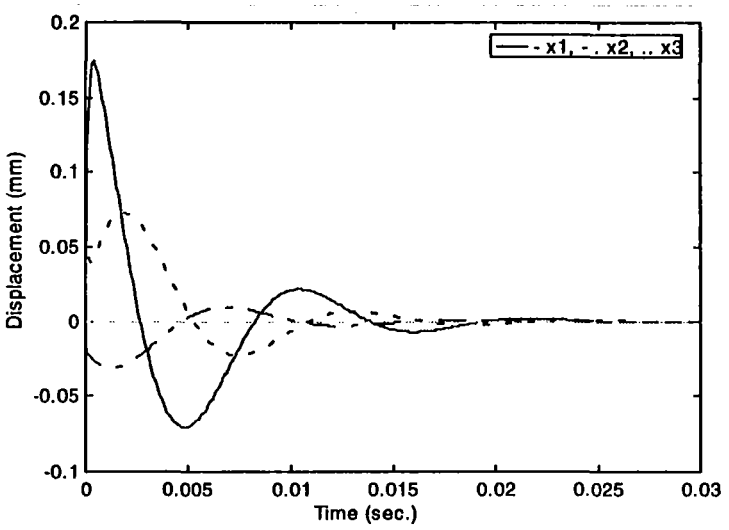

Figure 5. System response for impulse disturbance input.

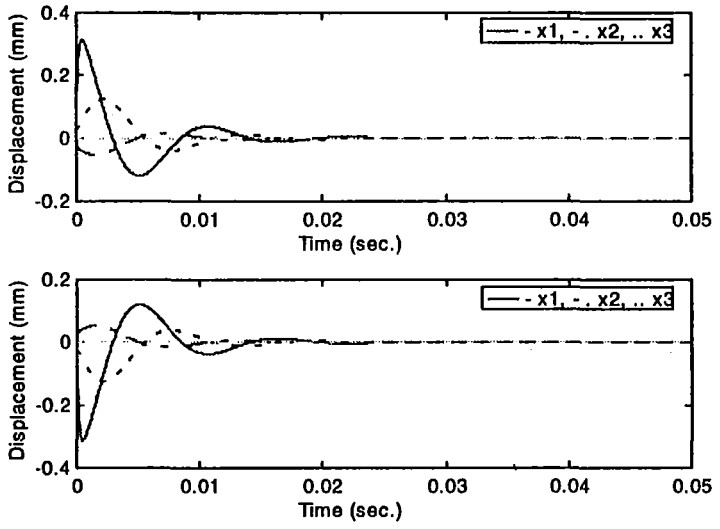

Figure 6. System response for different non-zero initial conditions.

In Fig. 7 we show the simulated results for case 1 only as the remaining cases are similar. It can be seen that for initial journal displacements of x_1=-0.2 mm and x_3=+0.2 mm, when rotating at speed of 10 and 20 rad/sec, it returns to its steady state condition in about 0.06 secs, so that it thereafter rotates about its geometric axis. However when rotating at speeds of 40 and 70 rad/sec it can be seen from Fig. 8 that the shaft begins to rotate about its principal inertial axis. The trade off between the sensitivity to transient and external periodic disturbances is determined by the choice of the performance weighting function $W_1(s)$.

Table 1.

Line	Unbalanced Eccentricity μ^T (mm)	Rotor mass (kg)	Speed Range ω (rad/sec)
1	μ^T={-0.009, -0.003, 0.005}	1.13	10,20,40,70
2	μ^T={-0.0009,-0.0003, .0005}	1.22	10,20,40,70
3	μ^T={-0.009, -0.003, 0.005}	1.16	10,20,40
4	μ^T={-0.0009,-0.0003, .0005}	1.52	10,20,40

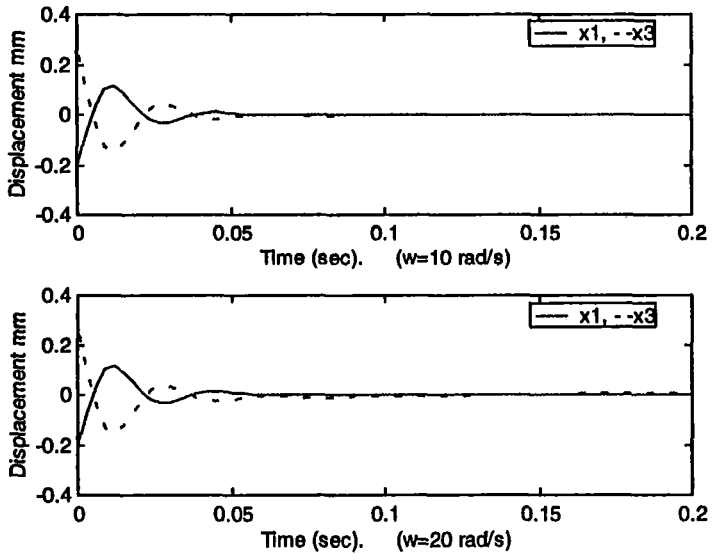

Figure 7. System responses with external periodic disturbance.

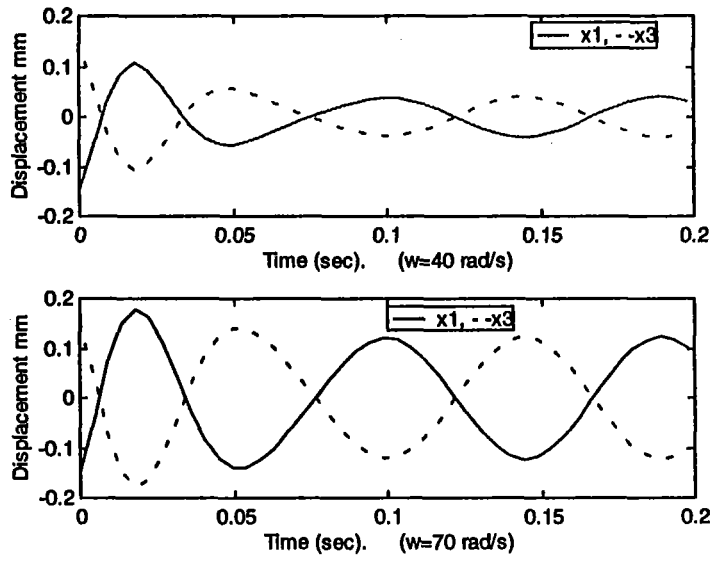

Figure 8. System responses with external periodic disturbance.

5. CONCLUSIONS

We have designed a H^{∞} controller for a magnetic bearing system operating at speeds up to 10,000 rpm. In our study we have considered the plant to have an unstructured multiplicative uncertainty. In the case where the system has external periodic disturbances it can be seen that it has low sensitivity to these disturbances when operation is at speeds above 40 rad/sec. Also using the designed controller, the rotor can be suspended in a stable manner, and has good robustness to self-excited disturbances.

ACKNOWLEDGMENTS

In this work the shaft mass and the shaft stiffness for the rotor system were calculated using the software package developed by Dr. J. Krodkiewski (ref. 7), from the Department of the Mechanical Engineering, University of Melbourne , Australia.

Part of this work was performed under the management of the Micromachine Centre as the Industrial Science and Technology Frontier Program, " Research and Development of Micromachine Technology", of MITI supported by New Energy and Industrial Technology Development Organisation.

APPENDIX I: BEARING SYSTEM EQUATION OF MOTION - SELF DISTURBANCES

The equations of the motion of the magnetic bearing system can be shown to be

$$[M_s]\{\ddot{x}\}+([K_s]+[K_x])\{x\}=K_i i$$

In this, the units of displacement x, mass of the shaft M_s and stiffness of the shaft K_s have the units of millimetre, kilogram, and newton/millimetre, respectively. The bearing actuator current sensitivity (K_i=23.06 N/A), and the bearing actuator static stiffness (K_x=171.00 N/mm), and i is the power amplifier output current.

APPENDIX II: BEARING SYSTEM EQUATION OF MOTION - PERIODIC DISTURBANCES

The equations of the motion for the magnetic bearing system having external periodic disturbances can be shown to be

$$[M]\{\ddot{x}\} + ([K_s] + [K_x])\{x\} = K_i i + F_d$$

where $F_d = M\ \mu\omega^2 e^{j\omega t}$ is the external periodic disturbance force produced by an unbalance mass attached to the rotor and M is the mass of the shaft and rotor. In the expression for F_d the rotor angular velocity is denoted by ω while μ is the eccentricity of the unbalance mass. In the simulations representative values for μ have been chosen.

REFERENCES

1. M. Dussunx.: The Industrial Applications of Active Magnetic Bearing Technology, *Proc. of the 2nd Int. Symp. on Magnetic Bearings,* Tokyo, Japan, July 1990, pp. 33.

2. K. Nonami and I. Takayuki.: μ Synthesis of Flexible Rotor Magnetic Bearing System, *4th Inter. Symp. on Magnetic Bearings,* ETH Zurich Swaziland, August 1994, pp. 73-78.

3. Y. N. Zhuravlyov; A. Mikhail; and E. Lantto: Inverse Problems of Magnetic Bearing Dynamics, *4th Inter. Symp. on Magnetic Bearings,* ETH Zurich, August 1994, pp. 79-84.

4. M. Fujita; K. Hatake; and F. Matsumura: Loop Shaping-Based Robust Control of a Magnetic Bearing, *IEEE Control Systems Magazine*, August 1993, pp. 57-64.

5. I. Postlehwaite; Mi-Ching Tsai; and D. W. Gu: Weighting Function Selection in H-Infinity Design, *Preprint 11th IFAC World Congress*, Tallin, Estonia, August 1990, Vol. 5, pp. 104-109.

6. R. Y. Chiang and M. G. Satonov: Robust-Control Toolbox, User's Guide, *The MATH WORKS, Inc.,* 1989.

7. J. Krodkiewski and R. B. Zmood: Use of Programmed Magnetic Bearing Stiffness and Damping to Minimize Rotor Vibration, *3rd Int. Symp. on Magnetic Bearings,* Alexandria, Virginia, July 29-31, 1992.

CROSS FEEDBACK CONTROL OF A MAGNETIC BEARING SYSTEM

Controller Design Considering Gyroscopic Effects

Markus Ahrens
International Center for Magnetic Bearings, ETH Zurich
Switzerland

Ladislav Kučera
International Center for Magnetic Bearings, ETH Zurich
Switzerland

ABSTRACT

For flywheel rotors or other rotors with significant ratios of moments of inertia ($J_z/J_x \not\ll 1$, see figure 2), the influence of gyroscopic effects has to be considered. While conservative or damped systems remain stable even under gyroscopic effects, magnetically suspended rotors can be destabilized with increasing rotational speed.
The influence of gyroscopic effects on the stability and behaviour of a magnetic bearing system is analyzed. The analysis is carried out with a rigid body model for the rotor and a nonlinear model for the magnetic bearing and its amplifier.
Cross feedback control can compensate gyroscopic effects. This compensation leads to better system performance and can avoid instability. Furthermore, the implementation of this compensation is simple. The main structure of a decentralized controller can still be used. It has only to be expanded by the cross feedback path.

INTRODUCTION

Magnetic bearings are used in a wide field of applications due to their advantages compared to other bearing types. The main advantages are that they operate contact free, they have low friction losses, adjustable damping and stiffness characteristics and the fact that no lubricants are necessary. They are therefore ideally suited for high speed and vacuum applications.
A magnetic bearing system is unstable in nature and therefore a controller is required. In order to design a controller a mathematical model of the plant is necessary.
The rotor can be described as a $\boldsymbol{MDGK}$-system (see equation 8). The gyroscopic matrix $\boldsymbol{G}$ describes the coupling between the rotor axes while rotating.
For rotors with a small ratio of moments of inertia ($J_z/J_x \ll 1$) the gyroscopic coupling is small and can be neglected. In this case the system can be divided into two identical subsystems (x-z and y-z plane) which can be controlled independently. For many magnetic bearing systems, decentralized controllers are used which control each bearing unit independently. In [Ble84] it is shown that gyroscopic systems can be controlled with decentralized controllers.
In [Mag71] and [MS76] it is shown that conservative stable systems cannot become unstable

with gyroscopic effects. Magnetically suspended rotors however, cannot usually be considered as conservative. There are mainly two reasons that stability cannot be guaranteed for magnetic bearing systems. In [Her91] it is shown that the plant is no longer positive-real, when digital controllers are used. In [ME93] it is shown that gyroscopic effects can cause instability when certain nonlinearities are considered.
For rotors with a ratio of moments of inertia which is not small ($J_z/J_x \not\ll 1$) (e.g. pumps, turbines and especially flywheels) or rotors with extremely high rotational speeds, the influence of gyroscopic effects has to be considered. In [MH84] it can be seen that centralized control (using LQR) considering gyroscopic effects can achieve better system performance than decentralized control. This is only valid however for the specified rotational speed. In [Ulb79] it is shown that a controller designed with LQR at a certain rotational speed can lead to instability at standstill. In [ONS89] cross feedback control is proposed. Here, the controller has a cross coupling which is displacement-proportional and can avoid instability of the precession mode.
In 1992 a project was started at the ETH Zurich[1] to develop a flywheel energy storage device using magnetic bearings. The following analysis was made within the scope of this project.

MODEL

This chapter describes the model structure used for the theoretical analysis of gyroscopic effects. The model structure is as extensive as necessary to solve the desired problems.
The authors used MAPLE [Hec93] for an analytical model, MATLAB [GLLT92] for linear modelling, controller design and transfer functions and ACSL [Mit93] for nonlinear simulations.

Magnetic Bearing

This section defines the nonlinear force and voltage equations of the electromagnets. The model will include the resistance of the coil R and the leakage inductance L_s. All other effects are neglected. All magnets (planes a and b, directions x and y, sides 1 and 2) have identical structures. The following equations are given for the magnets 1 and 2 of plane a and direction x. The equations for the other magnets are analogous.

Steady state definitions:

$x_{a1,2}$: air gap between electromagnet 1 (respectively 2) and the rotor.
x_0 : steady state air gap.
x_a : deviation from the steady state position.

$i_{xa1,2}$: current through the coil of electromagnet 1 (respectively 2).
i_0 : bias current.
i_{xa} : control current.

$F_{xa1,2}$: force of electromagnet 1 (respectively 2) acting on the rotor.
F_{xa} : total force acting on the rotor (including the disturbance force $F_{s,xa}$).

$u_{xa1,2}$: voltage across the coil of electromagnet 1 (respectively 2).

[1]The project was funded by NEFF (Nationaler Energie Forschungs-Fond).
Project partners are the Institute of Electrical Machines and the Chair of Power Electronics and Electrometrology.

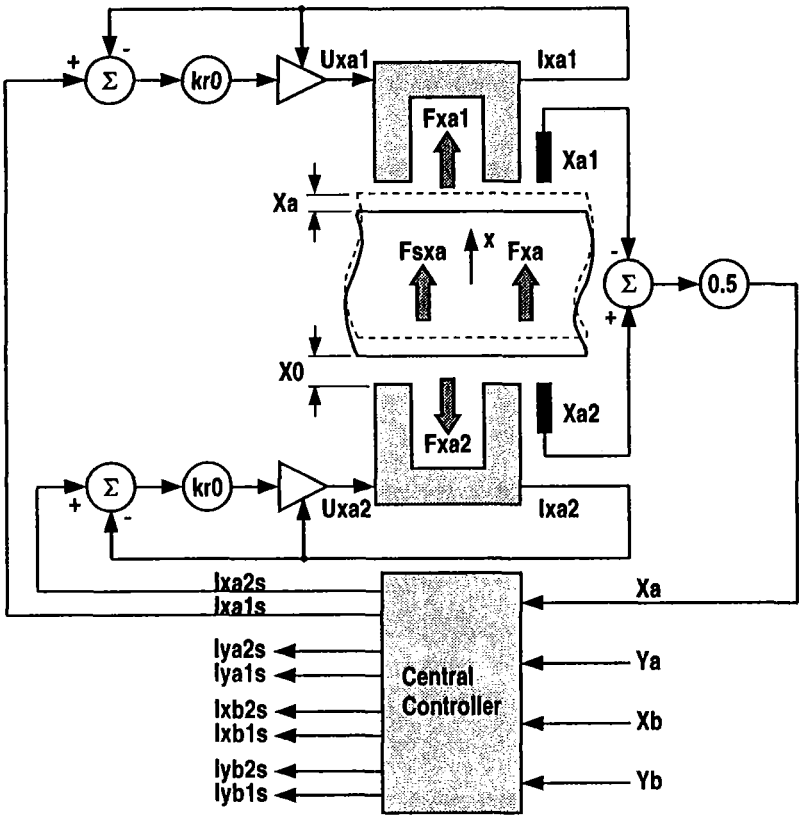

Figure 1: Definitions of the magnetic bearing model.

$$x_{a1} = x_0 - x_a, \qquad x_{a2} = x_0 + x_a \tag{1}$$

$$i_{xa1} = i_0 + i_{xa}, \qquad i_{xa2} = i_0 - i_{xa} \tag{2}$$

$$F_{xa1} = \frac{K}{4}\frac{i_{xa1}^2}{x_{a1}^2}, \qquad F_{xa2} = \frac{K}{4}\frac{i_{xa2}^2}{x_{a2}^2} \tag{3}$$

and

$$F_{xa} = F_{xa1} - F_{xa2} + F_{s,xa} \tag{4}$$

The constant $K = \mu_0 N^2 A$ represents electrical and geometrical characteristics of an electromagnet. $\mu_0 = 4\pi 10^{-7}\,(\mathrm{Vs})/(\mathrm{Am})$, N is the number of turns of the coil and A the area of one magnetic pole.

The linearized force equation with $k_s = \frac{K}{2}\frac{i_0^2}{x_0^3}$ and $k_i = \frac{K}{2}\frac{i_0}{x_0^2}$ is given by:

$$F_{xa} = 2k_s x_a + 2k_i i_{xa} + F_{s,xa} \tag{5}$$

The voltage across the coil of an electromagnet can be considered to be derived from an electrical effect which does not depend on x_a and is dependent upon R and L_s, and a second electromechanical effect which depends on x_a:

$$u_{xa1} = Ri_{xa1} + L_s\frac{\mathrm{d}i_{xa1}}{\mathrm{d}t} + \frac{K}{2}\frac{i_{xa1}}{x_{a1}}, \qquad u_{xa2} = Ri_{xa2} + L_s\frac{\mathrm{d}i_{xa2}}{\mathrm{d}t} + \frac{K}{2}\frac{i_{xa2}}{x_{a2}} \tag{6}$$

Rotor

In the following calculations a rigid body model is used. The equations of motion for a rotor can be described in body coordinates $\bar{q}$.
The equation of motion for the z-direction is independent of the equations of motion for the x- and y-direction. In the following analysis, the motion in the z-direction is neglected, because it is independent of gyroscopic effects.

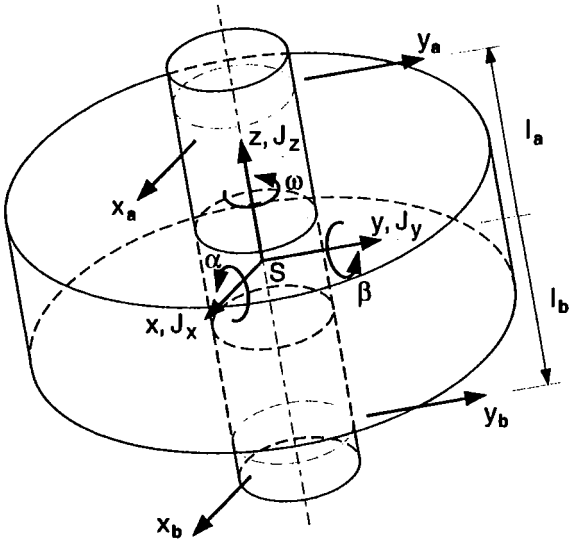

Figure 2: Definition of the moments of inertia and geometry definitions of the rigid body model, body coordinates $\bar{q}$ and bearing coordinates q. S defines the centre of gravity.

$$\bar{q} = \begin{pmatrix} \beta \\ x \\ -\alpha \\ y \end{pmatrix} \tag{7}$$

The equations of motion can be written as:

$$\boldsymbol{M}\ddot{\bar{q}} + (\boldsymbol{D} + \omega\boldsymbol{G})\dot{\bar{q}} + \boldsymbol{K}\bar{q} = \boldsymbol{F} \tag{8}$$

In equation (8), $\boldsymbol{M}$ is the symmetric mass matrix, $\boldsymbol{D}$ the symmetric damping matrix, $\boldsymbol{G}$ the skew-symmetric gyroscopic matrix, $\boldsymbol{K}$ the symmetric stiffness matrix and $\boldsymbol{F}$ the bearing forces. For the rigid body model the matrices are:

$$\boldsymbol{M} = \begin{pmatrix} J_x & 0 & 0 & 0 \\ 0 & m & 0 & 0 \\ 0 & 0 & J_x & 0 \\ 0 & 0 & 0 & m \end{pmatrix} \tag{9}$$

$$\boldsymbol{D} = \boldsymbol{0} \tag{10}$$

$$\boldsymbol{G} = \begin{pmatrix} 0 & 0 & J_z & 0 \\ 0 & 0 & 0 & 0 \\ -J_z & 0 & 0 & 0 \\ 0 & 0 & 0 & 0 \end{pmatrix} \tag{11}$$

$$\boldsymbol{K} = \boldsymbol{0} \tag{12}$$

$$\boldsymbol{F} = \boldsymbol{B_z f} \tag{13}$$

$$\boldsymbol{B_z} = \begin{pmatrix} l_a & l_b & 0 & 0 \\ 1 & 1 & 0 & 0 \\ 0 & 0 & l_a & l_b \\ 0 & 0 & 1 & 1 \end{pmatrix} \tag{14}$$

$$\boldsymbol{f} = \begin{pmatrix} F_{xa} \\ F_{xb} \\ F_{ya} \\ F_{yb} \end{pmatrix} \tag{15}$$

A transformation to bearing coordinates $\boldsymbol{q}$ leads to the following equations. The bearing coordinates are:

$$\boldsymbol{q} = \begin{pmatrix} x_a \\ x_b \\ y_a \\ y_b \end{pmatrix} \tag{16}$$

The transformation can be written as:

$$\boldsymbol{q} = \boldsymbol{T}\bar{\boldsymbol{q}} \tag{17}$$

where $\boldsymbol{T}$ is the transformation matrix:

$$\boldsymbol{T} = \begin{pmatrix} l_a & 1 & 0 & 0 \\ l_b & 1 & 0 & 0 \\ 0 & 0 & l_a & 1 \\ 0 & 0 & l_b & 1 \end{pmatrix} \tag{18}$$

The transformed equations of motions are:

$$\ddot{\boldsymbol{q}} = -\boldsymbol{T}\boldsymbol{M}^{-1}\omega\boldsymbol{G}\boldsymbol{T}^{-1}\dot{\boldsymbol{q}} + \boldsymbol{T}\boldsymbol{M}^{-1}\boldsymbol{B}_z\boldsymbol{f} \tag{19}$$

When a linearized bearing model is used, $\boldsymbol{f}$ can be written as:

$$\boldsymbol{f} = \boldsymbol{K}_s\boldsymbol{q} + \boldsymbol{K}_i\boldsymbol{i} \tag{20}$$

In equation (20), $\boldsymbol{K}_s$ is the force-displacement factor and $\boldsymbol{K}_i$ the force-current factor.

$$\boldsymbol{K}_s = \begin{pmatrix} 2k_{s,a} & 0 & 0 & 0 \\ 0 & 2k_{s,b} & 0 & 0 \\ 0 & 0 & 2k_{s,a} & 0 \\ 0 & 0 & 0 & 2k_{s,b} \end{pmatrix} \tag{21}$$

$$\boldsymbol{K}_i = \begin{pmatrix} 2k_{i,a} & 0 & 0 & 0 \\ 0 & 2k_{i,b} & 0 & 0 \\ 0 & 0 & 2k_{i,a} & 0 \\ 0 & 0 & 0 & 2k_{i,b} \end{pmatrix} \tag{22}$$

In this case $\boldsymbol{K}_s$ leads to a non-zero stiffness matrix $\boldsymbol{K}$.

For all further analysis, the location of the sensors is assumed to be identical with the location of the corresponding bearing forces (collocation).

Amplifier

The output voltage amplitude of an amplifier is limited to a lower and an upper boundary (u_{min} and u_{max}). The output current cannot exceed a maximal value i_{max} or become negative (in a two quadrant amplifier).

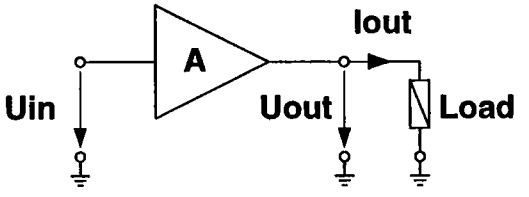

Figure 3: Diagram of the amplifier

$$u_{out} = \begin{cases} u_{max} & : \quad u_{in} \geq u_{max} \\ u_{in} & : \quad u_{min} < u_{in} < u_{max} \\ u_{min} & : \quad u_{in} \leq u_{min} \end{cases} \tag{23}$$

and

$$0 \leq i_{out} \leq i_{max} \tag{24}$$

Voltage saturation of an amplifier leads to reduced dynamics of the current. This is shown in figure 4 and 5 for an example. Current bandwidth can be approximated by a low pass of first order with variable cut-off frequency (depending on the magnitude of the current bouncing). A current controller has a fixed cut-off frequency which can be adjusted with the feedback gain kr_0 (see figure 4).

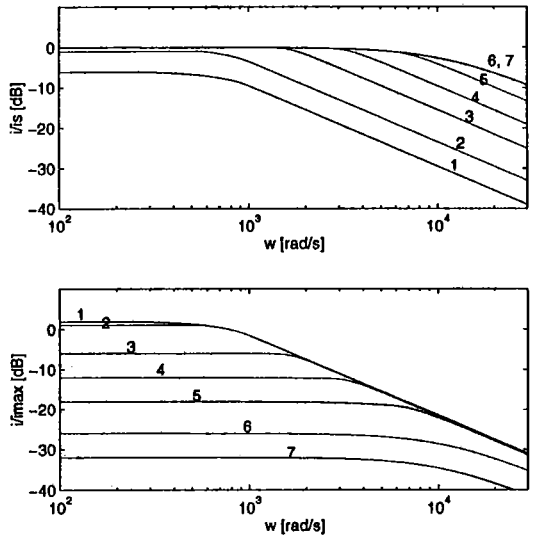

1: $\hat{i}_s = 10\,\mathrm{A}$
2: $\hat{i}_s = 5\,\mathrm{A}$
3: $\hat{i}_s = 2\,\mathrm{A}$
4: $\hat{i}_s = 1\,\mathrm{A}$
5: $\hat{i}_s = 0.5\,\mathrm{A}$
6: $\hat{i}_s = 0.2\,\mathrm{A}$
7: $\hat{i}_s = 0.1\,\mathrm{A}$

Figure 4: Dynamics of a current controller with saturated amplifier. The upper plot shows the transfer function $|G_1(j\omega)| = |\frac{i(j\omega)}{i_s(j\omega)}|$ and the lower plot the transfer function $|G_2(j\omega)| = |\frac{i(j\omega)}{i_{max}}|$ normalized to maximum current. $|G_2(j\omega)|_{max} = \frac{4}{\pi}$ and not 1 (the first spectral fourier coefficient of a periodic square wave).

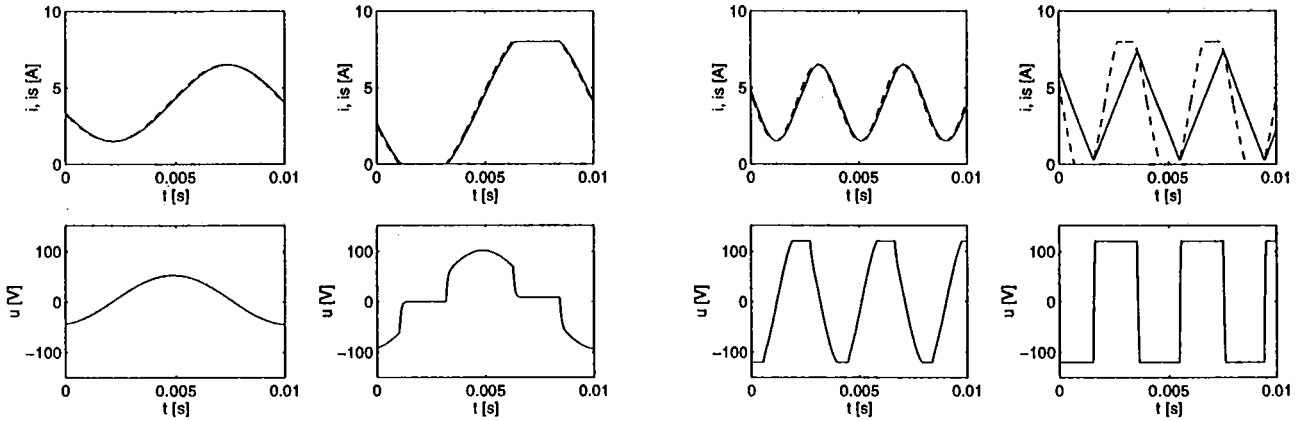

Current i and voltage u at 600 rad/s

Current i and voltage u at 1500 rad/s

Figure 5: Current i and voltage u at two frequencies.
i_s is the desired current and is plotted with dashed line. In the left hand plots $\hat{i}_s = 2.5\,\mathrm{A}$ and in the right hand plots $\hat{i}_s = 5\,\mathrm{A}$. The saturation current $i_{max} = 4\,\mathrm{A}$.

Digital Controller

The function of a digital controller can be divided into an input signal processing block, a controller and an output signal processing block. The following diagrams show the model structure of a state space current controller. Observers for all velocities of the rotor are part of the input block.
The input block models an AD-converter with quantized and sampled output. The derivation of the input signal is made by shifting the input signal N time steps and performing a backward integration (see figure 25). The purpose of the shifting factor N is to enlarge the resolution of the velocity signal at high sampling frequencies.

$$\dot{x}_{aq} = \frac{z^N - 1}{z^N T_s N} x_a \tag{25}$$

The output block models a DA-converter with a quantized and delayed output. The delay is caused by the calculation time of the processor.

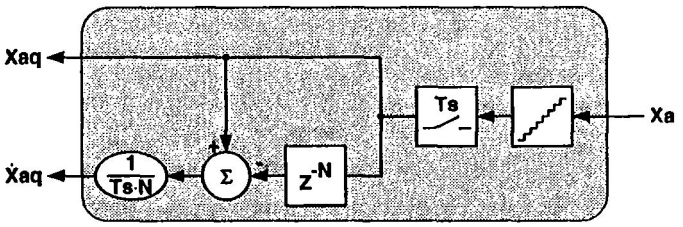

Figure 6: Input signal processing.

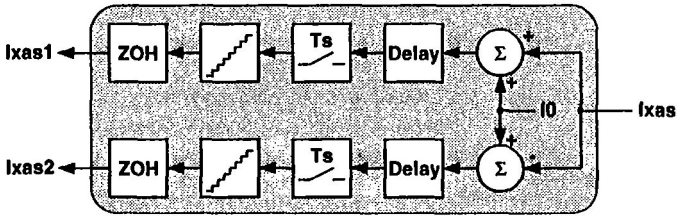

Figure 7: Output signal processing.

BEHAVIOUR OF MAGNETICALLY SUSPENDED GYROSCOPES

In this section, the basic behaviour of gyroscopes with magnetic suspension is shown. More information on the behaviour of gyroscopes in general can be found in [Mag71].
At first, system behaviour is shown for a linearized bearing model (refer to equation 20) using a decentralized PD-controller. In this case the rotor behaves like an elastically suspended gyroscope (suspension with a spring and damper). This is a damped mechanical system ($\boldsymbol{M} = \boldsymbol{M}^{\boldsymbol{T}} > 0, \boldsymbol{K} = \boldsymbol{K}^{\boldsymbol{T}} > 0, \boldsymbol{D} = \boldsymbol{D}^{\boldsymbol{T}} > 0$) and, therefore, stable ([Mag71],[MS76]).

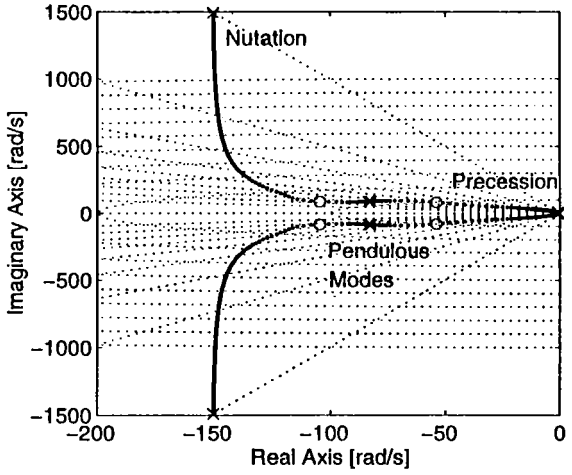

Figure 8: Poles of the system depending on the rotational speed, $\omega = 0 \ldots 1250\,\text{rad/s}$,
$\circ$: poles at $\omega = 0\,\text{rad/s}$,
$\times$: poles at $\omega = 1250\,\text{rad/s}$

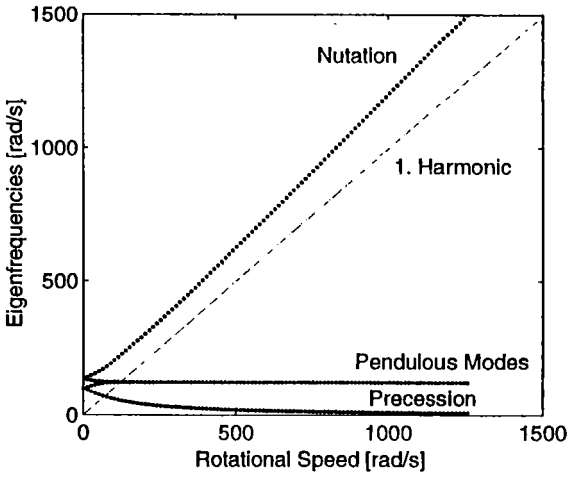

Figure 9: Campbell diagram of the rigid body model,
$\omega = 0 \ldots 1250\,\text{rad/s}$,

The non-rotating system has two eigenfrequencies which are equal for the x-z plane and the y-z plane. For the rotating rotor these eigenfrequencies become coupled and depend on the rotational speed. The four eigenfrequencies are a nutation, two pendulous and a precession frequency. The nutation frequency increases with the rotational speed ($\lim_{\omega\to\infty}\omega_N = \omega\frac{I_z}{I_x}$), while the precession frequency decreases ($\lim_{\omega\to\infty}\omega_P = 0$) [Mag71], [SBT94].

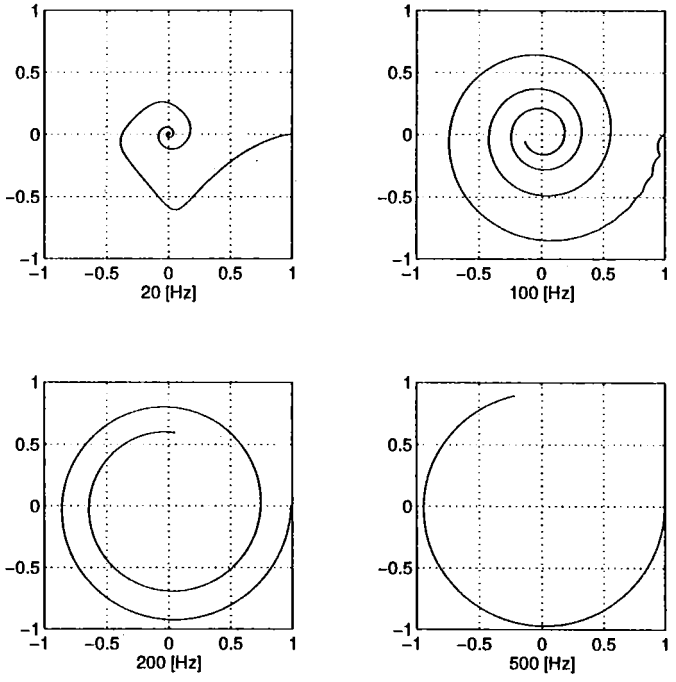

Figure 10: Response of the rotor in the upper plane due to an angular displacement ($\Delta x_a = -\Delta x_b$), The recording time was 1s for all plots, $\omega = 20\,\text{Hz}$, 100 Hz, 200 Hz and 500 Hz

It is assumed that all states (positions and velocities) can be measured or observed. Then the following feedback law can be used:

$$\boldsymbol{u} = -\boldsymbol{K}_r \boldsymbol{x} \tag{26}$$

In equation (26) $\boldsymbol{u}$ is the control input vector, $\boldsymbol{x}$ the state vector and $\boldsymbol{K}_r$ the feedback matrix.

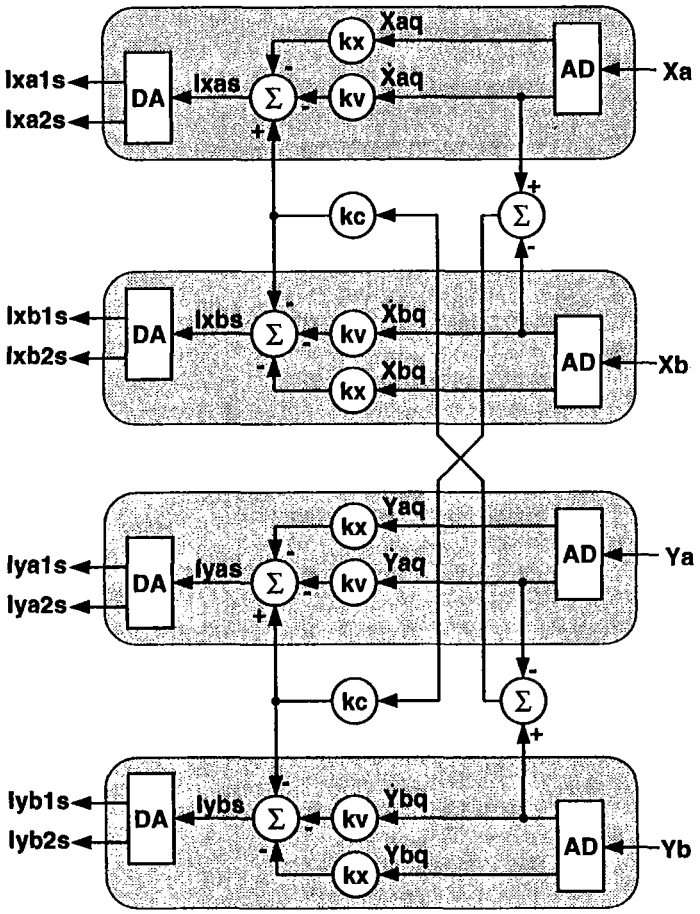

Figure 11: Decentralized controller with compensation of the gyroscopic cross coupling.

For many magnetic bearing systems, decentralized control is used. In that case, each magnetic bearing unit is a subsystem which is controlled independently [Ble84]. The feedback matrix $\boldsymbol{K}_r$ therefore only consists of diagonal elements. There is no cross coupling between the x- and y-direction and respectively the two radial bearing planes. The main advantages of decentralized control are simple controller structure and reduced computational time. For a system at standstill, and respectively for a system with weak gyroscopic coupling, decentralized control leads to good system performance which cannot be significantly improved with centralized control. In the case of a magnetic bearing system with strong gyroscopic coupling, the situation is different. The plant changes with the rotational speed. As mentioned before,

gyroscopic coupling leads to a decrease of system performance because the precession mode becomes limit stable. A consideration of digitization and other nonlinearities (see next section) shows that gyroscopic effects can cause instability. Therefore, gyroscopic coupling has to be considered for controller design.
A centralized controller can be designed at a certain rotational speed so that the system has the same poles as at standstill. In this case gyroscopic effects are compensated. This compensation leads to additional terms in the feedback matrix $\boldsymbol{K}_r$ which depend on rotor velocities and are proportional to the rotational speed. Furthermore, these additional terms only occur outside the diagonals of $\boldsymbol{K}_r$. A decentralized controller designed to operate at standstill therefore remains unaffected by this compensation. Figure 11 shows a simple realisation of a decentralized controller expanded with a compensation of the gyroscopic cross coupling.

The compensation factor k_c is:

$$k_c = \frac{C_{att}\omega J_z}{k_i(l_a - l_b)^2} \tag{27}$$

Further analysis shows that a system with complete compensation of gyroscopic effects is not robust to a delay time (see next section). An attenuation factor C_{att} is used to improve robustness. The structure of the compensator remains the same.

Figure 12 shows the behaviour of a rotor at a rotational speed of 1000 rad/s with a decentralized controller. The increase of system performance with cross feedback can be clearly seen (figure 13).

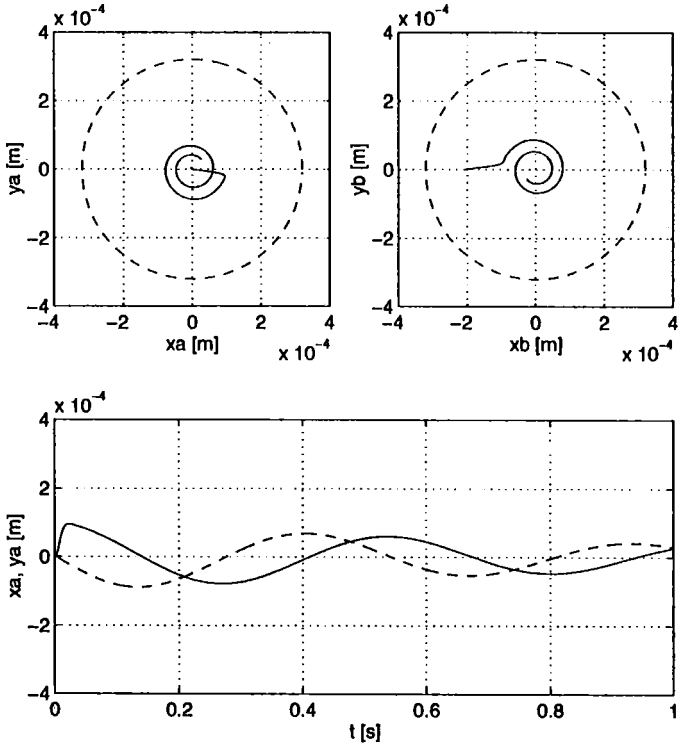

Figure 12: Decentralized controller and transient motion of the excited rotor (dashed line: retainer bearing), $\omega = 1000$ rad/s

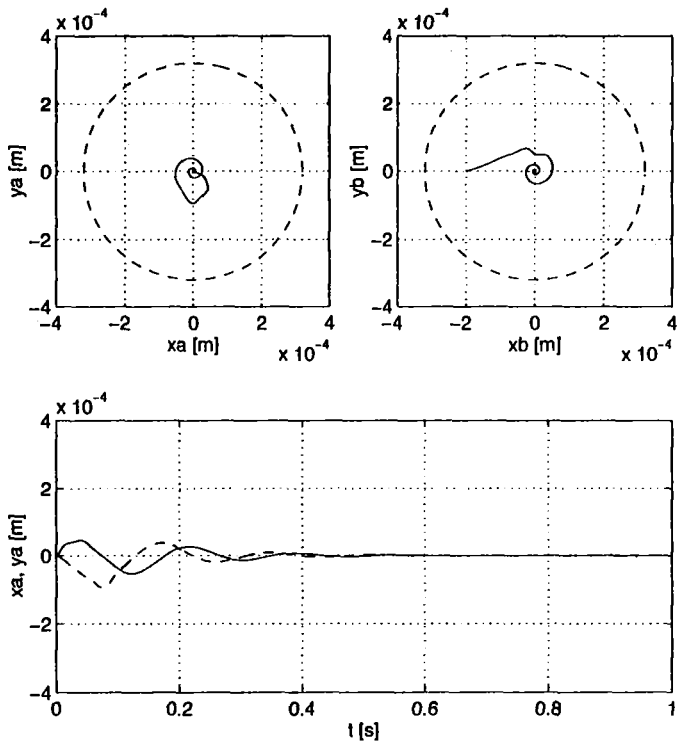

Figure 13: Decentralized controller with 70% compensation of the gyroscopic coupling and transient motion of the excited rotor (dashed line: retainer bearing), $\omega = 1000$ rad/s

It should be noted, that the expansion is small and, therefore, computation time will not increase much. Compared to a full centralized feedback matrix, computation time is nearly four times less. Furthermore, the implementation of this compensation is simple. The main structure of the decentralized controller can still be used. It only has to be expanded by the cross feedback path.

NONLINEARITIES AND SYSTEM PERFORMANCE

As mentioned before, a conservative or damped system cannot be destabilized by gyroscopic effects. A passive (positive-real) continous time controller would therefore be sufficient for stability. In [Her91] it is pointed out that the plant is no longer positive-real when digital controllers are used. Stability cannot therefore be guaranteed for a real nonlinear magnetic bearing with a digital controller.

Sampling Time

The choice of the sampling rate depends on the control of the fastest pole of the closed-loop system. The lowest sampling rate is given by Shannon's law and must be 2 times faster (in practice 5 ... 10 times) than the fastest closed-loop pole.

Typically the open-loop poles of a plant are slower than the closed-loop poles. The system "rotating rotor with gyroscopic coupling", however, behaves differently. At high rotational speed, the fastest open-loop pole can become faster than the closed-loop poles.
Sampling of a digital controller can be modelled with a ZOH (zero order hold) element. The transfer function is:

$$G_{zoh}(s) = \frac{1 - e^{sT_{samp}}}{s}\ ; \qquad G_{zoh}(j\omega) = \frac{1 - e^{-j\omega T_{samp}}}{j\omega} = \frac{2\sin(\frac{\omega T_{samp}}{2})}{\omega} e^{-j\frac{\omega T_{samp}}{2}} \tag{28}$$

It can be seen in equation (28) that a ZOH element introduces a phase shift of $\frac{\omega T_{samp}}{2}$. At the sampling frequency $f_{samp} = 1/T_{samp}$ the phase shift is $-180°$. Therefore, the stability margin for the nutation mode decreases. When the open-loop phase is under $-180°$ due to the phase shift caused by digitization, delay time, etc., instability can occur for the nutation mode (open-loop gain > 1).

The delay time is normally caused by computational time. Similarly to the sampling time, the delay time can be represented as a linear phase shift. This additional phase shifting leads to further reduction of the stability margin.

Current Controller and Amplifier Saturation

The dynamics of a current controller should be as fast as possible. Current controllers with slow dynamics have a phase shift of $-90°$ at the cut-off frequency. This phase shift leads to the same instability problems as mentioned before.
Saturation of the amplifier, i.e. limitation of voltage, leads to a delayed start of the current and, therefore, to an additional phase shift.
Current limitation mainly decreases the magnitude. The phase is unaffected (see also [Unb93b]) and, therefore, instability problems do not occur. A nonlinear simulation shows that the rotor is stable even with high current saturation (see figure 14).

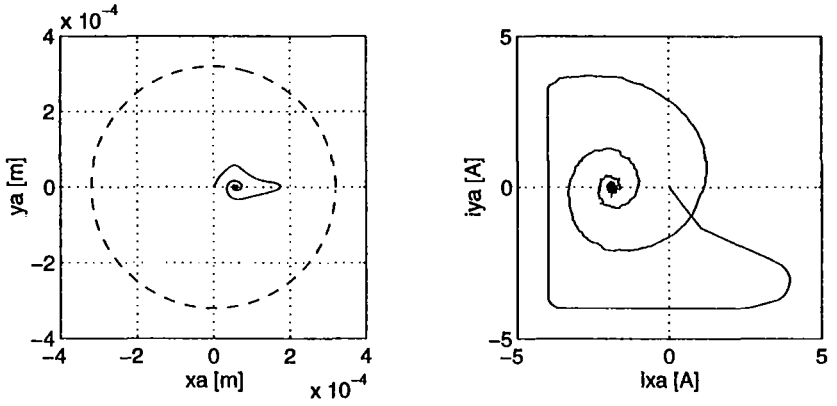

Figure 14: Transient motion of the rotor with an external disturbance force (dashed line: retainer bearing). The current is limited to 4 A.

Robustness of the Compensation

Nonlinearities such as digitization, delay time and amplifier saturation which lead to a delayed reaction of a compensator can cause instability of the system. The smaller these delays are, the better the compensation will work.
For systems with strong gyroscopic coupling, a controller with compensation has to be proposed to improve system performance. Complete compensation has been shown to be possible in linear simulations with MATLAB, but still leads to instability in practice. Nonlinear simulations (with ACSL) show that complete compensation is not robust to delay time effects. An attenuation factor C_{att} is therefore used. It gives the ratio of the implemented compensation compared to a complete compensation. The structure of the cross coupling remains the same, but robustness is much higher. A sufficient and robust solution can be found with an attenuation factor of 75%. With complete compensation, the system has the same behaviour as at standstill. With reduced compensation (e.g. 75%) the system behaviour is the same as for a reduced rotational speed (25% of the nominal rotational speed).
In this paper cross feedback control is analyzed for current control and voltage control with a fast current controller. Here, the rotor poles are independent of the poles of the current controller. For voltage control with a slow current controller, the relationship between the coefficients and the rotational speed is not obvious. In this case all system poles including the poles of the current controller depend on the rotational speed. Further analysis is therefore necessary for voltage controlled systems.
Simulations show that current errors caused by a current observer can easily cause instability. Current observers should therefore not be used for systems with a compensation of gyroscopic effects.

Nonlinear Force Characteristics

The nonlinear force characteristics of magnetic bearings is not crucial for an analysis of gyroscopic effects. Simulations show that this nonlinearity is negligible in the air gap region due to the differential setup of the magnets and the use of a bias current.

CONCLUSIONS

A theoretical analysis has shown that, for rotors with strong gyroscopic coupling, all nonlinearities which decrease the phase (digital control, delay time, slow current controller) can lead to instability at very high rotational speed.
The proposed compensation improves the transient behaviour of the rotor and, therefore, system performace. It can avoid the precession mode to become limit stable. The implementation of this compensation is simple. The structure of a decentralized control can still be used.
With analogue control which introduces no phase shift, stability problems can be reduced. The flexibility of digital control has however certain advantages (e.g. unbalance compensation).
In the next step, these theoretical results will be tested on the flywheel energy storage device.

REFERENCES

[Ack88] Jürgen Ackermann. *Abtastregelung.* Springer-Verlag, Berlin, 1988.

[Ble84] Hannes Bleuler. *Decentralized Control of Magnetic Rotor Bearing Systems.* PhD thesis, ETH Swiss Federal Institute of Technology, Zurich, 1984.

[GLLT92] Grace, Laub, Little, and Thompson. *MATLAB Control System Toolbox, User's Guide.* Natick, 1992.

[Hec93] Andre Heck. *Introduction to Maple.* Springer-Verlag, Berlin, 1993.

[Her91] Raoul Herzog. *Ein Beitrag zur Regelung von magnetgelagerten Systemen mittels positiv reeller Funktionen und $\mathcal{H}^\infty$-Optimierung.* PhD thesis, ETH Eidgenössische Technische Hochschule, Zürich, 1991.

[Mag71] Kurt Magnus. *Kreisel, Theorie und Anwendungen.* Springer-Verlag, Berlin, 1971.

[ME93] A.M. Mohamed and F.P. Emad. Nonlinear Oscillations in Magnetic Bearing Systems. *Transactions on Automatic Control*, 38, August 1993.

[MH84] Takeshi Mizuno and Toshiro Higuchi. Design of the Control System of Totally Active Magnetic Bearings. In *International Symposium on Design and Synthesis*, Tokyo, 1984.

[Mit93] Mitchell and Gauthier, Concord. *ACSL Reference Manual*, 1993.

[MS76] Peter C. Müller and Werner O. Schiehlen. *Lineare Schwingungen.* Akademische Verlagsgesellschaft, Wiesbaden, 1976.

[ONS89] Y. Okada, B. Nagai, and T. Shimane. Cross Feedback Stabilization of the Digitally Controlled Magnetic Bearing. In *Conference on Mechanical Vibration and Noise*, Montreal, 1989. ASME.

[SBT94] G. Schweitzer, H. Bleuler, and A. Traxler. *Active Magnetic Bearings.* vdf, Zurich, 1994.

[Ulb79] Heinz Ulbrich. *Entwurf und Lagerung einer berührungsfreien Magnetlagerung für ein Rotorsystem.* PhD thesis, TU München, 1979.

[Unb93a] Rolf Unbehauen. *Regelungstechnik I.* Vieweg, Braunschweig, 1993.

[Unb93b] Rolf Unbehauen. *Regelungstechnik II.* Vieweg, Braunschweig, 1993.

Session 6 -- Space Applications

Chairman: Nelson J. Groom
NASA Langley Research Center

DESIGN AND IMPLEMENTATION OF A DIGITAL CONTROLLER FOR A VIBRATION ISOLATION AND VERNIER POINTING SYSTEM

Daniel J. Neff and Colin P. Britcher
Department of Aerospace Engineering
Old Dominion University
Norfolk, VA

SUMMARY

This paper discusses the recommissioning of the Annular Suspension and Pointing System (ASPS), originally developed in the mid 1970's for pointing and vibration isolation of space experiments. The hardware was developed for NASA Langley Research Center by Sperry Flight Systems (now Honeywell Satellite Systems), was delivered to NASA in 1983. Recently, the hardware was loaned to Old Dominion University (ODU). The ASPS includes coarse gimbal assemblies and a Vernier Pointing Assembly (VPA) that utilize magnetic suspension to provide noncontacting vibration isolation and vernier pointing of the payload. The VPA is the main focus of this research. At ODU, the system has been modified such that it can now be operated in a 1-g environment without a gravity offload. Suspension of the annular iron rotor in five degrees-of-freedom has been achieved with the use of modern switching power amplifiers and a digital controller implemented on a 486-class PC.

INTRODUCTION

The Annular Suspension and Pointing System (ASPS) is a precision payload pointing system designed for use on the space shuttle. In the early 1970's, NASA's Earth-Orbital Systems Technology group established a need to develop a multi-purpose experiment mounting platform to meet the needs of solar, stellar, and earth viewing experiments planned for the 1980's [1]. The prototype hardware (ASPS) was developed for NASA Langley Research Center by Sperry Flight Systems (now Honeywell Satellite Systems). ASPS was delivered to NASA Langley Research Center in 1983, but was never recommissioned due to shifts in program priorities. In late 1992 the hardware was loaned to ODU so that it would be recommissioned and further developed.

GENERAL DESCRIPTION

The ASPS consisted of several systems, a payload mounting plate, the Vernier Pointing Assembly (VPA), two coarse gimbal assemblies, a mounting and jettison assembly, as shown in Figure 1, as well as a control electronics rack, various testing fixtures and assorted connection

hardware. The VPA contains an annular iron rotor with an L-shaped cross-section that supports the payload mounting plate. Five magnetic actuators, referred to as Magnetic Bearing Assemblies (MBAs) provide attractive magnetic forces to suspend the annular iron rotor in five degrees-of-freedom. The magnetic bearing assemblies control the payload tilt of ± 0.75 degrees (initial configuration). The VPA also contains a roll axis drive which can provide unlimited rotational motion about the axis perpendicular to the payload plate. Two coarse gimbal assemblies were stacked to form an elevation and a lateral gimbal pair, providing a mechanically limited travel of ± 100 degrees (from vertical) about the lower elevation gimbal axis, and ± 60 degrees about the upper lateral gimbal axis. The magnetic actuators were initially sized to accept payloads weighing up to 600 kg (later increased) with a center of mass positioned up to one and one half meters above the payload mounting plate [2].

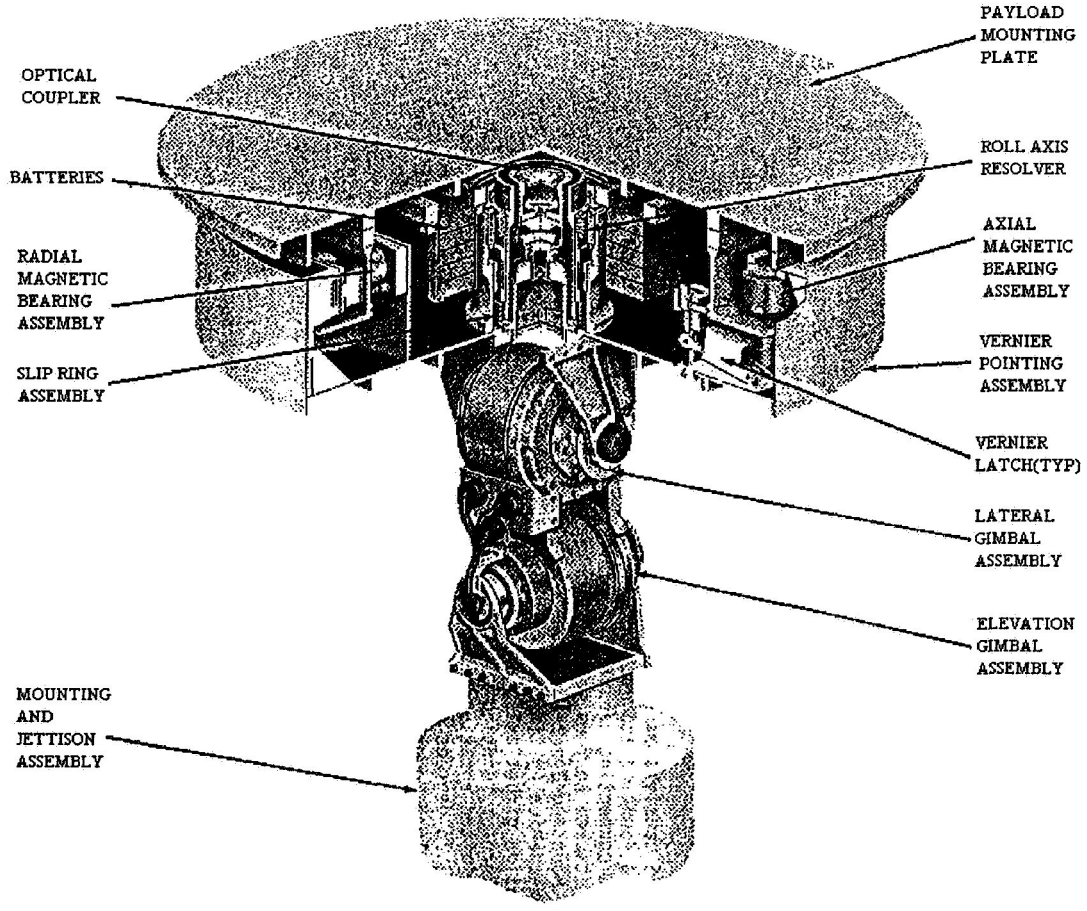

Figure 1 Annular Suspension and Pointing System

The mounting and jettison assembly supported the coarse gimbals and also contained pyrotechnics to jettison the ASPS (and payload) in the event of multiple failures which prevented stowage in orbit. The control electronics rack is an assembly of analog circuits made up of power amplifiers and data acquisition to control the vernier pointing assembly. The balance and testing fixture is a gravity off-load used to simulate a zero-gravity environment.

Hardware Status and Project Goals

Of the systems described above, only the VPA, control electronics rack, and balance and testing fixture were loaned to ODU. The goal of this project was to develop a modern digital control system to suspend the annular iron rotor against gravity in five degrees-of-freedom, and to develop the necessary hardware and software. Once the system became operational, future work could concentrate on improved control algorithms and hardware upgrades, with the objective of steadily improving performance [3].

COMPONENT DESCRIPTIONS

Vernier Pointing Assembly

The VPA provides the ASPS with its high resolution pointing capability. The VPA was originally composed of an annular iron rotor, three axial magnetic bearing assemblies, two radial magnetic bearing assemblies, a roll motor, a total of twelve proximity sensors, five vernier latches, a roll resolver and rotary transformer, and standby battery packs, as shown in Figure 2. However, the rotary transformer and standby batteries were not fully developed [2]. The three axial MBAs, two radial MBAs and roll motor actively control the six degrees-of-freedom of the annular iron rotor, whose mass is 21.59 kg. The axial MBAs control the translation and angular rotation of the payload about two axes and the radial MBAs control the lateral position, providing radial centering. The roll motor controls the sixth degree-of-freedom about the axis perpendicular to the payload plate. The axial MBAs react against the horizontal surface and the radial MBAs react against the vertical surface of the annular iron rotor. The displacements of the rotor are sensed by proximity sensors. Each axial and radial MBA incorporates a pair of proximity sensors. The roll motor has two pairs of proximity sensors to assist in compensating for stray forces and torques produced by the roll motor.

Magnetic Bearing Assembly

The electrical and mechanical descriptions of the axial MBAs is contained in Figure 3. The force capacity of the axial and radial magnetic bearing assemblies are ± 28.9N and ± 14.2N respectively. The operating range of the axial and radial assemblies were ± 5.6mm and

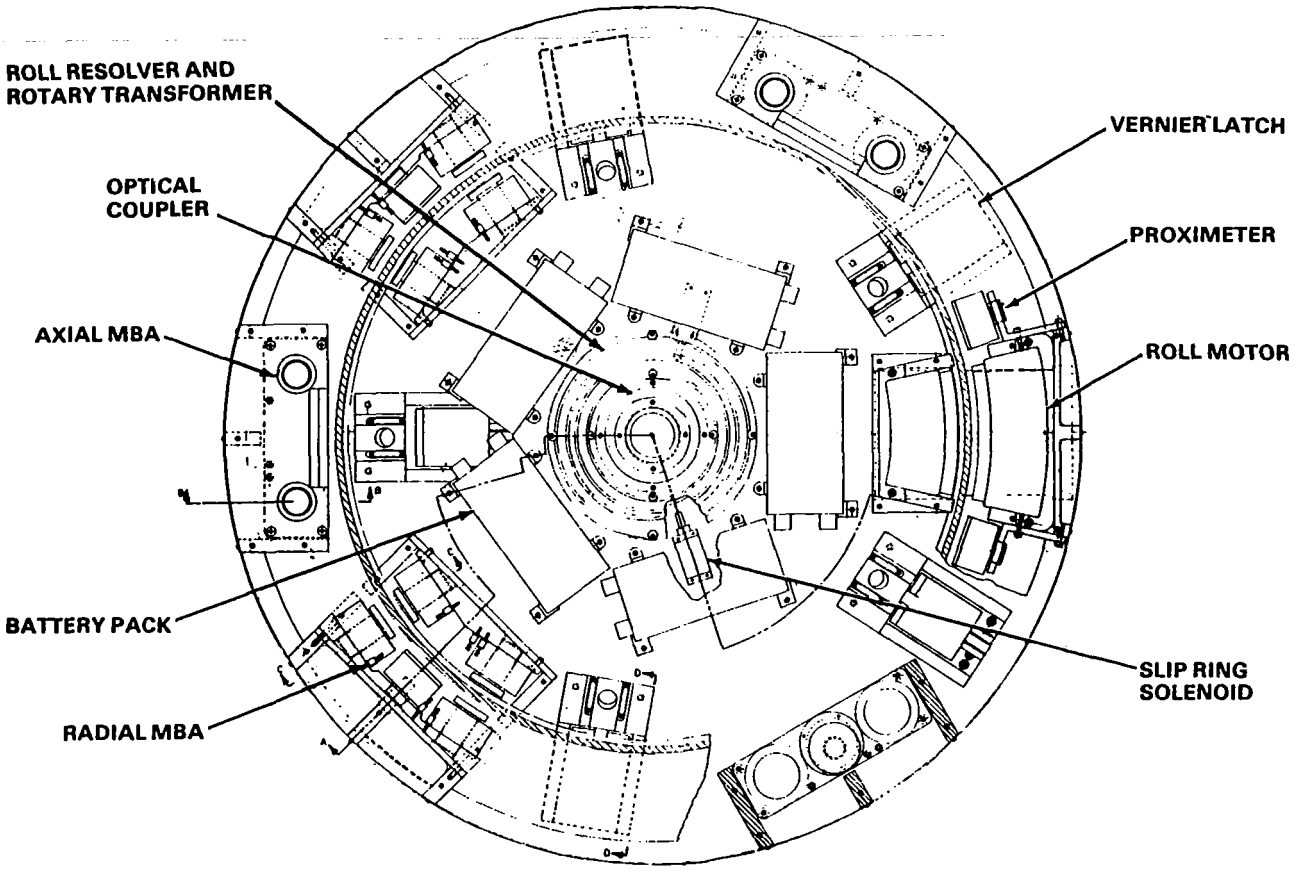

Figure 2 - The Vernier Pointing Assembly

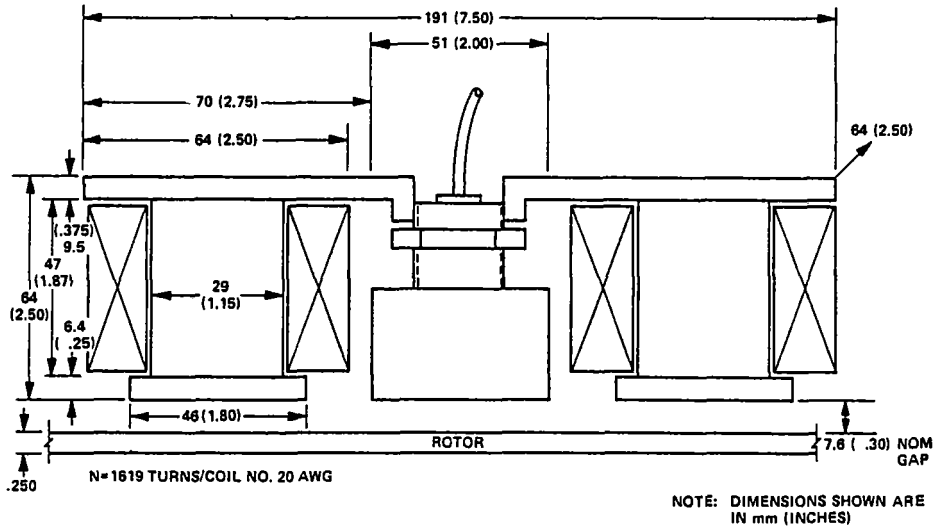

Figure 3 - Axial MBA Configuration (lower coils omitted for clarity)

$\pm$ 5.1mm respectively*. The magnetic actuators consist of a wire-wound magnetic coil and a core material manufactured out of 50% Nickel-Iron. The magnetic coils for the axial and radial MBAs are wound with 810 ± 1 turns of #20 AWG, HML insulated copper wire and 863 ± 1 turns of #22 AWG, HML insulated copper wire, respectively, with two coils connected in series.

Proximity sensors

The proximity sensors used on the ASPS were developed by Kaman Instrumentation, and are still commercially available. These noncontacting sensors use the principle of variable impedance caused by eddy currents that are induced in the conductive target by the sensor coil. The coil in the sensor is driven by a 10 MHz crystal-controlled oscillator. Excitation of the sensor coil generates an electromagnetic field that couples with the target. The gap between the sensor and target affects the strength of the electromagnetic coupling. The changing gap causes the impedance of the coil to vary, which unbalances the bridge network in the electronic package. The MBAs use two sensors one on each side of the iron rotor. The signals from each sensor are demodulated and differenced in an electronic package mounted on the VPA under one of the radial MBAs.

Roll Motor

The roll motor used on the ASPS is an AC Linear Induction Motor [2]. The motor also incorporates proximity sensors to permit compensation for the radial attractive forces produced in the two motor segment windings. The roll motor produces a maximum of 0.677 Nm of torque in its high excitation mode of operation. The radial force associated with the maximum torque is less then 1.56 N.

Vernier Latches

Five vernier latches, located on the baseplate of the VPA, support the iron rotor for launch and recovery maneuvers. The latches locate and lock the rotor into a center position. Locking the rotor down prevents damage to the MBAs, proximity sensors, and data transfer electronics during maneuvering.

Control Electronics Rack

The control electronic rack was a free standing rack that connected to the VPA through flexible cables, but was intended for laboratory test use only. The electronic assembly contains

*The axial MBA's have had the gap modified from a nominal gap of 7.6mm to 4.31mm in order to suspend the rotor in a one-g environment.

the nessesary hardware to drive the actuators, position sensors, and roll motor of the vernier pointing assembly. One of the major goals of the current work was to replace this system with up-to-date hardware, which will be discussed in more detail shortly.

Balance and Testing Fixture

The balance and testing fixture was used to simulate a zero-gravity environment. The apparatus consists of a counter-balancing system to unload the payload mounting plate and vernier pointing assembly in an attempt to simulate orbiter conditions. Tests using this fixture were performed on servo dynamics, decoupling control, stability during cross-axis disturbances, and a variety of other parameters [2,4].

HARDWARE ANALYSIS AND MODIFICATIONS

Magnetic Circuit Analysis

To estimate the force between the MBAs and the rotor the method of Virtual Work was used. Calculation of the change in magnetic energy in a device in which there are moving parts is a simple method of calculating the forces on moving parts in the device [5]. Simply stated, the change in energy, ΔW is equal to the force, F multiplied by the displacement of the body, Δd ($\Delta W = F\Delta d$). Assuming the permeability of Nickel-Iron to be infinite and that the permeability in the air gap remains constant as the body is displaced through a distance Δd, then the energy W is equal to

$$W = \frac{1}{2}\int_v \mu_o H^2 dV \approx \mu_o H^2 S\ell$$

where H is the field intensity in the gap, V is the volume, S is the pole face area and ℓ the air gap length (assuming two gaps, as Figure 4). Using Ampere's law for magnetic coils the field intensity can be found from $H2\ell = NI$ where N is the number of turns in the magnetic coils and I is the current in the coils. To calculate the force exerted on the rotor, shown in Figure 4 :

$$W_1 = \mu_o H_1^2 S\ell_1 = \mu_o \left(\frac{NI}{2\ell_1}\right)^2 S\ell_1 \quad \text{and} \quad W_2 = \mu_o \left(\frac{NI}{2\ell_2}\right)^2 S\ell_2$$

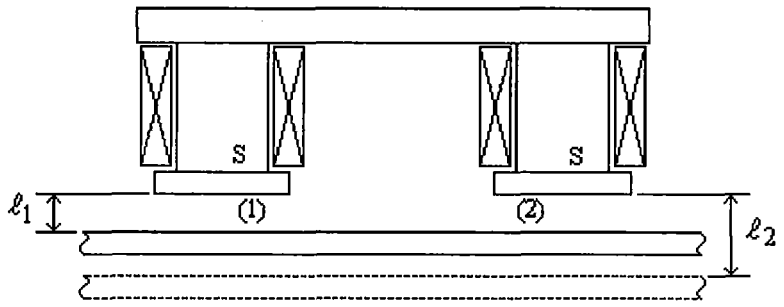

Figure 4 - Magnetic Circuit of an MBA with Movable Rotor.

The force between the rotor and the fixed part of the actuator can then be found by :

$$F = \left| \frac{(W_2 - W_1)}{(\ell_2 - \ell_1)} \right| = \frac{\mu_o N^2 I^2 S}{4\ell_1 \ell_2}$$

Where $\ell_1 = \ell_2 = 3.41\ mm$; $S = 1.58 \times 10^{-3}\ m^2$; $N = 1620$. By rearranging the above equation for current, I gives the following :

$$I = \frac{1}{N}\sqrt{\frac{\ell_1 \ell_2 F}{\mu_o S}} \quad = \frac{1}{N}\sqrt{\frac{g^2 F}{\mu_o S}}$$

Where $F = \frac{1}{3}M$ and M is equal to the mass of the rotor. The current needed to suspend the rotor at an air gap of $g = 3.41\ mm$ is therefore found to be 0.794 Amps. Alternative calculations using the more traditional circuit model give nearly identical results.

Control Approach

A block diagram of the proposed control system is shown in Figure 5. If the time interval between each input sample is small compared to the time constant of the actuator and process (high sampling rate), the system essentially acts as a continuous system [6]. This allows the A/D and D/A converters to be transparent in the preliminary control system design. The initial controller will be a simple proportional-derivative (PD) type. The plant comprises power amplifiers, the actuators, and the suspended mass. Feedback in the control loop is a measure of suspended mass (rotor) displacement from steady state conditions. In order to predetermine the proportional gain, K_p, and the derivative gain, K_D, accurate plant models are required. This is straightforward except for the MBAs, where the traditional linearized model is employed :

$$F = F_o + \frac{\partial F}{\partial i} i \approx \frac{\mu_o N^2 I_o^2 S}{g^2} + \frac{2\mu_o N^2 I_o S}{g^2} i \quad \text{where} \quad I^2 \approx I_o^2 + 2I_o i$$

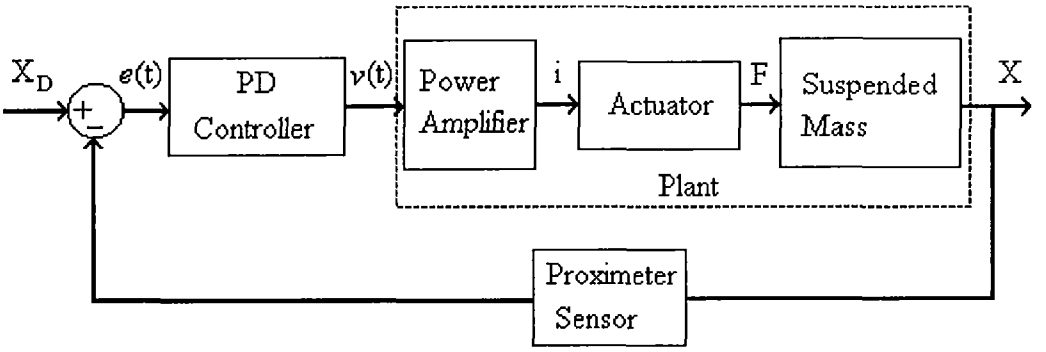

Figure 5 - Block diagram of the ASPS control system.

Figure 6 shows the control system transfer functions :

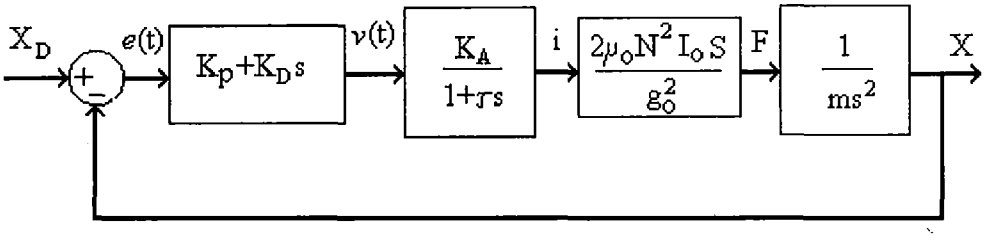

Figure 6 - ASPS component transfer functions

Finally, the transfer function representing the power amplifiers was verified by frequency response analysis of the amplifier using a signal analyzer. A break frequency of approximately 35 Hz was established. Table 1 summarizes all the required constants :

K_A	1.201 $\frac{\text{Amps}}{\text{volt}}$
τ	.00455 sec
μ_o	$4\pi \times 10^{-7} \frac{\text{H}}{\text{m}}$
N	810 $\frac{\text{turns}}{\text{coil}}$
I_o	1.25 amps*
S	1641.7 mm^2
g_o	3.41 mm
m	7.19 kg

Table 1 - Summary of constants used in transfer functions.

*Experimentally determined value.

With a ratio of $\frac{K_D}{K_p}$=0.1 the closed-loop transfer function of the system shown in Figure 6 is as follows :

$$K \frac{34.949\ s + 349.49}{0.0327\ s^3 + 7.19\ s^2}$$

The root locus plot of this system shows that the system is stable for a range of K from 0 to 10. An overall gain of 4.5 corresponding to a damping ratio of 0.7 can be determined graphically from Figure 7.

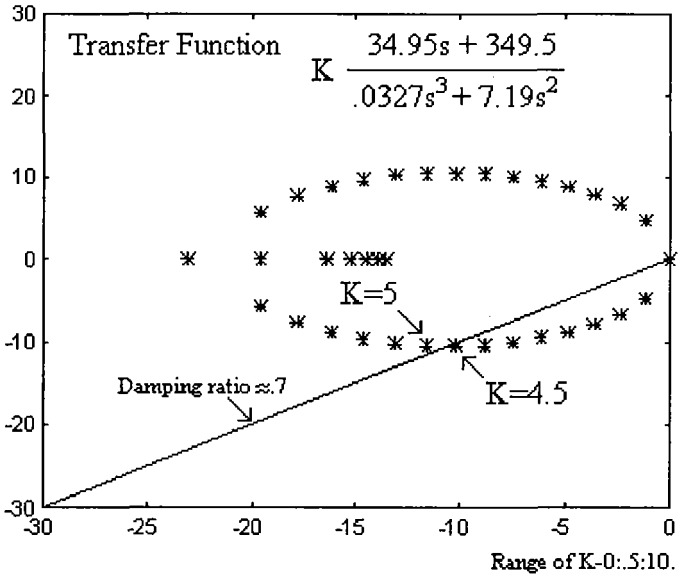

Figure 7 - Root locus for the PD controller.

Modifications to the Magnetic Bearing Assemblies

The first step in recommissioning the VPA was to modify the three axial MBAs so that the rotor could be suspended in a 1-g environment. To accomplish this the gap between the magnetic actuators and the rotor was reduced 54.5%, such that the current needed to suspend the rotor at the new gap was predicted (and verified by testing) to be low enough not to cause overheating of the magnetic coils. To implement the new air-gap, the top plate as shown in Figure 8 was remanufactured with a thickness change from 6.35 mm to 9.53 mm. This new thickness would extend the core material of the magnetic bearing assembly, and reduce the air gap between the top plate and the iron rotor from 7.62 mm to 3.41 mm. The radial magnetic bearing assemblies were not modified.

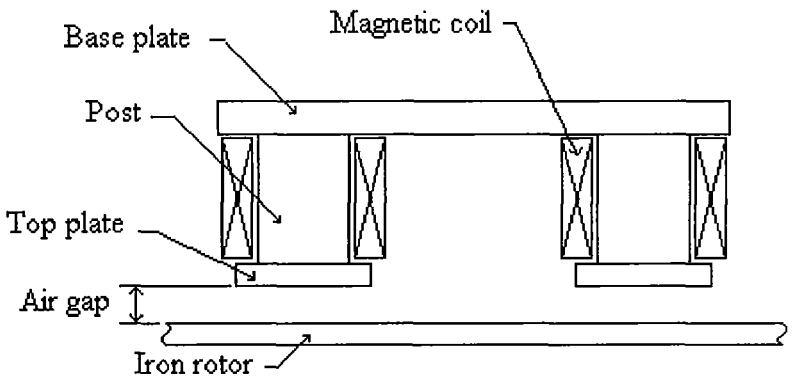

Figure 8 - Magnetic Bearing Assembly.

Digital Controller

The controller hardware comprises a 486DX4-33 PC with 12-bit A/D and D/A boards [7,8]. A counter/timer board was installed to interrupt the main program in order to perform the input/output at a regularly scheduled time interval. The power amplifiers selected to provide power to the magnetic actuators are commercial PWM types [9]. The switching frequency is 22kHz. The controller software was written using Microsoft Quick C and implemented the simple PD controller described earlier. Rate information is estimated by simple differencing of successive position samples. A block diagram of the new hardware is shown in Figure 9.

Each bearing station is controlled independently. This is possible since each has similar dynamics, and the geometry of the system is such that cross-coupling between actuators and system degrees-of-freedom is minimized. It should be noted that extensive coupling is introduced with a payload added, due to the large C.G. offset. Further, the magnetic actuators are quite non-linear, requiring a superior linearizing strategy if operation over the full range of displacements or tilt angles is anticipated. The original control system design incoporated many linearizing, mixing, and feedforward stages for these reasons [2].

OPERATION

The system is operational, with a typical time history from axial MBA station C shown in Figure 10. The large transient around 3 seconds corresponds to the release of the vernier latch at that station. As can be seen, excessive sensor noise currently hampers performance somewhat, but this appears to be due to improper wiring, grounding and shielding practices. Additional signal conditioning is currently being studied.

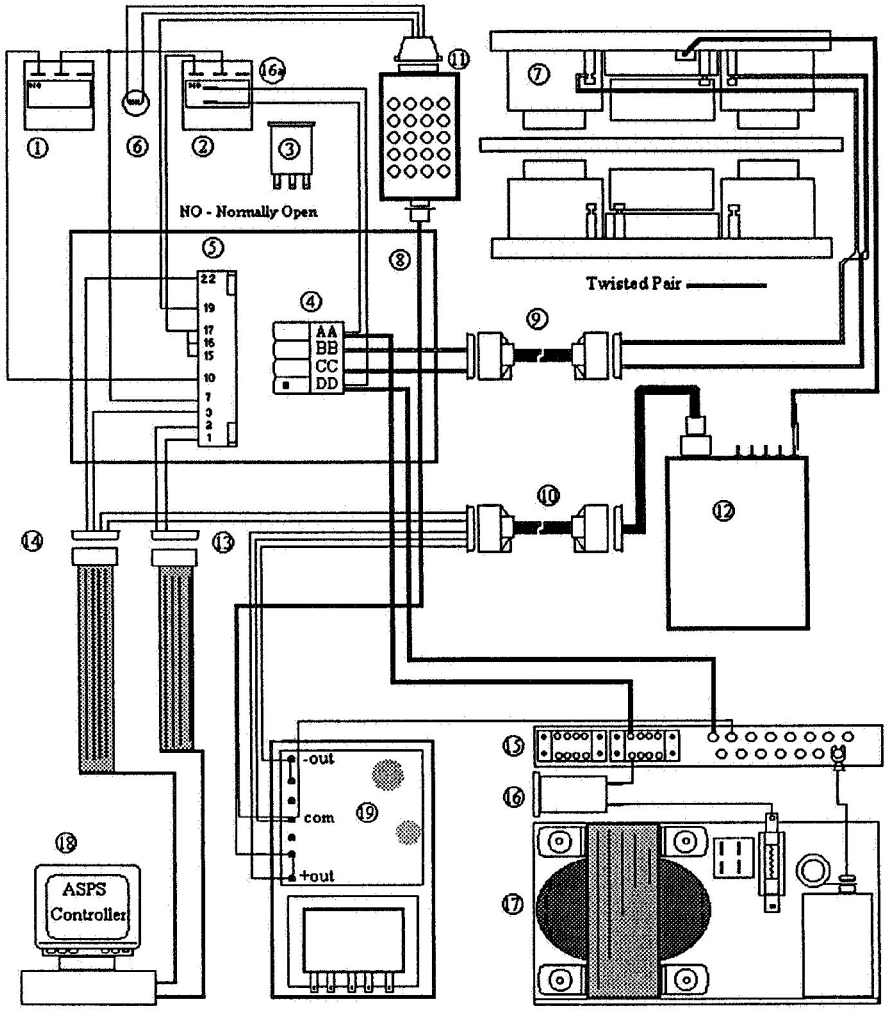

Figure 9 - Schematic Diagram of Revised ASPS Controller and Supporting Hardware

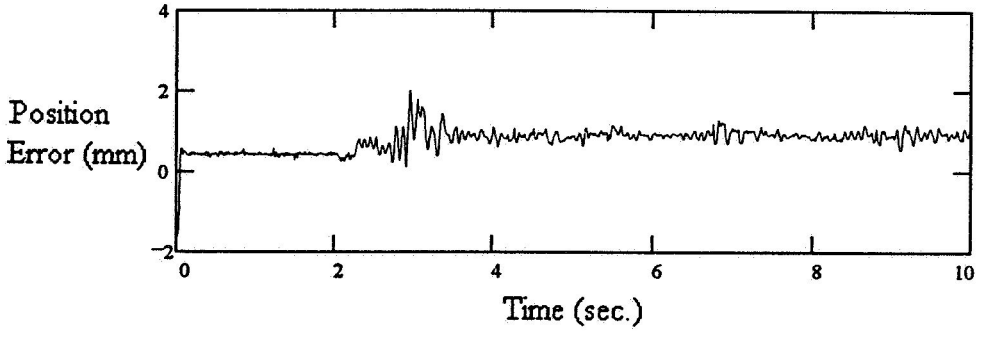

Figure 10 - Typical Time History, MBA station C, showing "launch" transient

CONCLUSIONS

The VPA has been successfully recommissioned and operated with five degree-of-freedom control.

ACKNOWLEDGEMENTS

This work was partially supported by NASA Grant NAG-1-1056, Technical Monitor Nelson J. Groom, and by the NASA/USRA Advanced Design Program administered by the Universities Space Research Association.

REFERENCES

1. Anderson, W.W.; Groom, N.J.; Woolley, C.T.: Annular Suspension and Pointing System. AIAA Journal of Guidance and Control, September-October 1979.
2. Cunningham, D.C., et al.: Design of the Annular Suspension and Pointing System (ASPS). NASA CR-3343, October 1980.
3. Britcher, C.P.; Groom, N.J.: Current and Future Development of the Annular Suspension and Pointing System. 4th International Symposium on Magnetic Bearings, Zurich, Switzerland, August 1994.
4. Sperry Corporation Flight Systems: Final Report - The Development of the ASPS Vernier System. Sperry Corporation Flight Systems, Phoenix, AZ. Contract No.NAS1-15008, June 1983.
5. Ida N.; Bastos, J.P.A.: Electromagnetics and Calculations of Fields. Springer-Verlag, New York, Inc., 1992.
6. Dorf, R.C.: Modern Control Systems, Sixth Edition. Addison-Wesley Publishing Company, 1992.
7. Keithley MetraByte Corporation: Users Guide of the DAS-1402 Data Acquisition Board
8. Keithley MetraByte Corporation: Users Guide of the DDA-06 Data Acquisition Board
9. Copley Controls Corporation: PWM Amplifier Catalog

A MAGNETIC BUMPER-TETHER SYSTEM USING ZFC Y123

Roy Weinstein, Drew Parks and Ravi-Persad Sawh
Institute for Beam Particle Dynamics and
Texas Center for Superconductivity
University of Houston
Houston, Texas

Victor Obot and Jianxiong Liu
Dept. of Mathematics
Texas Southern University
Houston, Texas

G. D. Arndt
NASA Johnson Space Center
Houston, Texas

SUMMARY

We consider the use of magnetic forces in a bumper system, to soften docking procedures. We investigate a system which exhibits no magnetic field except during the docking process, which, if desired, can automatically tether two craft together, and which provides lateral stability during docking. A system composed of zero field cooled $Y_{1.7}Ba_2Cu_3O_{7-\delta}$ (Y123) tiles and electromagnets is proposed. The Y123 high temperature superconductor (HTS) is mounted on one craft, and the electromagnet on the other. Results of small prototype laboratory experiments are reported. The electromagnet has, for convenience, been replaced by a permanent SmCo ferromagnet in these measurements. When the two craft approach, a mirror image of the ferromagnet is induced in the Y123, and a repulsive bumper force, F_B, results. F_B is velocity dependent, and increases with v. For presently available HTS materials, bumper pressure of ~3.7N/cm^2 is achieved using SmCo. This extrapolates to ~18N/cm^2 for an electromagnet, or a force of up to 20 tons for a 1m^2 system. After reaching a minimum distance of approach, the two colliding craft begin to separate. However, the

consequent change of SmCo magnetic field at the Y123 results in a reversal of current in the Y123 so that the Y123 is attractive to the SmCo. The attractive (tether) force, F_T, is a function of $R=B_{Fe}/B_{t,max}$, where B_{Fe} is the field at the surface of the ferromagnet, and $B_{t,max}$ is the maximum trapped field of the Y123, i.e., the trapped field in the so-called critical state. For $R \geq 2$, F_T saturates at a value comparable to F_B. For a range of initial approach velocities the two craft are tethered following the bumper sequence. Most of the kinetic energy of the collision is first converted to magnetic field energy in the Y123, and then into heat via the creep mechanism. About 15% of the work done against magnetic forces during collision remains stored as magnetic energy after 1 hour. Experiments have also been conducted on the spatial range of the bumper force for arrays of HTS tiles. For a single HTS tile ~ 2cm in diameter, the range of F_B is ~ 1cm. For a $1m^2$ array the range of F_B will be circa 50 cm.

INTRODUCTION

Assume two spacecraft approach for docking. On one is an unactivated electromagnet and, facing this, on the other craft is an array of HTS tiles. As the craft near, the HTS is cooled in zero field (i.e., zero field cooled, or ZFC) and the electromagnet is then turned on. As the craft approach, the superconductor first acts like a mirror image of the approaching ferromagnet, and repels it. The Bean model [1] gives a good qualitative representation of the forces. The field of the ferromagnet, B_{Fe}, first induces current J_c in the outer parts of the superconductor. These penetrate to some interior point, r_{min}. At r_{min} the current goes to zero. The direction of this current is such that the two magnets repel. As B_{Fe} increases, r_{min} decreases, and reaches the center of the superconductor when $B_{Fe}=B_{t,max}$. Here $B_{t,max}$ is the maximum field which can be trapped in the HTS. The maximum bumper force, F_B, occurs for the ratio $R=B_{Fe}/B_{t,max} \leq 1$.

If the craft have momentum they will approach unless and until stopped by F_B. After the relative motion is stopped, the magnets continue to repel, and hence the craft develop velocity in the reverse direction. In this phase, B_{Fe} at the surface of the superconductor decreases. The resulting supercurrent in the HTS depends upon the value of the ratio $R \equiv B_{Fe}/B_{t,max}$ at the point of closest collision. For a range of values of R the dominant resulting supercurrent reverses, and force on the ferromagnet, due to the supercurrent, becomes attractive. This can lead to tethering, as will be discussed further below. The maximum tether force occurs for $R \geq 2$.

EXPERIMENTAL STUDY

Measurement of Bumper Force

A device was constructed to measure the forces acting in the HTS-SmCo system. This is shown schematically in Fig. 1. Transducers were used to measure quantities of interest, and direct computer logging was used. Initially, only force, and separation distance of the Fe-HTS were measured. The HTS used was $Y_{1.7}Ba_2Cu_3O_{7-\delta}$ (Y123). The size of the Y123 tiles used were ~ 2cm diameter and 0.8cm thick, except where it was desired to reduce $B_{t,max}$ in order to increase R. In these cases the 0.8cm thickness was reduced. The SmCo magnets used were comprised of one or more pieces, each of which was 1" x 1" x 1/4". By varying the number of SmCo pieces used, B_{Fe} could be varied from 2,000 to 4,300 Gauss.

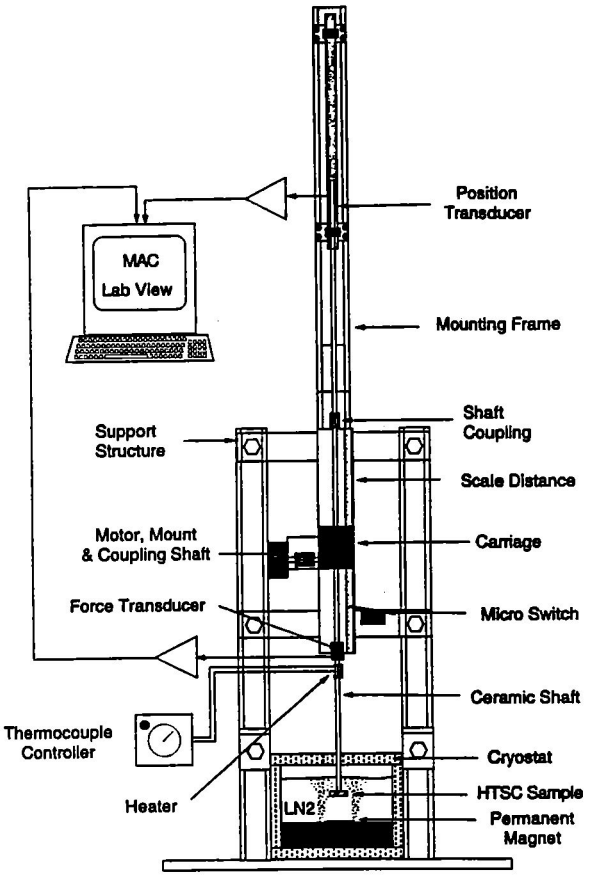

Fig. 1. Characterization apparatus for bumper/tether experiments.
Note: Transducers for magnetic field, temperature, and lateral forces have now been added to this device.

Figure 2 shows early measurements of the bumper force vs. distance in which it was learned that F_B depends upon the velocity of approach. This will be discussed below. The maximum values of F_B/Area observed were about 3.7N/cm^2. State-of-the-art HTS processing provides tiles of the size used for which $B_{t,max} \leq 2.1$Tesla.[2] However, the SmCo used was limited to about $B_{Fe} \sim 0.43$ Tesla. The maximum bumper force results from $B_{Fe}/B_{t,max} \sim 1$. Thus B_{Fe}, and not the HTS value of $B_{t,max}$, limited the magnitude of the bumper force when SmCo magnets were used. Electromagnets can be run, highly saturated, at up to $B_{Fe} \sim 2$

Tesla. Nevertheless, since $B_{t,max} \leq 2.1$ Tesla is available even today, the bumper force is limited by B_{Fe}, and not $B_{t,max}$ even when an electromagnet is used.

If we scale the results of the tests on our small prototype system to a system composed of HTS tiles with $B_{t,max} \geq 2.0$ Tesla, and $B_{Fe} \sim 2.0$ Tesla (for an electromagnet), then the bumper force scales to ~ 18.0N/cm^2. A system 1m^2 in size will exhibit bumper forces of $\geq$ 20 tons.

Velocity Dependence of Bumper Force

The HTS was zero field cooled (ZFC), and the force and work needed to bring the SmCo and HTS close together were measured. Repeated observations, such as presented in Fig. 2, made it clear that the bumper force, F_B, was velocity dependent. In this experiment, involving one tile of Y123, and one small SmCo magnet, the largest velocity of approach permitted by the specific equipment used was ~ 1m/sec. At this velocity, F_B was about 11N. In order to study the velocity dependence of the bumper force, the test apparatus was developed further to include motor drives of constant velocity. This study of F_B indicated that the dominant cause of the velocity dependency is the "giant creep" phenomenon. The creep effect describes a loss of magnetic field by a high temperature superconductor, after initial activation. In the creep mechanism, if the HTS trapped field B_t (t_1) is

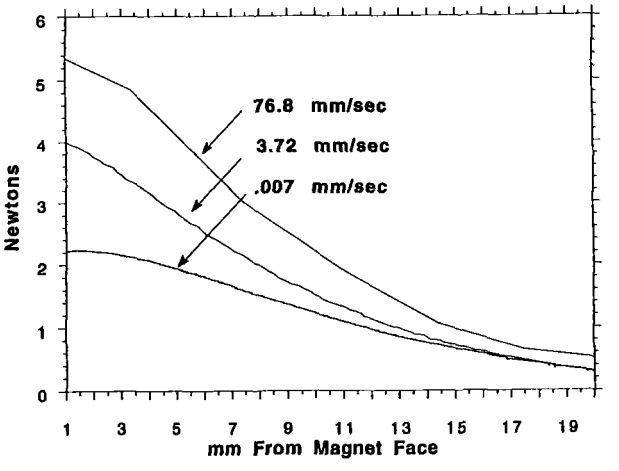

Fig. 2. Bumper force, in N, vs. separation of ferromagnet and HTS, in mm, with velocity of approach as a parameter. For this experiment a motor drive was added to the apparatus.

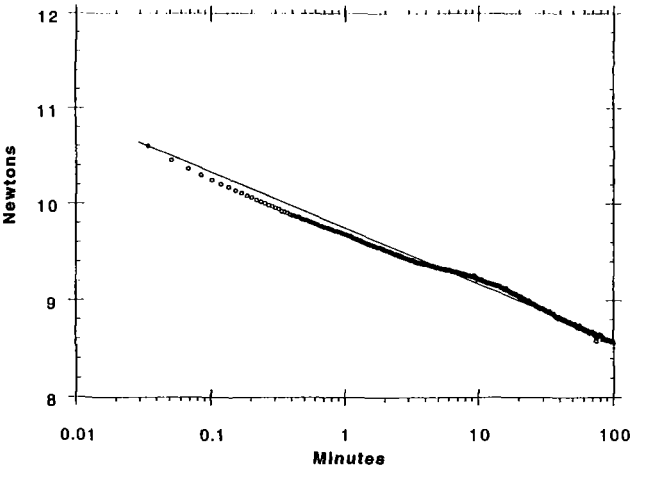

Fig. 3. Effect of creep on bumper force. The SmCo-HTS separation distance was closed rapidly. Following this F_B vs. time was observed.

measured at some time t_1, than at some later time, t_2,

$$B_t(t_2) = B_t(t_1)(1-\beta_1 \log(t_2-t_1)) \quad (1)$$

The creep rate for the materials and tile sizes used in this experiment have been measured repeatedly [3,4]. For a wide variety of processes and sizes, they are characterized in Eq. 1 by a value,

$$0.045 \leq \beta_1 \leq 0.055 \quad (2)$$

i.e., as a rule of thumb the trapped field in a tile of Y123 decreases at ~5% per decade of time.

In order to directly observe the creep effect on the bumper force, the maximum velocity available to us was used, and the Fe/HTS separation gap was closed to a very small separation in a few hundredths of a second. The separation was then left constant. The resulting force, as a function of time following the collision is shown in Fig 3.

The data of Fig. 3 is a good fit to

$$F(t_2) = F(t_1)(1-\beta_2 \log(t_2 - t_1)) \quad (3)$$

with

$$\beta_2 \sim 0.055 \quad (4)$$

This is as expected for a force proportional to ∇B_t, and hence to B_t.

At low collision velocities the field induced in the HTS is reduced by creep. At high velocities there is insufficient time for this, and hence a greater induced field results in the HTS, which in turn results in a larger value of F_B.

Energy Considerations

Our group earlier developed a model of the currents which flow in an HTS trapped field magnet [5]. The model describes the current as composed of two parts: (i) a volume current of constant current density, circulating around the field direction, as would a Bean current [1], and (ii) a constant surface current density on the outer periphery of the HTS, similar to an Amperian current density in a

ferromagnet. This current model provides excellent fits to the three dimensional field around trapped field HTS magnets.

The current model thus permits calculating trapped field energies. Using the current model [5], and a few points of measured trapped field, the magnetic field can be calculated for all space. From this the magnetic energy density can be calculated and then integrated. Typically, in these experiments, we found that 15% of the work done in the collision was still stored as magnetic energy in the HTS an hour after the collision.

In principle one can use such a measurement and calculation of stored energy, together with the creep equation (Eq. 1), to calculate the energy stored in the magnetic field of the HTS as a function of time. The creep rate, β, of Eq. 1 is both measured in this experiment, and known from previous work [Refs 3,4] for the time interval 1sec < t < 1 year. However, the creep rate for short times, t << 1 sec, is not available from our own measurements. Such data is available in the literature, and indicate a faster creep speed at very short times [6].

We used the measured creep, as shown in Fig. 3, and the measurement by others of creep at very short times, and concluded that most, if not all, of the kinetic energy lost in the collision is converted to magnetic field energy in the HTS. The magnetic energy is then converted to heat at a rate given by the creep mechanism.

The Bounce Back

After closest approach, the SmCo is repelled, by the HTS, and the separation increases. The nature of the Bean current [1] is such that the decreasing SmCo field results in a reversal of current in the outer regions of the HTS. The size of the region of reversal depends on the ratio $R = B_{Fe}/B_{t,max}$. For values of R of the order of 1, or larger, the repelling force reverses, and becomes an attractive force at a small separation distance. This can result in trapping the HTS and SmCo magnets close to each other, but not touching. The tether force depends upon the ratio $B_{Fe}/B_{t,max}$. See Figure 4. The tether force becomes maximum when $B_{Fe} \geq 2B_{t,max}$. This is also explained by the Bean model [1] which predicts that as the ferromagnet retreats, and B_{Fe} decreases at the surface of the HTS, J_c reverses, and an attractive field and force results, which is maximum when B_{Fe} is at least twice $B_{t,max}$.

Again we note that J_c, and B_t, for state-of-the-art HTS are quite sufficient for the HTS role in the device described here. Typical maximum trapped fields in our HTS tiles at 77K are 0.4-0.5 Tesla when not irradiated, 1.1 to 1.2 Tesla when proton irradiated [8] and 2.1 Tesla when processed with short isotropic columnar defects [7, 2]. $B_{t,max}$ had to be *reduced,* even in our unirradiated tiles, to observe cases in which the maximum tether force occurred. Thus the HTS used to observe tethering was not irradiated, and for some measurements the HTS tiles were thinned.

Fig. 5 shows the work done against F_B, in the movement toward closest approach, and by F_T in the retreat from closest approach. Fig 5 uses as input data the forces shown in Fig. 4c. In this example, the craft approach and their kinetic energy is gradually reduced by F_B, until the kinetic energy reaches zero at the distance of closest approach. Then F_T at first causes an acceleration in the opposite direction. However, when the craft reach point (a), in their retreat, F_T reverses and slows the retreat. The craft become energetically trapped in the region between (b) and the distance of closest approach. The craft will oscillate in this interval until dissipative forces bring them to rest at point (a).

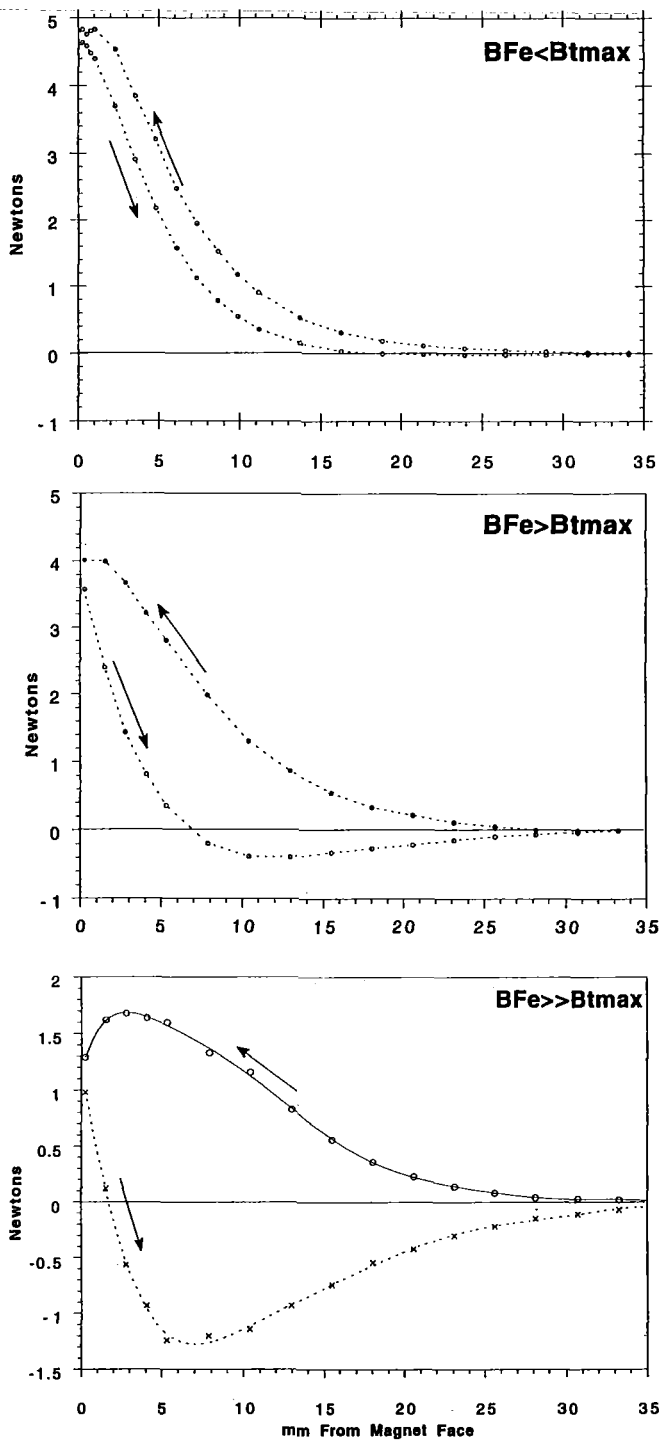

Fig. 4. F_B (arrow to left), and F_T (arrow to right) are shown for $R \equiv B_{Fe}/B_{t,max} = 0.67$ (top); 1.39 (middle); and 2.47 (bottom).

Range of the Magnetic Forces

The range of the bumper force, F_B, is about equal to the radius of the tile of HTS material. Most high quality HTS tiles have radius of 1-3 cm. Thus the range of F_B, for a single HTS tile, is 1-3 cm. (See Figure 4a.) Bumper operation can be useful at 1-3 cm as a backup for more traditional docking mechanisms in spacecraft. However, it would clearly be desirable to extend the range of the bumper force.

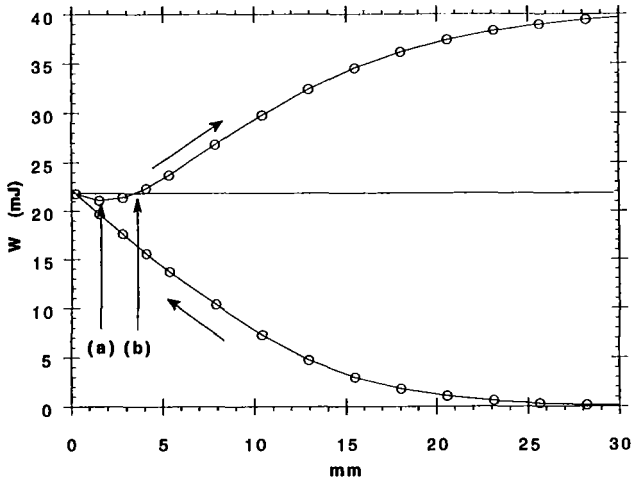

Fig. 5. Work done by spacecraft on magnetic field, in case of forces shown in Fig. 4c. On approach (arrow to right) spacecraft do work of 22mJ. At distance of closest approach, KE = 0. On bounce back spacecraft cannot separate beyond point (b).

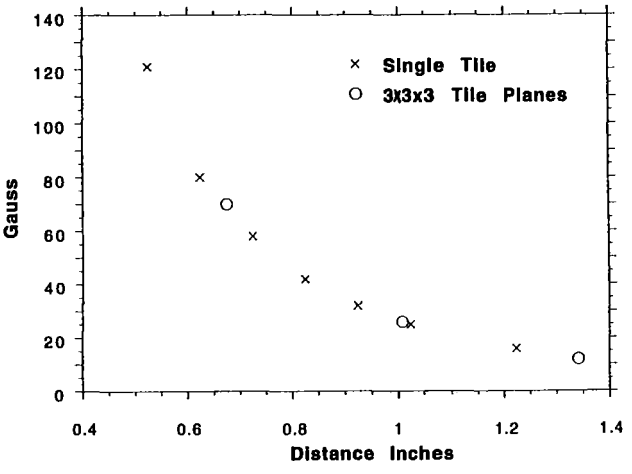

Fig. 6. Evidence for scaling, comparing trapped field of a single tile at distance Z from surface, to trapped field of an array of 3 x 3 x 3 tiles at a distance 3 x Z.

We have performed experiments to determine the scaling laws for *arrays* of HTS tiles. For these purposes we have used an array of 3 x 3 x 3 HTS tiles, and arrays of 1 x 5 x 5 and 2 x 5 x 5 tiles.

A single tile of HTS, of radius r_0, has a range of the order of r_0. One theoretically expects that an array of n x n x n HTS tiles will have a range of the order of n x r_0. This expectation has been confirmed experimentally for the 3 x 3 x 3 array of tiles. See Figure 6. Comparable extension of field range has been observed in 5 x 5 x 1 and 5 x 5 x 2 arrays. We expect therefore that an array of 50 x 50 tiles (of total size about 1m x 1m) will have a field range of about 50cm.

SUMMARY

A magnetic bumper-tether has been explored using 2cm diameter, 0.8 cm thick HTS tiles, ZFC, and similar size SmCo ferromagnets. Bumper forces, F_B, are observed up to $F_B \sim 11N$. F_B of the order of 20 tons can be achieved for arrays of the order of 1m x 1m for HTS tiles, used with an electromagnet. Because of creep, the bumper force is velocity dependent, having its highest values for the largest approach velocity, as is desirable. The bumper force maximizes for $R \equiv B_{Fe}/B_{t,max} \leq 1$.

The tether force, F_T, is comparable to the bumper force when $R \geq 2$. The tether force leads to automatic tethering for a range of values of R.

Bumper and tether forces, combined, will optimize in the interval $1 \leq R \leq 2$.

During the collision most of the mechanical work done in the collision is converted to magnetic field energy, and then to heat via the creep mechanism. One hour after the collision, 15% of the energy remains in the magnetic field.

The range of the bumper force for a single tile is only ~ 1cm. However the range of the force increases with the size of the total array of HTS tiles, and reaches, ~ 50 cm for an array of tiles 1m x 1m.

Work on this project continues, to determine the lateral stability of the bumper cycle, to test larger prototypes using arrays, and to make large-scale prototype collision tests. The theory of the dependence of F_B and F_T on R is being more fully developed. The present test device is being extended by adding magnetic field and temperature transducers, and force transducers to measure lateral forces.

This work was supported by NASA-JSC, NSF, ARO, and the State of Texas via TCSUH and the ATP Program.

REFERENCES

1. Bean, C.P.; Phys. Rev. Lett., 8, 250 (1962); Rev. Mod. Phys., 36, 31 (1964)

2. Weinstein, R.; Sawh, R.-P.; Ren, Y.; and Liu, J.: "The Effect of Isotropic Short Columnar Pinning Centers on J_c, T_c, and Creep," submitted to Eighth International Workshop on Critical Currents in Superconductors, Kitakyushu, Japan, April 1996.
3. Weinstein, R.; Ren, Y.; Liu J.; Chen, I.G.; Sawh, R.; Foster, C.; and Obot, V.; Proc. Intl. Symposium on Superconductivity, Vol 2, pg 855, Hiroshima, Springer Verlag (1993)
4. Weinstein, R.; Chen, I.G.; Liu, J.; Parks, D.; Selvamanickam, V.; and Salama, K.; Appl. Phys. Lett., 56, 1475 (1990)
5. Liu, J.; Chen, I.G.; Weinstein, R.; and Xu, J.; Jour. Appl. Phys., 73, 6530 (1993); Chen, I.G.; Liu, J.; Weinstein, R.; and Lau, K.; Jour. Appl. Phys., 72, 1013 (1992)
6. Gao, L.; Xue, Y.; Hor, P.; and Chu, C.W., Physica, C177, 438 (1991)
7. Weinstein, R.; et al, Invited Paper, Proc. International Workshop on Superconductivity, Kyoto, Japan (June 1994)
8. Weinstein, R.; Ren, Y.; Liu, J.; Sawh, R.; Parks, D.; Foster, C.; Obot, V.; Arndt, G.D.; and Crapo, A.; Proc. of Fourth World Congress on Superconductivity, Vol. I, pg. 158, Orlando (1994).

AN OVERVIEW ON AEROSPATIALE MAGNETIC BEARING PRODUCTS FOR SPACECRAFT ATTITUDE CONTROL AND FOR INDUSTRY

Alain SAMUEL
Bernard LECHABLE
AEROSPATIALE Espace et Défense - Les Mureaux - France

SUMMARY

For the last 25 years, AEROSPATIALE has worked on magnetic bearing technology and has been awarded contracts with many customers in order to develop equipment for flight and ground applications.

Two generations of magnetic bearing reaction wheels are already in flight, onboard observation satellites :

- first, on SPOT and ERS with 15 wheels in flight on 5 satellites,
- second, on HELIOS spacecraft with 3 wheels in flight.

Total cumulated flight time is now more than 65 years without any problem.

AEROSPATIALE Magnetic Bearings are based on the use of permanent magnets and on the control of the rotor around a zero force equilibrium point.

The present developments of magnetic bearing wheels for space applications focus on the versatility of a basic design which leads to a family of reaction and momentum wheels with tailored torque and kinetic momentum, leading to competitive mass and cost.

The present industrial applications concern kinetic energy accumulators, medical X-ray rotating devices, avionics equipment, cryotechnic compressors and vacuum pumps.

INTRODUCTION

AEROSPATIALE has been developing magnetic bearings for more than 25 years now. Our products were developed with the help of national and international organizations, who provided us with specifications, funding and technological support and allowed us to reach our present technical excellence and to offer top-performing products to our customers.

The present paper describes the chronology of Magnetic Bearing history at AEROSPATIALE, explains the inventive principle of the magnetic bearing and its applications in space as well as for industry, with a perspective on the new developments.

MAGNETIC BEARING HISTORY AT AEROSPATIALE

During the seventies, AEROSPATIALE worked on internal funding and with the help of some customers to develop all the technologies required for momentum wheels. They were designed for satellite applications such as :

- Energy storage wheels for COMSAT and INTELSAT. The program lasted until 1984 and allowed the realization of mockups and drawings of a 1.700 Nms energy storage wheel.

- Momentum and reaction wheels for CNES and ESA/ESTEC, with a 50 Nms and a 150 Nms model.

In 1978, AEROSPATIALE was awarded the contract for the development and the flight models of a 15 Nms reaction wheel dedicated to SPOT 1, first French optical observation satellite. This contract was renewed for SPOT 2 - SPOT 3 and for the two ERS European radar observation satellites which are each equipped with 3 reaction wheels.

Then, in 1985 the two axes wheel era began first with a 66 Nms momentum wheel mockup for ESA/ESTEC. Then, AEROSPATIALE was awarded the contract for the SPOT4 and HELIOS 1 programs, with 9 flight models of a 40 Nms and 0.45 Nm reaction wheel with an associated very low microvibration specification level. These same wheels will be used on ENVISAT (5), SPOT 5 (2 x 3), and probably on METOP(3 x 5).

Presently, a more powerful model is being developed for HELIOS 2 military observation satellite.

On the "industrial" side, the developments of different devices such as energy storage accumulators for telephone exchanges, test bench actuator for nuclear bar wear studies, X-ray tube bearings, tape recorder for satellite, artificial horizon gyroscope, ... etc.

Table 1. Magnetic Bearing Wheels History

MAGNETIC BEARING WHEELS HISTORY

1970	Beginning of R & D on Magnetic Bearings at AEROSPATIALE
1973	First patent on Magnetic Bearings
1973-1979	Development contracts on Magnetic Bearings Systems leading to the delivery of 15 equipments for customers such as CNES, COMSAT, ESTEC, INTELSAT
1980	Industrial development of Magnetic Bearing Wheels for observation satellites
February 1986	. First flight on SPOT 1 launched by ARIANE Flight n° 16 . Follow on series with SPOT 2, SPOT 3, ERS 1, ERS 2 . 15 Wheels launched and operating without any problem
1984 up to now	. New generation of Magnetic Bearings for ground and space applications : SPACE APPLICATIONS : Reaction wheels for SPOT 4 , HELIOS, PPF/ ENVISAT GROUND APPLICATIONS : Kinetic accumulators, Medical X-RAY devices . Avionic equipment, Vacuum compressors

Table 2. Flight Record

FLIGHT RECORD (11/95)

SPOT 1	**Launched 02/86**	**3 WHEELS**	**x 85700**	)	
SPOT 2	**Launched 01/90**	**3 WHEELS**	**x 51400**	)	
ERS 1	**Launched 07/91**	**3 WHEELS**	**x 38300**	)	**609600 h**
SPOT 3	**Launched 09/93**	**3 WHEELS**	**x 19300**	)	
ERS 2	**Launched 04/95**	**3 WHEELS**	**x 5400**	)	
HELIOS	**Launched 07/95**	**3 WHEELS**	**x 3100**	)	

CUMULATED FLIGHT WITHOUT FAILURE > 70 YEARS

Table 3. The Aerospatiale Magnetic Bearing

THE AEROSPATIALE MAGNETIC BEARING

· USE OF PERMANENT MAGNETS :

- PERMANENT FIELD OF FORCE
- EXISTENCE OF AN UNSTABLE EQUILIBRIUM
- ECONOMY OF ELECTRICAL ENERGY
- FULL TESTABILITY UNDER 1 g ENVIRONMENT

· USE OF COILS :

- MODIFY THE PERMAMENT FIELD
- ALLOW DYNAMIC CONTROL

· MAGNETIC CIRCUIT (IRON) :

- DETERMINE THE FLUX LINES

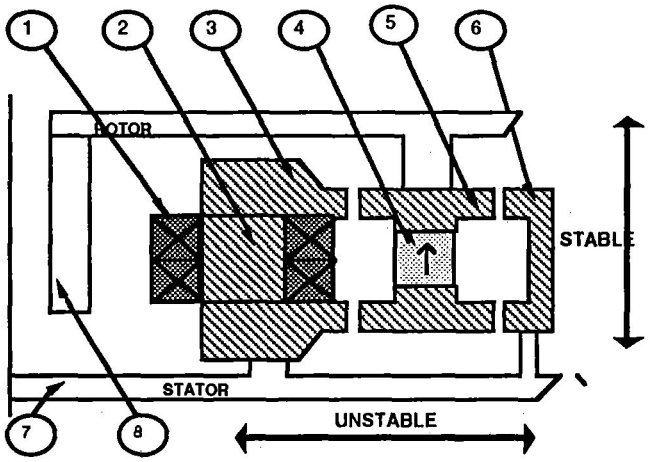

Magnetic bearing

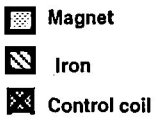

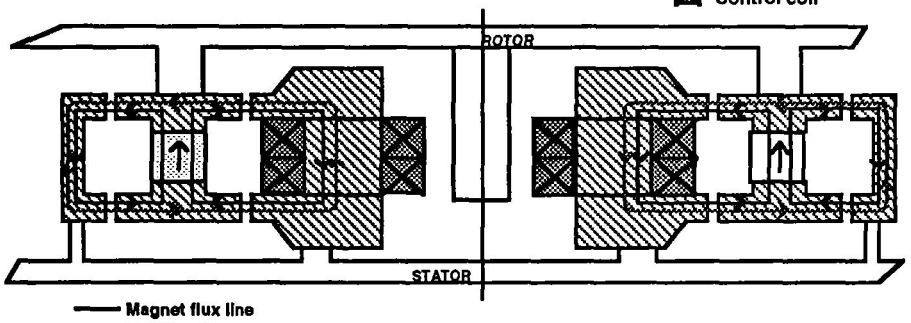

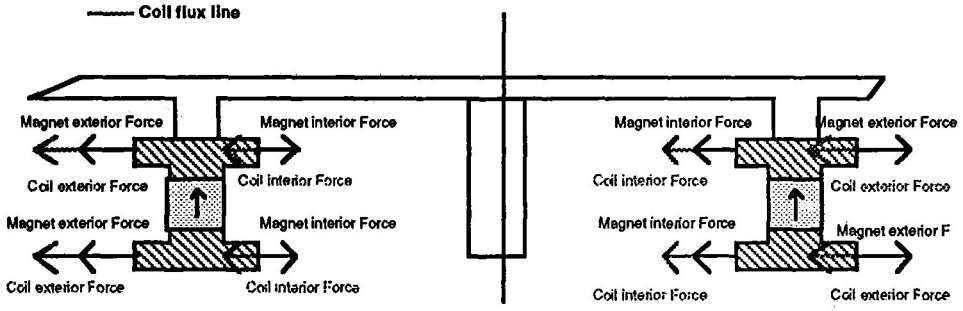

Coil and magnet flux lines and forces

WHEN CURRENTS CIRCULATE, RADIAL FORCES ARE INDUCED

AEROSPATIALE MAGNETIC BEARING

The AEROSPATIALE magnetic bearing principle is based on the use of permanent magnets which provide within the bearing :

- **a permanent field of force,**
- **an unstable equilibrium which is controlled by a servo loop.**

The reader will find a sketch on table 3. It shows the different parts of a typical bearing:

The magnet ④, is located on the rotating part ⑥, for this particular design. The magnet generates a magnetic field, which can be visualized through its flux lines. Those flux lines will follow a specific path from Northern pole to the Southern one of the magnet, which will be constrained through the iron parts.

The iron parts ②, ③, ⑤, ⑥ constitute the favorite way to curve a magnetic flux. Our skill is to design those parts in order to create the useful stiffness of the magnetic bearing. It is the shape of the iron teeth, on both parts of the air gaps, that give our bearings all their characteristics and qualities.

Together, permanent magnets and the iron circuit generate a field of forces and torques, which keeps the rotating parts within the teeth of the stator (the static rigidity on the stable axes) while creating an attraction (or a repulsion) towards both sides of the air gaps. This attraction sticks the rotating part to the stator!

The coil ① is used to restore stability within the bearing. Its electrically generated magnetic flux modulates the permanent flux of the magnet, so that the rotor will be positioned in the central part of the air gaps. Position sensors and an electronic control loop command the current in the coil to that effect.

As a consequence, this magnetic bearing needs a low electrical energy and is fully testable under 1g environment in any position.

Attraction forces within the air gaps are shown at the bottom of table 3. Without any external force and with a null coil current, those attraction forces are equal somewhere close to the middle of the air gaps, and they define a point of equilibrium.

This position is very unstable, and divergent forces increase when the rotor goes sidewards from this central equilibrium. The goal of the control loop is to transform this unstable equilibrium position into a stable one, so that the rotor levitates. The consequence of this design is the following :

as the rotor is stabilized on this equilibrium point, no significant force is exerted on it. Even with an additional force (the weight of the rotor by instance) the equilibrium point is only displaced. In consequence, no significant energy is required to keep the rotor in position, even in a 1g environment, as long as the air gap and the bearing stiffness are compatible with the external force. Due to this property, all our space wheels may be operated on ground, without any additional ground equipment.

THE PRESENT APPLICATIONS IN SPACE

Table 4. Aerospatiale Magnetic Bearing Wheels

AEROSPATIALE MAGNETIC BEARING WHEELS

CHARACTERISTICS	SPOT 1 reaction	SPOT 4 reaction	SPACEBUS momentum	*EVOLUTION reaction or momentum*
Kinetic Momentum Nms	15	40	65 ± 8	*40 to 90*
Torque Nm	0,2	0,45	0.1	*0.05 to 0.2*
Rotor Speed rpm	2 400	2 400	10 000	*5 000 to 10 000*
Constant speed power including motor power W	14 1	50 24	20 3	20 3
Max torque power including motor power W	115 64	232 140	155 118	155 118
Bearing power W	5	9	9	9
Mass kg (without WDE) (with WDE)	8,4 specific	17 specific	6.7 *9.9* (one channel)	*6 to 9* *9.2 to 12.2*
Onboard satellites (* when in flight)	3 x SPOT 1* 3 x SPOT 2* 3 x SPOT 3* 3 x ERS 1* 3 x ERS 2*	3 x HELIOS 1A* 3 x HELIOS 1B 3 x SPOT 4 6 x ENVISAT 6 x SPOT 5	SPACEBUS 3000 STENTOR	

The SPOT 1 Type Magnetic Bearing Wheel

Its magnetic bearing is a one active axis type with its unstable axis along the rotation axis of the wheel. The passive magnetic circuit of the bearing creates the stiffness on the passive axes (which are the radial and tilting axes) and a negative stiffness along the axis of the rotor. An inductive axial speed detector, an electronic control loop and an axial electromagnet allow the axial positioning of the wheel. An electronic logic lifts off the rotor, when power is turned on, with the help of a special transient supply. When power is turned off, the rotor comes towards a dry lubricated ball bearing. This bearing allows more than 100 emergency turns off, while the rotor runs at full speed.

A brushless torque motor creates the required reaction torque, which causes the rotation of the rotor (the kinetic momentum). Electronic circuits, incorporated into the ERPM, allow the commutation of the motor current for the 4 phases, depending on tachometer signals delivered on the stator and on a direction signal.

An axial locking device prevents the degradation of the wheel during transportation and launching. It may be screwed and unscrewed for storage and testing on ground, and a pyrotechnic cutter unlocks the rotor in space.

The design is dual redundant, to allow the functioning after any first failure. However, the magnetic bearing may not fail, so there is only one rotor. The electronic and electrotechnical parts are all dual redundant, except for the motor coils, which are specially protected. The mechanical and pyrotechnical parts of the locking device are unique, with a dual command, and a reliable design.

The SPOT 4 Type Magnetic Bearing Wheel

The magnetic bearing is here a two active axes type, with two radial unstable axes. This disposition allows a better radial control of the wheel, and hence, has been chosen to help reduce the wheel generated microvibrations. Two inductive radial position detectors, control loops and electromagnets allow the radial positioning of the wheel.

All its other devices (lift off logic, emergency ball bearings, torque motor, locking device and redundancy design) are comparable with those described above for the SPOT 1 wheel.

SPACEBUS Momentum Wheel

This wheel follows the main basic designs of the SPOT 4 wheel, with a two active axes type bearing and a brushless torque motor. Except for the dimensions and characteristic figures, the main technological differences lie in the 3 phased torque motor, the absence of any redundancy and a newly designed locking device (an inflatable vessel with an electrical valve).

Its basic characteristics are shown on table 4, and correspond to the needs of geostationary telecommunication satellites. But this wheel is being designed to easily fulfill all the characteristics of the "evolution" column of table 4. In fact, the evolutive elements are shown in table 5 as the rotor rim size (to adjust the required kinetic momentum with the allowed rotation speed) and the torque motor magnets height (to adjust the required torque with the max allowed current).

Table 5. SPACEBUS Momentum Wheel Adaptable Elements

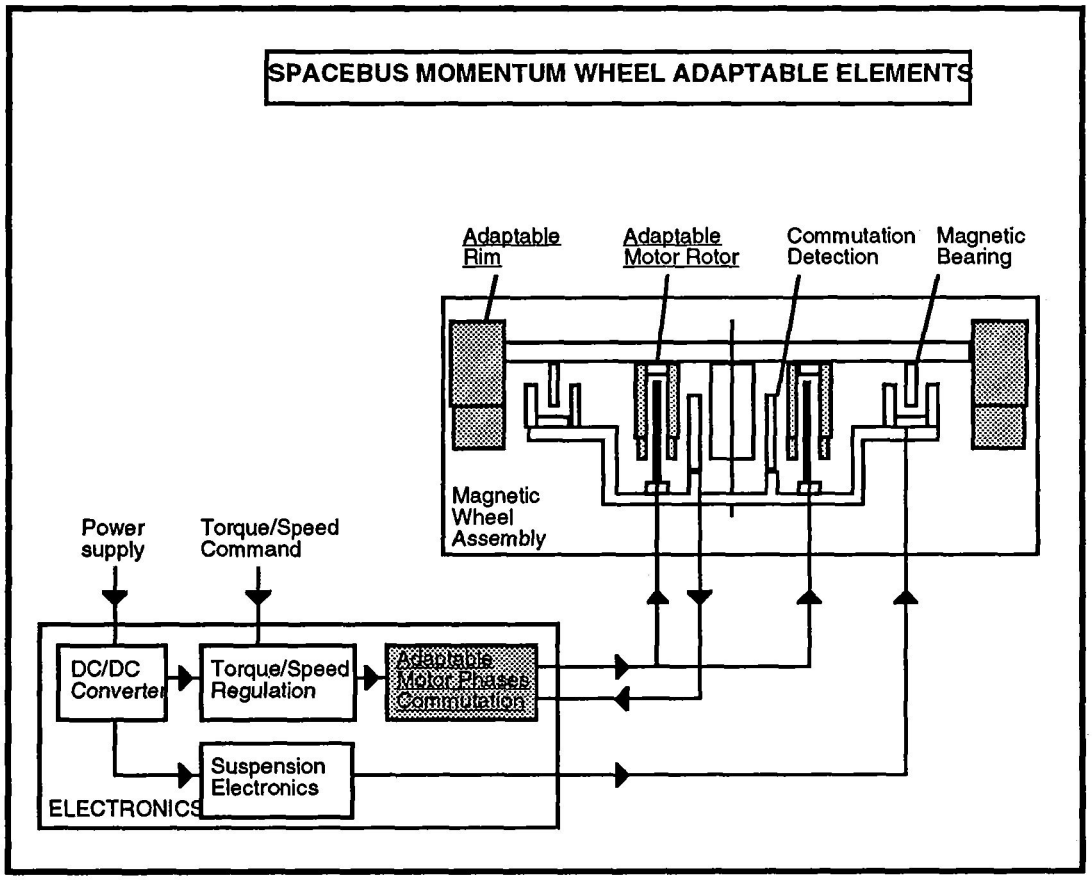

Table 6. Magnetic Bearings for Rotating Machines

MAGNETIC BEARINGS FOR ROTATING MACHINES

APPLICATIONS		STIFFNESS X	STIFFNESS Y	STIFFNESS Z	CURRENT ROTATIONAL SPEED	ROTOR MASS
Gyroscope Mini Pump Reaction Engine Simulator	MB 11-02 MB 11-03 MB 11-03	200 N/mm	200 N/mm	700 N/mm	24000 Tr/mm 90000 Tr/mm	0.35 kg
X-Raytube Chopper	MB 24-01 MB 24-02	200 N/mm	200 N/mm	40 N/mm	36000 Tr/mm	1.5 kg
Compressor Vibration Simulator for Nuclear Application	MB 24-04 MB 12-01	200 N/mm	200 N/mm	150 N/mm	36000 Tr/mm	1.5 kg
Turbomolecular Pump	MB 25-03	2000 N/mm	2000 N/mm	400 N/mm	42000 Tr/mm	2.5 kg
Wheel Energy Storage	MB 11-01	100 N/mm N/mm	100 N/mm	10000	12000 Tr/mm	360 kg

X, Y, Z passive or active axes - W current rotation speed

Table 7. Aerospatiale Magnetic Bearing Wheels

AEROSPATIALE MAGNETIC BEARING WHEELS

GENERATION		1985	1986	1987	1988	1989	1990	1991	1992	1993	1994	1995	1996	1997	1998	1999	2000	2001	2002
SPOT 1	SPOT 1 - 2 - 3	⌂⌂⌂	⌂⌂⌂ ■			⌂⌂⌂ ■				■									
	ERS 1 - 2						⌂⌂⌂	■		⌂⌂⌂		■							
SPOT 4	SPOT 4- HELIOS 1					—	—	—	—	—	⌂⌂⌂	⌂⌂⌂ ⌂⌂⌂ ■		●	●				
	ENVISAT												⌂⌂⌂ ⌂⌂⌂			●			
	SPOT 5*														⌂⌂⌂	⌂⌂⌂	●		
	METOP *															⌂⌂⌂	⌂⌂⌂ ⌂⌂⌂	⌂⌂⌂ ⌂⌂⌂	⌂⌂⌂
HELIOS 2	HELIOS 2											—⌂	—⌂	⌂⌂⌂	⌂⌂⌂	⌂⌂⌂	●		
SPACEBUS MOMENTUM WHEEL	SPACEBUS*											—	—⌂	—⌂	⌂	⌂⌂⌂ ⌂⌂⌂	⌂⌂⌂ ⌂⌂⌂	⌂⌂⌂ ⌂⌂⌂	⌂⌂⌂ ⌂⌂⌂

*Expected order
⌂ Flight items
■ Date of launch
⌂ Test Model
● Expected date of launch

CONCLUSION

This rapid survey of AEROSPATIALE products shows how efficient magnetic bearings are for different applications. They may be used either for increased reliability and reduced microvibration on satellites or for particular industrial uses with competitive characteristics.

Our industrial teams now are well trained either to manufacture existing products or to study and define new ones to fit specific needs.

Session 7 -- Superconductivity 2

Chairman: Hans Schneider-Muntau
National High Magnetic Field Laboratory (NHMFL)

ULTRALOW FRICTION IN A SUPERCONDUCTING MAGNETIC BEARING

Hans J. Bornemann, Michael Siegel, and Oleg Zaitsev
Forschungszentrum Karlsruhe GmbH, INFP, P.O. Box 3640
76021 Karlsruhe, Germany

Martin Bareiss and Helmut Laschütza
AEG Aktiengesellschaft, Bereich Infrarotmodule, Theresienstr. 2
74072 Heilbronn, Germany

SUMMARY

Passive levitation by superconducting magnetic bearings can be utilized in flywheels for energy storage. Basic design criteria of such a bearing are high levitation force, sufficient vertical and horizontal stability and low friction. A test facility was built for the measurement and evaluation of friction in a superconducting magnetic bearing as a function of operating temperature and pressure in the vacuum vessel. The bearing consists of a commercial disk shaped magnet levitated above single grain, melt-textured YBCO high-temperature superconductor material. The superconductor was conduction cooled by an integrated AEG tactical cryocooler. The temperature could be varied from 50 K to 80 K. The pressure in the vacuum chamber was varied from 1 bar to 10^{-5} mbar. At the lowest pressure setting, the drag torque shows a linear frequency dependence over the entire range investigated ($0 < f < 40$ Hz). Magnetic friction, the frequency independent contribution, is very low. The frequency dependent drag torque is generated by molecular friction from molecule-surface collisions and by eddy currents. Given the specific geometry of the set-up and gas pressure, the molecular drag torque can be estimated. At a speed of 40 Hz, the coefficient of friction (drag-to-lift ratio) was measured to be $\mu = 1.6 \times 10^{-7}$ at 10^{-5} mbar and T = 60 K. This is equivalent to a drag torque of 7.6×10^{-10} Nm. Magnetic friction causes ~1% of the total losses. Molecular friction accounts for about 13% of the frequency dependent drag torque, the remaining 87% being due to eddy currents and losses from rotor unbalance. The specific energy loss is only 0.3% per hour.

INTRODUCTION

A cooled superconductor can transport electrical currents without any losses. The new high temperature superconductor (HTSC) $YBa_2Cu_3O_7$ (YBCO), prepared by melt-texturation, has another extraordinary ability: It exhibits strong flux pinning and can trap magnetic fields. Due to this effect, a magnetic cushion is generated between a permanent magnet and the superconductor. This cushion provides stable levitation with vertical and horizontal restoring forces and almost frictionless rotation of the magnet. In contrast to conventional (low-temperature) superconductors, high-temperature superconductors require cooling by liquid nitrogen only (T = 77 K). They are more cost-effective and closer to practical applications. Active magnetic bearings have proven to be practical for rotating machinery. In contrast to those active systems which require elaborate control circuits to be operational, superconducting bearings are completely passive. Possible applications in the electric utility field are power systems, such as efficient high-speed flywheels for energy storage. Desirable properties of a bearing for a flywheel are high levitation forces, sufficient vertical and horizontal stiffness and low intrinsic drag.

The force F acting on a magnetic dipole m in an effective field H^{eff} is given by:

$$\vec{F} = -\mu_0 \nabla(\vec{m}\vec{H}^{eff}) \tag{1}$$

where μ_0 is a constant. Assuming the magnetic moment m is constant, the force in vertical direction, the levitation force F_z is:

$$F_z = -\mu_0 \left(\sum_{i=x,y,z} m_i \frac{\partial H_i^{eff}}{\partial z} \right) \tag{2}$$

here m is the magnetic moment of the superconductor, x, y, z represent the three geometric axes. According to (2), the levitation force F_z depends upon both m_i and H^{eff}. In the approximation of Bean's model [1], for a given effective magnetic field H^{eff}, the magnetic moment m_i of the superconductor in the critical state is proportional to the critical current density J_c and to the size of the shielding current loop d:

$$m \propto J_c \cdot d \tag{3}$$

Thus, high levitation forces and stiffness require a high effective magnetic field H^{eff} with high first and second order spatial derivatives and a superconductor with a large magnetic moment (i.e. high critical currents flowing over a considerable area). For melt-textured YBCO, macroscopic J_c values are typically around several 1000 A/cm^2 and d is several cm. H^{eff} should be at least several KOe. Preferably, permanent magnets based on Sm-Co or Nd-Fe-B compounds are used in the bearings.

Hysteresis loss in the superconductor is one of the main contributions to intrinsic bearing drag [2-4]. It is attributed to inhomogeneities in rotational symmetry of the permanent magnet. According to Beans' law [1], the energy loss due to magnetic drag for a superconductor in the critical state is given by:

$$E_{mag} \propto \frac{(\Delta H^{eff})^3}{J_c} \tag{4}$$

where ΔH^{eff} is the magnetic field inhomogeneity.

In order to establish an optimized bearing design, several studies have evaluated model bearing configurations. Bulk YBCO pellets were combined with permanent magnets of different size and geometry and in various configurations [5-7]. These experiments concentrated on studying static and dynamic interaction forces. The motivation for the work we report in this paper was to see to what extent friction can be reduced in a superconducting magnetic bearing. Minimum bearing friction is of particular importance in a flywheel system for diurnal load leveling. The goal for such a system is a net loss due to friction of 0.1% per hour (2.4% per day) [8]. Of course, in a flywheel system, other sources of friction exist such as eddy current drag and aerodynamic drag. Both depend upon frequency and can be quite high at high speeds. Nevertheless, the minimization of magnetic bearing drag is important. Not only does E_{mag} contribute to the overall friction in the system, but because it occurs in the superconductor, it presents an additional load for the cooling system.

According to eqn (4), magnetic drag can be reduced by using a homogeneous permanent magnet combined with a bulk superconductor with high J_c. Since J_c is known to increase with decreasing temperature, operation of the bearing at reduced temperatures is expected to further decrease E_{mag}.

EXPERIMENTS

Experimental Set-Up

Experiments were conducted in a vacuum chamber evacuated by a turbo molecular pump. The chamber is 9 cm in diameter and 7 cm high. Pressure could be set between 10^{-6} mbar and 1 bar. A bulk HTSC sample was placed on a cold plate and mounted on top of a cold finger. Cooling was provided by a AEG tactical cryocooler [9]. The hot end of the cold finger, outside the vacuum chamber, was air cooled using a small ventilator. Temperature sensors were located near the cold plate at the bottom of the sample holder and near the top of the sample. The lowest temperature reached was 40 K. We found this to be strongly dependent upon a series of experimental conditions, such as quality of the vacuum and ambient temperature in the lab (the efficiency of the stirling cryocooler depends upon the temperature at the warm end of the cold finger). During cool down, the permanent magnet was fixed in position by a movable holding and positioning device. When the HTSC element had reached the desired temperature, the device was retracted and the magnet was released (field cooled procedure). Spin-ups were accomplished with a valve controlled gas nozzle placed near the magnet using dry nitrogen gas. After the spin-up the position of the nozzle was lowered to avoid any interference with any possible gas streams that might leak through the valve. Rotational speeds were measured through a quartz window on top of the vacuum chamber using a LED sensor unit. During spin-down, speed, temperature and pressure were continuously monitored by a computerized data acquisition system.

A cool down experiment with a 80 g bulk HTSC sample is shown in Fig. 1. The sample cold plate alone gets cold in about 20 min. For better insulation and reduction of thermal losses, the superconductor had been wrapped in superinsulation foil. Still, a difference of about 2 K was measured between upper and lower sensor. We ascribe this difference which was observed for all experiments to losses by thermal radiation from the walls of the vacuum chamber.

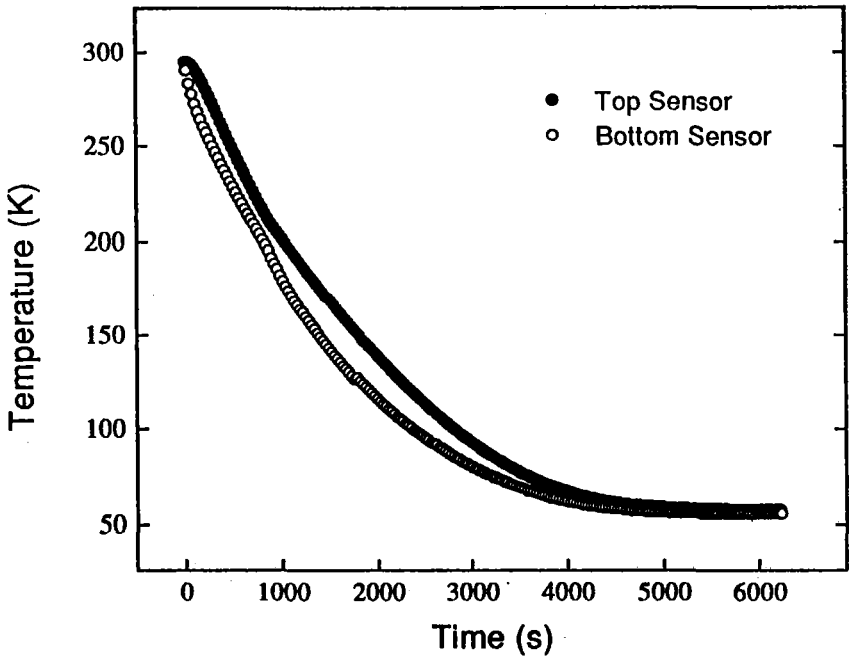

Fig.1: Cool down experiment for a 80 g bulk HTSC element. The difference in temperature between top and bottom temperature sensor is due to losses by thermal radiation from the walls of the vacuum chamber.

Spin-Down Experiments

A series of spin-down test was conducted with a homogeneous, disk shaped permanent magnet, measuring ø 25 mm x 9 mm high. The HTSC element was made of single grain, top seeded, melt-textured YBCO. Its dimensions were ø 32 mm x 17 mm high. With the magnet in place, the superconductor was cooled. Then the magnet was released and accelerated to a given speed up to 40 Hz. In Fig. 2 (a), a spin-down run from 35 Hz is shown for a pressure of 1 bar. Bearing gap, the distance between the upper surface of the HTSC element and the bottom of the magnet disk, was 6 mm, the surface temperature of the HTSC element was 60 K (top temperature sensor). Apparently, friction is very high. In only 45 min the freely rotating magnet disk was decelerated from 35 Hz to 0. The result of a similar experiment but in a vacuum of 10^{-5} mbar is presented in Fig. 2 (b). At this low pressure, friction is so low that a complete spin-down from 35 Hz was not practical. Instead, we started the experiment at the low frequency end. The magnet was accelerated and spin-down was recorded over a time period of about an hour. Then the magnet was accelerated again to the next higher frequency and so on. The insert shows

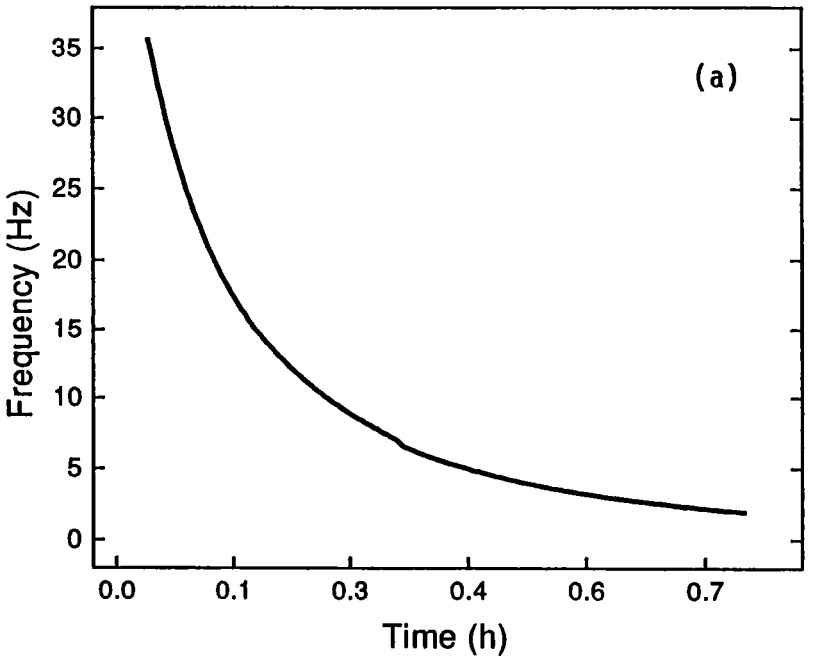

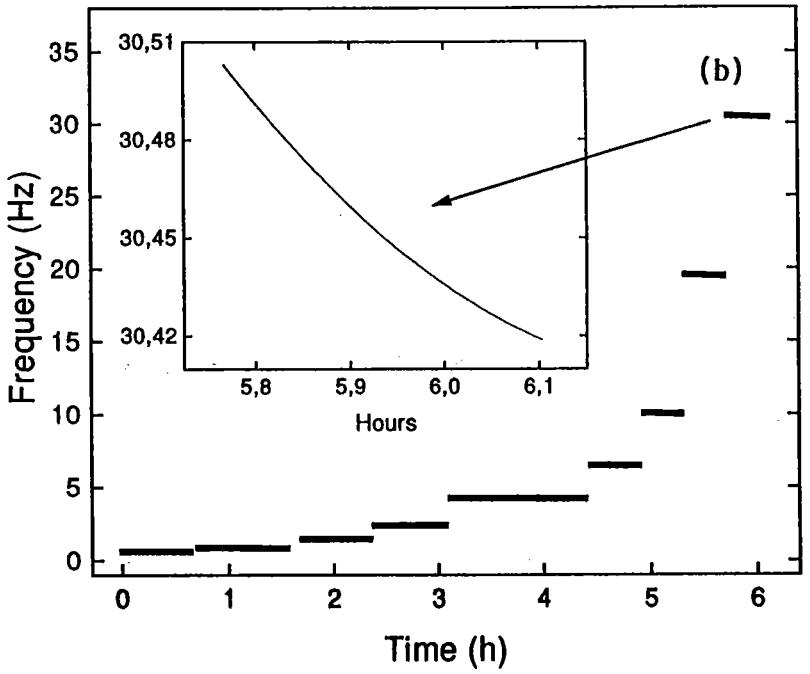

Fig. 2: Spin-down experiments at 60 K, bearing gap was 6 mm. (a) Pressure was 1 bar, (b) pressure was 10^{-5} mbar. The insert shows the spin-down from ~30 Hz on an expanded scale.

the spin-down recorded from ~30 Hz. It takes about 20 min for the frequency to drop by 0.09 Hz. The non-linearity of the curve indicates that there are frequency dependent contributions to the overall drag, such as molecular drag and eddy current drag.

Drag torque and coefficient of friction μ (drag-to-lift ratio, defined in [10]) vs frequency in the range from 0 to 40 Hz are shown in Fig. 3. Pressure in the vacuum chamber was 2 x 10^{-5} mbar, the temperature of the HTSC element was 60 K. Gap width was 7 mm. The drag torque shows a linear frequency dependence over the entire range indicating frequency dependent and frequency independent contributions to the total drag. The frequency independent contribution is due to magnetic hysteresis losses in the superconductor. From a least-squares fit to the data the magnetic drag torque Γ_{mag} was deduced. We find Γ_{mag} = 7.3 x 10^{-12} Nm. The frequency dependent contribution increases with increasing frequency. Eddy current losses, molecular drag and drag due to rotor unbalance are the main sources of frequency dependent drag [11]. At f = 40 Hz, the total frequency dependent drag torque was measured to be 7.6 x 10^{-10} Nm. Using the analytical expression derived by Chambers et al. [12] the molecular drag torque expected for our set-up can be calculated. We find Γ_{mol} = 1 x 10^{-10} Nm which is only 13 % of the frequency dependent contribution. Apparently, rotor unbalance and eddy currents give a significant contribution to the frequency dependent losses.

Nevertheless, friction is very low. At f = 40 Hz, the specific energy loss given by

$$\Delta E_{loss} = \frac{df}{dt \cdot f} \cdot 3600 \frac{s}{hour} \cdot 100\% \text{ (in \% per hour)} \qquad (5)$$

is only 0.3 % per hour.

The temperature dependence of the magnetic friction was deduced from measurements at frequencies below 1 Hz. With decreasing temperature, the energy loss E_{mag} due to magnetic drag is expected to decrease according to eqn (4), because J_C increases. Comparing the results at 60 K as shown in Fig. 3 (b) to a run made under identical conditions at 78 K, we find that E_{mag} is about 40% lower at 60 K. This is somewhat less than expected since intragrain J_C values typically increase by about a factor of 2, going from 77 K to 60 K, which should have resulted in a reduction of about 50% for E_{mag} according to eqn (4).

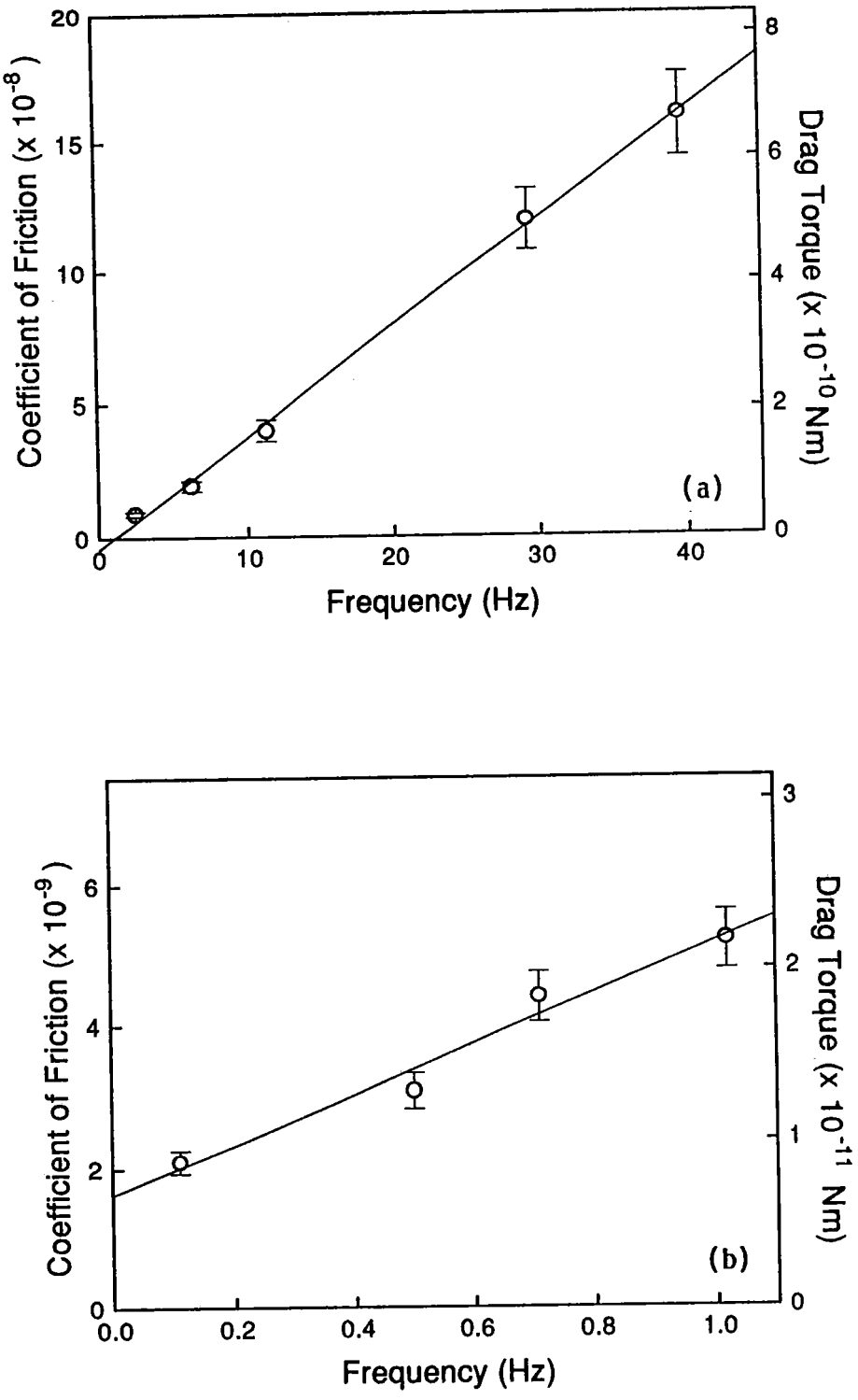

Fig. 3: Coefficient of friction μ and total drag torque vs frequency at T = 60 K. Pressure was 2 x 10^{-5} mbar. Gap width was ~7 mm. The solid curve is a linear least-squares fit to the data.

CONCLUSION

In conclusion, we have conducted a series of spin-down experiments with a superconducting magnetic bearing. Friction was studied as a function of operating temperature and pressure in the vacuum chamber. At atmospheric pressure, the drag torque due to gas friction is very high. At the lowest pressure setting (10^{-5} mbar), the drag torque shows a linear frequency dependence. For our set-up, using a homogeneous permanent magnet disk and a single grain HTSC element, magnetic friction was found to be insignificant compared to the other loss mechanisms. The experiments indicate that a further reduction of energy loss is accomplished by reducing eddy current and molecular drag.

ACKNOWLEDGMENTS

The HTSC element was prepared by Th. Burghardt. The authors would like to thank K. Weber for technical assistance. Financial support by the Deutsche Akademische Auslandsdienst (DAAD) under Contract No.13N5751 for one of us (OZ) is gratefully acknowledged.

REFERENCES

1. C. P. Bean, *Phys. Rev. Lett. 8*, 1962, pp. 250-253.
2. V.V. Nemoshalenko, E. H. Brandt, A. A. Kordyuk, and B. G. Nikitin, *Physica C 170,* 1990, 481-485.
3. H. J. Bornemann, T. Ritter, C. Urban, O. Zaitsev, K. Weber, and H. Rietschel, *Appl. Supercond. 2,* 1994, 439-447
4. J. R. Hull, T. M. Mulcahy, K. L. Uherka, R. A. Erck, and R. G. Abboud, *Appl. Supercond. 2,* 1994, 49-445.
5. M. Komori and T. Kitamura, *J. Appl. Phys. 69,* 1991, 7306.
6. P. Boegler, C. Urban, H. Rietschel, and H. J. Bornemann, *Appl. Supercond. 2,* 1994, 315-325
7. P. Tixador, P.Hiebel, E. Hotier, and X. Chaud, *Cryogenics* (in press)
8. R. F. Giese, Report for the International Energy Agency, Argonne National Laboratories, 1994.
9. AEG Split-Cycle Stirling Cooler Model SC 100
10. B. R. Weinberger and L. Lynds, *Appl. Phys. Lett. 59,* 1991, 1132-1134

11. H. J. Bornemann, A. Tonoli, T. Ritter, C. Urban, O. Zaitsev, K. Weber, and H. Rietschel, *IEEE Trans. on Appl. Supercond. 5,* 1995, 618-621.
12. A. Chambers, A. D. Chew and A. P. Troup, *Vacuum 43,* 1992, 9-13

ROTORDYNAMIC CHARACTERIZATION OF A HYBRID SUPERCONDUCTOR MAGNET BEARING

Ki B. Ma, Zule H. Xia, Rodger Cooley, Clay Fowler and Wei-Kan Chu
Texas Center for Superconductivity, University of Houston, Houston, TX 77204-5932, USA

ABSTRACT

A hybrid superconductor magnet bearing uses magnetic forces between permanent magnets to provide lift and the flux pinning force between permanent magnets and superconductors to stabilize against instabilities intrinsic to the magnetic force between magnets. We have constructed a prototype kinetic energy storage system, using a hybrid superconductor magnet bearing to support a 42 lb. flywheel at the center. With five sensors on the periphery of the flywheel, we have monitored the position and attitude of the flywheel during its spin down. The results indicate low values of stiffnesses for the bearing. The implications of this and other consequences will be discussed.

INTRODUCTION

A rotary bearing is a device designed to provide an interface between a rotating shaft (rotor) and a stationary structure (stator) that allows the transmission of normal thrust but not shear forces. With commonly encountered bearings such as ball bearings, this interface is made up of metallic spheres that roll on well lubricated tracks. Thrust forces are transmitted from the stator to the rotor via contact forces between the metallic spheres and the track, but dissipative shear forces, present as friction wherever there is relative motion between two solid bodies in physical contact, are still not entirely eliminated despite lubrication. This direct contact between the surface of a rotating solid object and the surface of a stationary object can be replaced by an indirect contact mediated by a fluid in motion. Hydrodynamical forces due to the fluid motion are responsible for the transmission of normal thrust support from the stator to the rotor, while creating a small gap that keeps them slightly apart at the same time. Dissipative shear forces across the fluid interface now appear in the form of viscous forces inherent in the motion of the fluid, but is generally much reduced in magnitude from frictional forces encountered with direct contact. Fluid film bearings, air bearings and fluid lubricants for roller bearings, all operate by the same phenomena.

Contact between the rotor and the stator is further reduced in magnetic bearings. When operating in vacuum, aerodynamic drag forces can be reduced to a minimum depending on the lowest pressure that can be attained. Normal thrust force is exerted via magnetic flux linkages between the rotor and the stator. These same magnetic flux linkages are also another potential source of dissipative shear forces, if their penetration through any surrounding metallic parts is

not engineered to be axisymmetric about the axis of rotation of the rotor. However, the most serious difficulty lies in the harmonic nature of the forces between magnets for time independent situations. Embodied in Earnshaw's theorem[1] as a special case, it implies that a stable equilibrium configuration cannot be with magnetostatic forces alone. Thus, alternating currents through coils are employed in passive magnetic suspension systems and active control circuitry is often found in the magnetic bearings of today. In these devices, the very means of maintaining stability requires some expenditure of energy.

With the advent of high temperature superconductivity, a new avenue to circumvent the inherent instability with magnetic systems becomes more readily accessible. The interaction between magnets and superconductors gives rise to two distinct effects which can be exploited for stable magnetic levitation. One is the Meissner effect; the other, the flux pinning effect. In the Meissner effect, the superconductor behaves as a perfect diamagnet and excludes magnetic fields completely from within its volume. As a result, a repulsive force develops between a superconductor and a magnet. The Meissner effect is dominant at lower magnetic fields (below the first critical field, $H_{c1}(T)$), and hence yields lower forces in general. Under higher magnetic fields, the superconductor allows partial or complete penetration of the external applied magnetic field into its interior. However, the rate of penetration of the field can be characterized as slow under most circumstances, and the behavior can be qualitatively described with the model of an almost perfect conductor. One consequence of this is that the superconductor develops a mechanical force opposing any motion that tends to change the magnetic field in its interior.[2] Thus, the force that develops between the superconductor and a magnet can be attractive or repulsive, depending on their relative position and orientation, and how they were brought into their present state.

To illustrate these properties, let us consider a magnet being brought to the vicinity of a cold (ie. below T_c, the temperature at which the superconductor changes from normal state to superconducting state) superconductor (melt-textured $YBa_2Cu_3O_7$) from a point far away. A continuously increasing repulsive force develops all the way. This could be interpreted as a consequence of the Meissner effect, and it is true at moderate distances, when the magnetic field at the superconductor due to the magnet is still lower than the first critical field. At smaller distances, however, the situation would have to be understood in terms of the flux pinning effect, which is only partially excluding the intensifying magnetic flux from the approaching magnet. This contention is supported by the following two observations: first, if we stop advancing the magnet towards the superconductor, the repulsive force gradually diminishes, signalling a reduction in the magnetic stress as the magnetic field continues to penetrate into the superconductor even though the magnet has stopped coming closer; and second, if we reverse the motion of the magnet, the repulsive force drops to values less than that recorded on the advance, and may reverse in direction to become an attractive force under certain circumstances.[3] Thus, the force between a superconductor and a magnet is not only dependent on its relative position and orientation, but also on the history of their relationship. As we shall see next, the attractive force is a signature of the flux pinning force as the Meissner effect can only give rise to repulsive forces.

The superconductor in the experiment described above was prepared in a zero field cooled condition, since it was already cold before the magnet started approaching. To contrast and

compare, we can cool the superconductor after the magnet has been brought to the vicinity of the superconductor. This is called the field cooled condition. No appreciable force develops between the magnet and the superconductor, indicating that the magnetic field that was present in the superconductor is not expelled to any considerable extent as the superconductor is cooled down through the transition temperature. Now, if we push the magnet closer towards the superconductor, a repulsive force develops; but if we pull the magnet away from the superconductor, an attractive force ensues. The same happens if we displace the magnet in the lateral directions.[4] This is in full accordance with the expectations of the flux pinning effect in which the superconductor resists any attempts to change the magnetic flux that was present at the moment when it last became superconducting. Here, we may note that although the force developed under field cooled conditions is much less than that developed under zero field cooled conditions, the magnetic stiffnesses developed are comparable.

Ever since the discovery of high temperature superconductors, there have been many schemes to harness the levitation force of superconductors on magnets for the fabrication of nearly frictionless bearings. These operate on the same principle as the magnetic bearings, with the superconductor replacing one of the magnets, usually that in the stator. Normal thrusts are now carried by a combination of flux pinning forces and diamagnetic repulsive forces from the Meissner effect.[5,6] More importantly, there will be no resistance against rotation if the magnet has been carefully crafted to be axisymmetric about the axis of rotation on the rotor, for this motion produces no changes in the magnetic field anywhere.[3]

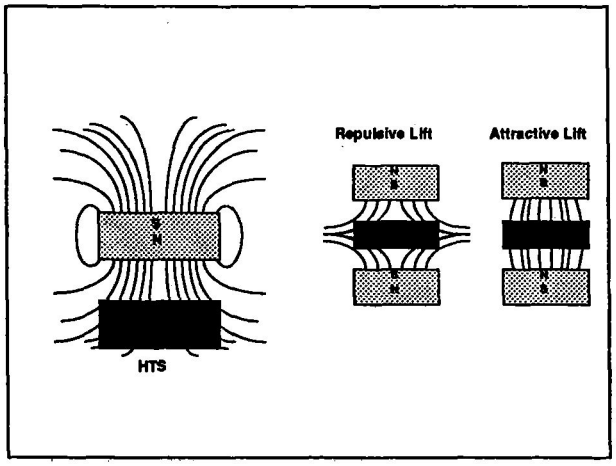

Fig. 1 On the left is an illustration of a superconductor magnet bearing. On the right are two versions of the hybrid concept. In the repulsive lift version, only the top magnet is freely levitated. In the attractive lift version, only the bottom magnet is freely suspended. All other components are presumed fixed.

At this point, we have to decide how we intend to put the magnet and the superconductor together to form the bearing. Field cooling is more natural and convenient, but it yields practically no thrust. However, even with zero field cooling, the levitation pressure that we can get is rather limited, to somewhere around 10 to 20 psi, and both short term stability and long term reliability are potential problems. On the contrary, levitation achieved with field cooled conditions appears to be more robust. So we decided to patch up the only shortcoming with the field cooled state by using additional magnets in the stator to provide the thrust needed.[7,8] With this hybrid approach, we gained the further advantage of the capability to achieve higher levitation pressure with less material. We do pay a price for this, as we have compromised the stability of the magnet superconductor configuration with the instability inherent in the magnetic force between the rotor magnet and the newly introduced stator magnet. As we shall soon see, we can lower this price to a small, acceptable level. This hybrid concept is illustrated in fig. 1.

We can arrive at this hybrid concept from the starting point with magnetic bearings also. Magnetic forces utilized in magnetic bearings can deliver sizable thrusts. The only thing that spoils this is their inherent instability which has to be overcome by means of active control. The hybrid approach simply replaces the active control circuitry with the passive differentially diamagnetic response of the high temperature superconductivity. Thus, we have combined the best of both worlds: the high thrust from the magnetic forces between magnets and the stability from the flux pinning forces between a magnet and a superconductor, all in a passive context in the sense of an absence of direct consumption of energy[4]. The one question that remains is whether the stability endowed by the magnet and superconductor combination is sufficient to overcome the instability of the magnet to magnet pair.

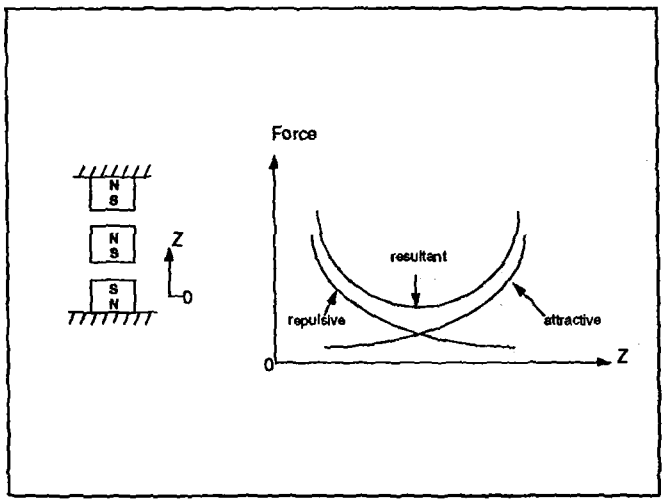

Fig. 2 Illustrating an example of a zero stiffness scenario. If the weight of the magnet exactly matches the value of the minimum resultant force at the midpoint, the magnet could be suspended in neutral equilibrium at that point.

In this tug of war between the instability of the magnet to magnet forces versus the stability coming from the flux pinning forces between the magnet and the superconductor, we can tip the balance towards stability either by increasing the flux pinning forces or decreasing the instability of the magnetic forces. The flux pinning forces are manifested in the critical current densities that the superconductors can carry, and limitations are set by intrinsic materials properties and processing techniques. On the other hand, although magnetic forces are inherently unstable, there is no lower bound to the magnitude of the instability. In other words, we can reduce the instability to a value as small as we please, in principle. We call this the zero stiffness concept, which is further illustrated in fig. 2.[9] What we have shown in this work is that in practice, we can reduce the instability in a magnet system capable of supporting a significant load down to a level that can be stabilized with a limited amount of superconducting material.

DESCRIPTION OF PROTOTYPE KINETIC ENERGY STORAGE SYSTEM

To demonstrate the practical utility of the hybrid magnet superconductor bearing, we have built a prototype kinetic energy storage system incorporating such bearings.[8] Being an energy storage system, it only makes sense to keep all source of energy loss down to a minimum. An extremely low loss is one of the potential benefits of the hybrid bearing. At the same time, the capacity for energy storage is also dependent on the mass involved, and the weight of this mass goes directly into the load on the bearing. Thus, for a device with useful energy storage capacity, the load on the bearing will also be substantial. This is where the high load carrying capability of the hybrid bearing becomes crucial.

The main component in a kinetic energy storage system that carries out the function of storing energy is the flywheel. In our prototype, the flywheel is composed of an aluminum disk, 12 in. in diameter, 1 in. thick, with two curvilinearly tapered stainless steel caps attached, one to each of both flat surfaces of the disk, making a total height from top to bottom of 7 in. The total weight of the flywheel comes out to 42 lbs. This load is shared almost equally between the top and bottom sets of magnets. The top set of magnets consists of a hollow cylinder magnet embedded in the top stainless steel cap on the rotor that is attracted to a similar hollow cylinder magnet contained in the stator. A piece of high temperature superconductor in the shape of an annular disk is inserted into the gap between these magnets for stabilization. The bottom set of magnets also consists of a hollow cylinder magnet embedded in the bottom stainless steel cap on the rotor, but is repelled by a solid cylinder magnet contained in the stator. While a piece of high temperature superconductor is inserted into the gap between magnets, an additional magnet attached to the case containing the superconductor occupies the volume of the hollow of the rotor magnet, to enhance the stabilizing prowess of the superconductor by decreasing the instability of the repelling magnets. This additional magnet also contributes to about one-sixth of the entire load on both bearings. Stability is further insured with a 4 in. ring magnet attached to the bottom of the flywheel, situated above a set of 12 superconductor pucks arranged in a ring and attached to the stator. Fig. 3 is a schematic representation of the magnet and superconductor placements.

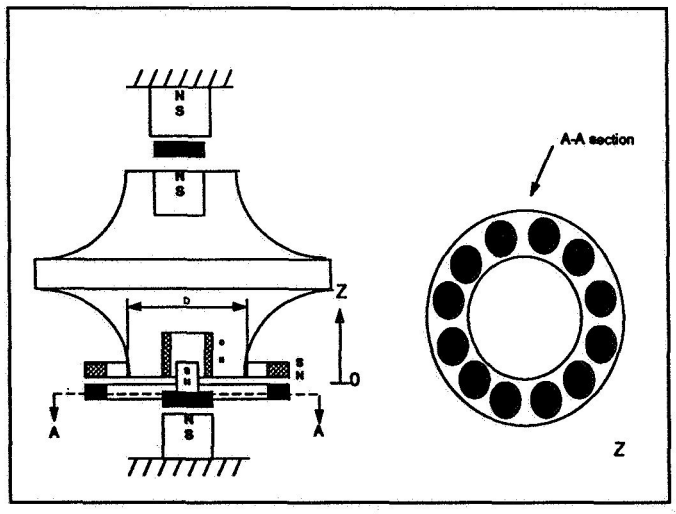

Fig. 3 Schematic representation of magnet and superconductor placements.

The above is the description of the barebone essentials of the storage system. To make it useful, it has to be efficiently interfaced with the outside world. Chief amongst the required accessories is a motor/generator with which to interconvert electrical and mechanical energies as energy is stored into or taken out from the system. A retractable non-contact magnetic clutch working with eddy currents is used as the link to transmit mechanical energy to and fro between the motor/generator and the rotating flywheel. Two chamfers, one near the top and one near the bottom of the flywheel, equipped with stepper motors to change their vertical positions, are used for positioning the flywheel vertically at the optimal height with respect to the magnets in the stators. Together with mechanical backup bearings placed on the top and the bottom of the flywheel, these two chamfers are also intended for use in arresting the motion of the flywheel in an emergency. The entire system is enclosed under a bell jar in vacuum, except for the superconductors which, naturally, have to be continuously immersed in liquid nitrogen. Thus, the superconductors are contained in vacuum-tight cavities made of stainless steel and supplied with cryogen through a plumbing system that includes a pump for liquid nitrogen and is open to the atmosphere. Considering that the superconductors have to be very close (< 5 mm.) to the

rotating magnets on the flywheel in vacuum, the design and fabrication of these cold stages could present a formidable challenge. Fig. 4 is a drawing of the assembled device.

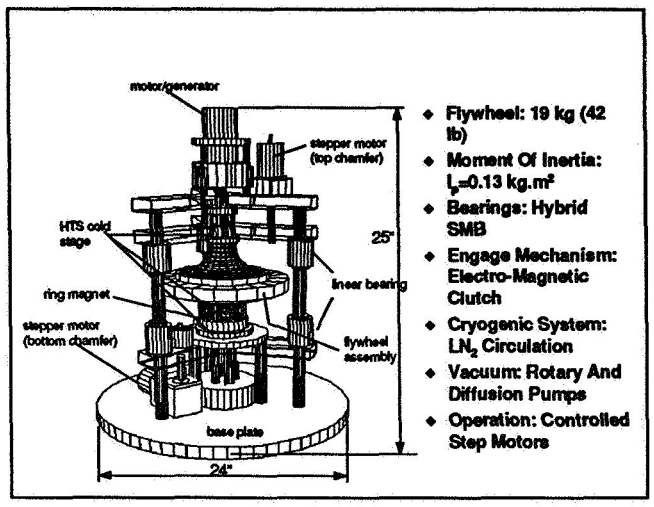

Fig. 4 Three dimensional drawing of our prototype kinetic energy storage system as assembled.

The first step in the operation of this kinetic energy storage system is to identify the optimal position of the flywheel with respect to the stator magnets, and the position of the top and bottom stator magnets with respect to each other. This is done with partial information from the mapping of the magnetic fields from the magnet components and the measurement of forces and stiffnesses between the magnet and the superconductor components before assembly. Final adjustments are made after assembly and before closing the bell jar, by observing the motion of the flywheel as the chamfers holding them in position are pulled apart from each other. After the bell jar is closed and the system is pumped down to its ultimate low pressure, we circulate liquid nitrogen through the cold stages, and spin the flywheel up to speed. Then we release the chamfers to allow the flywheel to levitate after the superconductors have undergone transition to the superconducting state, which is gauged by a certain amount of time after we started the liquid nitrogen pump, a period of time obtained with experience. We also tried releasing the flywheel first, after the superconductors are cold enough, and then spinning the flywheel up to speed from rest in a levitated state. There seems to be little difference in the result.

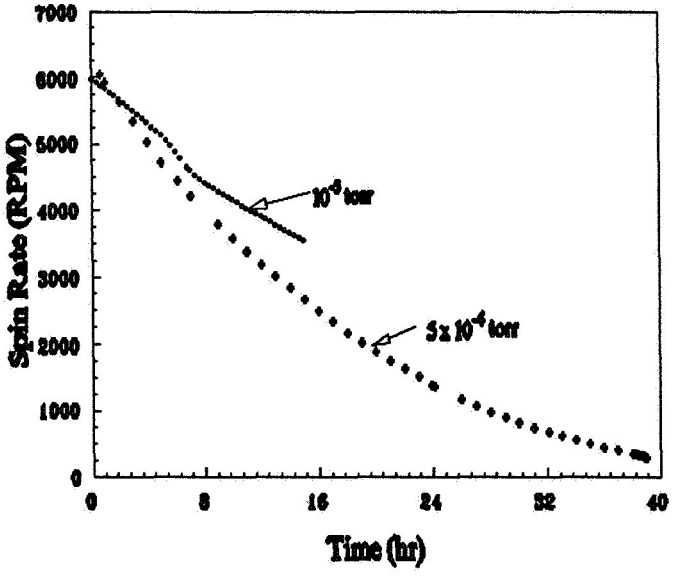

Fig. 5 Spin down curve of our prototype kinetic energy storage system under two different pressures.

Fig. 5 shows the spin down curves of our prototype kinetic energy storage system at two different pressures. Under a vacuum of 7×10^{-4} torr, we have been able to spin this flywheel up to a speed of 6000 RPM, storing an energy of 8 Whr. The initial rate of energy loss is about 5% per hour. The flywheel did not stop after 40 hours, at which time its speed has decreased to 240 RPM. The average rate of energy loss for this entire period is 2.5% per hour. With an improved vacuum of 10^{-5} torr, and

starting at the same speed, the initial rate of energy loss reduced to about 4% per hour. The run was ended after 15 hours for non-technical reasons. The extrapolated time to stop would be 75 hours, with mean energy loss rate of less than 2% per hour.

OBSERVATION OF ROTORDYNAMICS DURING SPIN DOWN

For the purpose of load levelling for the utilities, an energy loss rate of around 0.1% per hour would be desirable. Hence, reducing energy dissipation is still our first priority. Comparing the spin down results at different pressures with theoretical estimates, we have come to the conclusion that the majority of the dissipation is not due to aerodynamic drag from the residual gas. Thus, further improvement of vacuum would not be very fruitful at this point, and we have to look into the other major suspected reason: magnetic losses, of which there are quite a few different mechanisms: (i) even with the flywheel perfectly centered and its rotation axis perfectly aligned, any slight off axisymmetry of the rotor magnets would induce eddy currents in the surrounding metal parts, notably the stainless steel cold stages, and magnetic hysteresis losses in the superconductors in these cold stages; (ii) even with perfectly axisymmetric rotor magnets, if the flywheel is rotating about an off-center or slightly tilted axis, the magnetic field as seen by the stator parts would still have an alternating component, with the same consequences as regards to loss; and (iii) similarly, the metallic parts on the rotor would experience a fluctuating magnetic field giving rise to energy loss if either the stator magnets or the magnetic field trapped inside the superconductors are non-axisymmetric, or again, the flywheel is not rotating about an axis at the geometric center, or about an axis aligned with the geometric axis. The same result would happen if all the magnetic components are perfect, but the inertial properties of the flywheel is off the mark, either due to static imbalance or dynamic imbalance.

The purpose of following the spin down process in more detail is to assess the relative importance of the above mechanisms of energy dissipation. We have accelerated the deceleration of the flywheel in the observation by keeping the non-contact magnetic clutch engaged, so that the experiment may be performed in a shorter time span. The observation is carried out by monitoring the position of the flywheel surface at five different points, from which the position and orientation of the flywheel may be reconstructed. The placement of these position sensors is illustrated in fig. 6. A sixth sensor, consisting of a laser with a photodiode, monitors the total rotation rate of the flywheel by a chopping technique.

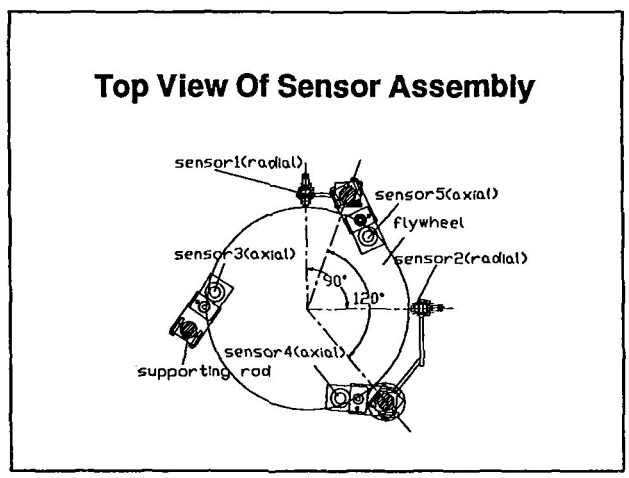

Fig. 6 Drawing for placement of position sensors.

RESULTS AND DISCUSSION

Let us start with the flywheel not rotating, but levitated. By comparing the readings of the position sensors after the flywheel is released into its levitated position and before, when it is clamped at an estimated optimum position, we found that the flywheel has tilted by about 0.2° and its center has shifted laterally by about 0.4 mm., not inconsiderable amounts, but still within the tolerance of our bearings because they were designed to operate with a large gap. The tilt and the displacement are in the same plane. A schematic drawing illustrating these deviations is shown in fig. 7. This result definitely indicates some sort of asymmetry in the system, but we cannot pinpoint its origin as yet.

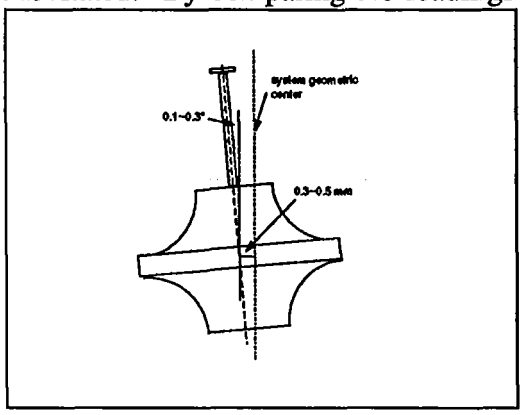

Fig. 7 Illustration of tilt and lateral shift of flywheel when levitated and stationary.

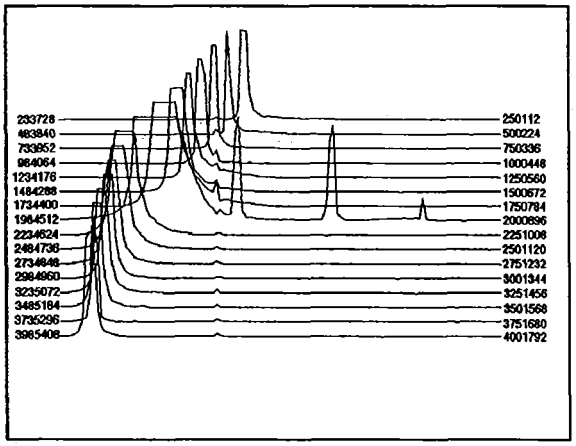

Fig. 8 Rotordynamic response of flywheel on spin down. The numbers are millsecond time markers.

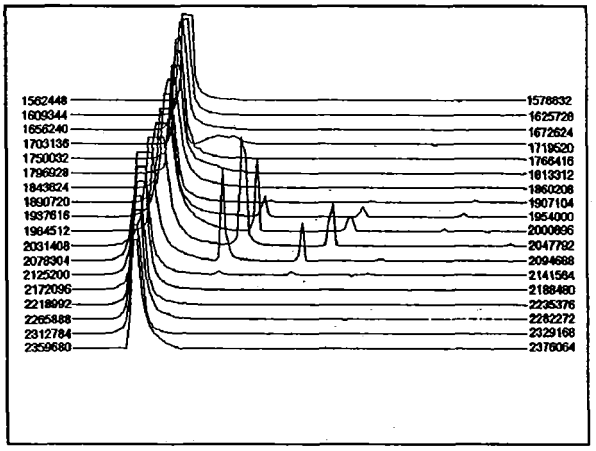

Fig. 9 Rotordynamic response of flywheel on spin down through the critical speed. The numbers are millsecond time markers.

On spinning up the flywheel, it goes through a critical speed regime as expected, and similarly on spin down. The rotordynamical response of the flywheel on spin down is shown in fig. 8. An expanded version in the transition region around the critical speed is shown in fig. 9.

Further examination of this region shows that this can be interpreted as several criticals closely clustered around 5 hz. Fig. 10 is a graph of the time evolution of the amplitude in the fundamental that is suggestive of this interpretation. This multiplicity is a result of multiple rigid body modes, with very similar stiffnesses. The value of 5 hz. agrees well with the value predicted from the spin whirl map, using the stiffness values measured before the magnets and superconductors were assembled. It also agrees with the simple formula

$$\omega^2 = k/M. \qquad (1)$$

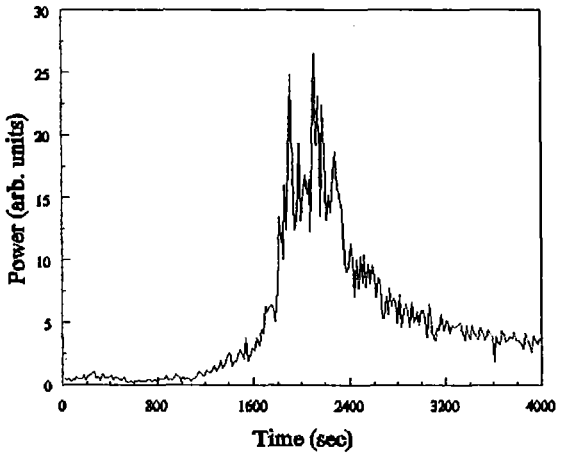

Fig. 10 Time evolution of the squared amplitude of vibration at the fundamental frequency of one of the position sensors.

The stiffnesses of the bearings can be estimated from this to be of the order of 30 N/mm. This value of the stiffnesses is rather low, and it does have its disadvantages. To some extent, these disadvantages are compensated for by gaps that can be large enough to accommodate the vibration amplitude when the flywheel goes through these criticals. These low stiffnesses also yield low critical speeds, which means that the flywheel can easily be boosted to operate in the supercritical regime, where the flywheel is self-centering and self-aligning. Measurements in this regime show that, as the rotational speed of the flywheel is increased, the vibration amplitudes of all the variables in this supercritical regime decrease as ω^{-2} with no offset for three of the sensors sensitive to tilt, and about 0.1 mm for the two sensors sensitive to lateral shift. Fig. 11 is a plot of the data which exhibits behavior according to this relationship. This result implies that the center of gravity of this flywheel coincides with its geometrical center to within 0.1 mm., and its principal moments of inertia coincides with its geometrical axis to a precision better than 0.002^0. It also means that the tilt and the lateral shift of the flywheel in its levitated, but stationary state is due more to the deviations of the rotor magnet from perfect axisymmetry, with a minor contribution from mass eccentricity, which we suspect comes from the mounting of the large ring magnet at the bottom. From the systems operation point of view, it also means that we do not have to be overly concerned with the inertial balance of the flywheel. Should it still be desirable to enhance the stiffness of the bearings, use of ion implantation techniques to create damage and pinning centers has been shown to be able to change the critical current density by orders of magnitude.[10] A corresponding, but perhaps more moderate increase in the stiffness can be expected.

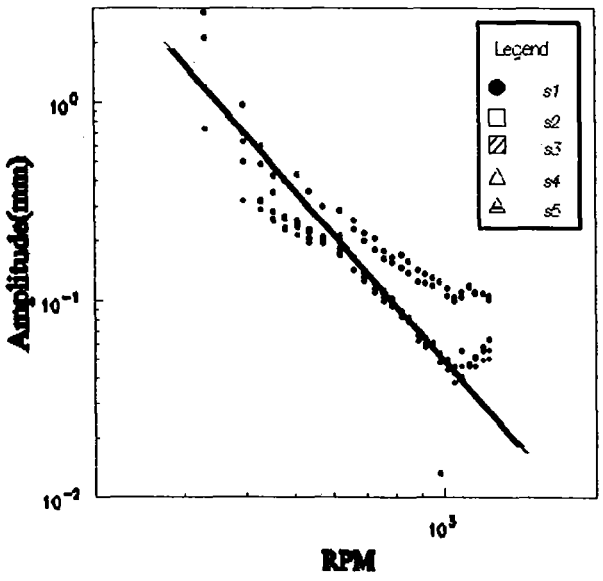

Fig. 11 Amplitude of oscillation measured at all the position sensors in the supercritical regime. The final upturn was observed to coincide with mechanical vibrations of the holding structure.

The effect of the vigorous oscillatory motion of the flywheel on the rate of energy loss is clearly evident in the spin down curve shown in fig. 12. With care, even the effect of minor resonances in the supporting mechanical structure, such as the pipes that carry liquid nitrogen, can be discerned. However, all these effects go away at high spins, and what we should focus attention on is the general and gradual increase in the rate of energy loss as spin is increased. If the energy loss is due to magnetic hysteresis in the superconductor, the spin down curve can be expected to be linear in time, whereas, if it is eddy current loss, the spin down curve would be exponential in time. Our curve is somewhat of a mix, and we are in the process of sorting this out in our next set of experiments with cold stages constructed out of electrically insulating material to eliminate eddy current loss.

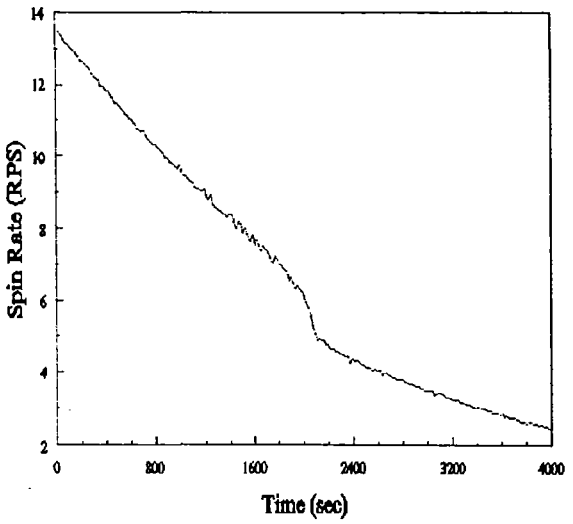

Fig. 12 Accelerated spin down curve for rotodynamic analysis of our prototype flywheel/bearing system. The sudden drop near the midpoint is where the system goes through its critical speed(s).

Throughout the spin down process, from high spins to low spins, we have observed that the flywheel is off axis and off center, but is keeping the same face outwards. This is indicated by the observation that the chopping signal is always in synchronism with the fundamental in the signal from all the sensors. One explanation of this is that the rotor magnets are not precisely axisymmetric, with the result that it is favorable to have one side always facing outside. However, it is expected that this should switch in going through the critical region. A phase slip of 180°

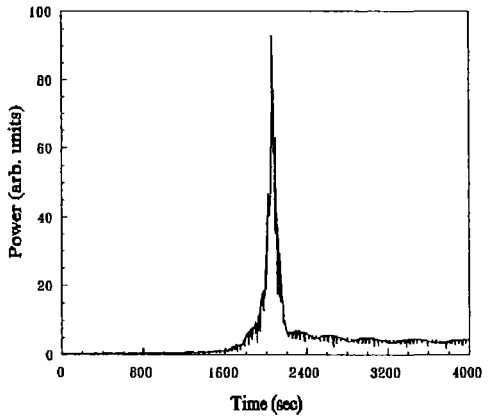

Fig. 13a Time evolution of the squared amplitude of vibrations of the tilt angle in the x-direction, defined arbitrarily to go through one of the three position sensors placed for tilt detection.

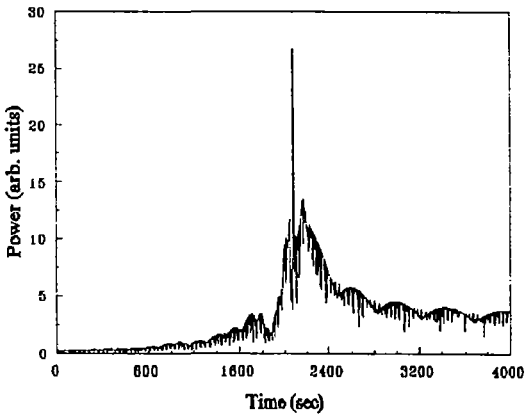

Fig. 13b Time evolution of the squared amplitude of vibrations of the tilt angle in the y-direction, perpendicular to the x-direction defined in fig. 13a.

during the transition could have been missed. The stator magnets are not exactly axisymmetric either, but perhaps deviate from axisymmetry to a smaller extent. The time evolution of the power spectrum of the tilt of the axis of the flywheel is slightly different for the two orthogonal directions, as shown in fig. 13 on the previous page.

FUTURE DEVELOPMENTS

The subsequent stages of development will see us pushing towards devices with higher and higher storage capacities. This will be achieved in two ways, increasing the maximum operating speed of the flywheel with a moderate increase in weight, or increasing the weight with a moderate increase in speed. It is estimated that machines with 1 kWhr to 10 kWhr can be reached in the next stage. This by no means represent a limitation for further growth.

Another issue is a materials issue. These high temperature superconductors show a promise of enhanced critical current density, and by implication stiffness, using ion implantation techniques to create an optimal amount of damage in the material which serves as pinning centers. This would certainly be a welcome development.

Finally, we should be focussing more attention on the overall problem of systems integration, such as designing a motor/generator that would couple into a low stiffness flywheel system effectively for energy storage and release. We are still in the process of designing a cold stage to enclose liquid nitrogen and high temperature superconductor in the vacuum chamber, without metallic parts. Reliability of the present operation procedure also needs improvement.

CONCLUSION

In conclusion, we would like to point out that kinetic energy storage system is a feasible application for hybrid superconductor magnet bearings, despite the objection of their low stiffnesses, which, in fact, offers some features that partially compensate for their disadvantage. Last, but not least, there is still some room for improvement of their stiffnesses.

ACKNOWLEDGEMENT

We would like to thank Dr. Quark Chen, Dr. Nan-jui Zheng and Mark Lamb for many a stimulating discussion. We acknowledge ARPA MDA 972-90-S-1001, US DOE Grant DE-FC48-95R810542 and the State of Texas through the Texas Center for Superconductivity for support on this work.

REFERENCES

1. Earnshaw, S., "*On the Nature of the Molecular Forces Which Regulate the Constitution of the Luminiferous Ether*," Trans. Cambridge Philos., Soc. 7, pp. 97-114.

2. Ma, K. B., et al, "*Phenomenology and Applications of Momentum Transfer Between Type II Superconductors and Permanent Magnets,*" Proceedings of the 1992 TCSUH Workshop, HTS Materials, Bulk Processing Bulk Applications, pp.419-425.

3. Moon, Francis, "*Superconducting Levitation - Applications to Bearings and Magnetic Transportation,*" John Wiley & Sons, Inc., 1994.

4. Ma, K. B.,et al, "*Applications of High Temperature Superconductors in Hybrid Magnetic Bearings,*" Proceedings of the 1992 TCSUH Workshop, HTS Materials, Bulk Processing Bulk Applications, pp.425-430.

5. Weinberger, B. R., et al, "*Magnetic Bearings Using High-Temperature Superconductors: Some Practical Considerations,*" Supercond. Sci. Technol., 3, 1990, pp.381-388.

6. McMichael, C., et al, "*Practical Adaptation in Bulk Superconducting Magnetic Bearing Applications,*" Appl. Phys. Lett. 60, pp.1893-1895.

7. McMichael, C., et al, "*Effects of Material Processing in High Temperature Superconducting Magnetic Bearings,*" Appl. Phys. Lett. 59, pp.2442-2444.

8. Chen, Q.Y., et al, "*Hybrid High Tc Superconducting Magnetic Bearings for Flywheel Energy Storage Systems,*" Appl. Supercond., Vol. 2, No.7/8, 1994, pp.457-464.

9. Xia, Z., et al, "*Hybrid Superconducting Magnetic Bearing and its Frictional Energy Loss and Dynamics,*" Proceedings of MAG'95, pp.321-329.

10. Gupta, Ram P., et al, "*Fluorine-Implanted Bismuth Oxide Superconductors,*" Appl. Phys. Lett., Vol.54, No.6, 1989, pp.570-571.

DEVELOPMENT OF Y-Ba-Cu-O SUPERCONDUCTORS FOR MAGNETIC BEARINGS[†]

V. Selvamanickam, K. Pfaffenbach, R. S. Sokolowski
Intermagnetics General Corporation
Latham, NY 12110

Y. Zhang and K. Salama
Texas Center for Superconductivity at University of Houston
Houston, TX 77204

SUMMARY

The material requirements, material manufacturing and magnetic properties that are relevant to fabrication of High Temperature Superconductor (HTS) magnetic bearings have been discussed. It is found that the seeded-melt-texturing method can be used to fabricate the single domain material that is required to achieve the best magnetic properties. Trapped-field mapping has been used as a non destructive tool to determine the single-domain nature of the HTS material and quantify the quality of the HTS disks. Both the trapped field and the levitation force of the Y-Ba-Cu-O disks are found to be strongly sensitive to the oxygen content.

INTRODUCTION

Magnetic bearings have been used extensively in applications ranging from turbomolecular pumps, machine tool spindles for grinding and milling, compressors and blowers, pumps for gas pipelines as well as rotating machinery in power generating plants that must operate in hostile environments. Yet, despite the growing acceptance of this new technology, it remains expensive and complex. However, the discovery of new high temperature superconductors in 1986 created an opportunity to dramatically improve the performance of magnetic bearings, increase their reliability and lower overall system operational costs. In a HTS magnetic bearing, the repulsive force between a superconductor and a permanent magnet enables levitation and therefore there are almost no frictional losses (ref. 1). Since these

[†] This work was partially supported by Air Office of Scientific Research Contract F49620-95-C-0023

are non-contact bearings, the need for lubricant disappears and the associated plumbing for delivering lubricant to and from the bearing surface, which adds to size and weight, is eliminated. Further, HTS bearings offer high-speed concomitantly with high stability and thousands of times lesser friction than the best roller bearings.

HTS MATERIAL REQUIREMENT

Figure 1 shows a schematic of a HTS magnetic bearing. The bearing is a passive type where the levitative force of a ring of superconducting disks keeps a magnet suspended in equilibrium. The four properties that affect the performance of magnetically levitated bearings are levitation pressure, stiffness, damping and drag. Levitation pressure, the most important property of these four, is directly dependent on the magnitude of magnetization of the superconducting material. The magnetization is determined by two factors : critical current density and the size of the induced current loop. The high temperature superconducting materials are categorized as type II superconductors where the critical current density is determined by the degree of flux pinning, which can be tailored in the material by the inclusion of fine-scale defects. Due to the anisotropic properties of high temperature superconductors, the critical current

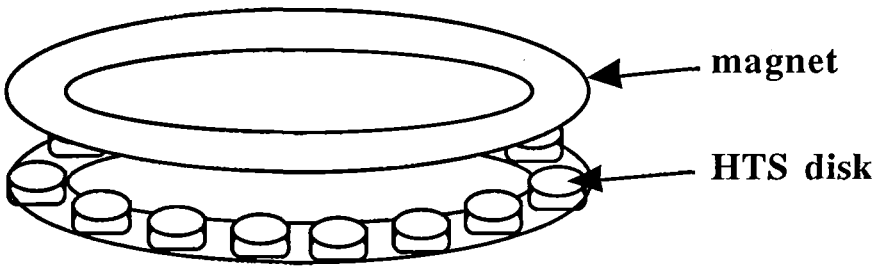

Fig. 1 Schematic of a passive superconductor magnetic bearing. The bearing is comprised of a permanent magnets levitated by a ring of superconductor disks.

density is also determined by the orientation of the strongly superconducting Cu-O planes with respect to the induced current. In order to achieve the maximum current density and hence the highest levitation pressures, it is essential to fabricate a material where the induced current flows only in the Cu-O planes. The second factor that influences the levitation pressure, namely the size of the induced current loop, can be maximized in a material where the current flows within a single grain without having to traverse

through grain boundaries. Taking the above factors into account, the preferable geometry of a superconducting material for use in a magnetic bearing is shown schematically in Fig. 2.
The superconductor consists of a single 'grain' where the strongly superconducting Cu-O planes are aligned perpendicular to the direction of an external magnetic field. In this case the current loop induced by the magnetic field flows in the entire sample along the Cu-O planes resulting in a high levitation pressure.

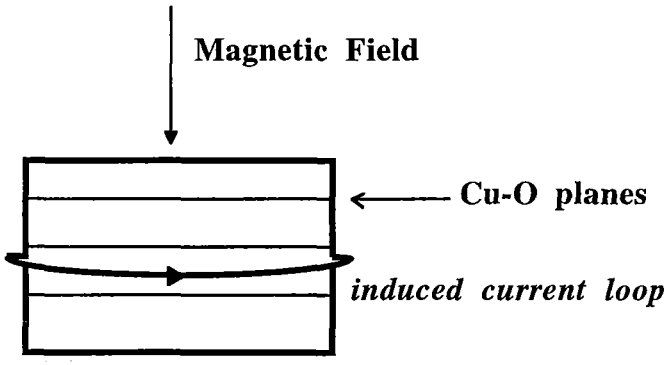

Fig. 2 Schematic of a microstructure that is desired to achieve high levitation pressure in a superconductor.

The microstructure shown in Fig. 2 cannot be achieved in $YBa_2Cu_3O_{7-x}$ by normal ceramic processing methods. Fig. 3 (a) is a schematic of the microstructure of a typical sintered $YBa_2Cu_3O_{7-x}$. As shown in Fig. 3 (a), this material consists of small grains of a few microns in dimension which are oriented randomly. Due to the small grain size and the random grain orientation, the flow of the induced current is restricted to within each individual grain as shown in Fig. 3 (a). As a result of the small size of the induced current loop, the levitation pressure of these sintered materials is low (ref. 2, 3). The sintered material shown in Fig. 3 (a) can be transformed into a material with grain size of about a centimeter by using a melt-texturing process (ref. 4). In this process, the sintered material is partially melted and solidified under controlled cooling conditions to yield a material which is locally textured as shown in Fig. 3 (b). This material would consist of about 10 to 20 grains which compares with thousands of grains in a sintered material. As a result of the large grain size, the size of the induced current loop is increased by several orders of magnitude. Furthermore, a number of fine-scale defects are created during the melt-texturing process which contributes to flux pinning which leads to high current density (ref. 5). Due to a combination of a large induced current loop and a high current density, the levitation pressure of melt-textured materials is much higher than that of sintered materials (ref. 2, 3, 6). Usually, the Cu-O planes of a few grains in a melt-textured material are aligned favorably with respect to the external magnetic field.

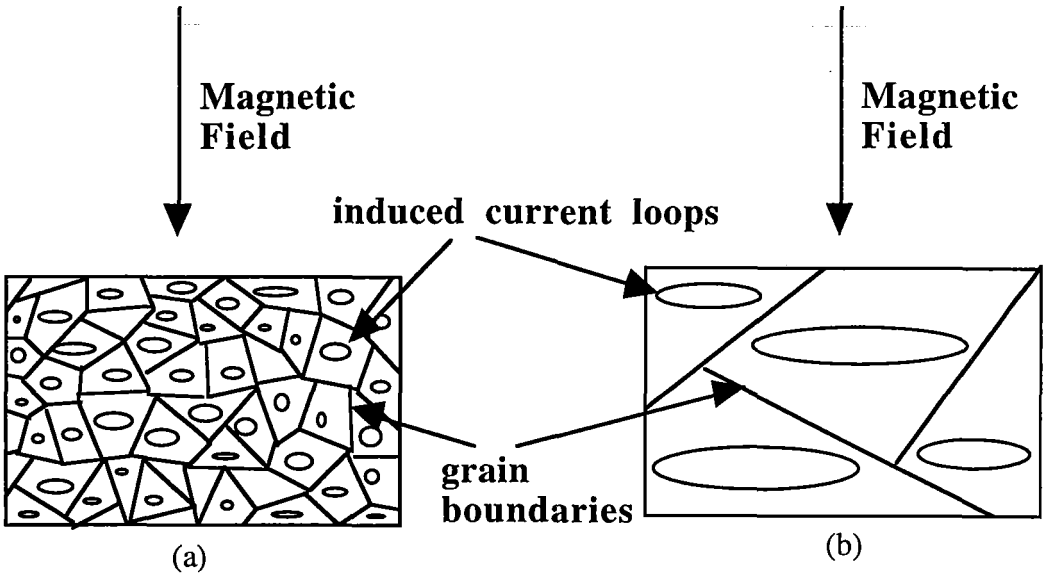

Fig. 3 Schematic of microstructure of (a) sintered superconductor having a number of small grains (grain size of a few microns) and (b) melt-textured superconductor having a few large grains (grain size of about a centimeter). The size of the current loop in the superconductor induced by an external magnetic field is much larger in melt-textured superconductors and therefore the levitation pressure is much higher.

However, in order to maximize the levitation pressure, the grains have to be formed during the melt-texturing process in a controlled way such that their Cu-O planes are aligned perpendicular to the magnetic field, as shown earlier in Fig. 2. For this purpose, an extended version of the melt-texturing process, namely seeded melt-texturing, has been developed. The detail of this process is shown in Fig. 4.

In this process, a sintered material similar to that shown in Fig. 3 (a) is partially melted and solidified under controlled cooling conditions as described before, but with the grain nucleation initiated with a 'seed'. This seed is preferably a material of $YBa_2Cu_3O_{7-x}$ superconductor family such as $SmBa_2Cu_3O_7$ or $NdBa_2Cu_3O_7$ which melts at a higher temperature than $YBa_2Cu_3O_{7-x}$ and does not react with the Y-Ba-Cu-O melt. These seeds are also grown by the melt-texturing process, cut, and shaped so that the Cu-O planes of their grains are oriented parallel to their large faces. As the schematic in Fig. 4 shows, the seed is then placed on top of the sintered material during the melt-texturing process which then acts as a template for textured growth of the $YBa_2Cu_3O_{7-x}$ grains. By this technique, a microstructure similar to that described in Fig. 2 can be achieved.

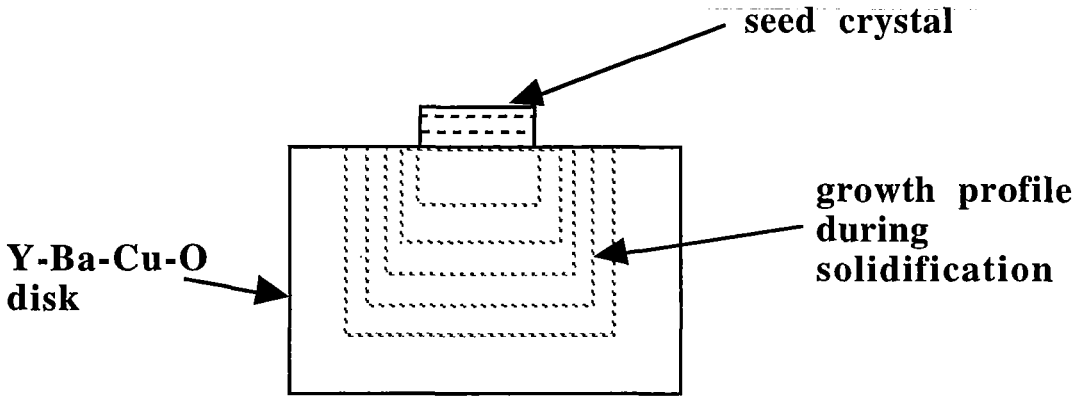

Fig. 4 Schematic showing the microstructure development in a $YBa_2Cu_3O_{7-x}$ disk during seeded melt-textured growth. Nucleation is initiated from the seed crystal of $SmBa_2Cu_3O_7$ which then acts as a template for subsequent growth as shown in the growth profile during solidification. By this technique, a microstructure similar to that shown in Fig. 2, which is required for high levitation pressures, can be achieved.

Since the material manufactured by seeded melt-texturing consists of one large 'grain', the size of the induced current loop is as big as the sample itself. Also, since the Cu-O planes of the grains of this material are all aligned perpendicular to the external magnetic field, the current flows only within these planes. As a result, materials fabricated by seeded melt-texturing exhibit the highest levitation pressures. Even higher levitation pressures can be attained by increasing the current density which can be achieved by controlled doping of the 'raw' material with platinum. Platinum doping has been observed to refine the size of Y_2BaCuO_5 particles which are created during the melt-texturing process (ref. 7). These particles and the defects such as stacking faults and dislocations associated with them have been found to be strong flux pinning centers in the melt-textured material (ref. 8). Refining the size of these particles leads to a higher defect density, hence a high current density which in turn results in high levitation pressures.

HTS MATERIAL FABRICATION

Powders of $YBa_2Cu_3O_{7-x}$ (Seattle Specialty Ceramics (SSC) Inc.) with 20 wt.% Y_2BaCuO_5 (SSC Inc.) and 0.5 wt.% Pt were pressed in the form of disks 1" in diameter. These disks were densified by

heat treating them at 950°C for 24 hours in air. Disks of $SmBa_2Cu_3O_7$ (SSC Inc.) with 10 wt.% Sm_2O_3 were also compacted and sintered at 1000°C for 24 hours. The Sm-Ba-Cu-O disks were then melt-textured with a MgO single crystal of <100> orientation similar to the schematic shown in Fig. 4. A sintered Y_2BaCuO_5 disk was used to support the Sm-Ba-Cu-O disk. The Sm-Ba-Cu-O disk was melted at 1135°C for 30 minutes and cooled fast to 1067°C and subsequently cooled at a rate of 0.5°C/h to 987°C. The melt-processed material was analyzed by optical microscopy and was found to contain a single domain extending half-way through the thickness of the sample. This process yielded a single grain of 20 mm in length that could be cleaved from the bulk sample. A single grain of 5 mm × 5 mm was cut and used for seeded-melt-texturing of Y-Ba-Cu-O disks.

The Y-Ba-Cu-O disks were melt-textured with the seed crystal of $SmBa_2Cu_3O_7$ as shown in Fig. 4. As in the case of Sm-Ba-Cu-O, the Y-Ba-Cu-O disk was also supported with a sintered Y_2BaCuO_5 disk during melt-texturing. The Y-Ba-Cu-O disk was melted at 1058°C in air and cooled fast to 1028°C from which it was cooled at a rate of 1°C/h to 930°C. Quench experiments during the slow cooling process revealed that the growth of the single domain of $YBa_2Cu_3O_{7-x}$ was only half-completed at 985°C and not fully completed even at 968°C. The melt-textured Y-Ba-Cu-O disk was analyzed by optical microscopy and then annealed in oxygen at 480°C for 48 hours. The magnetic properties of the disk were investigated following which it was annealed under the same conditions for 160 more hours.

HTS MATERIAL MAGNETIC PROPERTIES

Figure 5 shows the top surface of an as-melt-textured Y-Ba-Cu-O disk. The square impression of the Sm-Ba-Cu-O seed can be seen in the middle of the disk. Also, the growth fronts extending from the four sides of the seed to the periphery of the disk can be observed. This feature is representative of a single domain material which forms from a single grain seed. In order to verify if the material was composed of only one domain, trapped-field measurements were conducted. In the trapped-field measurements, the disk was field-cooled at 77 K in a magnetic field of 1.5 T. The disk was then transferred quickly to a trapped-field measurement rig where the field trapped in the sample was measured over the top surface using a hall probe (ref. 9). The measurements were taken over the entire top surface of the sample so that a complete map of the trapped field could be obtained. Figure 6 shows a 3-dimensional map of the trapped field in a melt-textured Y-Ba-Cu-O disk after an oxygen anneal of 48 hours. A single cusp in the field profile can be observed in Fig. 6 indicating the presence of a single domain. If more than one domain had been present, several cusps would have been obvious in the trapped field profile. The trapped-field measurement is

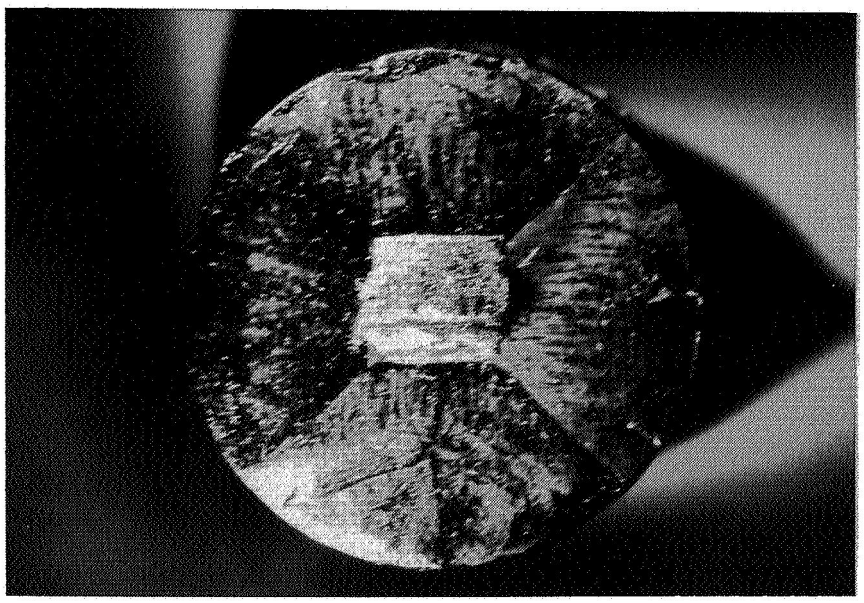

Fig.5 Top surface of a Y-Ba-Cu-O disk fabricated by the seeded-melt-texturing process. The square impression of the seed and the growth fronts emanating from the sides of the seed can be observed.

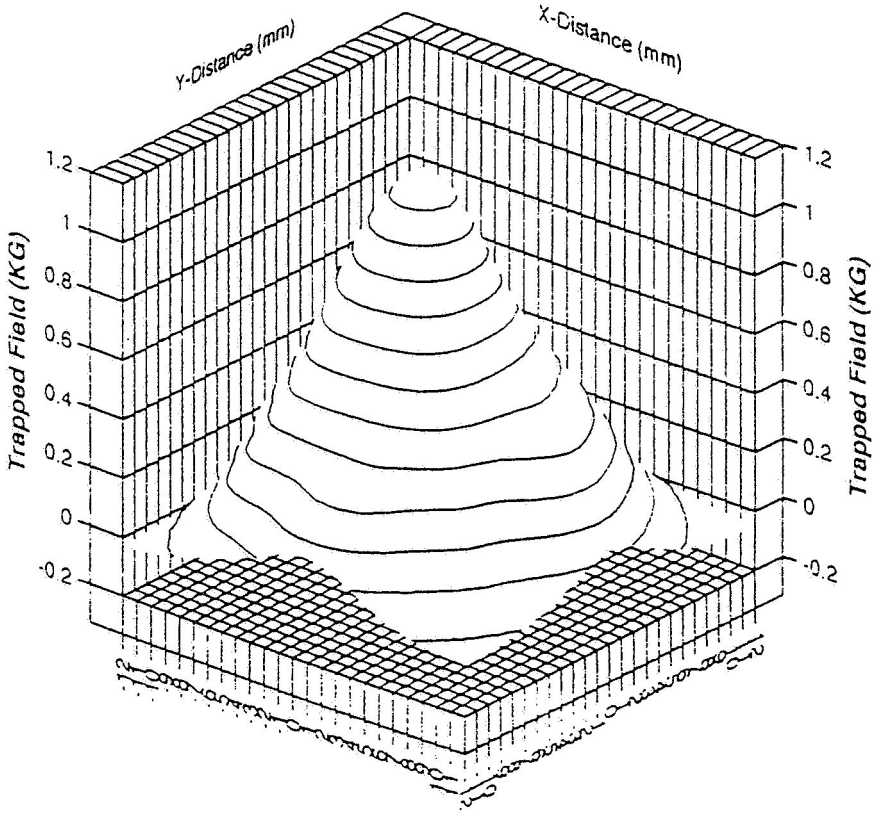

Fig.6 A 3-dimensional trapped field profile of a melt-textured Y-Ba-Cu-O disk after a short oxygen anneal. The presence of a single domain is evident from the single cusp in the trapped field profile.

among the best non-destructive tools available for the characterization of superconducting disks. The trapped-field profile can be used to quantify the quality of the disks and used to make appropriate modifications to the manufacturing process.

Figure 6 reveals that a maximum field of 1 kG was trapped in the disk. Since the seeded-melt-textured Y-Ba-Cu-O disks consist of a single domain, diffusion of oxygen is expected to be very slow in these materials. In order to increase the oxygen content to an optimum value, the disk described in figures 5 and 6 was annealed in oxygen for 160 more hours. Trapped-field measurements were then conducted on the disk as described previously. Figure 7 shows a 2-dimensional trapped-field map of the disk after the extended anneal. The presence of a single domain is obvious in this figure as evident by a single peak contour in the field profile. It can be also seen from the figure that the maximum trapped field in the disk has increased to 2.4 kG. Therefore, it is clear that a long oxygen anneal is required in order to achieve the maximum performance of single domain Y-Ba-Cu-O materials.

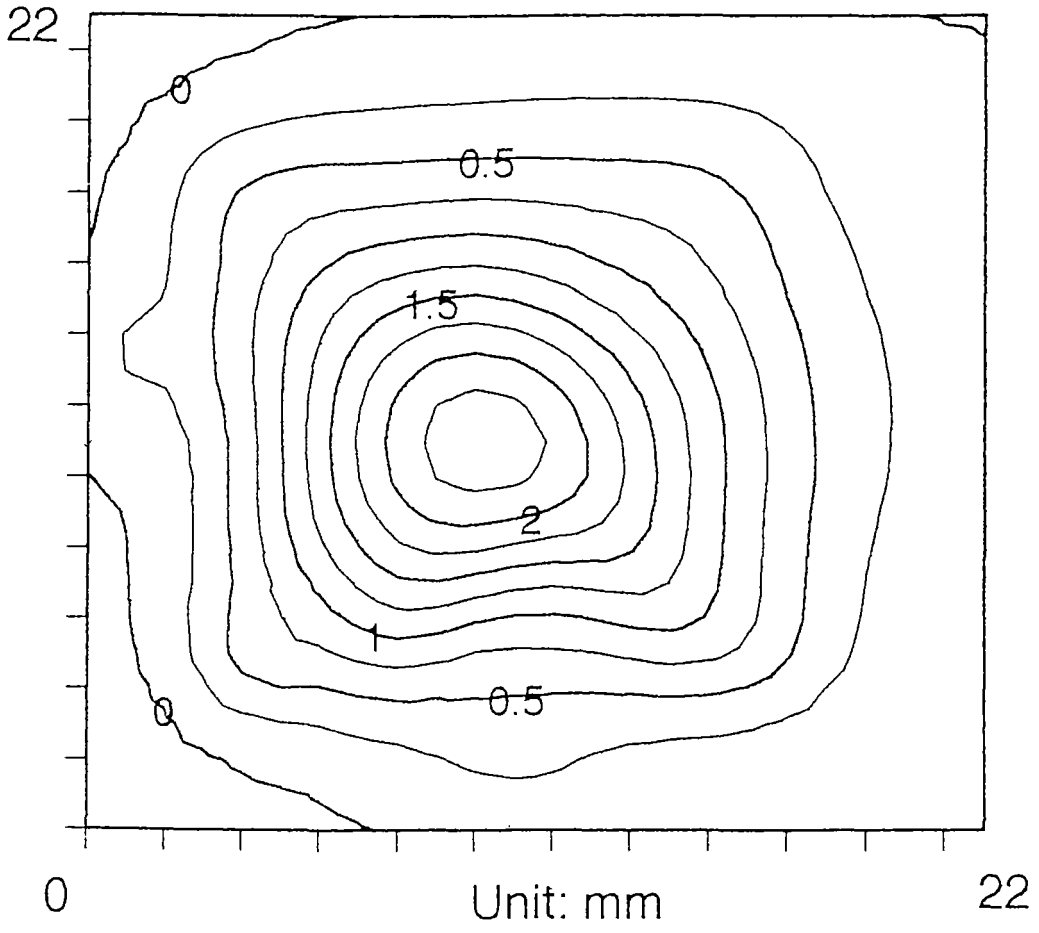

Fig. 7 A 2-dimensional trapped-field profile of a melt-textured Y-Ba-Cu-O disk after an additional oxygen anneal. The maximum trapped field has increased to 2.4 kG.

As mentioned earlier, magnetic levitation force is the most important property that determines the quality of a HTS magnetic bearing. The magnetic levitation force was determined in a test rig where the Y-Ba-Cu-O disk was cooled to 77 K in zero field and a 1" diameter permanent magnet of field strength of approximately 4 kG was moved in steps of 1 mm towards the disk . The levitation force was monitored at every step, as the magnet was moved first towards the disk and then away from the disk. The maximum levitation force was recorded at a distance of 0.5 mm which was the closest distance between the magnet and the disk. Figure 8 shows the levitation force of the melt-textured disk described in fig. 6 (after an oxygen anneal of 48 hours) over a distance of 30 mm.

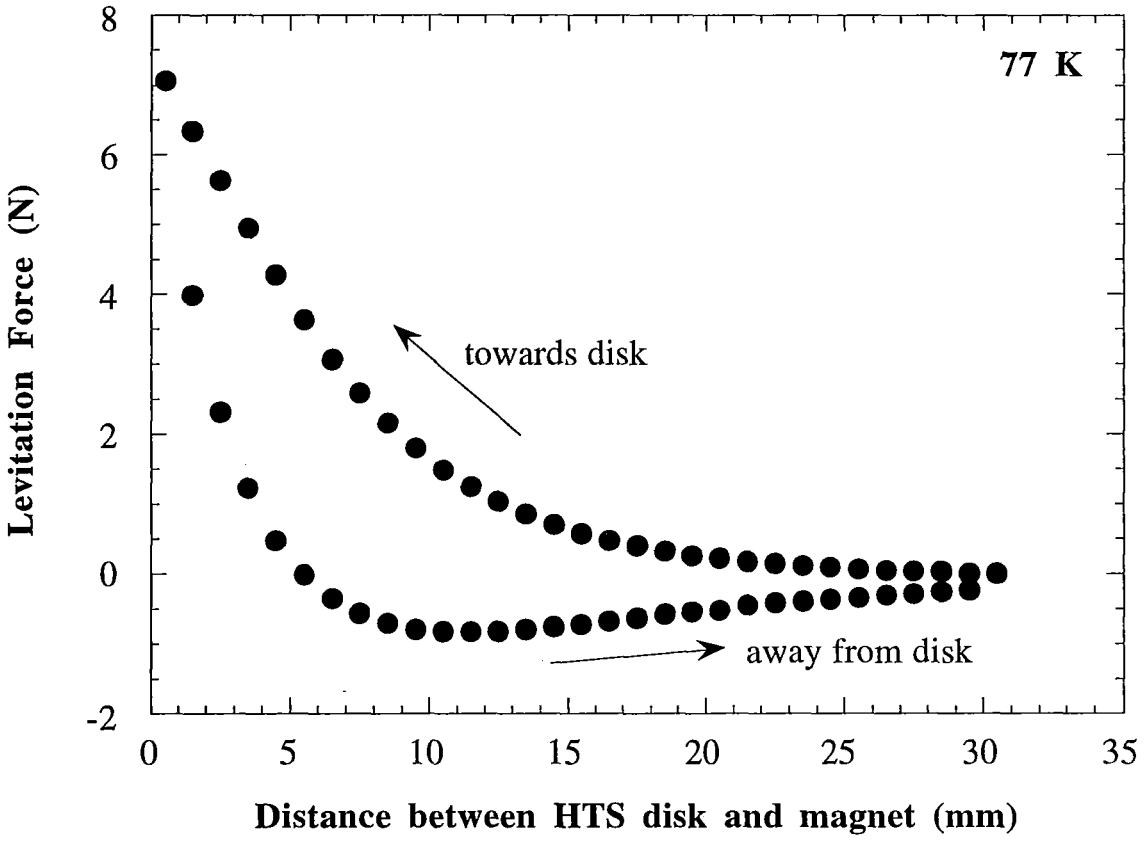

Fig. 8 Levitation force of a melt-textured disk as a permanent magnet is moved towards and then away from the disk. A maximum levitation force of 7 N is observed in the disk that was subjected to a short oxygen anneal.

It can be seen that the levitation force rises sharply as the magnet is brought closer to the disk and peaks at 7 N at a distance of 0.5 mm. A large hysteresis can be observed in the levitation force as the magnet is

moved away from the disk. In order to determine if the levitation force increased after an extended oxygen anneal, as did the trapped field, the same disk was characterized after the additional oxygen anneal of 160 hours. The levitation force characteristics of this disk are shown in fig. 9. It can be seen from the figure that the maximum levitation force has increased to about 16 N.

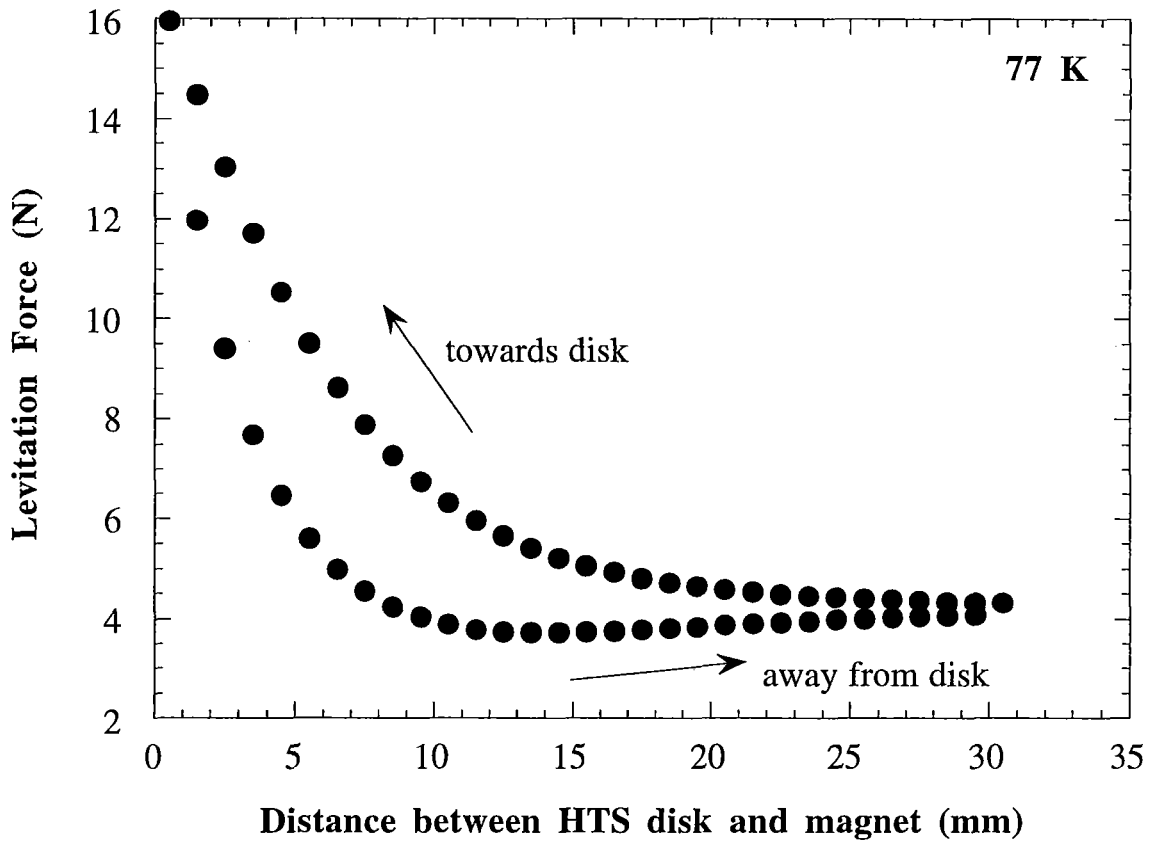

Fig. 9 Levitation force of a melt-textured disk after an additional oxygen anneal. The maximum levitation force can be seen to be improved to 16 N.

The results show that both the trapped field and the levitation force are more than doubled after the additional oxygen anneal. Additonal annealing in oxygen is being performed to determine if the magnetic properties could be further improved.

CONCLUSIONS

The development of Y-Ba-Cu-O superconductors for magnetic bearings has been addressed. It is found that seeded-melt-texturing of $YBa_2Cu_3O_{7-x}$ using a seed crystal of $SmBa_2Cu_3O_7$ can yield single-domain materials needed to achieve high levitation forces. The single-domain nature of the Y-Ba-Cu-O disks has been examined by trapped-field measurements. A levitation force of 16 N and a trapped field of 2.4 kG have been measured in the single-domain Y-Ba-Cu-O disks. Further development of these materials will involve optimizing the oxygen content, introducing defects for flux pinning and reducing microcracks which will all lead to higher levitation forces and trapped fields.

REFERENCES

1. Moon F. C. : Superconducting Levitation. John Wiley & Sons Inc. 1994.
   Chen Q. Y., Xia Z., Ma K. B., McMichael C. K., Lamb M., Cooley R. S., Fowler P. C., and Chu W. K. : Hybrid High T_c Superconducting Magnetic Bearings for Flywheel Energy Storage Systems. *Appl. Supercond.,* vol. 2, 1994, pp. 457 - 464.
2. Murakami M. : Melt Process, Flux Pinning, and Levitation. *Processing and Properties of High T_c Superconductors,* vol.1 ed. S. Jin, World Scientific, Singapore, 1993, pp. 213-270
3. Lehndorff B., Kürschner H-G., and Piel H. : Mapping of magnetic force and field distribution of melt-textured Y-Ba-Cu-O. *IEEE Trans. Appl. Supercond.,* vol. 5, no.2, June 1995, pp. 1814-1817.
4. Salama K., Selvamanickam V., Gao L., and Sun K. : High current density in bulk $YBa_2Cu_3O_x$ Superconductor. *Appl. Phys. Lett.,* vol. 54, no. 23, June 1989, pp. 2352-2354.
5. Murakami M., Morita M., Doi K., and Miyamoto K. : A new process with the promise of high J_c in oxide superconductors. *Jpn. J. Appl. Phys.,* vol. 28, no. 7, July 1989, pp. 1189-1194
6. Murakami M., Oyama T., Fujimoto H., Taguchi T., Gotoh S., Shiohara Y., Koshizuka N., and Tanaka S. : Large levitation force due to flux pinning in YBaCuO superconductors fabrication by melt-powder-melt-growth process. *Jpn. J. Appl. Phys.,* vol. 29, no.11, November 1990, pp. 1991-1994.
7. Ogawa N., Yoshida M., Hirabayashi I., and Tanaka S., : Preparation of YBCO bulk superconductor by Platinum doped melt growth method. *Supercond. Sci. and Technol.,* vol. 5, 1992, p. S89.
8. Mironova M., Lee D. F., Selvamanickam V., and Salama K., : Structure and Defects at Y_2BaCuO_5-$YBa_2Cu_3O_x$ interface in melt-textured YBCO superconductors. *Interface Science* , vol. 1, 1994, p.381.
9. Weinstein R., In-Gann Chen, Liu J., Parks D., Selvamanickam V., and Salama K., : Persistent magnetic fields trapped in high T_c superconductor. *Appl. Phys. Lett.*, vol. 56, no. 15, April 1990, pp.1475-1477.

Session 8 -- Applications 1

Chairman: Steven Van Sciver
National High Magnetic Field Laboratory (NHMFL)

DESIGN OF A BEARINGLESS BLOOD PUMP

Natale Barletta
Laboratory for Electrical Engineering Design (EEK)
Swiss Federal Institute of Technology
Zurich Switzerland

Reto Schöb
Sulzer Electronics AG
Winterthur, Switzerland

SUMMARY

In the field of open heart surgery, centrifugal blood pumps have major advantages over roller pumps. The main drawbacks to centrifugal pumps are however problems with the bearings and with the sealing of the rotor shaft. In this paper we present a concept for a simple, compact and cost effective solution for a blood pump with a totally magnetically suspended impeller. It is based on the new technology of the "Bearingless Motor" and is therefore called the "Bearingless Blood Pump". A single bearingless slice motor is at the same time a motor and a bearing system and is able to stabilise the six degrees of freedom of the pump impeller in a very simple way. Three degrees of freedom are stabilised actively (the rotation and the radial displacement of the motor slice). The axial and the angular displacement are stabilised passively. The pump itself (without the motor-stator and the control electronics) is built very simply. It consists of two parts only: the impeller with the integrated machine rotor and the housing. So the part which gets in contact with blood and has therefore to be disposable, is cheap. Fabricated in quantities, it will cost less than $10 and will therefore be affordable for the use in a heart-lung-machine.

MOTIVATION AND INTRODUCTION

In the field of open heart surgery, roller pumps are most often used to maintain the blood flow during an operation. However, they cause a lot of problems such as blood damage, material fatigue, particulate contamination and unlimited pressure at a given speed. Centrifugal pumps would therefore have major advantages. There are several centrifugal pumps commercially available i.e. from Biomedicus, Sarns Centrimed and St. Jude. All these pumps have a disposable pump head with a magnetically coupled driving system (see Fig. 2). This avoids the entry of blood into the electric motor. Unfortunately not all problems are solved by this construction. There are still severe problems related to the rotor-bearings and the sealing of the rotor shaft. Thromboemboli can be caused by dead water spaces around the shaft and heat

generation of bearings and seals. Leakage of seals can lead to infection and bearing-failures, when blood seeps into the bearing.

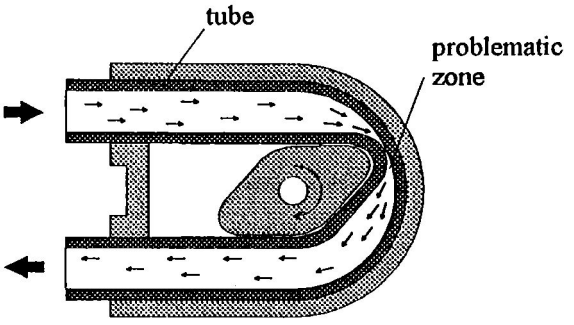

Fig. 1: Functional principle of a roller pump.

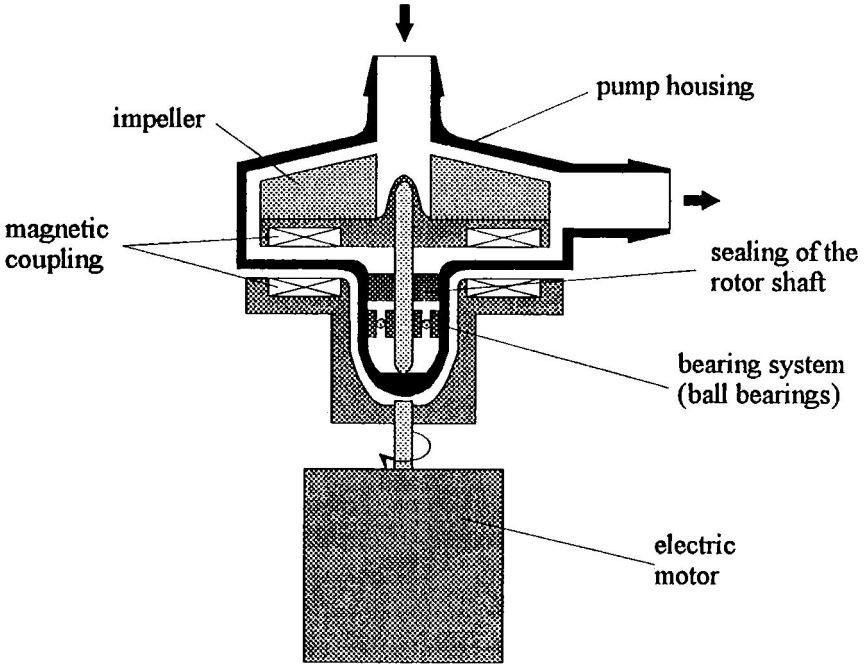

Fig. 2: Functional principle of a centrifugal blood pump with magnetic coupling and ball bearings.

These problems are mentioned by many authors i.e. in [1], [2], [3], [4] and [10]. One possibility to overcome these problems is to drive the pump impeller through the pump housing by an AC motor and to mount the impeller by magnetic bearings. Such constructions have been proposed i.e. in [5], [6], [7] and [8]. All these pumps are designed as artificial heart replacements or as ventri-cular assist devices (VAD). However, the concepts are not appropriate for use in heart surgery. Their drive- and bearing-system is not separable from the pump. The pump is therefore not disposable because the whole system would be too expensive to throw away after usage.

The requirements for a blood pump in the heart-lung-machine are: simple and cost effective construction of the disposable pump, easy mounting of the pump head in the drive system and in the heart-lung-machine and small priming volume (to save blood). A construction with active magnetic bearings can barely meet those specifications, mainly because of its high costs.

A very interesting solution for a disposable pump is presented by Mendler in [10]. The paper describes a seal-less centrifugal pump with a radial magnetic coupling. 4 of the 6 spatial degrees of freedom of the impeller are stabilised passively by magnetic forces. The other 2 degrees of free-dom are stabilised by a blood-flushed pivot bearing with minimal load and friction. Even if this pump could be a big step forward for centrifugal blood pumps, the pivot bearing remains a problematic point. The need for a cheap disposable blood pump with a fully magnetically suspended rotor is still in demand.

THE NEW APPROACH

Developments at the Laboratory for Electrical Engineering Design (EEK) of the Swiss Federal Institute of Technology (ETH) in Zurich and at several universities in Japan in the field of electrical drives and magnetic bearings have led to the so called "Bearingless Motor" (see [12], [13], [14], [15] and [16]). Recently the ETH Zurich founded a co-operation with two industrial companies: Sulzer Electronics AG, Switzerland and Lust Antriebstechnik GmbH, Germany, for the further development of this new technology. The expression "Bearingless Motor" was first used by Bichsel in [12]. In this content "bearingless" does not mean the lack of bearing forces, which are necessary in any case to stabilise the rotor, but the ommision of significant bearings. The principle of bearingless motor is based on the contactless magnetic bearing of the rotor. In contrast to conventional magnetic levitated drives, the bearing forces are not built up in separate magnetic bearings, which are placed on the left and right side of the motor, but in the motor itself. The active motor part generates not only the torque but also the radial magnetic bearing force, which is needed for the suspension of the rotor.

Normally two motor parts are needed for the full stabilisation of five spatial degrees of freedom. If the length of the rotor is small compared to its diameter, it is possible to stabilise three spatial degrees of freedom passively. Only one active radial bearing is needed. Figure 3 shows the functional principle of such a bearingless slice motor. It is arranged that the rotation and the radial position of the motor slice is controlled actively by the principle of the bearingless motor. The right part of Figure 3 shows an axial displacement of the rotor. The displacement results in attractive magnetic forces, which acts in the opposite direction of the displacement and therefore stabilizes the axial position of the rotor. The left part of the picture shows an angular displacement. It leads to stabilising magnetic forces too.

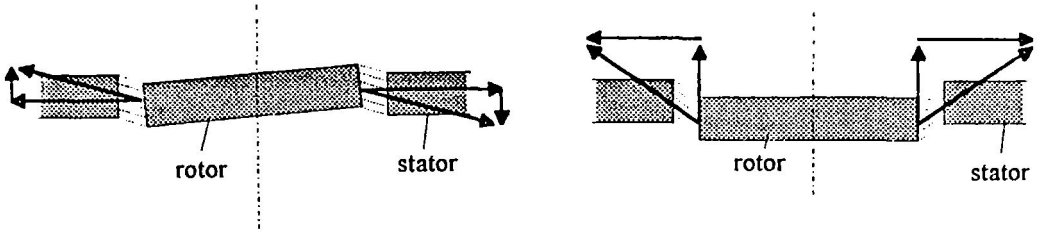

angular displacement axial displacement

Fig. 3: Passive stabilisation of the angular and axial displacement of the slice rotor

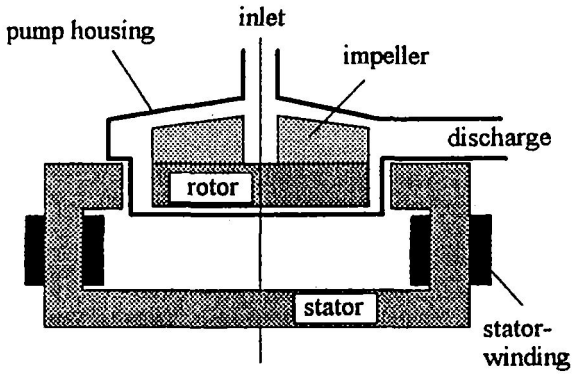

Fig. 4: Principle of the bearingless blood pump

With this "Bearingless Slice Motor", a simple, compact and cost effective solution for a blood pump with a disposable pump part becomes feasible. The rotor-slice can be directly integrated in a plastic impeller by injection moulding. The pump consists of two parts only: the impeller with the integrated motor-rotor and the housing. The principle of this "Bearingless Blood Pump" is shown in Figure 4.

MOTOR DESIGN

In a first step, two prototypes of bearingless slice motors, a synchronous machine and an induction machine, were built. Both motors worked with the same type of stator, which is shown in Figure 5. The stator with 24 slots has two separate two-phase windings. One with one pole pair to generate torque and in the case of the induction motor the machine flux, and one with two pole pairs to generate steering flux. Flux sensors were arranged in the air gap to control the flux and the speed of the motor. An optical sensor system was used to measure the radial position of the rotor.

The goals of these first prototypes were to demonstrate the functional principle of the bearingless slice motor and to prove that the demands of future application could be fulfilled. A

maximum speed of 6000 rpm and a torque of over 10 Ncm were reached with both motors. This exceeds the requirements for the blood pump.

After the feasibility of the bearingless slice motor was proved, two main problems had to be solved: the integration of the disposable pump part into the motor-stator and the measurement of the rotor position through the blood (the solution of the second problem will be described later). Figure 6 shows the disadvantages of the conventional motor design. It is not possible to exit the pump through the stator windings. It was necessary to build the stator in a way that the disposable pump part can be easily changed. Extensive investigations have been done at our lab to achieve this. The solution is a special motor design called temple motor. Its principle is shown in Figure 7.

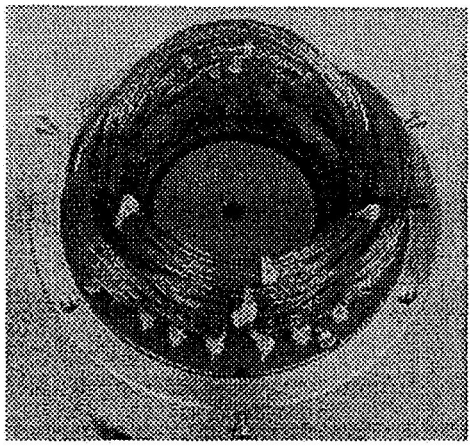

Fig. 5: First prototype of a bearingless slice motor

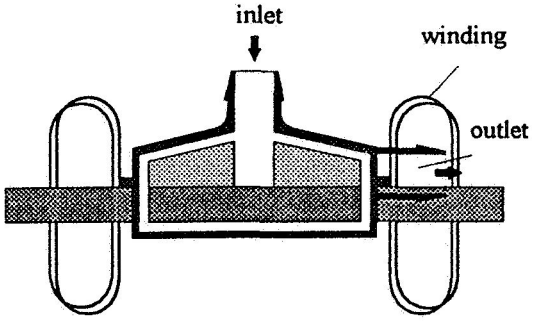

Fig. 6: Problems with the turn windings and the outlet of the disposable pump

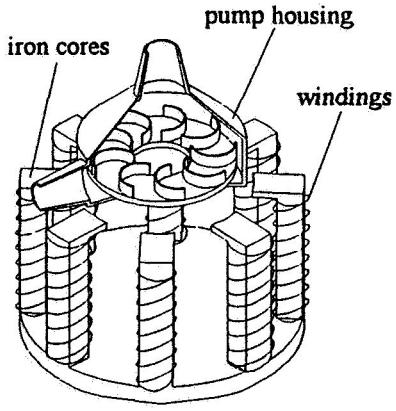

Fig. 7: Principle of the temple motor

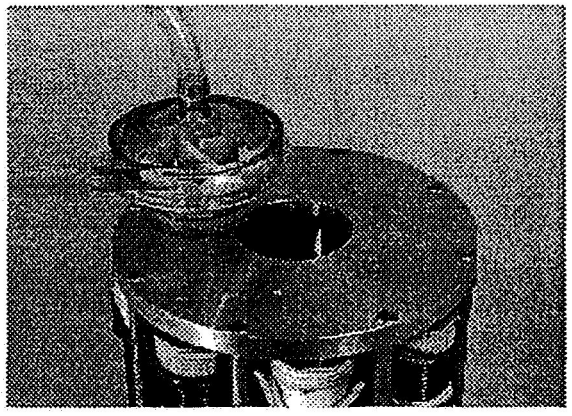

Fig. 8: First prototype of a temple motor for use in a bearingless blood pump

The motor coils are wound on L shaped iron cores and the cores are arranged like columns around the rotor in a way that the L shaped end of a core points to the rotor. With this

arrangement, the disposable pump can easily be pressed in at the top of the stator. The pump can be changed in only a few seconds. For applications in a heart-lung-machine, this is very important because it affects massively the overall setup time of the system.

In the second step an experimental prototype with the above described temple motor design was constructed. Figure 8 shows this prototype. It works after the principle of the bearingless synchronous motor. With this motor a speed of 4500 rpm and a maximum torque of 70 Ncm was reached. It gives the output power of 320 W and exceeds the requirements for the blood pump by a factor of 20. The prototype was already designed for pumping tests. The pump was built with parts of a commercially available blood pump (Saint Jude). After it was proved that bearingless pumping is possible with this arrangement, we immediately started the development of a smaller motor, which is more adapted to the duty of pumping blood. Figure 9 shows this smaller motor with the disposable pump. It reaches again speeds of 4500 rpm but at a lower torque of only 32Ncm. With the St. Jude impeller a maximum flow rate of 12 l/min and a maximum pump height of 5m was reached with water.

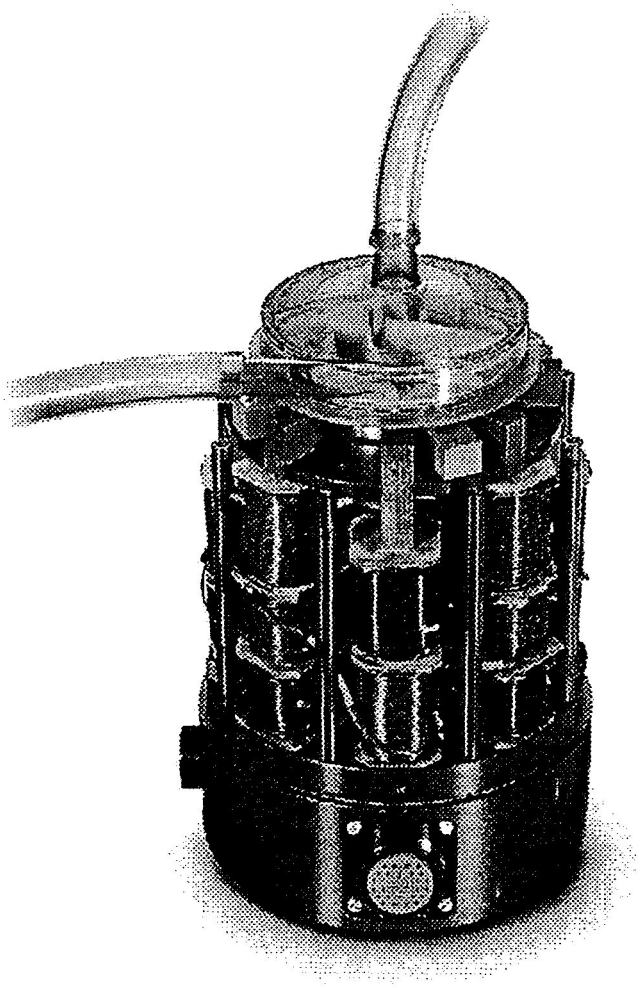

Fig. 9: Actual model of the motor with a disposable pump. The disposable part is built from parts of a commercial blood pump (St. Jude).

CONTROL

With the superposition of a steering-flux (with the pole pairs $p_2 = p_1 \pm 1$) to the motor-flux (with the pole pairs p_1), radial magnetic forces are built up in the bearingless motor. These forces are controlled by the current of the steering winding (with the pole pairs $p_2 = p_1 \pm 1$) and are used for the contactless mounting of the rotor in radial direction. The idea of a radial magnetic bearing in an a.c. motor which uses such a steering winding for the control of the magnetic tensile forces is published by several authors (i.e. [11], [13]). However, the proposed control schemes would work only under limited (steady state) conditions because they are based on the steering of the motor flux. A better control approach, which works also under transient conditions, is described in [15] and [17]. It is based on vector control and considers not only the Maxwell-forces but also the Lorentz-forces in the machine. The second point is especially important for the control of a bearingless synchronous motor with a large air gap like in our application. That is, why we use a vector control based control scheme for our bearingless slice motor. The digital controller is implemented on a self designed TMS 320C50-80 MHz based signal processor board. Commercial switched power amplifiers are used for the actuation of the motor windings. Figure 10 shows the complete blood pump with the necessary control electronics.

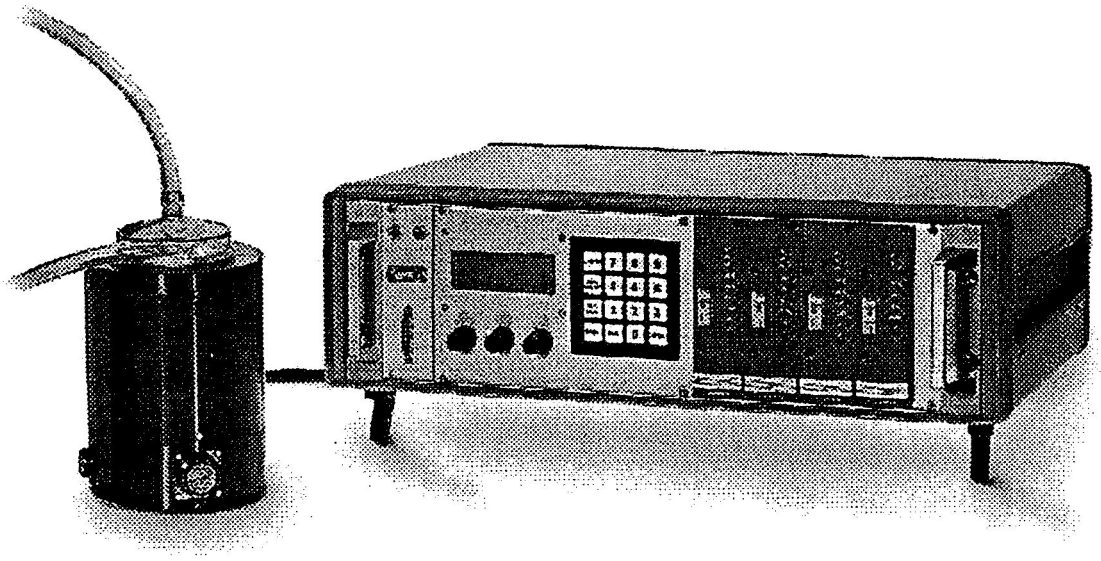

Fig. 10: Complete blood pump with the necessary control electronics.

SENSORS

An exact and fast determination of the flux has a major meaning for the overall quality of the position control. In the prototype system the flux is directly measured in the air gap with hall probes. To achieve immunity to radial rotor displacements it is measured differentially. The arrangement of the flux probes is shown in Figure 11. A total of four flux probes are needed with this method. A much bigger problem is the measurement of the radial rotor position. It is crucial that the position is exactly measured in the middle of the rotor. Otherwise there is a coupling

between the angular displacement of the rotor and the measurement. This coupling leads to instability of the radial position control. The red colour of the blood makes an optical measurement nearly impossible. Ultrasonic measurement is difficult because of the changing flow of the blood and the poor resolution of ultrasonic sensors. With inductive sensors a measurement, free of coupling, is not achievable. An interesting solution for the problem can be found by integrating the air gap flux over two halves of the circumference and by differentially weighting the corresponding magnitudes. If this is done in two quadrants, the radial position of the rotor can be determined. For this principle at least 8 flux probes have to be arranged in the air gap (see Figure 12).

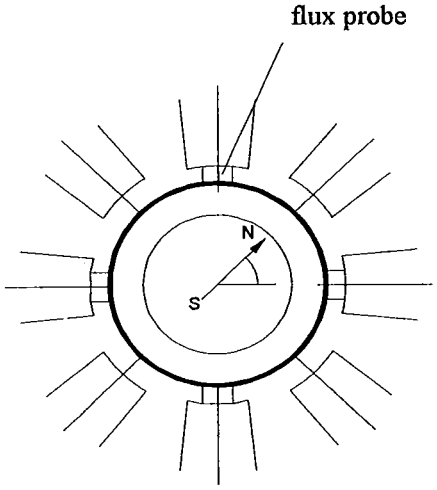

Fig. 11: Arrangement of the flux probes for measurement of the flux angle

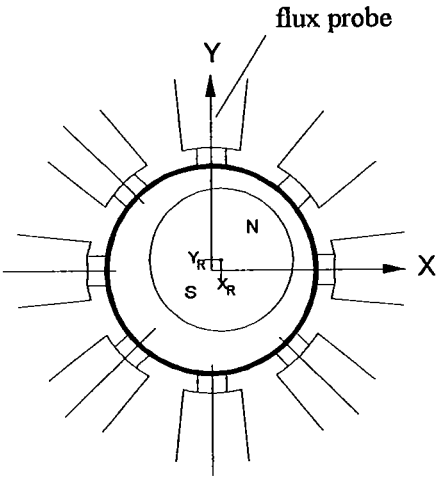

Fig. 12: Arrangement of the flux probes for measurement of the rotor position

TEST RESULTS

The test pump with St. Jude impeller reaches a maximum flow rate of 12 l/min and a maximum pump head of 5m with water at a rotor speed of 2200 rpm. The pumping power is not limited by the motor torque but by the axial forces which act on the rotor, due to the pressure differences on both sides of the impeller. The pressure-flow rate of the pump is more or less the same as of the original St. Jude pump. It is shown in Figure 13 for different rotor speeds. The requirements for the application in open heart surgery are easily achieved.

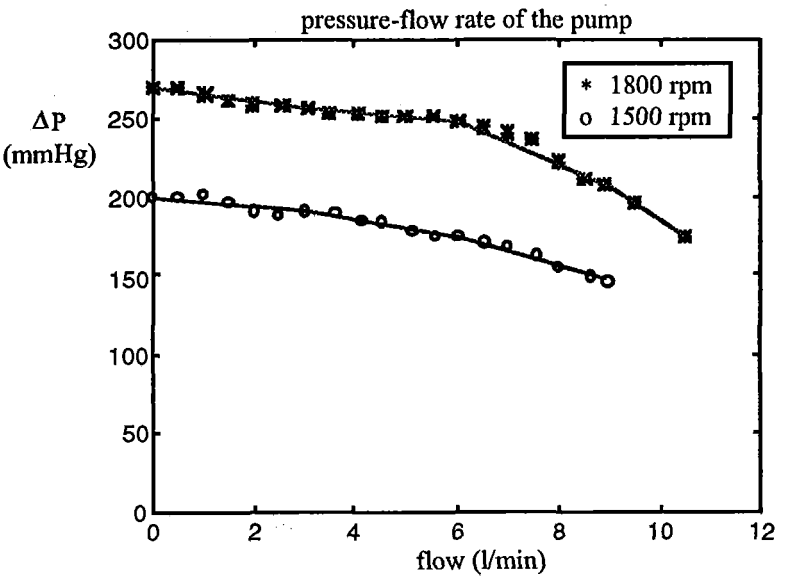

Fig. 13: Pressure-flow rate of the pump with St. Jude impeller for different rotor speeds.

CONCLUSION AND OUTLOOK

In this paper a new concept for a disposable blood pump with a totally magnetically suspended impeller was presented. The pump is based on the "Bearingless Motor" and is therefore called the "Bearingless Blood Pump". The disposable part of the system consists of two parts only: an impeller with the integrated machine rotor and a housing. Fabricated in quantities, it will cost less than $10 and will therefore be affordable for the use in a heart-lung-machine. It was demonstrated that the principle works successfully and that it meets all the requirements for practical use. The "Bearingless Blood Pump" is a reasonable solution to overcome the bearing- and shaft-seal-problems of today's centrifugal blood pumps.

Until now, all experiments have been done by using water. The objective was to prove the functional principle. Further investigations are now planned together with the German Heart Centre of Munich in the field of the pump optimisation to achieve low blood damage.

ACKNOWLEDGEMENTS

The project was supported jointly by the Laboratory for Electrical Engineering Design (EEK) of the Swiss Federal Institute of Technology (ETH) in Zurich and the companies Sulzer Electronics AG, CH-Winterthur and Lust Antriebstechnik GmbH, D-Lahnau.

REFERENCES

[1] Rhee, K. and Blackshear, P. L.: "Bearing and Bearing Seal Cavitation in Blood Pumps," International Workshop on Rotary Blood Pumps, Baden/Vienna, 1991.

[2] Olsen, D. B. and Wamler R. K.: "Continuous Blood-Flow Pumps with Internal and External Motors," International Workshop on Rotary Blood Pumps, Obertauern (Austria), 1988.

[3] Akamatsu, T.: "Developement of Nutating Centrifugal Blood Pump," International Workshop on Rotary Blood Pumps, Obertauern (Austria), 1988.

[4] Schistek, R.; Ghosh, P.; Unger, F.; and Matthias, H. B.: "Is it possible to Avoid Blood Contact of Sealing and Bearings in a Rotary Pump," International Workshop on Rotary Blood Pumps, Obertauern (Austria), 1988.

[5] Bramm, G.; Novak, P. and Olsen, D. B.: "Blood Pump for the Long Term Application with Magnetically Suspended Rotor to Reduce Blood Trauma," 2nd International Workshop of Austrian Society of Artificial Organs, 1981.

[6] Olsen, D. B. and Bramm, G., "Blood Pump with Magnetically Suspended Impeller," Trans. American Society of Artificial Internal Organs, Vol. 31, pp. 395-401, 1985.

[7] Akamatsu, T. and Nakazeki, T., "Recent Developement of a Centrifugal Blood Pump with Magnetically Suspended Impeller," 4th International Symposium on Artificial Heart and Assist Devices, Tokyo, 1992.

[8] Allaire, P. E.; Maslen, E. H.; Bearnson, G. D.; Olsen, D. B.: "Design of a Magnetic Bearing Supported Prototype Centrifugal Artificial Heart Pump," to be presented at the STLE/ASME Tribology Conference, Orlando, 1995.

[9] Mendler, N.; Podechtl, F.; Feil, G.; Hiltmann, P.; Sebening, F.: "Seal-less Centrifugal Blood Pump with Magnetically Suspended Rotor: Rot-a-Flot," Artificial Internal Organs, Vol. 19, Num.7, 1995.

[10] Yamane,T.; Ikeda,T.; Orita,T.; Tsutsui,T.; and Jikuya,T.: "Design of a Centrifugal Blood Pump with Magnetic Suspension," Artificial Internal Organs, Vol. 19, Num.7, 1995.

[11] Hermann, P. K.: Deutsche Offenlegungsschrift Nr.24 06 790

[12] Bichsel, J.: Beiträge zum lagerlosen Elektromotor, Dissertation ETH Zürich, 1990

[13] Chiba, A.; Power, D.T.; Rahman, M.A.: Characteristics of a Bearingless Induction Motor, IEEE Transactions on Magnetics, Vol. 27, No. 6, November 1991

[14] Schöb, R.: Beiträge zur lagerlosen Asynchronmaschine, Dissertation ETH Zürich, 1993

[15] Schöb, R.: Schweizerisches Patentgesuch Nr.00056/94-7

[16] Ohishi, T.; Okada, Y.; Dejima, K.: Analysis and Design of a Concentrated Wound Stator for Synchronous-Type Levitated Rotor, Fourth International Symposium on Magnetic Bearings, Zürich 1994

[17] Schöb, R.; Bichsel, J.: "Vector Control of the Bearingless Motor," 4th International Symposium on Magnetic Bearings, Zurich 1994.

[18] Hugel, J.: "The Vector Method for Determination of Torque nand Forces of the Lateral Force Motor," International Power Electronics Conference, Yokohama 1995.

MAGNETICALLY SUSPENDED LINEAR PULSE MOTOR FOR SEMICONDUCTOR WAFER TRANSFER IN VACUUM CHAMBER

Shin-ichi Moriyama, Naoji Hiraki
Kyushu Institute of Technology, 680-4, Kawazu, Iizuka, Fukuoka 820, Japan

Katsuhide Watanabe
Ebara Research Co., Ltd., 4-2-1, Honfujisawa, fujisawa, Kanagawa 251, Japan

Yoichi Kanemitsu
Kyushu University, 6-10-1, hakozaki, higashi-ku, Fukuoka 812-81, Japan

SUMMARY

This paper describes a magnetically suspended linear pulse motor for a semiconductor wafer transfer robot in a vacuum chamber. The motor can drive a wafer transfer arm horizontally without mechanical contact. In the construction of the magnetic suspension system, four pairs of linear magnetic bearings for the lift control are used for the guidance control as well. This approach allows us to make the whole motor compact in size and light in weight.

The tested motor consists of a double-sided stator and a transfer arm with a width of 50 mm and a total length of 700 mm. The arm, like a ladder in shape, is designed as the floating element with a tooth width of 4 mm (a tooth pitch of 8 mm). The mover mass is limited to about 1.6 kg by adopting such an arm structure, and the ratio of thrust to mover mass reaches to 3.2 N/kg under a broad air gap (1 mm) between the stator teeth and the mover teeth.

The performance testing was carried out with a transfer distance less than 450 mm and a transfer speed less than 560 mm/s. The attitude of the arm was well controlled by the linear magnetic bearings with a combined use, and consequently the repeatability on the positioning of the arm reached to about 2 μm. In addition, the positioning accuracy was improved up to about 30 μm through a compensation of the 128-step wave current which was used for the micro-step drive with a step increment of 62.5 μm.

INTRODUCTION

In the semiconductor manufacturing industries, the demand for a super clean robot without generation of dust particles and release of gas is increasing in connection with shifting the wafer

processes from a clean room to a vacuum chamber. One advantageous method for realizing such a robot is to drive a wafer transfer arm without mechanical contact by means of magnetic suspension techniques (ref.1). For example, we think of a three-dimensional robot as shown in Fig.1 (ref.2). The linear actuator comprises a linear motor and linear magnetic bearings and drives a wafer transfer arm horizontally. A floating body equipped with this actuator is rotatable in the horizontal plane by a rotary actuator, corresponding to a sort of outer rotor. The rotary actuator comprises a rotary motor, radial magnetic bearings and a passive thrust magnetic bearing, being driven vertically by a vertical feed screw assembly. The linear and rotary actuators are hermetically enclosed in a box-like case and a cylindrical wall respectively. Therefore we can operate this robot without any contamination of the vacuum environment in a wafer processing chamber.

In this work, we propose a magnetically suspended linear pulse motor (MSLPM) as the linear actuator of a wafer transfer robot as shown in Fig. 1. Selecting linear pulse motor from among candidate linear actuators is based on a view of precise wafer positioning by open-loop control and is advantageous to vacuum chamber robots which can hardly have sensors for locating the robot arms. In a design of the MSLPM, we must consider the following points. First, it is necessary to make the whole motor compact in size and light in weight because of reduction of the load on a floating body such as the outer rotor in Fig. 1. Second, the MSLPM is required to yield the desired thrust force against a broad air gap which must be arranged in consideration of a wall thickness of the box-like case. Last, the positioning of the arm has to be done with a high resolution from a viewpoint of continuous path control on wafer transfer robots. In this paper, we present a construction of the MSLPM satisfying these demands and discuss the performance.

CONSTRUCTION OF MSLPM

Figure 2 shows the basic structure of the MSLPM. The MSLPM consists of a linear pulse motor (LPM) and four pairs of upper and lower linear magnetic bearings (LMB) and has two features. One is that a ladder-like transfer arm is used as the floating mover of the MSLPM. We have to set a 1 mm air gap between the stator and the mover in consideration of a 0.5 mm wall thickness of the MSLPM case. Selecting such an arm structure is a countermeasure against a marked lowering of thrust force caused by the broad air gap. Another is that the LMB components, namely the electromagnet and the gap sensor, for the lift control are used for the guide control as well. By applying such a combined use, we can divide the MSLPM case into two parts and can realize compactness of the whole motor. The size of the MSLPM is roughly decided from the distance between center axes of the front and back electromagnets, h, and the width of the transfer arm, k. In consideration of an overall arrangement for the LPM and the LMB, we tried designing the MSLPM under the conditions $h = 164$ mm and $k = 50$ mm.

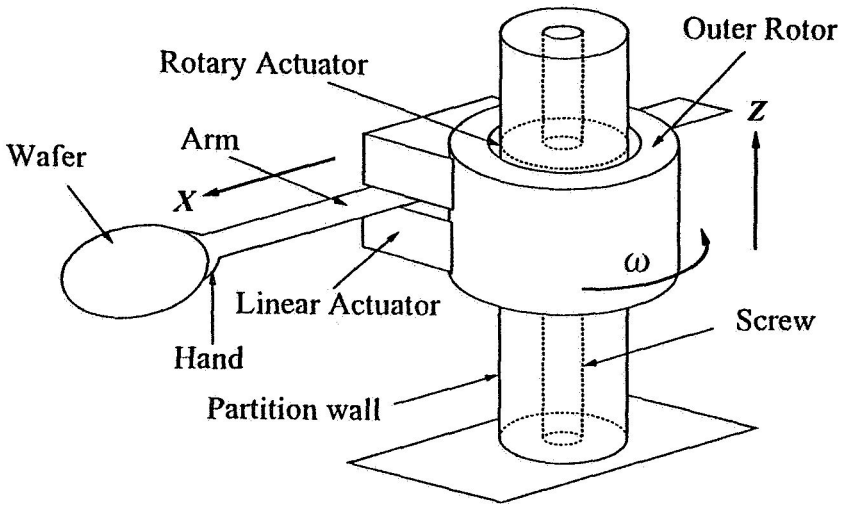

Figure 1. Conceptual diagram of a wafer transfer robot in a vacuum chamber.

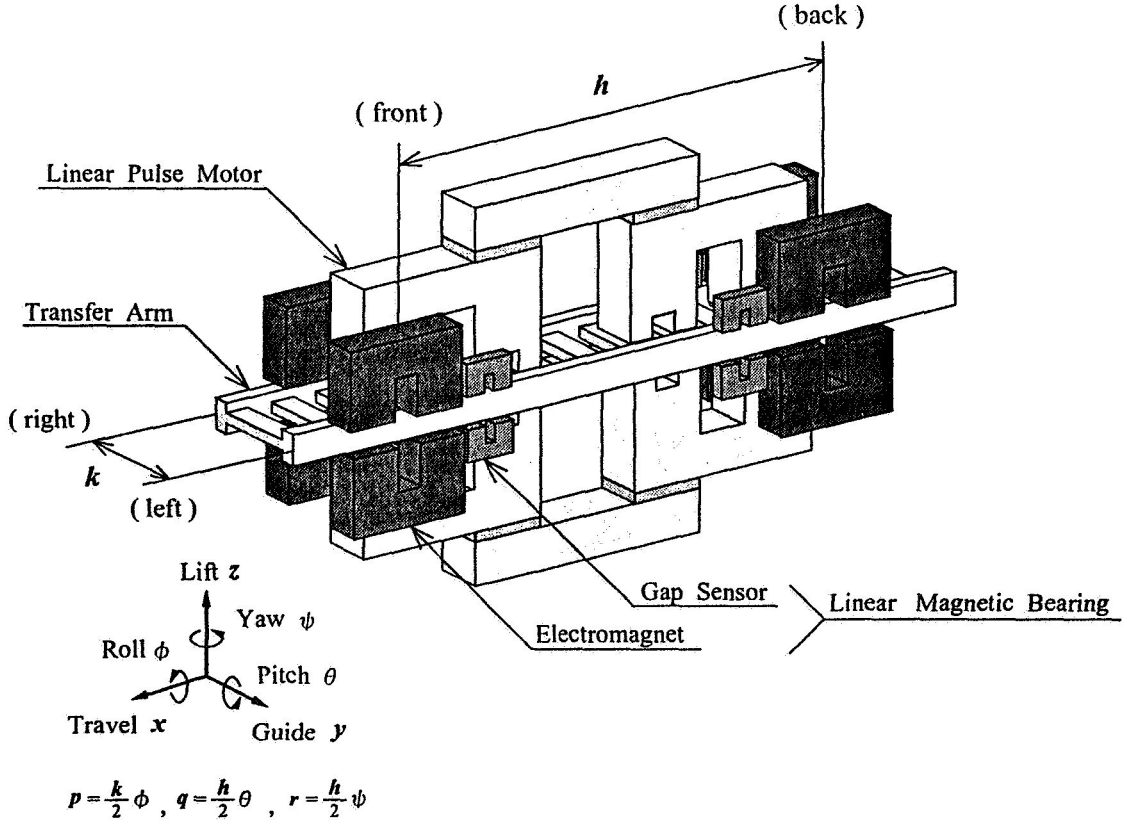

Figure 2. Basic structure of the MSLPM.

The MSLPM is a type of double sided LPM and has a cross sectional structure as shown in Fig.3. There are rungs of the ladder-like arm, namely teeth of the mover alone, between upper and lower parts of the stator. The tooth pitch determining the positioning resolution is twice the tooth width ($2a$). Four permanent magnets inserted in the stator produce a magnetic flux represented by the dotted lines. On the other hand, two pairs of upper and lower electromagnets, namely the A-phase electromagnet with an exciting current I_A and the B-phase one with I_B, form a magnetic flux represented by the solid lines. Therefore, if the total magnetic flux penetrating the mover is efficiently distributed at the tooth region other than the air space, it is possible for the stator to generate the required thrust force in the x -direction. From this point, it is better for the mover tooth to satisfy the condition t (thickness) $\geq a$ (width) $>> \delta$ (gap length). But at the same time we have to consider that the mover mass is larger with t and the positioning resolution is lower with a . Figure 4 shows the typical result of a 2-dimensional magnetic field analysis for the conditions $t = a = 4$ mm and $\delta = 1$ mm. In this analysis, we suppose that the A-phase current is supplied alone. It is found that the magnetic flux is efficiently centered at the two mover teeth under the left magnetic pole of the A-phase electromagnet. From such analytical results, we adopted the above-mentioned tooth dimensions for the ladder-like arm.

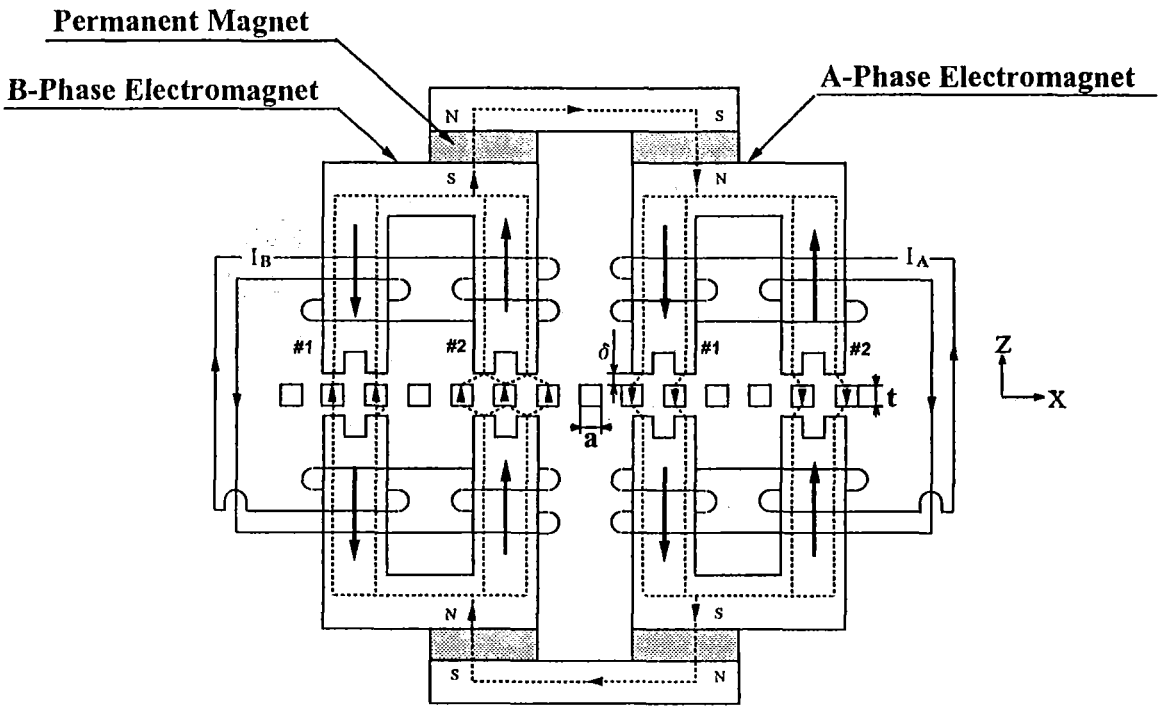

Figure 3. Cross sectional structure of the LPM.

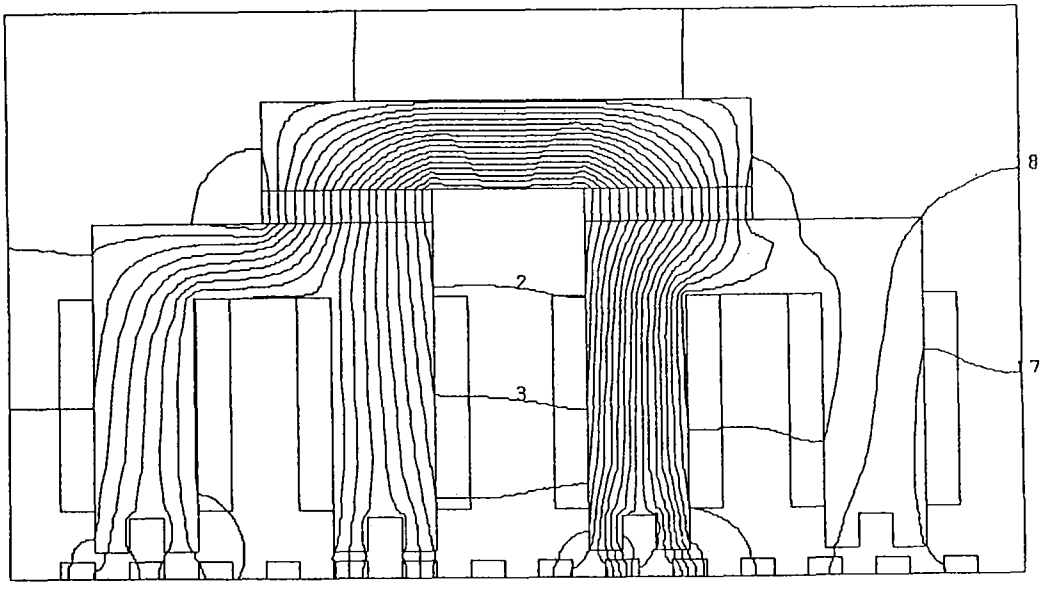

Figure 4. Magnetic flux distribution of the LPM.

In Fig.2, the four pairs of electromagnets are used for the attitude control with five degrees of freedom, that is, lifting (z), guiding (y), rolling (p), pitching (q) and yawing (r). Figure 5 shows a cross section of the two pairs installed at the front of the transfer arm or at the back. The electromagnets are arranged so that the center axes of them can be coincided with both edges of the arm. They are distinguished by the suffixes u (upper), d (lower), l (left), r (right), b (back) and f (front). The clearance between an electromagnet and the arm is expressed with the gap length $\delta_{ij}^{u(d)}$ and the stagger length λ_{ij} as

$$\delta_{ij} = \frac{1}{2}\left(\delta_{ij}^{u} - \delta_{ij}^{d}\right) = \delta_{ij}^{u} - \delta_{0} = \delta_{0} - \delta_{ij}^{d} \tag{1}$$

$$\lambda_{j} = \frac{1}{2}\left(\lambda_{lj} - \lambda_{rj}\right) = \lambda_{lj} - \lambda_{0} = \lambda_{0} - \lambda_{rj} \tag{2}$$

where $i = l, r$, $j = b, f$ and δ_0, λ_0 are the desired values. The attraction force which a pair of upper and lower electromagnets yields in the lifting direction is given by

$$f_{ij} = f_{ij}^{u} - f_{ij}^{d} \sim 2N\delta_{ij} + 2KI_{ij} \tag{3}$$

$$I_{ij} = \frac{1}{2}\left(I_{ij}^{u} - I_{ij}^{d}\right) \tag{4}$$

where N and K are the differential coefficients with respect to the gap length $\delta_{ij}^{u(d)}$ and the exciting current $I_{ij}^{u(d)}$ respectively. The attraction force which the two pairs yield in the

guiding direction is given by

$$f_{Tj}=f_{Tlj}^{u}+f_{Tlj}^{d}-f_{Trj}^{u}-f_{Trj}^{d}\sim 4N_T\lambda_j+4K_T I_{Tj} \tag{5}$$

$$I_{Tj}=\frac{1}{2}\left(I_{lj}^{u}+I_{lj}^{d}\right)-I_0=I_0-\frac{1}{2}\left(I_{rj}^{u}+I_{rj}^{d}\right) \tag{6}$$

where N_T and K_T are the differential coefficients with respect to the stagger length λ_{ij} and the exciting current $I_{ij}^{u(d)}$ respectively and I_0 is a bias current to feed the required attraction force to an electromagnet. From Eqs (1) ~ (6), we get the following controllable forces related to the attitude control:

$$f_z=f_{lb}+f_{rb}+f_{lf}+f_{rf}=-8Nz+8KI_z \tag{7}$$

$$f_p=f_{lb}-f_{rb}+f_{lf}-f_{rf}=-8Np+8KI_p \tag{8}$$

$$f_q=f_{lb}+f_{rb}-f_{lf}-f_{rf}=-8Nq+8KI_q \tag{9}$$

$$f_y=f_{Tb}+f_{Tf}=-8N_T y+8K_T I_y \tag{10}$$

$$f_r=-f_{Tb}+f_{Tf}=-8N_T r+8K_T I_r \tag{11}$$

where $z\sim r$ and $I_z\sim I_r$ are defined with the clearance variables δ_{ij}, λ_j and the current variables I_{ij}, I_{Tj} respectively. The above equations indicate that we can construct the five feedback loops against the attitude displacements $z\sim r$ through converting the supposed current variables $I_z\sim I_r$ to the real exciting currents I_{ij}^{u}, I_{ij}^{d}.

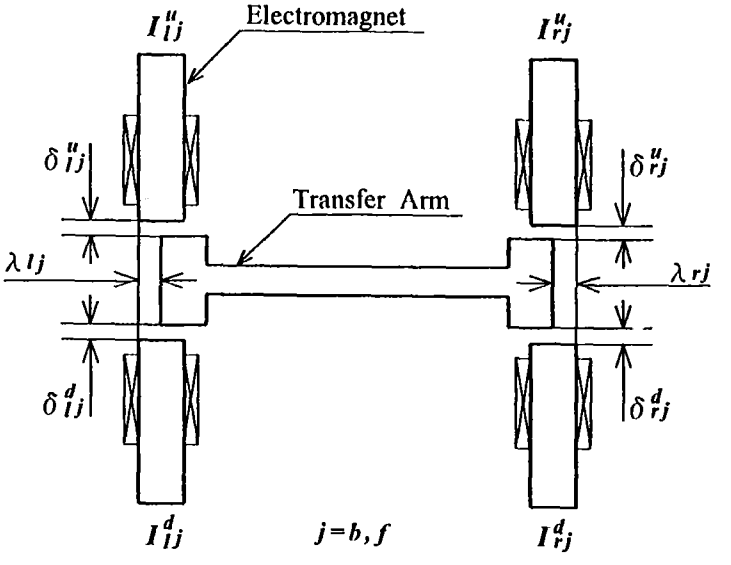

Figure 5. Cross sectional structure of the LMB electromagnets.

On the other hand, the four pairs of gap sensors in Fig.2 are used for the detection of the attitude displacements $z \sim r$. They are installed with the same arrangement as the electromagnets in Fig.5. Figure 6 shows a double-bridged circuit for the two pairs of sensors. The circuit involves the four sensors and the six resistors which are symbolized by the inductances L_{ij}^{u}, L_{ij}^{d} and the resistances $R \sim 4R$ respectively. The inductance given by

$$L_{ij}^{u(d)} \sim L_0 + \alpha\left(\delta_{ij}^{u(d)} - \delta_0\right) + \alpha_T\left(\lambda_{ij} - \lambda_0\right) \tag{12}$$

leads to the output signals

$$\hat{\delta}_{ij} \sim -\frac{GS_0\alpha}{L_0}\delta_{ij} \tag{13}$$

$$\hat{\lambda}_j \sim -\frac{G_T S_0 \alpha_T}{L_0}\lambda_j \tag{14}$$

where α and α_T are the differential coefficients with respect to the gap length $\delta_{ij}^{u(d)}$ and the stagger length λ_{ij} respectively and L_0 is the desired value. Since the signals $\hat{\delta}_{ij}$ and $\hat{\lambda}_j$ are proportional to the clearance variables δ_{ij} and λ_j respectively, we can easily convert them to the attitude displacements $z \sim r$.

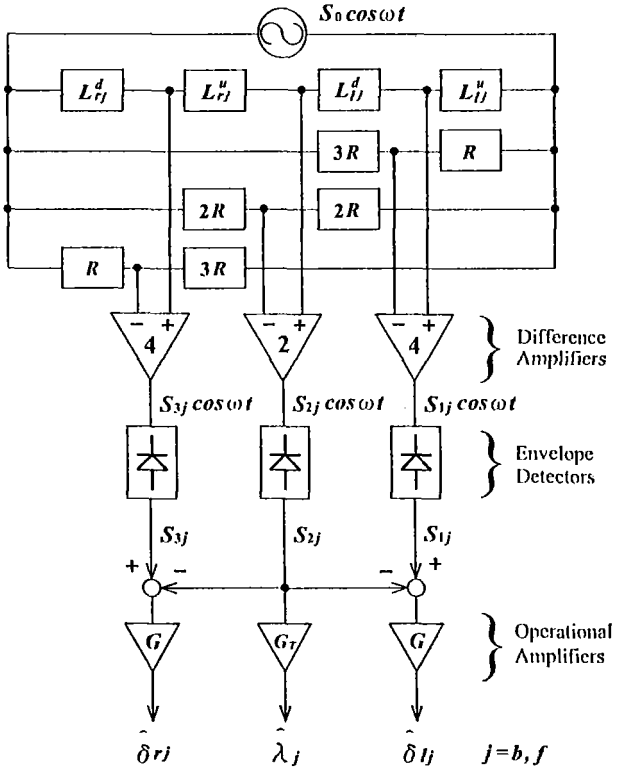

Figure 6. A double-bridged circuit for the gap sensors.

PERFORMANCE TEST

We made a MSLPM stator and a transfer arm as a trial. Figure 7 shows an apparatus for examining the performances of the tested MSLPM. The two stator parts are put in the upper and lower cases respectively. We could restrict the inside volume of each case to 212 mm by 74 mm by 61 mm. The arm has a total length of 700 mm and is movable to an optional position less than 450 mm. We also could limit the mass of the arm to 1.56 kg. The laser displacement meter is used for measuring the location of the arm over the performance test, and the load cell is used only for measuring the static thrust force of the MSLPM.

The performance test was carried out with two controllers as shown in Fig.7. The LPM controller forms an open-loop drive system for the micro-step positioning of the arm. The microprocessor supplies the command of the transfer speed, $\hat{v}$. And the logic sequencer produces the signals of the A-phase and B-phase exciting currents, $\hat{I}_A$ and $\hat{I}_B$, and the count of a series of timing pulses, $\hat{x}$. The count $\hat{x}$ is returned to the microprocessor as the positioning signal. If it reaches to the set position $\hat{x}_0$, then the command $\hat{v}$ is turned off. The timing pulses are generated at a frequency proportional to the command $\hat{v}$. The signals $\hat{I}_A$ and $\hat{I}_B$ change by each timing pulse according to waveform data stored in two read-only-memories beforehand. As a result, the LPM electromagnets are magnetized by 128-step wave currents and the arm is located by the micro-step drive with a step increment of $2a$ / 128 (62.5 μm).

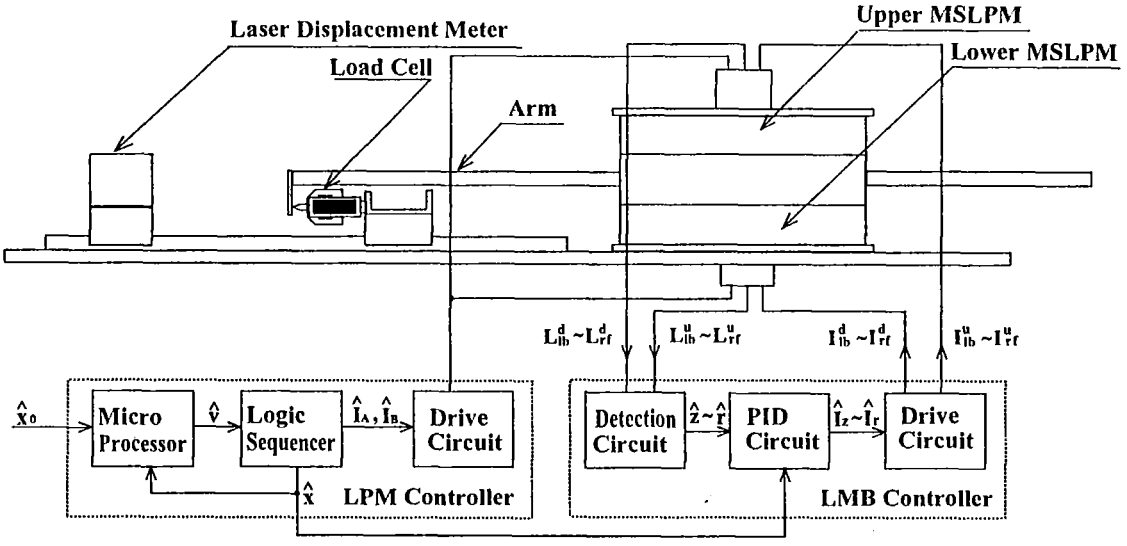

Figure 7. An apparatus for the performance test.

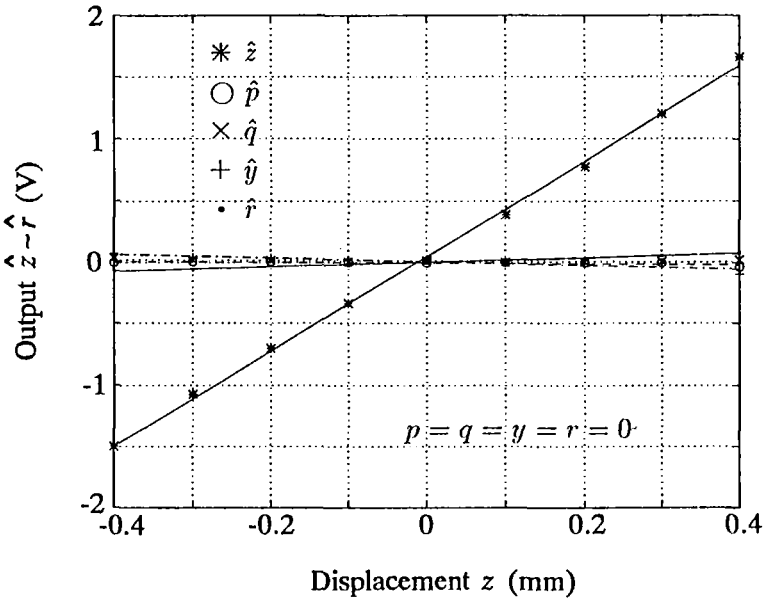

Figure 8. Dependence of output signals on the displacement z.

On the other hand, the LMB controller forms a feedback system for the attitude control of the arm. The detection circuit, which includes double-bridged circuits as shown in Fig.5, produces the displacement signals $\hat{z} \sim \hat{r}$, and the PID (proportional-integral-differential) circuit produces the control signals $\hat{I}_z \sim \hat{I}_r$. Regarding the signal $\hat{I}_q$, the positioning signal $\hat{x}$ from the LPM controller is considered to cancel an unbalance force in the pitching direction. The drive circuit controls the current of each LMB electromagnet according to the signals $\hat{I}_z \sim \hat{I}_r$, and consequently the arm is magnetically supported with a standard attitude. We carried out a calibration of the detection circuit before the performance test. We supported the arm by four micrometers in the lifting direction and by two in the guiding direction, and then moved in each direction of $z \sim r$. Figure 8 shows the typical result of the calibration. For the movement only in the z-direction, the signal $\hat{z}$ increases in proportion to the displacement z and the other signals are little produced. We obtained the same results for the signals $\hat{y} \sim \hat{r}$. We also estimated the following sensitivity from the inclination of a fitted line as shown in Fig.8: 3.95 V/mm for $\hat{z}$, 3.25 V/mm for $\hat{p}$, 1.89 V/mm for $\hat{q}$, 2.01 V/mm for $\hat{y}$ and 1.14 V/mm for $\hat{r}$.

The static thrust characteristic is one of fundamental performances of the MSLPM and must be estimated accurately. So we first measured the static thrust force while suspending the arm by the LMB. Figure 9 shows the typical results. There is little difference between the A-phase thrust force and the B-phase one. The maximum thrust force at $I_A = 0.7$ A or at $I_B = 0.7$ A can be estimated to 5.1 N. Thus the ratio of thrust force to mover mass becomes 3.2 N/kg.

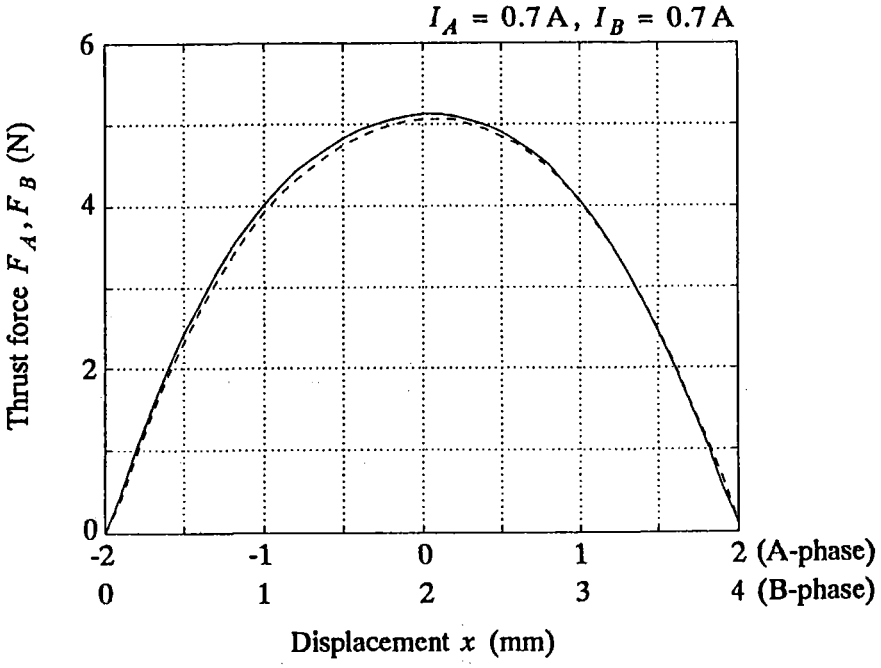

(a) Static thrust force versus displacement.

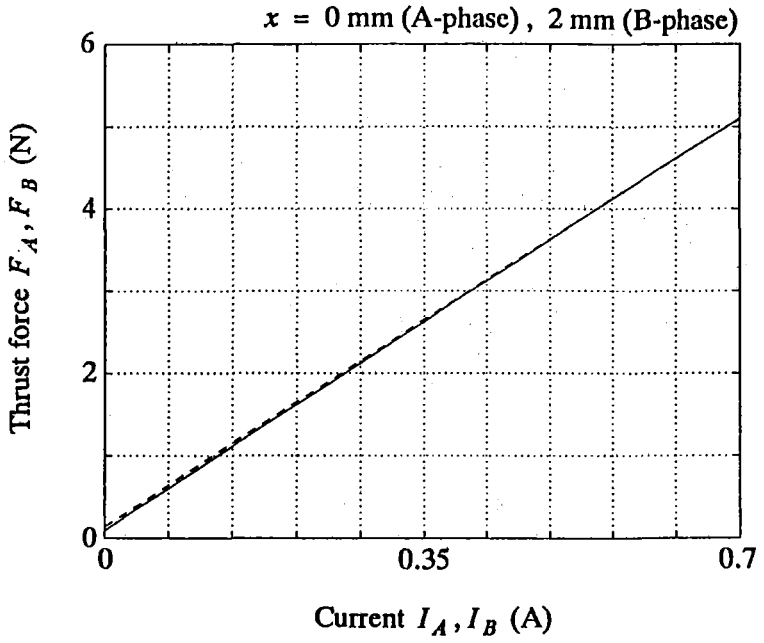

(b) Static thrust force versus exciting current.

Figure 9. Static thrust characteristics of the MSLPM. The solid and dotted lines indicate a A-phase force and a B-phase one respectively.

From the measuring results shown in Fig.9, we can express the thrust forces as

$$F_A = I_A \left\{ K_1 \cos\left(\pi \frac{x}{a}\right) - K_3 \cos\left(3\pi \frac{x}{a}\right) \right\} \tag{15}$$

$$F_B = I_B \left\{ K_1 \sin\left(\pi \frac{x}{a}\right) + K_3 \sin\left(3\pi \frac{x}{a}\right) \right\} \tag{16}$$

where $K_1 = 7.7$ A/N and $K_3 = 0.4$ N/A. In the above equations, each second term on the right hand side is regarded as a third harmonic component on the static thrust versus displacement characteristic. Here we neglect the third harmonic component because $K_3 << K_1$, and insert the sine wave currents

$$I_A = I_1 \sin\left(\pi \frac{\hat{x}}{a}\right) \tag{17}$$

$$I_B = -I_1 \cos\left(\pi \frac{\hat{x}}{a}\right) \tag{18}$$

to Eqs (15) and (16). Consequently, we can express the work load on the total thrust force $F = F_A + F_B$ as

$$\int_x^{x+a} F_1 \sin\left(\pi \frac{\hat{x}}{a} - \pi \frac{x}{a}\right) \mathrm{d}\hat{x} = \frac{1}{2} m \left(\frac{\mathrm{d}x}{\mathrm{d}t}\right)^2 \tag{19}$$

where $F_1 = K_1 I_1 = 5.4$ N and m is the mover mass. From the above equation, the starting speed

$$v_0 = \left(\frac{4\,a\,F_1}{\pi m}\right)^{1/2} \tag{20}$$

is derived, being estimated to 133 mm/s. Since the maximum slewing speed generally becomes several times the starting speed, we can expect a transfer speed of 300 mm/s to 500 mm/s.

Next, we examined the performances on the traveling of the arm. Figure 10 shows the typical results. The arm is accelerated up to a speed of 300 mm/s under the sine wave excitation as given by Eqs. (17) and (18), and then it is stopped at a set position of 400 mm after the slowdown to a waiting speed. The arm also is moved in reverse with the same speed pattern, and then it is returned at the original position. In this round trip, though the arm seems to be significantly displaced from the standard attitude in the r-direction, the displacement is smaller than the allowable value. Thus it can be said that the arm is moving horizontally while keeping sufficient clearance for the upper and lower cases. We carried out round trips and measured the stop position every time the arm was returned. As a result, the repeatability was estimated to about 2μm. Furthermore, we examined a limit of the steady speed in a trapezoidal speed pattern as shown in Fig. 10, and consequently obtained a maximum speed of 560 mm/s. On the other hand, the maximum speed measured with a step-speed pattern, namely the starting speed, was 125 mm/s. It is in good agreement with the expected value mentioned in the previous paragraph. This suggests that a work load of the MSLPM to the arm is perfectly converted into a kinetic energy of the arm. This ideal energy transformation together with the excellent repeatability may be a remarkable feature of the MSLPM.

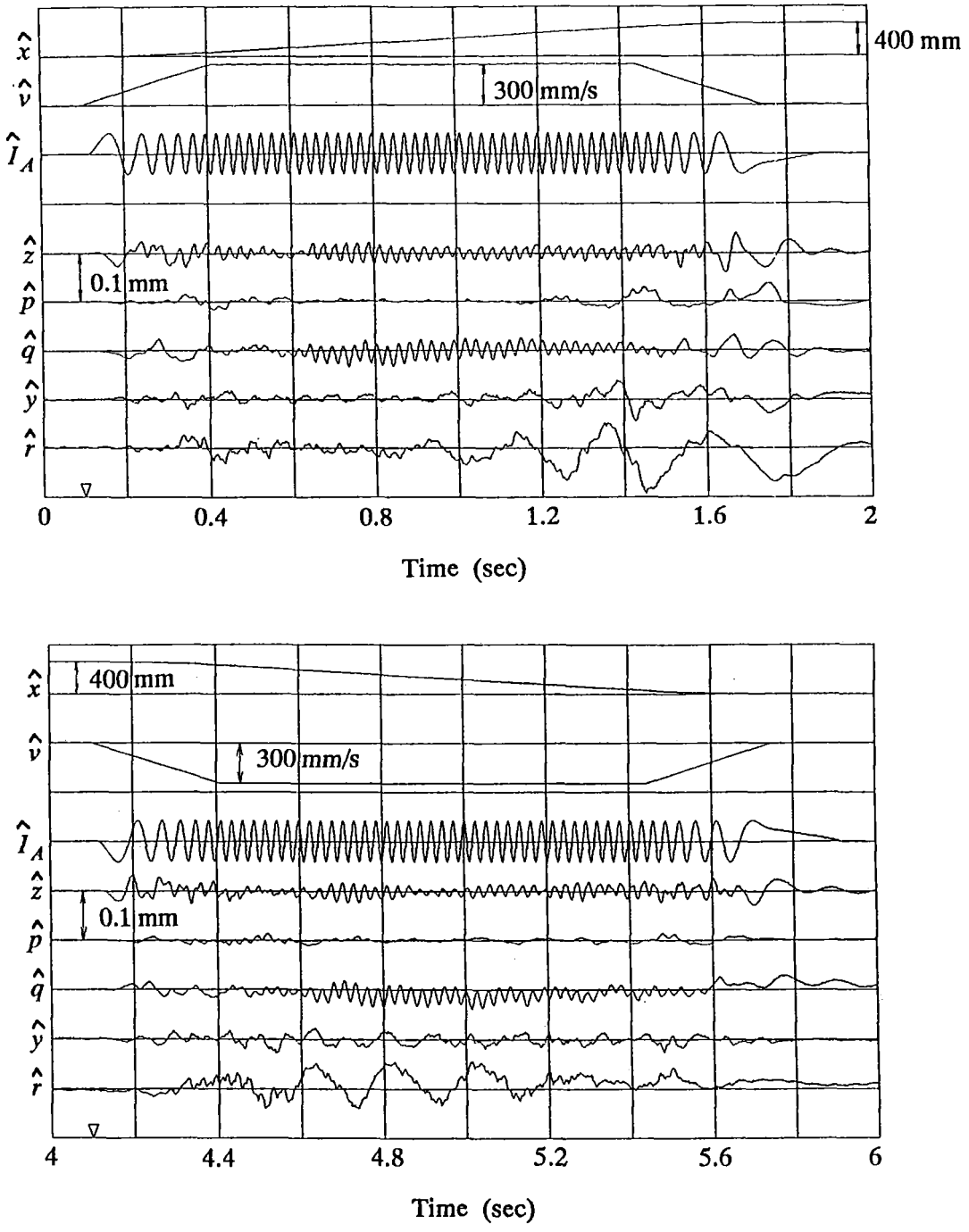

Figure 10. Time evolution of the positioning signal $\hat{x}$, the speed command $\hat{v}$, the A-phase signal $\hat{I}_A$ and the displacement signals $\hat{z} \sim \hat{r}$ during traveling the arm forward and backward. Each displacement of $z \sim r$ is expressed with a scale of 0.1mm/div. and the allowable value determined by the clearance between the arm and the MSLPM cases is as follows: ± 0.5 mm for z, ± 0.58 mm for p, ± 0.26 mm for q, ± 1.0 mm for y, ± 0.51 mm for r.

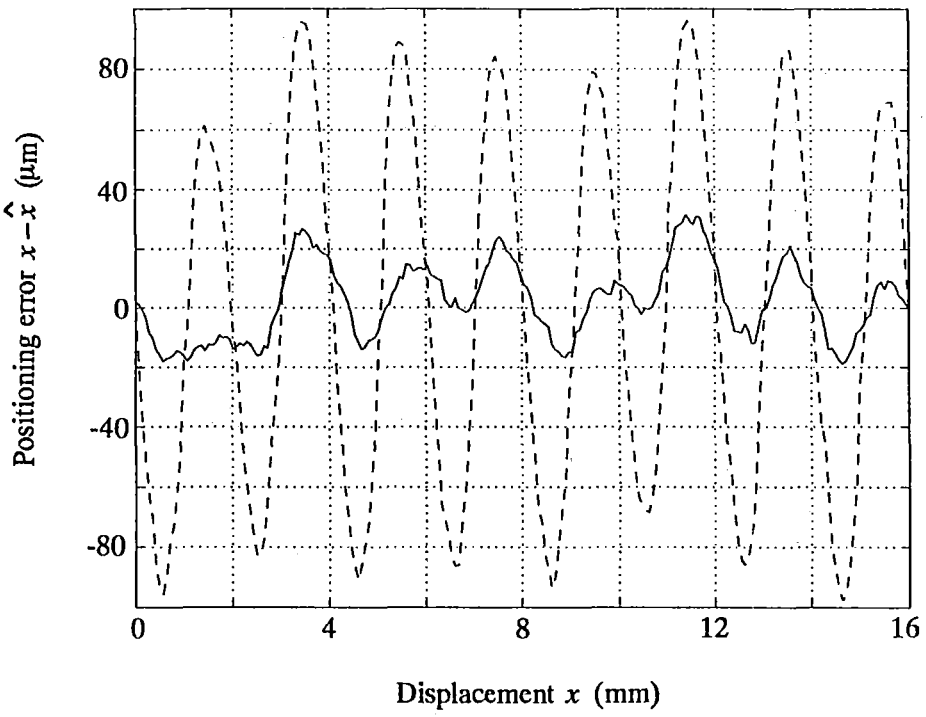

Figure 11. Positioning error on the micro-step drive. The dotted and solid curves indicate a step error for the sine wave excitation and one for the compensated excitation respectively.

Lastly, we examined the positioning error of the micro-step drive due to the sin wave excitation. As a result, it was found that there was a periodical error as shown by the dotted curve in Fig.11. The amplitude of the error $x-\hat{x}$ is more than the step increment of the micro-step drive. It is inferred that such an error is mainly due to a mismatching between the sine wave currents and the static thrust characteristics. From Eqs (15) ~ (18), the total thrust force involving the third harmonic component can be expressed by

$$F = F_1 \sin\left(\pi\frac{\hat{x}}{a} - \pi\frac{x}{a}\right) - F_3 \sin\left(\pi\frac{\hat{x}}{a} + 3\pi\frac{x}{a}\right) \tag{21}$$

where $F_3 = K_3 I_1 = 0.3\,\mathrm{N}$. Considering the condition $|x-\hat{x}| << a$ at $F=0$, we can find that there is a periodical error with the period $a/2$ (2 mm) and the amplitude $a F_3/\pi F_1$ (70 μm). This supposed error is similar to the measured one.

The positioning error due to the static thrust characteristics can be reduced by matching the exciting currents with higher-order harmonic components. The exciting currents matched with the third harmonic components in Eqs (15) and (16) are given by

$$I_A = I_1 \sin\left(\pi\frac{\hat{x}}{a}\right) + I_3 \tan\left(\pi\frac{\hat{x}}{a}\right)\cos\left(3\pi\frac{\hat{x}}{a}\right) \tag{22}$$

$$I_B = -I_1 \cos\left(\pi \frac{\hat{x}}{a}\right) + I_3 \cot\left(\pi \frac{\hat{x}}{a}\right) \sin\left(3\pi \frac{\hat{x}}{a}\right) \tag{23}$$

where $I_3 = I_1 K_3 / K_1$. The above equations lead to the ideal thrust forces without third harmonic component under the conditions $|K_3| << K_1$ and $|x - \hat{x}| << a$. By applying such a compensation to the 128-step wave currents, the positioning error became less than 30 μm, as shown by the solid curve in Fig.11.

CONCLUSION

We have constructed the magnetically suspended linear pulse motor in order to develop the linear actuator suitable to a wafer transfer robot in the ultra-high vacuum environment. The features and performances are as follows.

(1) The linear magnetic bearings combining the lift control and the guide control are used in the magnetic suspension system. By omitting them for the guide control, the case used for enclosing this motor hermetically can be divided into two parts. This is advantageous to a compactness of the linear actuator.

(2) The floating mover is the ladder-like arm with a total length of 700 mm and a width of 50 mm. The tooth width (pitch) is 4 mm (8 mm) and the air gap length is 1 mm. By adopting this arm, the mover mass is limited to about 1.6 kg and the ratio of thrust to mover mass reaches to 3.2 N/kg under the broad air gap.

(3) The attitude of the arm is well controlled by the magnetic suspension system, and consequently the clearance between the arm and the case is sufficiently maintained even during translation of the arm.

(4) The arm is horizontally movable with a transfer distance less than 450 mm and a transfer speed less than 560 mm/s by means of the micro-step positioning system. The positioning resolution, namely the step increment of the micro-step drive, is 62.5 μm. The positioning repeatability is about 2 μm and the positioning accuracy is about 30 μm. The performances indicate that this motor is sufficiently applicable to the wafer transfer robot.

REFERENCES

1. Ota, M.; Andoh, S.; and Inoue, H.: Mag-Lev Semiconductor Wafer Transporter for Ultra-High-Vacuum Environment, *Proc. 2nd Int Symp. on Magnetic Bearings*, July 12-14, 1990, pp. 109-114.
2. Wtanabe, K.; Kanemitsu, Y.; Shinozaki, H.; Hiraki, N.; and Moriyama, S.: Robot with Dust-Free and Maintenance-Free Actuators, US Patent 5,397,212.

PARAMETER DESIGN AND OPTIMAL CONTROL OF AN OPEN CORE FLYWHEEL ENERGY STORAGE SYSTEM*

D. Pang
Hua Fan College of Humanities and Technology
Shihtin, Taiwan

D. K. Anand
Professor of Mechanical Engineering
University of Maryland

J. A. Kirk
Professor of Mechanical Engineering
University of Maryland
College Park, MD 20742 USA

ABSTRACT

In low earth orbit [LEO] satellite applications spacecraft power is provided by photovoltaic cells and batteries. To overcome battery shortcomings the University of Maryland, working in cooperation with NASA/GSFC and NASA/LeRC, has developed a magnetically suspended flywheel for energy storage applications. The system is shown in Figure 1 and is referred to as an Open Core Composite Flywheel [OCCF] energy storage system.

Successful application of flywheel energy storage requires integration of several technologies, viz. bearings, rotor design, motor/generator, power conditioning, and system control.

In this paper we present a parameter design method which has been developed for analyzing the linear SISO model of the magnetic bearing controller for the OCCF shown in Figure 2. The objective of this continued research is to principally analyze the magnetic bearing system for nonlinear effects in order to increase the region of stability, as determined by high speed and large air gap control. This is achieved by four tasks: (1) physical modeling, design, prototyping, and testing of an improved magnetically suspended flywheel energy storage system, (2) identification of problems that limit performance and their corresponding solutions, (3) development of a design methodology for magnetic bearings, and (4) design of an optimal controller for future high speed applications.

Both nonlinear SISO and MIMO models of the magnetic system were built to study limit cycle oscillations and power amplifier saturation phenomenon observed in experiments. The nonlinear models

* This research was partially supported by a contract from NASA-Goddard Space Flight Center and FARE, Inc.

include the inductance of EM coils, the power amplifier saturation, and the physical limitation of the flywheel movement as discussed earlier. The control program EASY5 is used to study the nonlinear SISO and MIMO models.

Our results have shown that the characteristics and frequency responses of the magnetic bearing system obtained from modeling are comparable to those obtained experimentally. Although magnetic saturation is shown in the bearings, there are good correlations between the theoretical model and experimental data. Both simulation and experiment confirm large variations of the magnetic bearing characteristics due to air gap growth. Therefore, the gap growth effect should be considered in the magnetic bearing system design.

Additionally, the magnetic bearing control system will be compared to other design methods using not only parameter design but H^{∞} optimal control and μ synthesis.

INTRODUCTION

Although the control system and the magnetic bearing are an integral system, it is possible to independently evaluate and optimize the performance of the control system for a given plant.

The design of the flywheel energy storage (FES) plant is based on a pancake-shaped PM/EM magnetic bearing and a spokeless composite flywheel proposed earlier [1,2]. Based upon this design, four different prototypes of the FES system have been built and tested in the Magnetic Bearing Laboratory. The first prototype was built using a 3-inch magnetic bearing, a DC brushless motor, an aluminum flywheel and the prototype tested at a maximum speed of 9,333 RPM to demonstrate system feasibility. Next a 3-inch magnetic bearing stack using two magnetic bearings without a motor and an aluminum flywheel was spun by an air jet up to 7,000 RPM. Finally, a prototype consisting of two 4-inch magnetic bearings, a commercial off-the-shelf PM DC brushless motor, and an aluminum flywheel was built. The 4-inch magnetically suspended flywheel energy storage system was tested with a very limited performance. Anand, et al. [3] developed a new FES system using two newly improved magnetic bearings, a high efficiency PM DC motor/generator, and an aluminum flywheel. The system achieved a maximum speed of 6,800 RPM in air. With improvements to the magnetic bearings, the motor/generator, the power/control electronics, the vacuum chamber, and the composite flywheel, Wells, Pang, and Kirk [4] tested the final FES system shown in Fig. 1 at a maximum speed of 20,000 RPM with a total stored energy of 15.9 WH and an angular momentum of 54.8 N-m-s (40.4 lb-ft-s).

This research is specifically concerned with control system performance for the bearing shown in Fig. 1 and discussed in reference [5]. It must be noted that the results obtained in this study apply over a broad range of magnetic bearing parameters and can therefore be thought of as general conclusions. The magnetic bearings and Flywheel Energy Storage System shown in Fig. 1 has been extensively studied from a design viewpoint and reported in [5]. The control of this bearing was achieved by the proportional and derivative (PD) control system whose block diagram is shown in Fig. 2. This SISO model is duplicated to provide four independent and identical PD control systems used to control four degrees of freedom in the FES system of Fig. 1

There have been many advancements in the control system design and dynamic analysis for the FES system. For the original linear single-input-single-output (SISO) control system for the magnetic bearing,

Jayaraman [6] derived dynamic equations and analyzed dynamic responses of a linear multi-input-multi-output (MIMO) model. Zmood, et al., [7] developed a nonlinear SISO model of magnetic bearing to study limit cycle oscillations. Anand, et al., [3] used a parameter optimization method and the JEYCAD program [8] to create a control system with desired gain and phase margins. Fittro [9] developed a hybrid multi-layered neural network controller for a nonlinear SISO magnetic bearing models. Wells, Pang, and Kirk [4] built an adjustable stiffness and damping controller for the final FES system.

The design of the control system is constrained by the characteristics of the magnetic bearing such as load capability and linear range. Figure 3 shows typical experimental testing results of the magnetic bearing. Curves A and C are plotted as force and control current responses versus displacement at a fixed gain of the control system. Curves B and D are plotted at a higher gain. It shows that the net restoring force reaches its peak when the power amplifier becomes saturated and cannot supply more current. The distance between the center and the peak is called the linear range where the bearing should be operated. The slopes of curves A and B are the radial stiffness of the bearing. Notice that the linear range is dependent on the gain of the control system, the maximum control current of the power amplifier, and the magnetic saturation of the material. The bearings should be designed to have a maximum linear range with a proper load carrying capability.

Two design methods, the component design and the parameter design, have been developed for analyzing the linear SISO model of Fig. 2. The parameter design adjusts the critical parameter values to satisfy the gain margin and phase margin specifications for a robust control system. The parameters can be derived by the selection of the resistance and/or capacitance in the electrical circuit. The JEYCAD software program [8] was specifically written to provide a component design tool for this application. It allows the user to input the component data of the control system, and it will compute the appropriate transfer functions and the bearing characteristics. The JEYCAD program includes the Classic Control (CC) software program, which allows the designer to plot the frequency and time response of the control system and compare it to the performance specifications.

Both nonlinear SISO and MIMO models of the magnetic system are built to study limit cycle oscillations and power amplifier saturation phenomenon observed in experiments. The nonlinear models include the inductance of EM coils, the power amplifier saturation, and the physical limitation of the flywheel movement as discussed earlier. The control program EASY5 is used to study the nonlinear SISO and MIMO models.

Simulation and experimentation have identified that the inductance of the EM coils and the voltage limitation of the power amplifier are the causes for magnetic suspension failure. After these problems were corrected, the FES system achieved a maximum speed of 20,000 RPM and was stopped by current limitation of the motor controller. At 20,000 RPM, there is no gap growth effect and the gyroscopic motion does not yet cause any instability. At this speed, the existing control system design based on the linear SISO model has been proved to be robust and reliable.

MODELING AND VALIDATION

Physical modeling is critical to the success of the design and control for a magnetically suspended flywheel energy storage system. At low speeds, the system can be simplified and decoupled as a linear single-input-single-output (SISO) model. However, the linear model cannot explain some observed

phenomena such as the power amplifier saturation, the third harmonic noise, and the limit cycle oscillation. At high speeds, rotational stress causes flywheel deformation and air gap growth, which changes bearing characteristics. In addition, the gyroscopic effect of the flywheel couples the two radial axes motions so the system becomes a nonlinear multi-input-multiple-output (MIMO) problem. Detailed modeling is discussed in [5]. These models are refinements of earlier work and, in general, include non-linear effects and disturbances.

Experimental tests have been conducted on the magnetic bearings and the FES system to validate the modeling of (1) the magnetic bearing characteristics, (2) the gap growth effects, and (3) the frequency responses of the magnetic bearing system.

The experimental results of the bearing characteristics are used to validate the mathematical model of the magnetic bearing used here [5]. The theoretical values of passive radial stiffness and axial stiffness are computed with the empirical data from flux density measurements. The active stiffness, maximum radial force, linear range and stable range are affected by maximum control current and the current displacement ratio of the feedback control.

There are reasonably good correlations between the theoretical and experimental data for stiffness and the linear range. The maximum radial force has a large modeling error due to magnetic saturation. It is apparent that the increase of the radial force slows as the displacement increases from the center. Another indication is that the slope of the corrective force decreases as the current increases. However, the maximum radial force is not critical since the magnetic bearing mostly operates within the range of $\pm$ 0.038 mm (0.0015 in) where the modeling error for the radial force is small.

Because the rotational stress causes an outward deformation of the flywheel and increases the air gap at high rotating speeds, the characteristics of magnetic bearing will change as a function of the speed. It has been estimated that the air gap is increased between 0.10 and 0.41 mm (0.004 and 0.016 in) when a composite flywheel rotates between 40,000 and 80,000 RPM. The increase is more than 40% of the nominal air gap of 1.02 mm (0.04 in) at zero speed. The large variation of the air gap will change bearing characteristics and affect the FES system performance. This phenomenon, called gap growth effect, cannot be ignored and must be considered in the magnetic bearing system design.

The mathematical equations for the gap growth effects suggest that the air gap growth has great impact on the change of bearing characteristics at high rotational speeds. In order to simulate the gap growth effect on the magnetic bearing system, all the radial dimensions of the return rings are enlarged by the same magnitude as the gap growth. Simulation shows that as the air gaps increase by 10% and 21% of the original value, the passive stiffness decreases to 22% and 37%, and the force current stiffness to 14% and 28% of their original values. Because the change of the bearing characteristics is much larger than the change of the air gap, the gap growth effect cannot be ignored in the high speed applications. With reasonable confidence in the plant model briefly discussed above, and detailed in [5], it is appropriate that the control system performance be further analyzed and optimized.

The frequency response of the FES system is analyzed using control software EASY5. The simulation has the following assumptions:

(1) All the characteristics of the magnetic bearings are identical,

(2) All the control systems and displacement sensors are the same,

(3) The rotor dynamics of the system corresponds to a rigid body motion,

(4) There is no electrical saturation or time delay in the power amplifier,

(5) There is no magnetic saturation or nonlinearity in the magnetic bearings,

(6) The resistance of the EM coils can be ignored,

(7) The motor/generator has no effects on the magnetic bearing system.

The parameters of the control system, displacement sensor, and power amplifier for one-axis of the FES system are discussed in [5].

Figure 4 shows the displacement frequency responses of the FES system and its theoretical model. Both experimental and simulative results show similar trends with little difference. The FES system has a flat displacement frequency response until it reaches its natural frequency. The current frequency response of the system is almost constant throughout the frequency range. The voltage output always increases as the frequency increases but the trend in the actual system slows beyond 110 Hz. Similar conclusions can be reached from the current and frequency responses.

Validation of the characteristics and frequency responses of the magnetic bearing system indicate that there are good correlations between the theoretical model and experimental data.

PARAMETER DESIGN

The existing controller for the magnetic bearing system was designed with a parameter design method that achieves desirable gain margin and phase margin discussed in the previous section. The existing controller provides a stable system operation up to 20,000 RPM. However, the magnetic bearing system has air gap growth at high rotating speeds which causes bearing characteristics to change. In this section, an optimal control system is proposed using H^{∞} method and μ synthesis to account for gap growth effect and other plant uncertainties at high rotational speeds. Although the existing controller can achieve stable performance at the maximum gap growth, it is still desired to have better performance with larger bandwidth and faster settling time.

A parameter design method, proposed by Chang and Han [10], is used to find the desired gain margin and phase margin of control systems with adjustable parameters. Consider a system having an open loop transfer function G(s) and a unit feedback loop with the system having adjustable parameters. The characteristic equation of the control system can be written in the frequency domain and expressed in terms of a real part and an imaginary part, with both parts equal to zero.

$$F_r(j\omega) = F_r(\alpha, \beta, \gamma, \ldots, A, \theta, j\omega) = 0 \quad (1)$$

$$F_i(j\omega) = F_i(\alpha, \beta, \gamma, \ldots, A, \theta, j\omega) = 0 \quad (2)$$

Any two parameters can be solved from these equations by keeping the rest of the parameters constant.

In order to achieve the desired gain margin and phase margin of the control system, the following three loci are drawn on the two-parameter plane.

(1) The locus of A = 1 and $\theta = 0$

(2) The locus of A = gain margin and $\theta = 0$,

(3) The locus of A = 1 and θ = phase margin.

The first locus is a boundary of marginal stability of the control system. The second locus is a boundary of a constant gain margin and the third locus is a boundary of a constant phase margin. The enclosed region of these three loci will satisfy the minimum gain margin and phase margin. After the parameters are chosen, the parameters can be written as the form of circuitry components. The component values can be found by solving a set of linear equations.

Since the gain and time constant of the zero in the control system are the two most important parameters, they are selected using the parameter design. The two-parameter plane of the gain K and time constant τ_1 is plotted in Fig. 5. In order to achieve a gain margin of 4 and a phase margin of 40°, the K and τ_1 are chosen to be 1.04 and 0.0033.

The result of the parameter design was implemented in an adjustable stiffness and damping controller developed for the magnetic bearing system. The adjustable stiffness and damping controller allows the change in gain and zero in the electric circuit which affect bearing characteristics. The control system design has been proven to be robust by supporting the flywheel without any failure.

OPTIMAL CONTROL

H^∞ optimal control [5] offers a robust system performance by solving disturbance rejection and plant uncertainties. The H^∞ control system design minimizes the H^∞ norm of a pre-designed closed-loop transfer function. Because the H^∞ norm is the maximum singular value over all frequencies, the controller has good performance even at worst system conditions.

For a stable control system, the H^∞ norm of the transfer function must be less than 1. The objective of a H^∞ optimal control is to find a stabilizing controller K(s) such that the norm is minimized. A mixed sensitivity design is generally used to provide a direct and effective approach for the H^∞ optimal control. For a mixed sensitivity optimization problem, the objective is to find a stabilizing controller K(s) such that the norm of the weighted sum of the sensitivity function and the complementary sensitivity function is at a minimum.

The approach employing μ synthesis [5] provides a robust control design by solving parameter variations, unstructured uncertainties, and performance requirements. The μ synthesis can also be used to analyze robustness of the control system by calculating its structure singular value. The objective of the μ synthesis is to find a stabilizing controller and a diagonal scaling matrix such that a minima of a minima of the smallest uncertainty is found. This computation requires iterative processes. The controller is calculated using the H^∞ control method with a fixed scaling nature which is solved by optimization search techniques with a fixed controller. Theoretically, the μ synthesis controller is less conservative compared to the H^∞ optimal controller but the μ synthesis demands more computation time and sometimes does not converge.

Because of the gap growth, the average values for the stiffness increases for the H^∞ optimal control design. The weighting function W_1 is selected to achieve a bandwidth of at least 250 rad/s and a radial stiffness of 289 N/mm (1650 lb/in). The weighting function is designed to handle the parameter variation caused by the gap growth and unstructured uncertainties at 1000 rad/s. The H^∞ optimal controller is solved by using computer software MATLAB.

The closed loop frequency response of the FES system at the maximum gap growth is shown in Fig. 6. The system has a flat and smooth response with a bandwidth of 1000 rad/s. The step input response of the system shown in Fig. 7 has an overshoot of 4% and a settling time of 0.003 s.

An optimal controller applying μ synthesis was used to handle parameter variations of the stiffness and control energy limitation. The control system has the same physical plant as the H^∞ optimal controller and a zero order of the diagonal matrix is used to avoid a large order controller design. The control system is designed using MATLAB software. The system has a bandwidth of 70 rad/s at the maximum gap growth as shown in Fig. 8. The step input response of the system shown in Fig. 9 displays an overshoot of 9% and a settling time of 0.009 s.

CONCLUSION

The characteristics and frequency responses of the magnetic bearing system obtained from modeling are comparable to those obtained experimentally. Although magnetic saturation is shown in the bearings, there are good correlations between the theoretical model and experimental data. Both simulation and experiment confirm large variations of the magnetic bearing characteristics due to air gap growth. Therefore, the gap growth effect should be considered in the magnetic bearing system design.

The magnetic bearing control system was designed using three different methods, the parameter design, H^∞ optimal control, and μ synthesis. Because the existing controller using the parameter design never considers any plant uncertainty, it has the worst performance with a limited bandwidth, a large overshoot, and a long settling time. The H^∞ optimal controller takes into consideration the plant uncertainties, bandwidth, and disturbance attenuation, and achieves the best performance. However, the H^∞ optimal controller requires very large gain and control energy, which may not be possible in real applications. The optimal controller using μ synthesis considers parameter variations of passive stiffness and current force stiffness as well as control energy limitation. It achieves a good performance in bandwidth, settling time, and overshoot. Although its performance is not as good as the H^∞ optimal controller, it demands less gain and control energy.

REFERENCES

1. Kirk, J.A.: Flywheel Energy Storage Part I - Basic Concepts. *International Journal of Mechanical Science*, vol. 19, no. 4, 1977, pp. 223-231.

2. Kirk, J.A.; and Studer, P.A.: Flywheel Energy Storage Part II - Magnetically Suspended Superflywheel. *International Journal of Mechanical Science*, vol. 19, no. 4, pp. 233-245.

3. Anand, D.K.; Kirk; J.A.; Zmood, R.B.; Pang, D.; and Lashley, C.: Final Prototype of Magnetically Suspended Flywheel Energy Storage System. *Proceedings of 26th Intersociety Energy Conversion Engineering Conference*, Boston, MA, August 4-11, 1991.

4. Wells, S.; Pang, D.; Kirk, J.A.: Manufacturing and Testing of a Magnetically Suspended Composite Flywheel Energy Storage System. *Proceedings of 2nd International Symposium on Magnetic Suspension Technology*, NASA CP-3247, Seattle, WA, August 11-13, 1993.

5. Pang, D.: Magnetic Bearing System Design for Enhanced Stability. Ph.D. Dissertation, University of Maryland, College Park, MD, 1994.

6. Jayaraman, C.P.: Dynamic Analysis of Magnetic Bearing Stack. M.S. Thesis, University of Maryland, College Park, MD 1988.

7. Zmood, R.B.; Pang, D.; Anand, D.K.;and Kirk, J.A.: On the Nonlinear Operation of Magnetic Bearings. Internal Document, Magnetic Bearing Laboratory, University of Maryland, College Park, MD, 1990.

8. Jeyaseelan, M.: A CAD Approach to Magnetic Bearing Design. M.S. Thesis, University of Maryland, College Park, MD, 1988.

9. Fittro, R.L.: Neural Network Controller Design for a Magnetic Bearing Flywheel Energy Storage System. M.S. Thesis, University of Maryland, College Park, MD, 1993.

10. Chang, C.; and Han, K.: Gain Margins and Phase Margins for Control Systems with Adjustable Parameters. *Journal of Guidance, Control, and Dynamics*, Vol. 13, No. 3, May-June 1990.

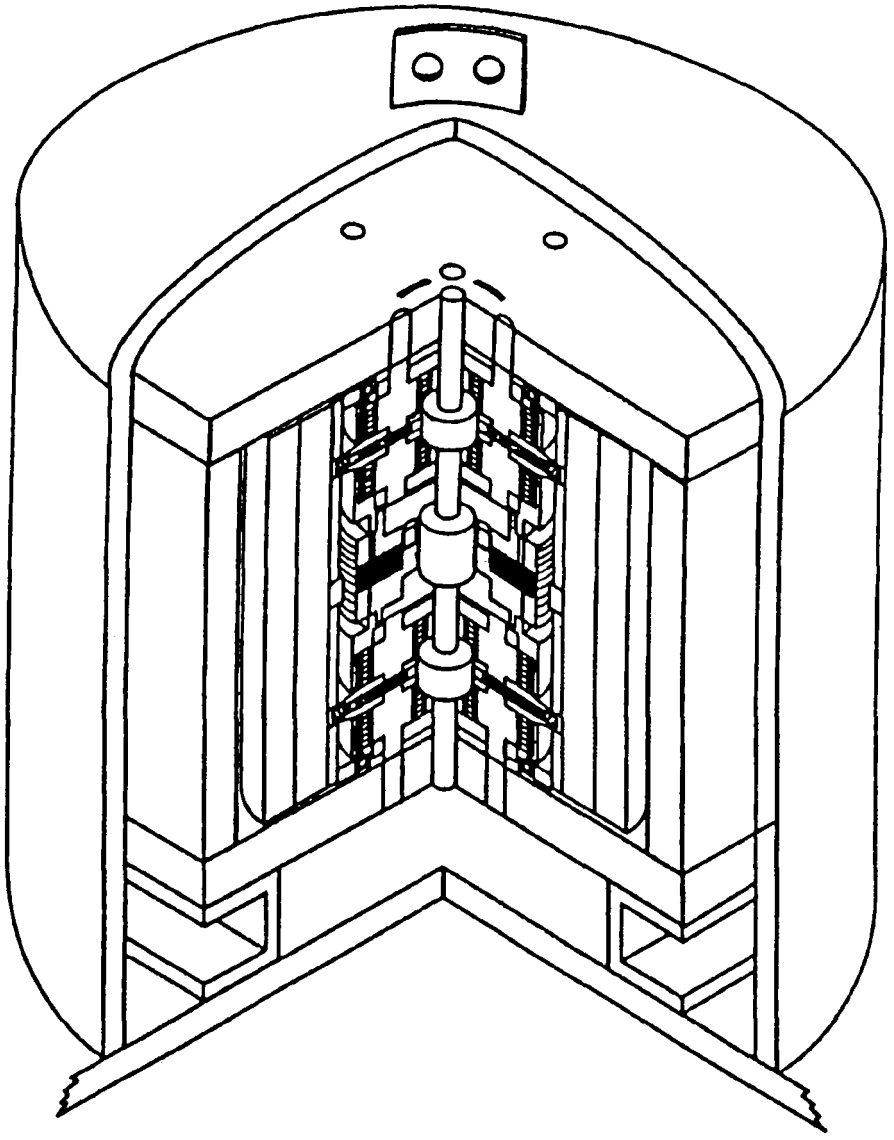

Figure 1 - Schematic of OCCF System

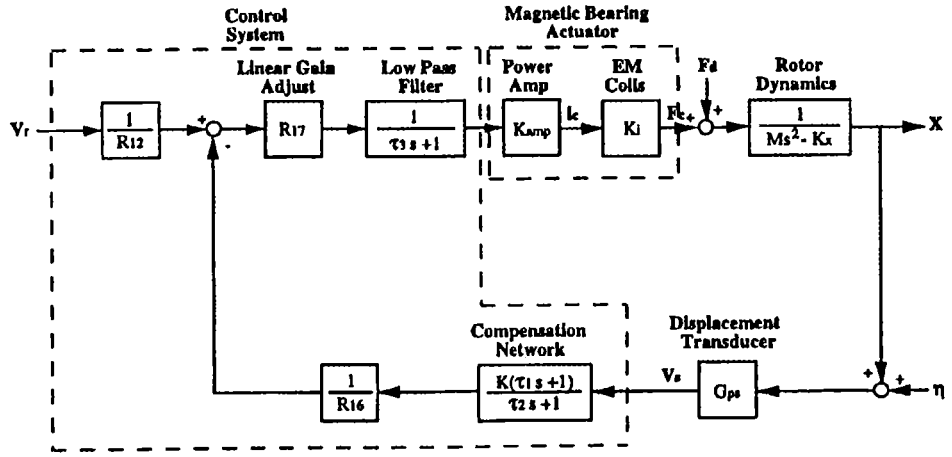

Figure 2 - Linear SISO Model of Magnetic Bearing System

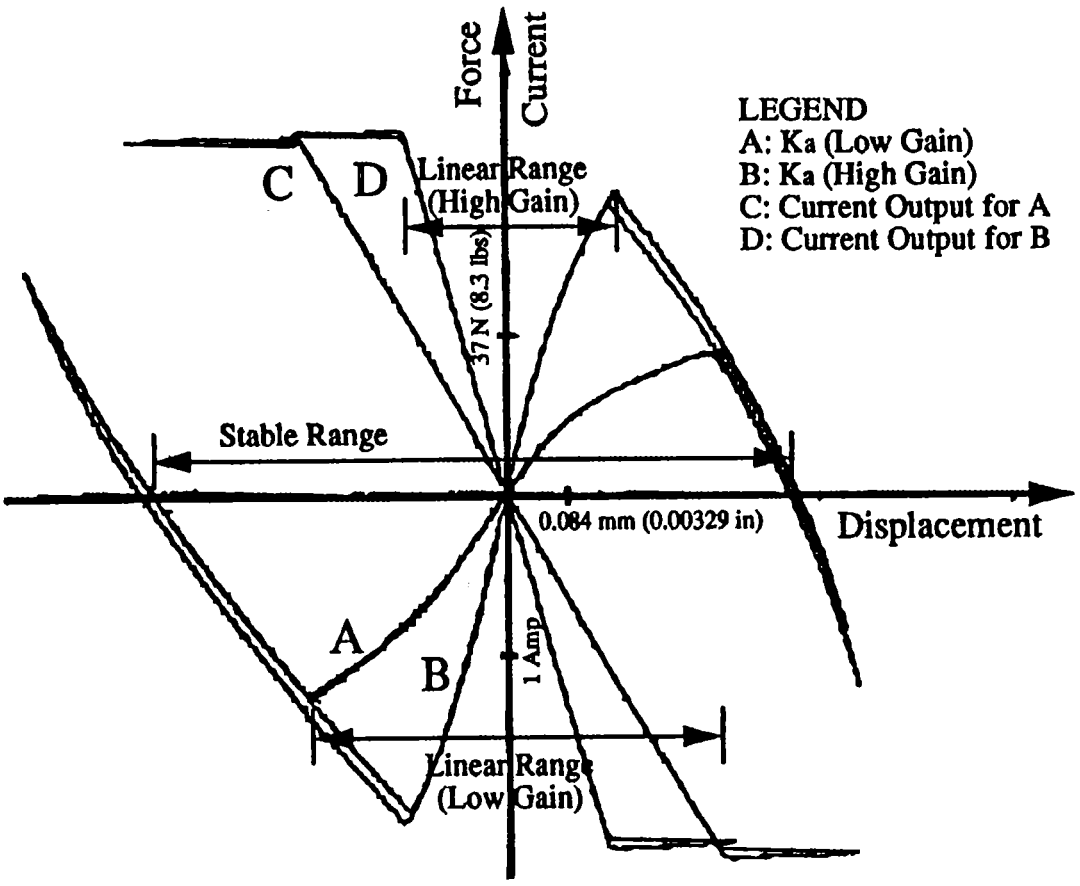

Figure 3 - Experimental Test of PM/EM Magnetic Bearing Characteristics

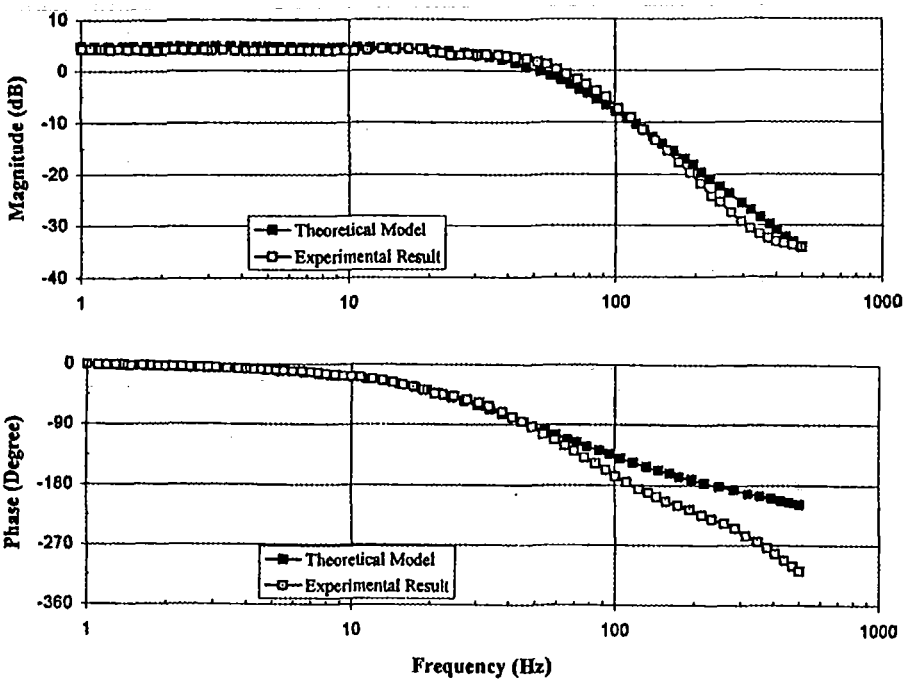

Figure 4 - Displacement Frequency Response of FES System

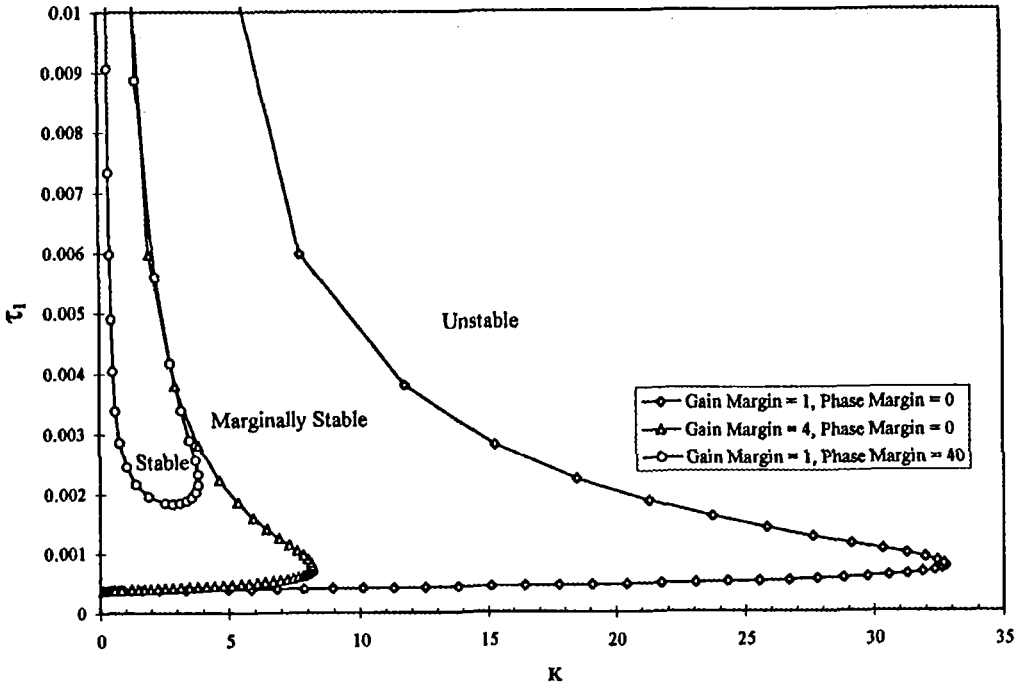

Figure 5 - Control System Parameter Design

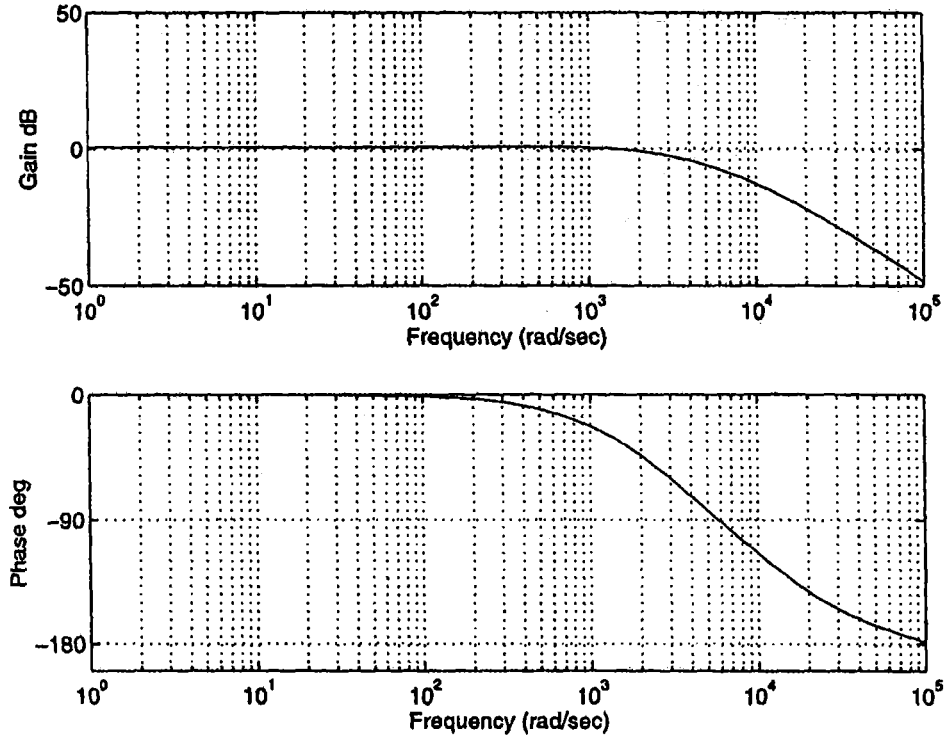

Figure 6 - Closed Loop Frequency Response Using H^{∞} Optimal Controller

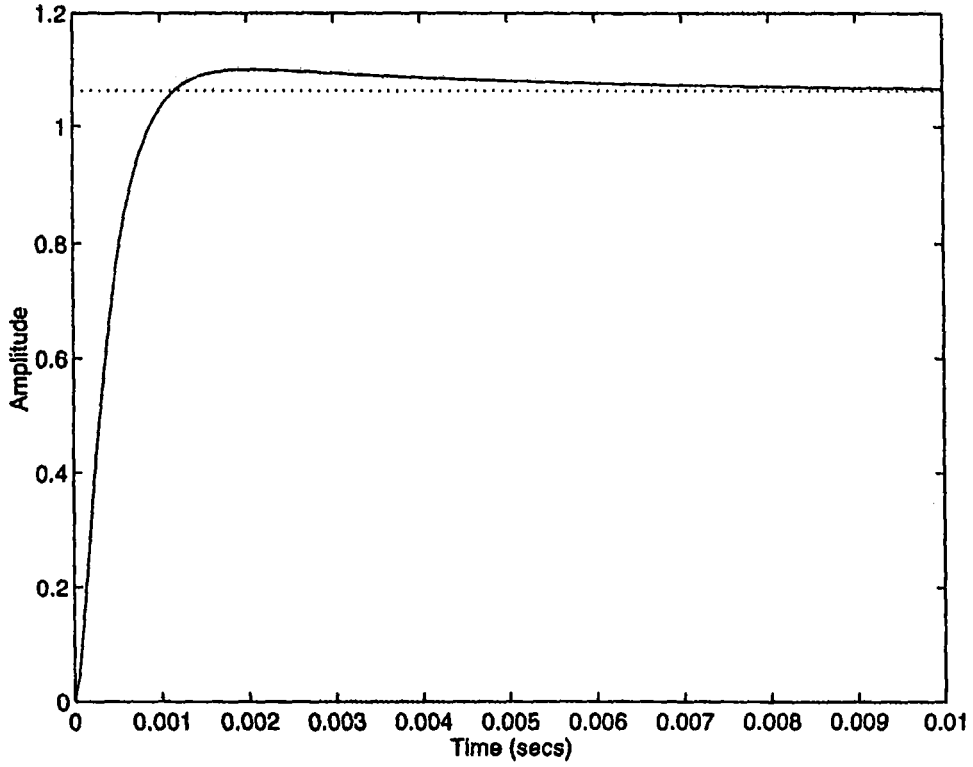

Figure 7 - Step Input Response Using H^{∞} Optimal Controller

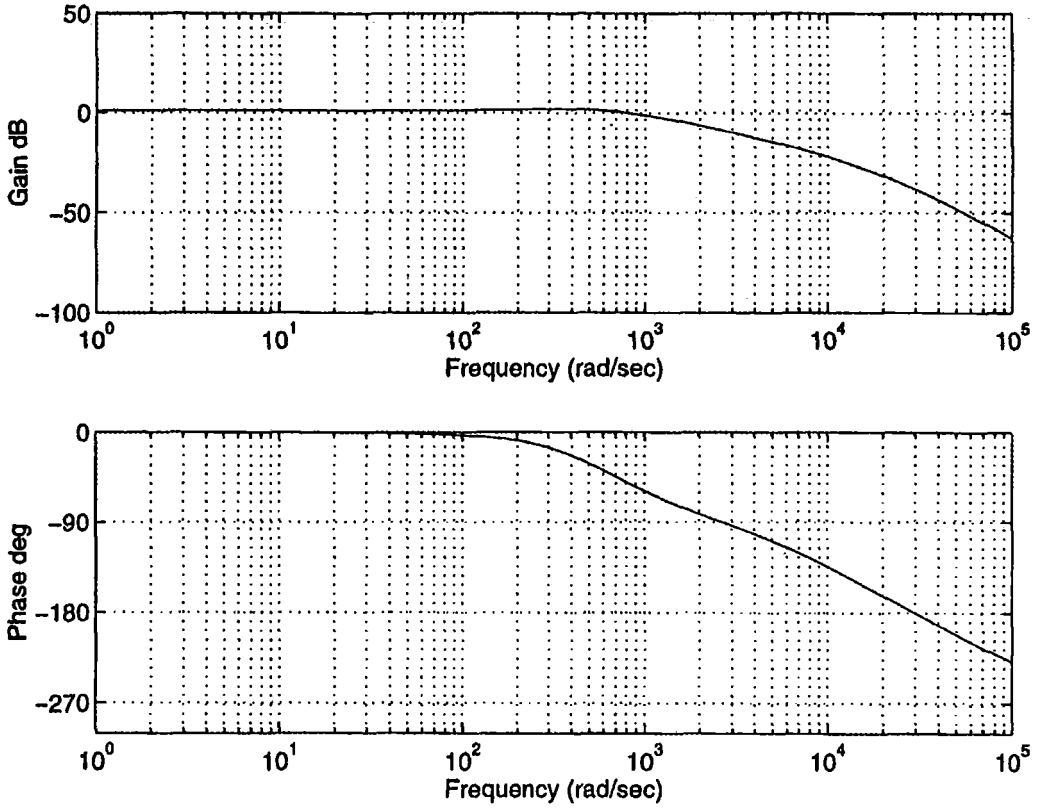

Figure 8 - Closed Loop Frequency Response Using μ Synthesis Controller

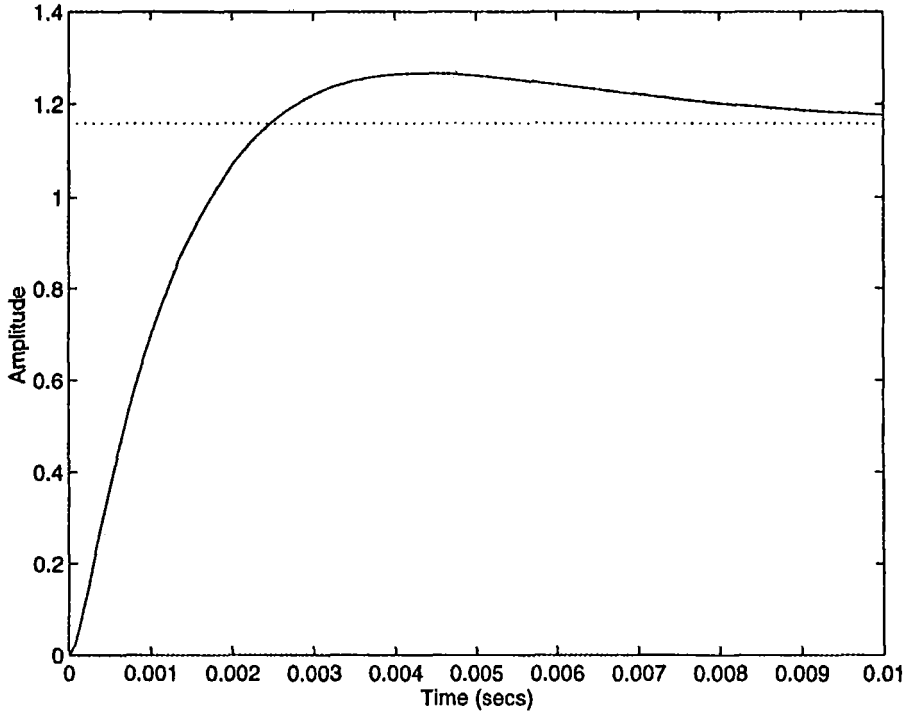

Figure 9 - Step Input Response Using μ Synthesis Controller

Session 9 -- Controls 2

Chairman: Carl Knospe
University of Virginia

NONLINEAR CONTROL OF LARGE DISTURBANCES IN MAGNETIC BEARING SYSTEMS

Yuhong Jiang and R. B. Zmood

Department of Electrical Engineering
Royal Melbourne Institute of Technology
Melbourne Victoria 3000, Australia

SUMMARY

In this paper, the nonlinear operation of magnetic bearing control methods is reviewed. For large disturbances, the effects of displacement constraints and power amplifier current and *di/dt* limits on bearing control system performance are analyzed. The operation of magnetic bearings exhibiting self-excited large scale oscillations have been studied both experimentally and by simulation. The simulation of the bearing system has been extended to include the effects of eddy currents in the actuators, so as to improve the accuracy of the simulation results. The results of these experiments and simulations are compared, and some useful conclusions are drawn for improving bearing system robustness.

1. INTRODUCTION

A magnetic bearing system with a long thin shaft can often have self-excited instabilities, especially when the shaft rotates at high speed. These instabilities can lead to severe rotor vibrations. This problem has been studied by many researchers using the H^{∞}, root locus, PID, and LQG methods (refs. 1, 2, and 3), for designing stable controllers using linearized models of the magnetic bearings and these approaches have been shown to give excellent results when the transient disturbances are small. However, due to bearing actuator nonlinearities and constraints, and particularly due to power amplifier nonlinearities, the above methods have proven to give poor robustness when the system is subjected to large disturbances.

The effects of nonlinear control of large disturbances in magnetic bearing systems have been studied in an earlier unpublished memorandum by Zmood et. al. (ref. 4). This analysis showed

that large scale self-excited oscillations can occur, and these results have been found to be due to a limit cycle which occurs in the bearing control system. This study indicated that reduction of the bearing control winding inductance not only allowed easier adjustment of the controller coefficients for stability but also significantly improved the bearing robustness in the presence of large disturbances. That work, however, did not include the effects of the eddy currents in either the bearing actuator or power amplifier models.

The present work is an extension of this earlier work of Zmood et. al. (ref. 4). The simulation of the magnetic bearing system has been extended to include the effects of the eddy currents in the power amplifier and the bearing actuator. Both transfer functions modelling eddy currents are first order. In this comparison, the results of the simulation using the eddy current models predict the experimental results more accurately. Some new useful design constraints are also derived for improving the magnetic bearing stability and robustness, such as the coil inductance, the height of the solid core of linear ferromagnetic material, and the gain coefficient. The results of the simulation and experimental work have shown that taking into account the system constraints in the controller design not only improves the large signal behaviour of the bearing and prevents self-excited oscillations, but also significantly improves its robustness.

2. MODEL OF THE MAGNETIC BEARING SYSTEM

To aid in understanding the bearing relaxation oscillation, it has been found necessary to make a number of simplifying assumptions about both the bearing actuator and the control system. While some of these assumptions have only a minor influence on the operation of the magnetic bearing, others limit the range of operating conditions which can be described.

2.1 The Magnetic Bearing Actuator

It will be assumed in developing a model for the bearing actuator that :

- The back e.m.f. induced in the actuator coils can be neglected;
- The coil resistance can be neglected;
- Eddy currents induced in the ferromagnetic components of the actuator are represented by a first order model;
- Magnetic saturation can be neglected;
- When the flywheel collides with the touchdown bearings the velocity immediately falls to zero;

- The actuator force is described by the equation $F_x = K_x x + K_i i_c$, where K_x and K_i are both positive;

Under the above assumptions, the equation of motion for the magnetic bearing are given by the following three conditions:

(1) When $-x_m < x(t) < x_m$, the equations of motion are given by

$$M\frac{d^2x}{dt^2} = k_i i_c - k_x x \tag{1}$$

$$L\frac{di_c}{dt} = V_c(t) \tag{2}$$

(2) When $x(t) = x_m$ and $i_c(t) > -i_{crit}$, or $x(t) = -x_m$ and $i_c(t) < i_{crit}$, the equations of motion are

$$\frac{dx}{dt} = 0 \tag{3}$$

$$L\frac{di_c}{dt} = V_c(t) \tag{4}$$

(3) When $x(t) = x_m$ and $i_c(t) \leq -i_{crit}$, or $x(t) = -x_m$ and $i_c(t) \geq i_{crit}$, the equations of motion are given by

$$M\frac{d^2x}{dt^2} = k_i i_c - k_x x \tag{5}$$

$$L\frac{di_c}{dt} = V_c(t) \tag{6}$$

where x is the journal displacement of the shaft and i_c is the coil current. For the above equations, the critical current is defined as $i_{crit} = k_x x_m / k_i$

2.2. Control System Block Diagram

A detailed block diagram for the magnetic bearing control is shown in Fig. 1. This figure shows the parameters for the compensator, low pass filter, and position transducer.

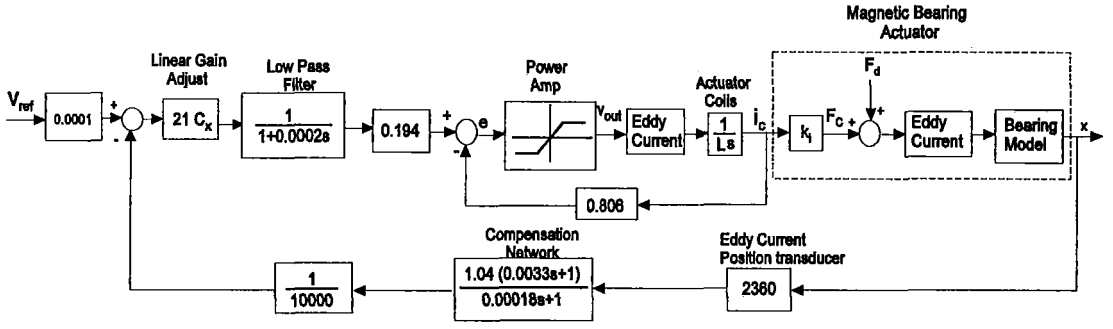

Figure 1. Detailed block diagram of magnetic bearing control system.

3. MODEL OF THE EDDY CURRENTS ON MAGNETIC BEARING ACTUATOR AND POWER AMPLIFIER

Eddy currents are to be found in any conductive material which is subjected to a time-varying magnetic field, and they therefore occur in all types of electrical equipment (ref. 5). In the magnetic bearing control system, the simulations more accurately predict the system performance when models of the eddy currents are included. The details of the eddy current transfer function models are described below.

3.1 Eddy Currents on the Magnetic Bearing Actuator

A first order transfer function model, describing the effects of the eddy currents on the transient performance of a magnetic bearing actuator, was presented by Zmood et. al. (ref. 6). In that paper, the transfer function of the bearing actuator was shown to be

$$F(s) = -K_x x(s) + K_i \frac{1+s(1-8/\pi)T_1}{1+sT_1} i_c(s) \tag{7}$$

This equation shows the functional relationship between the armature force *F(s)*, the armature displacement *x(s)*, and the coil current $i_c(s)$. The effect of the eddy currents is to introduce a

time-lag in the application of the force due to change in the coil currents. A block diagram for the bearing actuator including the armature mass is shown in Fig. 2.

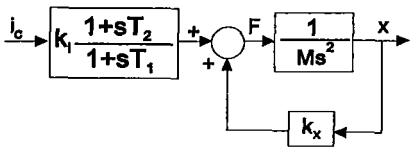

Figure 2. Block diagram of bearing actuator including eddy currents.

From Eq. (7), the transfer function representing the eddy currents in the bearing actuator can be seen to be

$$G_m(s) = \frac{1+T_2 s}{1+T_1 s} = \frac{1+0.3085\text{s}}{1+0.1636\times10^{-3}s}$$

where T_1 and T_2 are defined in Appendix I.

3.2 Effect of Eddy Currents on Power Amplifier

Using the method described in (ref. 6) the eddy current transfer function of the power amplifier is calculated to be

$$G_p(s) = \frac{1+T_1 s}{1+T_2 s} = \frac{1+0.1636\times10^{-3}s}{1+0.3085s}$$

The block diagram for the power amplifier including the inductance of the coil L, the eddy current transfer function $G_p(s)$, and the current i_c feedback is shown in Fig. 3,

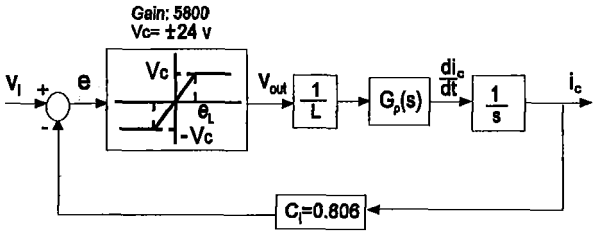

Figure 3. Block diagram showing power amplifier constraints and eddy current model transfer function.

where V_c is the maximum voltage of the power amplifier (V_c=*24.0* V), C_i is the current feedback parameter (C_i=0.806), and e_L is the maximum error signal for linear operation of the power amplifier ($e_L = V_c/gain = 24.0/5800$).

3.3 Constraint Analysis for Power Amplifier

To understand the operation of the power amplifier consider diagram shown in Fig. 3.

The output voltage of the power amplifier is given by

$$V_{out} = \begin{cases} 5800e, & -e_L < e < +e_L \\ V_c, & |e| \geq e_L \end{cases} \tag{8}$$

From Eq. (8) we obtain

$$V_{out} = V_c sat\left(\frac{V_i - 0.806 i_c}{e_L}\right) \tag{9}$$

From Eq. (9), the equation for the current slew rate is given by

$$s\, i_c = \frac{1}{L} V_c sat\left(\frac{V_i - 0.806 i_c}{e_L}\right) G_p(s) \tag{10}$$

Eq. 10 shows that the maximum current slew rate is determined by the inductance L, the maximum error signal e_L for linear operation and the maximum output voltage V_c. Those equations are used for the simulation of the magnetic bearing system control.

4. SIMULATION AND EXPERIMENTAL RESULTS

To clarify the significance of the many assumptions in the theoretical analysis presented above, some experiments as well as simulations have been performed. The simulation work has been performed using the simulation software package Advanced Continuous Simulation Language (ACSL) for the system shown in Fig. 1. In this work the model used for the bearing actuator is given by Eqs. (1) to (6) and for the power amplifier is given by Eqs. (8) to (10). The

initial conditions in all simulations have been taken to be $x(0)$=0.147 mm and $i(0)$= -0.1 A. Also in the simulation work, two different values of coil inductance L are used, these being 0.042 H and 0.072 H. The height b, of the solid core of linear ferromagnetic material has been taken to be 3 mm and 4 mm. In the experimental work, the coil inductance L is 0.042 H and the height b, of the solid core of linear ferromagnetic material is 3 mm. The simulation results show the system is stable for $7307 < C_x/C_i < 15275$. For C_x=19140 both the simulation and the experiments show the control system will have a limit cycle oscillation. The results of this work and their comparison are discussed below.

4.1 Simulation Results for Changes of the Coil Inductance L

In this section the control system coefficients are taken to be C_x=19140 and b=3 mm, and the system performance is examined for changing coil inductance L. Figs. 4 and 6 show the coil currents and the flywheel displacements waveforms of the magnetic bearing for L=0.042 H and L=0.0567 H, respectively. From the above figures, it will be noted that the coil current waveforms for the system simulation initially rise rapidly due to the effects of the eddy currents. The simulated dynamic response trajectories, in the i-x plane, for the bearing control system are shown in Figs. 5 and 7 with L=0.042 H and L=0.0567 H, respectively. There is a noticeable difference between their trajectories. The displacements waveforms of the system simulation for L=0.042 H dwell at the limits, $\pm x_m$, for only a very short period. However these is a considerable dwell time at the limits $\pm x_m$ when the coil inductance L is 0.0567 H.

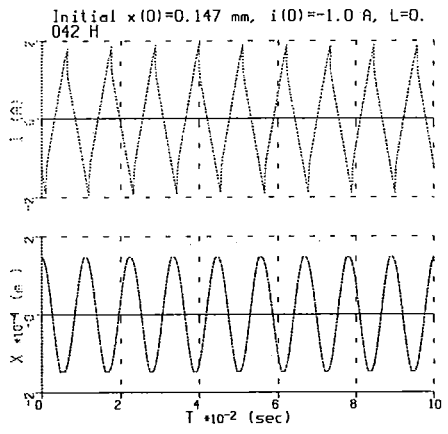

Figure 4. Simulation time response for C_x=19140 and L=0.042H.

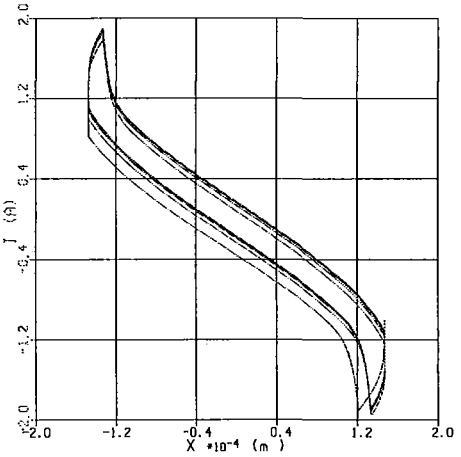

Figure 5. Simulation response trajectory in i-x plane for C_x=19140 and L=0.042H.

4.2 Simulation Results for Changes of the Eddy Current Transfer Function and the Controller Coefficients

In this section, the transfer function of the eddy currents has been changed to test the system stability, especially due to changes of the height b, of the solid core of

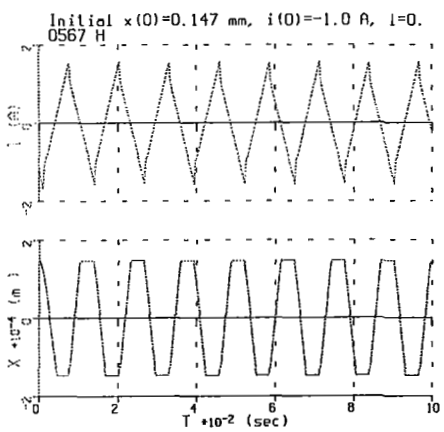

Figure 6. Simulation time response for C_x=19140 and L=0.0567H.

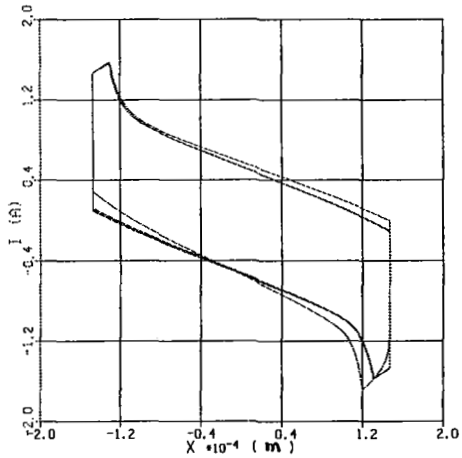

Figure 7. Simulation response trajectory in i-x plane for C_x=19140 and L=0.0567H.

linear ferromagnetic material and the gain coefficient C_x. All other coefficients are assumed fixed with $L=0.042$ H and $C_i=0.806$. The simulation results of the displacements and the currents for $b=4$ mm and $C_x=8000$ are shown in Figs. 8 and 9, respectively. From these figures it will be noted that the system is stable when changing the value b and the controller coefficients C_x. The simulation results show that the system should be stable for b=3 mm or b=4 mm and for $5889 < C_x < 12311$.

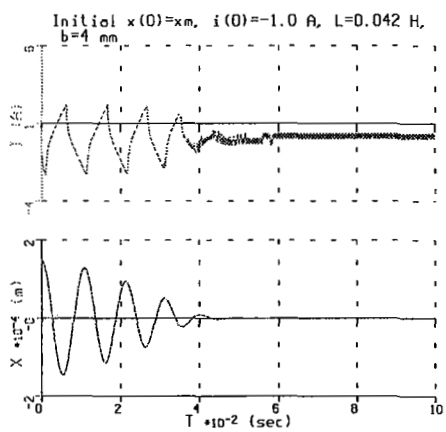

Figure 8. Simulation time response for C_x=19140, b=4 mm and L=0.042H.

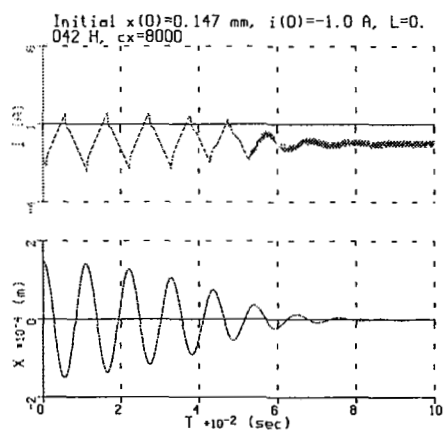

Figure 9. Simulation time response for b=3 mm, C_x=8000, and L=0.042H.

4.3 Experimental Results

In this section, the coil inductance L=0.042 H and the height of the solid core of linear ferromagnetic material b=3 mm for the experimental work. Fig. 10 shows the

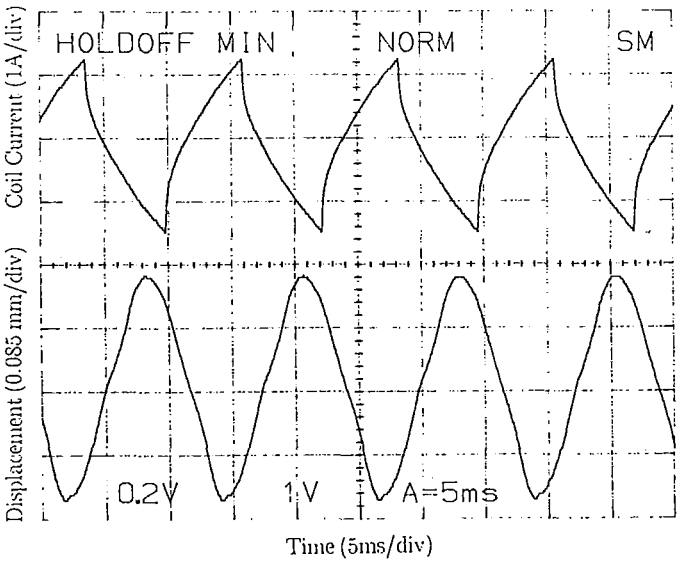

Figure 10. Experimental time response for C_x=19140, b=3 mm and L=0.042H.

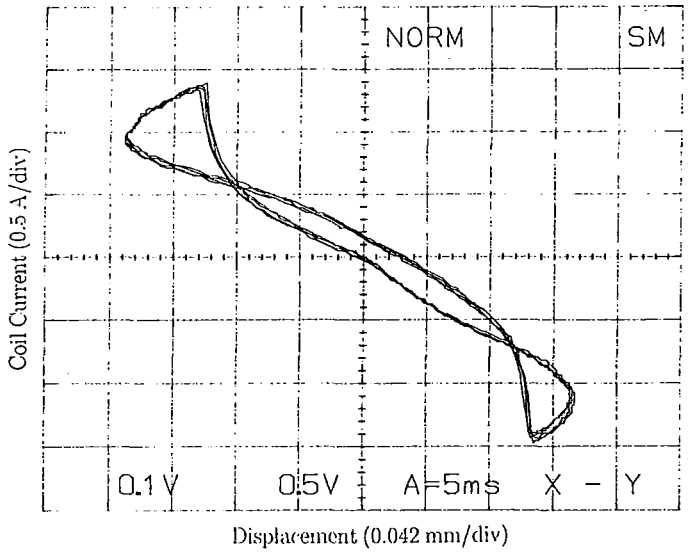

Figure 11. Experimental time response in i-x plane for C_x=19140, b=3 mm and L=0.042H.

experimentally measured coil current and flywheel displacement waveforms of the bearing and its control system for the controller coefficients C_x=19140 and C_i=0.806. The trajectory in the *i-x* plane for the same waveforms is shown In Fig. 11. The waveforms for the simulated system with the same operating conditions is shown in Figs. 4 and 5.

It is obvious that there is close correlation between the simulation and the experimental waveforms for L=0.042 H, C_x=19140 and b=3 mm. The coil current waveforms for the simulated system and the experimental system have a rapidly rising initial wavefront due to the effect of induced eddy currents. It will be noted that the results of the simulation using the eddy current model can predict the experimental results more accurately than the model without considering the eddy currents.

DISCUSSION

The large scale excited oscillations have been investigated and found to be due to a limit cycle which occurs in the magnetic bearing system. A simplified analysis of the magnetic bearing actuator and its control system, which includes the essential nonlinearities of the physical displacement constraints and the power amplifier saturation, has been undertaken. A useful design relationship in this work was obtained which shows that as the coil inductance decreases, the bearing control system becomes stable for a wider range of values of C_x. It has been observed that improved simulation results are obtained if the effects of the eddy currents on the operation of the bearing actuator and the power amplifier are included. The results of this investigation clearly indicate that reduction of the coil inductance not only improves the large signal operation of the magnetic bearing and prevents self-excited oscillations, but also significantly improves its disturbance robustness.

APPENDIX I. BEARING ACTUATOR MODEL

The transfer function of the magnetic bearing including the eddy currents is shown (ref. 6) to be

$$G_m(s) = \frac{x(s)}{I(s)} = -K_i\left(\frac{1+T_2 s}{1+T_1 s}\right)\frac{1}{Ms^2 + K_x}$$

where T_1=4δμb^2/π^2 and T_2=(1-8/π^2) T_1. In these equations, δ is the plate conductivity

($\delta = 0.3571 \times 10^{-8}$ Ωm for steel), μ is the plate permeability ($\mu = \mu_r \mu_0$ where $\mu_0 = 4\pi \times 10^{-7}$ H/m), b is the height of the solid core of linear ferromagnetic material ($b = 3 \times 10^{-3}$ m), m is the mass of the shaft ($m = 0.6583$ kg), K_x is the bearing actuator static stiffness ($K_x = 171.3$ N/mm), and K_i is the bearing actuator current sensitivity ($K_i = 23.06$ N/A).

REFERENCES

1. Y. N. Zhuravlyov; A. Mikhail; and E. Lantto.: Inverse Problems of Magnetic Bearing Dynamics. *4th Inter. Symp. on Magnetic Bearings*, ETH Zurich, August, 1994, pp. 79-84.

2. K. N. Hirochika and Y. Segawa.: H^{∞} Control of Milling AMB Spindle, *Fourth International Symposium on Magnetic Bearings.* ETH Zurich, Switzerland, August, 1994, pp. 23 - 26.

3. M. Fujita; K. Hatake; and F. Matsumura.: Loop Shaping Based Robust Control of a Magnetic Bearing. *IEEE Control System*, August, 1993, pp. 57-64.

4. R. B. Zmood; D. K. Anand; J. A. Kirk; and D. Pang.: The Behaviour of Magnetic Bearing Subjected to Large Disturbances. *RMIT Technical Report,* 1990, RMIT, Australia.

5. R. L. Stoll.: The Analysis of Eddy Currents. *Oxford University Press*, Oxford 1974.

6. R. B. Zmood; D.K. Anand; and J.A. Kirk.: The Influence of Eddy Currents on MagneticBearing Actuator Performance. *Proc. of IEEE*, Vol. 75, No. 2 (1987), pp. 259-260.

A HYBRID NONLINEAR CONTROL SCHEME FOR ACTIVE MAGNETIC BEARINGS *

F. Xia N. G. Albritton J. Y. Hung R. M. Nelms
Department of Electrical Engineering
200 Broun Hall
Auburn University, AL 36849-5201

SUMMARY

A nonlinear control scheme for active magnetic bearings is presented in this work. Magnet winding currents are chosen as control inputs for the *electromechanical* dynamics, which are linearized using feedback linearization. Then, the desired magnet currents are enforced by sliding mode control design of the *electromagnetic* dynamics. The overall control scheme is described by a multiple loop block diagram; the approach also falls in the class of nonlinear controls that are collectively known as the "integrator backstepping" method. Control system hardware and new switching power electronics for implementing the controller are described. Various experiments and simulation results are presented to demonstrate the concepts' potentials.

INTRODUCTION

The dynamic model used for this work is described now, followed by a brief discussion about several nonlinear control approaches.

System Modeling [6]

The dynamic model for one axis of an active magnetic bearing has several components. A second-order, linear differential equation describes dynamics of the rotor's mechanical position x with respect to opposing forces (F_1 and F_2), which are produced by the two windings of the bearing axis:

$$m\ddot{x} = F_1(i_1, x) - F_2(i_2, x) + \delta(t) \ . \tag{1}$$

* This work has been supported by the Center for Commercial Development of Space Power and Advanced Electronics with funds from NASA grant NAGW-1192-CCDS-AL, Auburn University, and the Center's Industrial Partners.

In the equation above, the rotor mass is represented by m, while the two winding currents are represented by i_1 and i_2. The variable $\delta(t)$ represents external force disturbances. Force produced by each winding of the bearing is a nonlinear function of winding current and air gap dimension $g(x)$, which is a function of the rotor position. Magnetic saturation is often ignored in fundamental electromagnetic analysis, yet the resulting relationship shows that force is proportional to the square of winding current, and inversely proportional to the square of air gap:

$$F_n(i_n, x) = k\frac{i_n^2}{g^2(x)} \quad , \quad n = 1, 2 \quad . \tag{2}$$

Efforts to increase the force/mass ratio of bearings often result in operation under magnetically saturated conditions. In this case, the relationship between force and winding currents is further complicated. In this work, the relationship described in (2) is used. Hence, the *electromechanical* dynamics for an active magnetic bearing can be described as a second-order nonlinear system with two inputs (the two winding currents).

Electromagnetic properties for each winding are described by a first-order nonlinear differential equation relating winding current dynamics to the voltage e applied to the winding:

$$e_n = Ri_n + \frac{\partial\lambda(i_n, g(x))}{\partial i}\frac{di}{dt} + \frac{\partial\lambda(i_n, g(x))}{\partial x}\frac{dx}{dt} \quad , \quad n = 1,2 \quad . \tag{3}$$

In the above model, R represents the winding resistance, and the function λ represents the magnetic flux linkage of the winding. In the simplest analysis that does not account for magnetic saturation, the flux linkage is proportional to winding current and inversely proportional to air gap dimension. Therefore, the electromagnetic dynamics are nonlinear. As is true with the electromechanical dynamics, the nonlinearity in the electromagnetic equations becomes more complex in the presence of magnetic saturation.

In summary, the overall dynamics for one axis of an active magnetic bearing are described by a fourth-order, nonlinear model having two inputs. Nonlinearities in the magnetic bearing are differentiable with respect to position, velocity, and current.

Nonlinear Control Options

Advanced control methods for active magnetic bearings have been actively pursued in recent years, and research literature in several fields describe significant achievements using nonlinear methods. Techniques like feedback linearization [1], adaptive control [2], [3], variable structure or sliding mode control [4], and fuzzy logic control [5] have all been examined for magnetic levitation systems. In this work, a

marriage of two nonlinear control techniques is used. Specifically, a feedback linearization controller is used to linearize and control electromechanical dynamics, while a variable structure controller is used to achieve the desired electromagnetic dynamics. Motivation for this hybrid control approach stems from several considerations described in the next section.

CONTROL ALGORITHM CONSIDERATIONS

Each of the nonlinear controllers mentioned in the introduction has unique merits. But it is believed that a hybrid control approach may be able to take advantage of several algorithms' benefits, and thus address the unique properties and needs of the various magnetic bearing subsystems. In addition, the overall control scheme would be divided into smaller subsystems, each of which may be easier to design than a full-state, nonlinear controller for the entire system dynamics.

Feedback Linearization Considerations

The feedback linearization control method is considered to help account for modeled nonlinearities in the system dynamics. This component shows great promise for compensating well-modeled smooth (differentiable) nonlinearities, yielding improved performance over classical PID control. However, the feedback linearization approach alone becomes very complex for active magnetic bearings when a design model that includes electromagnetic dynamics is used [1]. An intricate system of nonlinear coordinate transformation and nonlinear feedback is needed. In addition, a full-order feedback linearization type controller requires feedback of rotor position, velocity, and acceleration, as well as winding current. Despite these shortcomings the feedback linearization approach demonstrates significant improvement in dynamic response over more simple, linear control approaches [1], [6].

Variable Structure Considerations

Variable structure or sliding mode control is also a candidate to provide a measure of robust performance against disturbances and modeling errors that can be modeled by bounded, differentiable functions. The technique is especially attractive because the switching control signals are easily generated by modern switching amplifiers, whose superior efficiency is important for this application. Like the feedback linearization controller, however, the sliding mode controller is a full state feedback controller and requires position, velocity, and acceleration feedback in any design that accounts for electrical dynamics. Reduced feedback requirement is possible if electrical dynamics are ignored in the design model [4], but this is not an acceptable option for an active magnetic bearing, since the winding inductance is significant.

A Hybrid Nonlinear Control Approach.

To take advantage of merits from both types of controllers, a hybrid controller is

considered here. First, the feedback linearization method is used to design an improved controller for the second-order nonlinear *electromechanical* dynamics of the magnetic bearing. Application of feedback linearization to second-order dynamics doesn't require a coordinate transformation, uses a less complex nonlinear compensation component, and requires only rotor position and velocity feedback. The feedback linearization controller in this work treats the magnet winding currents as the control inputs. In reality, the winding currents are a state variable in any model that includes electrical dynamics. Thus, winding currents can be considered "pseudo" control signals. To enforce the desired winding currents, a variable structure or sliding mode controller is designed for the *electromagnetic* dynamics. The first-order electrical dynamics, though nonlinear, are easily and robustly controlled by the sliding mode control, which specifies a switching control signal. Control input for the electrical dynamics is a voltage, which is easily switched at high frequency by modern power electronics.

The hybrid nonlinear controller is illustrated by the multi-loop block diagram in Fig. 1. The outer-most feedback loop is a linear state feedback (PD or PID controllers are other options), used to stabilize the mechanical dynamics of the magnetic bearing. Outer loop controller design is based on a second-order linear state model with state variables being the bearing rotor position x and velocity $\dot{x}$, and control input being "force" v. Since the actual electromechanical dynamics are nonlinear, an intermediate feedback loop is used to cancel the modeled electromechanical nonlinearity, so the mechanical dynamics are specified by the outer loop controller output v. Design of the nonlinear intermediate loop is based on the feedback linearization principle, and results in specifying two reference winding currents $i_{\text{ref } 1,2}$ that cancel the force nonlinearities and also specify the desired linear mechanical dynamics.

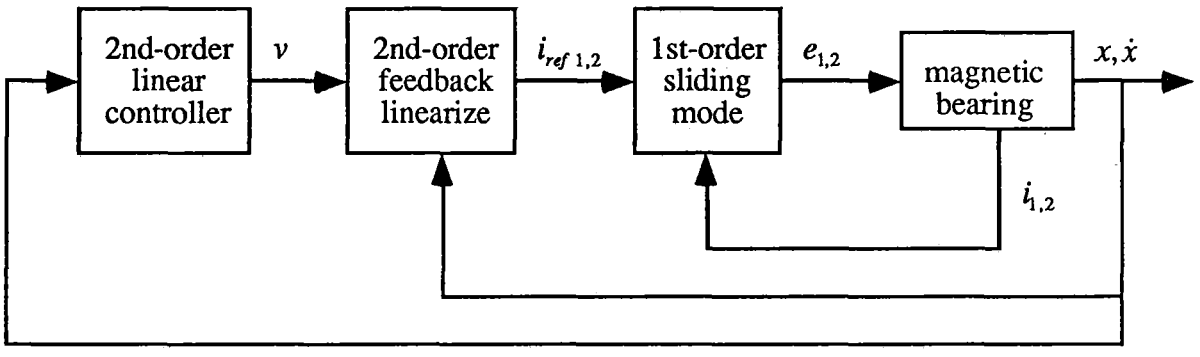

Fig. 1. Block diagram of the hybrid nonlinear controller.

Each winding possesses significant electromagnetic dynamics, however, and current is developed under the influence of applied voltage. Therefore, designs of the outer and intermediate feedback loops based on a second-order model are not entirely correct (the

full design model is fourth order). As discussed in the Introduction, the electromagnetic dynamics are modeled by two first-order nonlinear differential equations (one equation for each winding of the axis) with continuous partial derivatives. By using a variable structure (sliding mode) control for the current, it is theoretically possible to eliminate the electrical dynamics - in practice the electrical time constant is made very small. The innermost feedback loop represents a current feedback controller that uses the variable structure control scheme. A very simple approximation of the variable structure controller is realized using a pulse-density modulated amplifier, which is described in the section to follow.

The multiloop control scheme described here is similar in structure to a technique that has been recently named by some researchers as the "integrator backstepping" or "interlacing" approach [7] for robust nonlinear system design, but it has historical roots in well-known classical servo-mechanism design methods [8].

CONTROL SYSTEM COMPONENTS

Implementation of the control system at Auburn University is accomplished using a digital controller and a new switching power electronics design. Highlights of these two subsystems are presented here.

Digital Controller

The digital controller is built around an Analog Devices ADSP21020 floating-point digital signal processor. Several variations of feedback sensing and control signal interface circuits have been designed and tested at Auburn University [9]. One system uses analog input/output (I/O) port chips, which greatly simplify the hardware packaging. To take advantage of the processor data bus width (32 bits wide for fixed point data), a second system has been developed to access several I/O channels in parallel. For example, 4 channels of 8-bit A/D converters are accessed in parallel. An interface that does not use analog output electronics has also been developed for the second system. Replacing the analog output circuits is a single 16-bit wide digital word that carries the information to directly control the power electronic switches of the four switching power amplifiers. Each amplifer has 4 switches that are directly commanded by the DSP.

Control programs for the system are written using the C programming language. A few basic service functions have been developed in assembly language.

Resonant Switching Amplifier

The power amplifier architecture also presents a technological advance for switching amplifiers. In the past, pulse width modulation has been most commonly used in switching amplifiers. The ratio of semiconductor device conduction time and cutoff time, known as the duty cycle, is varied in proportion to a control signal. While average

efficiency can be very good, the majority of losses can be traced to the switching instances, when the power devices are changing state. A particularly stressful period for a device is during the time that a state transition occurs and voltage is present across the device.

To reduce switching losses in this work, a resonant type of converter is being used in the power amplifier. The amplifier "front-end" is designed to produce a high frequency voltage pulse sequence. Switching of the power devices is synchronized to the time instances in which voltage level equals zero, thus minimizing device stresses and losses. The amplifier design includes an H-bridge to steer the voltage pulse to the load (see Fig. 2). By varying the number of positive and negative voltage pulses to the load, an "average" voltage can be achieved. This scheme is also known as a pulse-density modulation, and is related to the delta-modulation concept used in digital communication systems.

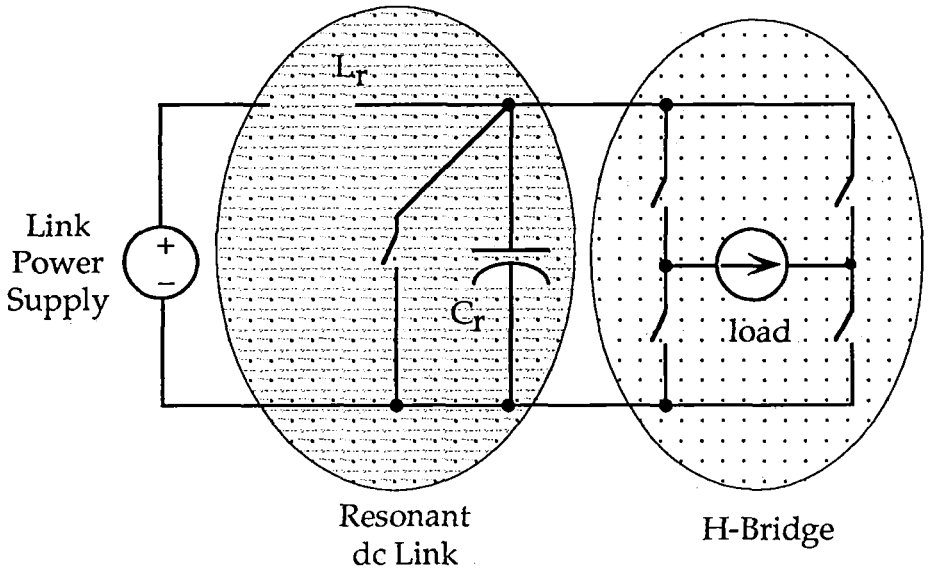

Fig. 2. Resonant-link, pulse-density modulated amplifier

With a very high frequency pulse train, the pulse density modulation scheme is a good approximation of the type of signals often used in sliding mode control designs. In this work, three control voltages can be achieved with this amplifier: "positive," "negative," and "zero" voltage. Controller design for this amplifier is also described in the reference [10].

SOME EXPERIMENTAL RESULTS

Various experiments are conducted to demonstrate the validity of the control

approach. The feedback linearization concepts is first tested using linear amplifiers. The variable structure controller for the current amplifer is tested in a separate experiment.

Feedback Linearization Component

The feedback linearization controller and a PD controller are compared by examining step responses and sinusoidal responses. Both controllers work well if the deviation from the design state is small. When the perturbation from the design state is large, however, the nonlinear controller exhibits a greater stability margin, as can be seen in the experimental data plotted in Fig. 3a. The PD controlled system does not respond favorably, as can be seen in Fig. 3b.

Variable Structure Component

Shown in Fig. 4 are the recorded oscilloscope traces of the current amplifier responses to step changes in current reference. The current reference is the lowermost trace. Voltage pulses being applied to the winding are shown in the center trace. The current response is the uppermost trace.

SOME SIMULATION RESULTS

The simulated response of the hyrid controller is shown in Fig. 5. The upper left plot shows the position response from an initial error of 1 mm. The velocity response is shown in the upper right plot. The two magnet winding currents are shown in the lower plots. These results show good promise for the hybrid control scheme.

CONCLUSIONS

A hybrid nonlinear control scheme and electronic hardware have been described. The hybrid controller consists of two components: a feedback linearization of the electromechanical dynamics, and a variable structure or sliding mode control of the electromagnetic dynamics. The design of each control component is based on a reduced order model of the subsystem under consideration, so the designs are less complicated than a full-state design of a single controller. In the feedback linearization design, the rotor position and velocity information is needed, while the sliding mode controller uses only current feedback. This hybrid control scheme can be interpreted as a type of "backstepping" or "interlacing" design. Experimental results of the various control system components have been presented, and simulation results for the complete system are encouraging.

References

1. J. Y. Hung, "Nonlinear control of a magnetic levitation system," *Proc. IEEE Industrial Electronics Conf.*, Kobe, JAPAN, 1991.

2. Sinha, P. K. (1987), Electrodynamic Suspension: Dynamics and Control, London, United Kingdom, Peter Peregrinus Ltd., 1987

3. B. Shafai, S. Beals, P. LaRocca, and E. Cusson, "Magnetic bearing control systems and adaptive forced balancing," *IEEE Control Systems*, vol. 14, no. 2, p. 4-13, April 1994.

4. A. Sinha, K. W. Wang, and K. L. Mease, "Robust and real-time rotor control with magnetic bearings," *AIAA/NASA/OAI Conference on Advanced SEI Technologies*, Cleveland, Ohio, p. 1-12, Sept 1991.

5. J. Y. Hung, "Magnetic bearing control using fuzzy logic," *IEEE Transactions on Industry Applications*, vol. 31, no. 6, Dec 1995. Originally presented at *IEEE Industry Applications Society Annual Meeting*, Toronto, Ontario, CANADA, pp. 2210–2215, Oct 1993.

6. F. Xia, "Nonlinear control of magnetic bearings: Design and implementation using digital signal processors," M.S. thesis, Auburn University, June 1995.

7. I. Kanellakopuolos, P.V. Kokotovic, A. S. Morse, "Systematic design of adaptive controllers for feedback linearizable systems," *IEEE Trans. Automatic Control*, vol. 36, no. 11, p. 1241-1253, Nov 1991.

8. G.S. Brown and D.P. Campbell, Principles of Servomechanisms, John Wiley & Sons, 1948, p. 269-277.

9. J. Y. Hung, "Magnetic bearing electronics and controller development," Auburn University Space Power Institute/CCDS project report, December 1994.

10. J. Y. Hung, R. M. Nelms, F. Xia, and M. Story, "Three-mode variable structure control of a pulse density modulated current feedback amplifier," *IEEE Int'l Symp. Industrial Electronics*, Athens, GREECE, pp. 736-740, July 1995.

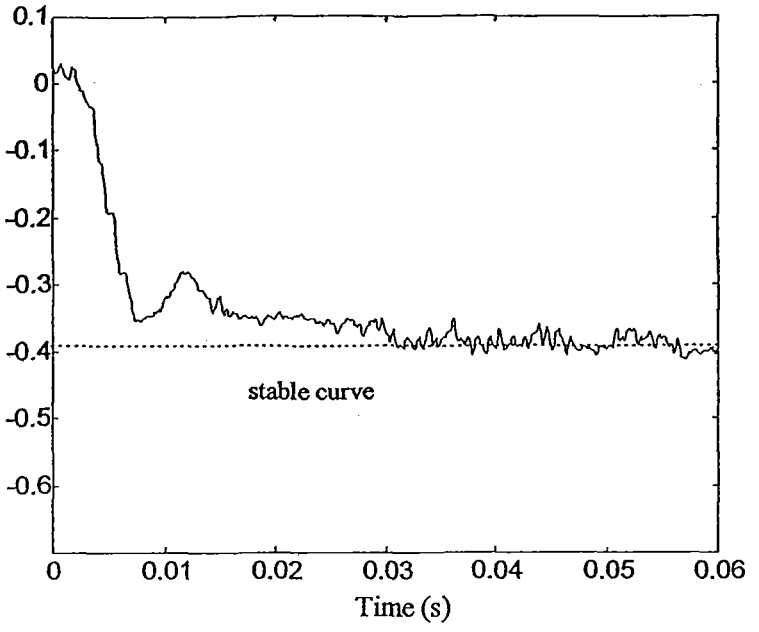

(a)

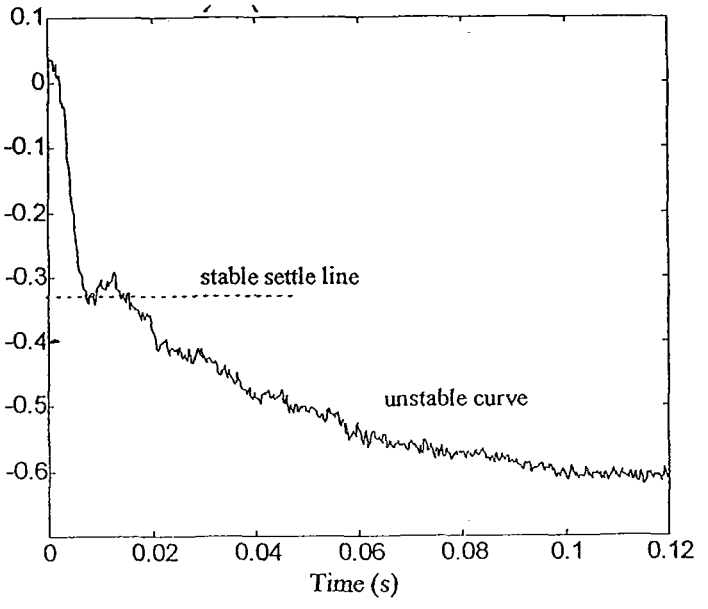

(b)

Fig. 3. Step responses of feedback linearization and PD controllers.

(a) Feedback linearization

(b) PD controller

Reference change exceeds stability limits of PD controller.

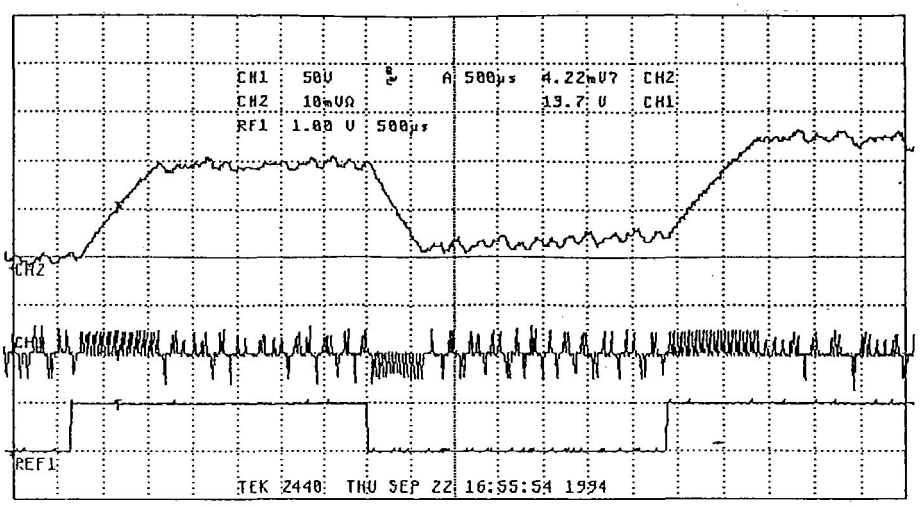

Fig. 4. Response of the resonant current amplifier.
Upper trace: load current
Middle trace: load voltage
Lower trace: reference current

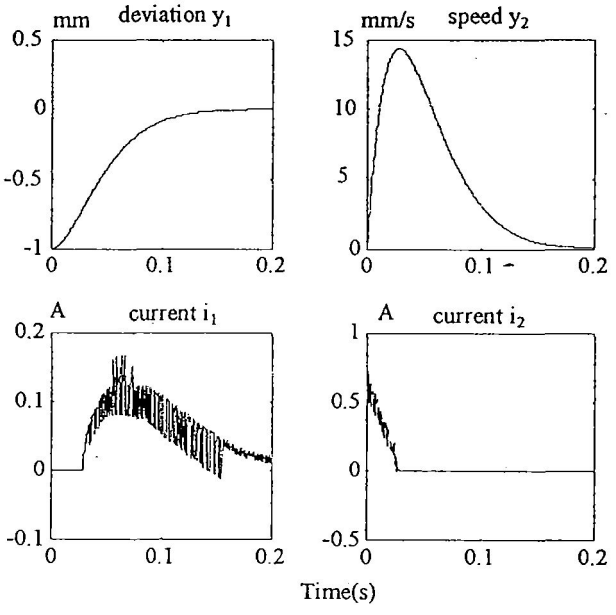

Fig. 5. Simulated response of the hybrid nonlinear controller.
Upper plots: position and velocity response.
Lower plots: magnet currents

DAMPING ROTOR NUTATION OSCILLATIONS IN A GYROSCOPE WITH MAGNETIC SUSPENSION[1]

Valentine N. Komarov
Research Institute for Applied Mathematics and Cybernetics
of Nizhny Novgorod State University, Nizhny Novgorod, Russia

SUMMARY

A possibility of an effective damping of rotor nutations by modulating the field of the moment transducers in synchronism with the nutation frequency is considered. The algorithms for forming the control moments are proposed and their application is discussed.

INTRODUCTION

Practical use of noncontact suspensions in gyroscopy is possible if the following requirements, at least, are fulfilled: the rotor must be stably suspended and stably rotate with given parameters; information about the angular motion of the body must be available.

The second problem of making the rotor rotate is, in turn, divided into three other problems: providing a necessary angular momentum for the rotor, which, most frequently, is equivalent to providing a certain rotation speed Ω for the rotor, providing a small, zero in the limit, nutation angle ϑ, and maintaining the achieved motion parameters within the given limits in the further operation of the unit. A way for solving these problems with respect to a gyro with a magnetoresonance suspension can be found in (ref. 1).

The small dissipative moments in a noncontact gyro leads to the fact that after acceleration the rotor rotates with a nutation angle defined mainly by the initial conditions. The damping of the nutation oscillations over a finite time can be achieved if, for the formation of the control moments (not only for nutation damping), we use modulation or self-modulation methods, when parameters of the suspension field or of the additional coil field (magnitude, direction, rotation speed, etc.) vary depending on an angular position of the aspheric rotor (ref. 2, 3, 4), due to which a nonconservative component appears in the moment effect on the rotor, which also provides an active damping of nutation. Let us consider one of the possible methods for an effective damping of the rotor nutation relative to a gyro with magnetic suspension.

[1]This research has been done under the support of the Russian Foundation for Fundamental Research (Project 95-01-00002)

THE EQUATIONS OF MOTION

Assuming the gyro rotor to be stably suspended in the suspension field, we represent the equations of its angular motions in the form of six first order equations with respect to the following phase variables (ref. 5): the value of angular momentum K , two angles ρ and σ , which determine its orientation (trihedron OY_j) relative to the suspension (trihedron OZ_k), and The Euler angles φ , ψ and ϑ , which prescribe the position of the rotor (trihedron (OX_i)) relative to the angular momentum $\vec{\mathbf{K}}$; φ is the angle of the proper rotation of the rotor about the axis of dynamic symmetry (OX_3) ; ψ is the angle of precession of this axis about the angular momentum $\vec{\mathbf{K}}$; ϑ is the nutation angle or the angle between the angular momentum and the axis OX_3.

Using the main equation of gyroscopy

$$\frac{d\vec{\mathbf{K}}}{dt} + \vec{\boldsymbol{\Omega}} \times \vec{\mathbf{K}} = \vec{\mathbf{M}} \tag{01}$$

written in the coordinate system OY_j and projecting the vector $\vec{\mathbf{K}}$ on the rotor axes OX_i

$$\left(\vec{\mathbf{K}} \cdot \vec{\mathbf{x}}_i\right) = K \cdot b_{i3} = I_i \cdot \Omega_i \,, \tag{02}$$

where I_i is the rotor's moment of inertia along OX_i, and Ω_i is the projection of the rotor's absolute angular velocity on the same axis, for an axisymmetric rotor $(I_1 = I_2 = A \neq I_3 = C)$ and the arbitrary moments we obtain

$$K\left(\frac{d\rho}{dt} + \Omega_{s2}\right) = M_1 \,, \quad K\left(\sin\rho\frac{d\sigma}{dt} - \Omega_{s1}\right) = M_2 \,, \quad \frac{dK}{dt} = M_3 \,, \tag{03}$$

$$K\frac{d\vartheta}{dt} = -\left(M_1\cos\psi + M_2\sin\psi\right) = -M_{con} \,,$$

$$\frac{d\varphi}{dt} - K\left(\frac{1}{C} - \frac{1}{A}\right)\cos\vartheta = \frac{M_2\cos\psi - M_1\sin\psi}{K\sin\vartheta} \,,$$

$$\frac{d\psi}{dt} - \frac{K}{A} = -\frac{M_2\cos\psi - M_1\sin\psi}{K}\operatorname{cotan}\vartheta - \Omega_3 \,,$$

where $M_j = \left(\vec{\mathbf{M}} \cdot \vec{\mathbf{y}}_j\right)$, $\Omega_3 = \Omega_{s3} + (M_2/K)\operatorname{cotan}\rho$, and Ω_{sj} are the projections onto the axes OY_j of the absolute angular velocity $\vec{\boldsymbol{\Omega}}_s$ of the coordinate system OZ_k. This velocity can be determined by the earth's rotation, by the rotation of an object on which the gyro is installed, by a forced rotation of the device casing performed to make its interaction with the rotor symmetric, etc.

The presence of different time-scale motions in real gyros, such as a "slow" precession motion of the angular momentum and a "fast" rotor rotation allows us to use, for studying the gyro dynamics, the averaging method in which even the first approximation reveals the basic laws of gyro behavior (ref. 5).

Omitting the standard procedure for normalizing the equations and finding in the latter a small parameter ε, which characterizes the ratio of the work of external forces per one rotation of the rotor to the kinetic energy accumulated by the gyro rotor, we write their standard form, which allows the asymptotic methods to be applied:

$$\rho^{\bullet} = \varepsilon\left(\frac{m_1}{k} - \omega_{s2}\right), \quad \sigma^{\bullet}\sin\rho = \varepsilon\left(\frac{m_2}{k} + \omega_{s1}\right), \qquad k^{\bullet} = \varepsilon m_3 , \tag{04}$$

$$k\vartheta^{\bullet} = -\varepsilon\left(m_1\cos\psi + m_2\sin\psi\right) ,$$

$$\varphi^{\bullet} + \gamma k\cos\vartheta = \varepsilon\left(\frac{m_2\cos\psi - m_1\sin\psi}{k\sin\vartheta}\right) ,$$

$$\psi^{\bullet} - k = -\varepsilon\left(\frac{m_2\cos\psi - m_1\sin\psi}{K}\operatorname{cotan}\vartheta - \omega_3\right) .$$

It is evident from the equations that free motion of the rotor (generating solution) represents a regular precession or the Euler–Poinsot motion with the constant angular velocities of the proper rotation $\varphi_0^{\bullet}$ and precession $\psi_0^{\bullet}$ for a constant nutation angle ϑ, such that

$$\psi_0^{\bullet} = k_0 , \qquad \varphi_0^{\bullet} = -\gamma k_0\cos\vartheta_0 , \qquad \left(\gamma = \frac{C-A}{A}\right) , \tag{05}$$

where k_0 is the constant value of the angular momentum $\vec{\mathbf{k}}$ which is immobile in the inertial space. For the periodic dependence of the right-hand sides of the equations of motion on the fast variables ψ and φ , to obtain the first approximation over the small parameter ε , the right-hand sides of the equations for the slow variables are averaged over the variables ψ and φ , whose dependences on τ are assumed to be the same as those in the unperturbed motion.

Let us now specify the requirements to be met by the moment controlling the rotor motion to perform the damping of the rotor's nutation oscillations over a finite period of time.

After the averaging of the equations of motion over the fast variables ψ and φ , the nutation angle varies according to

$$k\vartheta^{\bullet} = -\varepsilon m_{con}\left(\rho, \sigma, \vartheta, k\right) . \tag{06}$$

Since the initial values of the nutation angle ϑ are closer to 0 rather than $\pi/2$, and this angle must still decrease with time, we introduce variable $x = \sin\vartheta$ and linearize Eq. (06) with respect to this variable

$$kx^{\bullet} = -\varepsilon\left[m^0(\rho, \sigma, \vartheta, k) + xm^1(\rho, \sigma, \vartheta, k)\right] ,$$

where $m^0(\rho, \sigma, \vartheta, k) = m_{con}(\rho, \sigma, 0, k), \qquad m^1 = \partial m_{con}/\partial x|_{x=0}$.

Therefore, a monotonic decrease of the nutation angle ϑ to zero over a finite period of time is possible only if the condition $m^0 > |m^1|$ is fulfilled. In this case, there is no equilibrium state for the angle θ or x , and their **variation rates** are always negative, which allows the required effect to be achieved.

THE FORMATION OF THE CONTROL MOMENT

Let us discuss a possibility for damping the rotor nutations through its interaction with the field of a transducer for the angular position of the rotor. In a gyro with a magnetoresonance suspension, this transducer is embodied as a system of two four-leg magnetic circuits located on the same axis but on the different sides of the rotor with a coil (ref. 1) at each leg. An axial opening in the rotor leads to the fact that from the moment standpoint, the rotor will behave as anaspheric body, whose surface is described by a set of even harmonics (even Legendre polynomials), the first of which is the second harmonic responsible for the ellipsoidality or the uniaxial anisotropy. The moment defined by this harmonic will be considered below.

This moment is described by

$$\vec{\mathbf{M}} = -2a\left(\vec{\mathbf{s}}\cdot\vec{\mathbf{h}}\right)\left[\vec{\mathbf{s}}\times\vec{\mathbf{h}}\right], \tag{07}$$

where $a > 0$ is the interaction amplitude determined, in particular, by the field amplitude; $\vec{\mathbf{s}}$ and $\vec{\mathbf{h}}$ are the unit vectors of the symmetry axes of the ellipsoid and the field. (Since we allow for the anisotropic properties of the rotor determined by its opening, from the magnetic viewpoint it should be considered as an oblate ellipsoid tending to position itself with its axis perpendicular to the field's axis, which is reflected by the minus sign in Eq. (07).)

It can be assumed that the unit vector $\vec{\mathbf{s}}$ coincides with the unit vector of the dynamic symmetry axis OX_3 of the rotor, and, thus,

$$\vec{\mathbf{s}} = \vec{\mathbf{x}}_3 = \vec{\mathbf{y}}_1 \sin\vartheta\cos\psi + \vec{\mathbf{y}}_2 \sin\vartheta\sin\psi + \vec{\mathbf{y}}_3\cos\vartheta\,.$$

Using the spherical angles α_n and β_n, we prescribe the position of the unit vector $\vec{\mathbf{h}}$, which determines the symmetry axis of the magnetic field generated by the n-th pair of the coils belonging to different magnetic circuits but located on the same axis that passes through the center of the rotor

$$\vec{\mathbf{h}} = \vec{\mathbf{z}}_1 \sin\alpha_n\cos\beta_n + \vec{\mathbf{z}}_2 \sin\alpha_n\sin\beta_n + \vec{\mathbf{z}}_n\cos\alpha_n\,,$$

where $\alpha_n = \alpha$ is the same for all n and $\beta_n = \beta_0 + \pi n/2$.

Let us substitute these unit vectors into the expression for the moment (07) and find its component $m_{con} = m_1\cos\psi + m_2\sin\psi$ responsible for the variation of the nutation angle ϑ

$$M_{con} = 2a_n\left(h_1\sin\psi - h_2\cos\psi\right)h_3\cos\vartheta - \tag{08}$$

$$-\frac{1}{4}\left[2h_1h_2\cos 2\psi + \left(h_2^2 - h_1^2\right)\sin 2\psi\right]\sin 2\vartheta\,,$$

where

$$h_j = \left(\vec{\mathbf{h}}\cdot\vec{\mathbf{y}}_j\right), \qquad h_1 = \cos\rho\sin\alpha\cos\left(\sigma - \beta_n\right) - \sin\rho\cos\alpha\,,$$

$$h_2 = -\sin\alpha\sin\left(\sigma - \beta_n\right), \qquad h_3 = \sin\rho\sin\alpha\cos\left(\sigma - \beta_n\right) + \cos\rho\cos\alpha\,.$$

From Eq. (08) it follows that M_{con} is a periodic function of the precession angle ψ without the constant component $M^0_{con}(\rho, \sigma, 0, K)$, which can appear only in the case of a pulsed

switching-on of the field over the time periods, during which the moment does not change its sign. As it is evident from Eq. (08), the moment has a harmonic component with frequency $\psi^\bullet$ proportional to $\cos^2\vartheta$ and a component with double frequency $2\psi^\bullet$ proportional to $\sin 2\vartheta$. For $\vartheta = 0$ this results in

$$M_{con} = 2a_n\,(h_1 \sin\psi - h_2 \cos\psi)\,h_3\ .$$

Apparently, for the effective damping of nutation, i.e., dropping the angle ϑ down to zero over a finite period of time, the coil field with frequency $\psi^\bullet$ must be changed. (The speed of the rotor rotation about the symmetry axis OX_3 is equal to $\Omega_0 = K/C$, the nutation frequency $\psi^\bullet = K/A$, and, consequently, $\psi^\bullet = \Omega_0 C/A$). It should be noted that nutation oscillations of a cryogenic gyro can be damped in a similar manner (ref. 3).

Let us write $h_1 \sin\psi - h_2 \cos\psi$ in the form:

$$h_1 \sin\psi - h_2 \cos\psi = -\sin\rho\cos\alpha\sin\psi +$$

$$+\frac{1}{2}\left[(1+\cos\rho)\sin(\psi+\sigma-\beta_n) - (1-\cos\rho)\sin(\psi-\sigma+\beta_n)\right]\sin\alpha\ .$$

From the above expression it follows that the optimal switching-on of the field should follow the algorithm

$$a(\psi) = \begin{cases} a, & 2k\pi \le \psi+\sigma-\beta_n \le (2k+1)\pi \\ 0, & (2k+1)\pi \le \psi+\sigma-\beta_n \le 2(k+1)\pi\ , \end{cases} \tag{09}$$

i.e., the field is switched on over half the period of the nutation oscillations with frequency $\psi^\bullet$.

For this operation mode, two pairs of the control coils are switched on at any instant, which greatly improves the efficiency but leading, however, to a higher heat release that can be reduced due to a decrease in either the field amplitude, or the switching-on duration.

$$a(\psi) = \begin{cases} a, & \left(2k+\frac{1}{2}\right)\pi - \frac{\tau}{2} \le \psi+\sigma-\beta_n \le \left(2k+\frac{1}{2}\right)\pi + \frac{\tau}{2} \\ 0, & \text{outside the intervals} \end{cases} \tag{10}$$

Here $\tau < \pi$ is the switching-on duration. Apparently, the algorithm (09) is a particular case of (10) for $\tau = \pi$.

If all the coil pairs and their switching-on algorithms are identical, they create a total control moment

$$\langle M_{con}\rangle = 2\frac{a}{\pi}\,(1+\cos\rho)\,(2\cos\rho-1)\sin 2\alpha\sin\frac{\tau}{2}\cos^2\vartheta\ , \tag{11}$$

which leads to equation

$$K\vartheta^\bullet = -2\frac{a}{\pi}\,(1+\cos\rho)\,(2\cos\rho-1)\sin 2\alpha\sin\frac{\tau}{2}\cos^2\vartheta\ . \tag{12}$$

Apart from the variable ϑ , this equation also incorporates other quantities $K(t)$ and $\rho(t)$ that do not remain constant. If we write the rotor-affecting moments via the force function W (ref. 5), then, instead of the corresponding equations in (03), we can obtain

$$K\frac{d\rho}{dt} = \frac{1}{\sin\rho}\left(\frac{\partial W}{\partial\psi}\cos\rho - \frac{\partial W}{\partial\sigma}\right) ,$$

$$\frac{dK}{dt} = \frac{\partial W}{\partial\psi} ,$$

$$\frac{d\vartheta}{dt} = \frac{1}{K\sin\vartheta}\left(\frac{\partial W}{\partial\psi}\cos\vartheta - \frac{\partial W}{\partial\varphi}\right) .$$

Since the rotor opening is symmetric about its dynamic axis, then, consequently, $\partial W/\partial\varphi = 0$. The summation of the moments from all the pairs of the symmetric coils also results in $\partial W/\partial\sigma = 0$. These conditions yield the equations

$$K\frac{d\rho}{dt} = \frac{1}{\sin\rho}\frac{\partial W}{\partial\psi}\cos\rho , \qquad \frac{dK}{dt} = \frac{\partial W}{\partial\psi} ,, \qquad \frac{d\vartheta}{dt} = \frac{1}{K\sin\vartheta}\frac{\partial W}{\partial\psi}\cos\vartheta ,$$

from which we obtain two integrals

$$K_{z3} = K\cos\rho = Const , \qquad K_{x3} = K\cos\vartheta = Const , \tag{13}$$

the physical meaning of which is evident, i.e., on the strength of the control system and rotor symmetries, the projections of the angular momentum onto the symmetry axes of the suspension (K_{z3}) and the rotor (K_{x3}) remain constant. Representing K and $\cos\rho$ from Eq.(13) and substituting them into Eq. (12), we can find the law of the nutation angle ϑ variation with time. To simplify the solution, let us use the smallness of the misalignment angle ρ , which, along with the use of the second integral, yields

$$\vartheta^{\bullet} = -\nu\cos^3\vartheta , \qquad \left(\nu = \frac{4a}{\pi K_{x3}}\sin 2\alpha\sin\frac{\tau}{2}\right) \tag{14}$$

from which it is evident that the time of the nutation angle decrease from the initial value ϑ_0 to 0 is given by

$$T(\vartheta_0) = \frac{1}{\nu}\left\{\frac{\sin\vartheta_0}{2\cos^2\vartheta_0} + \frac{1}{2}\ln\left[\tan\left(\frac{\pi}{4} + \frac{\vartheta_0}{2}\right)\right]\right\} . \tag{15}$$

At least up to $\vartheta_0 \approx 20^0$, the dependence $T(\vartheta_0)$ is insignificantly different from the linear dependence $T(\vartheta_0) = \vartheta_0/\nu$, which simplifies the calculations.

Since on the right side of Eq. (14) there are no terms that are linear in $\sin\vartheta$, the interaction amplitude a (or the coil field value) can be any value other than zero, which affects only the time of the nutation damping rather than its character.

POSSIBLE REALIZATIONS

To conclude the study of the nutation damping, let us make some final remarks relative to the application of the method proposed:

a) As it is evident, the working part of the control moment of the n-th coil pair $\sim \sin(\psi + \sigma - \beta_n)$. At the same time, the projection of the rotor symmetry axis onto the direction $\vec{r}_n = \vec{z}_1 \cos\beta_n + \vec{z}_2 \sin\beta_n$, that corresponds to this pair is $(\vec{s} \cdot \vec{r}_n) = \vartheta \cos(\psi + \sigma - \beta_n) + \rho \cos(\sigma - \beta_n)$ for small ϑ and ρ . Since the moment transducer in the gyro incorporates four coil pairs, it is apparent that the control moment of any pair can be formed based on the signal taken from an adjacent pair.

However, this mode of operation, in which the signal is taken from one pair and there are switchings-over in the other pair, can lead to an electrical engagement of both channels disrupting thereby their normal operation. In this respect, we need to obtain a signal with frequency $\psi^\bullet$ by another method, for example, using a transducer to obtain a signal on one side of the rotor and a transducer to ensure control on the other side of the rotor. In this case, however, along with the moment effect, there will also be a force effect on the rotor or tension.

b) Another method is the switching-over mode of operation, in which, for a certain period of time, the transducers are used for obtaining the information and then for control with periodic repetitions of the process. There is no input signal in the control mode, and it results in a decrease of K. Consequently, the control signal can be formed by a device of an underexcited oscillator type to the input of which an external signal with frequency $\psi^\bullet$ is initially applied. In this case, control will be efficient only over the time period until the phase difference between the real signal from the rotor with frequency $\psi^\bullet$ and the signal from the oscillator achieves the critical value $(\Delta\varphi = \pi/2)$.

If at the initial time it was the frequency ω_0 , and the rotor deceleration could be simulated by the viscous friction when $\omega(t) = \omega_0 \exp(-\lambda t)$, the phase difference between the signals from the rotor and from the oscillator can be calculated as

$$\Delta\varphi = \int_0^t \omega_0 \left(1 - e^{-\lambda\tau}\right) d\tau = \omega \left(t + \frac{1}{\lambda} e^{-\lambda t} - \frac{1}{\lambda}\right) \approx \frac{1}{2}\omega_0 \lambda t^2.$$

If $T_0 = 2\pi/\omega_0$, $T_\lambda = \lambda^{-1}$, then

$$T_{con} = \sqrt{\frac{\Delta\varphi}{\pi} T_0 T_\lambda} \tag{16}$$

Let us consider the following example: if the rotor speed is $\Omega = 1000$ *r.p.s.* $(\psi^\bullet = 2\pi \cdot 1200\ sec^{-1})$, and the damping is such that $T_\lambda = 1\ hr$, the nutation can be damped during $T_{con} \approx 1.22\ sec$ until the phase difference becomes $\Delta\varphi = \pi/2$, after which we again need to switch over to the regime of signal reception and control moment formation.

c) The proposed mechanism of nutation damping is active for both constant and variable magnetic fields generated by the coils, but the constant field efficiency is greater. The maximum

gain in efficiency of the effect on the rotor can be obtained, provided the transducer coils are used for control alone and the input signal with frequency $\psi^{\bullet}$ for the control moment formation is taken from other devices.

REFERENCES

1. Odintsov, A. A.: Magnetic Gyroscope and Inertial System on its Basis. *Sudostroitel'naya promyshlennost', ser. Navigatsiya i giroscopiya*, no. 1, 1991, pp. 51-58 (in Russian).

2. Komarov, V.N.: On the Influence of the Self-Modulation on Nutation of a Noncontact Gyroscope. *Prikladnaya mekhanika*, vol. 20, no. 5, 1984, pp.104-109 (in Russian).

3. Komarov, V.N.; Urman, Yu. M.: Active Damping of Noncontact Gyroscope Rotor Nutation. *Izv. vuzov. Priborostroyeniye*, vol. 25, no.12, 1982, pp.- 44-47 (in Russian).

4. Komarov, V.N.: Regulating the Magnetic Gyroscope's Motion. *The Fourth International Symposium on Magnetic Bearings.* Zurich. Hochschulverlag AG an ETN,1994, pp.19-22.

5. Beletskiy, V.V.: Dynamics of Fast Rotations. *Proc. Res. Inst. for Mechanics. Moscow University*, no. 29, 1973, pp.97-118 (in Russian).

Session 10 -- Bearing/Actuator Design

Chairman: James Downer
Satcon Technology Corporation

DESIGN AND ANALYSIS OF AN ELECTROMAGNETIC THRUST BEARING

Bibhuti B. Banerjee
Dantam K. Rao
Precision Magnetic Bearing Systems, Inc.
Cohoes, NY

SUMMARY

A double-acting electromagnetic thrust bearing is normally used to counter the axial loads in many rotating machines that employ magnetic bearings. It essentially consists of an actuator and drive electronics. Existing thrust bearing design programs are based on several assumptions. These assumptions, however, are often violated in practice. For example, no distinction is made between maximum external loads and maximum bearing forces, which are assumed to be identical. Furthermore, it is assumed that the maximum flux density in the air gap occurs at the nominal gap position of the thrust runner. The purpose of this paper is to present a clear theoretical basis for the design of the electromagnetic thrust bearing which obviates such assumptions.

INTRODUCTION

The basic design analysis of an electromagnetic thrust bearing is well known (1, 2, 3, 4). In these analyses, the maximum bearing force is generally assumed to equal the external load. However, this assumption ignores the inertia forces due to the vibrating shaft. These inertial forces may be larger than the external loads under certain situations, thus invalidating the conventional design analysis.

Another assumption normally used is that the maximum force requirement occurs at the nominal or equal gap position, when the thrust runner is centered between the two stators. This assumption holds only if the maximum movement of the runner is negligibly small compared to the air gap. An adequate design should take the motion of the runner into account when computing the maximum ampere turns required.

NOMENCLATURE

A_p	single pole face area [m^2]
B_1, B_2	flux density in left and right electromagnet respectively [T]
c_{brg}	bearing damping coefficient [N-s/m]
k_{brg}	bearing stiffness coefficient [N/m]
m	total moving mass (shaft and runner) [kg]
f_c	coil copper factor
f_p	coil packing factor
F_1, F_2	force on runner from left and right electromagnet respectively [N]
F_{brg}	net bearing force on runner [N]
F_{dyn}	amplitude of dynamic component of external force on shaft [N]
F_{ext}	external force on shaft [N]
F_{stat}	static component of external force on shaft [N]
g_0	mean air gap [m]
g_1, g_2	air gap for left and right electromagnet respectively [m]
h_s	radial height of slot [m]
I_1, I_2	current in the left and right electromagnet coil respectively [A]
I_b	bias current in coil [A]
I_{dyn}	amplitude of the dynamic component of coil current [A]
I_{max}	maximum coil current [A]
I_{stat}	static component of coil current [A]
J	maximum coil current density [A/m^2]
l_s	axial length of slot [m]
N	number of turns in coil
R	resistance of coil [Ω]
t	time [s]
t_0	instant when bearing force is maximum [s]
V	power supply voltage [V]
x	axial displacement of runner [m]
x_{dyn}	amplitude of axial displacement of runner [m]
α	correction factor accounting for flux leakage and fringing
ϕ	phase lag of runner displacement with respect to dynamic component of external force [rad]
Φ	Flux in magnetic circuit [Weber]
μ_0	permeability of free space [$4\pi \times 10^{-7}$ N/A^2]
ω	frequency of dynamic external force [rad/s]
ψ	phase lag of coil current with respect to dynamic component of external force [rad]

THEORY

A double-acting electromagnetic thrust bearing, Fig. 1, is made up of two electromagnets (stators), one on each side of the thrust runner (rotor) and separated by an air gap. Such a system is inherently unstable. It is stabilized by sensing axial position and using this information to control the current in the stators via an electronic controller. The controller is typically of the proportional-integral-derivative (PID) type, and may be implemented in analog or digital form.

Force Capability

Each of the stators applies an attractive force on the runner. The free-body diagram of the thrust runner is shown in Fig. 2. For dynamic equilibrium, the equation of motion is

$$m\ddot{x} = F_{ext} - F_{brg} \tag{1}$$

where the external force and the resulting motion are

$$F_{ext} = F_{stat} + F_{dyn} \sin \omega t \tag{2}$$

$$x = x_{dyn} \sin(\omega t - \phi) \tag{3}$$

On substitution, we get

$$F_{brg} = F_{ext} - m\ddot{x} = F_{stat} + F_{dyn} \sin \omega t + m\omega^2 x_{dyn} \sin(\omega t - \phi) \tag{4}$$

The bearing has to be designed to accommodate the vector sum of the external force *and* the inertia force. The phase lag determines whether the inertia force adds to or subtracts from the external dynamic force, Fig. 3. For subcritical operation ($\phi < \pi/2$), neglecting the inertia force can result in an undersized thrust bearing that "bottoms out" during operation. For supercritical operation ($\phi > \pi/2$), the inertia force fights the external dynamic force, and ignoring this can result in an overdesigned bearing. If the phase lag is small

$$\phi << \pi/2 \tag{5}$$

the bearing must be designed for a load capacity of

$$F_{brg,\max} = F_{stat} + F_{dyn} + m\omega^2 x_{dyn} \tag{6}$$

This force requirement occurs at $\omega t = \pi/2$. Since the two electromagnets act in pull-pull mode, F_1 and

F_2 are always positive. The net bearing force is the difference of the two:

$$F_{brg} = F_1 - F_2 \tag{7}$$

The bearing force is at a maximum when one electromagnet is applying its maximum pull force and the other is turned off. Thus, for the double-acting arrangement, we must have

$$F_{1,\max} = F_{2,\max} = \left|F_{brg,\max}\right| \tag{8}$$

Each electromagnet must be designed for this load capability. For the special case where $F_{ext} = 0$, the bearing must still be capable of withstanding the inertia force at the natural frequency of axial vibration of the system. System design is then dictated by desired transient response, characterized by overshoot and settling time (5).

Ampere Turns

The thrust bearing consists of two electromagnetically biased and excited magnetic circuits with two air gaps per circuit. Each circuit has an outer and an inner pole in the stator, and back iron to complete the flux path in the stator, Fig. 1. The flux lines traverse the air gaps and complete their path in the runner. Both the runner and the stator are made of magnetically permeable material. The pole face areas are typically made equal in order to ensure uniform flux density in the stator.

The bearing force is related to the flux densities in the two electromagnets by

$$F_{brg} = \frac{A_p}{\mu_0}\left(B_1^2 - B_2^2\right) \tag{9}$$

while the two air gaps are given by

$$\begin{aligned} g_1 &= g_0 + x \\ g_2 &= g_0 - x \end{aligned} \tag{10}$$

The corresponding currents in the two electromagnets are

$$\begin{aligned} I_1 &= I_b + I_{stat} + I_{dyn}\sin(\omega t - \psi) \\ I_2 &= I_b - I_{stat} - I_{dyn}\sin(\omega t - \psi) \end{aligned} \tag{11}$$

The maximum external force, $F_{ext,\max}$ occurs when $\omega t = \pi/2$. This is given by

$$F_{ext,\max} = F_{ext}\big|_{\omega t=\pi/2} = F_{stat} + F_{dyn} \tag{12}$$

However, F_{brg} may not reach its maximum at the same instant due to the effect of rotor inertia. Let the bearing force reach a maximum at some time t_0. At this time t_0, then, we must also have, from (9)

$$\left(B_1^2 - B_2^2\right)\Big|_{t=T} = \left(B_1^2 - B_2^2\right)\Big|_{\max} \tag{13}$$

Since

$$B_1^2 \geq 0, \qquad B_2^2 \geq 0 \tag{14}$$

the difference reaches a maximum only when $B_2 = 0$ and B_1 is at a maximum, or $B_1 = 0$ and B_2 is at a maximum. Let's consider the former case:

$$F_{brg,\max} = \frac{A_p}{\mu_0}\left(B_{1,\max}^2 - 0\right) \tag{15}$$

$$B_2 = 0 \;\Rightarrow\; I_2 = 0 \;\Rightarrow\; I_{stat} + I_{dyn}\sin(\omega T - \psi) = I_b = I_{\max}/2 \tag{16}$$

$$I_1 = I_b + I_{stat} + I_{dyn}\sin(\omega T - \psi) = I_b + I_b = I_{\max} \tag{17}$$

$$B_{1,\max} = \left(\frac{\mu_0 N}{2\alpha}\right)\frac{I_1}{g_1}\Big|_{t=T} = \left(\frac{\mu_0 N}{2\alpha}\right)\frac{I_{\max}}{g_0 + x_{dyn}\sin(\omega T - \phi)} \tag{18}$$

We can rearrange (18) to determine the $(NI)_{\max}$ required to produce the magnetic flux density, $B_{1,\max}$:

$$(NI)_{\max} = \alpha\frac{2B_{\max}}{\mu_0}\left[g_0 + x_{dyn}\sin(\omega T - \phi)\right] \tag{19}$$

When the material operates up to saturation, $B_{\max} = B_{sat}$, and $(NI)_{\max}$ can be calculated, provided *t0* is known. The correction factor α may be determined using the techniques discussed in (2). The pole face area required may be determined using Eqn. (15) above.

The time t_0 when the bearing force developed is maximum can be determined analytically, using Eqn. (4). It is given by

$$T = (\pi - \delta)/\omega \tag{20}$$

Here, the angle δ can be calculated from

$$\delta = \tan^{-1}\left(\frac{F_{dyn} + m\omega^2 x_{dyn}\cos\phi}{m\omega^2 x_{dyn}\sin\phi}\right) \tag{21}$$

When the small phase lag condition of Eqn. (5) holds, the maximum force occurs at $x \approx x_{dyn}$. This

implies that the designer must ensure sufficient ampere turns to saturate the magnetic material of the left electromagnet for its maximum gap position of the runner. In general, however, the phase angle ϕ is not known beforehand, since the bearing design affects the system dynamics. Thus, an iterative process must be employed or bearing stiffness and damping parameters assumed in order to determine this phase:

$$F_{brg} = c_{brg}\dot{x} + k_{brg}x \tag{22}$$

For a given dynamic to static load ratio and a required vibration to gap ratio, the required stiffness may be calculated using the methodology outlined in [6].

Number of Turns and Maximum Current

Assuming a supply voltage v driving the coil of the left electromagnet, we must have

$$v = N\frac{d\Phi}{dt} + I_1 R \tag{23}$$

The resistive load is typically small compared to the inductive load, and may be neglected. Then,

$$\Phi = \frac{1}{N}\int v dt = \frac{1}{\omega N} V_{\max} \sin \omega t \tag{24}$$

assuming a sinusoidal supply voltage of the form $v = V_{\max} \cos \omega t$ [7]. The maximum flux level is therefore

$$\Phi_{\max} = B_{\max} A_p = \frac{V_{\max}}{\omega N} \tag{25}$$

The power supply voltage required is often determined by force slew rate requirements [8]. However, $V_{\max}$ is limited by available power supplies that operate at the frequency of interest. The number of turns is thus fixed as

$$N = \frac{V_{\max}}{\omega A_p B_{\max}} \tag{26}$$

This, in conjunction with Eqn. (19), fixes the maximum coil current:

$$I_{\max} = \frac{(NI)_{\max}}{N} \tag{27}$$

The maximum coil current density is typically fixed at around $J = 5 \times 10^6$ A/m^2, using which the coil wire gage may be obtained

$$A_w = \frac{I_{\max}}{f_c J} \tag{28}$$

The coil copper factor f_c — the ratio of bare copper cross-section to wire cross-section — is typically less than 0.7. The coil occupies a slot of axial length l_s and radial height h_s, so that the slot cross-section is

$$A_c = l_s h_s = \frac{(NI)_{\max}}{f_c f_p J} \tag{29}$$

EXAMPLE — HIGH SPEED FLYWHEEL

Let us consider a flywheel of mass 1 kg (2.2 lb) rotating at 6283 rad/s (60,000 RPM) and supported on magnetic thrust bearings. Let the magnitude of the dynamic external force be 445 N (100 lbf), so that

$$F_{ext} = 445 \sin 6283t$$

It is desired that the maximum excursion of the flywheel under this loading be limited to 2.5×10^{-5} m (1 mils). So, the runner motion is

$$x = 5 \times 10^{-5} \sin(6283t - \phi)$$

If ϕ satisfies Eqn. (5), we must design for

$$|F_{1,\max}| = |F_{2,\max}| = |F_{brg,\max}| = 445\,\text{N} + 1974\,\text{N} = 2419\,\text{N}$$

as required by Eqn. (6). It is evident that a bearing designed to withstand only the 445 N of dynamic external force would be inadequate for this system.

If the mean air gap is $g_0 = 2.5 \times 10^{-4}$ m (10 mils), $B_{\max} = 1.0$ T and Eqn. (19) is applied now, the maximum ampere turns required is

$$(NI)_{\max} = 438\,\text{A - turns}$$

assuming that the correction factor is $\alpha = 1$. This is about 40 A-turns more than for conventional designs, which assume saturation at the equal gap position. Also, using Eqn. (15), the pole-face area required is

$$A_p = 5.59 \times 10^{-4}\ \mathrm{m}^2 \quad (0.87\,\mathrm{in}^2)$$

We can now determine the number of turns N by applying Eqn. (26) and assuming a supply voltage of, say, 200 V:

$$N = 57\,\mathrm{turns}$$

The maximum current in the coil is

$$I_{\max} = 7.7\,\mathrm{A}$$

CONCLUSION

We have shown that two assumptions often employed in designing electromagnetic thrust bearings can lead to inadequate products. The inertia force must be taken into account when sizing the thrust bearing for load capacity. For subcritical operation, this inertia force increases the bearing load capacity requirement. However, if one designs for supercritical operation, the inertia force fights the external force and reduces the load capacity requirement. The bearing size may be *reduced* by taking advantage of this fact.

Moreover, during the vibration of the thrust runner in response to an excitation force, the maximum bearing load capacity is required at a position that is different from the nominal gap position. The implication is that the ampere turns required is more than that for the maximum-force-at-the-nominal-gap assumption. The maximum available voltage supply to energize the electromagnets then determines the maximum coil current and the number of turns.

REFERENCES

1. Habermann, H. and M. Brunet, "The Active Magnetic Bearing Enables Optimum Control of Machine Vibrations," ASME 85-GT-221.

2. Banerjee, B. B., "Analysis and Design of Magnetic Thrust Bearings," M. S. Thesis, Dept. of Mechanical and Aerospace Engg., University of Virginia, Charlottesville, 1988.

3. Allaire, P. E., A. Mikula, B. B. Banerjee, D. W. Lewis and J. Imlach, "Design and Test of a Magnetic Thrust Bearing," *Journal of the Franklin Institute*, vol. 326, no. 6, pp. 831 – 847, 1989.

4. Bornstein, K. R., "Dynamic Load Capabilities of Active Electromagnetic Bearings," ASME 90-Trib-50.

5. Inman, D. J., *Vibration*, Prentice Hall, Englewood Cliffs, New Jersey, 1989.

6. Rao, D. K., G. V. Brown, P. Lewis and J. Hurley, "Stiffness of Magnetic Bearings Subjected to Combined Static and Dynamic Loads," *Journal of Tribology*, vol. 114, pp. 785 – 789, 1992.

7. Ellison, A. J., *Electromechanical Energy Conversion*, George G. Harrap & Co. Ltd., 1965.

8. Maslen, E., P. Hermann, M. Scott and R. R. Humphris, "Practical Limits to the Performance of Magnetic Bearings: Peak Force, Slew Rate and Displacement Sensitivity," *Magnetic Suspension Technology Workshop*, NASA Langley Research Center, Hampton, Virginia, 1988.

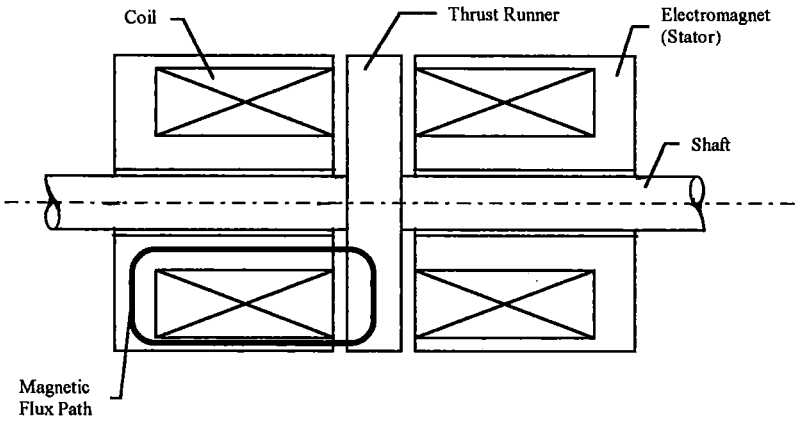

Figure 1. Double-Acting Electromagnetic Thrust Bearing

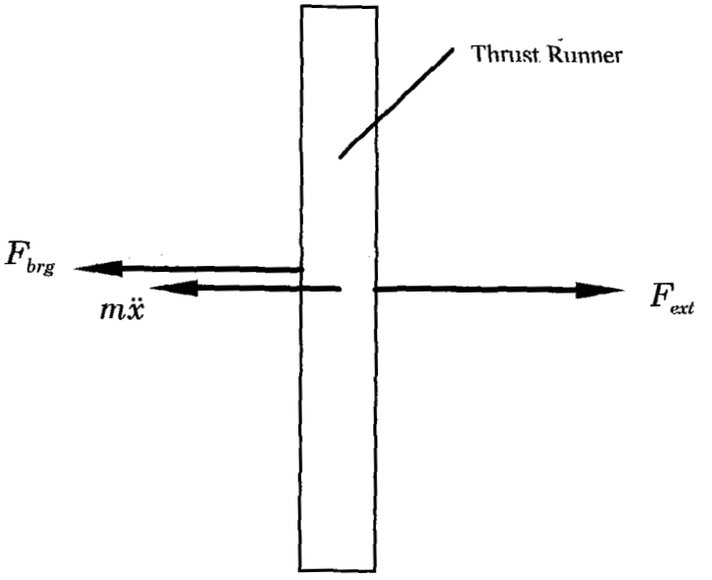

Figure 2. Free-Body Diagram of Thrust Runner for a Magnetic Thrust Bearing

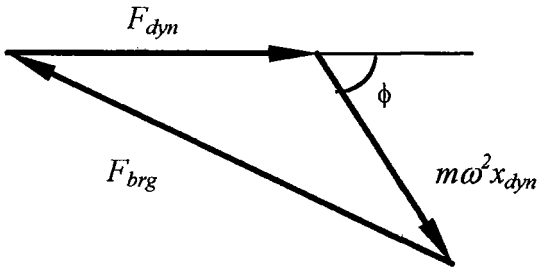

(a) Subcritical Operation

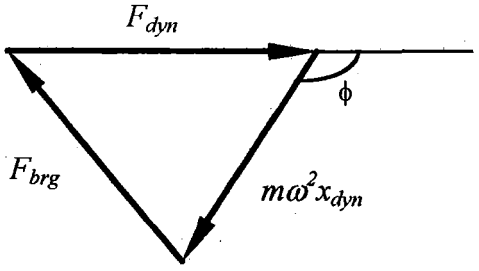

(b) Supercritical Operation

Figure 3. Phasor Diagrams for Motion of Thrust Runner

S27-37
82164
035631

RESULTS OF A PARAMETRIC STUDY ON 10,000 LB. AND 50,000 LB. PERMANENT MAGNETIC ACTUATORS

16 P.

Z. J. J. Stekly, C. Gardner, P. Domigan, C. McDonald, R. A. Farrell
Intermagnetics General Corporation

ABSTRACT

The purpose of this study was to generate design data and complete dynamic performance estimates for a high performance permanent magnet actuator. The basic configuration selected for analysis is an axisymmetric Nd-B-Fe permanent magnet actuator capable of providing force in one direction along its major axis. The actuator consisted of two main axisymmetric components separated by an air gap. The design was optimized for each value of force, gap and magnetic field to yield minimum weight and maximum lift to weight ratio. The following table is indicative of the results achieved.

Force (lbs)	Outer Diameter (inches)	L/W Ratio	Field Strength (T)	Air Gap (inches)
50,000	42.1	9:1	1.0	1.00
	22.0	45:1	1.8	0.25
10,000	10.5	30:1	1.0	0.79
	10.5	60:1	1.5	0.39

The basic conclusions is that, within the parameters considered, the 10,000 lb. and 50,000 lb. actuators are lightweight and compact. As expected for most permanent magnet devices, the smaller ones have higher lift to weight ratios. The question of dynamic performance and the control coil requirements for specific applications remains to be determined.

This work was performed by Field Effects, a division of Intermagnetics General Corporation, under a U.S. Department of Defense subcontract from Lockheed Martin Electric Boat Division, Groton, CT. "Distribution Statement A, **Approved for Public Release - Distribution Unlimited.**"

INTRODUCTION

This study was conducted to determine the characteristics of magnetic suspension systems for vibration isolation. Improved force attenuation and control was the prime motivation for studying magnetic suspension. Although the present effort concentrated on force attenuation, control system analysis was also needed to determine the force attenuation characteristics of magnetic actuators. Field Effects performed a single degree of freedom analysis of a Proportional, Integral, Derivative (PID) controller in order to make a first pass assessment of the force attenuation characteristics of magnetic suspension.[1]

CONFIGURATION

Two types of magnetic suspension are possible; attractive and repulsive. A repulsive system is stable in the direction of magnetization but unstable in the transverse directions while the reverse is true of an attractive system.[2] A repulsive system requires two magnetic assemblies compared to one for an attractive system and, therefore, is typically more costly to produce. Because of this, the attractive system was selected for study. The configuration selected is an axisymmetric configuration with a pole, permanent magnet material and return yoke in one assembly. A second assembly contains a control coil and lift plate, Figure 1.

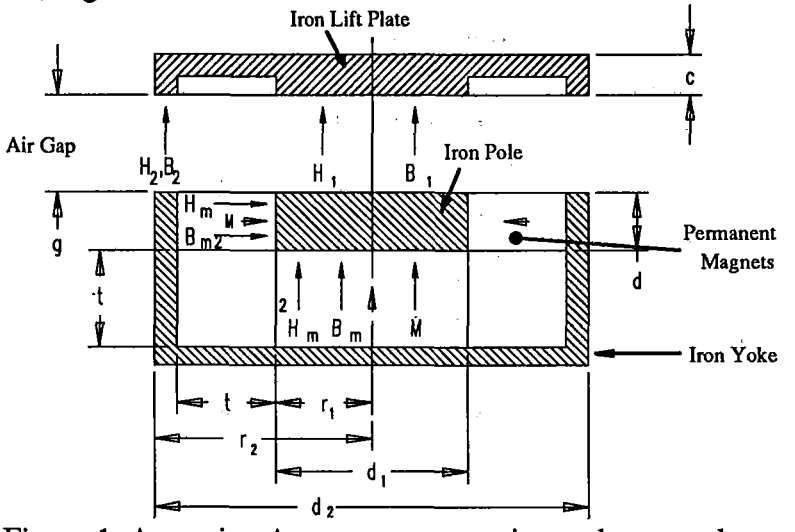

Figure 1. Attractive Actuator cross section and nomenclature

The results of the preliminary dynamic analyses are summarized by Figure 2, which compares the analytical one dimensional force attenuation of a magnetic actuator with

low pass filtered control to a typical rubber device with lift/stiffness ratio of 0.5 inch. This figure indicates that the magnetic actuator provides at least 30 dB more attenuation than the rubber one above frequencies of 10 Hz. It should be noted that this control system has not been optimized and therefore further improvements in the force attenuation characteristics are possible.

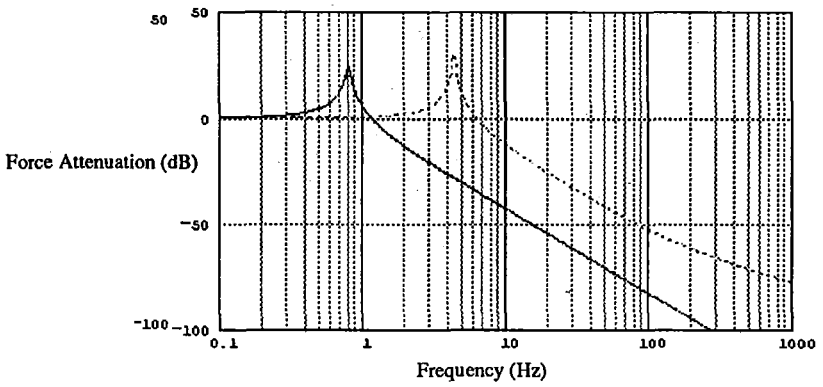

Figure 2. Force Attenuation Comparison Between Typical Rubber Device (dotted) And Magnetic Actuator with low pass filtered PID control (solid).

Equations were derived from first principals [3] to establish the relationship between design parameters such as gap and size to desired performance characteristics such as lift force, static stiffness and lift/weight ratio. A discussion of the analysis and equations are contained in the appendix.

10,000 Lb. Actuator Analytical Results

The initial actuator magnetic design focused on an attractive system capable of producing 10,000 lbs. of lift over a range of gaps which varied from 0.25 to 1 inch. The desired stiffness was 20,000 lbs./inch.

An ideal actuator has the following characteristics:

- Low stiffness for good acoustics.
- Large lift capacity.
- Light weight i.e. high lift/weight ratio.
- Small size.
- Large gap for shock mitigation.

As is often the case, these characteristics cannot be achieved without tradeoffs. In this case, optimization is based on minimum weight and diameter. Design curves using the analysis contained in the appendix were generated and are summarized for a 10,000 lb. lift actuator in Figure 3. This figure illustrates lift force, static stiffness (K), gap field and lift to weight ratio as a function of gap and actuator outside diameter. Lines of constant gap magnetic field of 1.0 T and 1.5 T are shown and trends for lift and stiffness as a function of gap and diameter indicated by arrows. The general conclusion is that higher gap fields, i.e., 1.5 T vs. 1.0T, lead to a smaller actuator and greater lift to weight ratios. A nominal operating region is also indicated encompassing actuators with lift to weight ratios ranging from 30-60 to 1. The nominal operating region is somewhat arbitrary but illustrates the range of design parameters that encompass an appropriate variation in the gap while still providing high lift to weight ratio.

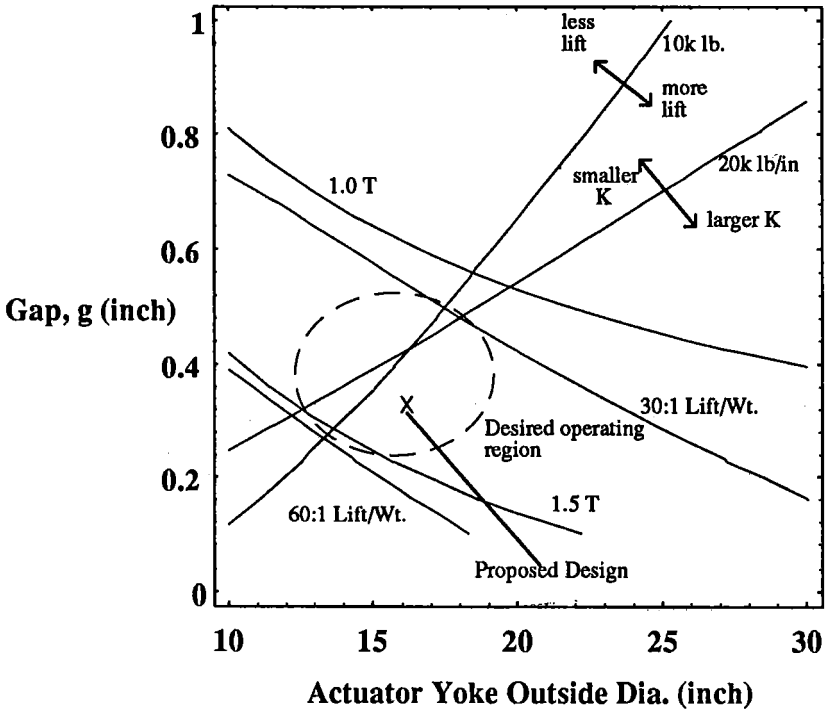

Figure 3. 10,000 Lb. Actuator Preliminary Design Curves.

As an example of design tradeoffs, Figure 3 illustrates that a 16 inch diameter actuator operating at 0.4 inch gap provides 10,000 lbs. of lift and 20,000 lbs./inch of stiffness. With the actuator diameter fixed at 16 inches, an increased gap results in lift, stiffness and lift/weight ratio all decreasing. These curves also indicate that for 10,000 lbs. of lift and a 60:1 lift/weight ratio, static stiffness will be above 20,000 lbs/inch, nominal operating gap will be ~0.2 inches. and the field in the gap will be greater than 1.5 T.

A 10,000 lb. lift actuator design concept for the design point indicated in Figure 3 is shown in Figure 4. The actuator is placed between a platform and the base. The permanent magnets, pole piece, and yoke are located in the upper assembly. The vertical

control coils are integral with the lift plate in the lower assembly. Eight lateral control coils are also located on the sides of the lift plate.

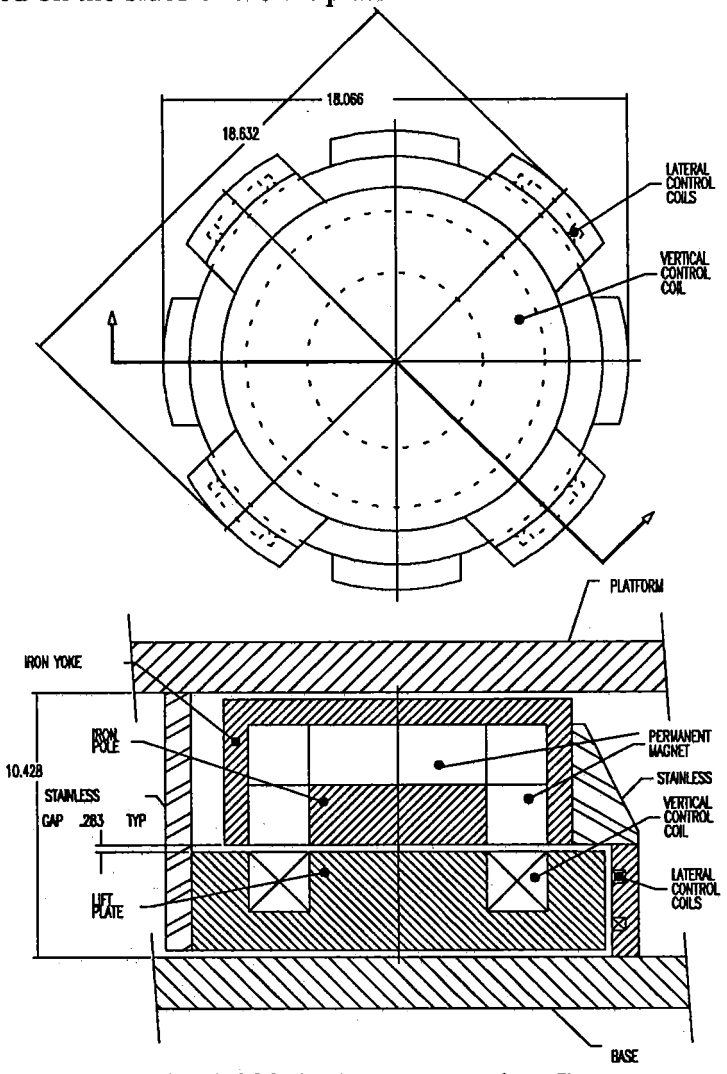

Figure 4. 10,000 lb. Actuator Design Concept.

This actuator concept is 18.7 inches in diameter, 10.4 inches high, has a 0.28 inch nominal gap and gap magnetic field of approximately 1.4 T.

50,000 LB. ACTUATOR ANALYTICAL RESULTS

As a part of this study, design curves for 50,000 lbs. of lift and 100,000 lb./inch stiffness, i.e., the same lift to stiffness ratio as the earlier 10,000 lb. case, were formulated using minimum magnet material as the optimization parameter. This represents a minimum cost approach as the magnet material cost dominates the cost of

the actuator. This approach also considerably simplifies the analysis compared to that used for the previously described 10,000 lb. lift case where minimum weight and diameter were the optimization parameters.

The force attenuation performance for the 50,000 lb. lift designs are essentially the same as shown in Figure 2 since the lift/stiffness ratio gives the same dynamics as the 10,000 lb./20,000 lb./inch case.

Contour curves for 10,000 and 50,000 lbs. lift as a function of gap and actuator diameter for gap magnetic fields of 1.5 and 1.8 T are given in Figures 5 and 6. Note that in these figures, both the 10,000 lb. and 50,000 lb. lift curves are obtained using minimum magnet material as the optimization criteria.

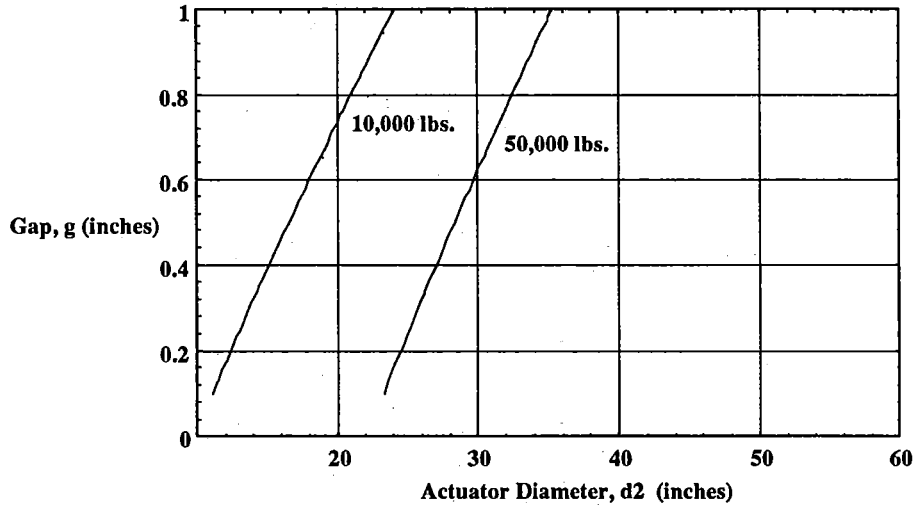

Figure 5. 1.5 T Lift Contours as a Function of Gap and Actuator Diameter.

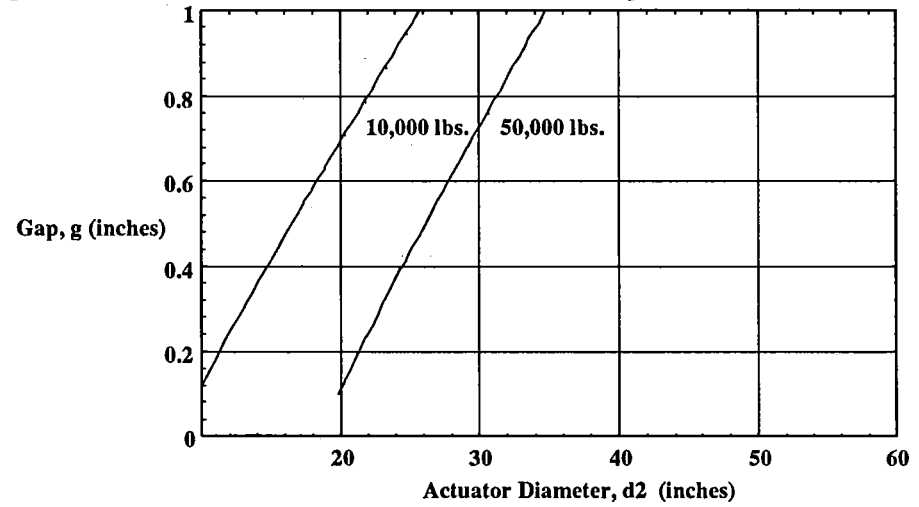

Figure 6. 1.8 T Lift Contours as a Function of Gap and Actuator Diameter.

These figures indicate that for 10,000 lbs of lift there are only minor differences between the 1.5 and 1.8 T curves, probably the result of the large fraction of permanent magnet material dominating magnet sizing. For 50,000 lbs. of lift, increased field yields

smaller actuators for the same gap as expected for designs where larger fractions of iron dominate. This data also demonstrates that large capacity actuators are more efficient from a lift force per unit actuator area standpoints. For example, Figure 5 indicates a 10,000 lb. actuator operating at 0.4 inch gap is approximately 16 inches in diameter while an actuator that provides a 5:1 improvement in lift at the same gap, i.e. 50,000 lbs., is only 1.7 times larger in diameter or 27 inches. The reason for this is that the thickness of permanent magnet material is fixed for a given field and gap. As a consequence, the permanent magnet takes up fractionally less of the area as the loads increase. (See equation A-12 in the appendix).

Figures 7 and 8 indicate stiffness and lift to weight contours respectively for the 1.5 T, 50,000 lb. lift design indicating how these parameters are affected by gap and diameter. Figure 8 shows, as one would expect, that the best lift to weight ratios are achieved with small gap, small diameter actuators.

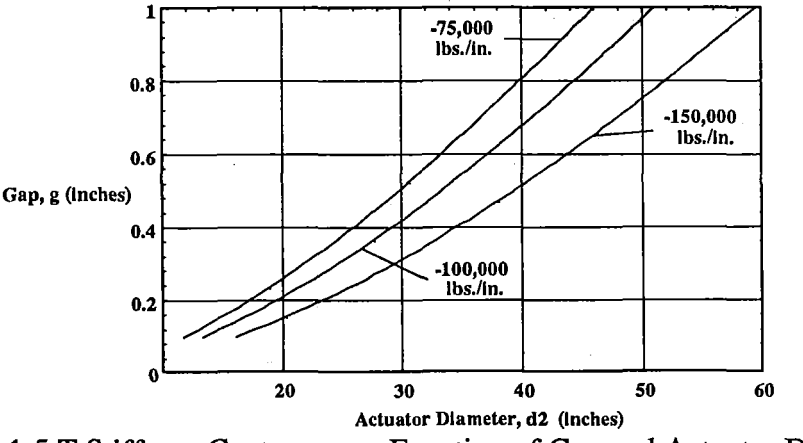

Figure 7. 1.5 T Stiffness Contours as a Function of Gap and Actuator Diameter.

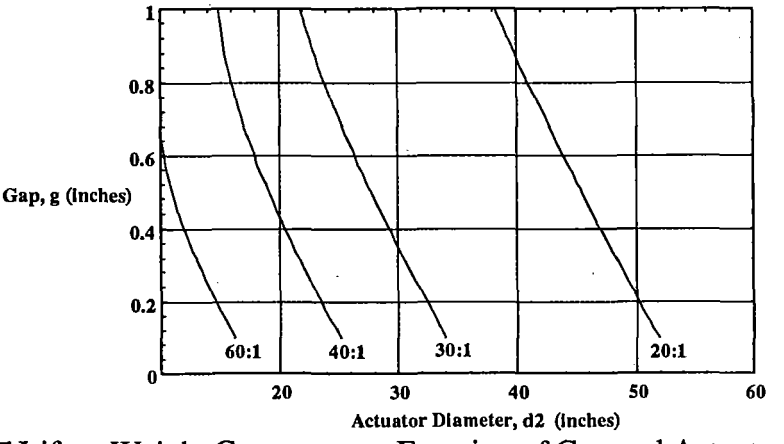

Figure 8. 1.5 T Lift to Weight Contours as a Function of Gap and Actuator Diameter.

Figure 9 indicates lift, stiffness and lift to weight contours for 1.0, 1.5 and 1.8 T gap fields, respectively. The maximum gap field analyzed was 1.8 T since this field is approximately the practical upper limit given the flux carrying capabilities of lower cost

iron alloys. Field Effects has built Nd-Fe-B permanent magnet devices with gap fields as high as 2 T using poles of a more expensive Vanadium Permendur alloy.[4,5]

Figure 9 clearly shows the tradeoff between gap and lift to weight ratio. At 1.5 T, given a requirement of 50,000 lbs of lift at a 0.1 inch gap, the lift to weight is ~42:1 while at a 1.0 inch gap the lift to weight is ~22:1. 1.0 T actuators have a maximum lift to weight of ~23:1 at 0.1 inch gap and ~10:1 at 1.0 inch gap or about half the performance of the 1.5 T actuator. The 1.8 T performance at 1.0 inch. gap is similar to that at the 1.5 T but has an improved lift to weight ratio (50:1 vs. 42:1) at 0.1 inch gap. Thus, given the flux carrying capacity of existing materials, a compact actuator design will have a gap field between 1.5 and 1.8 T.

Table I summarizes the effect of field and gap on actuator diameter, d2, and lift/weight ratio at the nominal 'design point' of 50,000 lb. lift and 100,000 lb./inch stiffness. The conclusion is that, if large gaps are required for shock mitigation reasons, high field actuators can achieve large gaps, i.e. 1 inch, at lift/weight ratios in the 22-26:1 range. Large gaps are not practical with low field actuators as the lift/weight ratio suffers dramatically.

Figure 10 illustrates two 50,000 lb. lift concepts for a 1.5 T attractive actuator designed for 0.25 inch and 1.0 inch nominal gaps. The 0.25 inch gap actuator is 30 inches in diameter, 12.9 inches high and has a lift/weight of 37:1, while the 1.0 inch gap is 41.3 inches in diameter, 20.5 inches high with a lift/weight of 22:1.

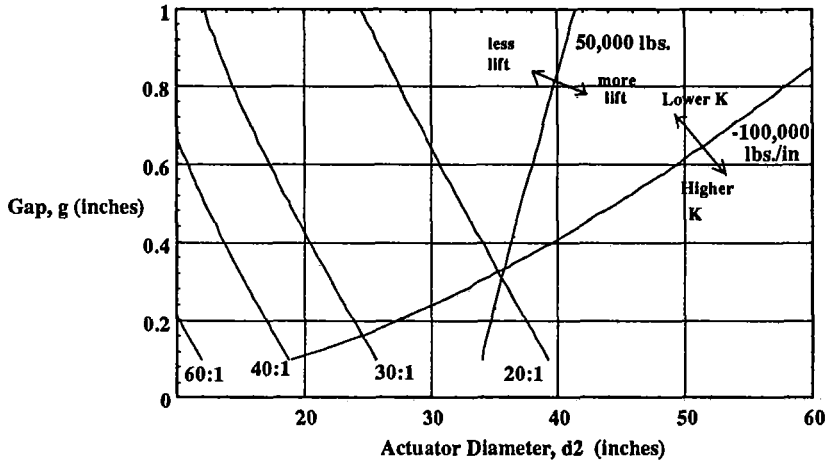

Figure 9 (a). 1.0 T Design Curves.

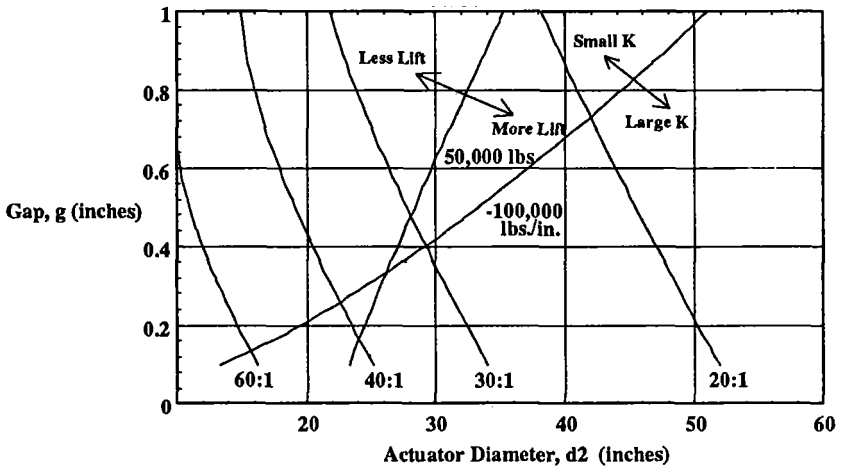

Figure 9 (b). 1.5 T Design Curves.

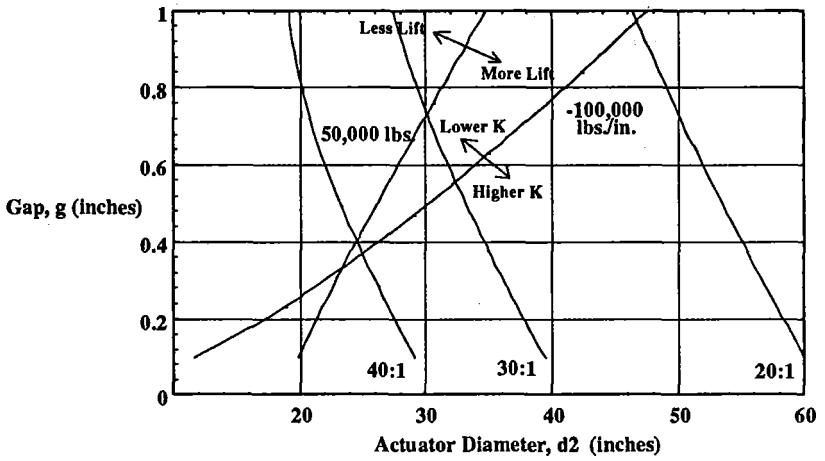

Figure 9 (c). 1.8 T Design Curves.

Table I:
50,000 lbs. and 100,000 lbs./inch Actuator Summary

Field (T)	Gap, g (in.)	.25	.5	.75	1.0
1.0	d2 (in.)	35	37	39	42
	L/W	22:1	15:1	11:1	9:1
1.5	d2 (in.)	25	28	32	35
	L/W	37:1	30:1	25:1	22:1
1.8	d2 (in.)	22	26	31	35
	L/W	45:1	38:1	30:1	26:1

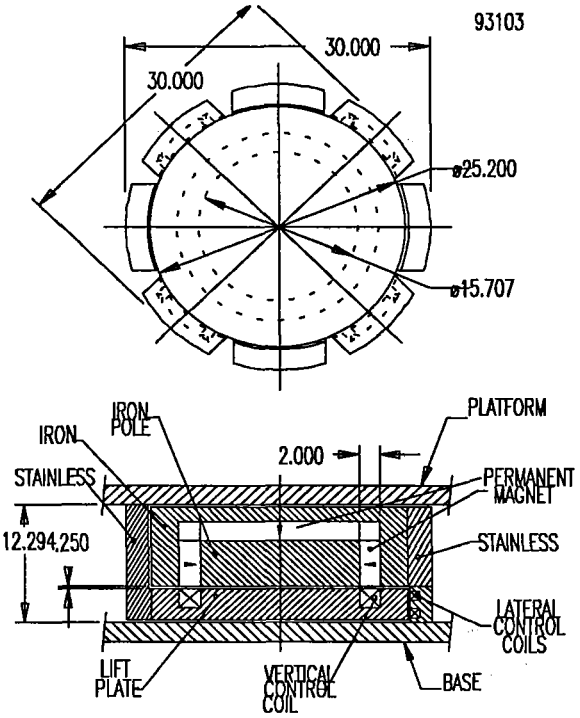

Figure 10a: 1.5 T, 0.25 in. Gap, 50,000 Lb. Lift Actuator Design Concept.

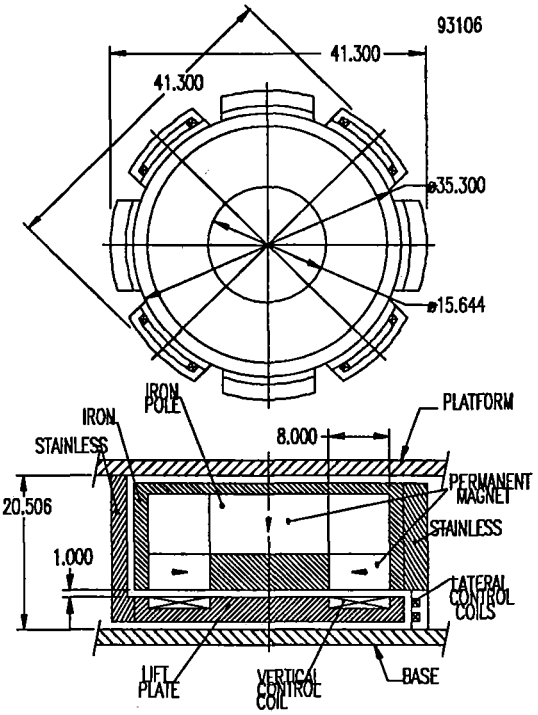

Figure 10b: 1.5 T, 1.0 gap, 50,000 Lb. Lift Actuator Design Concept.

Magnetic fringe fields are of concern for reasons of personnel or equipment exposure. Fields less than 5 Gauss are considered acceptable. PANDIRA[6], a finite difference magnetic analysis code, was used to estimate the fringe field at the gap centerline of the 50,000 lb. actuator design, Figure 11.

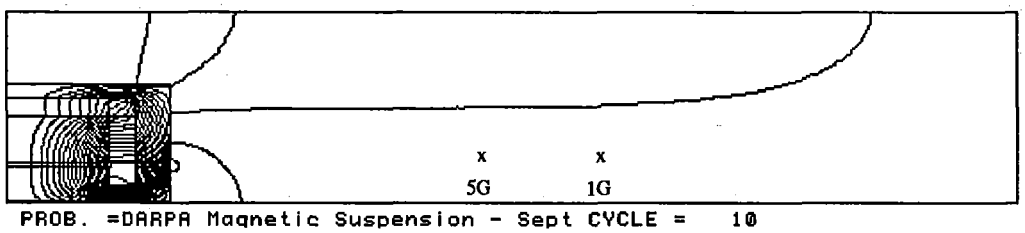

Figure 11. 50,000 lb. Actuator Fringe Field Plot.

The 5 and 1 Gauss points are located at 39.5 and 48.8 inches from the actuator center. The analysis also confirmed the uniformity of magnetic field within the gap at the pole and at the yoke.

CONCLUSIONS

The analysis performed indicates that a magnetic suspension system can provide 30 dB more force attenuation than rubber device above 10 Hz. Design optimization procedures, based on minimum weight and diameter, and a simplified version based on minimum magnet material, have been developed to size actuators and predict performance. In order to maximize actuator Lift to Weight ratio and minimize actuator size, gap field will be in the 1.5-1.8 Tesla range. Concept designs for 50,000 lb. lift actuators operating at 0.25 and 1.0 inch nominal gaps have been presented.

Larger capacity actuators are nearly twice as efficient as smaller actuators from a lift per unit foot print area perspective. For instance to achieve 50,000 lbs. of lift, five (1.5 T, 0.25 inch gap) 10,000 lb. actuators require a foot print of 37 inches by 56 inches while a single 50,000 lbs. actuator (1.5 T, 0.25 inch gap) requires only a 30 inches by 30 inches foot print. The 50,000 lb. actuators are approximately the same size as an equivalent lift capacity rubber device.

This analysis indicates that magnetic suspension is a viable technology based on force attenuation, lift to weight ratio and size. The critical characteristic, as far as the viability of this technology is concerned, is the force attenuation performance. Since magnetic suspension will be more costly than rubber devices, magnetic suspension must significantly improve performance.

ACKNOWLEDGMENTS

The assistance of Ms. Denise Silva and Ms. Julia Saia in preparing this manuscript is gratefully acknowledged.

REFERENCES

1. Katsuhiko, O.: *Modern Control Engineering,* Electrical Engineering Series, Prentice-Hall, Englewood Cliffs, NJ, 1970

2. Kraus, J.D.: *Electromagnetics,* McGraw-Hill, NY, 1984

3. Reitz, J. R.; Milford, F. J.; and Christy, R.W.: *Foundations of Electromagnetic Theory,* Addison Wesley Publishing Co., 1992.

4. Stekly, Z.J.J.; Gardner, C.; Baker, J.; Domigan, P.; Hass, M.,;McDonald, C.; and Wu, C.: *Design and Performance of 2T Permanent Magnet Wiggler for the Stanford Synchrotron Radiation Laboratory* presented at Synchrotron Radiation Instrumentation 1995, Argonne, IL.

5. Stekly, Z.J.J.; Gardner, C.; Domigan, P.: *A 2T Full Scale High Performance Periodic Permanent Magnet Model for Attractive (228KN) and Repulsive Maglev,* to be presented at NASA Magnetic Suspension Conference 1995, Tallahassee, FL.

6. POISSON, Super Fish Reference Manual LA-UR-87-126 LANL Code Group MS H829, LANL, N.M. Jani, 1987

APPENDIX

A-1 Magnetic and Force Analysis

The equations governing actuator design are discussed in this appendix. Figure A-1 illustrates a cross section of a generic actuator and the nomenclature used.

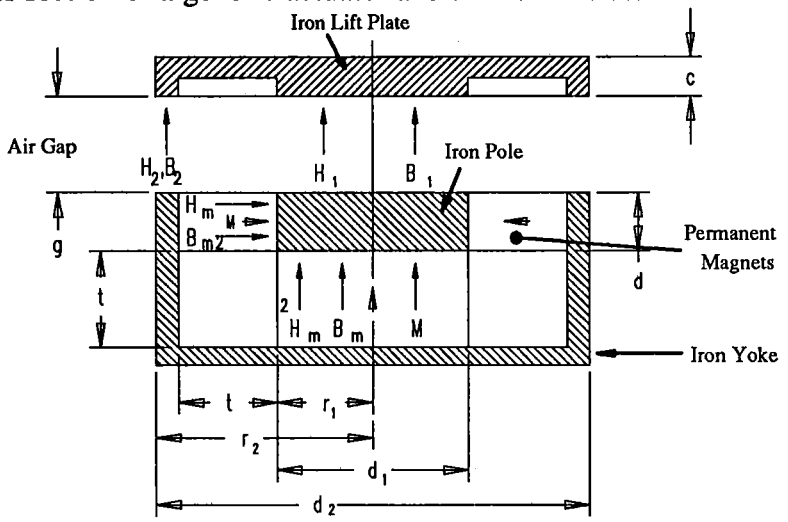

Figure A-1: Attractive Actuator cross section and nomenclature.

The location of the magnetic fields B_1, H_1 and B_2,H_2 in the gap and B_m, H_m within the permanent magnet material are indicated in the figure. The areas A_1, A_2, A_3, defined below, are for the inner pole, outer yoke and total for the permanent magnet material, respectively. The three basic magnetic equations involve continuity of magnetic flux, application of Ampere's Law and the relationship between fields and magnetization within the permanent magnet:

$$B_1A_1 = B_2A_2 = B_mA_3 \qquad [A1]$$

$$H_mt = -\frac{[B_1 + B_2]g}{\mu_o} \qquad [A2]$$

$$B_m = \mu_o(H_m + M_m) \qquad [A3]$$

The above equations assume that the iron has a very high magnetic permeability. Using all three equations to eliminate B_2, B_m, and H_m results in:

$$B_1 = \frac{\mu_o M}{\frac{g}{t}(1 + \frac{A_1}{A_2}) + \frac{A_1}{A_3}} \qquad [A4]$$

where:

M = magnetization
B_1 = pole gap flux
t = magnet thickness
r_1 = pole radius
d = pole depth
r_2 = outer radius of yoke
$A_3 = \pi r_1(r_1+2d)$, surface area magnet
$A_1 = \pi r_1$, pole area
$A_2 = \pi(r_2^2-(r_1+t)^2)$ yoke area
g = air gap

subscripts:

m = magnetic material
1 = inner pole
2 = outer yoke

The attractive force is equal to: $F = \frac{B_1^2}{2\mu_o} A_1 + \frac{B_2^2}{2\mu_o} A_2$ [A5]

This is equal to the magnetic pressure at the pole $B^2/2\mu o$ times the appropriate area which can be simplified to: $F = \frac{B_1^2}{2\mu_o} A_1[1 + A_1/A_2]$ [A6]

the stiffness, K is obtained by:

$$K = \frac{\partial F}{\partial g} = \frac{B_1}{\mu_o} A_1[1 + A_1/A_2]\frac{\partial B_1}{\partial g} \qquad [A7]$$

Performing the derivative indicated using equation A4 for B_1, substituting and simplifying results in:

$$K = \frac{F(1 + A_1/A_2)}{t} \bullet \frac{2B_1}{\mu_o M} \qquad [8]$$

Initially for the 10,000 lb. actuator design curves were obtained by choosing a value for the magnetization, $\mu_o M$ typical for Nd-B-Fe 1.1T magnet material and varying the remaining variables, based on experience, to determine B_1. The lift force, F and actuator stiffness, K were then calculated using the above equations. The iron pole, yoke, and lift plate dimensions were then determined by assuming the field in the iron was the same as that in the gap.

The lift to weight ratio could then be easily calculated as the ratio of F to actuator weight using the following:

$$L/W = \frac{F}{\rho_m V_m + \rho_{Fe} V_{Fe}} \qquad [A8]$$

where:

ρ_m = magnet density
V_m= magnet volume
ρ_{Fe} = iron density
V_{Fe} = iron volume

Because of the number of independent variables involved, this process was time consuming. It was also difficult to determine when an actuator design was "optimal". Therefore, a simplified design process was desirable.

A-2 Design Optimization

A designer wants to know what the lift, stiffness and lift/weight is as a function of gap and actuator diameter. Because of saturation effects, practical actuator designs will have a maximum gap field, B1 of between 1 and 2 Tesla. The designer is also limited by the properties of today's materials therefore, M is also known. This line of reasoning led us to conclude that we needed a design approach such that given the independent variables, B1, M, r2 and g, we could optimize the pole height, d and the magnet thickness, t.

The approach selected sought to minimize the volume of magnet material in the actuator. This simplified approach seeks to minimize actuator cost by minimizing the amount of the most expensive component of the actuator, the magnet material. We begin by approximating the magnet volume, V_m as the product of its surface area, A_3 and thickness, t as shown by:

$$V_m = A_3 t \qquad [A9]$$

We now substitute into [A4] to get:

$$V_m = \frac{A_3 g\left(1 + \frac{A_1}{A_2}\right)}{\left(\frac{M}{B_1} - \frac{A_1}{A_3}\right)} \qquad [A10]$$

Next we minimize V_m by taking the appropriate derivative of V_m and setting it equal to zero to get:

$$A_3 = \frac{2 A_1 B_1}{M} \qquad [A11]$$

To get an expression for t, we substitute [A9] and [A10] in [A11] and solve for t, the thickness of permanent magnet material:

$$t = \frac{2 B_1 g\left(1 + \frac{A_1}{A_2}\right)}{M} \qquad [A12]$$

DESIGN OF A LONG-STROKE NONCONTACT ELECTROMAGNETIC ACTUATOR FOR ACTIVE VIBRATION ISOLATION

Bibhuti B. Banerjee
Precision Magnetic Bearing Systems, Inc.
Cohoes, NY

Paul E. Allaire
Mechanical, Aerospace and Nuclear Engineering, University of Virginia
Charlottesville, VA

SUMMARY

A long-stroke moving coil Lorentz Actuator was designed for use in a microgravity vibration isolation experiment. The final design had a stroke of 5.08 cm (2 in) and enough force capability to isolate a mass of the order of 22.7–45.4 kg. A simple dynamic magnetic circuit analysis, using an electrical analog, was developed for the initial design of the actuator. A neodymium-iron-boron material with energy density of 278 T-kA/m (35 MGOe) was selected to supply the magnetic field. The effect of changes in the design parameters of core diameter, shell outer diameter, pole face length, and coil wire layers were investigated. An extensive three-dimensional finite element analysis was carried out to accurately determine linearity with regard to axial position of the coil and coil current levels. The actuator was constructed and tested on a universal testing machine. Example plots are shown, indicating good linearity over the stroke of approximately 5.08 cm (2 in) and a range of coil currents from -1.5 A to +1.5 A. The actuator was then used for the microgravity vibration isolation experiments, described elsewhere.

INTRODUCTION

A comparison of the microgravity requirements of space experiments with the actual environment available on spacecraft indicates the need for vibration isolation over a few decades in frequency [1]. While relatively high frequency disturbances may be attenuated using passive isolators, this approach fails in the very important but lower frequency regime of 0.1—10 Hz. Only active isolation at the payload-spacecraft interface with an appropriate actuator allows the synthesis of the desired isolator properties at these low frequencies and the adjustment of these properties using a control loop.

Mechanical or hydraulic actuators introduce a physical connection that may transmit undesirable vibrations and have friction and backlash [2]. Non-contacting actuators are therefore required. Among such actuators, acoustic or electrostatic types have inadequate force capabilities for realistic applications, being able to suspend masses only of the order of a few grams [2]. Electromagnetic actuators have a relatively higher force capability.

This paper discusses the design of a noncontacting electromagnetic actuator with a stroke of 5 cm (2 in) and enough force capability to isolate a mass (between 22.7 and 45.4 kg (50 and 100 lb)) connected by an umbilical to a source of low frequency vibrations. This large motion capability would provide rattle space for the isolated experiment. This rattle space is required in response to the very low frequency disturbances that may be passed on to the experiment without any attempt at isolation by the controller. The literature describes the design and use of magnetic actuators with single-stage motion capabilities of about 0.25 cm (0.1 in) or less [3, 4, 5, 6, 7]. Tandem coarse/fine schemes to overcome the small gap limitations of typical magnetic actuators and achieve isolation capabilities for very low frequency disturbances have been discussed [8, 9]. It is evident, however, that such strategies involve considerable mechanical complexity.

A single-stage long-stroke actuator with the basic advantages of a noncontacting magnetic isolation system is an attractive proposition. Force linearity with both position and current are highly desirable properties in order to simplify the feedback controller required. Moreover, in view of the ultimate goal of deployment in space, such a device has to be compact and lightweight. Power consumption and heat generation during operation—the costs associated with active control—also need to be minimized. Stroke limitations precluded the use of a moving-iron, magnetic thrust bearing-type actuator.

NOMENCLATURE

A_g, A_m	Cross-sectional area of air gap, magnet
avg	Average
B, **B**	Magnetic flux density (scalar, vector) (Tesla, T = Wb/m^2)
B_g	Radial flux density in air gap of Lorentz Actuator
B_{sat}	Saturation flux density
c, c_{cr}	Damping coefficient, critical damping coefficient
e, emf	Electromotive force (voltage)
f	Frequency (Hz)
F, $\hat{F}$	Force
F	Force (vector)
F_a	Force exerted by actuator

F_d	Direct disturbance force
F_T	Force transmitted to the base for a mass-excited system
fea	Finite element analysis
g_0	Acceleration due to gravity at sea level; 9.8 m/sec^2 (386 in/sec^2)
$G(s)$	Transfer function of plant
H	Magnetic field strength (A-turns/m)
$(-H_d, B_d)$	Magnet operating point on demagnetization curve (Appendix A)
$H(s)$	Transfer function of feedback controller
I	Current in conductor
k	Stiffness coefficient
l, $\mathbf{l}$	Length of conductor (vector $\mathbf{l} = \mathbf{l}_2 - \mathbf{l}_1$)
l_g, l_m	Length of air gap, magnet
L, L_C	Inductance, inductance of (Lorentz Actuator) coil
LAMA	Long Action Magnetic Actuator
m	Mass
max, min	Maximum, minimum
n	Number of turns of current-carrying conductor
Nd-Fe-B	Neodymium iron boron (magnet material)
R_C, R_S, R_t	Resistance of (Lorentz Actuator) coil, resistance of voltage source, total resistance in Lorentz Actuator circuit ($R_t = R_C + R_S$)
$\Re$	Reluctance of magnetic circuit (A-turn/Wb)
s	Laplace variable ($s = j\omega$)
Sm-Co	Samarium cobalt (magnet material)
t	Time
v	Source voltage
V_g, V_m	Volume of air gap, magnet
x	Displacement (absolute) of mass (microgravity experiment) m
z_{em}	Motional electrical impedance of Lorentz Actuator ($z_{em} = \alpha^2/z_m$)
z_m	Impedance of mechanical system driven by Lorentz Actuator ($z_m = F/\dot{x}$)
α	Electromechanical coupling coefficient (or power coefficient) for a Lorentz Actuator ($\alpha = NlB_g$)
ϕ	Magnetic flux (Weber, Wb)
ϕ_C,ϕ_m,ϕ_{sat}	Circuit flux, magnet flux, flux in saturated segment of magnetic circuit
η	Efficiency of electrical to mechanical power conversion by a Lorentz Actuator, as defined in Equation (4-15)
μ_0	Permeability of air ($\mu_0 = 4\pi \times 10^{-7}$ Wb/A-turn-m)
μ_r	Relative permeability of a medium
τ	Electrical time constant of the Lorentz Actuator ($\tau = L_C/R_C$)
τ_m	Equivalent mechanical time constant of the Lorentz Actuator ($\tau_m = m(R_C + R_S)/\alpha^2$)
ω_n	Natural frequency
ξ	Damping ratio

THEORY

The moving-coil-type Lorentz Actuator operates on the same principle as the voice-coil of a speaker [10]. Current is passed through a coil wound on a sleeve. The sleeve surrounds the core of the actuator and can move axially in either direction. The geometry of the actuator is shown in Figure 1. The coil is much longer than the width of the pole-face, so that the number of turns of coil wire directly underneath the pole-face in the flux path is the same for every coil position between the extremes of the stroke limit. The circumferential current flow in the coil is normal to the radial magnetic field across the pole-face gap generated by a permanent magnet in the shell of the actuator.

As shown in Figure 1 (inset), when a conductor of length $\mathbf{l} = \mathbf{l}_2 - \mathbf{l}_1$ and carrying current I is placed in a magnetic field of average flux density **B** over the length of the conductor, a Lorentz force **F** is produced in a direction mutually perpendicular to both **l** and **B**:

$$\mathbf{F} = \int_{\mathbf{l}_1}^{\mathbf{l}_2} I(d\mathbf{l} \times \mathbf{B}) \tag{1}$$

For the Lorentz Actuator, this relation reduces to

$$F = nlIB_g = \alpha I \tag{2}$$

where $l = 2\pi r$ is the length of one turn of the coil, and the electromechanical coupling coefficient (or power coefficient) $\alpha \equiv nlB_g$ indicates the efficiency of energy conversion for the actuator.

The motion of the coil at a velocity $\dot{x}$ in the magnetic field results in the generation of an induced voltage (a "back-emf") given by

$$e = \alpha \dot{x} \tag{3}$$

The Lorentz Actuator coil has resistance R_C and inductance L_C. The electrical circuit may be represented as in Figure 2. For this circuit, with $R_t = R_C + R_S$, and $L = L_C$, we have

$$v = L\dot{I} + R_t I + \alpha \dot{x} \tag{4}$$

The Lorentz Actuator drives a mechanical "circuit" that may be generically represented as a mass-spring-damper system. Thus, we also have

$$\alpha I = m\ddot{x} + c\dot{x} + kx \tag{5}$$

where the system is made up of a mass m, a spring of stiffness k and a damper with damping coefficient c. For microgravity vibration isolation, k and c are the umbilical stiffness and damping respectively.

Equations (4) and (5) may be used to obtain the transfer function of the Lorentz Actuator. On taking the Laplace transforms,

$$\begin{aligned}(Ls + R_t)I(s) &= V(s) - \alpha s X(s) \\ (ms^2 + cs + k)X(s) &= \alpha I(s)\end{aligned} \tag{6}$$

Division to eliminate *I(s)* and manipulation yields the transfer function

$$\frac{X(s)}{V(s)} = \frac{\alpha}{\beta s^3 + \gamma s^2 + \delta s + \varepsilon} \tag{7}$$

where the coefficients in the denominator are

$$\beta = mL, \quad \gamma = mR_t + cL, \quad \delta = kL + cR_t + \alpha^2, \quad \varepsilon = kR_t \tag{8}$$

For this actuator, *cs* and *k* are small compared to ms^2. So, equation (7) simplifies to

$$\frac{X(s)}{V(s)} = \frac{\alpha}{s(mLs^2 + mR_t s + \alpha^2)} \tag{9}$$

Also, the electrical transients decay very rapidly, so that the electrical time constant is small and *L* can be neglected. Then equation (9) reduces to

$$\frac{X(s)}{V(s)} = \frac{1/\alpha}{s(\tau_m s + 1)} \tag{10}$$

where $\tau_m = mR_t / \alpha^2$ may be termed the equivalent mechanical time constant of the Lorentz Actuator. The actuator designed was used to drive a mass of 34 kg (75 lb). It was powered by a linear transconductance amplifier with a transconductance ratio of 0.5 A/V, for an effective total resistance R_t of 2 Ω (irrespective of coil resistance). Thus, the mechanical time constant for this application was $\tau_m \approx$ 19.24 sec. In contrast, the electrical time constant for the actuator was $\tau = L_C/R_C$ = 1.1 milli-sec, which is negligibly small.

The electrical and mechanical system equations are coupled by the coefficient α. Strong coupling results in a high power conversion efficiency η, given by

$$\eta = \frac{\alpha I\dot{x} - c\dot{x}^2}{\alpha I\dot{x} + R_t I^2} \tag{11}$$

Nonlinearity in a Lorentz Actuator is primarily caused by the coil moving out of the uniform magnetic field in the air gap as its position varies over the entire stroke. This results in the electromechanical coupling coefficient becoming a nonlinear function of displacement, instead of being a constant. In addition, if a voltage source is used to power the Lorentz Actuator, Equations (4) and (5) take nonlinear forms given by

$$v = L\dot{I}(x) + R_t I(x) + \alpha(x)\dot{x}$$
$$\alpha(x)I(x) = m\ddot{x} + c\dot{x} + kx \tag{12}$$

For the Lorentz Actuator designed, the use of a long coil length and of current feedback ensures good linearity. A longer coil length, however, also results in an increased inductance and a higher electrical time constant for the actuator.

INITIAL DESIGN

While the main reason to pick the Lorentz Actuator over an actuator like a magnetic thrust bearing is the much longer stroke capability possible, there are other advantages too. Unlike the magnetic bearing, it is open-loop and neutrally stable, thus eliminating the need for a redundant control system and backup power supply. Nor is a constant bias current necessary for steady state operation, so that the power requirements under these conditions are very small. The linearity offered by a Lorentz Actuator greatly simplifies control system design and operation. The relatively low force capability is not an issue for microgravity applications, since the forces required are quite small (of the order of one pound).

The initial design was developed using the basic techniques of linear magnetic circuit analysis. Neodymium iron boron (Nd-Fe-B), with a high maximum energy product of 278 T-kA/m (35 MGOe), was chosen as the magnet material[1]. This commercially available material has the composition $Nd_{15}Fe_{77}B_8$. This choice was dictated by the need for a compact actuator which would nonetheless exhibit a linear force-vs.-current trend. Samarium cobalt (Sm-Co) was also considered, but a comparison showed that the magnetic and mechanical properties of Nd-Fe-B are superior because of its iron content. Nd-Fe-B is 15% lighter, which is significant for a space application, and cheaper. The two areas of advantage for Sm-Co—relative inertness and better thermal stability—were not of much importance here.

Fringing and leakage of the magnetic field were not modeled, but an attempt to minimize their deleterious effects was made by applying a rule of thumb that requires the gap ratio—the ratio of the shell-to-core gap to the pole-face gap—to be about 3:1 or higher. A design algorithm was developed to carry out the Lorentz Actuator design [12].

Some observations on sizing the magnet may be made. For a magnet of length l_m and cross-sectional area A_m operating at the point $(-H_d, B_d)$ on its normal demagnetization curve [12] and producing a flux density B_g in an air gap of length l_g and cross-sectional area A_g in a typical Lorentz Actuator geometry, we have

$$B_g A_g = B_d A_m \tag{13}$$

and

$$H_d l_m = -\frac{B_g}{\mu_0} l_g \tag{14}$$

[1]Crumax® 355, a product of Crucible Magnetics, Crucible Materials Corporation, 101 Magnet Drive, Elizabethtown, Kentucky 42701.

Here, μ_0 is the permeability of air, and the reluctance of the iron path is assumed to be negligible compared to that of the air gap. Multiplying these two equations and rearranging gives us

$$B_g^2 = -\mu_0 (B_d H_d) (V_m / V_g) \tag{15}$$

where the volumes of the magnet and the air gap are represented, respectively, by $V_m = A_m l_m$ and $V_g = A_g l_g$. A greater volume of magnet material can thus result in a higher value of the air gap flux density, provided the same energy product ($B_d H_d$) is maintained. Generally, changing either the length l_m or the cross-section A_m of the magnet to change the volume of the magnet results in changing the operating point of the magnet on the demagnetization curve, so that the energy product is also changed. Dividing Equation (13) by (14) yields the slope of the load-line:

$$\frac{B_d}{\mu_0 H_d} = -\frac{l_m}{A_m}\frac{A_g}{l_g} \tag{16}$$

An increase in the length of the magnet must be accompanied by a corresponding increase in its cross-sectional area, or vice-versa, so as to maintain the same slope of the load-line. In effect, this does not change the operating point, so that the energy product also stays the same, even though the volume of the magnet has increased.

It was found that a reduction of the core diameter helped to improve position linearity. While increasing the axial length of the air gap by axially elongating the pole-face helped improve the gap flux density and actuator force, imparting a "lip" to the actuator enhanced position linearity. The magnet protrudes radially outside the pole-piece and the base, reducing the leakage factor significantly [13].

A number of design iterations were carried out for a circuit of magnet iron, with a saturation flux density, B_{sat} of 1.2 T (Tesla). The Nd-Fe-B magnet required for the resulting design could not be made in one piece—the large outer diameter (8.13 cm (3.20 in)) would require it to be made up of sectors. It was decided to analyze this design using finite elements.

FINITE ELEMENT ANALYSIS

An effort was made to try to come up with a more compact design, within a constraint of 5.08 cm (2 in) as the outer diameter of the magnet, this dimension being the manufacturer's limit for a one-piece Nd-Fe-B magnet. It was hypothesized that a reduction of the core diameter to saturate the core would enable us to satisfy this constraint, with its concomitant reduction in the magnet diameter. This would deliberately violate the rule of thumb about the minimum gap ratio required, and yet minimize flux leakage and its consequent nonlinearity problem, since a magnetic material, when saturated, has the permeability of air. Finite element analysis [14] was used in this context to produce a better design.

A detailed finite element analysis enabled the realistic consideration of flux leakage and fringing effects. The effect of magnetic saturation of part of the circuit could be studied, as also that of using different geometric configurations to minimize weight and cost. Properties of magnetic materials were input as *B-H* tables, so that operation in the nonlinear region of a material's *B-H* curve was permitted.

The model also included the effect of change in the air gap flux due to the varying magnetic flux associated with changing coil current.

A finite element analysis package[2] suitable for solving a three-dimensional axisymmetric problem on a personal computer was used. The initial design of the Lorentz Actuator, as specified in the last section, was then modeled. The amount of flux leakage observed was judged high enough to cause unacceptable variations in force with changes in position of the coil.

A number of designs, incorporating a constraint of 4.95 cm (1.95 in) (to allow for machining losses with a 5.08 cm (2 in) cylindrical ingot, the largest available) on the outer diameter of the magnet, were analyzed by this technique. The finite element mesh consisted predominantly of quad elements, though some triangular ones were also used. The mesh used for the final design is shown in Figure 3, along with a typical flux plot (Lorentz Actuator final design, coil in its innermost position carrying a current of 2.5 A (into the plane of the page)). A total of 499 elements made up the axisymmetric finite-element model, with the air gap and shell-to-core gap regions being very finely meshed into 162 elements.

The generation of the required force while maintaining linearity, with respect to both coil position and coil current, and compactness is the crux of the problem. Position linearity requires that, for a constant coil current, the actuator force remain the same irrespective of the axial position of coil, within the stroke bounds. On the other hand, current linearity at a given coil position calls for the actuator force to vary linearly with changes in the coil current between its upper and lower design limits. Current linearity, therefore, requires that the average flux density across the effective air gap remain constant with variations of the coil current. The effective air gap is generally longer (in the axial direction) than the air gap radially beneath the pole-face due to flux leakage.

The design iterations were driven by the conflicting needs of satisfying the force requirement and maintaining linearity. While the limit on the outer diameter of the magnet provided the design envelope in the radial direction, the total stroke of 5.08 cm (2 in) dictated that the coil be considerably more than 5.08 cm (2 in) long to ensure that the same number of turns of the coil "cut" the effective air gap. This helped ensure force linearity with position from one end of the stroke to the other. The thickness of the air gap depended on a compromise between reducing it to decrease the circuit reluctance so as obtain increased flux density and force, and increasing it to accommodate a greater number of (radial) layers of coil wire (of the same gage) in order to increase the force.

FINAL DESIGN

The final design, obtained after a number of iterations with the finite element model, is shown in Figure 4. The magnetic material used for the circuit was a nickel-iron alloy with 48% nickel content[3]. In bar form, this material exhibits very high permeability and nominally saturates at approximately 1.5 T. A coil current density of 155 A/cm^2 (1000 A/in^2) was picked for continuous use to ensure cool operation, even though a fivefold increase in the current density is possible for peak loads. Other design data for this actuator, which was built and tested, are provided in Table 1.

---

[2]MAGGIE, a product of The MacNeal-Schwendler Corporation, 815 Colorado Boulevard, Los Angeles, CA 90041

[3]High Permeability "49"® Alloy, from Carpenter Technology Corporation, Carpenter Steel Division, 5355 Morse Drive, Decatur, GA 30035-3810.

The results obtained by finite element analysis indicated that this design would have a high degree of position and current linearity. The predictions and actual measurements are presented in the following section.

TEST RESULTS

A universal testing machine was used to test the Lorentz Actuator for load capacity at various coil positions and coil currents. Because of thermal considerations, currents of up to ±1.5 A only were tested. The resulting data were then analyzed and compared with the predictions based on finite element analysis. These results are presented in Figure 5 for positive coil currents. Almost identical results for negative coil currents are not presented here for the sake of brevity.

The motivation for this figure is to check for position linearity. Least squares fitting of a regression line has been carried out for each set of experimental data. The slope of each of these regression lines would have been zero for perfect position linearity. A small amount of leakage flux exists in the air between axial distances of 0.76 cm (0.3 in) and 5.84 cm (2.3 in), even though this was neglected in the predictions. Furthermore, the tolerance of 0.13 mm (5 mils) for the magnet inner diameter was a compromise between the requirements of accuracy and cost. Combined with unknown inaccuracies introduced during the vendor's assembly procedure, it resulted in more flux leakage than expected from finite element analysis. (This is corroborated by the analysis of flux measurements, which follows). As the coil moves further towards the closed end, more turns of the coil "cut" this leakage flux, so that the magnitude of the force increases. Since the coil length has been chosen to take advantage of the fringing flux at the open end even at the innermost position of the coil, there is no corresponding reduction on this account with inward coil motion.

The next figure, Figure 6, presents the data from the perspective of current linearity. Again, linear regression lines have been fitted to the experimentally obtained data, revealing that the current linearity observed is very good (note the extremely good correlation). The higher slope of the least square line compared to the predicted results line is indicative of higher forces in each case than predicted, again because of the reasons mentioned earlier. Also, as expected from the discussion for position linearity in the previous paragraph, the slope of the least square line increases as the coil moves inward.

A gaussmeter was used to measure the radial flux density in the air gap over an axial travel of 2.03 cm (0.8 in) to 11.43 cm (4.5 in) from the base. Flux densities were measured along axial lines at 45 ° intervals circumferentially around the annular air gap, using a probe of 0.25 mm (10 mils) thickness. The unbroken line ("avg") in Figure 7 represents the average of each set of eight values observed at a particular axial distance. The values observed in the pole-face region are lower than predicted by finite element analysis (dashed line "fea"), but spread out over a longer axial length. The "error bars" along this line represent the spread between the maximum and minimum values observed at the corresponding points. The fact that this spread is much higher in the shell-to-core region than elsewhere is attributable to inaccuracies in machining and assembly mentioned earlier.

An error analysis was performed to verify that the differences between the measured and predicted flux over the pole-face gap were within the limits resulting from dimensional and magnetic tolerances. The analysis predicted an error of ±5.64% in the magnetic flux in this region. The actual error over this range was calculated to be −3.83%, well within the predicted limits [12].

CONCLUSION

The theory for the design of a long-stroke electromagnetic actuator for space vibration isolation has been presented. A preliminary design was verified and optimized using finite element analysis. The actuator was then constructed and tested for load capacity and gap flux. It exhibited excellent force linearity with respect to position and current.

This actuator was used in an actively controlled vibration isolation testbed in the laboratory where both springs and an air dashpot were used as umbilicals. Reduction ratios of 40 dB or greater were achieved, as desired, in each case tested [12, 15].

REFERENCES

[1] Nelson, E. S., "An Examination of Anticipated *g*-Jitter on Space Station and Its Effect on Materials Processes," *NASA TM–103775*, April 1991.

[2] Naumann, R. J. and D. D. Elleman, "Containerless Processing Technology," *Materials Sciences in Space*, Ed. B. Feuerbacher, Springer Verlag, Berlin, 1986.

[3] Owen, R. G. and D. I. Jones, "Columbus Applications Study (WP. 1.1)," Technical Note No. BTN 001, University College of North Wales, School of Electronic Engineering Science, Bangor, Gwynedd, Sep. 1988.

[4] Havenhill, D. D. and K. D. Kral, "Payload Isolation Using Magnetic Suspension," AAS 85 014, *Annual AAS Guidance and Control Conference,* Keystone, Colorado, Feb. 2–6, 1985.

[5] Allen, T. S., D. D. Havenhill and K. D. Kral, "FEAMIS: A Magnetically Suspended Isolation System for Space Based Materials Processing," AAS 86 017, *Annual AAS Guidance and Control Conference*, Keystone, Colorado, Feb. 1–5, 1986.

[6] Hibble, W., P. J. Wolke and M. Smith, "A Magnetic Isolation and Pointing System for the Astrometric Telescope Facility," *Workshop on Magnetic Suspension Technology*, NASA Langley, Hampton, Virginia, Feb. 2–4, 1988.

[7] Jones, D. I., A. R. Owens, R. G. Owen and G. Roberts, "Microgravity Isolation Mount: Design Report," Technical Note BTN 009, University College of North Wales, School of Electronic Engineering Science, Bangor, Gwynedd, Sep. 1989.

[8] Hamilton, B. J., J. H. Andrus and D. R. Carter, "Pointing Mount with Active Vibration Isolation for Large Payloads," AAS 87 033, *Annual AAS Guidance and Control Conference*, Keystone, Colorado, Jan. 31–Feb. 4, 1987.

[9] Allan, A. P. and C. R. Knospe, "A Six Degree-of-Freedom Magnetic Bearing for Microgravity Vibration Isolation," *International Symposium on Magnetic Suspension Technology*, NASA Langley, Hampton, Virginia, August 1991.

[10] Carlson, A. B., D. G. Gisser and F. K. Manasse, "Magnetics and Electromechanics," Chapter 17, *Electrical Engineering: Concepts and Applications*, Addison Wesley Publishing Company, Reading, Massachusetts, 1989.

[11] Olson, H. F., *Solution of Engineering Problems by Dynamical Analogies*, Second Edition, D. Van Nostrand, Princeton, New Jersey, 1966.

[12] Banerjee, B. B., "Active Vibration Isolation of Microgravity Experiments with Umbilicals Using Magnetic Actuators," Ph. D. Dissertation, Univ. of Virginia, Charlottesville, May 1994.

[13] McCaig, M. and A. G. Clegg, *Permanent Magnets in Theory and Practice*, John Wiley & Sons, New York, 1987.

[14] Allaire, P. E., *Basics of the Finite Element Method*, Wm. C. Brown Publishers, 1985.
[15] Banerjee, B. B., Allaire, P. E., and Grodsinsky, C. M., "Active Vibration Isolation of Microgravity Experiments with Spring Umbilicals Using an Electrodynamic Actuator," 3rd. International Symposium on Magnetic Suspension Technology, NASA CP- , 1995.

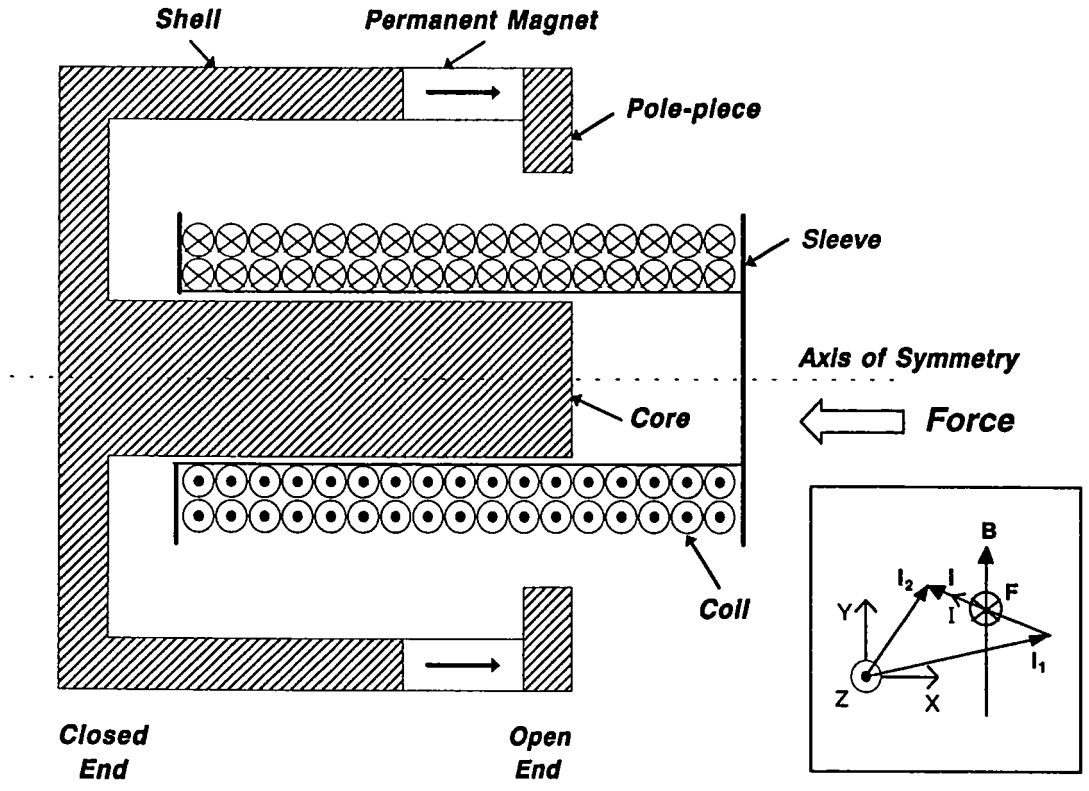

Figure 1. Cross-Section of a Lorentz Actuator (Not to Scale) and the Lorentz Force on a Conductor in a Magnetic Field (Inset)

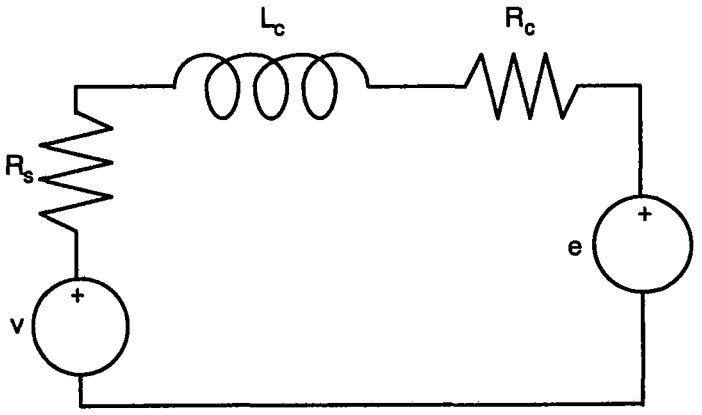

Figure 2. Electrical Circuit for Lorentz Actuator

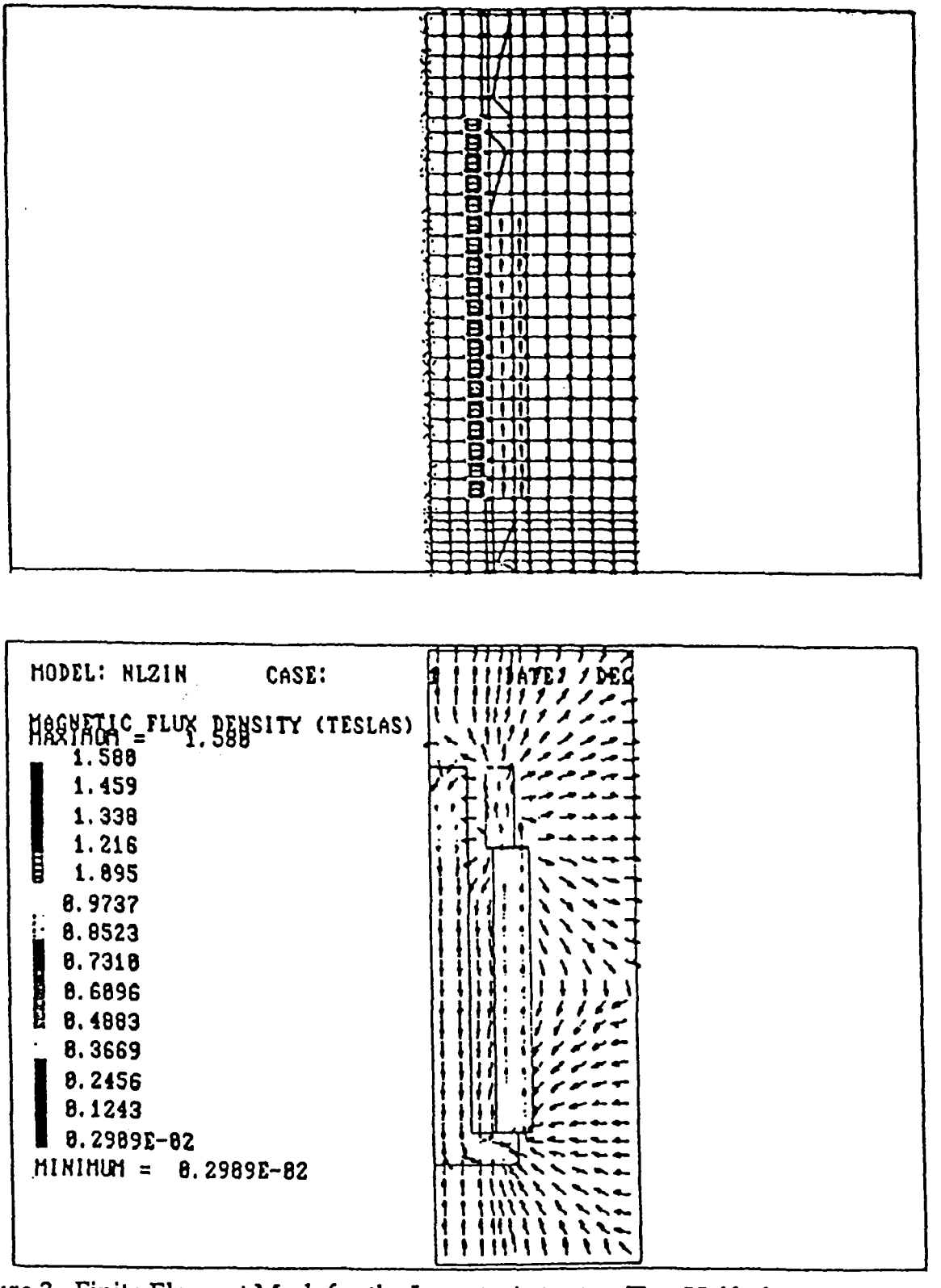

Figure 3. Finite Element Mesh for the Lorentz Actuator (Top Half of an Axisymmetric Cross-Section, with Air Elements Surrounding it) and Flux Plot for Coil at 0.3 in (0.76 cm), Current = +2.5 A

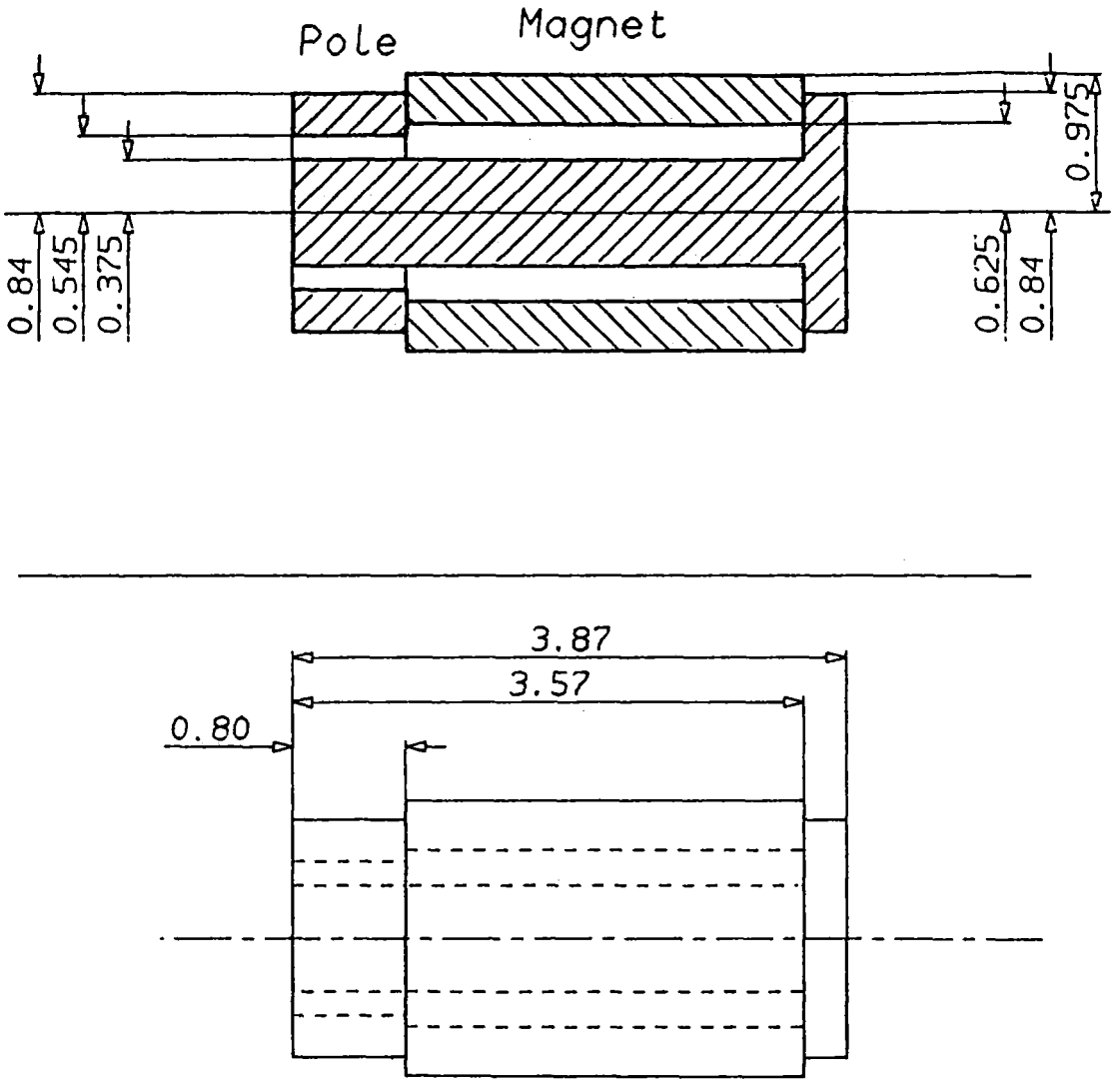

Figure 4. Lorentz Actuator: Final Design

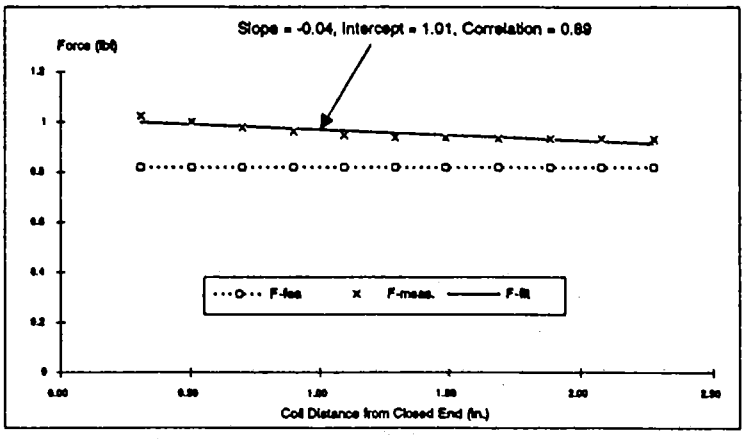

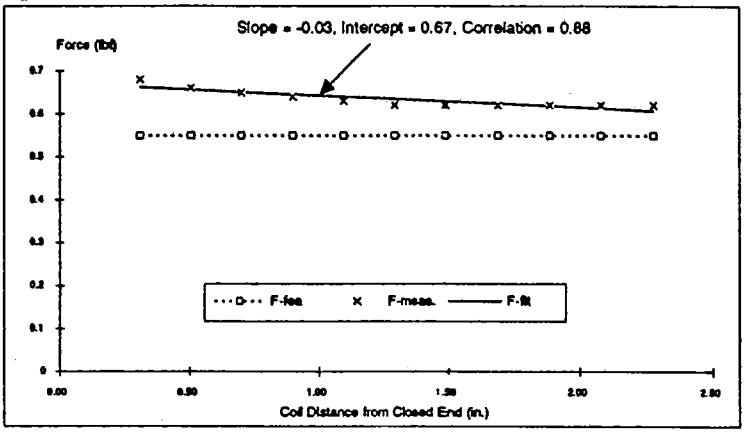

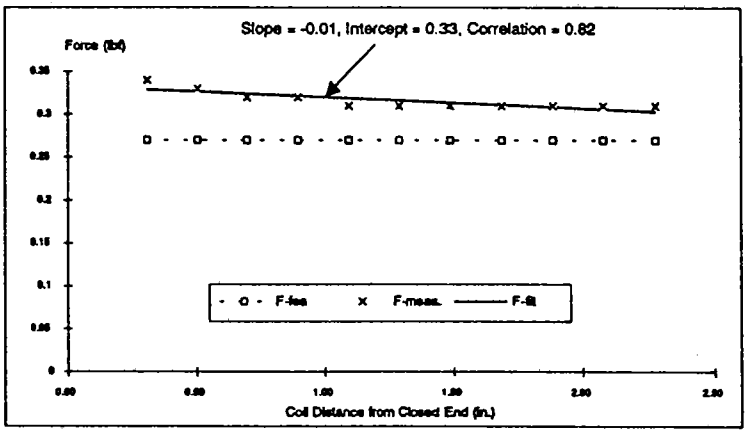

Figure 5. Position Linearity: Measured and Predicted Forces for Positive Coil Currents (I = 1.5A, 1.0A & 0.5A respectively, starting at the top)

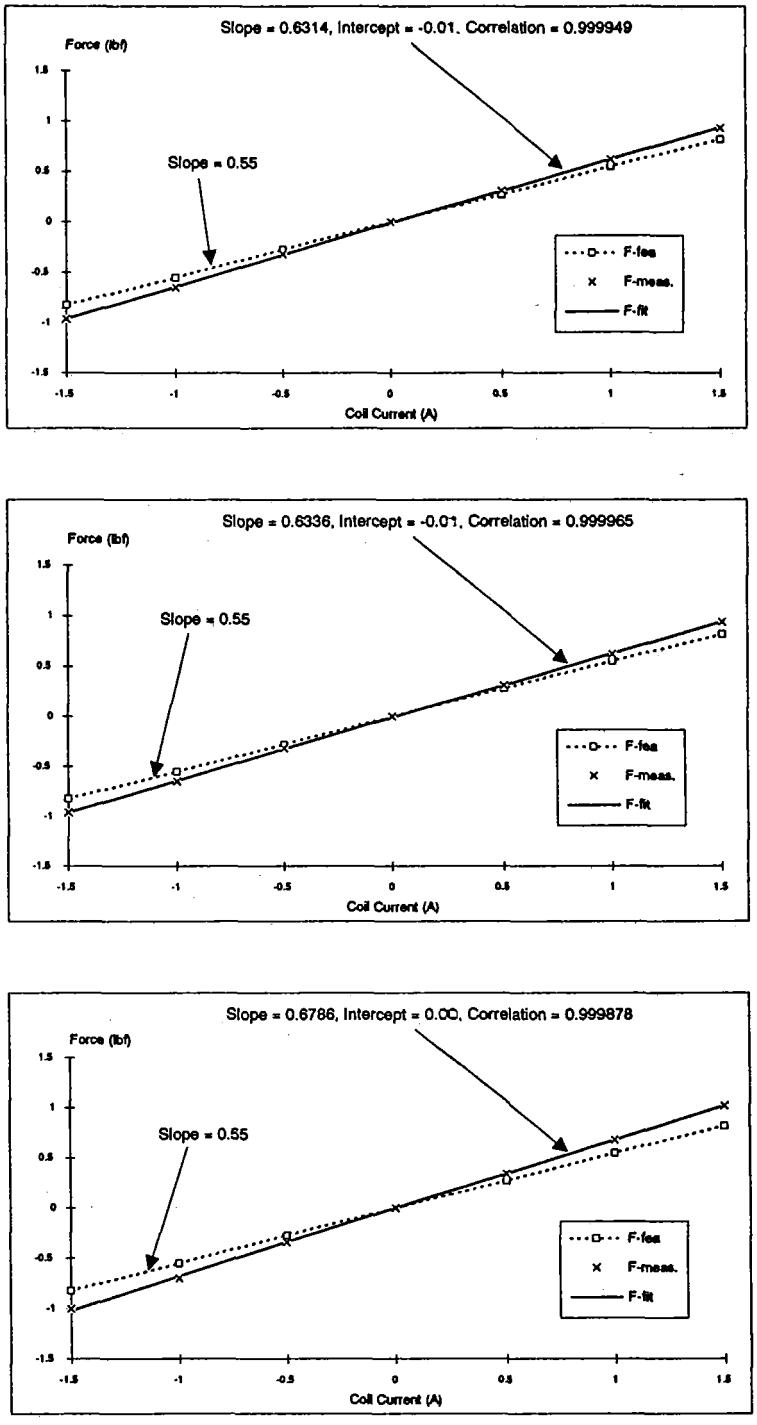

Figure 6. Current Linearity: Measured and Predicted Forces for Three Coil Positions ('out,' 'mid' and 'in' respectively, starting at the top)

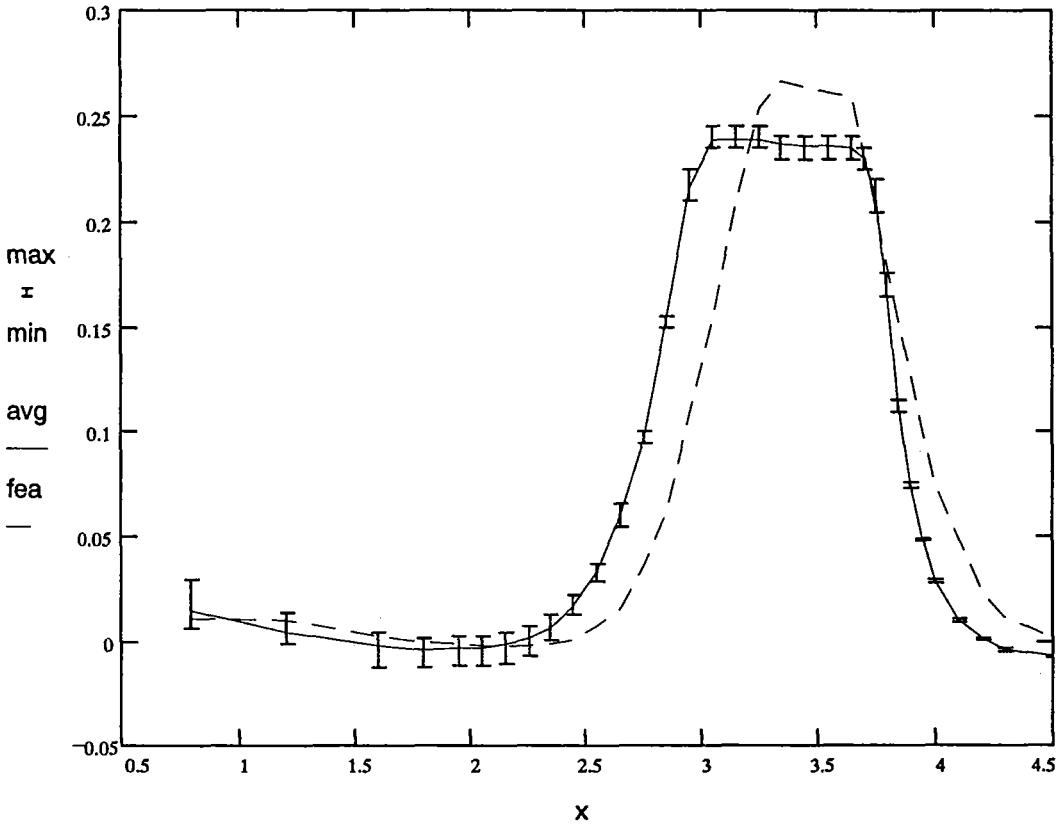

Figure 7. Radial Flux Density (Tesla) vs. Axial Distance (inches, from Closed End) in Lorentz Actuator Air Gaps (Current in Coil = 0 A)

Table 1. Lorentz Actuator: Final Design Specifications

Total length	.....	9.83 cm (3.87 in)
Magnet outer diameter	.....	4.95 cm (1.95 in)
Magnet inner diameter	.....	3.18 cm (1.25 in)
Magnet length	.....	7.04 cm (2.77 in)
Shell outer diameter	.....	4.27 cm (1.68 in)
Shell base length	.....	0.76 cm (0.30 in)
Pole-face length	.....	2.03 cm (0.80 in)
Core diameter	.....	1.90 cm (0.75 in)
Air gap	.....	0.43 cm (0.17 in)
Shell-to-core gap	.....	0.64 cm (0.25 in)
Gap ratio	.....	1.47 : 1
Axial length of coil	.....	10.16 cm (4 in)
Wire (#22, 130°C) diameter	.....	0.68 mm (26.7 mils)
Total number of turns	.....	150 x 4
Coil resistance (measured)	.....	2.7 Ω
Inductance (measured, fully in)	.....	3 mH
Maximum coil current	.....	2.5 A
Air gap flux density (average)	.....	0.2135 T
Maximum force generated	.....	5.56 N (1.25 lbf)
Theoretical power coefficient	.....	1.88 N/A (0.42 lbf/A)
Actual power coefficient	.....	2.22 N/A (0.50 lbf/A)
Actuator weight (excl. coil)	.....	1.03 kg (2.28 lb)

REPORT DOCUMENTATION PAGE

Form Approved
OMB No. 0704-0188

1. AGENCY USE ONLY *(Leave blank)*	2. REPORT DATE	3. REPORT TYPE AND DATES COVERED
	July 1996	Conference Publication

4. TITLE AND SUBTITLE

Third International Symposium on Magnetic Suspension Technology

5. FUNDING NUMBERS

WU 505-64-70-03

6. AUTHOR(S)

Nelson J. Groom and Colin P. Britcher, Editors

7. PERFORMING ORGANIZATION NAME(S) AND ADDRESS(ES)

NASA Langley Research Center
Hampton, VA 23681-0001

8. PERFORMING ORGANIZATION REPORT NUMBER

L-17591A

9. SPONSORING/MONITORING AGENCY NAME(S) AND ADDRESS(ES)

National Aeronautics and Space Administration
Washington, DC 20546-0001

10. SPONSORING/MONITORING AGENCY REPORT NUMBER

NASA CP-3336
Part 1

11. SUPPLEMENTARY NOTES

Nelson J. Groom: Langley Research Center, Hampton, VA; Colin P. Britcher: Old Dominion University, Norfolk, VA

12a. DISTRIBUTION/AVAILABILITY STATEMENT

Unclassified–Unlimited
Subject Category 18
Availability: NASA CASI (301) 621-0390

12b. DISTRIBUTION CODE

13. ABSTRACT *(Maximum 200 words)*

In order to examine the state of technology of all areas of magnetic suspension and to review recent developments in sensors, controls, superconducting magnet technology, and design/implementation practices, the Third International Symposium on Magnetic Suspension Technology was held at the Holiday Inn Capital Plaza in Tallahassee, Florida on December 13–15, 1995.

The symposium included 19 sessions in which a total of 55 papers were presented. The technical sessions covered the areas of bearings, superconductivity, vibration isolation, maglev, controls, space applications, general applications, bearing/actuator design, modeling, precision applications, electromagnetic launch and hypersonic maglev, applications of superconductivity, and sensors. A list of attendees appears on page xv of the document.

14. SUBJECT TERMS

Magnetic bearings; Magnetic suspension; Large gap magnetic suspension; Small gap magnetic suspension; Maglev; Sensors; Superconducting magnetic suspension systems; Control systems

15. NUMBER OF PAGES

407

16. PRICE CODE

A18

17. SECURITY CLASSIFICATION OF REPORT	18. SECURITY CLASSIFICATION OF THIS PAGE	19. SECURITY CLASSIFICATION OF ABSTRACT	20. LIMITATION OF ABSTRACT
Unclassified	Unclassified	Unclassified	